ASME
SETTING THE STANDARD

Transactions of the ASME, Journal of Turbomachinery (ISSN 0889-504X) is published quarterly (Jan., Apr., July, Oct.) by The American Society of Mechanical Engineers, Three Park Avenue, New York, NY 10016. Periodicals postage paid at New York, NY and additional mailing offices.
POSTMASTER: Send address changes to Transactions of the ASME, Journal of Turbomachinery, c/o THE AMERICAN SOCIETY OF MECHANICAL ENGINEERS, 22 Law Drive, Box 2300, Fairfield, NJ 07007-2300.
CHANGES OF ADDRESS must be received at Society headquarters seven weeks before they are to be effective. Please send old label and new address.

Journal of Turbomachinery

Published Quarterly by ASME

VOLUME 129 • NUMBER 1 • JANUARY 2007

TECHNICAL PAPERS

(Contents continued on inside back cover)

This journal is printed on acid-free paper, which exceeds the ANSI Z39.48-1992 specification for permanence of paper and library materials. ♾™
♻ 85% recycled content, including 10% post-consumer fibers.

Journal of Turbomachinery **Volume 129, Number 1** **JANUARY 2007**

The ASME Journal of Turbomachinery is abstracted and indexed in the following:

Aluminum Industry Abstracts, Aquatic Science and Fisheries Abstracts, Ceramics Abstracts, Chemical Abstracts, Civil Engineering Abstracts, Compendex (The electronic equivalent of Engineering Index), Corrosion Abstracts, Current Contents, Ei EncompassLit, Electronics & Communications Abstracts, Energy Information Abstracts, Engineered Materials Abstracts, Engineering Index, Environmental Science and Pollution Management, Excerpta Medica, Fluidex, Fuel and Energy Abstracts, INSPEC, Index to Scientific Reviews, Materials Science Citation Index, Mechanical & Transportation Engineering Abstracts, Mechanical Engineering Abstracts, METADEX (The electronic equivalent of Metals Abstracts and Alloys Index), Metals Abstracts, Oceanic Abstracts, Pollution Abstracts, Referativnyi Zhurnal, Shock & Vibration Digest, Steels Alert

Predicting Transition in Turbomachinery—Part I: A Review and New Model Development

T. J. Praisner
Turbine Aerodynamics,
United Technologies Pratt & Whitney,
400 Main St., M/S 169-29,
East Hartford, CT 06108

J. P. Clark
Turbine Branch,
Turbine Engine Division,
Propulsion Directorate,
Air Force Research Laboratory,
Building 18, Room 136D,
1950 5th St.,
WPAFB, OH 45433
e-mail: john.clark3@wpafb.af.mil

Here we report on an effort to include an empirically based transition modeling capability in a Reynolds Averaged Navier-Stokes solver. Well known empirical models for both attached- and separated-flow transition were tested against cascade data and found unsuitable for use in turbomachinery design. Consequently, a program was launched to develop models with sufficient accuracy for use in design. As a first step, accurate prediction of free stream turbulence development was identified as a prerequisite for accurate modeling. Additionally, a demonstrated capability to capture the effects of free stream turbulence on pre-transitional boundary layers became an impetus for the work. A computational fluid dynamics (CFD)-supplemented database of 104 experimental cascade cases was constructed to explore the development of new correlations. Dimensional analyses were performed to guide the work, and appropriate non-dimensional parameters were then extracted from CFD predictions of the laminar boundary layers existing on the airfoil surfaces prior to either transition onset or incipient separation. For attached-flow transition, onset was found to occur at a critical ratio of the boundary-layer diffusion time to a time scale associated with the energy-bearing turbulent eddies. In the case of separated-flow transition, it was found that the length of a separation bubble prior to turbulent reattachment was a simple function of the local momentum thickness at separation and the overall surface length traversed by a fluid element prior to separation. Both the attached- and separated-flow transition models were implemented into the design system as point-like trips. [DOI: 10.1115/1.2366513]

Introduction

In axial-flow turbomachinery, the design trend is toward increasing airfoil loading in an effort to reduce weight and cost of future systems. Transition prediction is critical for accurate loss predictions of high lift airfoils, and the full multi-moded (Mayle [1]) nature of the transition process must be considered. Lakshminarayana [2], Simoneau and Simon [3], Simon and Ashpis [4], Dunn [5], and Yaras [6] all provide detailed reviews of the state of the art in predictive techniques for turbomachinery, and they point to the need for improved models for transition.

Elevated levels of free stream turbulence ($Tu > 1.0\%$) have a significant effect on pre-transitional, or "quasi-laminar (QL)" boundary layers. Further, it is the authors' opinion that the quality of the laminar boundary layer at transition onset must be predicted accurately before transition modeling can be used most effectively. Therefore, it is important to capture accurately the fieldwise development of free stream turbulence quantities. To that end, the ability of the k-ω turbulence model of Wilcox [7] to predict the development of Tu was validated against the experimental data of Ames [8]. Additionally, an accurate technique for modeling the effects of Tu on laminar boundary layers within the framework of the k-ω model was developed.

In testing against cascade data it was found that open-literature models for attached and separated-flow transition were not sufficiently accurate for implementation in a design system. Consequently, an effort was launched to develop new correlations for attached- and separated-flow transition. A dimensional analysis was performed considering all transition-relevant quantities available within the framework of a Reynolds Averaged Navier-Stokes (RANS) simulation performed with a two-equation turbulence model. A database of the resulting dimensionless groups was constructed from open-literature and Pratt & Whitney in-house cascade data. The cascade data were supplemented with quantities based on the aforementioned modeling techniques for free stream turbulence development and its effects on laminar boundary layers. An investigation of the resulting database enabled the development of new models for attached- and separated-flow transition. The details of this process are documented below.

A computational-methods section will be presented first with discussions on boundary conditions, free-stream-disturbance propagation and quasi-laminar boundary layers. Then, sections concerning attached- and separated-flow transition are presented, where reviews of the state-of-the-art and current model development details are discussed. Validation and benchmarking of the new models is presented in Part II of this paper.

Computational Methods

Steady-state and time-resolved turbine flow fields were predicted using the three-dimensional (3D), Reynolds Averaged Navier-Stokes (RANS) code described both by Ni [9] and Davis et al. [10]. Numerical closure for turbulent flow is obtained via the k-ω model of Wilcox [7]. An O-H grid topology was employed for all simulations, and approximately 600,000 grid points per passage were used for three-dimensional simulations executed for this study (without tip clearance). The viscous grid provides near-surface values of y^+ less than 1 over no-slip boundaries and gives approximately 7 grid points per momentum thickness in airfoil and end wall boundary layers. These grid densities and spacings provide essentially grid-independent solutions for capturing ther-

Contributed by the International Gas Turbine Institute (IGTI) of ASME for publication in the JOURNAL OF TURBOMACHINERY. Manuscript received October 1, 2003; final manuscript received March 1, 2004. IGTI Review Chair: A. J. Strazisar. Paper presented at the International Gas Turbine and Aeroengine Congress and Exhibition Vienna, Austria, June 13–17, 2004, Paper No. 2004-GT-54108.

mal fields, surface heat transfer, and transition-related streamwise gradients in gas turbines. The code is accurate to second order in space and time and multi-grid techniques are used to obtain rapid convergence. Uniform-temperature, constant heat-flux, and adiabatic-wall thermal boundary conditions are available and were employed when appropriate. The inlet boundary conditions used for each simulation are described as necessary.

Development of Freestream Disturbances. Free stream disturbances have been shown to play an important role in transition (see, e.g., Abu Ghannam and Shaw [11] and Mayle [1]). In order to develop a RANS-based transition-prediction system, some form of free stream turbulence modeling must be implemented in the solver. Two-equation turbulence models, which provide modeling of the convection, dissipation, and diffusion of free stream disturbances, are currently the state of the art in turbomachinery design systems. However, the ability of any two-equation model to capture accurately the development of free stream turbulence quantities in prototypical turbomachinery flow fields should be demonstrated before empirical modeling based on free stream disturbances can be applied.

Two-equation turbulence models present the user with two quantities that must be specified at the inlet of a simulation. (1) The turbulence kinetic energy, k, is directly proportional to the local turbulence intensity and velocity and, when simulating experimental data, is typically set based on measured levels. (2) The dissipation parameter should be set to match the experimental decay rate of free stream turbulence when it is derivable from published data. When it is necessary to estimate inlet boundary conditions for two-equation turbulence models, there are a number of techniques that may be employed.

When simplifications for zero pressure-gradient steady flow are applied to the k-ω equations (Wilcox, [12]) one can obtain the following relations for the free stream development of k and ω:

$$k(x) = k_{in}\left(\frac{1}{\omega_{in}}\right)^{1.2}\left[\frac{3x/40}{U_\infty} + \frac{1}{\omega_{in}}\right]^{-1.2} \tag{1}$$

$$\omega(x) = \left(\frac{3x/40}{U_\infty} + \frac{1}{\omega_{in}}\right)^{-1} \tag{2}$$

where x is streamwise distance, k_{in} and ω_{in} are inlet quantities, and U_∞ is the free stream velocity. If the measured turbulence decay rate upstream of the cascade is known, Eqs. (1) and (2) can be used to solve for the inlet values of k and ω. The predicted decay rate of free stream turbulence obtained from Eqs. (1) and (2) varies with x to the -0.62 power, and this falls within the range of -0.60 to -0.68 reported by Baines and Peterson [13] and Hinze [14].

If the free stream turbulence decay rate upstream of the test section is not known then there are three other means of deriving the inlet value of the specific dissipation rate, ω_{in}. First, if the decay rate is not reported for a configuration with grid generated turbulence, and either the grid location, or the bar size of the grid is known, then the decay rate can be estimated quite accurately by using the following relation which is similar to one from Baines and Peterson [13]:

$$Tu(x) = 1.12\left(\frac{x}{d}\right)^{-0.65} \tag{3}$$

Here d is the cross-stream dimension of the bar elements that comprise the grid. If the experimentally estimated dissipation rate is available, the inlet value for ω can be estimated based on the relation from Wilcox [7]:

$$\omega = \frac{2}{3}\frac{\varepsilon}{C_\mu u'^2} \tag{4}$$

where ε is the measured dissipation rate and $C_\mu = 0.09$.

Finally, as a third, less-preferred methodology, the authors have found that the following relation from Wilcox [7] gives a reasonable estimate for ω at the inlet in cases where the length scale for an experimental configuration is reported as well as the inlet turbulence level:

$$\omega = \frac{u'}{C_\mu \lambda} \tag{5}$$

where λ is the measured integral length scale and u' is deduced from the free stream turbulence level. Use of Eq. (5) for grid-generated turbulence typically results in inlet values for ω close to those obtained with Eq. (1).

Using these techniques for deriving k and ω boundary conditions, comparisons were made between computational fluid dynamics (CFD) simulations with the k-ω model and the measured free stream development of turbulence quantities in the vane cascade from Ames [8] and Ames and Plesniak [15]. In his reports, Ames provides detailed measurements of turbulence quantities within the passage of the C3X vane. In one case free stream turbulence was generated with a passive grid, providing a turbulence intensity of 8%, nominally, at the inlet to the cascade.

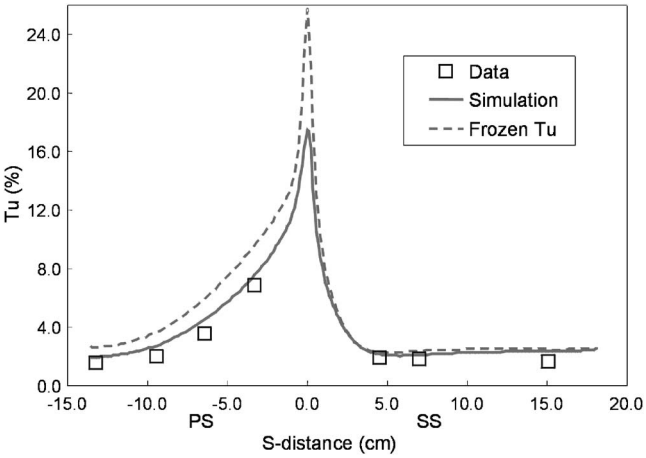

Fig. 1 Measured and predicted distributions of free stream turbulence around the C3X airfoil. Data are from Ames [8].

Figure 1 is a comparison of the measured and predicted turbulence levels around the airfoil. Also shown is the distribution of Tu obtained if "frozen" turbulence (constant u') is assumed within the passage. The frozen-turbulence method results in over predictions of local levels of Tu of up to 40% on the pressure side and in the stagnation region while giving good estimates on the suction side. Overall, better agreement is obtained with the prediction supplied by the k-ω model. Although, experimentally, the isotropy of the free stream turbulence is significantly reduced by the potential field of the airfoil, the evolution of the simulated *isotropic* turbulence is within ±0.5% of the measured levels based on the stream-wise component of turbulence on both the pressure and suction sides of the airfoil.

For accurate multi-row modeling of multi-stage turbomachinery turbulence fields, it is also important to capture accurately the development of the turbulence length scale/dissipation rate. Figure 2 is a comparison of the predicted and experimentally estimated dissipation rates around the airfoil tested by Ames [8]. While the agreement between CFD and data is not as good here as for the turbulence intensity, it is shown in Part II of the present work that this level of fidelity appears adequate for making multi-row predictions of attached- and separated-flow transition. Again, further validation of the ability of the k-ω model to predict the development of free stream disturbances in multi-stage environments will be presented in Part II of this paper.

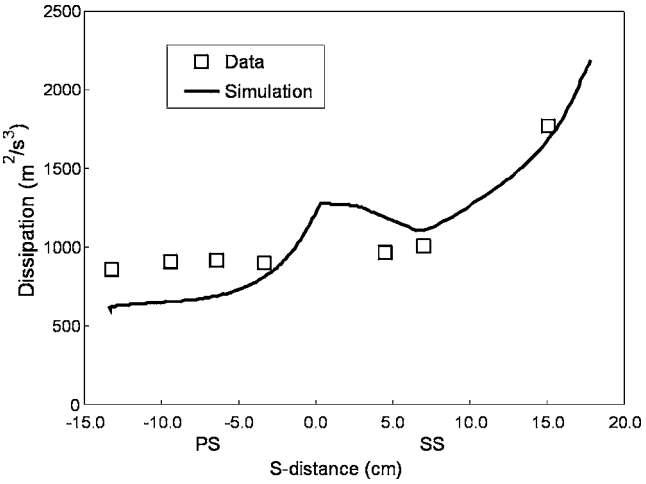

Fig. 2 Comparison of measured and predicted turbulence dissipation around the C3X airfoil. Data are from Ames [8].

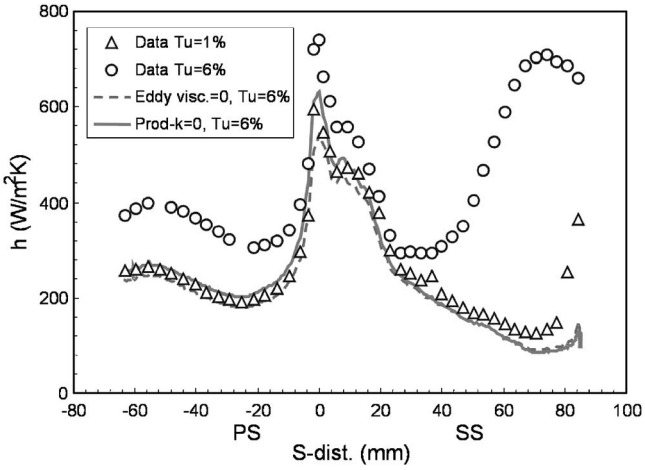

Fig. 3 Measured convective heat transfer coefficient distributions from Arts et al. [22] and CFD predictions run with fully laminar boundary layers

Modeling Pre-Transitional Boundary Layers. Moss and Oldfield [16] concluded from their experimental study of the effects of turbulence level and length scale on heat transfer in laminar boundary layers that, "accurate prediction of heat transfer enhancement due to free stream turbulence is not possible using the turbulence level alone." Considering Reynolds' analogy, it seems that accurate predictions of quasi-laminar thermal *and* momentum boundary layers cannot be obtained without attention to turbulence length scale (i.e., specific dissipation) as well as intensity.

The importance of capturing turbulence intensity and length-scale effects on laminar boundary layers was emphasized by Boyle et al. [17], where the authors developed a model that considers both turbulence level and length scale to increase turbulent viscosity above zero in laminar regions to account for what they refer to as "turbulence enhancement." Boyle and co-workers reported a "noticeable" improvement in spatially averaged laminar-region heat transfer predictions using their model, but no model tested produced accurate *local* heat load levels. Similarly, Roach and Brierley [18] point to the importance of modeling the effects of turbulence level and length scale on pre-transitional boundary layers. However, the authors assumed that the integral quantities of quasi-laminar boundary layers are the same as the equivalent purely laminar ($Tu=0$) boundary layer. Sharma et al. [19] reviewed experimental evidence that turbulence from upstream rows imparts a significant influence on the pre-transitional boundary layers on turbine airfoils. Additionally, the importance of capturing the effects of free stream turbulence on laminar boundary layers has been identified in experimental studies of convective heat transfer rates by Ames [20] and Van Fossen et al. [21].

The phenomenon of a quasi-laminar boundary layer is demonstrated in the cascade heat transfer data of Arts et al. [22]. Figure 3 is a plot of measured heat transfer distributions from Arts et al. [22] with nominal inlet free stream turbulence levels of 1% and 6%. Additional flow conditions for both data sets in Fig. 3 were $\mathrm{Re}_c=1\times10^6$ and $M_{\mathrm{exit}}=0.77$, where Re_c is Reynolds number based on true chord. Heat transfer augmentations in the leading-edge and pressure-side regions of the airfoil of up to approximately 50% are evident. Given that the only difference between the two conditions is the turbulence level, the enhanced energy transfer across the quasi-laminar boundary layer in the high Tu case is primarily due to the penetration of free stream turbulence into the laminar boundary layer.

The data from Arts et al. [22] were employed to assess various methods for modeling quasi-laminar boundary layers. Uniform surface-temperature conditions were held for each of the simulations, and this was consistent with the measurements. CFD simulations (Fig. 3) were run fully laminar on both the suction and pressure sides of the airfoil employing common modifications from literature to simulate laminar regions. One such technique tested, which is commonly employed in transitional RANS simulations, involves setting the eddy viscosity, μ_T, from the turbulence model to zero within laminar regions. Also tested was the technique reported by Schmidt and Patankar [23] in which the production term in the k equation is set to zero in laminar regions.

The heat transfer distribution predicted by setting the eddy viscosity equal to zero with $Tu=6\%$ is shown in Fig. 3. The results for this simulation duplicate the convective heat-load distribution from a purely laminar simulation (not shown). Results from setting the production of k equal to zero with $Tu=6\%$, shown in Fig. 3, indicate only a slight increase in the predicted heat-load levels around the airfoil compared to the prediction with $\mu_T=0$. From these simulations it is concluded that neither method for modeling *laminar* flow with elevated free stream turbulence accurately predicts the wall gradients of the quasi-laminar boundary layer. Subsequently, a model was developed based on studies performed with the data of Arts et al. [22]. Results based on the new model for quasi-laminar boundary layers are shown in Fig. 4 and labeled as "QL model." As seen in this figure, the results from the QL model are more accurate in quasi-laminar regions than the results shown in Fig. 3. The current method is based on physical reasoning which links the production terms in the k and ω equations to

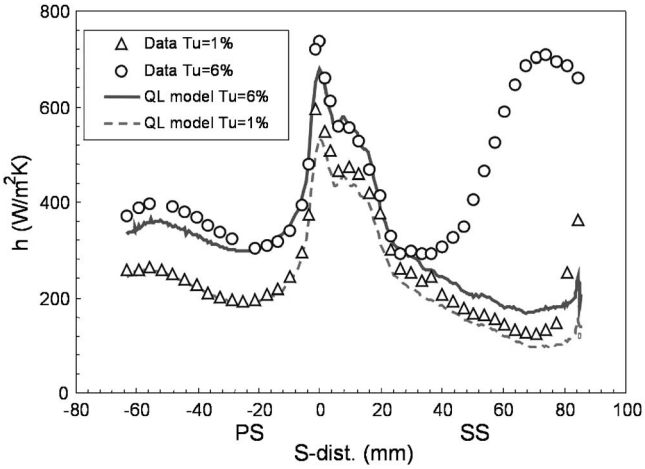

Fig. 4 Results from CFD simulations run with the QL model for capturing pre-transitional quasi-laminar boundary layers

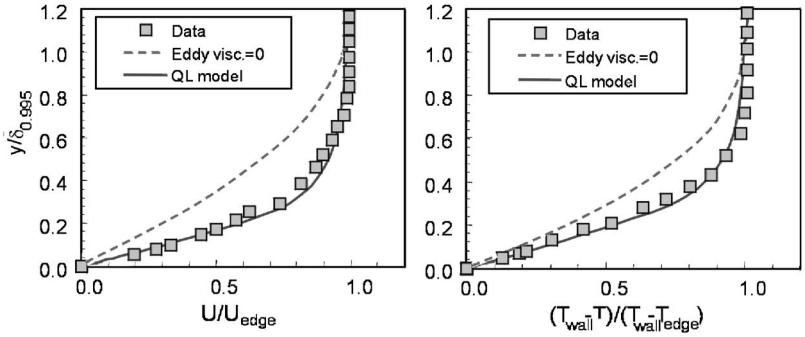

Fig. 5 Non-dimensional momentum and thermal boundary layer profiles in a quasi-laminar boundary layer just prior to transition. Data are from Blair [25].

the concept of self-sustaining turbulence in turbulent boundary layers. The analogy is drawn that in laminar regions of the boundary layer, where disturbances are damped by the action of viscosity, the production of both k and ω should be negligible. Implicit in this analogy is that the eddy viscosity in a quasi-laminar boundary layer is independent of the mean strain. Minimizing the production terms in the k and ω equations, in contrast to setting $\mu_T=0$, allows for the convection and diffusion of free stream turbulence into quasi-laminar (QL) boundary layers. For the length scales (i.e., dissipation rates) and turbulence intensities present in the data of Arts et al. [22], the QL model was found to capture convective heat loads to within ±10% in quasi-laminar regions for all conditions reported.

Additional testing of the QL model was performed with the cascade data of Ames [8] with similar accuracy for convective heat loads for levels of Tu up to 12% from a simulated combustor (Praisner et al. [24]). Additionally, predictions of stagnation-point heat transfer levels from the QL model are within ±10% of the correlation of Van Fossen et al. [21] for a range of turbomachinery-specific turbulence and dissipation levels.

To verify that the quasi-laminar boundary layer *shape* is also modeled accurately by the QL model, a study was performed with the favorable pressure-gradient, flat-plate data of Blair [25]. Figure 5 is a plot of non-dimensionalized velocity and temperature profiles in the quasi-laminar flow region immediately upstream of transition onset with $K=0.2\times10^{-6}$ and $Tu=3\%$, where K is the acceleration parameter. Also shown are results from CFD predictions performed with the laminar regions simulated by setting $\mu_T=0$ (purely laminar) and the QL model. Both the momentum and thermal boundary layer shapes are well matched with the QL model as compared to the method of setting $\mu_T=0$. Also, the predicted convective heat transfer levels within the quasi-laminar region were as accurately captured as those in the benchmarking against the data of Arts et al. [22].

For the momentum boundary layer shown in Fig. 5 the predicted values of momentum-thickness Reynolds number, Re_θ, are 23% and 6% below the measured value for the $\mu_T=0$ technique and QL model, respectively. In turn, the shape factors predicted with the $\mu_T=0$ technique and QL models are 21% and 3% above the measured level of 2.57, respectively. Also, the approximate location of transition onset for the case with $Tu=6\%$ in Fig. 4 is at $s=28$ mm on the suction side. The QL-model predicted values of Re_θ for this streamwise location differ by 15% between the two turbulence levels considered. These results, taken together with the flat-plate results for Re_θ, indicate that a transition prediction system that does not accurately capture the turbulence-enhanced transfer characteristics of quasi-laminar boundary layers may provide inaccurate quantities for transition onset prediction.

Additionally, if one assumes the Re_θ value for the $\mu_T=0$ technique is essentially an exact numerical solution for a condition with $Tu=0\%$, these results are in contrast with the assumption made by Roach and Brierley [18] that integral quantities of pre-transitional boundary layers are unaffected by free stream turbulence. The aforementioned authors supported their assumption by referencing turbulent boundary layer data with elevated Tu levels. Since turbulence levels within turbulent boundary layers are of the order 10–15% with low free stream Tu, it is not surprising that they are not appreciably affected by elevated levels of free stream turbulence. In contrast, because laminar boundary layers contain low levels of turbulence, they are more susceptible to significant momentum- and heat-transfer enhancement with the addition of turbulence convected and diffused from the free stream. The results presented here are supported by the results of Yaras [6] who reported increases in measured Re_θ values as high as 30% in pre-transitional boundary layers subjected to elevated levels of Tu measured.

Results obtained with the QL model for various values of turbulent Prandtl number, Pr_T, show little variation in boundary layer qualities. Variation of Pr_T from a molecular level of 0.7 to a turbulent level of 0.9 resulted in variations in predicted heat flux and skin-friction levels of less than 5% in quasi-laminar regions. This may be related to the fact that turbulent mixing in quasi-laminar boundary layers is significantly lower than in turbulent boundary layers. While not comprehensively validated, it appears that there may be no need to employ different turbulent Prandtl numbers for laminar and turbulent regions of the flow field in simulations that employ the QL model.

Finally, it was found that the effects of roughness on pre-transitional boundary layers were not accurately captured with the combination of the QL model and the modified wall boundary condition for ω from Wilcox [7] for rough walls. This is not surprising considering that the formulation of Wilcox's modification was specific to turbulent boundary layers. However, the assumption of admissible roughness is typically valid for all but the high-pressure turbine in large commercial and military engines. Resolution of pre-transitional boundary layers subjected to significant levels of roughness is a topic that requires more attention.

Modeling Attached-Flow Transition

The ability to capture the development of turbulence level and dissipation rate outside boundary layers as well as viscous layer details demonstrated above gives one confidence that transition modeling in such flows is possible. Accordingly, a database of experimental test cases was constructed to evaluate methods for transition onset prediction in turbomachines. The construction involved performing laminar simulations of experimental cascade configurations with appropriate free stream and wall boundary conditions. Inlet levels of turbulence and dissipation rate were set employing the aforementioned techniques for matching the decay rate of Tu. The k-ω-based QL model for capturing the pre-transitional boundary layers was employed as well. For each experimental case considered, the measured and predicted airfoil static-pressure distributions were in close agreement. Transition

onset was considered to occur in the data sets where wall-gradient quantities first began to deviate from fully laminar simulations. Only cascade geometries of turbomachinery-specific airfoils were considered, and both open-literature and in-house data were used to build the database of 57 cases. The 57 cases themselves consisted of seven different geometries tested in experiments with various boundary conditions.

Review of Models for the Onset of Transition. The most successful physical model for the transition process is that due to Emmons [26], Schubauer and Klebanoff [27], and Narasimha [28]. In this model, transition is considered to be the result of the random formation of "spots" of turbulence in the boundary layer over some finite region in the streamwise direction. These turbulent spots grow as they convect downstream, and the intermittency (i.e., the fraction of time the flow is turbulent) increases in the streamwise direction until the entire surface is covered with them. At that point, the boundary layer is considered fully turbulent.

The foregoing would suggest that an assessment of the effects of various flow field parameters on transition must be an evaluation of the way in which they affect the formation and subsequent growth of turbulent spots and/or wake-induced turbulent strips. Several authors have conducted experimental studies in that regard (e.g., Clark et al. [29], Gostelow et al. [30], and Halstead et al. [31]), and others (e.g., Chen and Thyson [32], Dey and Narasimha [33], and Solomon et al. [34]) have incorporated information on turbulent-spot formation and kinematics into integral methods for calculating intermittency and, by extension through a "linear combination model" after Dhawan and Narasimha [35], skin friction. Still others (e.g., Suzen and Huang [36] and Steelant and Dick [37]) have made use of the "universal" intermittency distribution to derive transport equations for intermittency that are solved alongside the RANS equations or used some combination of the correlations of Abu-Ghannam and Shaw [11], Drela [38], and Solomon et al. [34] to evaluate intermittency (e.g., Gier et al. [39], Thermann et al. [40], Roux et al. [41], and Roberts and Yaras [42]) through transition. Subsequently, some of the same authors modified the calculated eddy viscosity according to the fraction of time the flow is predicted to be turbulent through the transition zone. As previously stated, pre-transitional boundary layers with elevated *Tu* levels may not be adequately modeled by setting μ_T equal to zero upstream of transition onset.

The review article of Mayle [1] spurred renewed interest in the ideas of Emmons [26] and Narasimha [28] for the prediction of transition in turbomachines, and much of the recent work described above followed recommendations from that paper closely. In particular, the concept of the universal intermittency distribution as described in detail by Narasimha [43] has been used to build correlations for transition onset (Mayle [1]), as well as turbulent-spot generation rates and transition length (Fraser et al. [44] and Gostelow et al. [30]).

At the root of many correlations used to predict transition onset is the $F(\gamma)$ technique of Narasimha [43], whereby measured streamwise variations of intermittency, γ, are plotted in the form

$$F(\gamma) = [-\ln(1-\gamma)]^{1/2} \tag{6}$$

Narasimha [28] first proposed that all turbulent spots are formed randomly in time and spanwise location at a single streamwise station in the flow. Under that hypothesis, which is now known generally as "concentrated breakdown," Eq. (6) becomes

$$F(\gamma) = \left(\frac{n\sigma}{U_\infty}\right)^{1/2}(x - x_t) \tag{7}$$

for constant-velocity flow along a flat plate. In Eq. (7), x_t is the streamwise location where all spots are formed, n is the number of spots formed at that position per unit time and per unit spanwise distance, U_∞ is the free stream velocity, σ is Emmons [26] nondimensional spot-propagation parameter, and x is a location on the flat-plate surface further downstream than x_t.

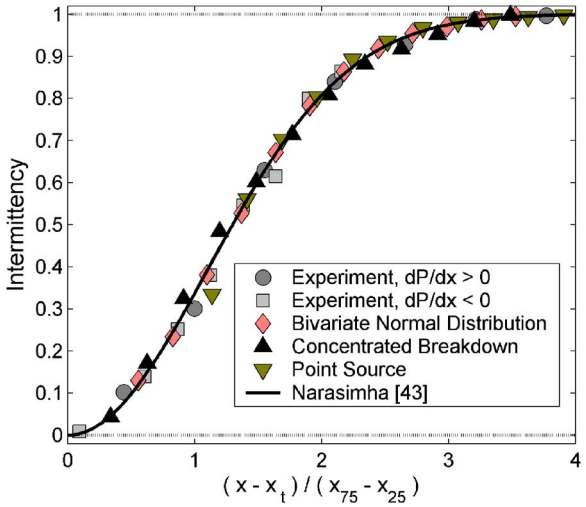

Fig. 6 A comparison between the "universal" curve of Narasimha [43] and both experimental data and simulations from Clark [49]

Dhawan and Narasimha [35] also showed that variations of intermittency through the transition zone possess a high degree of similarity if the streamwise distance is suitably nondimensionalized. They demonstrated that the transitional intermittency variations from a number of experiments collapsed on a single curve when the streamwise distance was represented by

$$\xi = \frac{x - x_t}{x_{75} - x_{25}} \tag{8}$$

where x_{75} and x_{25} are the streamwise positions where the intermittency is 0.75 and 0.25, respectively. The same authors also showed that the available intermittency data were well represented by the equation

$$\gamma = 1 - e^{-0.412\xi^2} \tag{9}$$

Equation (9) has become known as the universal intermittency distribution (Narasimha [45,46]). Like Eq. (7), Eq. (9) is a consequence of the assumption of concentrated breakdown as applied to the transition model of Emmons [26] in constant velocity, flat-plate flow.

Many authors have shown that it is possible to linearize intermittency distributions using Eqs. (6) and (7) and, consequently, to plot the data in the universal form of Eq. (9) (e.g., Owen [47]). This is true even under conditions of changing pressure gradient and/or free stream velocity (Sharma et al. [48], Gostelow et al. [30], and Fraser et al. [44]). As an illustration of this phenomenon, representative data from Clark [49] are plotted in Fig. 6. Experimental intermittency distributions for flat-plate flows under both favorable and adverse pressure gradient conditions are plotted, and both agree with the universal curve very well. This is surprising in the case with the favorable pressure gradient since the local velocity varies by a factor of more than 6.7 over the streamwise distance represented in the figure. Note that both the spot shape parameter and the free stream velocity itself are considered constant and brought outside an integrand in the derivation of Eq. (7), and neither of these assumptions is valid in the experiment of Clark [49]. Intermittency variations predicted with a time-marching simulation of the transition zone like that described by Narasimha [50] are also plotted in Fig. 6. These predicted intermittency distributions are taken along the centerline of a flat-plate flow at Mach 0.5. Spot propagation parameters were as measured by Clark et al. [29], and three different distribution functions for spot generation were considered. The universal curve fits the pre-

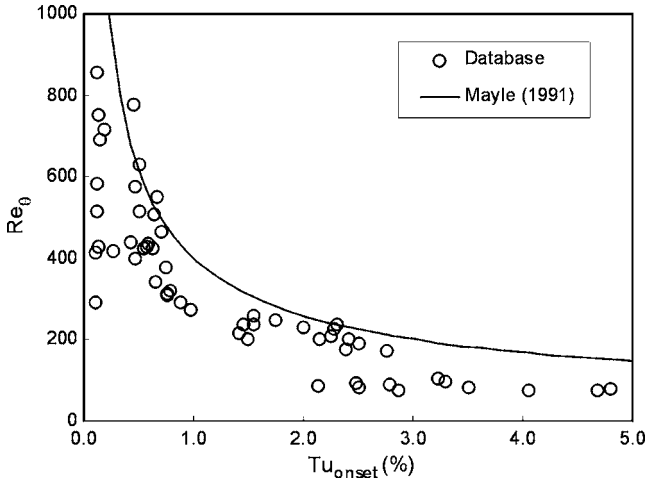

Fig. 7 A comparison between the current database for attached-flow transition onset and the correlation of Mayle [1]

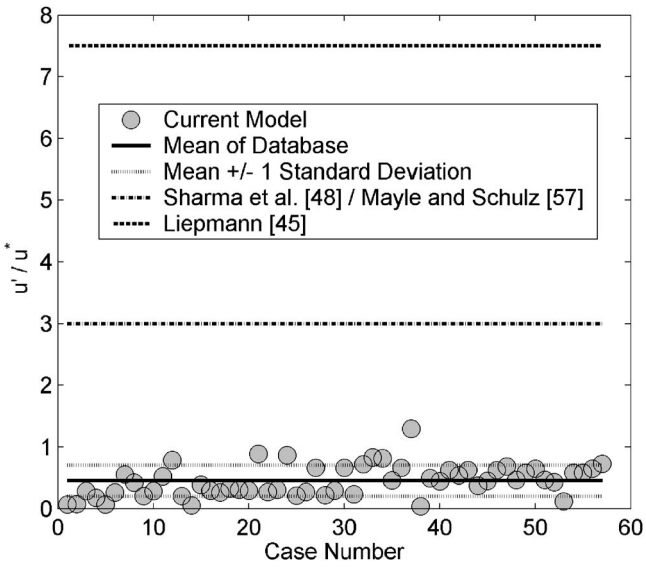

Fig. 8 A comparison between the transition onset criteria of Liepmann [54], Sharma et al. [48], and Mayle and Schulz [57] and the current attached-flow database

dicted intermittency distributions very well, not just when concentrated breakdown prevails, but also for both a bivariate normal (in streamwise and spanwise directions) spot generation function and a point source located off the plate centerline.

Observations like those presented here with respect to the universal curve are not new (see, e.g., Dhawan and Narasimha [35]). In more recent times Mayle [1] used the $F(\gamma)$ technique to develop a correlation for transition onset, where onset was taken to be the x intercept of the $F(\gamma)$ plot. Also, correlations for length as well as turbulent-spot generation rates under a variety of flow conditions (Mayle [1], Gostelow et al. [30], and Fraser et al. [44]) have been derived. From the discussion above, it does not follow that if it is possible to linearize experimental data by plotting $F(\gamma)$, then the transition is consistent with a flat-plate flow undergoing transition via a concentrated breakdown of the laminar boundary layer. When the current database for attached-flow transition onset is compared to one such correlation from Mayle [1], as in Fig. 7, there is considerable scatter. Testing against the database revealed a success rate of approximately 50% in predicting onset within 10% of the measured location in terms of surface distance. Also, transition onset typically occurs at lower Reynolds numbers than predicted by the Mayle [1] relation. Similar results to those in Fig. 7 are reported by Simon and Ashpis [4] for comparisons made between data and the Mayle [1] correlation. In light of these findings, it might be better to develop correlations for transition onset and turbulent-spot production rates, for example, from direct measurements like those first reported by Hofeldt [51]. Such direct measurements are difficult, however, and little data are available at present to create such correlations.

Both Tani [52] and Reshotko [53] review a number of models that are not based on the concept of universal intermittency, and they both point out that one of the first was due to Liepmann [54]. Many authors refer to Liepmann [55] as the source of this idea, but the 1945 publication is the correct one. Liepmann supposed that transition onset occurs when the local Reynolds stress in the perturbed laminar boundary layer equals the local friction velocity. Liepmann's idea has been recast and used by others. For example, Van Driest and Blumer [56] correlated the local vorticity Reynolds number, which like the friction velocity depends on the normal gradient of streamwise velocity in two dimensional (2D) flow, at transition onset with free stream turbulence and pressure gradient. Recently, Mayle and Schulz [57] referred to the formulation of Liepmann's criterion due to Sharma et al. [48] as appropriate for transition onset. Sharma et al. [48] argued that the local Reynolds stress itself depends on the local root mean square of streamwise velocity perturbations and stated that transition onset occurs when

$$\frac{u'}{u^*} = 3.0 \tag{10}$$

based on experimental data related to a turbine airfoil suction-side flow field. In Eq. (10), u^* is the local friction velocity and u' is the fluctuating component of the local streamwise velocity. Liepmann [54] argued the same case based on his own experimental data. Following Liepmann's analysis and recasting his correlation in the form of Eq. (10) results in a constant on the right-hand side equal to 7.5 rather than 3. In addition, Roach and Brierley [18] report that the constant in Eq. (10) varies from 3.0 to 7.4 for the ERCOFTAC T3 test cases.

If one assumes that u' within the quasi-laminar boundary layer is modeled to a reasonable level of accuracy with the QL model, it might be possible to predict transition onset based on a relation like that in Eq. (10). In Fig. 8 the quantity u'/u^*, evaluated at transition onset, is plotted for all cases in the current database. For comparison both the constants of Sharma et al. [48] and Liepmann [54] are also plotted. Transition onset seems to occur at much lower levels of u'/u^* than those indicated by Sharma et al. [48] and Liepmann [54] over the entire database.

The poor correlation of the database in Fig. 8 may likely be a result of the assumption of isotropic turbulence within the quasi-laminar boundary layer inherent in the QL model. Also, one notes that the studies of Sharma et al. [48] and Liepmann [54] predate the use of conditional sampling techniques for boundary-layer measurements (see, e.g., Suder et al. [58] and Kim et al. [59]). So, it could be that the local rms of velocity fluctuations in the boundary layer was largely influenced by the passage of turbulent spots over the fixed hot wires in the experiments of both Liepmann [54] and Sharma et al. [48]. As such, the criteria represented by Eq. (10) might be more indicative of turbulent-spot detection than of the state of a quasi-laminar boundary layer at transition onset. The foregoing argument is supported by the results of a simple calculation. Consider a boundary layer profile undergoing transition to be a linear combination of laminar and fully turbulent profiles weighted on the intermittency, as suggested first by Dhawan and Narasimha [35], and let onset occur in a Blasius boundary layer on a flat plate at a local streamwise Reynolds number of 250,000.

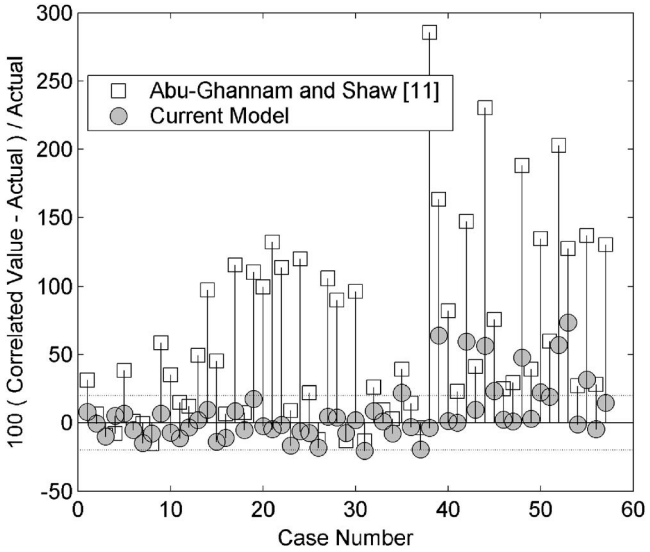

Fig. 9 A comparison of the efficacy of the current transition-onset model for attached flow with that of Abu-Ghannam and Shaw [11]

If one represents the turbulent profiles by a 1/7th power law and presumes there is no change in boundary layer thickness at transition onset (strictly speaking, there can be no change in the local momentum thickness), then at $y^+=25$, the local rms becomes about three times the local friction velocity if the intermittency is 10%. This is in keeping with the results of Sharma et al. [48]. In any regard, the results shown in Fig. 8 suggest that with the current modeling of pre-transitional boundary layers, accurate RANS-based transition predictions cannot be obtained with a model of the type in Eq. (10).

A correlation for transition onset that was developed independently of the concept of intermittency is due to Abu-Ghannam and Shaw [11]. Their work was recast by Drela [38] using the boundary layer shape factor as a correlating parameter and collectively these relations were used by a number of others (e.g., Fraser et al. [44], Gier et al. [39], and Roux et al. [41]). Abu-Ghannam and Shaw [11] measured the time-mean near-wall streamwise velocity with a hot wire, and they determined the start of transition to occur where that parameter began to deviate from the reference laminar level. As such, their method is consistent with demarcating transition start by an increase in the local skin friction over the laminar level, and that is in essence the technique used to determine onset for the current database. The percent difference between the momentum-thickness Reynolds number predicted with the correlations of Abu-Ghannam and Shaw [11] and the actual values found in the current database is plotted in Fig. 9. It was found that the correlation of Abu-Ghannam and Shaw [11] produces errors in the momentum-thickness Reynolds number in excess of 20% in 39 of the 57 cases in the database. Testing against the database revealed a success rate of approximately 68% in predicting onset within 10% of the measured location in terms of surface distance. Testing of the correlation utilizing inlet turbulence levels instead of local (at transition onset) levels, which is consistent with the original formulation of the model, did not improve the correlation of the database.

Early in the course of this work, three separate transition-length correlations were evaluated in conjunction with the onset model of Abu-Ghannam and Shaw [11] to predict the development of intermittency through transition for flow fields in the current database. These were the models of Gostelow et al. [30], Fraser et al. [44], and Solomon et al. [34]. However, the modeling of transition length was eventually discarded, and abrupt trips at onset were used exclusively in this effort. This decision was made for a number of reasons. First, the present authors found it was inadvisable to stack any correlation for length upon another correlation for transition onset since each relation must have its own attendant uncertainty. Moreover, it was noted that all three aforementioned length models depended on correlations for turbulent-spot production rates that were derived from experimental data using the $F(\gamma)$ technique. On account of the discussion presented above relative to the $F(\gamma)$ technique, none of these models were adopted. Finally, the implementation of a transition-length model requires that a streamline-based application of the modeling be implemented. That is, it becomes necessary to track particles from transition onset through 3D flow fields along airfoil surfaces. So, without the use of an intermittency-transport equation (Suzen and Huang [36]), such a model becomes difficult to implement. Since an abrupt trip, applied in a simulation, implies the sudden increase in turbulence production in the context of this work, and because there is some finite distance over which the boundary layer and turbulence model respond to that, a finite transition length is obtained in practice (Praisner et al. [24]).

New Model for Attached-Flow Transition. Morkovin [60] coined the term bypass transition, and he has often alerted designers to the implications of such phenomena. In his NATO AGARDograph he stated that designers must become "rather sensitive to bypasses when transition risks imply risks to the basic mission of the design." Morkovin also pointed out that "it is easy to criticize; it is another matter to offer a constructive suggestion to the designer." With these ideas in mind and with the current capability to predict local flow features at the onset of transition for experiments pertinent to turbomachinery design, the database was analyzed to build a new model for attached-flow transition onset.

It was postulated that the boundary-layer momentum thickness at the onset of transition (θ) depends upon a number of *local* flow variables at the edge of the boundary layer and the local wall temperature (T_w). These flow variables were taken to include the density (ρ), the dynamic viscosity (μ), the sonic speed (a), the driving temperature for heat transfer (T_g), the thermal conductivity of the fluid (k), the specific heat at constant pressure (c_p), the magnitude of the flow velocity (U_∞), the streamwise velocity gradient (dU_∞/ds, the root mean square of streamwise velocity fluctuations (u'), and their length scale (λ).

Applying the Buckingham-Pi Theorem via the "step-by-step" technique of Massey [61], it is possible to represent the physical process as a function of seven non-dimensional parameters. The relation is

$$\mathrm{Re}_\theta = f(M, T_g/T_w, K, Tu, Pr, \lambda/\theta) \tag{11}$$

The non-dimensional parameters in Eq. (11) are the momentum-thickness Reynolds number at transition onset (Re_θ), the Mach number (M), the gas-to-wall temperature ratio (T_g/T_w), the acceleration parameter (K), the local turbulence intensity (Tu), the molecular Prandtl number (Pr), and the ratio of turbulent length scale to momentum thickness (λ/θ). Note that the physical dimensions used to define the indicial matrix are mass (m), length (L), time (t), temperature (T), and heat (H). Because heat is invoked as a dimension, it is assumed that there is no substantial conversion of mechanical energy into thermal energy. So, the results are restricted to flows of gases with moderately supersonic Mach numbers, but this is not a limitation for the gas-turbine situation.

The non-dimensional parameters in Eq. (11) were tabulated at transition onset for each case in the database, and the results were correlated to determine the combination of non-dimensional parameters that provided the best collapse of the data. The best correlation for transition onset was found when

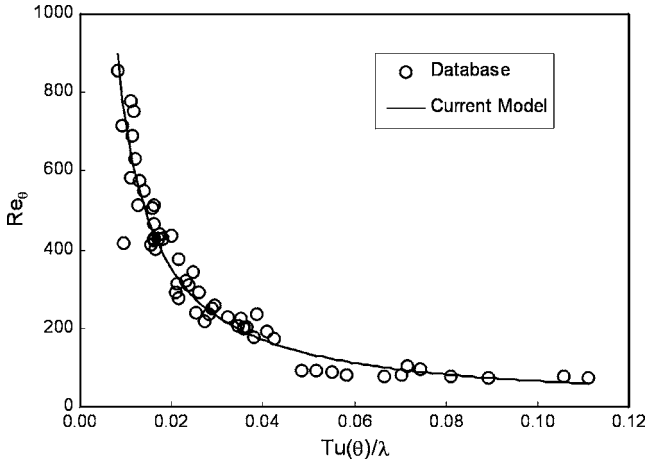

Fig. 10 The current model for the onset of attached-flow transition compared to the database

$$\mathrm{Re}_\theta = A\left(Tu\frac{\theta}{\lambda}\right)^B \tag{12}$$

where A and B are constants equal to 8.52 and −0.956, respectively. The entire database is plotted in Fig. 10. Equation (12) implies that the local momentum thickness at transition onset is a function of only *one* non-dimensional parameter that is a product of two of the basic non-dimensional parameters derived directly from the step-by-step method of Massey [61].

An ability to determine the edge of the boundary layer in a robust manner is an important aspect of transition modeling techniques based on integral and edge quantities. The edge of the boundary layer was taken to be the distance from the wall at which the local vorticity dropped to 1% of the maximum value in the O grid at that streamwise grid location. This method, reported by Michelassi et al. [62], provides a robust and accurate edge detection technique for laminar boundary layers. Variations in the percentage of the maximum vorticity used to define the boundary layer edge between 0.8% and 1.8% resulted in variations in the coefficient of correlation of the least-squares fit for Eq. (12) on the range from 0.95 to 0.96.

As seen in Table 1, all the non-dimensional parameters, save the molecular Prandtl number, varied markedly at transition onset over this database. For example, transition onset occurred under both favorable and adverse pressure gradients. The strength of the pressure gradients covers the range from above relaminarization ($K > 3\times10^{-6}$) on the favorable side through Thwaite's separation criterion ($K\,\mathrm{Re}_\theta^2 < -0.09$, see White [63]) under decelerating conditions. Both adiabatic flows and those with velocity profiles that were affected by the temperature dependence of viscosity were part of the database. Also, the range of Mach numbers covered incompressible through transonic flows. The *local* turbulence intensity varied by two orders of magnitude, and while the maximum value may at first consideration seem low, one must remember that the *inlet* turbulence intensity was much higher. Further, the ratio of local turbulence length scale to momentum thickness at onset varied by an order of magnitude. Again, the molecular Prandtl number was essentially constant for all points in the database.

Table 1 Variation of non-dimensional parameters at transition onset

Variable	Range
Re_θ	73–856
$K\times10^6$	−1.9 to 4.8
$K\mathrm{Re}_\theta^2$	−0.15 to 0.06
M	0.05–1.24
T_g/T_w	1.0–1.41
Tu_{onset} (%)	0.11–5.09
λ/θ	4.26–66.2
Pr	0.71–0.71

Physical Significance of the Current Attached-Flow Model. Equation (12) was incorporated into the airfoil design system directly with the factor and power in the equation set equal to 8.52 and −0.956, respectively. However, it is possible to recast the relation in such a way that gives insight into its possible physical significance. One notes that the constant B in the relation is very close to −1. If that value is accepted, then, after some algebraic manipulation, Eq. (12) becomes:

$$100\left(\frac{u'}{\lambda}\right)\left(\frac{\rho'\theta^2}{\mu}\right) = A_1 \tag{13}$$

where A_1 is another constant that may be evaluated directly as the mean of values occurring at transition onset in the database. Here, A_1 was found to be 7.0 ± 1.1. Note that Eq. (13) implies that transition onset occurs when the ratio of a boundary-layer diffusion time ($\rho\theta^2/\mu$) to a time scale associated with the large-eddy turbulent fluctuations ($t_e=\lambda/u'$) becomes a critical value.

It is instructive to consider the implications of Eq. (13) for a Blasius boundary layer undergoing transition. The usual form of the laminar diffusion time scale, t_d, is $\rho\delta^2/\mu$ (see, e.g., Schlichting [64], and Hofeldt et al. [65]) where δ is the thickness where the local velocity becomes 99% of the free stream value and ρ is the fluid density. The ratio of 99% velocity thickness to momentum thickness in a Blasius boundary layer is 5:0.664. Substituting into Eq. (13), taking A_1 equal to 7.0, and rearranging gives

$$t_e = 0.25t_d \tag{14}$$

Now, the time for a Blasius boundary layer to grow to a thickness δ is 1/25th the laminar diffusion time scale (Schlichting [64]). So, transition onset would occur for the Blasius boundary layer when the local eddy time scale approached a level associated with a growth of ≈6 boundary layer thicknesses. Schlichting [64] gives the smallest unstable wavelength of a Blasius boundary layer as $\approx6\delta$. So, Eq. (14) implies that the onset of bypass transition occurs when the local eddy time scale reaches a time scale associated with the wavelength of a Tollmien-Schlichting (TS) wave.

Although one typically does not associate TS activity with bypass transition, it has been noted by Herbert [66] that the ultimate breakdown associated with the appearance of "spikes" in hot-wire records and the first formation of turbulent spots in natural transition occurs over a length scale of about 1 TS wavelength. Also, Walker and Gostelow [67] have measured frequencies consistent with TS activity in boundary layers undergoing bypass transition in adverse pressure gradients. Additionally, Mack [68] noted that often TS frequencies persist in boundary layers undergoing natural transition beyond the range of applicability of small disturbance theory. Volino [69,70] also reported that for separated-flow transition, TS frequencies were detected for both low and high levels of Tu. Again, the real implication of this discussion is that when the ratio of the turbulent-eddy time scale to the laminar diffusion time reaches a critical value, bypass transition occurs. Further, the critical value of this ratio is nearly constant over a range of flow conditions consistent with gas-turbine engines.

Modeling Laminar Separation and Turbulent Reattachment

"Of all the transition modes, there is none more crucial to compressor and low-pressure turbine design and none more neglected than separated-flow transition" (Mayle [1]). As attempts are made to reduce airfoil counts, and hence component cost and weight, airfoil loadings need to increase. Highly loaded airfoils are more

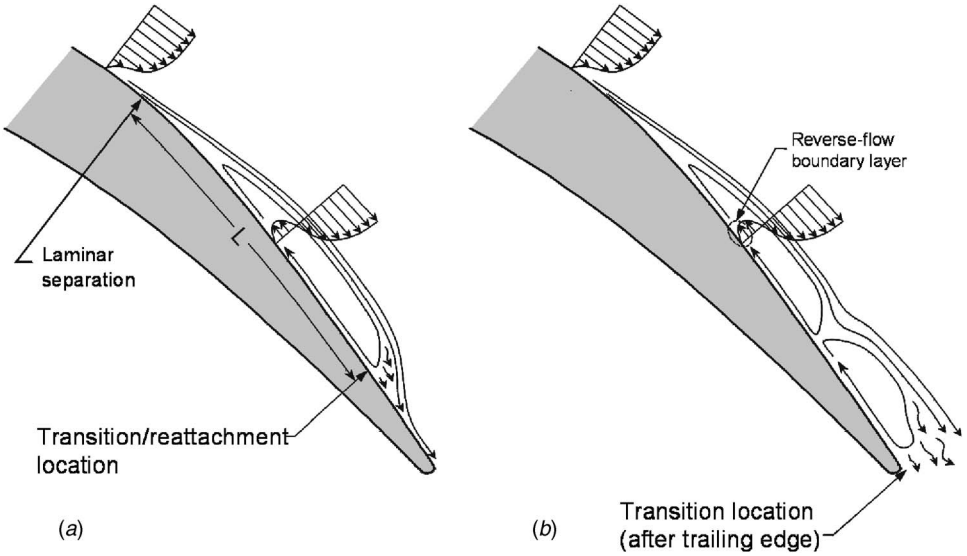

Fig. 11 Schematic representation of suction-side, laminar-separation characteristics showing both reattached (*a*) and stalled (*b*) conditions

prone to experiencing laminar separations (Fig. 11) and stall. In the stalled condition profile losses can increase as much as 500% over the case where the separation reattaches to the airfoil. Laminar separations occur in the leading-edge, suction-side regions of compressors and the aft suction-side regions of low-pressure turbine (LPT) airfoils. Airfoil stall causes compressor surge and poor performance of LPTs at cruise conditions.

If the laminar shear layer formed by a separation transitions to a turbulent state close enough (i.e., in a stream-wise sense) to the separation location, it typically reattaches to the airfoil surface as a result of turbulent mixing that entrains high-momentum fluid into the near-wall region. This scenario is schematically depicted in Fig. 11(*a*). However, if transition of the shear layer occurs sufficiently far downstream of separation, the layer typically does not reattach, resulting in a stalled condition as shown in Fig. 11(*b*). It is therefore critical that a design system be capable of predicting the existence of a laminar separation and whether or not the laminar separation will reattach.

As a first step in developing a transition modeling capability for separated flow, a proof-of-concept study was executed with the goal of determining if a separated-flow transition model could be effectively implemented in a RANS code. For this study, CFD simulations of cascade experiments were run with imposed abrupt trips, set according to experimental hot-film data. Figure 12 is a plot of separation and reattachment locations as a function of exit Reynolds number for a cascade airfoil with $Tu=5\%$. The total suction-side surface length of the airfoil for this case was 37.1 mm, and both experimental and computational results are shown in Fig. 12.

It can be seen in Fig. 12 that the separation and reattachment locations from simulations utilizing the QL model for the pretransitional boundary layers are in close agreement with the data at all but the lowest simulated Reynolds number. The deviation from the data at the lowest Reynolds number is a result of stall occurring in the simulation and subsequent unsteadiness in the steady simulation. For a Reynolds number of 1.5×10^5 a simulation was also run with the turbulent viscosity set to zero in laminar regions and the results are also plotted in Fig. 12. For this simulation the separation location occurs upstream of the measured location. This is consistent with the quasi-laminar boundary layer shape, and hence near-wall momentum, not being accurately modeled by setting $\mu_T=0$. The calculated loss levels from the simulations shown in Fig. 12 were in good agreement with the measured values. The conclusion of this study was that the RANS code with abrupt trips and some form of modeling for quasi-laminar, pretransitional boundary layers would provide an accurate framework for separated-flow transition modeling.

So, in addition to the attached-flow transition studies, a CFD-supplemented database of laminar separations with turbulent reattachment was constructed based on 47 in-house and open-literature experimental cascade data sets. The test cases for the separated-flow database include laminar separations with turbulent reattachment on both compressor- and turbine-specific geometries. Some of the data sets included in the database are from airfoils on the verge of stall. Like the attached-flow database, the separated-flow database covers a significant range of turbomachinery-specific flow parameters.

Review of Models for the Onset of Separated-Flow Transition. One common method for predicting the transition location of a near-wall bounded shear layer involves the use of a correlation that was developed for attached-flow transition such as either the Mayle [1] or Abu-Ghannam and Shaw [11] model. These models rely on a non-dimensional boundary layer thickness (Re_θ or shape factor) for the prediction of transition onset and were developed with data for attached-flow transition. As depicted

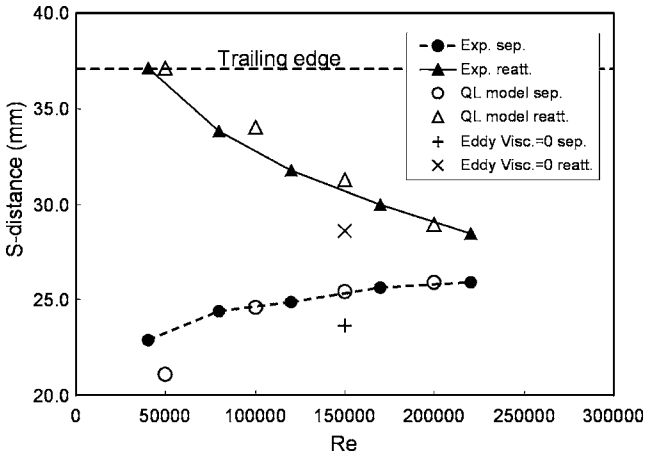

Fig. 12 Measured and predicted separation and reattachment locations. Transition was specified in the simulations based on data.

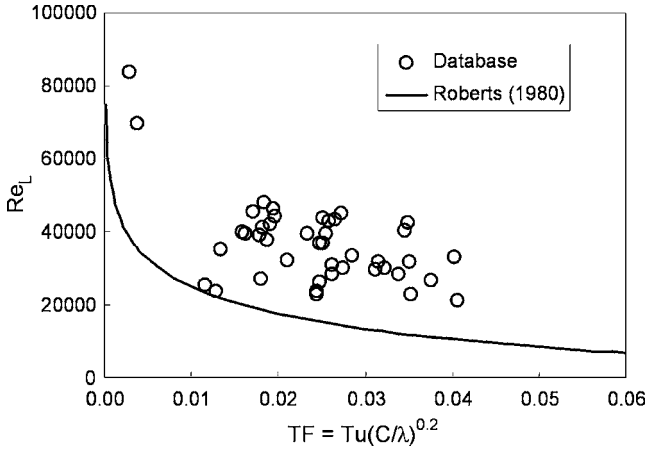

Fig. 13 A comparison between the separated-flow transition model of Roberts [71] and the separated-flow transition database

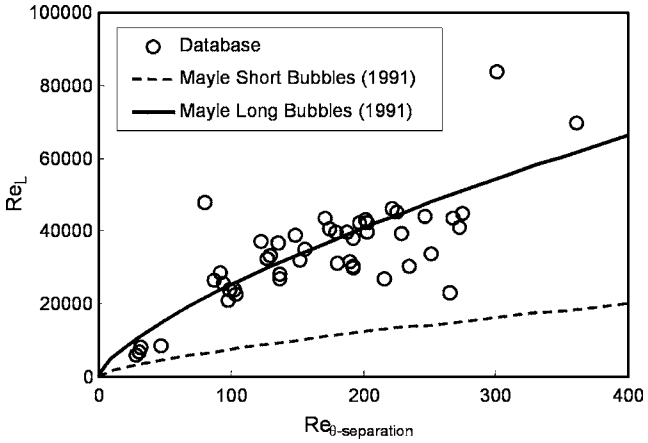

Fig. 14 A comparison between the separated-flow transition models of Mayle [1] and the separated-flow transition database

in Fig. 11, in the separated region, the only attached boundary layer that exists is the reverse-flow boundary layer within the separation bubble. The primary issue with employing an attached-flow transition model in a region where the flow is separated is that the physical significance of Re_θ fundamentally changes once the boundary layer separates.

A rather unique model for the prediction of separated-flow transition was reported by Roberts [71], in which the distance from the separation location to the shear layer transition location (L in Fig. 11) is related to free stream turbulence quantities. This model is unique in that it considers both turbulence intensity *and* length scale in predicting separated-flow transition onset. Figure 13 is a comparison between predictions performed with the model of Roberts [71] and the separated-flow database. Plotted in this figure is Reynolds number based on L versus the local "turbulence factor" which is defined as $TF=Tu(C/\lambda)^{0.2}$, where C is the airfoil chord. The highest level of turbulence factor considered in the development of the Roberts [71] model was approximately 0.06. This model was developed for external flows with low free stream turbulence levels ($<0.2\%$). The only database cases that are well correlated by this model are the cases in which $Tu<0.6\%$ (Fig. 13). The Roberts model [71] does not correlate database cases with $Tu>0.6\%$ well enough for implementation in a design system. Additionally, alteration of the model by leaving out the length scale in the calculation of TF, as suggested as a possible modification by Roberts [71], did not improve the correlation of the database.

Other separated-flow transition models have been reported by Walker [72], Mayle [1], and Hatman and Wang [73]. These models relate separation length to the conditions of the laminar boundary layer at the separation location. RANS-based simulations employing models of this type have proven to be at least trend accurate in the prediction of separated transition (see, e.g., Volino [69,70] and Houtermans et al. [74]). The separated-flow transition database was employed to test the models of Mayle [1] for "long" and "short" bubbles and a comparison of the predicted and measured bubble lengths is shown in Fig. 14. It can be seen in this figure that neither the long- nor the short-bubble model provides sufficient accuracy for design purposes. Similar results were obtained for comparisons between the models due to Walker [72] and Hatman and Wang [73] and the separated-flow database. These results are supported by Volino [69,70] who reported that the correlations of Hatman and Wang [73], Mayle [1], and Davis et al. [75] give "rough" estimates for the transition behavior of his experimental test cases.

New Model for Separated-Flow Transition. In RANS-based simulations the authors believe that the multi-moded [1] nature of transition is best captured by employing two separate models for attached and separated transition. So, following the body of material concerning models for separated-flow transition summarized above, a new model has been developed based on the separated-flow database. The same dimensional-analysis technique used for the attached-flow model was employed in the development of this model. The best correlation of the database was obtained when the length of the bubble was related to the state of the boundary layer at separation. The form of the current model is:

$$\frac{L}{S_{\text{sep}}} = C\text{Re}_{\theta-\text{sep}}^{D} \tag{15}$$

where C and D are constants equal to 173.0 and −1.227, respectively, L is the distance between separation and transition onset, and S_{sep} is the surface distance from the stagnation point to the separation location.

The separated-flow database is shown in Fig. 15 along with the current transition model (Eq. (15)). The reasonably good correlation of the database with the recasting of Walker's original idea [72] supports the assertion that for viscously dominated, near-wall bounded separations, the bubble size scales on the state of the boundary layer at separation. While Eq. (15) does not explicitly contain turbulence quantities, they are still important in the determination of Re_θ at the separation location if a model, such as the

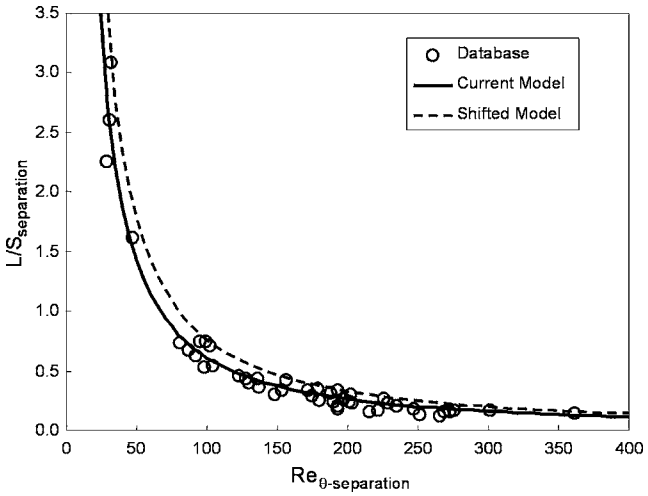

Fig. 15 The current model and database for separated-flow transition. The model with a conservative shift is also shown.

current QL model, is employed to capture the effects of free stream turbulence on the pre-separation quasi-laminar boundary layer. Additionally, it should be noted that Eq. (15) was implemented in the design system in a conservative fashion by setting C at a level 20% higher than the least-squares-fit value plotted on Fig. 15 as "current model." This conservatively defined correlation is also plotted in Fig. 15 as "shifted model" and represents an upper bound for bubble sizes in the database.

If modeling of the effects of free stream turbulence on the pre-transitional/separation boundary layers is not used in conjunction with the attached- and separated-flow models presented here, a conservative predictive system for low-Reynolds number separated flows results. As demonstrated earlier (Figs. 5 and 12), onset/separation values of Re_θ are under-predicted (by 15% or more) when quasi-laminar effects are not modeled. This, taken with the inverse relation between Re_θ and the length of the separated region presented in Eq. (15), results in an over prediction of bubble length and hence a conservative prediction of the performance of an airfoil with separated flow. That is, the analytically determined stall Reynolds number is larger when Eq. (15) is used in the absence of pre-transitional modeling, and thus airfoils designed in that fashion may have better than predicted Reynolds-lapse characteristics. Such was the case for the L1M airfoil designed at AFRL and tested by Bons et al. [76]. The designers of the L1M used an entirely different design system than that employed in this study and made use of Eq. (15) without the benefit of pre-transitional modeling. The L1M airfoil had a design Zweifel coefficient of 1.34, and it was stall free for the range of Reynolds numbers tested in the experiment, as predicted. The lowest Reynolds number achieved in the experimental verification of the airfoil performance was 20,000. At that Reynolds number, the suction-side bubble was predicted to close at 92% of the axial chord, whereas the measured re-attachment was at approximately 80%.

In his experimental assessment of the Pack B airfoil, Volino [69,70] reported that boundary layer reattachment occurs essentially simultaneously with transition onset for separated flow transition. This supports the assertion made by Lou and Hourmouziadis [77] that the transition length is very short because of the lack of wall damping in the shear layer. Also, Walker et al. [78] reported that abrupt transition is a relatively (compared to transition-length models for separated flow) realistic model of the transition region in laminar separation bubbles. So, as in the case of attached-flow transition, abrupt transition is assumed for the implementation of the current separated-flow model. Validation of the many assumptions involved in the development of both models as well as their implementation is reported in Part II of this work.

Physical Significance of the Current Separated-Flow Model. While the concept of long and short bubbles has been discussed in literature relating to separated-flow transition for many decades, the present results suggest that the concept may not be important in turbomachinery configurations. The present database is in conflict with reports of Hatman and Wang [73] and Houtermans et al. [74] where the existence of two bubble regimes seems evident from data. In the current database, no long bubbles, that significantly alter airfoil pressure distributions, were found that *also* reattached to the airfoil. In other words, separations that do not reattach, and hence alter the turning characteristics and loadings of airfoils, are not referred to as bubbles here as they are not closed. Large reattaching bubbles that significantly alter pressure distributions are possible on flat-plate configurations such as that employed by Hatman and Wang [73] if reattachment occurs downstream of the simulated trailing edge. Therefore, their correlation may still be useful in predicting where the laminar shear layer transitions downstream of an airfoil trailing edge. The present database shows a continuous distribution of separation behavior up to the point of stall. This is consistent with the results of Houtermans et al. [74] for their short bubble regime. The data regarded as reflecting long bubble behavior by Houtermans et al. [74] is here interpreted as arising from stalled conditions. So, the authors believe that the short bubble regime primarily describes separation behavior *with* reattachment. In this work, if separated-flow transition onset is predicted to occur downstream of the airfoil trailing edge, then the airfoil is run fully laminar.

Conclusions

The ability to model accurately the development of free stream disturbances has been shown to be an important aspect of any transition modeling capability. Evidence has been presented that capturing the effects of free stream turbulence on pre-transitional boundary layers may enhance the accuracy of empiricisms used for the prediction of transition. The k-ω model, along with the current method for modeling quasi-laminar boundary layers, was employed to supplement 104 cascade data sets from literature and in-house studies (i.e., Pratt & Whitney proprietary data) to build databases for attached- and separated-flow transition. Existing models for both transition mechanisms were assessed with the databases and deemed not to have sufficient accuracy for design purposes. Consequently, dimensional analysis was employed as a guide for the extraction of pertinent flow variables from flow field predictions of the experiments, and new models were developed.

Two correlations were developed, one for the onset of attached-flow transition and the other for the length of a separation bubble prior to turbulent reattachment. The current models are based on *local* flow field parameters, and they appear to have greater efficacy than a number of extant correlations. In particular, the model for attached-flow transition appears to have a physical basis with respect to the fundamental mechanism of bypass transition in compressible flow. That is, it was found that the onset of transition occurs when the ratio of a boundary-layer diffusion time to a time scale associated with the local, energy-bearing turbulent fluctuations at the edge of the shear layer reaches a critical value. Further, it was found that the critical value of the ratio was nearly constant over a wide range of flow field conditions consistent with turbomachinery airfoils. By contrast, no such underlying physical basis was apparent from considerations of the separated-flow model: it appeared to be more of a straight correlation of variables.

The models have been implemented as point-wise trips in a 3D RANS solver that forms part of a turbomachinery design system. It should be noted that both the attached- and separated-flow models are based solely on two-dimensional data and applications of them in three-dimensional flow fields may elucidate deficiencies. In addition, no modeling has been implemented to account for the effects of roughness on pre-transitional/separation boundary layers. Part II of this paper [79] focuses on the validation of the current models for use in an airfoil design system

Acknowledgment

The authors would like to thank Pratt & Whitney for granting permission to publish this work. In particular, they are grateful to Dr. Jayant Sabnis, Gary Stetson, and Joel Wagner for their support. Inspiration for this work is a result of the authors' participation in the Minnowbrook conferences that are sponsored by the U.S. Air Force Office of Scientific Research and NASA (see, e.g., NASA CP 1998-206958). Professor T. V. Jones and Professor Jim S.-J. Chen taught the authors the importance of starting any technical effort from basic principles, and additional insights were gleaned from discussions with A. A. Rangwalla, M. F. Blair, F. Ames, D. Zhang, L. Bertuccioli, and J. Duke.

References

[1] Mayle, R. E., 1991, "The Role of Laminar-Turbulent Transition in Gas Turbine Engines," ASME J. Turbomach., **113**, pp. 509–537.
[2] Lakshminarayana, B., 1991, "An Assessment of Computational Fluid Dynamic Techniques in the Analysis and Design of Turbomachinery—The 1990 Freeman Scholar Lecture," ASME J. Fluids Eng., **113**, pp. 315–352.

[3] Simoneau, R. J., and Simon, F. F., 1993, "Progress Towards Understanding and Predicting Heat Transfer in the Turbine Gas Path," Int. J. Heat Fluid Flow, **14**, pp. 106–128.
[4] Simon, F. F., and Ashpis, D. E., 1996, "Progress in Modeling of Laminar to Turbulent Transition on Turbine Vanes and Blades," NASA Technical Memorandum No. 107180.
[5] Dunn, M. G., 2001, "Convective Heat Transfer and Aerodynamics in Axial Flow Turbines," ASME Paper No. 2001-GT-0506.
[6] Yaras, M. I., 2002, "Measurements of the Effects of Freestream Turbulence on Separation-Bubble Transition," ASME Paper No. GT-2002–30232.
[7] Wilcox, D. C., 1998, *Turbulence Modeling for CFD*, 2nd ed., DCW Industries, Inc., La Canada, CA.
[8] Ames, F. E., 1994, "Experimental Study of Vane Heat Transfer and Aerodynamics in Elevated Levels of Turbulence," NASA Contract Report No. 4633.
[9] Ni, R. H., 1999, "Advanced Modeling Techniques for New Commercial Engines," *Proceedings of the XIV International Symposium on Air Breathing Engines*, Florence, Italy, 5–10 September.
[10] Davis, R. L., Shang, T., Buteau, J., and Ni, R. H., 1996, "Prediction of 3-D Unsteady Flow in Multi-Stage Turbomachinery Using an Implicit Dual Time-Step Approach," AIAA Paper No. 96–2565.
[11] Abu-Ghannam, B. J., and Shaw, R., 1980, "Natural Transition of Boundary Layers—The Effects of Turbulence, Pressure Gradient, and Flow History," J. Mech. Eng. Sci., **22**(5), pp. 213–228.
[12] Wilcox, D. C., 1988, "Reassessment of the Scale-Determining Equation for Advanced Turbulence Models," AIAA J., **26**, pp. 1299–1310.
[13] Baines, W. D., and Peterson, E. G., 1951, "An Investigation of Flow Through Screens," Trans. ASME, **73**, pp. 467–480.
[14] Hinze, J. O., 1975, Turbulence, 2nd ed., McGraw–Hill, New York, p. 272.
[15] Ames, F. E., and Plesniak, M. W., 1995, "The Influence of Large Scale, High Intensity Turbulence on Vane Aerodynamic Losses, Wake Growth, and Exit Turbulence Parameters," ASME Report No. 95-GT-290.
[16] Moss, R. W., and Oldfield, M. L. G., 1992, "Measurements of the Effect of Free-Stream Turbulence Length Scale on Heat Transfer," ASME Report No. 92-GT-244.
[17] Boyle, R. J., Bunker, R. S., and Giel, P. W., 2003, "Predictions for the Effects of Turbulence on Turbine Blade Heat Transfer," ISABE Report No. 2003 1178.
[18] Roach, P. E., and Brierley, D. H., 2000, "Bypass Transition Modeling: A New Method Which Accounts for Freestream Turbulence Intensity and Length Scale," ASME Report No. 2000-GT-278.
[19] Sharma, O. P., Renaud, E., Butler, T. L., Milsaps, K., Dring, R. P., and Joslyn, H. D., 1988, "Rotor-Stator Interaction in Multi-Stage Axial-Flow Turbines," AIAA Report No. 88–3013.
[20] Ames, F. E., 1995, "Advanced *k*-epsilon Modeling of Heat Transfer," NASA Contract Report No. 4679.
[21] Van Fossen, G. J., Simoneau, R. J., and Ching, C. Y., 1994, "Influence of Turbulence Parameters, Reynolds Number, and Body Shape on Stagnation-Region Heat Transfer," NASA Technical Report No. 3487.
[22] Arts, T., de Rouvroit, L. M., and Rutherford, A. W., 1990, "Aero-Thermal Investigation of a Highly Loaded Transonic Linear Turbine Guide Vane Cascade," von Karman Institute for Fluids Dynamics Technical Note No. 174.
[23] Schmidt, R. C., and Patankar, S. V., 1988, "Two-Equation Low-Reynolds-Number Turbulence Modeling of Transitional Boundary Layer Flows Characteristic of Gas Turbine Blades," NASA Contract Report No. 4145.
[24] Praisner, T. J., Clark, J. P., Grover, E. A., Bertuccioli, L., and Zhang, D., 2004, "Challenges in Predicting Component Efficiencies in Turbines with Low Reynolds Number Blading," NASA/TM-2004-212913, p. 58
[25] Blair, M. F., and Werle, M. J., 1981, "Combined Influence of Freestream Turbulence and Favorable Pressure Gradients on Boundary Layer Transition and Heat Transfer," UTRC Report No. R81–914388–17.
[26] Emmons, H. W., 1951, "The Laminar Turbulent Transition in a Boundary Layer. Part 1," J. Aeronaut. Sci., **18**, pp. 490–498.
[27] Schubauer, G. B., and Klebanoff, P. S., 1955, "Contributions on the Mechanics of Boundary Layer Transition," NASA TN Paper No. 3489.
[28] Narasimha, R., 1957, "On the Distribution of Intermittency in the Transition Region of a Boundary Layer," J. Aeronaut. Sci., **24**, pp. 711–712.
[29] Clark, J. P., Jones, T. V., and LaGraff, J. E., 1994, "On the Propagation of Naturally-Occurring Turbulent Spots," J. Eng. Math., **28**, pp. 1–19.
[30] Gostelow, J. P., Blunden, A. R., and Walker, G. J., 1994, "Effects of Freestream Turbulence and Adverse Pressure Gradients on Boundary-Layer Transition," ASME J. Turbomach., **116**, pp. 392–404.
[31] Halstead, D. E., Wisler, D. C., Okiishi., T. H., Walker, G. J., Hodson, H. P., and Shin, H. W., 1997, "Boundary Layer Development in Axial Compressors and Turbines: Part 3 of 4—LP Turbines," ASME J. Turbomach., **119**, pp. 225–237.
[32] Chen, K. K., and Thyson, N. A., 1971, "Extension of Emmons' Theory to Flows on Blunt Bodies," AIAA J., **9**(5), pp. 821–825.
[33] Dey, J., and Narasimha, R., 1990, "Integral Method for the Calculation of Incompressible Two Dimensional Transitional Boundary Layers," J. Aircr., **27**(10), pp. 859–865.
[34] Solomon, W. J., Walker, G. J., and Gostelow, J. P., 1996, "Transition Length Prediction for Flows with Rapidly Changing Pressure Gradients," ASME J. Turbomach., **118**, pp. 744–751.
[35] Dhawan, S., and Narasimha, R., 1958, "Some Properties of Boundary Layer Flow During the Transition From Laminar to Turbulent Motion," J. Fluid Mech., **3**, pp. 418–436.
[36] Suzen, Y. B., and Huang, P. G., 2000, "Modeling of Flow Transition Using and Intermittency Transport Equation," ASME J. Fluids Eng., **122**, pp. 273–284.
[37] Steelant, J., and Dick, E., 2001, "Modeling of Laminar-Turbulent Transition for High Free Stream Turbulence," ASME J. Fluids Eng., **123**, pp. 22–30.
[38] Drela, M., 1995, "MISES Implementation of Modified Abu-Ghannam-Shaw Transition Criterion," MIT Technical Report.
[39] Gier, J., Ardey, S., and Heisler, A., 2000, "Analysis of Complex Three-Dimensional Flow in a Three-Stage LP Turbine by Means of Transitional Navier-Stokes Simulation," ASME Paper No. 2000-GT-645.
[40] Thermann, H., Mueller, M., and Niehuis, R., 2001, "Numerical Simulation of Boundary Layer Transition in Turbomachinery Flows," ASME Paper No. 2001-GT-0475.
[41] Roux, J., Lefebvre, M., and Liamis, N., 2002, "Unsteady and Calming Effects Investigation on a Very High Lift LP Turbine Blade—Part II: Numerical Analysis," ASME Paper No. GT2002–30228.
[42] Roberts, S. K., and Yaras, M. I., 2003, "Measurements and Prediction of Freestream Turbulence and Pressure-Gradient Effects on Attached-Flow Boundary-Layer Transition," ASME Paper No. GT2003–38261.
[43] Narasimha, R., 1985, "The Laminar Turbulent Transition Zone in the Boundary Layer," Prog. Aerosp. Sci., **22**, pp. 29–80.
[44] Fraser, C. J., Higazy, M. G., and Milne, J. S., 1994, "End-Stage Boundary Layer Transition Models for Engineering Calculations," Proc. Inst. Mech. Eng., Part C: J. Mech. Eng. Sci., **208**(C1), pp. 47–58.
[45] Narasimha, R., 1990, "Modeling the Transitional Boundary Layer," NASA CR 187487.
[46] Narasimha, R., 1991, "Recent Advances in the Dynamics of the Transition Zone," ISABE Report No. 91 7006.
[47] Owen, F. K., 1970, "Transition Experiments on a Flat Plate at Subsonic and Supersonic Speeds," AIAA J., **8**(3), pp. 518–523.
[48] Sharma, O. P., Wells, R. A., Schlinker, R. H., and Bailey, D. A., 1982, "Boundary Layer Development on Airfoil Suction Surfaces," ASME J. Eng. Power, **104**, pp. 698–706.
[49] Clark, J. P., 1993, "A Study of Turbulent-Spot Propagation in Turbine-Representative Flows," D. Phil, University of Oxford, Oxford, England.
[50] Narasimha, R., 2003, "Review of Recent Research in Bangalore on the Transition Zone," NASA/TM-2004-212913, p. 63.
[51] Hofeldt, A. J., 1996, "An Investigation of Naturally-Ocurring Turbulent Spots Using Thin-Film Gages," Ph.D. thesis, University of Oxford, Oxford, England.
[52] Tani, I., 1969, "Boundary-Layer Transition," Annu. Rev. Fluid Mech., **1**, pp. 169–196.
[53] Reshotko, E., 1976, "Boundary Layer Stability and Transition," Annu. Rev. Fluid Mech., **8**, pp. 311–349.
[54] Liepmann, H. W., 1945, "Investigation of Boundary Layer Transition on Concave Walls," NACA Wartime Report No. W-87 (also NACA ACR 4J28).
[55] Liepmann, H. W., 1943, "Investigations of Laminar Boundary Layer Stability and Transition on Curved Boundaries," NACA Wartime Report No. W-107 (also NACA ACR 3H30).
[56] Van Driest, E. R., and Blumer, C. B., 1963, "Boundary Layer Transition: Free Stream Turbulence and Pressure Gradient Effects," AIAA J., **1**, pp. 1303–1306.
[57] Mayle, R. E., and Schulz, A., 1997, "The Path to Predicting Bypass Transition," ASME J. Turbomach., **119**, pp. 405–411.
[58] Suder, K. L., O'Brien, J. E., and Reshotko, E., 1988, "Experimental Study of Bypass Transition in a Boundary Layer," NASA TM Report No. 100913.
[59] Kim, J., Simon, T. W., and Kestoras, M., 1994, "Fluid Mechanics and Heat Transfer Measurements in Transitional Boundary Layers Conditionally Sampled on Intermittency," ASME J. Turbomach., **116**, pp. 405–416.
[60] Morkovin, M. V., 1978, "Instability, Transition to Turbulence, and Predictability," NATO AGARDograph No. 236.
[61] Massey, B. S., 1986, *Measures in Science and Engineering*, Ellis-Horwood, Ltd., Chichester, UK, pp. 125–127.
[62] Michelassi, V., Rodi, W., and Giess, P.-A., 1998, "Experimental and Numerical Investigation of Boundary-Layer and Wake Development in a Transonic Turbine Cascade," Aerosp. Sci. Technol., **3**, pp. 191–204.
[63] White, F. M., 1991, *Viscous Fluid Flow*, 2nd ed., McGraw-Hill, New York, pp. 273–274.
[64] Schlichting, H., 1979, *Boundary Layer Theory*, 7th ed., McGraw-Hill, New York, pp. 90–91, 470.
[65] Hofeldt, A. J., Clark, J. P., LaGraff, J. E., and Jones, T. V., 1998, "The Becalmed Region in Turbulent Spots," NASA/CP 1998–206958, pp. 95–98.
[66] Herbert, T., 1988, "Secondary Instability of Boundary Layers," Annu. Rev. Fluid Mech., **20**, pp. 487–526.
[67] Walker, G. J., and Gostelow, J. P., 1990, "Effects of Adverse Pressure Gradients on the Nature and Length of Boundary-Layer Transition," ASME J. Turbomach., **112**, pp. 196–205.
[68] Mack, L. M., 1975, "Linear Stability Theory and the Problem of Supersonic Boundary Layer Transition," AIAA J., **13**(3), pp. 278–289.
[69] Volino, R. J., 2002, "Separated Flow Transition Under Simulated Low-Pressure Turbine Airfoil Conditions—Part 1: Mean flow and Turbulence Statistics," ASME Paper No. 2002-GT-30236.
[70] Volino, R. J., 2002b, "Separated Flow Transition Under Simulated Low-Pressure Turbine Airfoil Conditions: Part 2—Turbulence Spectra," ASME Paper No. 2002-GT-30237.
[71] Roberts, W. B., 1980, "Calculation of Laminar Separation Bubbles and Their Effect on Airfoil Performance," AIAA J., **18**(1), pp. 25–31.

[72] Walker, G. J., 1989, "Modeling of Transitional Flow in Laminar Separation Bubbles," *Proceedings of the Ninth International Symposium on Air Breathing Engines*, pp. 539–548.
[73] Hatman, A., and Wang, T., 1999, "A Prediction Model for Separated Flow Transition," ASME J. Turbomach., **121**, pp. 594–602.
[74] Houtermans, R., Coton, T., and Arts, T., 2003, "Aerodynamic Performance of a Very High Lift LP Turbine Blade With Emphasis on Separation Prediction," ASME Paper No. 2003-GT-38802.
[75] Davis, R. L., Carter, J. E., and Reshotko, E., 1985, "Analysis of Transitional Separation Bubbles on Infinite Swept Wings," AIAA Paper No. 85–1685.
[76] Bons, J. P., Hansen, L. C., Clark, J. P., Koch, P. J., and Sondergaard, R., 2005, "Designing Low-Pressure Turbine Blades With Integrated Flow Control," ASME Paper No. GT2005–68962.
[77] Lou, W., and Hourmouziadis, J., 2000, "Separation Bubbles Under Steady and Periodic-Unsteady Main Flow Conditions," ASME Paper No. 2000-GT-0270.
[78] Walker, G. J., Subroto, P. H., and Platzer, M. F., 1988, "Transition Modeling Effects on Viscous/Inviscid Interaction Analysis of Low Reynolds Number Airfoil Flows Involving Laminar Separation Bubbles," ASME Paper No. 88-GT-32.
[79] Praisner, T. J., Grover, E. A., Rice, M. J., and Clark, J. P., 2004, "Predicting Transition in Turbomachinery, Part II—Model Validation and Benchmarking," ASME Paper No. GT-2004–54109.

Predicting Transition in Turbomachinery—Part II: Model Validation and Benchmarking

T. J. Praisner
E. A. Grover
M. J. Rice

Turbine Aerodynamics,
United Technologies Pratt & Whitney,
400 Main St., M/S 169-29,
East Hartford, CT 06108

J. P. Clark
Turbine Branch,
Turbine Engine Division,
Propulsion Directorate,
Air Force Research Laboratory,
Building 18, Room 136D,
1950 5th St.,
WPAFB, OH 45433
e-mail: john.clark3@wpafb.af.mil

The ability to predict boundary layer transition locations accurately on turbomachinery airfoils is critical both to evaluate aerodynamic performance and to predict local heat-transfer coefficients with accuracy. Here we report on an effort to include empirical transition models developed in Part I of this report in a Reynolds averaged Navier-Stokes (RANS) solver. To validate the new models, two-dimensional design optimizations utilizing transitional RANS simulations were performed to obtain a pair of low-pressure turbine airfoils with the objective of increasing airfoil loading by 25%. Subsequent experimental testing of the two new airfoils confirmed pre-test predictions of both high and low Reynolds number loss levels. In addition, the accuracy of the new transition modeling capability was benchmarked with a number of legacy cascade and low-pressure turbine (LPT) rig data sets. Good agreement between measured and predicted profile losses was found in both cascade and rig environments. However, use of the transition modeling capability has elucidated deficiencies in typical RANS simulations that are conducted to predict component performance. Efficiency-versus-span comparisons between rig data and multi-stage steady and time-accurate LPT simulations indicate that loss levels in the end wall regions are significantly under predicted. Possible causes for the under-predicted end wall losses are discussed as well as suggestions for future improvements that would make RANS-based transitional simulations more accurate.
[DOI: 10.1115/1.2366528]

Introduction

The need to incorporate transition modeling in turbomachinery prediction and design methods has been described many times in related literature. A representative example is found in Greitzer et al. [1] where the authors describe turbulence and transition as being the key small-scale phenomena of interest in unsteady-flow research. Indeed, the effect of unsteadiness on boundary-layer transition in turbomachines has been studied extensively (see, e.g., Hodson [2], Doorly and Oldfield [3], LaGraff et al. [4], and Halstead et al. [5]). One of the most detailed investigations on unsteady phenomena involved in transition on low-pressure turbines is that due to Halstead et al. [6]. However, it is not always apparent how designers can capitalize on such work (Wadia [7]), no matter how rigorous and detailed it is. Still, there have been attempts to incorporate knowledge of transition physics into airfoil design systems in the past, and some success has been achieved with boundary-layer calculation methods (see, e.g., Sharma et al. [8]). Also, thanks to the Minnowbrook conferences, in the past decade there has been a greater degree of communication among members of the transition community engaged in research aimed at the turbomachinery environment and those working at a more fundamental level (see, e.g., LaGraff and Ashpis [9]). Consequently, the incorporation of existing transition models (see Part I [10]) into Reynolds averaged Navier-Stokes (RANS)-based design systems within industry has started to emerge (see, e.g., Dorney and Ashpis [11], Gier et al. [12], Höhn and Heinig [13], Thermann et al. [14], Roux et al. [15], and Walker et al. [16]), but it is unclear whether or not the state of the art in airfoil design has been affected yet.

In Part I of this work, Praisner and Clark [10] summarize the current state of the art in transition modeling for both attached and separated boundary layer flows. The available literature on the subject is extensive, and the authors draw on a range of it to determine whether or not transitional simulations are practicable in a RANS-based design system for turbomachinery airfoils. The work resulted in new models for attached- and separated-flow transition. The resulting transition modeling system that was developed in Part I of this report is validated here against a number of cascade and rig tests.

Motivation

While RANS-based computational fluid dynamics (CFD) simulations typically provide accurate predictions of pressure fields and flow capacities, limited success has been achieved in the accurate prediction of viscous losses. This situation needs attention since the trend in both industry and government is toward the reduction of development time and cost of new engines. From this follows a need to reduce the amount of experimental testing performed in the design cycle. This in turn creates challenges for aerodynamic designers because they must often provide aerodynamic embodiments that provide performance improvements over legacy designs that themselves were positively affected by a great deal of testing. As a result, tools are needed that accurately capture the salient flow phenomena that determine component and, ultimately, engine performance. Ordered by decreasing level of fidelity, the aerodynamicist needs design tools that can provide:

1. Absolute efficiency predictions
2. An ability to predict performance differences between designs
3. Accurate efficiency deltas between operating points for a given design

Ideally these predictive capabilities should be robust enough for the design of turbomachines for many aircraft applications: single aisle, wide-body, military.

Contributed by the International Gas Turbine Institute (IGTI) of ASME for publication in the JOURNAL OF TURBOMACHINERY. Manuscript received October 1, 2003; final manuscript received March 1, 2004. IGTI Review Chair: A. J. Strazisar. Paper presented at the International Gas Turbine Institute and Aeroengine Congress and Exhibition, Vienna, Austria, June 13–17, 2004, Paper No. 2004-GT-54109.

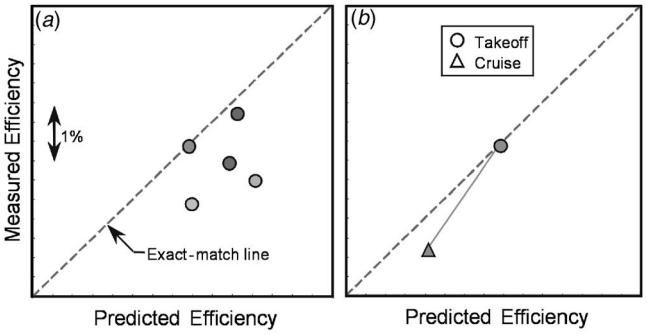

Fig. 1 Measured-versus-predicted efficiencies for five LPTs at takeoff conditions (*a*), and for an LPT at takeoff and cruise conditions (*b*)

Figure 1(*a*) is a plot of measured-versus-predicted efficiency levels for five low-pressure turbines (LPTs). The predicted values were obtained from fully turbulent steady CFD simulations run with ideal (i.e., smooth) end walls. First, the absolute levels of efficiency can not be accurately predicted with fully turbulent CFD simulations as executed here, as evidenced by the fact that only one of the five predictions falls on the "exact-match" line. Second, the ranking of the five designs from the CFD results is far different than the actual (measured) ranking. So, the fully turbulent simulations executed for this effort also do not predict performance differences, even qualitatively, between designs. Finally, the measured and predicted results for a LPT at takeoff and cruise Reynolds numbers are shown in Fig. 1(*b*) While the absolute efficiency is well predicted by the turbulent simulation for the takeoff condition, the cruise efficiency level is significantly over predicted. The results in Fig. 1(*b*) indicated that turbulent CFD simulations of LPTs are also not able to predict efficiency deltas between design points for a given design. So, fully turbulent CFD is not capable of fulfilling any of the aerodynamicist's three requirements for an effective design tool as regards the LPT.

It is believed that inaccuracies in efficiency predictions obtained from fully turbulent, steady RANS simulations are a consequence of an inability to predict accurately:

1. Non wall-bounded shear flows which include:
   1.1. Mixing of flow distortions/wakes
   1.2. Losses associated with end wall/secondary flows
   1.3. Effects of cavity and main-gas-path interactions
2. Unsteady effects
3. The transitional nature of attached and separated airfoil boundary layers.

The goal of this study is to develop a tool that can accurately model the transitional nature of airfoil boundary layers in axial-flow turbomachinery. However, some attention will be paid to unsteady effects and non-wall bounded shear flows, and an effort has been made to elucidate other RANS modeling issues through the systematic validation of the transition-prediction capability.

This validation/benchmarking effort focuses on LPT airfoils because the high aspect ratios that typify these airfoils can allow for the clear discrimination of profile loss levels from other loss mechanisms. Additionally, LPT airfoils display the full multi-moded (Mayle [17]) nature of turbomachinery-related transition, and an inability to predict attached- and separated-flow transition in the LPT can mean the difference between success and failure of the design.

Particular attention will be paid to the prediction of loss and efficiency levels in this report as they are the primary quantities of concern to the aerodynamic designer. Only a fraction of the benchmarking cases executed for validation and benchmarking of the modeling capability are presented here. The cases that are presented were chosen to demonstrate the systematic approach of the validation effort. Benchmarking with profile-loss data from high aspect ratio cascades is presented first, and this is followed by comparisons between predicted and measured spanwise loss data from cascades. Next, results from validation studies with spanwise efficiency data from multi-stage LPT rigs are presented. Finally, comparisons are made between measured and predicted levels of integrated and mid-span efficiency levels for engines and rigs.

Computational Methods

Steady-state and time-resolved turbine flowfields were predicted using the three-dimensional (3D) RANS code described collectively by Ni [18], Ni and Bogoian [19], and Davis et al. [20]. Numerical closure for turbulent flow is obtained via the k-ω turbulence model as described by Wilcox [21]. An O-H grid topology was employed with approximately 40,000 grid points per passage for two-dimensional (2D) simulations and approximately 600,000 grid points per passage for three-dimensional simulations without tip clearance. These grid counts provided essentially grid-independent solutions with values of y^+ of the order 1 and approximately 7 grid points per momentum thickness. In steady mode the code is accurate to second order in space, multi-grid techniques are used to obtain rapid convergence, and a mixing-plane model is employed at each inter-row boundary. To account for losses generated by the mixing of flow distortions, the exit flow field from each row is circumferentially "mixed out" by a control-volume analysis that assumes a constant-area condition for the mixing process. The resulting one-dimensional span-wise profiles are then passed into the downstream row.

When run in time-accurate mode, the code employs implicit dual time stepping to solve for the periodic, unsteady flow field, and a sliding grid interface exists at inter-row boundaries. The code is accurate to second order in space and time, and multi-grid techniques are used for the inner subiterations. For the time-accurate LPT rig simulations, up to 27 million grid points, distributed across 102 CPUs, were needed per simulation. Finally, free stream values of k and ω were set for each validation case according to the methods outlined in Praisner and Clark [10] (i.e., Part I).

The attached- and separated-flow transition models developed in Praisner and Clark [10] were incorporated into the solver without any additional modifications or tuning to data beyond their development. As stated in Praisner and Clark [10], predicted transition locations were handled as abrupt trips in the code. Extrapolation outside of the development space of each model is allowed in the code. However, if extrapolation occurs in a simulation, detailed feedback is output to the user indicating the dimensionless parameters that were outside the bounds of the database used to build the correlation.

Attention was paid to postprocess the predicted flow fields consistently with the data reduction techniques used for each benchmark data set. The boundary conditions used for each simulation are described in detail below, as warranted. For simplicity, end wall flows were treated as fully turbulent for all computational results presented. As mentioned in Part I of this report, no modeling for roughness effects on pre-transitional laminar boundary layers exists in the current transition-prediction system. Consequently, only validation cases for which aerodynamically smooth surface conditions existed are presented.

Steady 2D Validation Results

Figure 2 is a plot of measured and predicted convective heat load distributions around the high-pressure turbine inlet guide vane of Arts et al. [22]. Results are shown from CFD simulations with fully turbulent, fully laminar, and transitional modeling of the boundary layers on the airfoil. Note that modeling of the effects of free stream turbulence on the pre-transitional boundary layers (Praisner and Clark [10]) was employed for the transitional

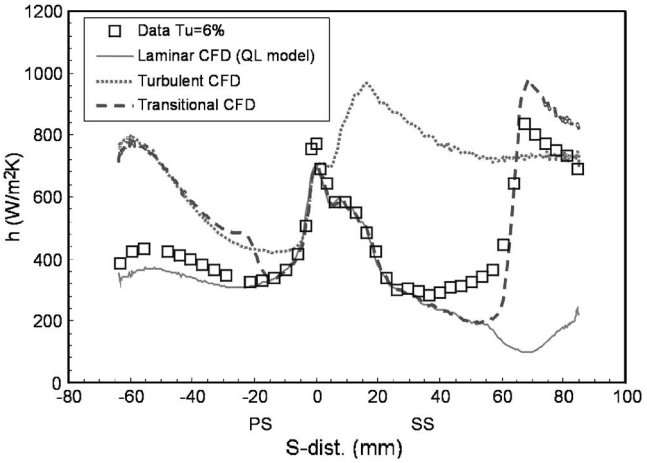

Fig. 2 Measured and predicted heat-load distributions at the midspan of an high-pressure turbine vane cascade. Data are from Arts et al. [22].

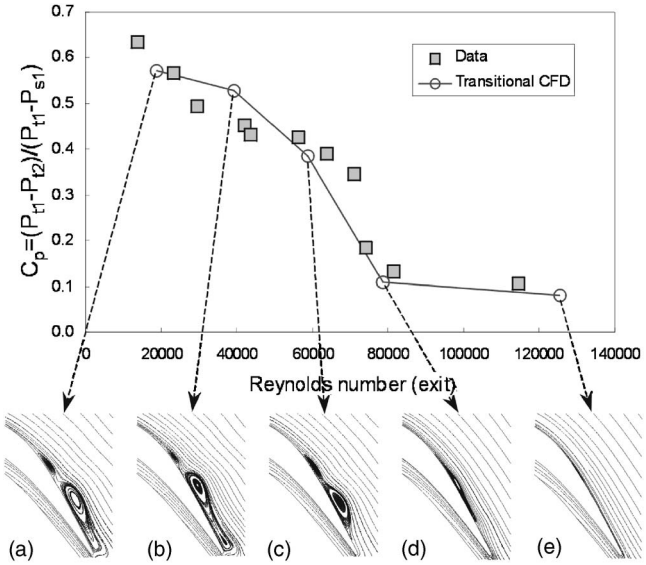

Fig. 3 Measured and predicted profile losses versus Reynolds number for Pack B. Data are from Bons et al. [25].

and laminar simulations. The suction and pressure sides of the airfoil are denoted by PS and SS under the abscissa. Additional flow conditions for both data sets in Fig. 2 were $Tu=6\%$, $\mathrm{Re}_c = 1\times10^6$ and $M_{\mathrm{exit}}=0.92$.

It is possible to use Fig. 2 to illustrate a general conclusion of the transition modeling effort. Transition onset on the suction side, as marked by a deviation from the fully laminar solution, occurs at a surface distance of approximately 35 mm. Then, a gradual increase above the laminar level is noted between $s=35$ and 60 mm. However, at $s=60$ mm there is a sudden increase in the slope of the heat transfer distribution. This sudden change in slope is consistent with a subtransition (Narasimha [23]) caused by the impingement of the cross-passage shock on the airfoil surface. Note that Narasimha [24] interprets a subtransition as indicative of an alteration of spot-propagation characteristics. The authors believe the shock/boundary-layer interaction in Fig. 2 is more apt to be a source of additional spot generation. The case is made that the considerable and spatially limited increase in measured heat transfer rate at the shock location ($s=60$ mm) may not be explained by altered spot-propagation rates alone. This implies that "concentrated breakdown" may occur at more than one location on the suction side. The attached-flow model does not predict transition onset to occur at the initial transition location, but instead, predicts onset at the location of shock impingement (i.e., at the experimental sub-transition point). In the course of developing the database of experimental attached-flow transition cases, observations like these played a part in rejecting both existing transition length correlations and the universal intermittency distribution behind them as guides to modeling transition in favor of point-like trips.

On the pressure side the approximate transition onset location is relatively well predicted at $s=20$ mm. However, downstream of the onset location on the pressure side, the boundary layer is subjected to very high acceleration ($K>6.0\times10^{-6}$), and the apparent transition length evidenced by the data appears to be dramatically drawn out as a result. The application of an abrupt trip on the pressure side gives rise to the gross over prediction of heat-load levels downstream of transition onset on the pressure side.

Overall the agreement between the transitional simulation and the data is better than the turbulent and laminar simulations. However, the results presented in Fig. 2 demonstrate significant deficiencies in heat load predictive capabilities. It should be noted that the experimental case provided by Arts et al. [22] is not well suited for evaluating viscous losses arising from the transitional nature of the airfoil boundary layers. This is a result of the loss levels being dominated by shock losses. In fact mid-span losses were well predicted by both fully turbulent and transitional simulations.

Benchmarking against steady incompressible cascade data was performed with the Pack B data from Bons et al. [25]. The Pack B airfoil is a low Mach number design for a typical highly loaded LPT airfoil. Figure 3 is a comparison between the measured and predicted profile losses with a free stream turbulence level (Tu) of 1% and incompressible-flow conditions. For calculation of the loss coefficient plotted in Fig. 3, Pt and Ps are the total and static pressures, respectively, and 1 and 2 denote inlet and exit locations, respectively. Also, the profile loss data in Fig. 3 are plotted against *exit* Reynolds number, Re_2, while the original data were reported based on inlet values. The data with $Tu=1\%$ was employed for benchmarking because stall conditions are evident in the data set for exit Reynolds numbers below 70,000.

In the context of high-lift designs, the most important feature of the data in Fig. 3 is the Reynolds number at which the airfoil stalls. In Figure 3 the transitional predictions accurately capture the stall Reynolds number of 80,000. The stall Reynolds number is here taken to be the location at which loss begins to increase significantly above levels typical of attached flow transition. Streamline topologies for each of the simulated Reynolds numbers are also shown in Fig. 3. For $\mathrm{Re}_2=127{,}000$ (Fig. 3(*e*)) the suction-side boundary layer is predicted to remain attached to the airfoil and transition just downstream of the minimum pressure location. For $\mathrm{Re}_2=78{,}000$ (Fig. 3(*d*)) the suction-side boundary layer is predicted to undergo a laminar separation with turbulent reattachment with only a small distortion to the overall streamline topology. For $\mathrm{Re}_2<78{,}000$ (Figs. 3(*a*)–3(*c*)), the size of the separation bubble increases significantly in the surface-normal direction and significant unsteadiness precluded convergence of the simulations with respect to the loss. No attempts were made to perform time-accurate simulations for $\mathrm{Re}_2<70{,}000$, so loss levels calculated from the steady simulations are approximate.

In addition to benchmarking with pre-existing data, an effort was conducted to design new airfoils with the goal of increasing the loading by 25%. Computer-aided optimizations were performed with two-dimensional transitional CFD simulations in which the airfoil pitch was systematically increased from the starting geometry of the Pack B airfoil. For each pitch increase the airfoil shape was re-optimized to minimize profile loss. Ultimately two airfoils were designed: one aft loaded (Pack D-A) and the

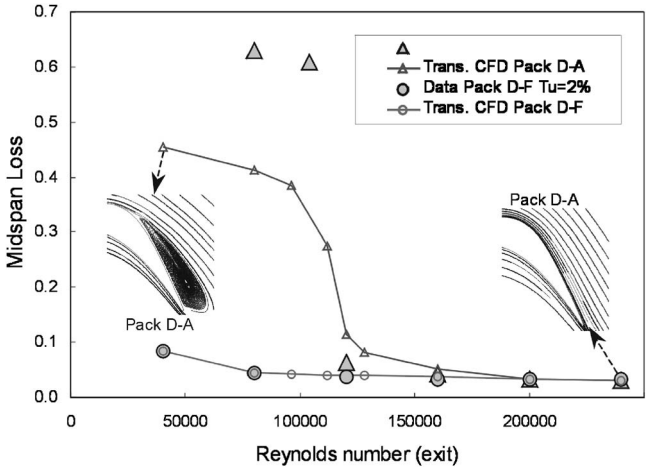

Fig. 4 Measured and predicted profile losses plotted versus exit Reynolds number for the Pack D-A and Pack D-F airfoils

other front loaded (Pack D-F). An exit Reynolds number of 128,000, which is typical of cruise conditions, was held for the designs of the Pack D airfoils. A Zweifel load coefficient of 1.40 was achieved with both Pack D designs. For reference the Pack B has a Zweifel load coefficient of approximately 1.15, where the load coefficient is defined as:

$$C_L = 2\frac{\tau}{b_x}\sin^2\beta_2\left(\frac{C_{x1}}{C_{x2}}\cot\beta_1 + \cot\beta_2\right) \quad (1)$$

In Eq. (1), τ is the pitch, b_x is the axial chord, β_1 and β_2 are the inlet and exit flow angles, and C_{x1} and C_{x2} are the inlet and exit axial velocities, respectively. Both the Pack D-A and D-F airfoils violated standard design practices at Pratt & Whitney for LPT designs. In addition, no airfoils were present in the database of cases used to develop the two transition models with $C_L > 1.2$. Finally, it was not necessary to use extrapolation of the transition models beyond their development space in the design of the Pack D airfoils

Low Mach number testing ($M < 3$) of the Pack D geometries was conducted with a passive-grid generated free stream turbulence level of 2% at an engine-specific turbulence length scale of approximately 10% of axial chord. Profile loss-versus-Reynolds-number data and transitional CFD predictions are shown in Fig. 4 for the Pack D-A airfoil. The data depicted in this figure are from Sjolander [26] and the computational results presented were performed *before* the experimental data were recorded (i.e., they are true pre-test predictions). As indicated by the loss data, the Pack D-A airfoil has a stall Reynolds number of approximately 120,000 for the free stream conditions considered. Transitional simulations accurately predict the stall Reynolds number for the Pack D-A airfoil in that the airfoil experienced non-reattaching separations for $Re_2 < 120{,}000$. Loss levels for Reynolds numbers higher than the stall Reynolds number are also well predicted. The significant under prediction of losses for Reynolds numbers below 120,000 is related to the fact that a steady solution could not be obtained once stall occurred. Also, the streamline topology shown in Fig. 4 for the lowest Reynolds number indicates that the separation in the stalled condition for this high-lift, aft-loaded design is more dramatic than that of the lower lift, mid-loaded Pack B design. As in the Pack-B validation study, time-accurate simulations were not run for Reynolds numbers below the stall value.

Also shown in Fig. 4 is the loss data for the Pack D-F airfoil with the same free stream conditions as those held for the Pack D-A testing. For the Reynolds numbers and free stream conditions considered in testing, the Pack D-F airfoil did not experience stall. The predicted loss levels are within the experimental uncertainty, for all Reynolds numbers for this airfoil. Additionally, the loss levels of the Pack D-F airfoil matched, with experimental uncertainty, those of the base line, Pack B design at all Reynolds numbers for the same flow conditions. The Pack B data are not shown in Fig. 4 for clarity. So, in addition to predicting the stall Reynolds number accurately for the Pack D-A design, the transition modeling capability predicted the performance benefits of a front-loaded design.

Figure 5 is a plot of measured and predicted static-pressure distributions for the aft region of the Pack D-F airfoil at $Re_2 = 56{,}000$ and the Pack D-A airfoil at $Re_2 = 160{,}000$. The local variation in the pressure distributions caused by laminar separations on both airfoils is evident in the data. These separation-related features in the static-pressure distributions are reasonably well captured by the transition modeling system. As the computational separation bubbles for both cases are very thin in the wall normal dimension, no streamline images were included in Fig. 5.

The results of the 2D steady validation effort show that, for systematic reductions in Reynolds number, the interplay of the attached- and separated-flow transition models captures loss-versus-Reynolds-number behavior for the test cases considered. In other words, the attached-flow model predicts transition in a manner that results in the formation of a laminar separation at the appropriate Reynolds number. Following the formation of a lami-

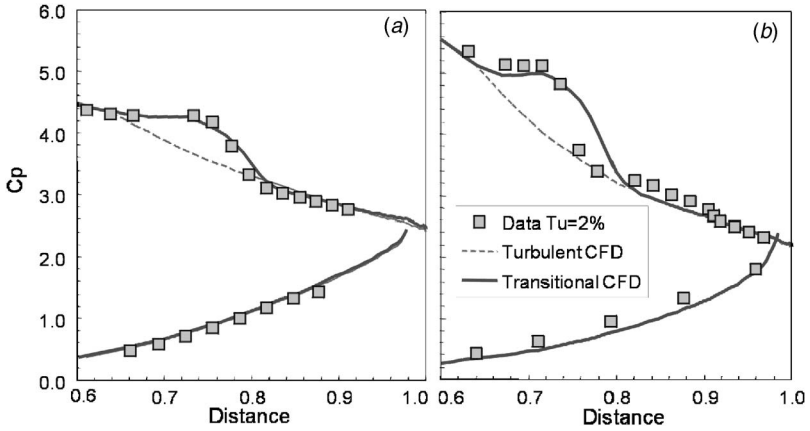

Fig. 5 Measured and predicted pressure loadings for the aft region of (*a*) the Pack D-F airfoil at $Re_2 = 56{,}000$ and (*b*) the Pack D-A airfoil at $Re_2 = 160{,}000$. Data are from Sjolander [26].

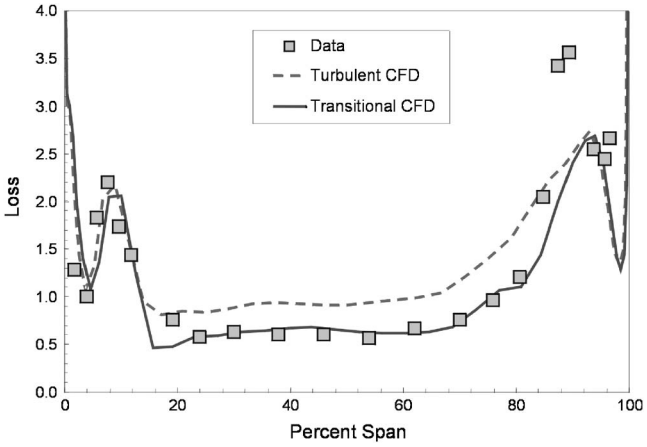

Fig. 6 Annular cascade loss-versus-span data with fully turbulent and transitional CFD predictions. Data are from Soderberg et al. (1988).

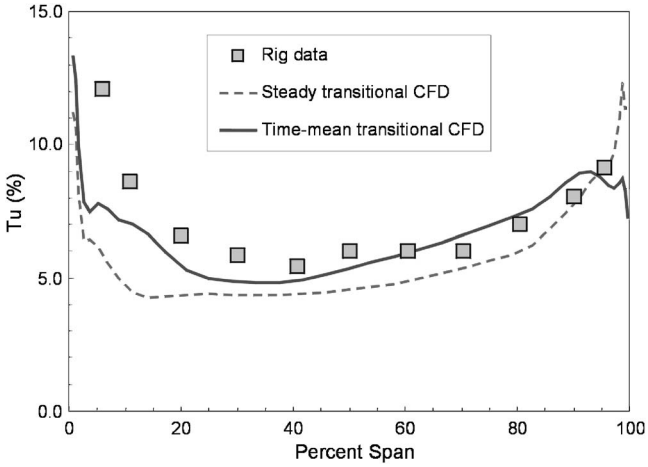

Fig. 7 Measured and predicted (steady and time-accurate) radial turbulence-intensity distributions downstream of the first two stages of a LPT rig. Data are from Binder et al. [27].

nar separation, the separated-flow model predicts the proper growth of the separation bubble with decreasing Reynolds number to the point of stall.

Steady 3D Validation Results

Building upon the 2D validation results, benchmarking was conducted against *spanwise* loss data that were obtained with actual LPT vane hardware. Spanwise loss data with turbulent and transitional CFD results are shown in Fig. 6. The flow conditions for the experiment were: $M_2=0.65$, $\mathrm{Re}_2=375{,}000$, and $Tu=2\%$. Distributions of k and ω that were physically consistent with the measured inlet end wall boundary layers were set at the inlet. Total-pressure losses are referenced to the inlet mid-span total pressure.

The transitional simulation provides a more accurate prediction (within 10%) in the 20–80 % span region compared to the fully turbulent simulation (50% over prediction). While the secondary losses are matched well in the inside-diameter (i.d.) region (0–20 % span), the peak secondary loss level is under predicted in the outside-diameter (o.d.) region by approximately 35%. The primary difference between the i.d. and o.d. geometries for this cascade was that the o.d. end wall was highly oblique relative to the airfoil stacking line as compared to the i.d. end wall.

Steady 3D Multi-Stage Validation Results

Critical to capturing the physics of attached- and separated-flow transition in a multi-stage environment is an ability to predict accurately the development of turbulence quantities through the machine. There is a paucity of experimental data in the open literature that can be used to validate the predictive capability developed here, but one useful study is that due to Binder et al. [27]. The authors measured spanwise profiles of turbulence intensity at various streamwise locations in a mutli-stage LPT rig. In Fig. 7 measurements are compared with levels predicted both with steady and time-resolved transitional simulations. The steady prediction is within 3% of the measured value between 20% and 80% of the span where the flow field is dominated by the wakes from upstream airfoil rows as opposed to secondary flows. The time mean of the time-accurate prediction is even better, falling within 1% over the same spanwise range. This gives some credence to the use of the k-ω turbulence model in conjunction with the transitional modeling capability for predicting the efficiency of multi-stage rigs. The largest inaccuracies obtained from the simulations occur at 5% span and the cause of this is unclear.

Steady multi-stage validation of the transition modeling capability was conducted with efficiency data from a four-stage LPT rig (Rig A) of a large commercial engine. As in the cascade benchmarking, inlet boundary layer turbulence quantities were set according to experimental data with $Tu=2\%$ in the free stream. The exit Reynolds number for the first vane in the rig was 200,000, which for this LPT is characteristic of cruise conditions. Figure 8 is a plot of the measured radial efficiency profile from the four-stage rig and the corresponding turbulent and transitional CFD results. End walls were modeled as "ideal" in that cavity and platform-overlap details were not considered in the geometry. Measured efficiency levels are matched to within ±0.25% between 40% and 70% span with the transitional simulation while the turbulent one under-predicts efficiency levels in this region by approximately 1%. The accuracy of the transitional simulation in the mid-span region is encouraging in that the development of the free stream turbulence and length scale through all eight rows of airfoils plays an important role in determining transition onset locations, and hence performance. The most pronounced deviation from data occurs in the o.d. region for both the transitional and turbulent simulations.

Cavity and main-gas-path interactions have been shown to play an important role in determining end wall efficiency levels both experimentally and computationally by Schlienger et al. [28] and Gier et al. [29]. However, since inter-row cavities were not mod-

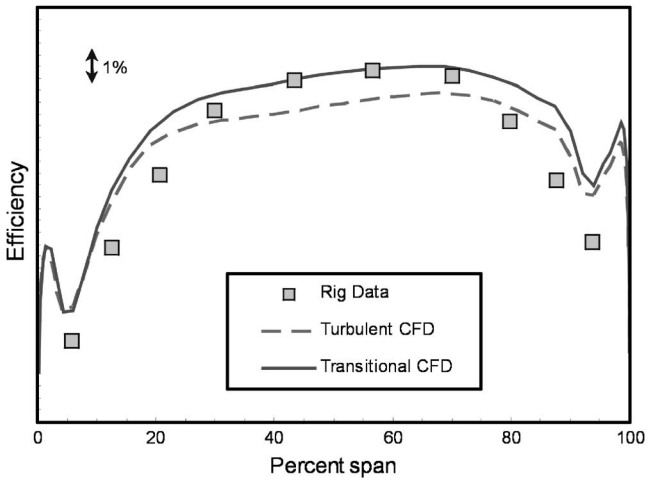

Fig. 8 Four-stage LPT rig (Rig A) efficiency-versus-span data at cruise conditions with fully turbulent and transitional steady CFD predictions

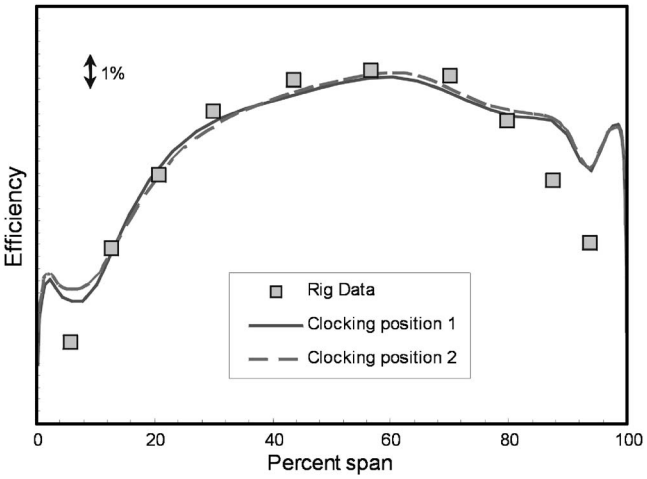

Fig. 9 Measured and predicted (time-accurate) efficiency-versus-span results for Rig A. Predictions for two clocking positions of the first stage at cruise conditions are shown.

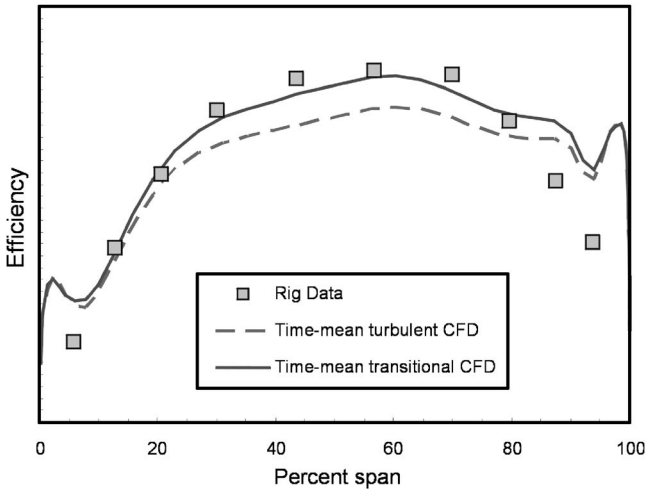

Fig. 10 Rig A efficiency-versus-span data with time-accurate transitional and turbulent CFD predictions at clocking position 1 at cruise conditions

eled for this study, the losses associated with cavity/main-gas-path interactions are not present in the simulations. So, at least part of the over prediction of end wall efficiency levels is due to the ideal-end wall simplifications in the simulations.

Time-Accurate 3D Multistage Validation Results

Time-accurate transitional simulations of Rig A were performed to assess the behavior and accuracy of the transition modeling in an unsteady environment. Again, ideal end walls were assumed for all time-accurate simulations. Airfoil counts for each row of airfoils in the LPT were such that a half-wheel simulation would have been needed for a true-count prediction with circumferentially periodic boundaries. As a result, airfoil scaling was employed to reduce the total number of passages modeled in the simulations. However, the airfoil counts were selected to keep the level of scaling to less than 7% on a row-by-row basis. Comparing spanwise efficiency profiles from steady transitional simulations run with and without airfoil scaling revealed no more than a 0.14% variation in local efficiency between scaled and un-scaled cases. Additionally, the integrated efficiency levels of the scaled and un-scaled steady cases were within 0.02% of each other.

Alteration of airfoil counts necessitated an evaluation of clocking effects that might be present in the scaled simulation and not in the experiment. To accomplish this, both rows of the first stage were indexed through one pitch by increments of 20% of local pitch. As clocking effects are thought to have a pronounced effect on boundary-layer transition behavior (see, e.g., Sharma et al. [30] and Höhn and Heinig [13]), transitional CFD was employed for the clocking study. Typically 20 periodic cycles were required for convergence of the LPT efficiency signal with 100 time steps per blade passing. The resulting time-mean integrated efficiency levels, for all clocking positions considered, varied by less than ±0.05%. Spanwise efficiency profiles corresponding to the two most disparate clocking positions are shown in Fig. 9. There are minimal variations, at any spanwise location, related to the first stage clocking. These results are consistent with the fact that the vortexing of the original design was not tailored to take advantage of clocking effects. Based on the weak effect of clocking from the first-stage study, clocking effects of the second and third stages were not investigated.

Figure 10 is a plot of efficiency-versus-span data for Rig A as compared to time-accurate transitional and turbulent CFD predictions at clocking position 1. Similar to the steady results, the mid-span efficiency levels are better matched with the transitional simulation. The time-accurate transitional simulation provides a significant improvement in accuracy for the 10–30 % span region over the steady transitional results. Note that the same efficiency variations between steady turbulent and steady transitional simulations exist for the time-accurate simulations. This suggests that wall-bounded loss generating mechanisms are not the primary cause of the differences between the steady and time-mean efficiency profiles. Also, as described by Denton [31], the acceleration or deceleration of a velocity defect can cause increased or decreased loss generation associated with the mixing process. So, a possible cause for the poorer accuracy of the steady simulations, as compared to the time-accurate results, is believed to be the assumptions associated with the mixing-plane implementation. The mixing-plane calculation assumes a zero pressure-gradient condition for the mixing calculation at each row interface, which is not valid for the case in which distortions are convected through potential fields of downstream rows. Work is currently under way to determine if this effect is in fact responsible for the variations in predicted efficiency levels between steady and time-accurate simulations.

Specific information of the character of the predicted mid-span transition location on the suction side of a select airfoil for Rig A is shown in Fig. 11. In the steady prediction, the boundary layer was predicted to experience laminar separation and turbulent reattachment at approximately 70% and 78% of the total surface

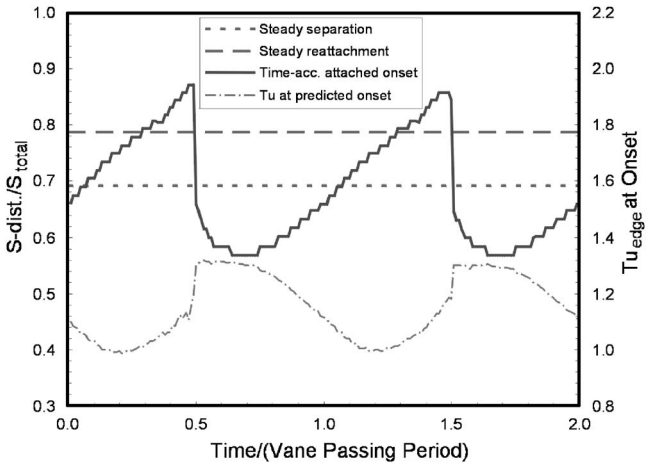

Fig. 11 Mid-span transition information from the second row of steady and time-accurate simulations of Rig A

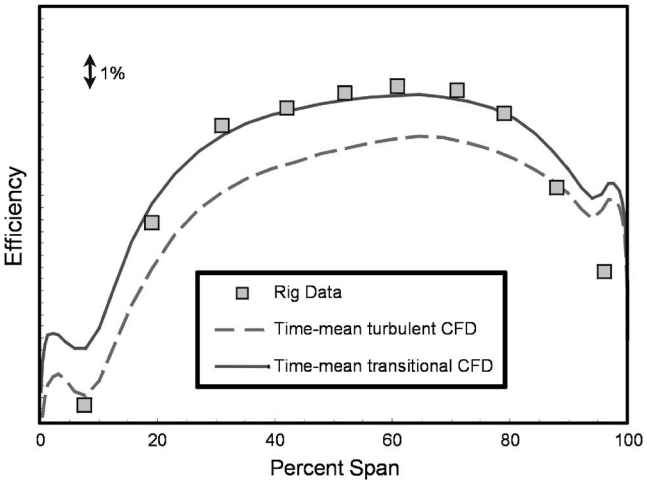

Fig. 12 Rig B efficiency-versus-span data at cruise conditions. Time-accurate predictions are shown.

distance, respectively. However, when run in time-accurate mode, the simulation predicted a complete suppression of the separation. Instead, attached-flow transition was predicted, and the transition-onset location fluctuated with time in response to the wake impingement from the upstream row. Both the onset location and the local free stream turbulence level at the edge of the boundary layer are also plotted against time in Fig. 11. It is interesting to note that at some instances the boundary layer remained attached while experiencing a predicted transition onset location father aft than both the separation and reattachment locations predicted in the steady simulation. Also, while there is no provision in the code for modeling the effect of the becalmed region that is known to follow an impinging wake on the airfoil suction side (see, e.g., Mayle [17]), the periodic-unsteady flow does appear to have a significant effect on the resistance of the boundary layer to separation.

Efficiency-versus-span data for a *second* LPT rig, Rig B, is shown in Fig. 12. Time-accurate turbulent and transitional predictions are also shown. This rig is also from a large commercial engine and was run at an exit Reynolds number for the first vane equal to 170,000, which again is characteristic of cruise conditions. As in the case of the previously presented time-accurate rig results, the transitional simulation provides the most accurate prediction between 10% and 80% span. Also, the most pronounced inaccuracies produced by the transitional simulation occur in the end wall regions. In contrast to the transitional results, the fully turbulent assumption results in as much as a 2% under prediction of the efficiency between 10% and 80% span.

Results presented for the LPT rigs considered in this report are typical of results obtained from steady and time-accurate comparative studies performed with other LPT rig data sets where end wall losses did not propagate into the mid-span region. For two other LPTs considered in the validation effort (and not reported here) that had either lower airfoil aspect ratios or unusually high levels of end wall steepness, penetration of end wall losses into the mid-span region confounded the interpretation of the benchmaking results.

Integrated Efficiency Predictions

Figures 13(*a*) and 13(*b*) are plots of measured-versus-predicted LPT efficiencies from fully turbulent and transitional CFD simulations, respectively. All predicted values plotted in Fig. 13 were obtained from steady CFD simulations. Based on these results, steady transitional simulations more accurately capture the performance differences between design points than the turbulent simulations. This is most obvious in the case with the largest variation

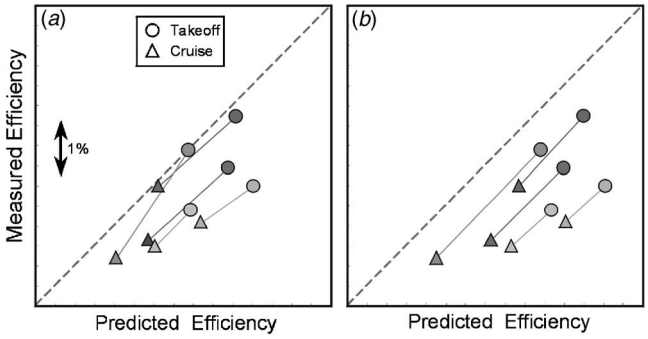

Fig. 13 Measured-versus-predicted integrated efficiencies for five LPTs at takeoff and cruise conditions. Fully turbulent results are shown in (*a*) and transitional results are shown in (*b*).

between the measured takeoff and cruise efficiencies of 1.7%. The efficiency delta for this case predicted by turbulent simulations is 1.1% while the transitional simulations predict a 1.7% delta. That the transitional simulations predict accurate efficiency deltas for a given configuration suggests that the loss mechanisms that are not modeled accurately in the transitional simulations are relatively, compared to profile losses, independent of Reynolds number.

An important feature of Figs. 13(*a*) and 13(*b*) is that the accuracy of the transitional simulations is, on average, less than that of fully turbulent ones. Reviewing the spanwise-efficiency validation results such as those in Fig. 8, the cause for the lower accuracy in absolute efficiency predictions associated with transitional simulations becomes apparent. Fully turbulent simulations under predict mid-span efficiency levels, which in turn compensates for the over prediction of efficiency levels in end wall regions (Fig. 8). So, the fact that turbulent simulations appear to provide more accurate efficiency predictions is both fortuitous and spurious.

Measured-versus-predicted *mid-span* efficiency levels from steady turbulent and steady transitional simulations of a number of LPTs are shown in Figs. 14(*a*) and 14(*b*), respectively. Mid-span efficiency levels were obtained by integrating both measured and predicted levels over the central 20% of span. Note that one of the cases presented in Fig. 14 is for a low Reynolds number condition that results in stalled airfoils in the transitional simulation. In Fig. 14(*a*), turbulent predictions result in as much as a 2% under prediction of mid-span efficiencies. In contrast, the transitional simulations are within approximately 0.25% of measured levels. These comparisons indicate that profile losses, and hence the transitional nature of the airfoil boundary layers, are most accurately modeled in the transitional simulations. Since only small variations between steady and time-accurate predictions of mid-span efficiencies exist (Figs. 8 and 10), Fig. 14(*b*) changes little if plotted for time-accurate simulations.

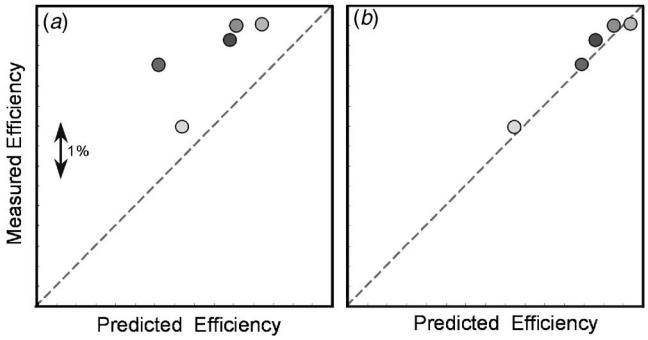

Fig. 14 Measured-versus-predicted *mid-span* efficiencies for four LPTs. Fully turbulent results are shown in (*a*) and transitional results are shown in (*b*).

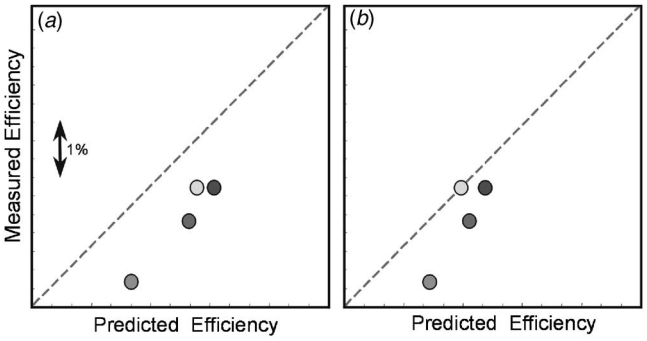

Fig. 15 Measured-versus-predicted integrated efficiencies for three LPTs. Steady transitional results are shown in (*a*) and time-accurate transitional results are shown in (*b*).

Spanwise-integrated steady efficiency predictions of a limited number of the LPTs are compared to measured levels in Fig. 15(*a*) while time-accurate results for the same LPTs are shown in Fig. 15(*b*). The efficiency over predictions for time-accurate simulations are, on average, approximately half those from steady transitional simulations. These results are consistent with the comparisons made between steady and time-accurate spanwise efficiency results for the four-stage LPT rig presented in the preceding section.

It was shown in previous sections of this paper that secondary loss predictions from the CFD simulations can be inaccurate for annular cascade data, particularly in the o.d. region (e.g., see Fig. 6.). Since secondary losses are generally known to be independent of Reynolds number, it is believed that the inability of the RANS simulations presented here to capture accurately the end wall losses, contributes to the inaccurate absolute efficiency predictions. An additional cause for the poor absolute predictions is believed to be the simplified geometric modeling of the end walls. However, the primary cause for over-predicted efficiency levels from steady simulations (as presented here) may be attributable to assumptions made in the inter-row mixing-plane implementation. This was demonstrated in the significant reductions in efficiency over predictions between steady and time-accurate simulations (Fig. 15).

Conclusions

Three levels of fidelity that might be provided by RANS simulations for efficiency predictions of turbomachinery components are: (1) absolute efficiency levels, (2) performance differences between designs, and (3) efficiency deltas between operating points for a given design. The goal of this work was to model the transitional nature of boundary layers on turbomachinery airfoils in RANS simulations to determine if efficiency-prediction improvements could be realized in any of the aforementioned categories. Attached- and separated-flow transition models, developed in Part I of this paper, were incorporated into a RANS-based system for airfoil design, and a validation and benchmarking study was conducted.

The transition models were implemented here using point-wise trips with no transition length modeling or use of the universal intermittency distribution. The models provided a significant improvement in the accuracy of predicted profile losses for both cascades and multi-stage LPT rigs over the fully turbulent assumption. Validation against cascade data also demonstrated that the new modeling capability accurately captures the interplay between the physics of attached- and separated-flow transition modes for the test cases considered. To further demonstrate the modeling capabilities, two low-pressure turbine airfoils were designed that had Zweifel load coefficients of 1.4 (a 25% increase over the base line level). The stall Reynolds numbers of both airfoils were accurately predicted with the transition-modeling capability in advance of testing. Further, one design (i.e., the front-loaded one) was resistant to stall for *exit* Reynolds numbers below 50,000 while also matching the performance level of the base line design. So, by incorporating modeling of the physics of transition into the design system at an adequate level, it was demonstrated that the design space for LPT airfoils was significantly extended.

More accurate predictions of profile losses were demonstrated both for airfoils that experienced attached-flow transition (where fully turbulent RANS over predicts loss) and for those that experienced separated-flow transition (where fully turbulent RANS under predicts loss). However, considering the relative merits of the attached- and separated-flow models, it appears that the former is more effective than the latter. This is not surprising since, as seen in Part I of this work [10], the attached-flow model is grounded in the basic physics of bypass transition, while the separated-flow model is more of a straightforward correlation of variables. Consequently, the authors believe that future work should focus on modeling separated flow transition. In addition, a modeling capability that captures the effects of surface roughness on pre-transitional boundary layers is needed.

It was found that the addition of transition modeling to the design system proved effective for determining efficiency deltas between design points and profile losses for individual low-pressure turbines. No improvements were realized concerning the accuracy of predicted *absolute* levels of efficiency and the ability to predict efficiency deltas between engine designs. However, the ability to predict mid-span performance allows one to infer much about secondary-flow and cavity/main-gas-path interaction loss mechanisms and the ability of RANS simulations, employing two-equation turbulence models and ideal end walls, to capture them properly. This means that, particularly for low-aspect-ratio components, further work is necessary in the pursuit of accurate predictions of secondary-flows and cavity/main-gas-path interactions.

Acknowledgment

The authors would like to thank Pratt & Whitney for granting permission to publish this work. In particular, they are grateful to Dr. Jayant Sabnis, Gary Stetson, and Joel Wagner for their support. Inspiration for this work is a result of the authors' participation in the Minnowbrook conferences that are sponsored by the U.S. Air Force Office of Scientific Research and NASA (see, e.g., NASA CP 1998-206958). Professor T. V. Jones and Professor Jim S.-J. Chen taught the authors the importance of starting any technical effort from basic principles, and additional insights were gleaned from discussions with A. A. Rangwalla, M. F. Blair, F. Ames, T. Fukuda, O. P. Sharma, S. S. Magge, D. Zhang, G. Barter, and J. Dailey.

References

[1] Greitzer, E. M., Tan, C. S., Wisler, D. C., Adamczyk, J. J., and Strazisar, A. J., 1994, "Unsteady Flows in Turbomachines: Where's the Beef?" *Unsteady Flows in Aeropropulsion*, ASME AD-40, New York, pp. 1–11.
[2] Hodson, H. P., 1984, "Boundary Layer and Loss Measurements on the Rotor of an Axial-Flow Turbine," ASME J. Eng. Gas Turbines Power, **106**, pp. 391–399.
[3] Doorly, D. J., and Oldfield, M. L. G., 1985, "Simulation of Wake Passing in a Stationary Turbine Rotor Cascade," AIAA J. Propulsion, Vol. **1**(4), pp. 316–318.
[4] LaGraff, J. E., Ashworth, D. A., and Schultz, D. L., 1989, "Measurement and Modeling of the Gas Turbine Blade Transition Process as Disturbed by Wakes," ASME J. Turbomach., **111**, pp. 315–322.
[5] Halstead, D. E., Wisler, D. C., Okiishi, T. H., Walker, G. J., Hodson, H. P., and Shin, H. W., 1997, "Boundary Layer Development in Axial Compressors and Turbines: Part 1 of 4—Composite Picture," ASME J. Turbomach., **119**, pp. 114–126.
[6] Halstead, D. E., Wisler, D. C., Okiishi, T. H., Walker, G. J., Hodson, H. P., and Shin, H. W., 1997, "Boundary Layer Development in Axial Compressors and Turbines: Part 3 of 4—LP Turbines," ASME J. Turbomach., **119**, pp. 225–237.
[7] Wadia, A., 2003, personal communication.
[8] Sharma, O. P., Wells, R. A., Schlinker, R. H., and Bailey, D. A., 1982, "Boundary Layer Development on Airfoil Suction Surfaces," ASME J. Eng. Power, **104**, pp. 698–706.

[9] LaGraff, J. E., and Ashpis, D. E., editors, 1998, "Minnowbrook II: 1997 Workshop on Boundary Layer Transition in Turbomachines," NASA/CP-1998–206958.
[10] Praisner, T. J., and Clark, J. P., 2004, "Predicting Transition in Turbomachinery, Part I—A Review and New Model Development," ASME Report No. GT-2004–54108.
[11] Dorney, D. J., and Ashpis, D. E., 1998, "Study of Low Reynolds Number Effects on the Losses in Low-Pressure Turbine Blade Rows," AIAA Paper No. 98–3575.
[12] Gier, J., Ardey, S., and Heisler, A., 2000, "Analysis of Complex Three-Dimensional Flow in a Three-Stage LP Turbine by Means of Transitional Navier-Stokes Simulation," ASME Paper No. 2000GT-645.
[13] Höhn, W., and Heinig, K., 2000, "Numerical and Experimental Investigation of Unsteady Flow Interaction in a Low Pressure Multistage Turbine," ASME Paper No. 2000-GT-437.
[14] Thermann, H., Mueller, M., and Niehuis, R., 2001, "Numerical Simulation of Boundary Layer Transition in Turbomachinery Flows," ASME Paper No. 2001-GT-0475.
[15] Roux, J., Lefebvre, M., and Liamis, N., 2002, "Unsteady and Calming Effects Investigation on a Very High Lift LP Turbine Blade—Part II: Numerical Analysis," ASME Paper No. GT-2002–30228.
[16] Walker, G. J., Henderson, A. D., Hughes, J. D., and Coupland, J., 2003, "Modeling of Unsteady Transitional Flow on Axial Compressor Blades," NASA/TM-2004-212913, p. 57.
[17] Mayle, R. E., 1991, "The Role of Laminar Turbulent Transition in Gas Turbine Engines," ASME J. Turbomach., **113**, pp. 509–537.
[18] Ni, R. H., 1982, "A Multiple-Grid Scheme for Solving the Euler Equations," AIAA J., **20**(11), pp. 1565–1571.
[19] Ni, R. H., and Bogoian, J. C., 1989, "Prediction of 3-D Multistage Turbine Flowfield Using a Multiple-Grid Euler Solver," AIAA Paper No. 89–0203.
[20] Davis, R. L., Shang, T., Buteau, J., and Ni, R. H., 1996, "Prediction of 3-D Unsteady Flow in Multi-Stage Turbomachinery Using an Implicit Dual Time-Step Approach," AIAA Paper No. 96–2565.
[21] Wilcox, D. C., 1998, *Turbulence Modeling for CFD*, 2nd ed., DCW Industries, La Canada, CA.
[22] Arts, T., de Rouvroit, L. M., and Rutherford, A. W., 1990, "Aero-Thermal Investigation of a Highly Loaded Transonic Linear Turbine Guide Vane Cascade," von Karman Institute for Fluids Dynamics Technical Note No. 174.
[23] Narasimha, R., 1985, "The Laminar Turbulent Transition Zone in the Boundary Layer," Prog. Aerosp. Sci., **22**, pp. 29–80.
[24] Narasimha, R., 1991, "Recent Advances in the Dynamics of the Transition Zone," ISABE Report No. 91–7006.
[25] Bons, J. P., Sondergaard, R., and Rivir, R., 2001, "The Fluid Dynamics of LPT Blade Separation Control Using Pulsed Jets," ASME Paper No. 2001-GT-0190.
[26] Sjolander, S., 2003, personal communication.
[27] Binder, A., Schröder, T. H., and Hourmouziadis, J., 1988, "Turbulence Measurements in a Multistage Low-Pressure Turbine," ASME Paper No. 88-GT-79.
[28] Schlienger, J., Pfau, A., Kalfas, A. I., and Abhari, R. S., 2003, "Effects of Labyrinth Seal Variation on Multistage Axial Turbine Flow," ASME Paper No. GT-2003–38270.
[29] Gier, J., Stubert, B., Brouillet, B., and de Vito, L., 2003, "Interaction of Shroud Leakage Flow and Main Flow in a Three-Stage LP Turbine," ASME Paper No. GT2003–38025.
[30] Sharma, O. P., Ni, R. H., and Tanrikut, S., 1994, "Unsteady Flows in Turbines—Impact on Design Procedure," in AGARD Lecture Series 195, Turbomachinery Design Using CFD.
[31] Denton, J. D., 1993, "Loss Mechanisms in Turbomachines," ASME J. Turbomach., **115**, pp. 621–656.

Experimental and Computational Comparisons of Fan-Shaped Film Cooling on a Turbine Vane Surface

W. Colban

K. A. Thole

Mechanical Engineering Department,
Virginia Tech,
Blacksburg, VA

M. Haendler
Siemens Power Generation,
Muelheim a. d. Ruhr, Germany

The flow exiting the combustor in a gas turbine engine is considerably hotter than the melting temperature of the turbine section components, of which the turbine nozzle guide vanes see the hottest gas temperatures. One method used to cool the vanes is to use rows of film-cooling holes to inject bleed air that is lower in temperature through an array of discrete holes onto the vane surface. The purpose of this study was to evaluate the row-by-row interaction of fan-shaped holes as compared to the performance of a single row of fan-shaped holes in the same locations. This study presents adiabatic film-cooling effectiveness measurements from a scaled-up, two-passage vane cascade. High-resolution film-cooling measurements were made with an infrared camera at a number of engine representative flow conditions. Computational fluid dynamics predictions were also made to evaluate the performance of some of the current turbulence models in predicting a complex flow such as turbine film-cooling. The renormalization group (RNG) k-ε turbulence model gave a closer prediction of the overall level of film effectiveness, while the v^2-f turbulence model gave a more accurate representation of the flow physics seen in the experiments. [DOI: 10.1115/1.2370747]

Introduction

The nozzle guide vanes in a gas turbine, located directly downstream of the combustion section, are particularly susceptible to thermal failure, with gas temperatures commonly reaching levels above component latent melting temperatures. Combustion temperatures continue to rise in an effort to increase the efficiency and power output from gas turbine engines. This rise has led to the increased demand to devise better cooling schemes and more resilient materials from which to manufacture the turbine vanes. Many cooling strategies are typically used at the same time, including impingement cooling, internal passage cooling, and external film cooling. Although designing various cooling configurations, consideration must also be given to the structural integrity of the vanes, since turbine vanes are under extremely high thermal stresses.

Ideally, film cooling aims to inject cooler temperature fluid over the surface of the vane, shielding it from the high-temperature freestream gases. This goal is sometimes difficult to achieve, however, as the nature of the flow through the turbine passage tends to be uncompromising with conditions, including high freestream turbulence, secondary flows, high surface curvature, rapid flow acceleration, and high-pressure gradients, all of which have been shown to affect cooling performance. Film cooling offers the engine designer an enticing way to extend part life; however, the use of too much coolant flow from the compressor takes a toll on the overall engine efficiency. To counteract this consequence, engine designers are constantly on the lookout for ways to maintain or even increase the cooling performance but with less coolant.

Alternative hole geometries are sometimes used by engine designers, such as the diffused or so-called fan-shaped holes, to maximize the performance of the injected coolant. By expanding the exit of the cooling hole in the lateral direction, the effective momentum of the surface coolant can be reduced prior to injection. Goldstein et al. [1] showed that fan-shaped holes provide better surface attachment at higher blowing ratios, as well as better lateral spreading of the coolant than cylindrical holes. A slight deviation of this design is the laidback fan-shaped hole, wherein a forward expansion is also included, further inhibiting jet liftoff. The major drawback for noncylindrical hole geometries is increased initial manufacturing costs. The benefits, however, of fan-shaped holes are many, including increased part life (fewer replacements needed), less required coolant (increased engine efficiency), and fewer holes needed (increased structural stability of the vane).

Computational fluid dynamics (CFD) is becoming an essential design tool in the gas turbine industry because it is both cheaper and faster than performing experiments. However, in order to rely on CFD results, it is first necessary to validate the predictions with measurements to ensure computational reliability. In this study, detailed comparisons of the measured adiabatic effectiveness data are made to CFD predictions using both the renormalization group (RNG) k-ε and v^2-f turbulence models.

The standard k-ε turbulence model is a Reynolds-averaged Navier-Stokes (RANS) model with two transport equations—one for the turbulent kinetic energy (k) and one for the eddy viscosity (ε)—which are used to approximate the turbulent viscosity (μ_t). The RNG k-ε model involves renormalization group theory and adds a term to the eddy viscosity transport equation, which makes the model better for high strain flows than the standard k-ε model. One major drawback of the RNG k-ε model in wall-bounded flows, such as film cooling, is the assumption of isotropic turbulence. The existence of the wall introduces anisotropy in the normal fluctuations, the presence of which are not accounted for in the wall functions used to approximate the behavior in the boundary layer in the k-ε turbulence models. Wall functions lose their reliability in three-dimensions or separated flow regimes, such as sometimes seen in film cooling.

Durbin [2] incorporated turbulence anisotropy in the near wall region into the existing k-ε RANS model by adding two transport equations—one for the normal fluctuations (v^2) and one for an elliptic relaxation function (f)—and effectively removed the ne-

Contributed by the Turbomachinery Division of ASME for publication in the JOURNAL OF TURBOMACHINERY. Manuscript received January 12, 2006; final manuscript received January 29, 2006. Review conducted by D. Wisler.

cessity of wall functions. The v^2-f turbulence model correctly models the blocking phenomenon near the wall that is responsible for attenuating the normal turbulent fluctuations, eliminating the requirement of damping functions in wall bounded flows.

Film-cooling effectiveness has been predicted using both the RNG k-ε and the v^2-f turbulence models in our paper. The complete passage, including the contoured end wall was modeled in the RNG k-ε simulation for a baseline case. A spanwise periodic section of the vane passage was modeled using the v^2-f turbulence model for the same blowing ratios that were measured experimentally.

This study is the first to present detailed high-resolution adiabatic film-cooling effectiveness measurements for a turbine vane with multiple rows of fan-shaped film-cooling holes at engine representative blowing ratios. Contours and laterally averaged values of adiabatic film-cooling effectiveness are presented for both the pressure and suction sides. Adiabatic film-cooling effectiveness data are critical information for engine designers, necessary to predict not only metal temperatures but also to validate CFD predictions.

Past Studies

Because of its crucial role in preventing thermal failure in gas turbine engines, film cooling has been an extensively researched topic over the last 30–35 years [3,4]. Flat-plate studies have encompassed a variation of every possible geometrical parameter, including surface angle, entrance length, hole spacing, compound angle, lateral expansion angle, forward expansion angle, area ratio, and multiple row configurations. External conditions have also been thoroughly investigated for flat plates, including such effects as turbulence intensity, pressure gradient, and the state of the approaching boundary layer. An excellent review of the relevant shaped hole literature, which primarily focused on flat-plate studies, was given by Bunker [5]. Although flat plate studies are a key first step in understanding the flow physics for a given cooling hole geometry, to completely understand the flow physics and evaluate a given film-cooling design, it must be tested on the actual turbine vane. It stands to reason that the flow physics on a highly curved surface, such as a turbine vane, coupled with multiple cooling row interaction, could yield results that are different from the flat-plate special case. Some studies have presented results for partially and/or fully cooled nozzle guide vanes, but the deficiency of many of those studies is the lack of high-resolution effectiveness measurements.

Studies involving a single row of fan-shaped cooling holes on a vane surface have been performed by Zhang et al. [6], Zhang and Pudupatty [7], and Colban et al. [8]. Using the same experimental procedure and facilities for both studies, effectiveness measurements were made with fan-shaped holes on the suction side by Zhang et al. [6] and on the pressure side by Zhang and Pudupatty [7]. Results indicated an increase in effectiveness on the suction side for the blowing ratio range from 0.5 to 1.5 and a decrease in effectiveness on the pressure side for the blowing ratio range from 1.5 to 2.5.

Colban et al. [8] presented adiabatic effectiveness measurements for eight single rows of fan-shaped holes on both the pressure and suction sides in the same facilities as this paper. Their results indicated that in regions of high convex curvature, particularly on the suction side near the leading edge, jet liftoff was prevalent and increased with blowing ratio. Colban et al. [8] also noted a decrease in effectiveness with increased blowing on the pressure side, which was attributed to partial jet liftoff and hot gas entrainment.

Despite the knowledge gained by studying single-row cooling on the vane, it is still necessary to study multiple-row film cooling on the vane. Goldstein et al. [9] showed that on a flat plate, a single row of cooling holes separated with increasing blowing ratio, resulting in decreased film effectiveness. However, with a double-row cooling configuration, the upstream row provided the impetus for the downstream row to stay attached to the surface. This resulted in an increased film effectiveness with blowing ratio. The study by Goldstein et al. [9] suggested that an accurate study of vane film cooling would not be complete unless all of the engine-present film-cooling rows were tested together.

Effectiveness measurements were made by Guo et al. [10] in a transonic facility for a turbine airfoil with multiple rows of fan-shaped holes. Results showed higher values of effectiveness for fan-shaped holes than for cylindrical holes. However, the decay in effectiveness on the pressure side was faster for fan-shaped than for cylindrical holes, which was most likely the result of a better lateral coverage for the fan-shaped holes. Sargison et al. [11] also measured effectiveness in an annular turbine cascade with multiple rows of cylindrical, fan-shaped, and converging slot holes. They reported similar levels of performance for the fan-shaped and converging slot holes, both of which had superior performance than cylindrical holes.

Effectiveness measurements on the pressure side were made for three rows of fan-shaped holes and isothermal showerhead blowing by Schnieder et al. [12]. They reported that the presence of isothermal showerhead blowing caused increased mixing of the first pressure side row, lowering effectiveness. However, with showerhead cooling, perhaps the increased mixing of the first pressure side row might actually improve effectiveness. Polanka et al. [13] also studied the effect of showerhead blowing on the first downstream pressure side row, using cylindrical instead of fan-shaped holes. They reported that showerhead blowing caused the jets to stay attached, where they would normally separate without upstream blowing. Polanka et al. [13] suggested that increased turbulent mixing caused by the showerhead dispersed the jet toward the wall, reducing liftoff.

Colban et al. [8] presented effectiveness for fan-shaped holes combined with upstream showerhead blowing. Their results indicated that upstream showerhead blowing increased jet dispersion toward the vane surface for the first row of film-cooling holes downstream on the pressure side, a result consistent with the results of Polanka et al. [13]. Although Colban et al. [8] presented a complete set of high-resolution data for single-row fan-shaped holes on a turbine vane, it is further necessary to understand the row-to-row interaction, as the state of the approaching boundary layer has been shown to have a significant effect on the performance of a film-cooling jet [14].

There have been a limited number of computational studies involving shaped hole film cooling on a flat plate. Kohli and Thole [15] used the standard k-ε model with nonequilibrium wall functions to show the importance of modeling the interior plenum conditions correctly. A similar flat-plate study was performed by Hyams and Leylek [16], who investigated the effect of hole geometry on the thermal and flow field using the high Reynolds number k-ε model with generalized wall functions. They showed that laterally diffused shaped holes had the highest adiabatic effectiveness levels downstream of the hole exit location.

Computational film-cooling studies on a turbine vane surface with fan-shaped holes have been done by Hildebrandt et al. [17], Ferguson et al. [18], and Heidmann et al. [19]. Only Heidmann et al. [19], however, modeled more than one row of holes on the vane. Their study used the k-ε model to simulate a periodic section of the vane with six staggered rows of cylindrical showerhead holes, four rows of fan-shaped holes on the pressure side, and two rows of cylindrical holes on the suction side. The numerical results presented by Heidmann et al. [19] were not validated with experiments; thus, the validity of the method was not established. The single-row numerical results of Ferguson et al. [18] showed good agreement with experimental results for blowing ratios of <1.5 using the RNG k-ε model with a two-layer wall treatment. Above a blowing ratio of 1.5, the agreement was not so good.

Nothing, to the author's knowledge, as of yet has been published applying the v^2-f turbulence model to film-cooling flow applications. However, because the v^2-f model is valid all the way

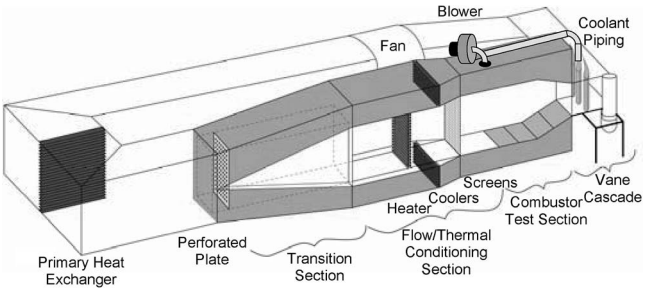

Fig. 1 Schematic of the low-speed recirculating wind tunnel facility

to the wall, with no need for wall functions or damping models in the viscous sublayer, it stands to reason that it should be expected to perform at least as good as the existing two-equation models if not better. The v^2-f model has been used with success in modeling three-dimensional turbulent boundary layers [20] as well as separated flow conditions, such as the backward-facing step and vortex shedding flows [21].

Of the previous fan-shaped film-cooling studies that have been performed on a vane, the obvious deficiency is for high-resolution data for the fully cooled situation. This study offers the first completely cooled turbine vane study with fan shaped film cooling giving detailed experimental adiabatic film cooling effectiveness results. Similarly, past computational studies of film cooling have been limited in their scope.

Experimental Facilities

The experiments were performed in the VTExCCL large-scale, low-speed, recirculating wind tunnel facility shown in Fig. 1. This facility was identical to the one used by Colban et al. [8] and was described in detail by that study. The main features of the facility were a flow split section that divided the flow into two channels, one that was heated to by a 55 kW heater bank and used as the mainstream combustor exit flow and the other that was cooled using a 40 kW chiller in series with a heat exchanger and used as coolant flow.

The test section was a linear, two-passage cascade with a contoured upper end wall. The inlet freestream turbulence intensity was measured to be 1.2% a distance of 0.2 C upstream of the vane leading edge with a hot wire anemometer. Typical mainstream temperature was 60°C, with a nominal difference between the mainstream and coolant of 20°C, yielding a density ratio of 1.06. The pressure at the test section inlet was nearly atmospheric. A list of pertinent geometrical parameters for the test section is given in Table 1, along with certain relevant inlet conditions.

Test Section Design. To match the engine static pressure distribution around the vane to that found in the engine, a contoured surface was implemented for the upper end wall. The contoured end wall, which contracted to roughly 54% of the inlet span height, is shown schematically and graphically in Fig. 2. A detailed account of the contour design was given by Colban et al.

Table 1 Operating conditions and vane parameters

Scale	3X
C (m)	0.53
$S_{max,PS}$ (m)	0.52
$S_{max,SS}$ (m)	0.68
U_{inlet} (m/s)	10
Re_{inlet} (-)	3.0×10^5
ΔT_{FC} (°C)	20
Vane pitch (m)	0.465

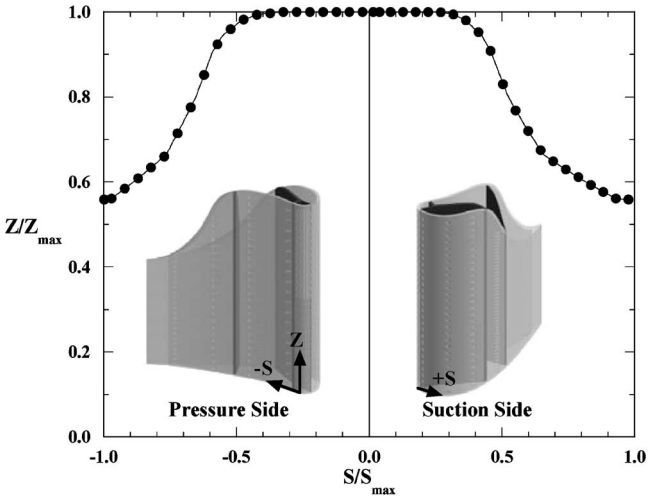

Fig. 2 Contoured end-wall surface definition

[8]. The contoured end wall resulted in an excellent match of the experimental static pressure distribution at the midspan to that of the engine. Also, since this investigation was not focused on any three-dimensional effects of the contour on the vane cooling, a rigorous investigation, including CFD predictions and experimental examination, was used to verify the presence of a two-dimensional flow regime in the area where the measurements were taken. All of the film-cooling effectiveness measurements were made between 5% and 32% span, while the flow was essentially two-dimensional below 40% span.

A schematic of the vane test section is shown in Fig. 3. Bleed valves were used to ensure flow periodicity between the two passages, and the flexible wall was used to make minor adjustments to the flow distribution around the center vane. Also shown in Fig. 3 are the plenum locations relative to the holes, as well as the hole designations, to be used throughout the rest of the report.

A detailed discussion of the vane design and construction was given by Colban et al. [8]. The vane contained four interior plenums, which allowed for flow-rate control among the rows of holes to obtain the desired blowing ratio distribution. Coolant was supplied to the plenums from the upper channel in the wind tunnel using the blower shown in Fig. 1. Discharge coefficients, which were presented in the study of Colban et al. [8], were used to set the combined flow rates through each plenum based on the desired blowing ratios.

The test vane contained showerhead cooling with five in-line rows, four fan-shaped pressure side rows, and four fan-shaped suction side rows of film-cooling holes. The diameter of the cylindrical inlet section of the fan-shaped holes was 0.38 ± 0.015 cm. The diameters of each hole were measured to verify that the correct flow area was used to determine the total mass flow rate and individual blowing ratios because of slight manufacturing varia-

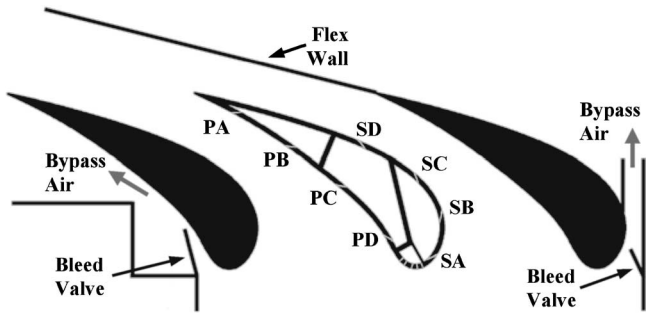

Fig. 3 Schematic of experimental test section

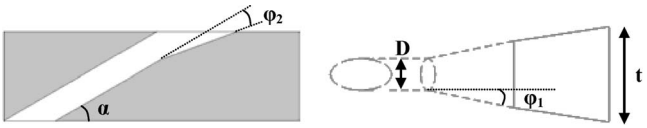

Fig. 4 Fan-shaped cooling hole detailed geometry

tion resulting from the five-axis water-jet machining process. Slight variations did occur in fan shape of the holes as a result of the manufacturing process. Some hole-to-hole variation can be seen in the effectiveness contours, which were attributed to variation in hole shape as well as experimental uncertainty. An illustration of the fan-shaped hole geometry is shown in Fig. 4, and relevant parameters for the film-cooling holes are listed in Table 2. The cylindrical showerhead holes had fairly high-surface inclination angle of 60 deg along with a 90 deg compound angle. The fan-shaped holes had a surface inclination angle of 30 deg and lateral and forward expansion angles of 10 deg.

High-resolution surface temperature measurements were obtained with an infrared (IR) camera. Thermocouples placed in the vane surface were used to calibrate the images, which were taken from below the test section at 45 deg relative to the surface for optical access. Postprocessing of the images required a three-dimensional transformation, calibration, conduction correction, and assembly. A detailed description of the complete measurement technique can be found in Colban et al. [8].

Two blowing ratios were defined for this study. For the showerhead region, blowing ratios are reported based on inlet velocity U_{in},

$$M_{\infty} = \frac{m_c}{A_h U_{\text{in}} \rho_{\text{in}}} \tag{1}$$

For the fan-shaped holes, however, it is more appropriate to report blowing ratios in terms of local velocity U_{local},

$$M = \frac{m_c}{A_h U_{\text{local}} \rho_{\text{in}}} \tag{2}$$

Three sets of blowing ratios were measured for the fan-shaped holes, while the showerhead blowing ratio of $M_{\infty}=2.0$ was held constant for all cases. The range of measured blowing ratios, shown in Fig. 5, was chosen to encompass typical operating conditions in an industrial gas turbine. As described earlier, blowing ratios were set by using previously measured discharge coefficients.

Experimental Uncertainty. Surface temperatures were measured for a reference case with hot mainstream flow and cool plenum flow, but no surface film cooling. This procedure yielded values of surface effectiveness without blowing between 0.04 and 0.12. A one-dimensional conduction correction was then applied to the data using the reference values, as described in Ethridge et al. [22]. The partial derivative and sequential perturbation method as explained by Moffat [23] was used to determine uncertainties for the experimentally reported effectiveness values. High values of $\eta=0.9$ had uncertainties of ±0.012, whereas low values of $\eta=0.2$ had an uncertainty of ±0.011.

Table 2 Film-cooling hole parameters

Fan shaped			Showerhead	
D (cm)	0.38		D (cm)	0.24
α (deg)	30		α (deg)	60
φ_1 (deg)	10		β (deg)	90
φ_2 (deg)	10		t (cm)	0.48
t (cm)	0.81		t/P (-)	0.22
	t/P (-)	$S_{\text{exit}}/S_{\text{max}}$ (-)		
Row PA	0.540	−0.840		
Row PB	0.405	−0.615		
Row PC	0.405	−0.384		
Row PD	0.270	−0.135		
Row SA	0.405	0.090		
Row SB	0.405	0.214		
Row SC	0.405	0.345		
Row SD	0.810	0.519		

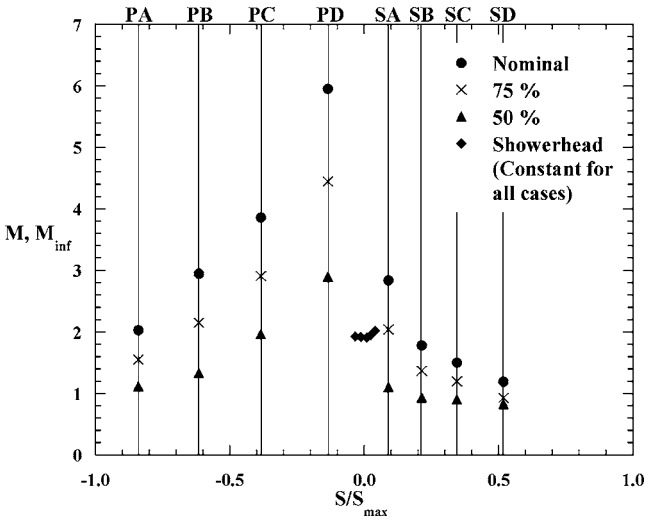

Fig. 5 Test matrix of blowing ratios for each case

Computational Methodology

CFD predictions were done with both the RNG k-ε and v^2-f [2] turbulence models. The RNG k-ε was chosen because it is perhaps the most common turbulence model currently used in industry and serves as a baseline computational comparison for the v^2-f model. The v^2-f model was chosen to see if the improvements made in the near-wall modeling would offer a significant improvement in predictive capability over the current industry standard. The constraints of the two models dictated different approaches in selecting the computational domain and in meshing. All the CFD predictions were done using FLUENT 6.0.1, a commercially available CFD solver with a special module for the v^2-f model.

RNG k-ε Model. The computational domain for the RNG k-ε simulation consisted of one periodic vane passage. A two-dimensional view of the domain is shown in Fig. 6. The domain began one chord length upstream of the vane leading edge, using a velocity inlet condition. The exit boundary was located 1.5 C downstream of the trailing edge, a distance suggested by Hermanson and Thole [24] so as not to affect the upstream flow field. The interior plenum geometry was consistent with the experimental setup, using mass flow inlet boundaries. The mass flow rates were specified such that the average blowing ratios exiting the holes would correspond to the experimentally desired values. The contoured end wall was also modeled to see how far down the vane span the effects of the contour reached. The RNG k-ε domain included the entire vane height and all of the cooling holes, 215 of which were fan-shaped holes and 130 of which were cylindrical showerhead holes.

Approximately 2.2 million unstructured tetrahedral cells were used to mesh the domain. This resulted in ~1500 volumetric cells to define each fan-shaped hole (Fig. 7(*a*)), and ~400 volumetric cells to define each cylindrical hole. Because the RNG k-ε turbulence model is not valid within the laminar sublayer, nonequilibrium wall functions were used to model the viscous effects of the boundary layer near the wall. This required cells with centroids located within a range of $30<y^+<60$ near the vane surface. Convergence required ~1000 iterations on four parallel processors.

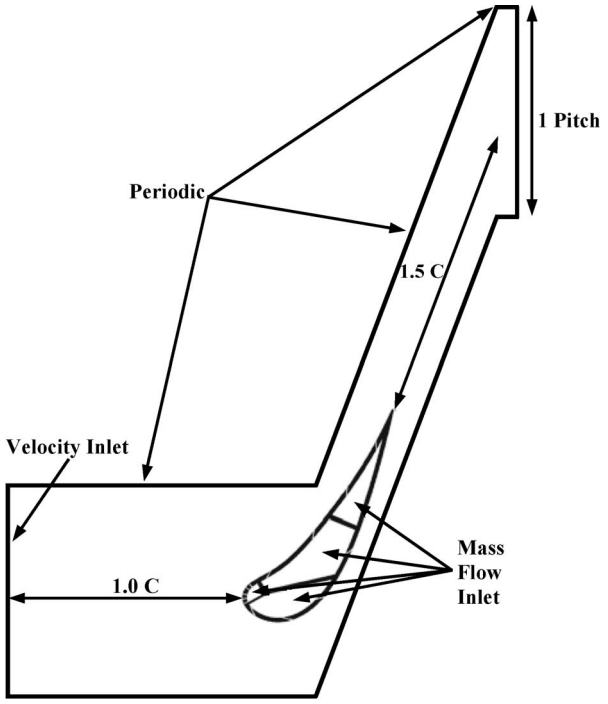

Fig. 6 2D view of the CFD domain (the RNG *k-ε* model featured the entire span and contour, whereas the *v²-f* prediction featured only a 6 cm spanwise periodic section)

The simulations took approximately two days to converge. Convergence was determined not only from residuals, but also by monitoring area-averaged surface temperatures on both the suction and pressure sides. The drag coefficient around the vane was also monitored as a check on aerodynamic convergence. A grid independence study was also performed by adapting the grid up to 3.9 million cells, but no significant change in results was observed so the initial grid size of 2.2 millions cells was deemed sufficient.

***v²-f* Model.** Unlike the RNG k-ε model, the v^2-f model is valid to the wall. This required a structured grid in the vicinity of the wall, resolving the boundary layer to within $y^+ < 3$. Consequently, modeling the entire span was not a possibility for the v^2-f model due to the higher cell density required near the wall. For this reason, only a 6 cm spanwise periodic section was included in the computational domain, which is shown schematically in Fig. 6. Both the experimental results and the RNG k-ε CFD results showed periodicity below the midspan; thus, it was valid to model only the small periodic section, thus making the computations feasible.

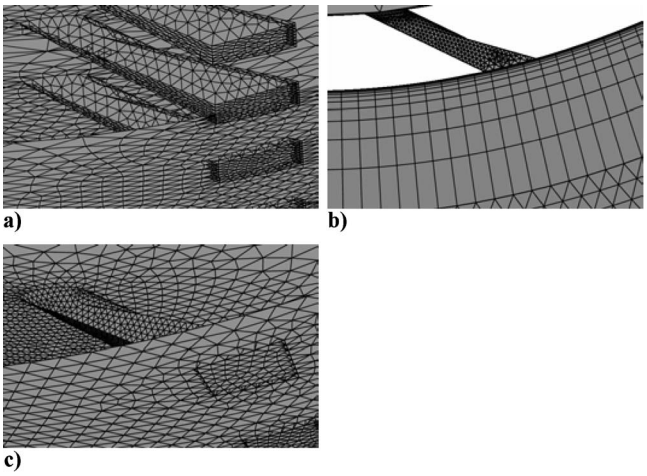

Fig. 7 Computational grid sample of (*a*) the RNG *k-ε* surface mesh, (*b*) the *v²-f* boundary layer mesh, and (*c*) the *v²-f* surface mesh

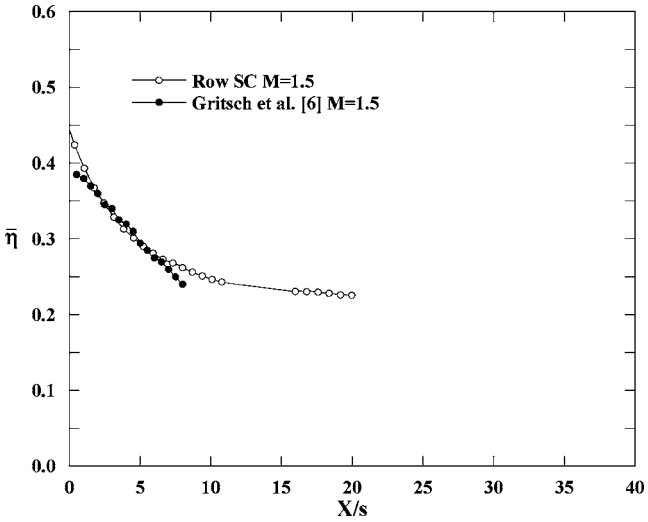

Fig. 8 Comparison of results to previously published data

The v^2-f model grid contained ~1.6 million cells in order to get the near-wall resolution. The vane surface was meshed with an unstructured grid, and a boundary layer mesh was applied to the vane surface (shown in Fig. 7(*b*)). Consequently, there were prismatic cells to a distance of 1.5 cm from the wall, at which point the remainder of the domain was meshed with unstructured tetrahedral cells. The surface mesh resolution is shown for the v^2-f simulations in Fig. 7(*c*). Solutions were run for 500 iterations on a first-order upwind scheme, before being switched over to a second-order upwind scheme with SIMPLEC coupling for 1500 iterations. The v^2-f model computations were run on three parallel processors and required approximately three days to reach convergence. As with the RNG k-ε model, the surface temperatures and drag coefficient were monitored as additional convergence criteria.

Results

Prior to performing the multiple-row adiabatic film-cooling measurements, the experimental method and data reduction procedure were validated for a single-row and compared to existing published data. Figure 8 shows laterally averaged single-row effectiveness downstream of row SC, a row that was located in a relatively flat region of the vane. Because of differences in hole geometry and spacing, the distance downstream of the hole exit was normalized with respect to the equivalent exit slot width s, where s was the ratio of the hole breakout area to the hole spacing P. The results show excellent agreement with the flat-plate study by Gritsch et al. [25], thus validating both the experimental and data reduction methods.

Pressure Side. Adiabatic film-cooling effectiveness contours for each case are shown in Fig. 9 for the pressure side. In total, five images were required to completely capture the pressure side, with measurements taken in the nominally 2D flow region of the vane. The showerhead cooling was largely ineffective at cooling the leading edge region, which Colban et al. [8] attributed to jet liftoff from the high surface angle. The first row of fan-shaped holes showed liftoff by a narrowing in the jet contour just downstream of the hole exit. However, downstream near $S/S_{max} = -0.20$, the jets began to spread laterally. This was a result of the

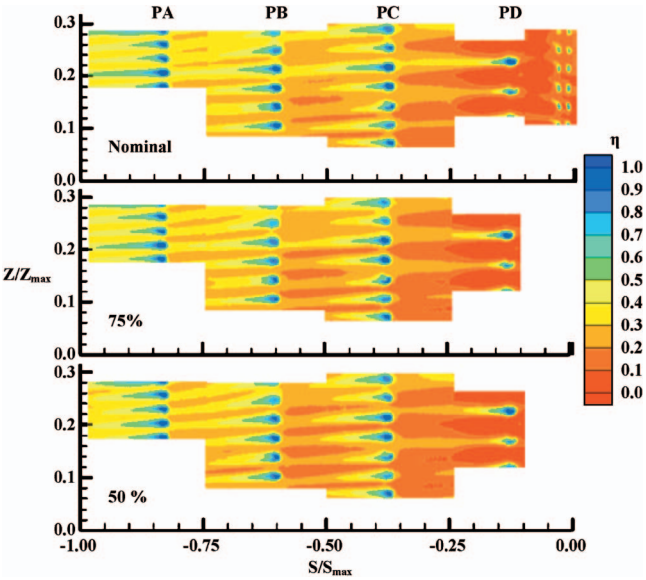

Fig. 9 Pressure side experimental results

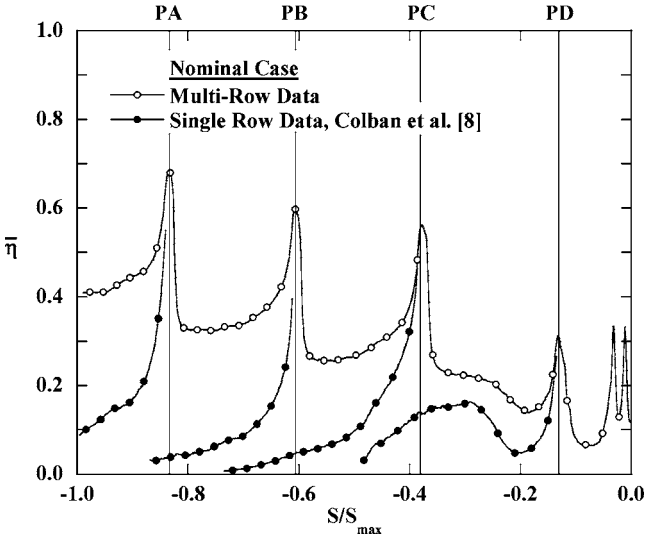

Fig. 11 Comparison of multirow and single-row data on the pressure side at nominal conditions

holes in row PD being placed in a region of concave curvature on the pressure side. The jets lifted off initially, but downstream they impinged on the vane surface, which caused lateral spreading. These results were consistent with the cylindrical film-cooling study performed by Ito et al. [26] on a concave pressure surface.

Overall, there was an increase in η with distance from the leading edge, which is evident from the increased η levels between the jets in rows PC, PB, and PA. Laterally averaged η values (shown in Fig. 10) also show an increase in cooling effectiveness with increased blowing. This result differs from the single-row results for the pressure side [8], which showed a decrease in film effectiveness with increased blowing. The belief is that the upstream coolant caused increased turbulent mixing in the downstream jet (both laterally and normal to the surface). The enhanced mixing coupled with the upstream coolant caused better film-cooling jet diffusion and, consequently, more effective surface cooling. Figure 11 shows the single-row data from Colban et al. [8] plotted with the multirow data for the nominal case. The multirow data has overall much higher η, which became increasingly pronounced with surface distance. The increase in η from single-row cooling to multirow cooling is due to a combination of two effects. First, the upstream coolant filled in the gaps or spaces between the downstream rows, leading to a greater cooled surface area. Second, as mentioned before, the upstream film cooling makes the downstream row more effective by increasing the amount of turbulent mixing and reducing the normal momentum. This was particularly evident for row PD, which separated from the surface for both the single-row and multirow tests. The difference, however, was that the amount of liftoff was significantly reduced for the multirow cases, indicating that the upstream showerhead blowing had the effect of keeping the jets attached to the surface. This finding was consistent with the flat-plate study of Goldstein et al. [9] and the airfoil study of Polanka et al. [13], both of which used cylindrical holes.

Computational film-cooling effectiveness contours are shown in Fig. 12 for the pressure side. Results from both turbulence models show a spanwise skewness in jet trajectory for row PD (row PC as well for the v^2-f model). This directionality was caused by the orientation of the showerhead cooling. However, the experimental results did not indicate a directional influence from the showerhead on the downstream rows (Fig. 9).

Differences between the two models show that the RNG k-ε

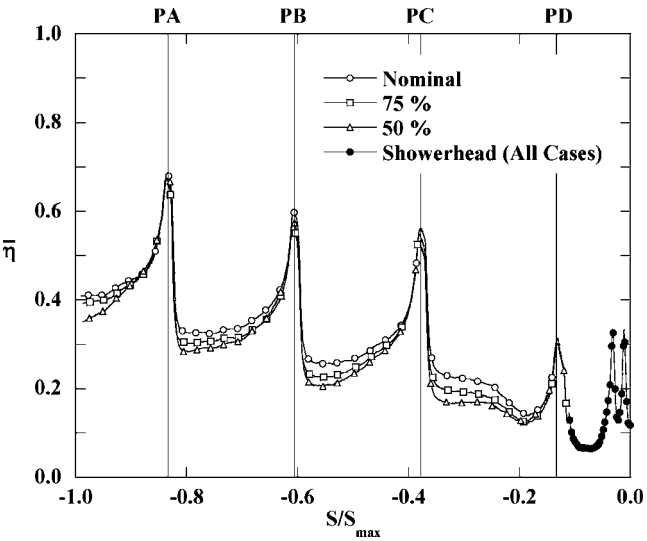

Fig. 10 Experimental laterally averaged adiabatic film-cooling effectiveness on the pressure side

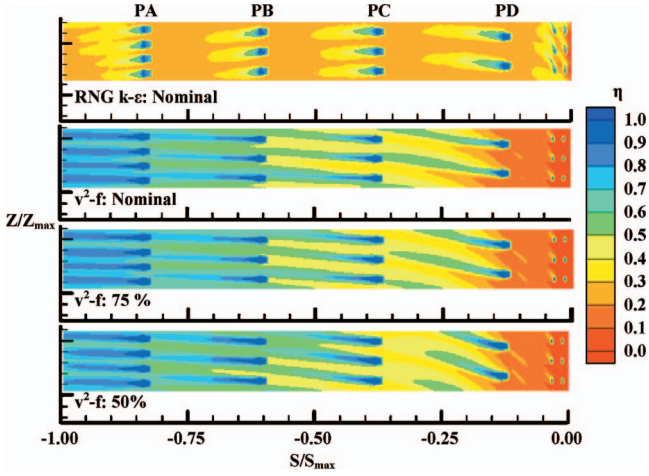

Fig. 12 CFD contours for the pressure side

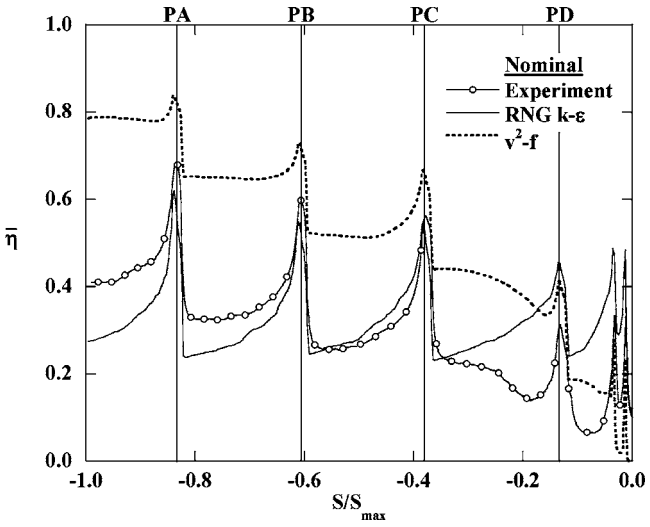

Fig. 13 Pressure-side comparison of laterally averaged film effectiveness with computations

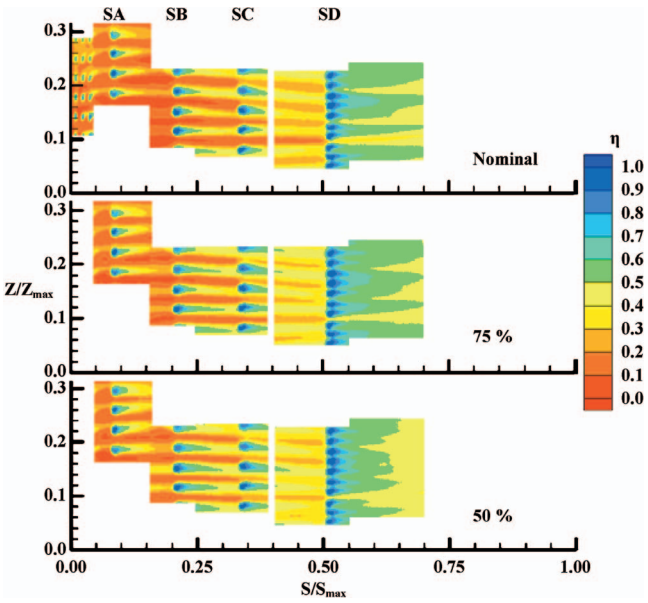

Fig. 15 Experimental results on the suction side

predictions were more accurate in terms of the overall level of film-cooling effectiveness. However, the RNG k-ε prediction showed a wider coolant footprint than the experimental results, whereas the v^2-f predictions showed a much narrower coolant footprint similar to the experimental results. Another physical trend shown by the v^2-f that was not picked up by the RNG k-ε prediction was the spreading of the coolant downstream of the first fan-shaped row due to liftoff and reattachment. Neither model accurately predicted the showerhead behavior. The RNG k-ε model underpredicted the showerhead liftoff, while the v^2-f model overpredicted the amount of liftoff in the showerhead region.

A comparison of laterally averaged effectiveness at nominal conditions between the experimental results and both computational models is shown in Fig. 13. Again, the RNG k-ε model more accurately predicted the overall levels of η, while the v^2-f model grossly overpredicted η on the pressure side. It is interesting to note that the v^2-f model predicted a continual rise in effectiveness, indicating a buildup of coolant from upstream rows. The RNG k-ε model however, showed no row-to-row increase in effectiveness, which can be seen not only in the laterally averaged values of Fig. 13, but in the contour of Fig. 12.

The difference in behavior between the two models in the near leading-edge region can be seen by examining the streamlines. Streamlines for the nominal blowing conditions are shown in Fig. 14 for both turbulence models. The RNG k-ε model showed the streamlines stay attached to the surface with little lateral spreading, whereas the v^2-f model showed greater lateral spreading after an initial jet liftoff. Also, the skewness in the jets for both models was illustrated by the streamlines as a compound effect from the showerhead film cooling, which had a 90 deg compound angle with respect to the main flow.

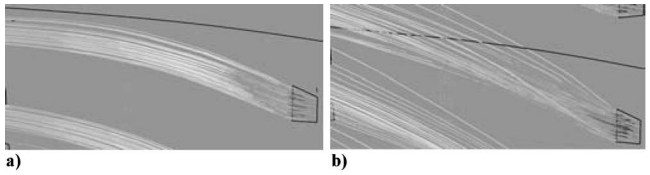

Fig. 14 Streamlines near the leading edge for (*a*) RNG k-ε and (*b*) v^2-f models at nominal conditions

Suction Side. Contours of η are shown for the experimental results on the suction side in Fig. 15. Significant showerhead liftoff occurred, as on the pressure side, causing poor leading-edge region cooling. The jets on the first two suction side rows (SA and SB) separated from the surface at high blowing ratios due to the high curvature and acceleration in that region. Overall, η increased with surface distance from the stagnation line on the suction side, as seen from the laterally averaged η values in Fig. 16. Near the leading edge, η decreased with blowing ratio because of the jet separation. However, as we progress along the suction side, the curvature decreases, and the amount of liftoff consequently also decreases. This led to a reversal in trend of η with blowing rates by the end of the suction side.

The effect of multiple cooling rows as opposed to the single-row results of Colban et al. [8] for the nominal flow conditions are shown in Fig. 17. In contrast to the pressure side, where showerhead liftoff also occurred, the effect of the showerhead on the first suction side row was not as significant. On the suction side, the separated showerhead coolant could not remain close enough to

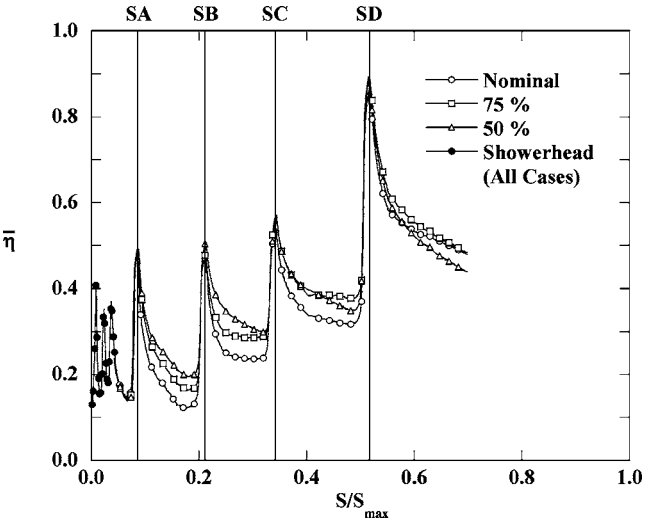

Fig. 16 Experimental laterally averaged adiabatic film-cooling effectiveness on the suction side

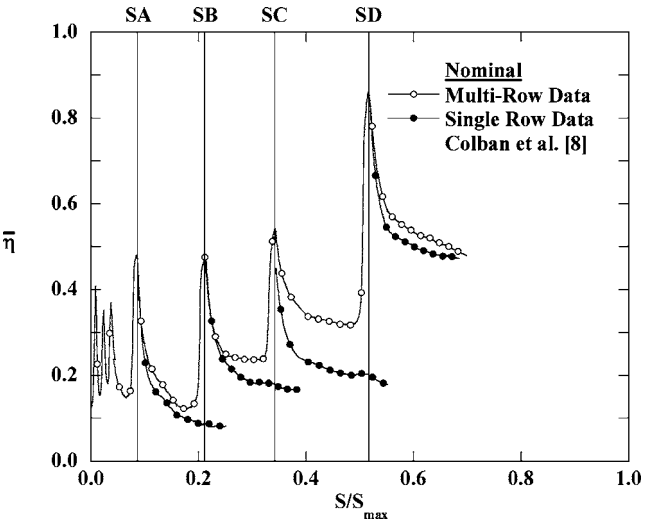

Fig. 17 Comparison of multirow and single-row data on the suction side at nominal conditions

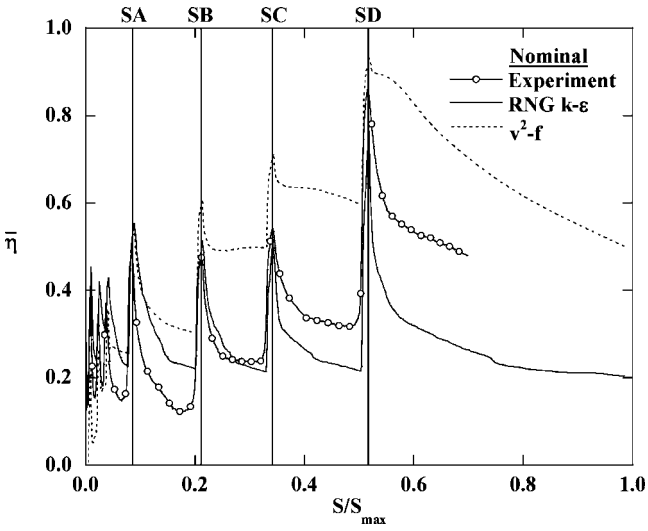

Fig. 19 Suction-side comparison of laterally averaged film effectiveness with computations

the surface to have an effect on the downstream rows because of the severe surface curvature. Rows SB and SC show a more significant effect of upstream cooling, with results mirroring the trends observed on the pressure side. Further downstream, row SD showed little effect of upstream cooling. This was because of the extremely close hole spacing for row SD, there was no room for extra coolant between the holes.

Contours of η are shown in Fig. 18 for the CFD results on the suction side. Just as row PD on the pressure side, row SA was directionally influenced by the showerhead cooling. The v^2-f results mimic the experimental results near the leading edge in that they also predicted liftoff for the first two rows of fan-shaped holes, and that liftoff also increases with blowing ratio. The v^2-f model also closely predicts the amount of liftoff in the showerhead region. As shown in the laterally averaged η values for the nominal case in Fig. 19, the RNG k-ε model exhibits a much faster decay in η downstream of the attached fan-shaped rows than was measured in the experiments. On the other hand, the v^2-f model exhibits more lateral spreading of the attached jets than was measured experimentally, leading to less decay in η with distance downstream. The streamlines on the suction side (Fig. 20) also show the greater lateral spreading of the fan-shaped holes predicted by the v^2-f model as compared to the RNG k-ε model.

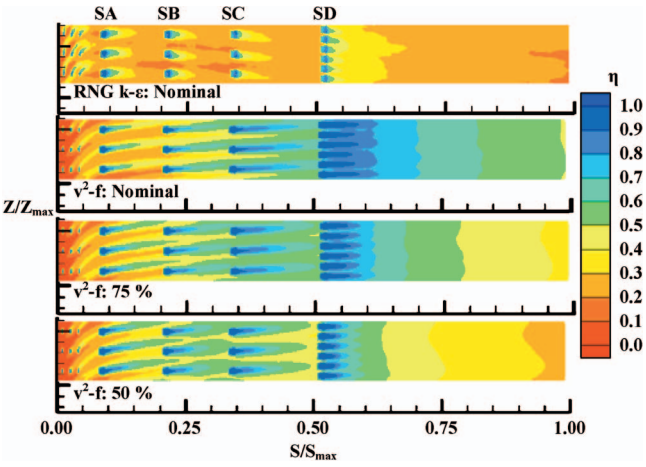

Fig. 18 CFD contours for the suction side

Conclusions

This study presented a detailed experimental and computational investigation of film cooling on a gas turbine vane with fan-shaped holes. Multirow data were presented at a range of engine representative blowing ratios on both the pressure and suction sides and compared to CFD predictions using both the RNG k-ε and v^2-f turbulence models.

Experiments showed that on the pressure side the showerhead blowing was not very effective, with excessive liftoff leading to little cooling in that region. Downstream, the first pressure side fan-shaped row exhibited liftoff and reattachment, as evidenced by a narrowing and widening in jet contours, although the liftoff was not as significant as the single-row case. Overall, η levels increased on the pressure side with both surface distance and blowing ratio.

Showerhead blowing was also relatively ineffective on the suction side, again exhibiting substantial liftoff and low film-cooling effectiveness. In the near leading-edge region of high curvature on the suction side, jet liftoff was accentuated by blowing ratio yielding much lower levels of η at high blowing rates.

The CFD predictions did not agree well with the experimental results, for the most part, at best capturing either the correct η levels or the correct physics, but not both. The v^2-f model more nearly predicted the actual flow physics, whereas the RNG k-ε model offered a better match with the experimental data in terms of correct effectiveness levels. Although there have been matching CFD predictions for flat-plate film cooling, clearly more advances in CFD turbulence modeling are required before the highly complex flow of film cooling on a gas turbine vane can be modeled accurately.

Acknowledgment

The authors are grateful to Siemens Power Generation for their funding and support of this project.

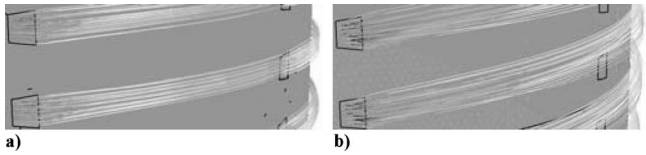

Fig. 20 Streamlines near the leading edge for (*a*) RNG k-ε and (*b*) v^2-f models at nominal conditions

Nomenclature

A = area
C = vane true chord
C_D = discharge coefficient
D = film-cooling hole diameter
f = elliptic relaxation function
k = turbulent kinetic energy
k_{cond} = thermal conductivity
m = mass flow rate
M = blowing ratio using local velocity, $M=m_c/A_h U_{\text{local}}\rho_{\text{in}}$
M_∞ = blowing ratio using inlet velocity, $M_\infty=m_c/A_h U_{\text{in}}\rho_{\text{in}}$
P = hole spacing measured normal to streamwise direction
P = vane pitch
Re = Reynolds number, $\text{Re}=U_{\text{in}}C/\nu$
s = equivalent slot width, $s=A_{\text{break}}/P$
S = distance along the vane surface
t = hole breakout width
T = temperature
U = velocity
v^2 = normal velocity fluctuations
X = distance downstream of the hole exit
y^+ = wall coordinate
Z = distance measured along the vane span

Greek

α = inclination angle
β = compound angle
ε = eddy viscosity, surface emmissivity
μ_t = turbulent viscosity
ν = kinematic viscosity
η = adiabatic film-cooling effectiveness, $\eta=(T_\infty - T_{\text{ad}})/(T_\infty - T_c)$
ρ = density
φ_1 = lateral diffusion angle
φ_2 = forward expansion angle

Subscripts

ad = adiabatic
break = hole breakout area
c = coolant
exit = hole exit
h = metering area of film-cooling holes based on D
in = inlet condition
local = local conditions
max = maximum
plenum = plenum conditions
surf = surface
∞ = freestream conditions

References

[1] Goldstein, R. J., Eckert, E. R. G., and Burggraf, F., 1974, "Effects of Hole Geometry and Density on Three-Dimensional Film Cooling," Int. J. Heat Mass Transfer, **17**, pp. 595–607.
[2] Durbin, P. A., 1991, "Near-Wall Turbulence Closure Modeling Without 'Damping Functions'," Theor. Comput. Fluid Dyn., **3**, pp. 1–13.
[3] Kercher, D. M., 2003, Film-Cooling Bibliography: 1940–2002: private publication.
[4] Kercher, D. M., 2005, Film-Cooling Bibliography Addendum: 1999–2004, private publication.
[5] Bunker, R. S., 2005, "A Review of Shaped Hole Turbine Film-Cooling Technology," ASME J. Heat Transfer, **127**, pp. 441–453.
[6] Zhang, L., Baltz, M., Pudupatty, R., and Fox, M., 1999, "Turbine Nozzle Film-Cooling Study Using the Pressure Sensitive Paint (PSP) Technique," ASME Paper No. 99-GT-196.
[7] Zhang, L., and Pudupatty, R., 2000, "The Effects of Injection Angle and Hole Exit Shape on Turbine Nozzle Pressure Side Film-Cooling," ASME Paper No. 2000-GT-247.
[8] Colban, W., Gratton, A., Thole, K. A., and Haendler, M., 2006, "Heat Transfer and Film-Cooling Measurements on a Stator Vane With Fan-Shaped Cooling Holes," ASME J. Turbomach., **128**, pp. 53–61.
[9] Goldstein, R. J., Eckert, E. R. G., Chiang, H. D., and Elovic, E., 1985, "Effect of Surface Roughness on Film Cooling Performance," ASME J. Eng. Gas Turbines Power, **107**, pp. 111–116.
[10] Guo, S. M., Lai, C. C., Jones, T. V., Oldfield, M. L. G., Lock, G. D., and Rawlinson, A. J., 1998, "The Application of Thin-Film Technology to Measure Turbine-Vane Heat Transfer and Effectiveness in a Film-Cooled, Engine-Simulated Environment," Int. J. Heat Fluid Flow, **19**, pp. 594–600.
[11] Sargison, J. E., Guo, S. M., Oldfield, M. L. G., Lock, G. D., and Rawlinson, A. J., 2001, "A Converging Slot-Hole Film-Cooling Geometry—Part II: Transonic Nozzle Guide Vane Heat Transfer and Loss," ASME Paper No. 2001-GT-0127.
[12] Schnieder, M., Parneix, S., and von Wolfersdorf, J., 2003, "Effect of Showerhead Injection on Superposition of Multi-Row Pressure Side Film-Cooling With Fan Shaped Holes," ASME Paper No. GT2003–38693.
[13] Polanka, M. D, Ethridge, M. I., Cutbirth, J. M., and Bogard, D. G., 2000, "Effects of Showerhead Injection on Film Cooling Effectiveness for a Downstream Row of Holes," ASME Paper No. 2000-GT-240.
[14] Riess, H., and Bölcs, A., 2000, "The Influence of the Boundary Layer State and Reynolds Number on Film-cooling and Heat Transfer on a Cooled Nozzle Guide Vane," ASME Paper No. 2000-GT-205.
[15] Kohli, A., and Thole, K. A., 1997, "A CFD Investigation on the Effects of Entrance Crossflow Directions to Film-Cooling Holes," *32nd National Heat Transfer Conference*, **12**, pp. 223–232.
[16] Hyams, D. G., and Leylek, J. H., 1997, "A Detailed Analysis of Film Cooling Physics—Part III: Streamwise Injection With Shaped Holes," ASME Paper No. 97-GT-271.
[17] Hildebrandt, T., Ganzert, W., and Fottner, L., 2000, "Systematic Experimental and Numerical Investigations on the Aerothermodynamics of a Film Cooled Turbine Cascade With Variation of the Cooling Hole Shape—Part II: Numerical Approach," ASME Paper No. 2000-GT-298.
[18] Ferguson, J. D., Leylek, J. H., and Buck, F. A., 2002, "Film Cooling on a Modern HP Turbine Blade Part III: Axial Shaped Holes," ASME Paper No. GT-2002–30522.
[19] Heidmann, J. D., Kassab, A. J., Divo, E. A., Rodriguez, F., and Steinthorsson, E., 2003, "Conjugate Heat Transfer Effects on a Realistic Film-Cooled Turbine Vane," ASME Paper No. GT2003–38553.
[20] Parneix, S., Durbin, P. A., and Behnia, M., 1998, "Computation of 3-D Turbulent Boundary Layers Using the V2F Model," Flow, Turbul. Combust., **60**, pp. 19–46.
[21] Durbin, P. A., 1995, "Separated Flow Computations With the k-e-v^2 Model," AIAA J., **33**, pp. 659–664.
[22] Ethridge, M. I., Cutbirth, J. M., and Bogard, D. G., 2000, "Scaling of Performance for Varying Density Ratio Coolants on an Airfoil With Strong Curvature and Pressure Gradient Effects," ASME Paper No. 2000-GT-239.
[23] Moffat, R. J., 1988, "Describing the Uncertainties in Experimental Results," Exp. Therm. Fluid Sci., **1**, pp. 3–17.
[24] Hermanson, K. S., and Thole, K. A., 2000, "Effect of Inlet Conditions on Endwall Secondary Flows," J. Propul. Power, **16**, pp. 286–296.
[25] Gritsch, M., Schulz, A., and Wittig, S., 1998, "Adiabatic Wall Effectiveness Measurements of Film-Cooling Holes With Expanded Exits," ASME J. Turbomach., **120**, pp. 549–556.
[26] Ito, S., Goldstein, R. J., and Eckert, E. R. G., 1978, "Film Cooling of a Gas Turbine Blade," ASME J. Eng. Power, **100**, pp. 476–481.

The Effect of Hot-Streaks on HP Vane Surface and Endwall Heat Transfer: An Experimental and Numerical Study

T. Povey
Department of Engineering Science,
University of Oxford,
Parks Road,
Oxford, OX1 3PJ, UK

K. S. Chana
QinetiQ,
Cody Technology Park,
Ively Road,
Farnborough, GU14 0LX, UK

T. V. Jones

J. Hurrion

Department of Engineering Science,
University of Oxford,
Parks Road,
Oxford, OX1 3PJ, UK

Pronounced nonuniformities in combustor exit flow temperature (hot-streaks), which arise because of discrete injection of fuel and dilution air jets within the combustor and because of endwall cooling flows, affect both component life and aerodynamics. Because it is very difficult to quantitatively predict the effects of these temperature nonuniformities on the heat transfer rates, designers are forced to budget for hot-streaks in the cooling system design process. Consequently, components are designed for higher working temperatures than the mass-mean gas temperature, and this imposes a significant overall performance penalty. An inadequate cooling budget can lead to reduced component life. An improved understanding of hot-streak migration physics, or robust correlations based on reliable experimental data, would help designers minimize the overhead on cooling flow that is currently a necessity. A number of recent research projects sponsored by a range of industrial gas turbine and aero-engine manufacturers attest to the growing interest in hot-streak physics. This paper presents measurements of surface and endwall heat transfer rate for a high-pressure (HP) nozzle guide vane (NGV) operating as part of a full HP turbine stage in an annular transonic rotating turbine facility. Measurements were conducted with both uniform stage inlet temperature and with two nonuniform temperature profiles. The temperature profiles were nondimensionally similar to profiles measured in an engine. A difference of one-half of an NGV pitch in the circumferential (clocking) position of the hot-streak with respect to the NGV was used to investigate the affect of clocking on the vane surface and endwall heat transfer rate. The vane surface pressure distributions, and the results of a flow-visualization study, which are also given, are used to aid interpretation of the results. The results are compared to two-dimensional predictions conducted using two different boundary layer methods. Experiments were conducted in the Isentropic Light Piston Facility (ILPF) at QinetiQ Farnborough, a short-duration engine-sized turbine facility. Mach number, Reynolds number, and gas-to-wall temperature ratios were correctly modeled. It is believed that the heat transfer measurements presented in this paper are the first of their kind.
[DOI: 10.1115/1.2370748]

Introduction

Heat transfer rates in the first stage turbine have been studied for many years. Increases in turbine inlet temperature, to achieve higher thrust and efficiency, have been made possible by the development of advanced materials (high-temperature super-alloys of nickel and thermal barrier coatings), and by employing more sophisticated cooling systems. Modern turbine blades are cooled with a combination of film cooling, impingement cooling, and passage cooling. For given level of material and design sophistication, however, inlet temperatures are limited in practice by the energy cost associated with requiring an increase in the cooling air flow rate: the cooling air is usually extracted from the engine compressor, and therefore the energy associated with compression is the most significant term in calculating the overall cycle performance. In engines in which hot-streaks are pronounced, an additional performance penalty is incurred in designing for higher temperatures than the mass-mean gas temperature: if the hot-streak migration process is not fully understood the designer must effectively design for the peak gas temperature, and budget for this in the overall engine performance calculation.

This paper seeks to address the problem of quantifying the influence of inlet temperature distortion (ITD) on vane surface and endwall heat transfer rates. A detailed aerodynamic survey of the HP vane was conducted, and heat transfer rates were measured at a number of locations over the vane surface and endwalls. These data are unique, as they have been taken in a facility equipped with an ITD generator that simulates combustor-representative hot-streaks at the HP stage inlet. Both heat transfer and aerodynamic measurements were performed for three inlet temperature profiles. Blind predictions of heat transfer using an integral method, and using the TEXSTAN code were also conducted, and these are presented. Although the streamline pattern within a vane passage cannot be affected by ITD, it can be affected by platform-slot or cooling-hole injection, and a study that combines engine-representative ITD, engine geometry, and cooling flow, for engine-representative main flow, is clearly desirable.

HP Vane and Endwall Heat Transfer Studies

HP vane aerodynamics and heat transfer are more amenable to reasonably accurate numerical prediction than other vane/blade rows. Only the trailing edge region of the vane is subject to the strong forced periodic oscillations in the pressure field that are caused by the relative motion of vane rows [1]. In addition, the

Contributed by the International Gas Turbine Institute (IGTI) of ASME for publication in the JOURNAL OF TURBOMACHINERY. Manuscript received October 1, 2004; final manuscript received February 1, 2005. IGTI Review Chair: K. C. Hall. Paper presented at the ASME Turbo Expo 2005: Land Sea and Air, Reno, NV, June 6–9, 2005, Paper No. GT2005-69066.

leading edge region is unaffected by the strong localized regions of unsteadiness associated with viscous phenomena such as trailing edge wakes, secondary flow features, and shock wave boundary layer interactions that affect downstream vane rows. The primary factors that affect heat transfer rate are secondary flows, high freestream turbulence, and shock boundary layer interaction in the trailing edge region of the vane. In addition, the migration of hot-streaks as they pass through the vane passage, deforming under the influence of the pressure field set within the passage, must be considered. It is easy to demonstrate (on physical grounds) that hot-streaks do not directly influence the streamline pattern within a stator passage: the temperature essentially acts as a marker for the streamline (the same is not true as the streak enters the rotor passage where preferential migration has been shown to occur).

Turbulence and Heat Transfer. Many authors have studied the effect of increased free-stream turbulence on the heat transfer rate at the vane surface. High turbulence has been shown to promote earlier transition from a laminar to a turbulent boundary layer [2–4]. Universal correlations—even for a relatively limited class of vane geometry—for predicting both the point of transitional onset, and the length of transition, have so far evaded investigators, however. This must be due to the number of parameters that appear to be significant for the physics of the transitional boundary layer: surface curvature, surface roughness, Reynolds number, turbulence intensity, turbulence length scale, and pressure gradient are a nonexhaustive list. Despite the limitations, the data that are available have proven very useful, and are used extensively when applying integral methods [5] for predicting heat transfer rate.

Secondary Flow and Heat Transfer. The importance for predicting and analyzing heat transfer of understanding secondary flow processes within the HP turbine cannot be overstated. A very accurate picture of the dominant secondary flow mechanisms has been developed through the work—outstanding among others—of Klein [6], Langston et al. [7] and Sieverding [8]. In predicting vane suction surface (SS) and vane endwall heat transfer, regions in which the near-wall flow can be dominated by secondary flow, it is essential for the secondary flow pattern to be well characterized. Likewise, in experimental investigations the secondary flows must be representative of those of an engine. In practice, this means that it is insufficient to use anything but either actual engine components or geometrically similar counterparts.

Vane Surface. A number of early studies of HP vane surface heat transfer supported a model of high leading and trailing edge heat transfer, with span-wise variation particularly on the SS of the vane close to the endwalls, a region of strong secondary flow. An increasing appreciation of the importance of correctly modeling secondary flows led to experiments by Dunn and Stoddard [9] who used actual engine hardware, Wedlake et al. [10], and Taulbee et al. [11]. A particularly comprehensive aerothermal survey of a highly loaded modern HP vane and endwall, at conditions of M, Re, Tu, and T_g/T_w representative of an engine, was conducted by Harvey et al. [12] (also: Harvey [13], Harvey and Jones [14]). In addition to simulating in unprecedented degree actual turbine conditions (the cascade geometry was also fully representative of engine components), the study included very detailed aerodynamic and heat transfer measurements, surface flow visualization experiments, and predictions of both surface streamline pattern (3-D DENTON Euler Solver) and heat transfer (Integral Method). It is now recognized that to understand vane and endwall heat transfer it is necessary to achieve conditions very close to those of an engine, and that a multi-faceted approach similar to that described is required.

Endwall. A large number of studies of heat transfer and cooling on HP vane endwalls have been conducted. An early study of film cooling effectiveness with slot ejection [15] confirmed the difficulty of cooling the pressure-surface-corner region of the endwall: low-momentum coolant was swept across the passage by the strong cross-passage pressure gradient, collecting in the SS corner. This useful, if with hindsight rather predictable, conclusion is supported by numerous later studies. Although it had been generally agreed for a number of years that secondary flow can significantly affect heat transfer, one of the first studies to relate a secondary flow pattern—determined using flow visualization—to an experimentally measured heat transfer distribution for a vane endwall, was that of Gaugler and Russell [16].

There have been a number of recent endwall studies, both of secondary flow control mechanisms (to reduce losses in the turbine), and of the endwall heat transfer process (see, for example: Harvey et al. [17] Kang et al. [18], Kang and Thole [19]). Other investigations have sought to: determine the extent to which improved film coverage may be achieved by influencing the near-wall secondary flow pattern using angled holes [20]; develop optimized endwall film-cooling configurations [21,22]; investigate contoured endwall effects [23]; and investigate the effect of backward facing injection slots on film cooling performance [24]. The wealth of recent literature demonstrates how active an area of research this currently is.

In 2000, a significant European research project commenced for Aerothermal Investigations on Turbine Endwalls and Blades (the AITEB program). The project attracted a large number of industrial partners, whose primary objective was the development of more robust design package (correlation based models, and numerical simulations) for heat transfer prediction in the typically highly loaded—both thermally and aerodynamically—environment of the HP turbine. A key part of this program is a study of HP vane endwalls, with slot-ejected platform cooling. The work-packages that constitute the program are summarized by Haselbach and Schiffer [25]. The authors note that there may be a trend towards flatter combustor exit temperature profiles, which, for the same mean gas temperature, would push near-wall gas temperatures higher than at present. This would require more aggressive platform cooling than is currently the norm: if there exists a strong radial temperature profile such that the near-endwall flow is cooler than at midspan, there is clearly a lesser requirement on the platform cooling system. Whether or not the high platform-cooling burden is alleviated by radial temperature distortion at the combustor exit, it is clearly the case that an improved understanding of the heat transfer distribution on the endwall is essential.

Studies of Nonuniform Inlet Temperature Effects

There are two design philosophies for HP stages influenced by hot-streaks. For integer vane/injector-port count ratio, the hot-streak can be aligned with the leading edge or with the center of the passage. For noninteger ratios, clearly a combination of both situations is unavoidable. The former imposes a greater heat load on the HP vane, and necessitates higher cooling flow rates, but has the effect of cooling and breaking up the hot streak, moderating the unsteady thermal and mechanical loading imposed on the rotor by the hot-streaks. The latter results in a lower heat load on the HP vane, allowing a reduction in cooling flow, but results in higher unsteady aerothermal loading of the rotor. Both strategies are investigated in this study.

Although there have been numerous studies of heat transfer rates in first stage turbines, there have been relatively few experimental studies to quantify the impact of hot streaks on heat transfer. In an early experiment of Butler et al. [26] conducted in a large-scale low-speed rotating facility (the United Technologies LSRR facility), the authors concluded that the nature and degree of flow redistribution occurring during convection though a HP vane passage was not affected by the inlet temperature profile. This important result had been proven theoretically many years earlier by Munk and Prim [27], who noted that inflow temperature nonuniformities cannot alter the streamline pattern of a stationary

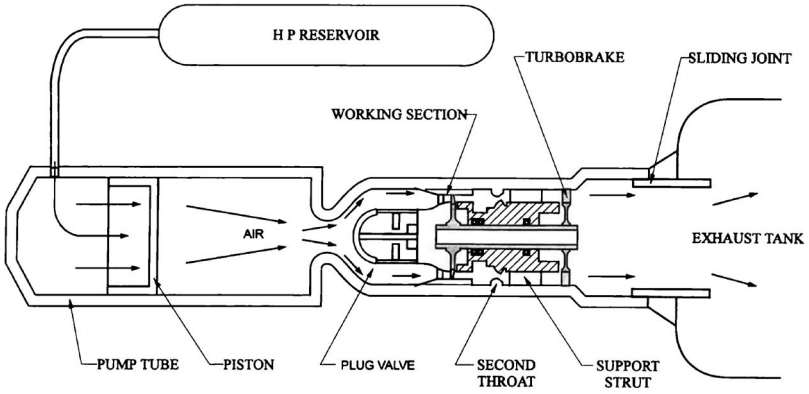

Fig. 1 Schematic of the ILPF

blade row, the latter being influenced only by inlet total pressure nonuniformities. It is important not to infer—incorrectly—from this statement that mixing does not occur within the passage. It is true only that ITD does not give rise to additional mixing.

It is the case, therefore, that changes in heat transfer associated with the introduction of temperature nonuniformity (for the same mean temperature) arise, in the case an HP vane passage, because of changes in driving temperature rather a change in heat transfer coefficient. The results of the first truly comprehensive study of heat transfer on an HP vane and endwall with and without temperature nonuniformity [28] support this assertion. Measurements were performed with the *hot-streak* aligned with the leading edge of the vane, and aligned with the vane mid passage. This paper presents a summary of those results. The measurements were taken in a rotating annular turbine facility (the Isentropic Light Piston Facility at QinetiQ, Farnborough, UK) in which M, Re, Tu, and T_g/T_w were all correctly modeled, as was the geometry. The HP vane count was 32, and 32 hot-streaks were simulated. The measurements are the first of their kind, to the authors' knowledge.

The HP vane of the present study was operated as part of a complete stage, and, later, as part of a 1.5 stage turbine with a downstream IP vane. The effect of hot-streaks both on the downstream rotor and on the IP vane has been studied. The results of these investigations are reported in companion papers by Povey et al. [29], for the case of the IP vane, and Chana and Jones [30], for the case of the HP rotor. While the result of Munk and Prim [27] holds for all blade/vane rows, for flow passing between vane/blade rows which are in relative motion, the inlet total pressure fields and incidence angles are altered by the introduction of ITD. Because of this effect, both the inviscid flow and the secondary flow structures are altered. In this case, it is very difficult to separate the changes in heat transfer that arise because of changes in heat transfer coefficient, and those that arise because of changes in the local driving temperature, even if, in some cases, there may be good reason to suspect that one of these processes is dominant. (It is experimentally very difficult, especially in the case of nonuniform inlet temperature, to deduce the local gas temperature with sufficient resolution and accuracy to resolve this question of predominance.)

There are examples from engine test experience of local overheating within the HP turbine, and on the HP rotor pressure surface (PS) and blade tip in particular. These effects are difficult to explain without invoking hot-streak migration within the turbine. A number of studies of hot-streak migration within the HP turbine blade passage have been conducted, and the effect is now reasonably well understood. The principal effect is incidence angle induced temperature segregation [26,31,32], which can lead to preferential migration of hotter gas towards the PS of the rotor blade.

That there is growing interest in the effects of nonuniform inlet temperature on turbine heat transfer is evidenced by the number of programs developed to study these effects. Experimental programs in five different rotating facilities have been recorded. In chronological order of first publication these are:

(i) The Warm Core Turbine Test Facility at the NASA Lewis Research Center, Cleveland, Ohio, USA [33,34].
(ii) The Low Speed Rotating Rig (LSRR) at the United Technologies Research Center, East Hartford, Connecticut, USA [26,35].
(iii) The Rotating *Blow-down* Facility at the Massachusetts Institute of Technology, Cambridge, Massachusetts, USA [31,32].
(iv) The Isentropic Light Piston turbine-test Facility (ILPF) at QinetiQ, Farnborough, Hampshire, UK [28,30].
(v) The Turbine Research Facility (TRF) at the Wright-Patterson Air Force Base, Dayton, Ohio, USA [36].

Hot-streak experiments have also been conducted in nonrotating facilities. Varadarajan and Bogard [37] (see also Jenkins and Bogard [38]) measured adiabatic effectiveness on the SS of a film-cooled nozzle guide vane for uniform inlet temperature and for a hot-streak incident on the leading edge of the vane. Experiments were conducted in a large-scale two-dimensional cascade of two vane passages (at The University of Texas at Austin, Austin, Texas, USA). Re was correctly modeled, but, because a linear cascade was used, the effect of realistic secondary flows could not be quantified. Investigations of the effects of mainstream turbulence on the vane film cooling and hot-streak dispersion were conducted in the same facility [39].

In addition to experimental studies, there have been a large number of numerical studies to investigate the aerothermal, aerodynamic, and aeromechanical impact of hot streaks in the high-pressure turbine. Publications in the period 2000 to 2004 include: Busby et al. [40], Dorney and Sondak [41], Gundy-Burlet and Dorney [42], Orkwis et al. [43], Prasad and Hendricks [44], Dong et al. [45], Hurrion [28], Sondak et al. [46], and He et al. [47].

The Isentropic Light Piston Facility

The ILPF is a short duration wind tunnel, capable of testing an engine size turbine at the correct nondimensional parameters for fluid mechanics and heat transfer. The facility has been used to test both a single HP turbine stage [48] and a 1.5 turbine stage turbine [49]. For the experiments described in this paper, only the HP stage was installed. During a run M, Re, Tu, and T_g/T_w are all representative of engine conditions. A novel feature of the facility is the aerodynamic turbo-brake [50], which is on the same shaft as the turbine and is driven by the turbine exit-flow. At the design speed, the turbobrake power is matched with the turbine, and thus constant speed is maintained during a run. A schematic of the facility is presented in Fig. 1. Air from a high-pressure reservoir drives a piston down a piston tube, isentropically compressing and

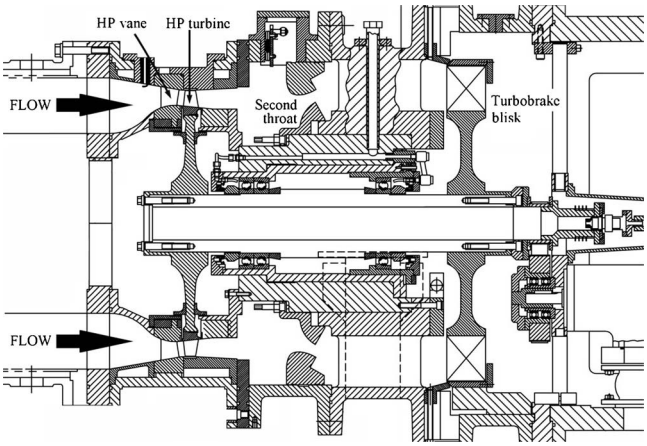

Fig. 2 The working section of the ILPF: HP turbine stage and turbobrake

heating the working gas (air) inside the tube. When the desired pressure is reached, the compressed air is suddenly discharged, by means of a fast acting valve, into the working section. Typically, steady conditions are achieved for 500 ms.

The working section of the facility is shown diagrammatically in Fig. 2. The desired turbine pressure ratio is set by means of an adjustable second throat.

The design operating conditions of the ILPF are given in Table 1. Measurements confirmed that the same stage inlet conditions were achieved both with and without ITD.

Temperature Distortion Factors

Measurements of temperature at the exit-plane of combustors show large radial and circumferential variations in temperature. The flow is, in addition, highly unsteady. The time-mean temperature field measured at the exit plane of a combustor typical of a modern military engine is presented in Fig. 3. Peak temperatures are in excess of 2200 K, while at the hub and casing endwalls there are relatively cool regions of flow, with temperatures as low as 1500 K. Circumferential variations (hot-spots) arise because of the discrete nature of fuel and dilution air jets. In addition, combustor lining coolant flow causes a strong radial temperature gradient.

To quantify temperature nonuniformity, temperature distortion factors (TDFs) are used. There are several definitions in current use, many of which are essentially the same. Combustor flow is highly turbulent, and, because hot and cold gas streams are subject to aggressive mixing, typical time-mean combustor exit temperature profiles are generally rather smooth spatially. It may be sufficient, therefore, to describe an ITD with a single numerical

Table 1 Operating point of the HP turbine stage with and without ITD.

Parameter	Predicted uniform inlet temperature	Measured: Uniform inlet temperature	Measured: ITD
p_{01}, bar	4.6	4.6±2%	4.6±2%
T_{01}, K	444	444±2%	444±2%
M_2^{hub}	1.054	1.034±2%	1.063±2%
M_2^{case}	0.912	0.925±2%	0.926±2%
ω, r.p.m.	9500	9500±2%	9500±2%
p_3^{hub}, bar	1.434	1.428±2%	1.451±2%
p_3^{case}, bar	1.439	1.435±2%	1.453±2%
p_{02r}, bar	2.697	2.707±2%	No data

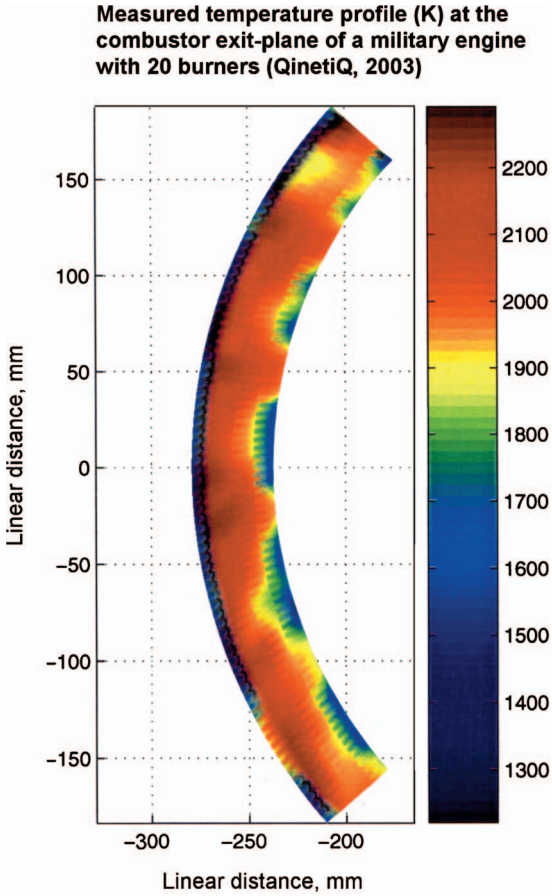

Fig. 3 Typical measured combustor exit temperature profile

value. A distinction is sometimes drawn, however, between the overall TDF (OTDF), which is a measure of the divergence of the hottest gas streak from the mean temperature, and the radial TDF (RTDF), which is a measure of the nonuniformity of the circumferentially averaged temperature field. The definitions that are used are as follows:

$$\text{OTDF} = \frac{T_{\max} - \bar{T}^{\text{area}}}{\Delta T_{\text{comb}}}, \quad \text{RTDF} = \frac{\bar{T}^{\text{circ}}_{\max} - \bar{T}^{\text{area}}}{\Delta T_{\text{comb}}}$$

where $\bar{T}^{\text{area}}$ is the area mean temperature, $\bar{T}^{\text{circ}}$ is the circumferential mean temperature (expressed as a function of radial height), ΔT_{comb} is the temperature rise across the combustor, and T is the local temperature (a function of span, or area). The subscript "max" identifies that the maximum of the quantity has been taken. Where a description of the form of the profile is required, the local OTDF (LOTDF) and local RTDF (LRTDF) forms follow naturally:

$$\text{LOTDF} = \frac{T - \bar{T}^{\text{area}}}{\Delta T_{\text{comb}}}, \quad \text{LRTDF} = \frac{\bar{T}^{\text{circ}} - \bar{T}^{\text{area}}}{\Delta T_{\text{comb}}}$$

The usefulness of these TDF definitions is not universally understood. In the engine situation, the parameter quantifies how completely hot and cold gas streams mix. There is no direct analogy in the test-facility situation. It is worth noting, however, that, where heat transfer similarity is concerned, and where both $\bar{T}^{\text{area}}/T_w$ and T_{cool}/T_w (where T_{cool} is the temperature of the cold gas introduced to simulate ITD in the test rig situation), equivalent TDFs may be defined.

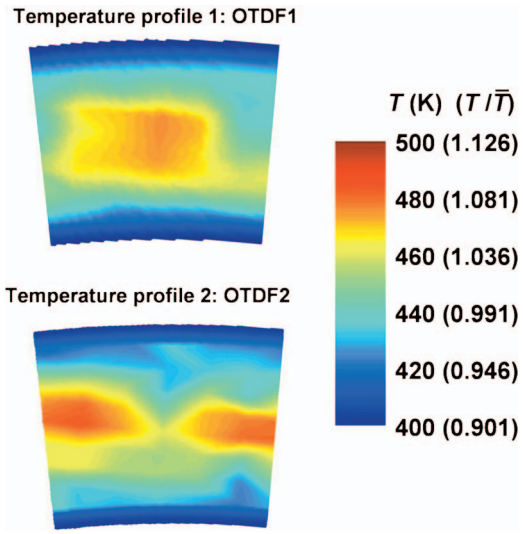

Fig. 4 Measured inlet temperature profiles: OTDF1 and OTDF2

$$\mathrm{LOTDF}_{\mathrm{rig}} = \frac{T - \bar{T}^{\mathrm{area}}}{\bar{T}^{\mathrm{area}} - T_{\mathrm{cool}}}, \quad \mathrm{LRTDF}_{\mathrm{rig}} = \frac{\bar{T}^{\mathrm{circ}} - \bar{T}^{\mathrm{area}}}{\bar{T}^{\mathrm{area}} - T_{\mathrm{cool}}}$$

It can be shown that if $\mathrm{LOTDF}_{\mathrm{rig}}$ (rig situation) is matched to LOTDF (engine situation), the nondimensional vane inlet temperature profile ($T/\bar{T}^{\mathrm{area}}$) will also be approximately matched. This is so whether or not there is similarity of mixing processes (rig to engine) upstream of the vane inlet plane.

The Temperature Distortion Generator

In a typical civil engine, fuel-injector-to-vane-count ratios near 1:2 are not uncommon. Count ratios are often noninteger, however, and therefore the possible benefits associated with hot-streak clocking are difficult to realize in practice. HP vane surface cooling systems must be designed for peak combustor exit temperatures. There has been, therefore, considerable interested in the effects of hot streak clocking (relative circumferential position).

The ITD generator used in the ILPF is described in detail by Chana et al. [51]. Hot-streaks, rotatable with respect to the NGV leading edge, are generated by blowing cool air through struts upstream of the HP NGVs. The number of hot streaks was the same as the HP vane count: 32. Experimental results for two clocking positions are discussed in this paper. The temperature profiles measured at the inlet plane of the HP vane (average of area surveys at three locations around the annulus) are presented in Fig. 4. The scale is presented both as time-mean temperature, and as temperature ratio, $T/\bar{T}^{\mathrm{area}}$: it is worth noting that where hot-streak migration physics is concerned, it is sufficient to match $T/\bar{T}^{\mathrm{area}}$ alone, although a number of parameters—essentially identical—have been used by other authors. The two profiles for which data is presented are referred to as OTDF1 (hot-streak aligned geometrically with the vane midpassage) and OTDF2 (hot-streak aligned with the vane leading edge). Thus, the effect of clocking the hot-streak with respect to the HP vane could be investigated.

The maximum and minimum measured gas temperatures were approximately 480 and 412 K (note that measurements were not conducted very close to the wall—within 5% span of the endwall). The mean temperature was the same for both uniform and nonuniform inlet temperature: 444 K. Because cool air was injected to create an ITD, a higher main flow temperature was required. This was achieved by increasing the pump-tube compression ratio. The peak-to-mean and minimum-to-mean temperature ratios were approximately 1.08 and 0.93, respectively.

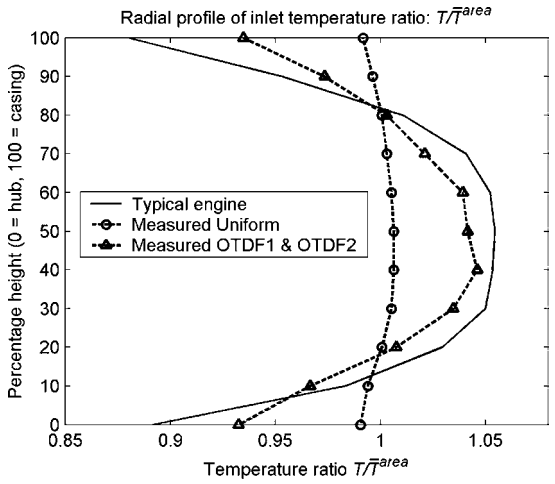

Fig. 5 Comparison of the ILPF radial temperature profile with typical engine profile

There was no significant difference between the radial temperature profiles (circumferentially averaged), $\bar{T}^{\mathrm{circ}}/\bar{T}^{\mathrm{area}}$, for OTDF1 and OTDF2. The measured radial profile is presented in Fig. 5 and is compared to the temperature profile of a typical engine (measurements were not taken very close to the endwall—within 5% span of the endwall—and the temperature at the nearest point was used in this region). The measured temperature profile without ITD is also given, and is indicated in Fig. 5 by "Measured Uniform." The measured radial profiles for OTDF1 and OTDF2 were very similar in both magnitude and form to the engine profile. The peak measured value of $\bar{T}^{\mathrm{circ}}/\bar{T}^{\mathrm{area}}$ was 1.045, while the peak engine value was 1.055. The minimum measured value of $\bar{T}^{\mathrm{circ}}/\bar{T}^{\mathrm{area}}$ was 0.93, while the corresponding engine value was 0.89. There are many ways of comparing the intensities of peaks of nonuniform temperature profiles. A useful comparison may be made in terms of a nondimensional intensity factor such as the ratio (rig-to-engine) of nondimensionalzed peak-to-min temperature differences in the radial profile:

$$\frac{(\bar{T}^{\mathrm{circ}}_{\mathrm{max}}/\bar{T}^{\mathrm{area}} - \bar{T}^{\mathrm{circ}}_{\mathrm{min}}/\bar{T}^{\mathrm{area}})_{\mathrm{rig}}}{(\bar{T}^{\mathrm{circ}}_{\mathrm{max}}/\bar{T}^{\mathrm{area}} - \bar{T}^{\mathrm{circ}}_{\mathrm{min}}/\bar{T}^{\mathrm{area}})_{\mathrm{engine}}}$$

In terms of this parameter, the ratio was approximately 0.7:1.0. The nondimensional temperature field of the experiment was therefore similar in magnitude to that of a typical engine.

Instrumentation and Processing

The HP vane was instrumented with static pressure tappings at 10, 50, and 90% spans on both the pressure and suction surface of the vane. Surface heat transfer measurements were conducted using thin-film platinum resistance heat transfer gauges of the type described by Oldfield and Doorly [52]. On the vane pressure and suction surfaces, a thin Upilex™—polyimide—substrate was used to support the gauges, as shown in Fig. 6 (two-layer substrate). To conduct measurements on the endwalls, gauges were painted and fired directly onto vanes made from Macor™, a machinable glass, as shown in Fig. 7 (single-layer substrate).

Uncertainty in Nusselt Number. Equations for the transient thermal response of a thin-film gauge on a two-layer substrate are presented by Doorly and Oldfield [53]. The corresponding equations for a single-layer substrate are given by, for example, Jones [54]. A full uncertainty analysis for thin-film heat transfer measurements is quite involved. Povey [55], considers the following sources of uncertainty:

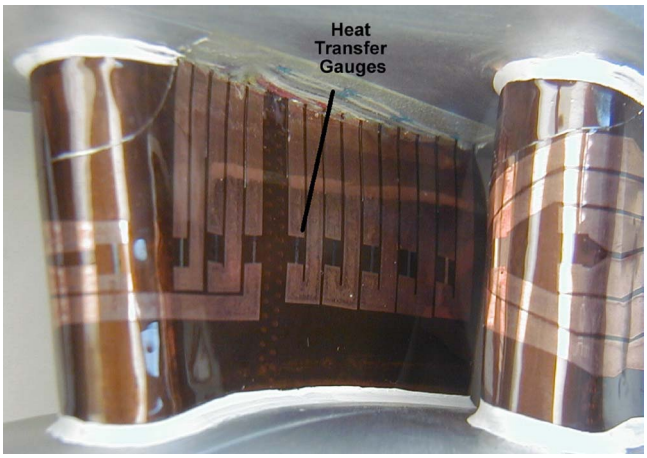

Fig. 6 Thin film gauges on the HP vane PS at 50% span

(i) Uncertainty in directly measured physical parameters (T_0, p_0, p, R_{20}, I, V_g, etc.) and derived physical parameters (T_w, T_{aw}).
(ii) Uncertainty in experimentally determined physical (thermal) properties where a full independent analysis of the experimental uncertainty must be conducted ($\rho_1 c_1 k_1, \rho_2 c_2 k_2, a/k_1, \alpha$).
(iii) Process uncertainties: analog-to-digital conversion, averaging a fluctuating signal over a finite period, numerical uncertainties associated with discrete Fourier transform processing, etc.
(iv) Additional uncertainties arising from, for example, gauge lead temperature coefficient of resistance, etc.

It is essential (order of magnitude changes) to consider the time dependency of the sensitivity coefficients of each parameter, and also to perform separate analyses that include only those uncertainties that affect gauge-to-gauge, run-to-run, and absolute uncertainties. In the ILPF, the heat flux history to the vane and endwall surfaces can be approximated by a step in heat transfer of 500 ms duration. The analytical solution for T_w (gauge on two-layer substrate) for a step function in $\dot{q}$ has been calculated by Doorly [56]. The author shows that $T_w(t)$ is initially dominated by the thermal product of the surface substrate layer, $\rho_1 c_1 k_1$. Once the thermal wave has penetrated the upper layer, the gauge acts very much like a direct heat-flux gauge [57], and the surface temperature rises much more slowly (for $\rho_2 c_2 k_2 > \rho_1 c_1 k_1$); $T_w(t)$ is now most strongly linked to $\rho_2 c_2 k_2$, the thermal product of the lower layer. The time at which the second term becomes dominant in describing $T_w(t)$ is termed the switch point, and for a 100 μm Upilex™ layer over aluminum, this occurs at approximately $t_{sp} \approx 70$ ms.

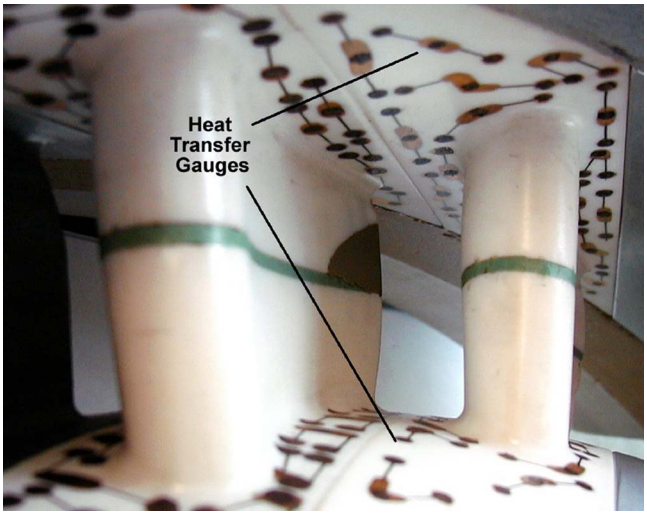

Fig. 7 Heat transfer gauges on the HP vane hub and case endwalls

Table 2 Measurement precision and absolute uncertainty.

	Precision		Absolute uncertainty	
Variable	Uniform	ITD	Uniform	ITD
T_0	±1 K	±3 K	±5 K	±7 K
T_{aw}	±1 K	±3 K	±5 K	±7 K
T_w	±1.5 K	±1.5 K	±1.5 K	±1.5 K
$T_{aw}-T_w$	1.9%	3.6%	5.6%	7.6%
$\bar{\dot{q}}$	1.5%	1.5%	3.4%	3.4%
Nu_{aw}	2.4%	3.9%	6.6%	8.3%

A mean value of heat transfer $\bar{\dot{q}}$ was obtained by averaging during the period 350 to 450 ms. For $t \gg t_{sp}$, the heat flux uncertainty is highly insensitive to uncertainty in both $\rho_1 c_1 k_1$ and $\rho_2 c_2 k_2$, and depends primarily on the uncertainty in the value of a/k_1. The same result can easily be obtained using a perturbation analysis technique using experimental data. The value of a/k_1 was determined experimentally by methods described by Piccini et al. [58]: the uncertainty was approximately 3.0%. The absolute uncertainties in the values of in T_w and $\bar{\dot{q}}$ (precision ≈1.5%) were approximately 0.5% and 3.4%, respectively.

The uncertainty in Nusselt number is dominated by the uncertainty in the term $T_{aw}-T_w$, the uncertainty in T_{aw} arising as the result of uncertainty in T_0, with a negligibly small additional contribution from uncertainty in p/p_0. T_0 is measured during a run using ten thermocouples in the leading edge plane of the HP NGVs. Absolute uncertainties are based on estimates of boundary layer thickness etc., and, for the case of ITD, accuracy in matching a nonuniform temperature field based on a finite number of point measurements. Estimates of measurement precision and absolute uncertainty are given in Table 2, below.

Numerical Methods for Heat Transfer Rate Prediction

The measured HP vane surface heat transfer rate distribution was compared to predictions conducted using an integral method, and using the TEXSTAN code. An outline of these codes and the input conditions are given below.

Integral Method Predictions. Surface heat transfer rate was calculated using the integral method technique of Kays and Crawford [5]. This gives an approximate solution to the momentum and energy equations in a region of varying free-stream velocity, and for varying fluid properties for an isothermal surface. The velocity profile of the vane was accurately known from experiment. The stagnation point heat transfer and enhancement due to turbulence were calculated using the correlations of Lowery and Vachon [59], which have been verified by other authors. The point of transitional onset was predicted with a correlation that was developed by Abu-Gannam and Shaw [2]. The correlation of Fraser et al. [4] was used for the transition length, although this is notoriously difficult to predict accurately. Enhancement factors for free-stream turbulence effects were treated using the correlations of Krishnamoorthy and Sukhatme [60]. These have been compared with a wide range of experimental data and have been shown to offer reasonable accuracy over a wide range of conditions. Predictions of heat transfer rate at 50% span were made at the mean inlet total temperature of 444 K, and using a total pressure of 4.6 bar. The measured surface aerodynamics given in Fig. 8 was used. Predic-

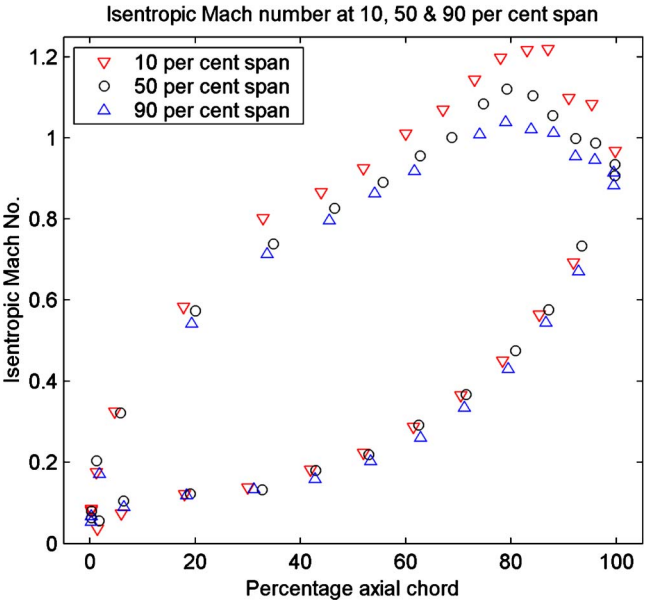

Fig. 8 HP vane isentropic Mach number at 10, 50, and 90% span

tions were made for an isothermal wall at 300 K, to replicate the conditions of the experiment. One of the difficulties of comparing experimental and predicted results in terms of Nusselt number is the choice of total temperature that is used to derive Nusselt number from heat transfer rate. Ideally, a local recovery temperature would be used, but in the case of nonuniform inlet temperature in particular, this can be very difficult to determine. For this reason, a local recover temperature based on the mean inlet total temperature of 444 K, and the measured aerodynamics, was used throughout.

TEXSTAN Predictions. Nusselt number measurements were also compared to predictions conducted using Academic Version 1999 of the boundary layer code TEXSTAN [61]. The code was run using the measured 50% span pressure distribution, to output surface heat transfer rate. No allowance for the surface curvature was included. Predictions were performed at a number of inlet turbulence levels. The turbulence model used was that of Lam and Bremhorst [62], a two-equation *k*-epsilon model. The inlet total temperature was set to 444 K, and the total pressure to 4.6 bar. The boundary layer was initiated 0.1 mm from the leading edge at a nominal thickness. Transition location was determined using the same correlation as for the integral method above. The Nusselt number was then calculated using an adiabatic wall temperature based on an inlet total temperature of 444 K and the measured aerodynamics. The isothermal wall temperature was set to 300 K.

Experimental Results

Interpretation of the measurements of HP vane surface heat transfer rate was informed by investigations of HP vane aerodynamics and surface flow visualization (using an oil paint method). These experiments were conducted for uniform and nonuniform inlet temperatures and will now be described.

Aerodynamics. The HP vane surface Mach number distributions at 10, 50, and 90% span are presented in Fig. 8. The passage was fully choked, with a peak Mach number at 10% span of approximately 1.22, and a peak Mach number at 90% span of approximately 1.03. A sudden drop in Mach number across the shock on the SS of the vane can be seen at approximately 87% axial chord at 10% span. A QinetiQ TRANSCode prediction (not shown) was in good agreement with the measurements.

The measured steady pressure distribution showed little change

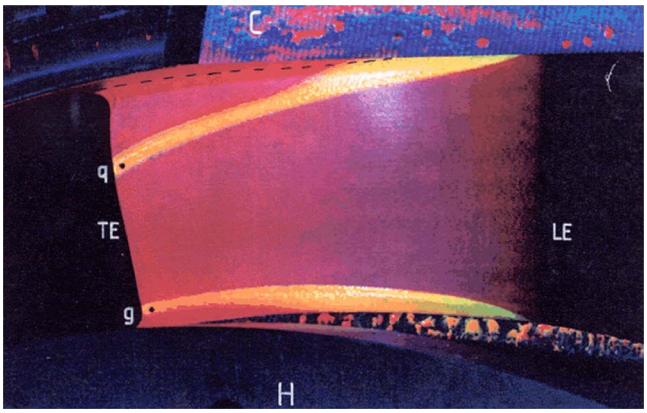

Fig. 9 Surface flow visualization on the HP vane SS [13]

with the introduction of ITD (see also Hurrion [28]). The most pronounced effect of ITD on the HP vane was on the unsteady pressure measurements in the trailing edge region (not discussed in this paper). As expected, the effect of ITD on the operating point of the rotor (both steady and unsteady) was more pronounced than that on the HP vane. This is because, although ITD does not affect the inviscid flow field within the HP vane passage, temperature distortions cause a change both in rotor-relative inlet total pressure and in rotor-relative incidence angle.

Surface Flow Visualization. A photograph of a surface flow visualisation experiment is presented in Figure 9. In this photograph of the SS of the vane, the leading edge (LE) and trailing edge (TE) are marked, and the surface streamlines are highlighted by using layers of oil paint dissimilar in color. The hub and casing platforms are marked "H" and "C" respectively. On the SS, there was significant radial flow migration on to the surface of the vane. The hub endwall vortex was relatively small in extent, and migrated to approximately 10% span. The point at which the vortex leaves the vane is marked "g." At the casing, the vortex was considerably larger, as expected, and migrated to approximately 30% span. The point at which the vortex leaves the vane is marked "q." The PS flow was largely parallel to the endwalls. The heat transfer rate at midspan is therefore likely to be largely unaffected by the secondary flows, while on the SS at 10% span, but also—especially −90%, one would expect a reduction in heat transfer rate for uniform inlet temperature as a result of the secondary flows.

HP Vane Surface Nusselt Number. The measured HP vane surface Nusselt number distribution for uniform inlet temperature is presented in Fig. 10. Nu was calculated using an adiabatic wall temperature based on the mean inlet temperature of 444 K, using a tangential chord length of 70.1 mm, and using the measured wall temperature. In Fig. 10, error bars indicate the absolute uncertainty in the measurement, which was 6.6%. The precision of the measurement was approximately 2.4%. Two runs are presented that agree (on average) to within less than 1%. The results are plotted against percentage surface distance (SD).

The stagnation point peak measured Nu was approximately 2500. The Nu distribution on the PS of the vane suggests gradual transition from a laminar to a turbulent boundary layer. The point of transitional onset was at approximately 10% SD, where the minimum value of Nu was approximately 1200. The value of Nu increased continuously from 10% SD to the trailing edge of the vane, where the peak Nu was approximately 2750. The increase towards the trailing edge is expected because the flow accelerates in this region, and therefore thinning of the boundary layer occurs.

On the SS, the transition process was more clearly defined. At 25% SD, the value of Nu (1300) suggests a laminar boundary layer, whilst at 70% SD the level suggests a fully turbulent bound-

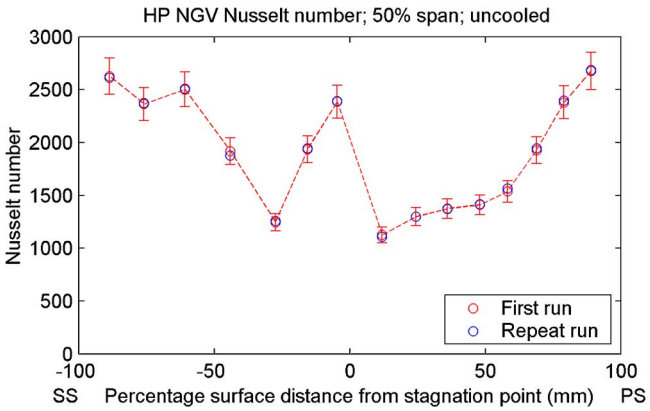

Fig. 10 Measured HP vane surface Nusselt number distribution

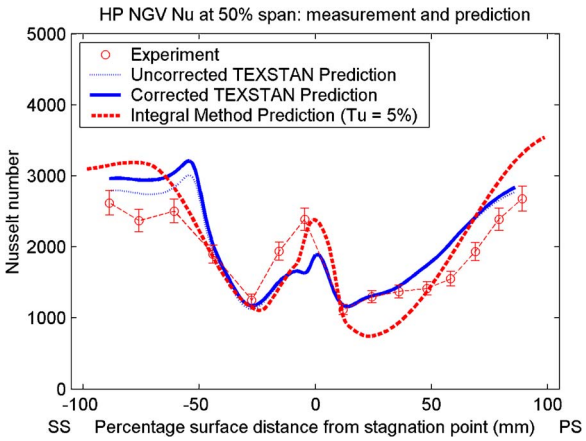

Fig. 12 Integral method and TEXSTAN predictions for HP vane surface Nu compared to experimental data

ary layer. From 70% SD to the trailing edge of the vane, the Nu is almost constant (approximately 2500). It is not possible to determine the length of the transitional region exactly, but the available data place a maximum bound on the length of 45% SD; it is likely to be significantly shorter than this.

Comparison of Measured HP Vane Surface Nusselt Number With TEXSTAN and Integral Method Predictions. The integral method prediction for HP vane surface Nusselt number distribution is compared to the experimental data at 50% span in Fig. 11. Predictions were made for a free-stream turbulence level of 5%. Experimental points are marked as open circles. The blind prediction and the prediction for a fully laminar boundary layer are presented. The latter is useful in comparing prediction and experiment in the transitional region.

The leading edge Nu number is in excellent agreement with the experimental value. Similarly, the predicted Nu on the SS plateau (towards the trailing edge of the vane) is in reasonable agreement with the measured results, the predicted value being approximately 30% greater. On the PS of the vane, the predicted onset and length of transition are in reasonable agreement with the experimental results, although the predicted Nu distribution is somewhat higher than the measured values from 30% SD onwards. It is clear that on the SS, however, the correlations for onset and length of transition do not accurately represent what was measured. The prediction is for fully developed turbulent flow at 25% SD, while the experimental results suggest transitional flow at 50% SD.

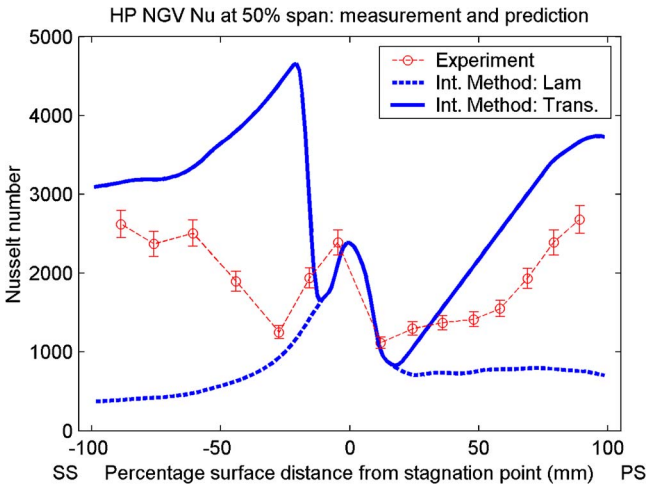

Fig. 11 Integral Method prediction for HP vane surface Nu compared to experimental data

Similarly, the prediction is for transitional onset at 10% SD, while measurements suggest a fully laminar boundary layer at 25% SD. The large discrepancies between the measured and predicted distributions of Nu on the SS arise because the transitional region is poorly modeled. The results highlight a common problem in predicting transitional behavior in regions of strong streamwise pressure gradient.

The same correlations as those used in the Integral Method code were used for prediction of transitional onset and length of transition in the TEXSTAN code, resulting in similar discrepancies between predicted and measured values. Imposing start and end points of transition resulted in good agreement between measured and predicted values of Nu. The Integral Method and the TEXSTAN predictions—for forced transition—are compared to the experimental measurements in Fig. 12. The TEXSTAN results are presented using a gas temperature of 444 K ("Uncorrected") and using a recovery temperature based on a total temperature of 444 K ("Corrected"). When the transition locations are imposed, the predictions agree well with experimental results. On the SS, the TEXSTAN prediction is everywhere within 30% of the measured results, with the greatest discrepancy in the leading edge region. On the SS, the TEXSTAN and Integral Method predictions are very similar in magnitude and form. On the PS, the TEXSTAN prediction is somewhat closer to the experimental results than the Integral Method prediction and the discrepancy between TEXSTAN prediction and experiment was everywhere less than 20%.

Overall, the TEXSTAN prediction is in slightly better agreement with the experimental results than the Integral Method, but both codes have similar limitations: in particular, the problem with the accurate prediction of the point of transitional onset and the length of transitional region.

Comparison of HP Vane Surface Nusselt Number With and Without Inlet Temperature Distortion. The measured Nusselt number at 50% span is presented in Fig. 13. Results are given for uniform inlet temperature, and for ITDs OTDF1 and OTDF2. Nu was calculated using local recovery temperature based on a mean inlet temperature (444 K) and on the tangential chord of the vane. Error bars represent absolute uncertainty in the data points: 6.6% for uniform inlet temperature, and 8.3% for ITD. Precision (repeatability) uncertainties were 2.4% and 3.9%, respectively, although in practice significantly better repeatability was obtained between runs.

The stagnation point Nu was similar (within ~10%) for uniform inlet temperature and for ITD. The exact location of the peak is not significant, as different instrumentation was used for uniform temperature and ITD measurements, and the number of gauges was insufficient to determine exactly the location of the stagnation point. On the PS of the vane, there was little change in

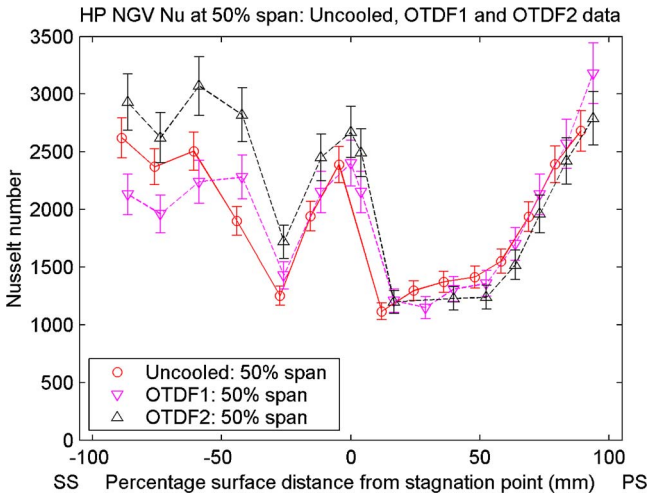

Fig. 13 Comparison of HP vane surface Nusselt number distribution with and without ITD at 50% span

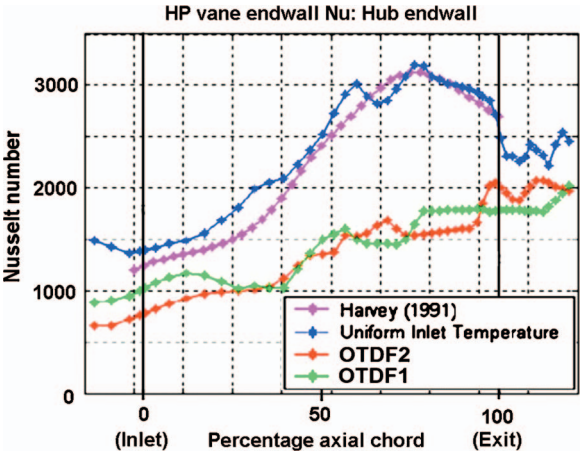

Fig. 15 Nusselt number on the HP vane hub endwall with and without ITD

Nu with ITD. Differences between the measurements were of the order of 10% or lower. On the SS, in contrast, there was a marked change with the introduction of ITD. On the SS, the general form of the measurements was similar for the three temperature profiles: high Nu (~2500) at the leading edge stagnation point; a reduction in Nu in the laminar boundary layer region; a rapid increase in Nu as the flow undergoes transition; a plateau in Nu towards the trailing edge in the fully turbulent boundary layer region. The measurements conducted for OTDF2 show that the value of Nu is consistently higher on the SS than for either uniform inlet temperature or for OTDF1. In contrast, the measured Nu distribution for OTDF1 was similar to that for uniform inlet temperature over the early SS, but lower towards the trailing edge than for either of the other two profiles.

The results are now discussed with reference to Figure 14, which is a schematic representation of the streamlines at 50% span for ITDs OTDF1 and OTDF2. In Fig. 14, a schematic cross section of the temperature profile is presented, depicting the clocking position of the hot-streak with respect to the vane leading edge. Regions of high, intermediate, and low temperature are indicated by red, green, and blue, respectively. Although the ITD generator was configured so that the hot-streaks were aligned—geometrically—with the HP vane midpassage (OTDF1), and with the vane leading edges (OTDF2), circulation in the approach to the vane leading edge region introduces a shift in the location of the peak with respect to the vane leading edge. The left side of the figure is a schematic of OTDF1. Because of the effect of circulation, the low temperature region is not incident equally on the pressure and suction surfaces of the vane, but moves towards the SS. Thus, there is a reduction in driving gas temperature only on the SS of the vane: consider the results presented for OTDF1 in Fig. 13. Likewise, for OTDF2, circulation causes the hot-streak to impact the SS of the vane, rather than equally on both surfaces: consider the results presented for OTDF2 in Fig. 13. The results demonstrate that the effect of ITD on heat transfer is significant, and highlight the necessity of correctly calculating the displacement effect of circulation ahead of the vanes if clocking is to be used to advantage in engine design.

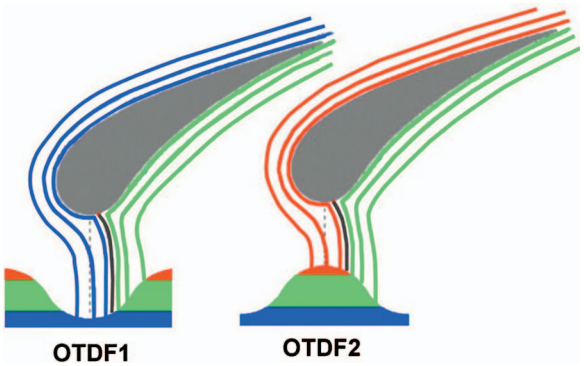

Fig. 14 Schematic of the 50 percent span streamlines for OTDF1 and OTDF2

Comparison of HP Vane Endwall Nusselt Number With and Without Inlet Temperature Distortion. The midpassage Nu on the HP vane hub endwall is shown in Fig. 15. Heat transfer measurements were conducted throughout the passage (approximately 40 locations) and the data were fitted with a three-dimensional spline. Nu based on mean inlet total temperature (T_{01}=444 K) was then calculated from the spline fit. Results are presented for uniform inlet temperature, and for ITDs OTDF1 and OTDF2. Nu is plotted against percentage axial chord (0% = leading edge, 100% = trailing edge).

For uniform inlet temperature, the hub endwall Nu at inlet to the vane passage was approximately 1400. Close to the trailing edge Nu plateaus at approximately 3000, then falls rapidly to approximately 2300 downstream of the vane. Harvey [13] conducted similar measurements on the vane endwall, which are presented for comparison. The data are in agreement, and this lends confidence to the results.

The results for OTDF1 and OTDF2 are very similar, and show a significant reduction—over the results for uniform inlet temperature—in midpassage Nu based on mean inlet temperature. Between 0 and 95% axial chord the reduction in Nu is between 30 and 50%. The reduction in Nu (as defined above) implies either a reduction in driving temperature, or a reduction in the heat transfer coefficient. These effects are, in fact, impossible to separate, and this highlights a common problem with heat transfer investigations. The aerodynamic survey (presented above) gave strong evidence, however, that there was little change with ITD in the vane flow-field. This is in accord with the theoretical result of Munk and Prim [27], which states that no additional redistribution of the mainstream flow (because here viscous forces are negligible) is expected with ITD. It seems likely, therefore, that the observed change in Nu is largely driving-temperature-induced, rather than caused by a change in heat transfer coefficient. The reduction of Nu on the hub endwall suggests that the mean gas temperature in the near-endwall region is lower for OTDF1 and OTDF2 than for uniform inlet temperature. This is expected, and demonstrates the beneficial effect on endwall heat load of ITD. It

is worth noting that whether the radial temperature profile arises primarily because of combustor lining coolant flow, or because of slot injection at the combustor/turbine interface, the above result would still hold: the endwall heat load is significantly lower than might be expected for a uniform inlet temperature flow of the same mean temperature.

If the heat transfer coefficient is assumed unchanged, the driving temperature may be approximated using the following expression

$$\frac{\mathrm{Nu}_{TD}}{\mathrm{Nu}_U}(T_g^{\mathrm{ass}} - T_w) + T_w = T_g^{\mathrm{act}}$$

where Nu_U and Nu_{TD} are the Nusselt numbers for uniform inlet temperature and for ITD, respectively, and T_w, T_g^{ass}, and T_g^{act} are the wall temperature, the assumed gas temperature, and the actual gas temperature, respectively. Using values of T_w=310 K, and T_g^{ass}=444 K the above expression reduces to

$$T_g^{\mathrm{act}} = \frac{\mathrm{Nu}_{TD}}{\mathrm{Nu}_U}(134) + 310$$

Accepting the assumptions implicit in the above analysis the local driving temperature can be calculated. For reductions in Nu with ITDs of 30 and 50%, the driving temperatures calculated using the above expression are T_g^{act}=404 K and T_g^{act}=377 K respectively. The measured flow temperature at the closest location to the endwall was 412 K. The above-calculated temperatures are somewhat lower than this. The suggestion is that, while the results are in rough accord with the measured temperature distributions, the near-wall flow temperature (which was not measured) was even lower than expected. The evidence suggests a driving temperature induced reduction in Nusselt number, with driving temperatures in the range 377 K to 404 K in the near-wall flow.

It is worth nothing that towards the trailing edge (from 80% axial chord onwards) the reduction in Nu with ITD was lower than elsewhere in the passage. It is likely that this was predominantly the result of secondary flow induced mixing, which acts to raise the gas temperature in the near-wall region (for OTDF1 and OTDF2) by mixing with it gas from the mainstream, which is likely of higher temperature. Thus, the values of Nu with and without ITD are more similar than in regions unaffected by secondary flow: for fully mixed out flow, of course, it is expected that the values of Nu would be the same.

It should be understood that while this analysis provides a very satisfying semi-quantitative explanation of the observed heat transfer rates with and without ITD, the accuracy of the analysis is limited because the driving gas temperature is not directly known. Even in the case of uniform inlet temperature, the driving temperature is not uniform. Secondary flows develop, which, resulting from intimate contact with cooler metal surfaces, are of lower temperature than the inlet temperature. In addition, because the vane is operating in the transonic regime, the recovery temperature can differ by several degrees from the mainstream temperature.

The midpassage Nusselt number on the HP vane casing endwall is shown in Fig. 16. Results are presented for uniform inlet temperature and for IDTs OTDF1 and OTDF2. The results are presented in the same way as for the hub endwall. For uniform inlet temperature, the measured Nu is in excellent agreement with the results of Harvey [13]. A smooth increase in Nu in the downstream direction from 1100 to 2750 was observed. Results for the two distorted temperature fields were similar: there was a significant reduction in Nu over the entire chord of the casing endwall at midpassage. At the leading edge, Nu was reduced from 1100 to 770, a reduction of 30%. In the region close to the trailing edge, Nu was reduced from 2750 to 1800, a reduction of 35%. The magnitude of the reduction in Nu with ITD was everywhere between 25 and 35%.

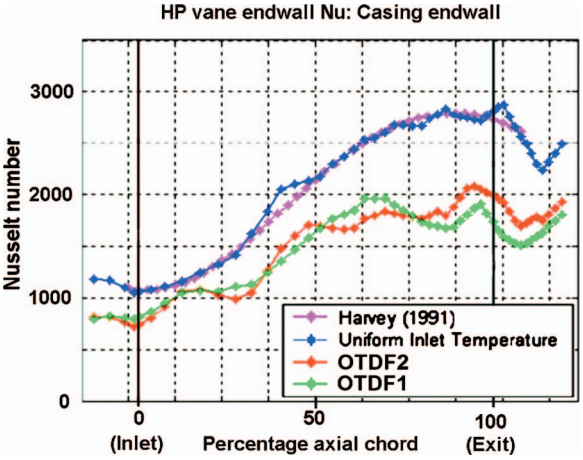

Fig. 16 Nusselt number on the HP vane case endwall with and without ITD

Conclusions

Aerodynamic and surface heat transfer measurements were conducted on HP nozzle guide vane and endwall with both uniform and engine-representative turbine inlet temperature distribution functions. In addition, surface flow visualization experiments were performed, to aid interpretation of the results. The measured surface Nusselt number distribution on the HP vane (run with a uniform inlet temperature) has been compared to two numerical predictions. The first was made using an integral method that was written specifically for this purpose, and the second was made using the TEXSTAN code. This is the first time, to the authors' knowledge, such a comprehensive survey of the effect of hot-streaks on the HP vane heat transfer has been conducted, in which all relevant nondimensional parameters were also matched.

Aerodynamic measurements indicated that the HP vane operating point was unaffected by the introduction of ITD. In the trailing edge region, there was a small influence with the introduction of ITD on the unsteady pressure distribution of the vane. Surface flow visualization experiments showed that the secondary flows were relatively small in extent (extending 10% and 30% of span from the hub and the case, respectively), and that the midspan flow was essentially unaffected by radial flow migration.

The Nusselt number results for uniform inlet temperature indicated relatively early transitional onset on both the pressure surface (10 mm) and the suction surface (22 mm) of the vane. The transition to fully turbulent flow was relatively rapid on the SS, although on the PS the transitional region was less clearly defined. Both the integral method code and the TEXSTAN code were markedly poor at predicting the point of transitional onset and the length of the transitional region, especially on the suction surface of the vane. By setting the start and end points of transition in the integral method code and in the TEXSTAN code, a reasonable match between prediction and experimental data was achieved. Discrepancies were everywhere lower than 35% in magnitude, and 20% or less over much of the vane surface. In terms of the mean level, the TEXSTAN prediction was somewhat better than the integral method prediction, although both codes predicted higher heat transfer rates in the turbulent region than were measured.

Measurements of the effect of an engine-representative turbine inlet temperature distribution on the HP vane heat transfer at midspan were conducted for two clocking positions of a hot-streak with respect to the vane. Measurements were performed with the *hot-streak* aligned with the leading edge of the vane, and aligned with the vane mid passage. The heat transfer rate on the SS at 50 percent span was substantially increased—over the uniform inlet temperature result—when the *hot-streak* was aligned with the vane leading edge, and was slightly decreased when the *hot-streak*

was aligned with the vane midpassage. The same result was not observed on the PS at 50% span, which was insensitive to changes in ITD. The results were explained qualitatively in terms of a model that included the effect of circulation in the approach to the vane leading edge. The results demonstrate that hot-streaks can have a significant impact on HP vane heat transfer, and highlight the need to carefully characterize the streamline pattern in this region if the effects of clocking are included in the turbine design process.

Detailed measurements of the heat transfer rate to the HP vane passage end-walls with and without ITD were conducted. The results for uniform inlet temperature were in excellent agreement with measurements conducted in the same facility by Harvey (1991); this was in support of the robustness of the measurements. With the introduction of ITD there was a large decrease in heat transfer rate over the entire endwall surface at both hub and the casing. Along the mid-passage streamline, the decrease in Nu (based on mean inlet temperature) with ITD at the hub endwall was between 30 and 50%. Along the casing endwall, the reduction was between 25 and 35%. The reduction was very similar for both clocking positions of the hot-streak, suggesting the effect is not affected by the relative circumferential positions of the *hot-streak* and the HP vane. The form of the results (and other evidence discussed in the text) suggested that the decrease in heat transfer rate was the result of a lower local total temperature of the gas near the endwalls rather than a decrease in the heat transfer coefficient. The driving gas temperatures were calculated by assuming the same heat transfer coefficient as measured for uniform inlet temperature, and were in approximate agreement with temperatures measured close to the endwall at inlet to the vane. The results demonstrate that ITD can have a very significant effect on the endwall heat transfer.

Acknowledgments

The assistance of S. J. Anderson and A. H. Mole in the acquisition of data contained in this report is gratefully acknowledged. This work was conducted as part of, and was funded under, the Brite Euram Forth Framework on Turbine Aerothermal External Flows, Contract Number BRPR-CT97-0519. The UK Department of Trade and Industry through the CARAD Programme also provided funding.

Nomenclature

a = thickness of Upilex™ (upper substrate) layer
c = specific heat capacity
I = gauge supply (constant) current
k = thermal conductivity
M = isentropic Mach number
$p; p_0; p_{01}$ = static pressure; total pressure; total pressure at stage inlet
R_{20} = gauge resistance at 20°C
Re = Reynolds number
Tu = turbulence intensity
$T_0; T_{01}$ = total temperature; total temperature at stage inlet
T_{cool} = temperature of injected coolant flow
$T_{g'}; T_g^{\text{ass}}; T_g^{\text{act}}$ = local gas temperature; assumed; actual
$T_{\max}; \Delta T_{\text{comb}}$ = peak combustor exit temperature; temperature rise across combustor
$T_w; T_{aw}$ = local wall temperature; adiabatic wall temperature
$\bar{T}^{\text{area}}$ = area mean temperature
$\bar{T}^{\text{circ}}$ = circumferential mean temperature (expressed as a function of radial height)
V_g = gauge output voltage
α = temperature coefficient of resistance
ρ = material density
ω = angular speed of turbine

Abbreviations

HP = high-pressure
ITD = inlet temperature distortion
NGV = nozzle guide vane
OTDF & RTDF = overall & radial temperature distortion factors
PS; SS = pressure surface; suction surface
SD = surface distance
TDF = temperature distortion factor

Subscripts

1 = HP vane inlet; upper substrate index (Upilex™, Macor™)
2 = HP vane exit; lower substrate index (aluminium)
3 = HP rotor exit
r = rotor relative
hub; case = Evaluated at hub; case
max; min = maximum; minimum

References

[1] Parker, R., and Watson, J. F., 1972, "Interaction Effects Between Blade Rows in Turbomachines," Proc. Inst. Mech. Eng., **186**(21), pp. 331–340.
[2] Abu-Ghannam, B. J., and Shaw, R., 1980, "Natural Transition of Boundary Layers—The Effects of Turbulence, Pressure Gradient and Flow History," J. Mech. Eng. Sci., **22**(5), pp. 213–228.
[3] Narasimha, R., 1985, The Laminar-Turbulent Transition Zone in the Boundary Layer," Prog. Aerosp. Sci., **22**, pp. 29–80.
[4] Fraser, C. J., Higazy, M. G., and Milne, J. S., 1994, "End-Stage Boundary Layer Transition Models for Engineering Calculations," J. Mech. Eng. Sci., **208**, pp. 47–58.
[5] Kays, W. M., and Crawford, M. E., 1993, *Convective Heat and Mass Transfer* (Mechanical Engineering Series), 3rd ed., McGraw-Hill, New York.
[6] Klein, A., 1969, "Investigation of the Entry Boundary Layer on the Secondary Flows in the Blading of Axial Turbines," (English Translation) BHRA T-1004.
[7] Langston, L. S., Nice, M. L., and Hooper, R. M., 1977, "Three Dimensional Flow Within a Turbine Cascade Passage," ASME J. Eng. Power, **99**, pp. 21–28.
[8] Sieverding, C. H., 1985, "Secondary Flows in Straight and Annular Turbine Cascades," A. Ş Uçer, P. Stow, and Ch. Hirsch, eds., *Thermodynamics and Fluids of Turbomachinery*, Vol. II, NATO, pp. 621–624.
[9] Dunn, M. G., and Stoddard, F. J., 1979, "Measurement of Heat-Transfer Rate to a Gas Turbine Stator," ASME J. Eng. Power, **101**(2), pp. 275–280.
[10] Wedlake, E. T., Brooks, A. J., and Harasgama, S. P., 1988, "Aerodynamic and Heat Transfer Measurements on a Transonic Nozzle Guide Vane," ASME Paper No. 88-GT-10.
[11] Taulbee, D. L., Tran, L., and Dunn, M. G., 1989, "Stagnation Point and Surface Heat Transfer for a Turbine Stage: Prediction and Comparison With Data," ASME J. Turbomach., **111**(1), pp. 28–35.
[12] Harvey, N. W., Wang, Z., Ireland, P. T., and Jones, T. V., 1989, "Detailed Heat Transfer Measurements in Linear and Annular Cascades in the Presence of Secondary Flows," AGARD PEP 74B, pp. 24-1–24.12.
[13] Harvey, N. W., 1991, "Heat Transfer on Nozzle Guide Vane End Walls," D.Phil thesis, Department of Engineering Science, University of Oxford, Oxford, UK.
[14] Harvey, N. W., and Jones, T. V., 1990, "Measurement and Calculation of Endwall Heat Transfer and Aerodynamics on a Nozzle Guide Vane in Annular Cascade," ASME Paper No. 90-GT-301.
[15] Blair, M. F., 1974, "An Experimental Study of Heat Transfer With Film Cooling on Large-Scale Turbine Endwalls," ASME J. Heat Transfer, **96**, pp. 524–529.
[16] Gaugler, R. E., and Russell, L. M., 1984, "Comparison of Visualised Turbine Endwall Secondary Flows and Measured Heat Transfer Patterns," ASME J. Eng. Gas Turbines Power, **106**, pp. 168–172.
[17] Harvey, N. W., Rose, M. G., Coupland, J., and Jones, T. V., 1998, "Measurement and Calculation of Nozzle Guide Vane End Wall Heat Transfer," ASME Paper No. 98-GT-66.
[18] Kang, M. B., Kohli, A., and Thole, K. A., 1999, "Heat Transfer and Flowfield Measurements in the Leading Edge Region of a Stator Vane Endwall," ASME J. Turbomach., **121**, pp. 184–190.
[19] Kang, M. B., and Thole, K. A., 1999, "Flowfield Measurements in the Endwall Region of a Stator Vane," ASME Paper No. 99-GT-188.
[20] Friedrichs, S., Hodson, H. P., and Dawes, W. N., 1996, "Distribution of Film Cooling Effectiveness on a Turbine Endwall Measured Using the Ammonia and Diazo Technique," ASME J. Turbomach., **118**, pp. 613–621.
[21] Friedrichs, S., Hodson, H. P., and Dawes, W. N., 1999, "The Design of an Improved Endwall Film-Cooling Configuration," ASME J. Turbomach., **121**, pp. 772–780.

[22] Knost, D. G., and Thole, K. A., 2004, "Adiabatic Effectiveness Measurements of Endwall Film-Cooling for a First Stage Vane," ASME Paper No. GT-2004–53326.
[23] Oke, R., Simon, T., Shih, T., Zhu, B., Lin, Y. L., and Chyu, M., 2001, "Measurements Over a Film-Cooled Contoured Endwall With Various Coolant Injection Rates," ASME Paper No. 2001-GT-140.
[24] Colban, W. F., and Thole, K. A., 2003, Combustor Turbine Interface Studies—Part I: Endwall Effectiveness Measurements," J. Turbomach., **125**, pp. 193–202.
[25] Haselbach, F., and Schiffer, H. P., 2004, "Aerothermal Investigations of Turbine Endwalls and Blade," ASME Paper No. GT-2004-53078.
[26] Butler, T. L., Sharma, O. P., Joslyn, H. D., and Dring, R. P., 1989, "Redistribution of Inlet Temperature Distortion in an Axial Flow Turbine Stage," J. Propul. Power, **5**(1), pp. 64–71.
[27] Munk, M., and Prim, R. C., 1947, "On the Multiplicity of Steady Gas Flows Having the Same Streamline Pattern," Proc. Natl. Acad. Sci. U.S.A., **33**, pp. 137–141.
[28] Hurrion, J., 2002, "The Effect of an Inlet Temperature Profile on the Heat Transfer to Gas Turbine Blades," D.Phil. thesis, University of Oxford, Oxford, UK.
[29] Povey, T., Chana, K. S., and Jones, T. V., 2003, "Heat Transfer Measurements on an Intermediate Pressure Nozzle Guide Vane Tested in a Rotating Annular Turbine Facility—and the Modifying Effects of a Non-Uniform Inlet Temperature Profile," MIS Q., **217**, Part A: Journal of Power and Energy, pp. 421–431.
[30] Chana, K. S., and Jones, T. V., 2002, "An Investigation on Turbine Tip and Shroud Heat Transfer," ASME Paper No. GT-2002-30554.
[31] Shang, T., 1995, "Influence of Inlet Temperature Distortion on Turbine Heat Transfer," Doctoral thesis, Department of Aeronautics and Astronautics, MIT, Cambridge, MA.
[32] Shang, T., and Epstein, A. H., 1996, "Analysis of Hot Streak Effects on Turbine Rotor Heat Load," ASME Paper No. 96-GT-118.
[33] Schwab, J. R., Stabe, R. G., and Whitney, W. J., 1983, "Analytical and Experimental Study of Flow Through an Axial Turbine Stage With Nonuniform Inlet Radial Temperature Profiles," NASA Technical Memorandum 83431, AIAA 83-1175.
[34] Stabe, R. G., Whitney, W. J., and Moffitt, T. P., 1984, "Performance of a High-Work Low Aspect Ratio Turbine Tested With a Realistic Inlet Radial Temperature Profile," NASA Technical Memorandum 83655, AIAA Paper No. 84–1161.
[35] Roback, R. J., and Dring, R. P., 1993, "Hot Streaks and Phantom Cooling in a Turbine Rotor Passage: Part 1—Separate Effects," ASME J. Turbomach., **115**(4), pp. 657–666.
[36] Barringer, M. D., Thole, K. A., and Polanka, M. D., 2004, "Developing a Combustor Simulator for Investigating High Pressure Turbine Aerodynamics and Heat Transfer," ASME Turbo Expo 2004, Vienna, Austria, June 14–17, ASME Paper No. GT-2004-53613.
[37] Varadarajan, K., and Bogard, D. G., 2004, "Effect of Hot Streaks on Adiabatic Effectiveness for a Film Cooled Turbine Vane," ASME Paper No. GT-2004–54016.
[38] Jenkins, S. C., and Bogard, D. G., 2004, "The Effects of the Vane and Mainstream Turbulence Levels on Hot Streak Attenuation," ASME Paper No. GT-2004–54022.
[39] Jenkins, S. C., Varadarajan, K., and Bogard, D. G., 2003, "The Effects of High Mainstream Turbulence and Turbine Vane Film Cooling on the Dispersion of a Simulated Hot Streak," ASME Paper No. GT-2003–38575.
[40] Busby, J., Sondak, D., Staubach, B., and Davis, R., 2000, "Deterministic Stress Modelling of Hot Gas Segregation in a Turbine," ASME J. Turbomach., **122**(1), pp. 62–67.
[41] Dorney, D. J., and Sondak, D. L., 2000, "Effects of Tip Clearance on Hot Streak Migration in a High-Subsonic Single Stage Turbine," ASME Paper No. 2000-GT-441.
[42] Gundy-Burlet, K. L., and Dorney, D. J., 2000, "Effects of Radial Location on the Migration of Hot Streaks in a Turbine," J. Propul. Power, **16**(3), pp. 377–387.
[43] Orkwis, P. D., Turner, M. G., and Barter, J. W., 2000, "Linear Deterministic Source Terms for Hot Streak Simulations," ASME Paper No. 2000-GT-0509.
[44] Prasad, D., and Hendricks, G. J., 2000, "A Numerical Study of Secondary Flow in Axial Turbines With Application to Radial Transport of Hot Streaks," ASME Turbo Expo 2000, ASME Paper No. 2000-GT-0448.
[45] Dong, S. Y., Liu, S. L., and Zhu, H. R., 2001, "Inviscid Numerical Simulation of Unsteady Flow in a Turbine Stage With Inlet Temperature Distortion," J. Northwest. Polytechnical Univ., **19**(3), pp. 345–348.
[46] Sondak, D., L., Gupta, V., Orkwis, P. D., and Dorney, D. J., 2002, "Effects of Blade Count on Linearized and Nonlinear Hot Streak Clocking Simulations," J. Propul. Power, **18**(6), pp. 1273–1279.
[47] He, L., Menshikova, V., and Haller, B. R., 2004, "Influence of Hot Streak Circumferential Length Scale in Transonic Turbine Stage," ASME Paper No. GT-2004–53370.
[48] Hilditch, M. A., Fowler, A., Jones, T. V., Chana, K. S., Oldfield, M. L. G., Ainsworth, R. W., Hogg, S. I., Anderson, S. J., and Smith, G. C., 1994, "Installation of a Turbine Stage in the Pyestock Isentropic Light Piston Facility," ASME Paper No. 94-GT-277.
[49] Povey, T., Chana, K. S., Jones, T. V., and Oldfield, M. L. G., 2003, "The Design and Performance of a Transonic Flow Deswirling System—An Application of Current CFD Design Techniques Tested Against Model and Full-Scale Experiments," *Advances of CFD in Fluid Machinery Design*, R. L. Elder, A. Tourlidakis, and M. K. Yates, eds., IMechE Professional Engineering Publishing, London, pp. 65–94.
[50] Goodisman, M. I., Oldfield, M. L. G., Kingcombe, R. C., Jones, T. V., Ainsworth, R. W., and Brooks, A. J., 1992, "An Axial Turbobrake," ASME J. Turbomach., **114**, pp. 419–425.
[51] Chana, K. S., Hurrion, J. R., and Jones, T. V., 2003, "The Design, Development and Testing of a Non-Uniform Inlet Temperature Generator for the Qinetiq Transient Turbine Research Facility," ASME Paper No. GT-2003-38469.
[52] Oldfield, M. L. G., and Doorly, J. E., 1996, "New Heat Transfer Gauges for Use on Multi-Layered Substrates," ASME Paper No. 86-GT-96.
[53] Doorly, J. E., and Oldfield, M. L. G., 1987, "The Theory of Advanced Heat Transfer Gauges," Int. J. Heat Mass Transfer, **30**(6), pp. 1159–1168.
[54] Jones, T. V., 1989, "Recent Developments in Transient Heat Transfer Measurements," Eurotherm Seminar No. 9, Heat Transfer in Single Phase Flows, July 10–11, Bochum.
[55] Povey, T., 2003, "On Advances in Annular Cascade Techniques," D.Phil. thesis, Department of Engineering Science, University of Oxford, Oxford, UK.
[56] Doorly, J. E., 1985, "The Development of a Heat Transfer Measurement Technique for Application to Rotating Turbine Blades," D.Phil. thesis, University of Oxford, Oxford, UK.
[57] Epstein, A. H., Guenette, G. R., Norton, R. J. G., and Yuzhang, G., 1986, "High Frequency Response Heat Flux Gauges," Rev. Sci. Instrum., **57**(4), pp. 639–649.
[58] Piccini, E., Guo, S. M., and Jones, T. V., 2000, "The Development of a New Direct-Heat-Flux Gauge for Heat Transfer Facilities," Meas. Sci. Technol., **11**, pp. 342–349.
[59] Lowery, G. W., and Vachon, R. I., 1975, "Effect of Turbulence on Heat Transfer from Heated Cylinders," Int. J. Heat Mass Transfer, **18**(11), pp. 1229–1242.
[60] Krishnamoorthy, V., and Sukhatme, S. P., 1989, "The Effect of Free-Stream Turbulence on Gas Turbine Blade Heat Transfer," ASME J. Turbomach., **111**, pp. 497–501.
[61] Crawford, M. E., and Kays, W. M., 1976, "STAN5: A Program for Numerical Computation of Two-Dimensional Internal and External Boundary Layer Flows," NASA Contractor Report CR-2742.
[62] Lam, C., and Bremhorst, K., 1981, "A Modified Form of the k-Epsilon Model for Predicting Wall Turbulence," ASME J. Fluids Eng., **103**, pp. 456–460.

Experimental Evaluation of Active Flow Control Mixed-Flow Turbine for Automotive Turbocharger Application

Apostolos Pesiridis

Ricardo F. Martinez-Botas[1]

Imperial College London,
Department of Mechanical Engineering,
United Kingdom

In the current paper we introduce an innovative new concept in turbochargers—that of using active control at the turbine inlet with the aim of harnessing the highly dynamic exhaust gas pulse energy emanating at high frequency from an internal combustion engine, in order to increase the engine power output and reduce its exhaust emissions. Driven by the need to comply to increasingly strict emissions regulations as well as continually striving for better overall performance, the active control turbocharger is intended to provide a significant improvement over the current state of the art in turbocharging: the Variable Geometry Turbocharger (VGT). The technology consists of a system and method of operation, which regulate the inlet area to a turbocharger inlet, according to each period of engine exhaust gas pulse pressure fluctuation, thereby actively adapting to the characteristics of the high frequency, highly dynamic flow, thus taking advantage of the highly dynamic energy levels existent through each pulse, which the current systems do not take advantage of. In the Active (Flow) Control Turbocharger (ACT) the nozzle is able to adjust the inlet area at the throat of the turbine inlet casing through optimum amplitudes, at variable out-of-phase conditions and at the same frequency as that of the incoming exhaust stream pulses. Thus, the ACT makes better use of the exhaust gas energy of the engine than a conventional VGT. The technology addresses, therefore, for the first time the fundamental problem of the poor generic engine-turbocharger match, since all current state of the art systems in turbocharging are still passive receivers of this highly dynamic flow without being able to provide optimum turbine inlet geometry through each exhaust gas pulse period. The numerical simulation and experimental work presented in this paper concentrates on the potential gain in turbine expansion ratio and eventual power output as well as the corresponding effects on efficiency as a result of operating the turbocharger in its active control mode compared to its operation as a standard VGT. [DOI: 10.1115/1.2372778]

Introduction

The benefits accrued by the use of variable geometry devices for exhaust gas flow control to the turbine are well known and include improved transient response, fuel economy, and more importantly reduced emissions in the face of ever stringent emissions regulations, Ikeya et al. [1], Tsujita et al. [2], and Minegashi et al. [3]. The common problems encountered with VGT were reliability (for long periods of time while exposed to high temperature and corrosive exhaust gases), complexity because of the VGT actuation mechanism and control system, and subsequent, high cost [4]. However, recent research has tended to provide acceptable solutions to most of these problems and today VGTs have already had a significant impact in the design of diesel engines.

A fundamental issue that has so far not been addressed satisfactorily, however, is the less than ideal combination of a reciprocating engine providing energy to drive a rotodynamic machine such as a turbocharger turbine. Yet even with the advent of VGTs, this mismatch is not eliminated, since a VGT responds to operating point changes only, i.e., for steady-state operation the nozzle setting of a VGT regulates the turbine inlet area to one constant, optimal value. However, regardless of the engine operating at steady-state or transient mode, the inlet conditions to the turbocharger still include a highly pulsating flow field with widely varying pressure and mass flow rate levels at all times [5]. It may still be possible to harness that energy by continually altering the effective throat area of the turbine by means of a fast-response nozzle.

Automotive turbochargers almost in their entirety are equipped with radial turbines, due to the efficiency superiority of radial designs when compared to other turbine types relative to a given, small size. But radial turbines are limited in their potential, due to their radial leading edge. A mixed flow turbine differs from a radial turbine in that the leading edge is swept radially downward, as opposed to the zero blade angle of the radial turbine. Research has shown a substantial amount of exhaust gas energy to be available at velocity ratios of less than 0.7 [6]—the point of highest energy recovery for a radial turbine. For a nonzero blade angle the velocity ratio and thus the peak efficiency point moves to a lower velocity ratio, which means a higher pressure ratio. Shifting the peak efficiency point to a higher pressure ratio is advantageous in a turbocharger application, which is subjected to pulsating flows from the reciprocating engine, where the greater energy of the flow is contained at high pressures [7].

Extensive research work has already been carried out by the turbocharger research group at Imperial College on mixed flow turbine (MFT)-based, fixed geometry turbochargers (FGTs) and obtained promising results so far. Thus, it was decided to expand the scope by studying a novel variable geometry turbocharger capable of actively controlling the flow into the turbine, in com-

[1]Address all correspondence to this author.

Contributed by the International Gas Turbine Institute (IGTI) of ASME for publication in the JOURNAL OF TURBOMACHINERY. Manuscript received October 1, 2004; final manuscript received February 1, 2005. IGTI Review Chair: K. C. Hall. Paper presented at the ASME Turbo Expo 2005: Land, Sea and Air, Reno, NV, June 6–9, 2005, Paper No. GT2005-68830.

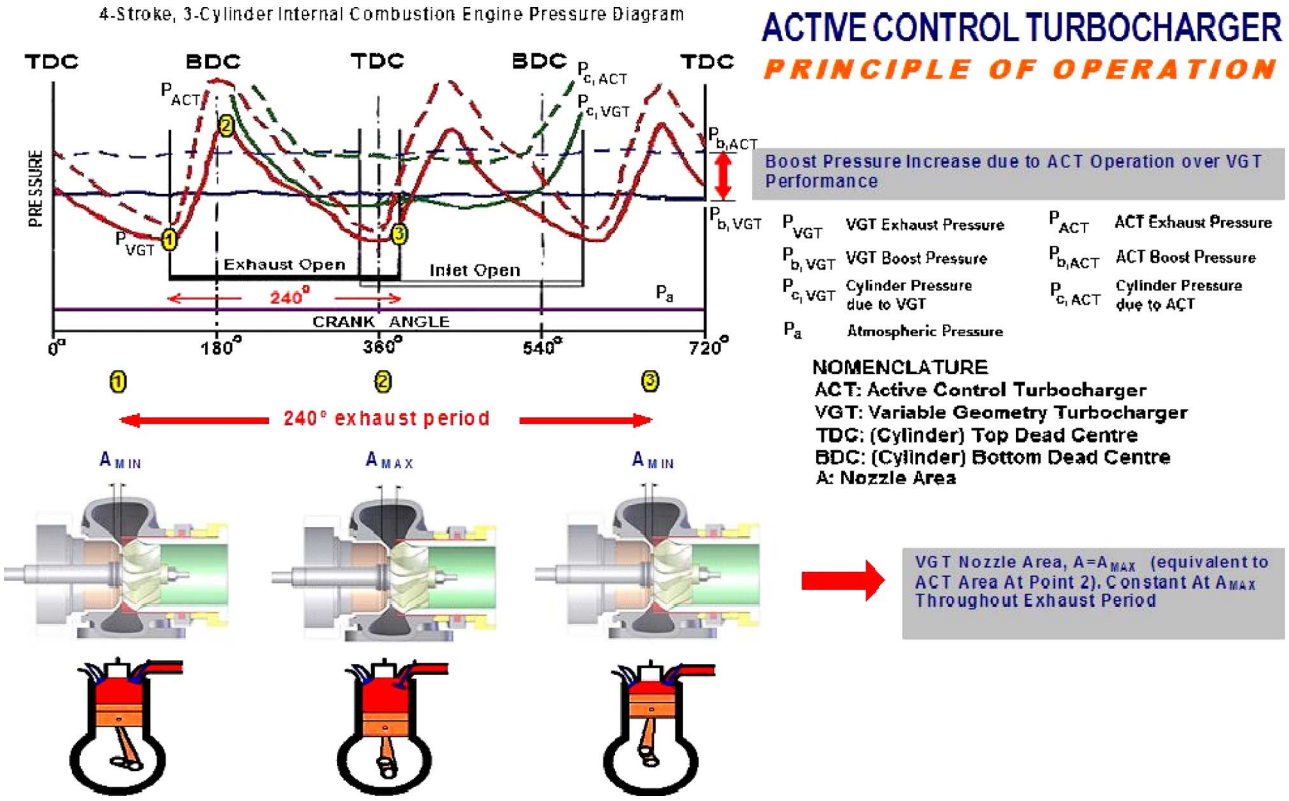

Fig. 1 The active control concept for turbochargers. Exhaust process cycle (240° CA) for one cylinder, where the nozzle gap (1) is in the minimum gap position at the start of the exhaust process, and progressively opens up to the fully open position (2) at peak pressure and then retracts back to the minimum vane gap position (3) at the end of the exhaust process

bination with the present MFT installed. The Active Control Turbocharger (ACT) is a special type of VGT, where the nozzle (in this case a sliding wall type) is able to alter the inlet area at the throat of the turbine inlet casing (volute) through optimum amplitudes, at variable out-of-phase conditions and at the same frequency as that of the incoming exhaust pulses (Fig. 1). For this purpose it is actuated by a suitable electrodynamic shaker, which—supplied by a powerful amplifier—is capable of meeting the frequency and amplitude requirements of this intensive and continuous operation.

In early production VGTs, open-loop control systems were used to provide the required boost pressure without taking into account engine volumetric efficiency. Current production VGT systems provide closed-loop control with engine volumetric efficiency being taken into account. An undue reduction in volumetric efficiency causes specific fuel consumption and emissions penalties. Excessive volumetric efficiency reduction is the result of excessive negative pressure drop across the engine, i.e., when the exhaust manifold pressure instantaneously exceeds the inlet manifold pressure. In variable geometry mechanisms this is the result of excessive inlet area restriction. However, there are a number of mechanisms available to prevent this from happening. Minimum turbine inlet area limits need to be imposed in order to avoid this excessive pressure buildup and in the case of ACT operation the minimum inlet area per cycle can be phased in such a way as to avoid the valve overlap period of the engine. Minimal valve overlap is, therefore, a desirable engine characteristic. The minimal inlet areas that were tested were phased in such a way as to occur 30°, 60°, 90°, and 240° after the start of the exhaust gas pulse. Since the valve overlap period occurs at any point after 180° of crankshaft rotation from the time of the exhaust valve opening the 240° and 30° cases are susceptible to poorer results. However, the actual phasing will be a function of exhaust manifold length as well as geometry and the wave dynamics of the particular exhaust process under consideration.

Our aim in this paper is to introduce the concept of Active (Flow) Control in a turbocharger turbine. In addition, the experimental setup of the laboratory is described and the design and operating details pertaining of the ACT are explained. Numerical simulation results are provided showing a nominal benefit to be expected due to ACT operation over the current VGT operation. Finally, experimental results obtained so far are discussed.

Literature Review

Mixed Flow Turbines. The concept of a mixed flow turbine was initially studied for the first time in the early 1950s for aerospace application. By the early 1970s the possibility of using mixed flow turbines was introduced to overcome the problems associated with a radial turbine. For the past three decades research has concentrated in proving the superiority of the mixed flow turbine in terms of lower velocity ratio operation and higher mass flow rate [8–11]. Apart from these, the mixed flow turbine has also been developed as part of engine development in recognition of its advantages [1–3,12]. Despite some disadvantages, such as a larger weight in comparison to a radial turbine, giving rise to dynamic problems as well as being more complicated to design for stress reduction as indicated by Rodgers [13], the mixed flow turbine offers a potential alternative to the radial turbine for engine operation.

Variable Geometry Turbocharging. Although the concept of VGT is not entirely new (the first examples appearing in the early 1960s), their development did not gain impetus until fairly re-

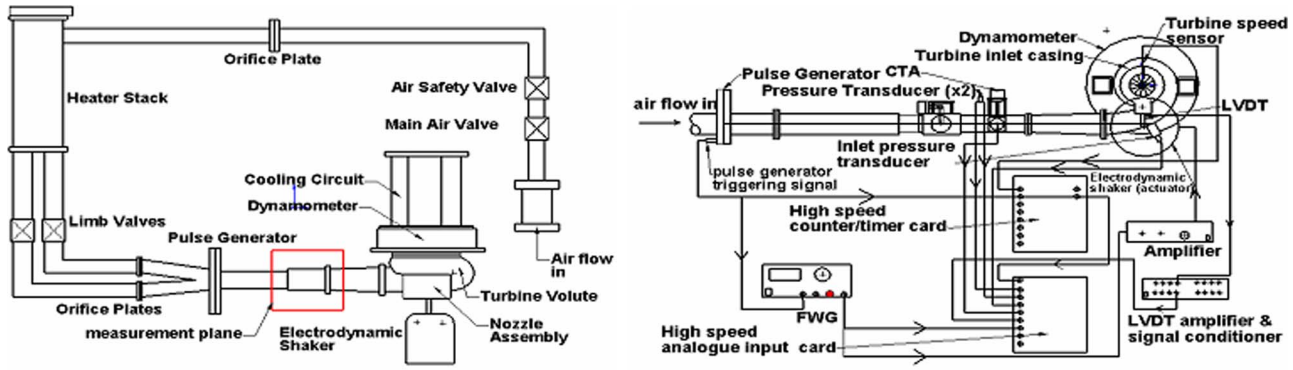

(*a*) (*b*)

Fig. 2 (*a*) **Turbocharger test rig schematic and** (*b*) **laboratory schematic of major high-speed data acquisition hardware and software as well as the setup for ACT control**

cently. Up until the early 1980s, VGTs were rarely used, except on gas turbine plants and experimental turbochargers, but today they constitute standard equipment for both SI and CI internal combustion engines.

Many VGT devices have been tested over the years, such as movable volute tongues, pivoting nozzle vanes, movable sidewalls and sliding nozzles. Comparison of the performance of the various VGT types has shown that pivoting vanes and sliding nozzles afford higher performance and better reliability and are the designs of choice for turbochargers produced today [14–16]. The current project utilized a lightweight sliding nozzle for VGT and ACT testing (Fig. 3 later).

Most available published work on VGTs is still based on steady-state data. Exceptions have used averaged pulsating data in combination with VGT, from which empirical factors are derived to compare steady and unsteady data [17]. The present experimental facility, however, offers the ability for both steady and pulsating flow testing of the VGT for the first time. The scope of steady state testing of a VGT is to focus the development of optimal ACT operating schedules. From past research, however, it has been shown that the turbine performance during pulsating flow departs substantially from the quasisteady assumption [6,7,18]. Thus unsteady-state VGT testing is required in order to define alternate and perhaps more optimal ACT operating schedules and more importantly to provide a basis to compare against ACT data since unsteady tests provide a closer match to real life engine operation.

It is clear from a review of literature that there has not been any attempt as yet to apply active flow control means on a turbocharger turbine with published results. This confirms the novelty of the idea and the results are presented in this paper.

Experimental Test Facility

The turbocharger aerodynamic test facility is a simulated reciprocating engine test bed for turbocharger testing. In Fig. 2(*a*) a schematic of the laboratory setup for ACT testing is illustrated. Three screw compressors supply air at room temperature up to a maximum mass flow rate of 1.2 kg/s. A 76 kW heater stack is used to bring the air to the required test condition. The pulsations are generated by a pair of counter-rotating plates situated 755 mm upstream of the inlet measurement plane. The unsteady flow generated replicates an engine exhaust manifold, albeit at a lower temperature; the nondimensional mass flow rate and speed parameters are correctly matched. The airflow is split into two pipes soon after leaving the heaters; this feature allows testing of twin entry turbochargers. The current turbine is part of a single entry system, thus the air flow is merged prior to entering the volute.

The hot exhaust gases of a real engine are simulated in this rig with the supply of warm air scaled according to the equivalent conditions, which are summarized in Table 1.

The present facility introduces three new features to the research already carried out by this group previously on MFTs. In addition to other instrumentation, a permanent magnet, eddy current dynamometer is now used as the loading device in place of the previous compressor, as well as a novel Active (flow) Control Turbocharger (Fig. 2(*a*)).

Instrumentation. The instrumentation for control, monitoring, data logging, and data reduction has been modified and upgraded to an automated system through the use of two computers, which now undertake the entire experimental task.

One computer handles all normal control functions such as airflow and pulse generator frequency regulation, as well as steady-state monitoring and data logging through the use of distributed, network I/O modules to the static pressure, temperature, and frequency counters. The second computer is used for high speed data acquisition as well as to control the electrodynamic shaker that actuates the ACT. For this task, two high-speed, data acquisition cards are utilized. In addition, an external function waveform generator is used as part of the ACT control system.

Figure 2(*b*) shows the hardware setup for high-speed data logging and ACT control. Various sensors along the pipework upstream of the turbine and on the turbine itself are utilized. Pressures from the measurement plane, and turbine inlet casing stations, CTA (constant temperature anemometer), LVDT nozzle position, and FWG (Function waveform generator) signals are directed to the high-speed analog input data acquisition and control card, while the signal from the magnetic pickup sensor measuring pulse generator frequency, and the signal from the turbine speed optical sensor are directed toward the high-speed, counter-timer card.

In addition, an eddy current dynamometer is used to measure

Table 1 Design conditions

Parameter	Design condition	Equivalent Design condition	Units
Pressure ratio	2.91	2.91	—
Inlet temperature	923	344	K
Mass flow rate	0.414	0.678	kg/s
Rotational speed	98 000	60 000	rpm

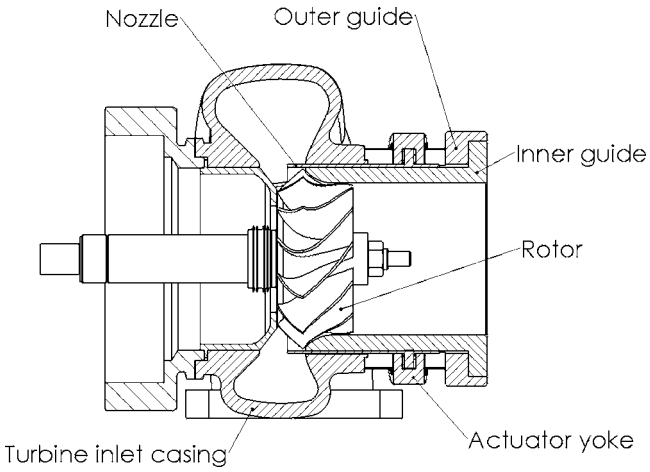

Fig. 3 ACT sectional view with Mixed Flow Turbine. The thin section nozzle can be seen protruding axially at the inlet to the turbine. The supporting guides and part of the actuator yoke are, also, shown

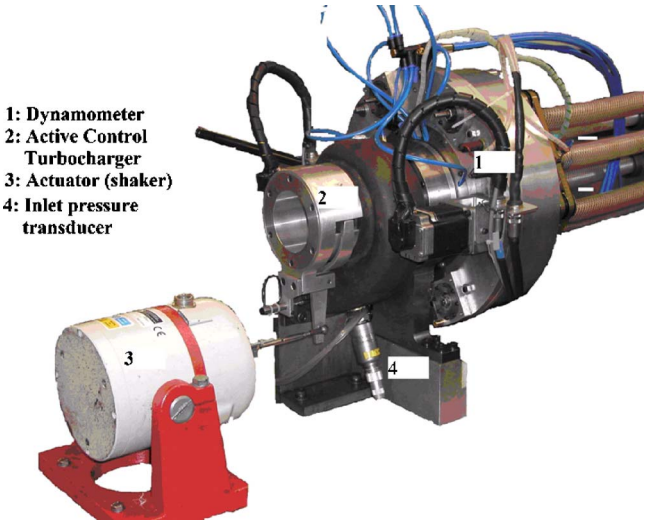

Fig. 5 Active control turbocharger with electrodynamic shaker and dynamometer

the power, from which the efficiency of turbocharger turbines can be estimated. Because of the wide operating conditions of the turbocharger turbines, the power range requirement of the dynamometer is large. When engine simulations are carried out using quasisteady methods to model the pulsating flow conditions in the engine manifold and its turbocharger, a turbine map with very wide operating conditions is required. A possible method to obtain such a map is by using the compressor of the turbocharger to load the turbine. Unfortunately, the range of data using this method would be insufficient given the surge and choke margins of the compressor. An eddy current dynamometer used as the loading device thus offers a much broader range of testing without the associated aerodynamic limitations of the compressor it replaces. The dynamometer utilizes the principle of eddy-current braking by incorporating neodymium-iron-boron magnets in a spider creating a low inertia axial flux rotor.

Active Control Turbocharger

Design. The main ACT components can be seen in Figs. 3–5. A nozzleless Holset H3B turbocharger turbine was modified to accept a nozzle for VGT testing. Due to the very small space available and dynamic requirements, a very thin (1.5 mm thickness) section, tubular form, sliding nozzle was designed. Two embedded attachment points at the end away from the turbine inlet casing are used to mount the nozzle on to its actuating arm (yoke) via two small bearing pads, which fit between the nozzle and the yoke and

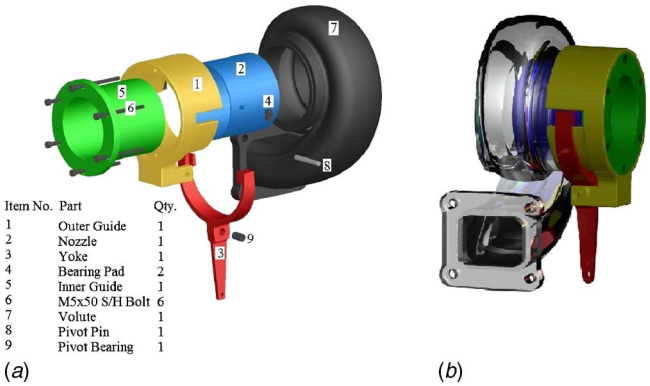

Fig. 4 (*a*) Active control turbocharger exploded view and (*b*) assembled turbocharger

assist in translating the pivoting movement of the yoke into a linear motion by the nozzle. The nozzle itself is guided toward the throat by an inner guide, which serves both as a bearing surface to the nozzle as well as forming the exducer section of the turbine. An outer guide houses the entire assembly and at its lower end is shaped into a bracket on which the yoke is attached and can freely pivot about. The entire assembly is held together and attached to the face of the turbine by six 50 mm M5 bolts. The throat width to the turbine is 26 mm wide and the nozzle can block 21.5 mm off that passage width before reaching the stops.

The materials used for the assembly were 6082-T6 aluminium alloy, for the entire assembly except for the nozzle, providing light weight, with adequate strength to overcome (in the case of the yoke) fatigue, which is the major issue in this type of operation. At its most severe type of operation, the yoke achieved a safety factor of 10 with respect to the maximum bending stress applied to it at its corners by the bearing pads. The nozzle was of carbon fiber reinforced plastic (CFRP) construction, providing adequate strength for an ultralow weight against the high pressure airflow used during testing—the low nozzle weight being critical for the ACT in achieving good force performance.

An electrodynamic shaker was used to drive the nozzle in the ACT mode. The shaker was chosen so as to be able to provide the required force for the limiting frequencies and amplitudes expected during testing (60 Hz and approximately 20 mm, respectively). Direct coupling of the shaker and nozzle was not possible due to the nozzle being driven from the exhaust side of the turbine, thus forcing the shaker to be offset to the side of the exducer. The simplest way to drive the nozzle from this position was with a single-piece, pivoting yoke-type actuator arm. This makes the design simpler, more compact, and more importantly, allows for far better fatigue endurance with the added advantage of significant vibration damping due to the rocker-arm type operation of the yoke used to drive the nozzle, which largely damps out what would otherwise have been severe vibrations through the turbocharger. The total mass of all moving parts (Parts No. 2, 3, 4, 8 and 9 in Fig. 3(*a*)) is only 0.241 kg, which was important in order to be able to achieve the force performance required for testing, even though a penalty in terms of vibration results, since at present it is not possible to balance both sides of the yoke, as the top part (nozzle) is significantly lighter to the bottom part that also contains approximately 0.2 kg of the moving part of the shaker.

Operation. The electrodynamic shaker is connected to the lower part of the yoke through an adjustable lever (Fig. 2) used to

Table 2 Nozzle VGT settings for the 26 mm wide throat area

Nozzle restriction into throat (mm)	ϑ_{VGT}
0	1 (fully open area)
4	0.846
8	0.692
12	0.538
16	0.385
20	0.231
21.5	0.173 (fully restricted area)

set the nozzle restriction (ϑ_{VGT}) in the VGT mode or the null point (ϑ_{null}) in the ACT mode. For VGT testing once ϑ_{VGT} is set, its value does not change through either steady or unsteady testing, while for ACT testing ϑ_{null} is set as the midpoint between the maximum intended open nozzle area point ($\theta_{VGT}=\theta_{max}$) and the minimum area available (see Table 2). The amplitude, frequency, and form of the controlling signal is controlled by a function waveform generator, which sends a control input signal in the form of a selected waveform to a 100 W amplifier as well as to the controlling computer. From the amplifier the signal is routed to the shaker and transformed into motion by the nozzle. High speed pressure transducers located at the measurement plane as well as just upstream of the nozzle are used to measure the inlet pressure level. Timing is achieved through the use of the magnetic pickup sensor on the pulse generator to define accurately the pulse period and its start and end. The pulse generator opening signal is used to trigger the FWG, which in turn causes the nozzle to move in response to its signal. The known length of the pipework from the pulse generator to the nozzle is used to derive the pressure wave travel time (which travels at the acoustic velocity) for the inlet temperature of the test at hand from:

$$t = \frac{l}{\sqrt{\gamma RT}} \tag{1}$$

In addition, the total system (control input to feedback) time response is known through testing and a time constant is thus derived that is input into the controlling software that controls the operation of the ACT. Thus, the shaker is always in phase with the inlet pressure signal. Additional out-of-phase, resulting due to the fact that the total energy travel time is dependent on both the acoustic velocity of the pressure wave in addition to the local flow velocity, is detected through suitable software and adjusted as required, thus achieving a reasonably accurate phasing of inlet pressure and nozzle motion signals. All acquired data are phase shifted (lagged) eventually, from their measurement location (Fig. 2(*b*)) to the turbine inlet entry according to the procedure described by Szymko and Martinez-Botas [19].

For VGT testing, ϑ_{VGT} can be set by adjusting the lever only. For ACT testing ϑ_{null} is adjusted manually, while $\Delta\vartheta_{ACT}$ (amplitude) and the shaker frequency are preset on the waveform generator according to the test parameters required. Typical ϑ_{VGT} test points used during testing are included in Table 2 (in normalized throat open area form):

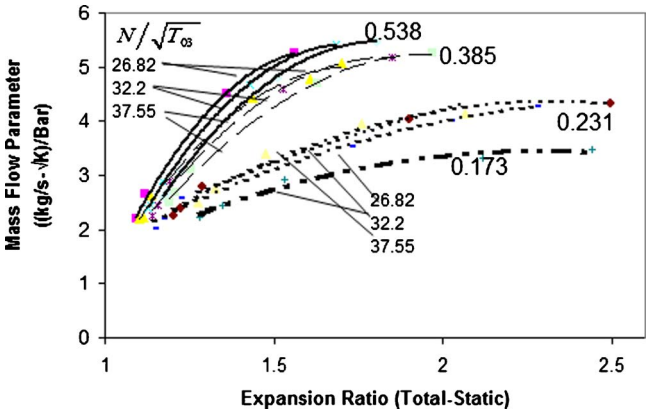

Fig. 7 Overall steady state VGT map for 70% equivalent speed. At each normalized throat open area (0.538, 0.385, 0.231, 0.173) constant speed parameter curves can be seen (26.8, 32.2, and 37.5)

Steady-State Test Results

The steady-state VGT results can be seen in Figs. 6–8. Turbine map plots of efficiency against velocity ratio and MFP versus ER are presented for the three constant speed parameters (26.82, 32.2, and 37.55 rps/$\sqrt{}$K, which in equivalent turbine speed terms represent 50%, 60%, and 70% of the design speed, respectively). The 50% equivalent turbine speed corresponds to approximately 29 400 rpm, while 70% to 41 400 rpm.

From the efficiency plots it immediately becomes apparent that there is a large efficiency drop as the throat restriction increases. This was expected as with every VGT mechanism disturbing the flow to the turbine, in the form of stagnating flow on the outside surface of the sliding nozzle as well as increased turbulence off the sharp edged tip of the nozzle. It is significant to note that for relatively small restrictions (down to 0.692 or even 0.538) the drop in efficiency is typically less than 10%, while it becomes higher at larger restrictions.

On the other hand, from the mass flow parameter against expansion ratio plots, it can be seen that even though the smaller restrictions do not suffer a significant drop in efficiency, they do not produce initially any appreciable increase in expansion ratio, whereas at approximately the same restrictions, where the efficiency drop becomes significant the expansion ratio gain becomes more pronounced (Fig. 8). Therefore, the effect that the throat restriction has on expansion ratio increase becomes evident.

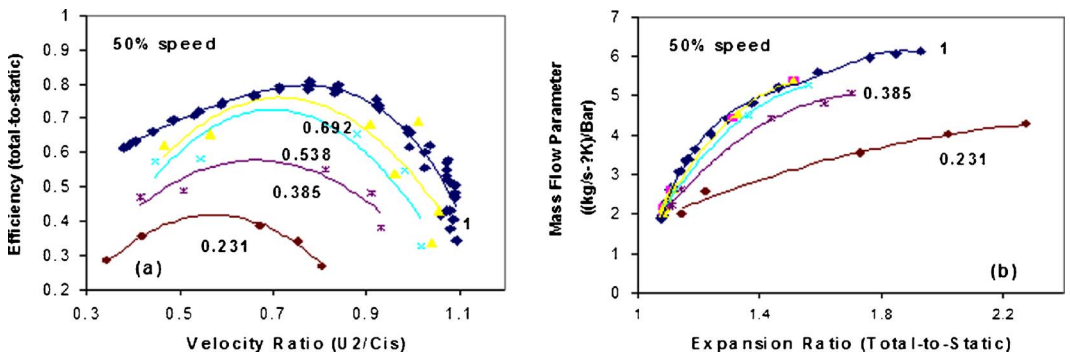

Fig. 6 (*a*) to (*f*) Steady state turbine maps for 50%, 60%, and 70% equivalent speeds

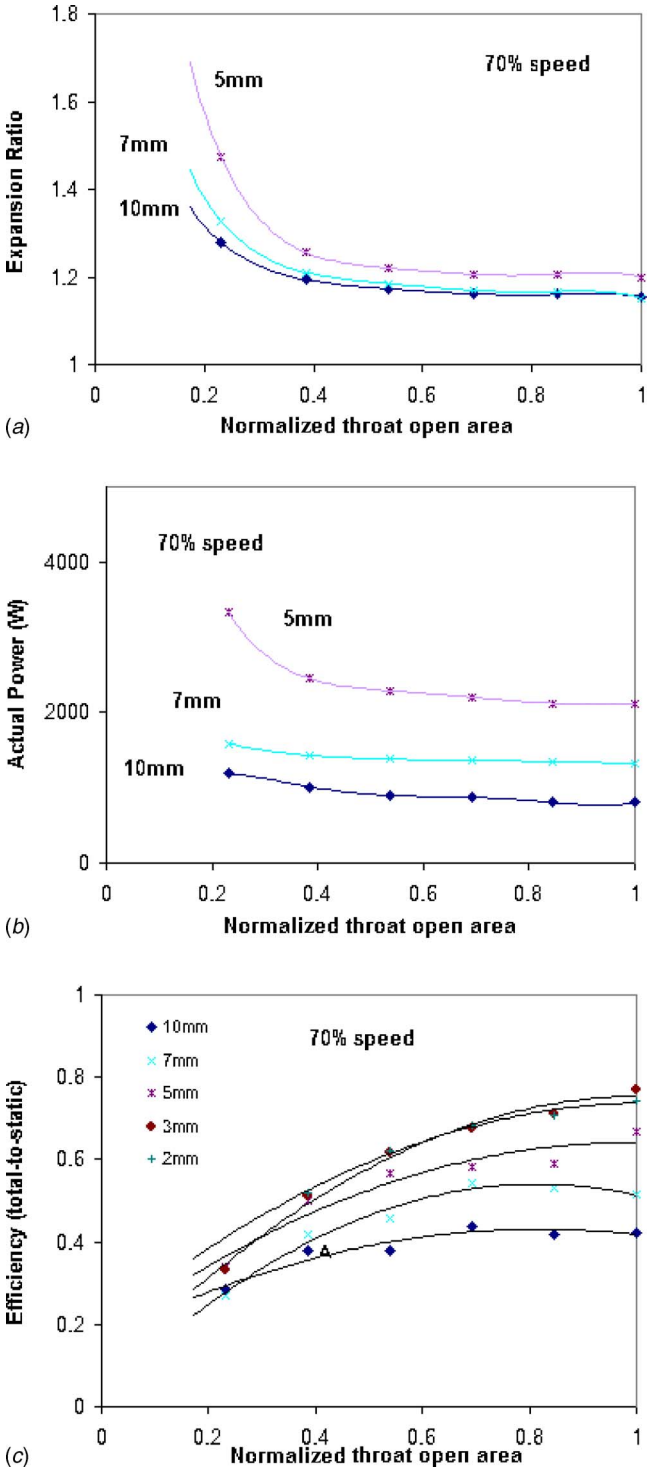

Fig. 8 (*a*) Turbine expansion ratio, (*b*) actual power, and (*c*) efficiency plots with changing turbine inlet areas at 70% equivalent speed for different loads

Unfortunately, due to project constraints it was not possible to match an optimal MFT-oriented nozzle design to the present MFT. Instead, a straight nozzle was used with the MFT rotor as opposed to a downward inclined nozzle in the radial direction to follow the MFT leading edge angle, thus resulting in interspace diffusion effects causing degradation of VGT performance, since the resulting triangular interspace between the nozzle and rotor causes this flow diffusion and therefore a decrease of the velocity component, C, hence less actual energy recovered by the turbine itself.

Table 3 Conventional turbocharger comparison with ACT performance (max. nozzle restriction)

Parameter	Cycle-averaged VGT data	Equivalent data for ACT
Inlet pressure (bar)	1.584	1.68
Mass flow rate (kg/s)	0.2531	0.1538–0.3498
Turbine speed (rps)	685.9	694.2
Actual Power (W)	17859	18716
Isentropic Power (W)	24770	28510
Cycle-averaged efficiency	0.721	0.679

Active Control Turbocharger

Numerical Simulation. Our main aim of the numerical simulation was to demonstrate the ability of an ACT to enhance the exhaust gas energy recovery in the turbine, by comparison to a conventional VGT, since outside the optimum engine/turbocharger matching point the energy recovery capability suffers significantly.

A standard one-dimensional (1-D) matching calculation was used and is based on a procedure described in the literature [8], along with elements from the model of Chen et al. [20], where a tapered duct is considered as a simplification for a 1-D quasi-steady calculation. The main, general assumptions, therefore, made in this model involve a quasisteady approach and a high response actuator responding to a sine wave control input. In addition, standard 1-D compressible isentropic flow equations Y [21] were applied for the derivation of the main thermodynamic parameters. For a known inlet temperature, pressure, Mach number and area, and a known exit area as modified by the nozzle, all exit parameters may be obtained by obtaining the exit Mach number first.

Due to the nature of the engine-turbocharger match (volume machine combined with a speed machine) the cycle averaged power output of the turbocharger is less than what it could be if the turbine inlet pressure level (and the exhaust gas energy level in general) could be raised instantaneously to its peak pressure instead of fluctuating substantially between atmospheric levels and its peak value. The ideal case, therefore, is for an ACT turbocharger to virtually eliminate exhaust gas pulsation at entry to the turbine rotor so that the turbine inlet pressure at any instant of time is equal to the peak pressure of an equivalent pulse in a standard VGT-equipped turbocharger. This, however, is not possible due to limitations on the maximum nozzle displacement, efficiency drop, and the fact that at the end of the pulse period the inlet pressure levels are near atmospheric and therefore, it is not possible to increase the inlet pressure significantly at this stage.

An example of the gain afforded by an ACT can be seen in Table 3, where a significant increase in pressure and power levels can be seen by comparison to a conventional turbocharger (6.1% and 4.58%, respectively). It may, also, be observed that this power increase comes at the expense of efficiency (a drop of 5.82%), which was expected, but this did not have a very detrimental effect on the power recovered.

In addition, Fig. 9 illustrates the variation of the most important parameters affecting ACT operation over the pulse cycle. Actual power and pressure recovery are evident at the start and end of the pulse, while at or near the peak the effect is negligible or the same as in VGT. Efficiency drop is proportional to the increase in pressure, as can be seen in Fig. 9(*c*).

Operating Schedule Based on Steady-State VGT Test Results. The purpose of the steady-state VGT tests carried out was to develop a realistic nozzle ACT schedule (in terms of nozzle displacement amplitude and null points) for different operating conditions (turbine speed, dynamometer load, and pulse generator frequency). From Fig. 7 it may be observed that on the initial

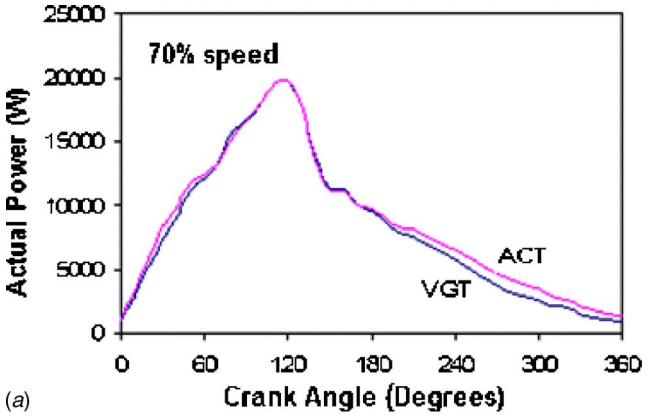

(*a*)

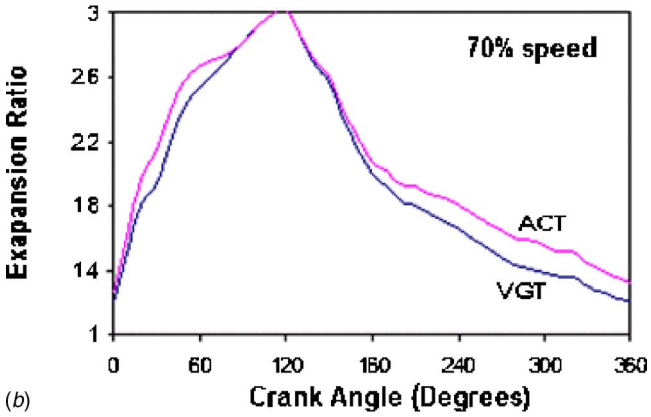

(*b*)

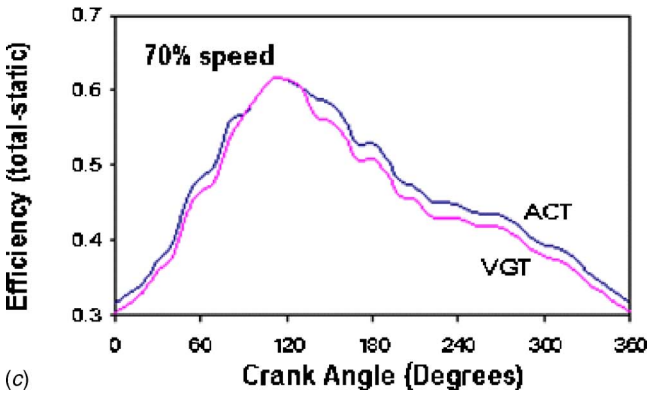

(*c*)

Fig. 9 A comparison of VGT and ACT simulation results. (*a*) Benefit in actual power, (*b*) pressure recovered, and (*c*) efficiency drop during one pulse

steep gradient part of the MFP over ER curves, for a constant MFP (which is what quasisteadily applies to an ACT nozzle) large nozzle amplitudes are required to achieve modest inlet pressure gains. Above approximately 1.4 bar, the slope becomes significantly flatter, offering much larger gains in terms of pressure. However, at the same time there is a corresponding decrease in efficiency (Fig. 8(*c*)). The measure of energy availability and corresponding actual energy recovered by the turbine is given by the following equations:

$$W_{t,\mathrm{is}} = \dot{m}_t C p_{\mathrm{exh}} T_3 \left[1 - \left(\frac{P_{03}}{P_4} \right)^{1-\gamma_{\mathrm{exh}}/\gamma_{\mathrm{exh}}} \right] \qquad (1')$$

$$W_{t,\mathrm{act}} = \eta_{t_{-s}} W_{t,is} \qquad (2)$$

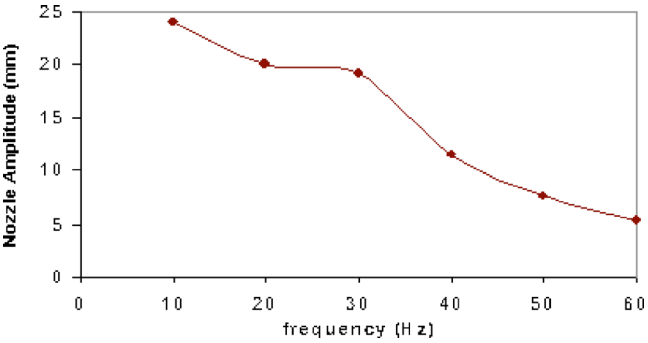

Fig. 10 Available nozzle amplitude performance over the test frequency range

In an effort to recover more energy out of the exhaust gases, increasing the pressure drop across the turbine is one way of achieving this aim provided, however, that the resultant efficiency drop can be held within tolerable limits, according to Eqs. (1) and (2). Therefore, the disparity between the FGT efficiency and the efficiency at any intermediate nozzle position ($\Delta\eta_{t-s}$) needs to be minimal. From Fig. 6, a minimum efficiency drop occurs only at the ends of the velocity ratio range as between 0.6 and 0.7 the FGT efficiency reaches its peak, whereas the VGT efficiencies exhibit a flatter curve thus increasing the disparity at the FGT peak efficiency velocity ratio range.

In Fig. 8 it may be seen that only at the higher loads and in any case only at significant throat area restrictions (below 0.5 or 50% open for the higher loads) does energy become available for increased recovery. At very low powers (10, 7, and even 5 mm dynamometer gaps) a high percentage of energy may be recovered. At 5 mm gap, some energy may be recovered but in any case at low powers a throat area of 25% open or less is required for any sort of appreciable effect.

In addition, ACT operation is also limited by the frequency of the generated pulse. In Fig. 10 it may be observed that due to actuator dynamic performance the maximum amplitudes are available, only at the lower frequencies (below 30 Hz). It, therefore, becomes apparent that the most beneficial area for ACT energy extraction is at inlet pressures above 1.4 bar and at velocity ratios below 0.6 (or at very high velocity ratios—above approximately 0.9) and at frequencies of less than 30 Hz.

Figure 11 shows the traces of the control input signal from the FWG (activated by the pulse generator magnetic pickup sensor signal) and the corresponding feedback signal from the LVDT for a 90° case. The system lag (mainly due to the mechanical response of the actuator) is indicated as well. For simplicity the FWG provides a sine wave to the shaker as the controlling signal.

A typical pressure waveform is not a sine wave but was con-

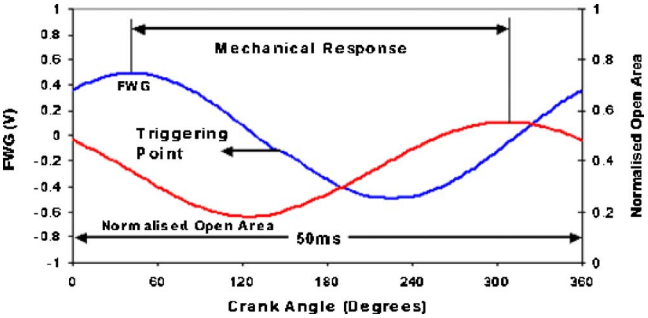

Fig. 11 Nozzle (LVDT position signal) lag in relation to the FWG control input waveform (35 ms lag in this case) during a 50 ms pulse period (20 Hz)

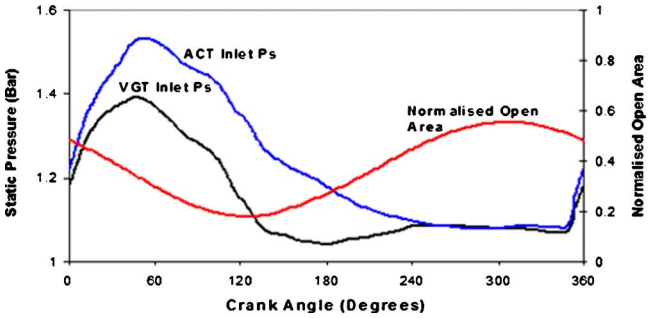

Fig. 12 Pressure recovery achieved by an ACT compared to a VGT at 50% equivalent speed at 20 Hz (simulated exhaust gas frequency)

sidered similar enough to a sine wave in order for the latter to be selected as the controlling waveform. The instantaneous position of the nozzle is evaluated from:

$$\theta_{\mathrm{ACT}} = \theta_{\mathrm{ACT,min}} + \Delta\theta_{\mathrm{ACT}}[1 - (\sin(\omega t)/\sin(\omega t)_{\mathrm{min}})] \quad (3)$$

where

$$\Delta\theta_{\mathrm{ACT}} = \theta_{\mathrm{VGT}} - \theta_{\mathrm{ACT,min}} \quad (4)$$

ACT Experimental Test Results. Experiments have so far concentrated on investigating, primarily, the effects of the nozzle throat area variation on pressure recovery, when the nozzle responds to a sinusoidal waveform input signal. Various phasing schemes have been attempted in order to match inlet pressure and nozzle displacement traces for improved energy recovery. Unlike the original idea to extract energy only at the lower (near ambient), energy levels of the pulse (peak-to-peak match), where the minimum area provided by the nozzle occurs when the maximum throat area and the peak of the pulse are in phase (i.e., the minimum area occurs 240° after pulse generator opening). Three other minimum nozzle area (maximum restriction) phase settings were tested: one, 30° after pulse generator opening, the second at 60° (at the nominal peak of the pulse), and the third at 90° (Fig. 12). In addition, various nozzle amplitudes, $\Delta\theta_{\mathrm{ACT}}$, have been tested and comparisons against different VGT test points could be made.

Nozzle lag by comparison to the inlet pressure trace is of the order of 100° during peak-to-peak phasing at 20 Hz. At the same frequency when operating with the 90° out-of-phase control scheme, the nozzle lag is of the order of 210° (see Fig. 11 and the mechanical response period in crank angle terms).

In Fig. 12, a 90° out-of-phase control scheme is illustrated. This type of control can be very useful as it takes advantage of the higher energy content of the gas while the pulse generator is still open, as opposed to peak-to-peak phasing where energy recovery is primarily attempted through the utilization of the low energy gas stream (at near ambient levels) when the pulse generator is closed. From this graph a clear pressure rise results (2.8% in cycle average terms). This test corresponded to an area variation due to nozzle displacement of between 17.3% to 38.4% open throat area, with the VGT operating constantly at the latter figure throughout the fluctuations of the exhaust pulses. With reference to the different out-of-phase control schemes tested, while at the pressure peak the other settings have a maximum throat area, the 90° setting due to its phasing has less than 40% available throat area. The consequence of this is a higher pressure drop but a reduction in efficiency that may locally reduce the amount of power recovered. This is a well recorded tradeoff of variable inlet area turbines. However, in cycle-average terms there is a clear benefit from this type of operation, as indicated by Table 4 for the case of 60 Hz at 4 mm load in relation to the original 240° control scheme.

In low power VGT conditions where there is more restriction from this device, the benefit to be gained by ACT operation is higher than at the higher engine speed/load conditions, where VGTs restrict the inlet to the turbine less. This is due to the smaller efficiency drop occurring at the lower available isentropic powers. Conversely, the turbocharger will again comparatively benefit at the very high powers as the efficiency drop tends to follow a constant rate that improves slightly as exemplified by the loads of 2 mm in Fig. 8(*c*).

There is a discrepancy between experimental and numerical gain in inlet pressure recovery. However, direct comparisons cannot be drawn due to the fact that the two operating points are significantly different. Since the results illustrated concern low power tests, higher benefit can be expected at the higher power setting, where there is more potential for energy recovery.

Table 4 ACT energy extraction benefit over VGT at 60 Hz, 4 mm load

	VGT	ACT1 240°	ACT2 90°	240° % Increase	90° % Increase
Wact (W)	5495	5667	5902	3.13	7.41
ER	1.55	1.69	1.74	9.18	12.57

Conclusions

The application of a VGT operation to a nozzleless FGT equipped with a MFT rotor, requires large throat restrictions for appreciable gains in ER to be achieved, but also with significant efficiency losses too. The latter are part of the nonoptimal design match between the straight nozzle and the inclined MFT leading edge causing interspace losses.

In terms of employing the turbocharger for ACT operation, there is a clear potential as confirmed by simulation results and early ACT tests, however, this is hampered by high losses and therefore the energy recovery is not as high as theoretically possible. By focusing on certain parts of the operating envelope (low pulse frequency operation, operation at low or very high powers and large area restrictions) the potential of the present ACT may be demonstrated. The ACT results even for this first prototype suggest a notable improvement in power (typically between 3% and 7%) when compared to a standard VGT operation.

Nomenclature

U = blade tip speed
$\dot{m}$ = mass flow rate
FGT = fixed geometry turbocharger
VGT = variable geometry turbocharger
ACT = active control turbocharger
C = gas inlet velocity
ER = turbine expansion ratio or pressure ratio
P = pressure
T = temperature
Cp = specific heat at constant pressure
MFP = mass flow parameter, $\mathrm{MFP}=\dot{m}\sqrt{T_0}/P_0$
$U_{\mathrm{inlet}}/C_{\mathrm{is}}$ = velocity ratio
$U_{\mathrm{inlet}}/C_{\mathrm{is}}=U_3/\sqrt{[2C_PT_{01}[1-(P_3/P_{04})^{(\gamma-1)/\gamma}]]}$
MFT = mixed flow turbine
LVDT = linear variable displacement transducer
CFRP = carbon fiber reinforced plastic
FWG = function waveform generator
P = pressure
N = turbine rotational speed
$N/\sqrt{T}$ = pseudo nondimensional speed parameter

Greek Symbols

γ = ratio of specific heats
η = efficiency

θ, $\Delta\theta$ = nozzle position and position amplitude, respectively
ω = angular velocity

Subscripts

is = isentropic
act = actual
min = minimum area
max = maximum area
0 = total/stagnation condition
2 = pulse generator
3 = turbine inlet
4 = turbine exit
t = turbine
t-s = total to static
null = null position of actuator or nozzle

References

[1] Ikeya, N., Yamaguchi, H., Mitsubori, K., and Kondoh, N., 1992, "Development of Advanced Model of Turbochargher for Automotive Engines," SAE Paper No. 920047.

[2] Tsujita, M., Niino, S., Isizuka, T., Kakinai, A., and Sato, A., 1993, "Advanced Fuel Economy in Hino New P11C Turbocharged and Charge-Cooled Heavy Duty Diesel Engine," SAE Paper No. 930272.

[3] Minegashi, H., Matsushita, H., and Sakakida, M., 1995, "Development of a Small Mixed-Flow Turbine for Automotive Turbochargers," ASME Paper No. 95-GT-53.

[4] Watson, N., and Janota, M. S., 1982, *Turbocharging the Internal Combustion Engine*, Wiley Interscience, New York.

[5] Baines, N. C., 2002, "Radial and Mixed Flow Turbines Options for High Boost Turbocharger," *7th Int. Conference on Turbocharger and Turbocharging*.

[6] Hakeem, I., 1995, "Steady and Unsteady Performance of Mixed Flow Turbines for Automotive Turbochargers," Ph.D. thesis, Imperial College of Science, Technology and Medicine, London, England.

[7] Palfreyman, D., and Martinez-Botas, R. F., 2002, "Numerical Study of the Internal Flow Field Characteristics in Mixed Flow Turbines," ASME Paper No. GT 2002–30372.

[8] Baines, N. C., Wallace, F. J., and Whitfield, A., 1979, "Computer Aided Design of Mixed-Flow Turbines for Turbochargers," Trans. ASME: J. Eng. Gas Turbines Power, **101**, pp. 440–449.

[9] Abidat, M., Chen, H., Baines, N. C., and Firth, M. R., 1992, "Design of a Highly Loaded Mixed Flow Turbine," Proc. Inst. Mech. Eng., Part A, **206**, pp. 95–107.

[10] Arcoumanis, C., Hakeem, I., Khezzar, L., and Martinez-Botas, R. F., 1995, "Performance of a Mixed Flow Turbocharger Turbine Under Pulsating Flow Conditions," ASME Paper No. 95-GT-210.

[11] Karamanis, N., and Martinez-Botas, R. F., 2002, "Mixed-Flow Turbines for Automotive Turbochargers: Steady and Unsteady Performance" Int. J. Engine Research Vol 3, No. 3, IMechE.

[12] Yamaguchi, H., Nishiyama, T., Horiai, K., and Kasuya, T., 1984, "High Performance Komatsu KTR150 Turbocharger," SAE Paper No. 840019.

[13] Rodgers, C., 1990, "Review of Mixed Flow And Radial Turbine Options," AIAA Paper 90-2414.

[14] Flaxington, D., and Szuzupak, D. T., 1982, "Variable area radial-inflow turbine," *2nd Int. Conf. on Turbocharging and Turbochargers*, Proc. of the IMechE, Paper No. C36/82.

[15] Franklin, P. C., and Walsham, B. E., 1986, "Variable Geometry Turbochargers in the Field," *3rd Int. Conf. on Turbocharging and Turbochargers*, Proc. of the IMechE, Paper No. C121/86, pp. 241–250.

[16] Kawaguchi, J., Adachi, K., Kono, S., and Kawakami, T., 1999, "Development of VFT (Variable Flow Turbocharger)," SAE Paper No. 1999-01-1242.

[17] Capobianco, M., and Gambarotta, A., 1992, "Variable Geometry and Waste-Gated Automotive Turbochargers: Measurements and Comparison of Turbine Perforamance," J. Eng. Gas Turbines Power, **114**, pp. 553–560.

[18] Palfreyman, D., and Martinez-Botas, R. F., 2004, "The Pulsating Flow Field in a Mixed Flow Turbine: An Experimental and Computational Study," ASME Paper No. GT 2004-53143.

[19] Szymko, S., and Martinez-Botas, R., 2006, "Experimental Evaluation of Turbocharger Turbine Performance Under Pulsating Conditions," ASME Paper No. GT 2005-68878.

[20] Chen, H., Hakeem, I., and Martinez-Botas, R. F., 1996, "Modelling of Turbocharger Turbine Under Pulsating Inlet Conditions," Proc. Inst. Mech. Eng., Part A, **210**, pp. 397–408.

[21] Yahya, S. M., 1981, "Gas Tables for Compressible Flow Calculation," 2nd ed., Wiley Eastern Limited, New York.

A Direct Performance Comparison of Vaned and Vaneless Stators for Radial Turbines

S. W. T. Spence
R. S. E. Rosborough
D. Artt
G. McCullough

School of Mechanical & Aerospace Engineering,
Queen's University Belfast,
Ashby Institute,
Stranmillis Road,
Belfast BT9 5AH, UK

An extensive performance investigation has been conducted on a radial turbine with three different vaneless volutes and three corresponding vaned stators. Previously published comparisons have been based on turbines with unmatched flow rates, meaning that the impact of stator losses was not isolated from rotor and exit losses. Each vaned stator configuration tested in this investigation matched the flow rate of the corresponding vaneless volute to within 1%. The volutes and the vaned stators were all machined in order to achieve high quality and comparable surface finishes. At all operating conditions, the vaneless volutes were shown to deliver a significant efficiency advantage over the vaned stators. However, the vaneless volute turbines did not demonstrate any greater tolerance for off-design operating conditions than the vaned stator configurations. Full performance data are presented for the six different turbine configurations tested and a one-dimensional turbine performance model is evaluated as a means of predicting and extrapolating turbine performance. [DOI: 10.1115/1.2218518]

Introduction

A radial flow turbine is employed in almost all turbocharging applications for its compactness, robustness, economic production, and relatively low specific speed. The radial turbine comprises two main elements; a rotating component that extracts work from a swirling fluid, and a stationary component that produces the swirl by accelerating a high pressure fluid. The stationary component, referred to as the stator, can be either a series of angled guide vanes around the periphery of the rotor or alternatively a vaneless housing where the flow accelerates through a throat in the tangential inlet section of the housing. In some cases both approaches are combined where a larger vaneless housing directs flow through a row of stator vanes into the rotor.

While there are other important roles for radial turbines, such as small gas turbine engines, turbo-compounding, and cryogenic expanders, turbocharging is the most common application. For packaging and economic reasons, in the past practically all turbochargers used a vaneless turbine stator, referred to as a volute. However, air management challenges on modern engines with high EGR flows have promoted the use of VGTs which combine a volute with a row of stator vanes. The stator vanes have an adjustable element, usually a moveable vane endwall or pivoting vanes, permitting variation of the stator throat area.

Ideally a vaneless volute should provide a free vortex flow at rotor inlet with properties that are uniform around the circumference of the rotor. Bhinder [1] proposed a linear relationship between A and r, where A is the cross-sectional area of the volute at any given azimuth angle and r is the radius of the centroid of the cross-sectional area at the same angle. Bhinder's approach assumed incompressible flow and vaneless volutes designed on this criterion did not demonstrate uniformity of flow conditions around the rotor circumference. Chapple et al. [2] made allowance for the compressible nature of the flow when proposing a method for determining volute geometry. They also described how the analysis was modified to account for frictional effects by employing the approach conventionally used to predict frictional losses in pipe flows. Turbine performance maps were presented to show improvements in overall stage efficiency with the new volute design approach and good accuracy in the prediction of mass flow rate at the specified design point. The angle of the volute tongue, which is the angle through which the flow entering the volute is turned before it clears the trailing edge of the tongue, has also been identified as an important factor in volute design, although the optimum values proposed by different researchers vary considerably [2,3]. There have been several methods proposed for predicting the losses incurred through the volute, all of which are based on a mixture of fundamental fluid flow theory and empiricism [2,4,5]. A comprehensive nondimensional approach to the design of vaneless volutes has been presented by Whitfield et al. in a series of publications [6–8] and it is not proposed to repeat the design methodology in any more detail in this publication.

Vaned stators for radial turbines have used guide vanes ranging from simple flat plates to complex cambered aerofoil shapes. Many different formats of simple 1D stator loss models have been proposed to assist the turbine design process, although all rely heavily on empiricism and do little to help improve the existing level of technology. One of the more useful loss models applicable to vaned stators is that used by Glassman [9], which originates from work on axial flow cascades by Stewart et al. [10].

One of the persistent difficulties with the improvement of radial turbine technology has been the lack of comprehensive published data sets providing back-to-back comparisons of the effect of different design parameters. Satisfactory comparisons cannot be made on the basis of isolated tests on different turbines. The two main radial turbine test programs providing extensive amounts of comparable test data are those undertaken by NASA, for example, [11–14] and also by Ricardo & Co., for example, [15,16], and Hiett and Johnston [17]. Bhinder [1] stated that when all other factors are equal, the peak efficiency of a vaneless turbine will be 2–3% lower than that of a turbine with a vaned stator. However, this assertion was not supported with experimental data. Only one published performance comparison of vaned and vaneless stators with the same turbine rotor has been found: Baines and Lavy [18]. The vaneless volute was cast iron while the vaned stators were machined and therefore likely to have a much better surface finish

Contributed by the Turbomachinery Aero Division of ASME for publication in the JOURNAL OF TURBOMACHINERY. Manuscript received January 22, 2005; final manuscript received January 11, 2006. Review conducted by D. Prasad.

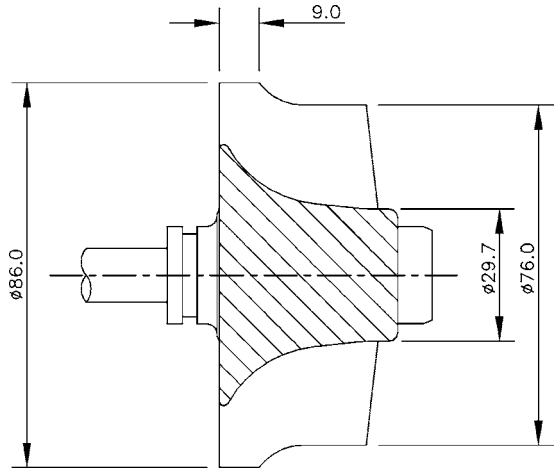

Fig. 1 Meridional view of the turbine rotor

than the vaneless volute. The authors originally aimed to compare performance of the vaned and vaneless stators at points of matched mass flow rate, although they reported that this had not been completely achieved in the experimental comparisons. The vaned turbine was shown to be around 15% more efficient than the vaneless configuration. Internal flow investigations in the vaneless volute identified large variations in flow angle and velocity around the volute exit, which the authors cited as the reason for poorer stage efficiency due to varying rotor incidence angle around the circumference. While the results provided a useful indication, unfortunately the variation in surface finishes and the discrepancy in the flow rates meant that the intended direct comparison of vaned and vaneless stators had not been achieved. Rodgers [19] also states that further efficiency reductions of several percentage points occur due to the exclusion of vaned nozzles.

In the present program of work the authors have sought to address the issue of efficient stator design through a series of performance tests on a turbine using the same rotor but a range of different stator configurations. This article presents a performance comparison of vaned and vaneless stators over a range of conditions and at particular design points of matching mass flow rate.

Turbine Design

Three different vaneless volutes, each with a different A/r value, were produced and tested with a radial turbine rotor. For comparison, three different vaned stators were designed and tested corresponding to each of the vaneless volutes.

The turbine rotor used for the tests was a commercially available rotor originating from a Holset turbocharger. In turbochargers, peak turbine efficiency is often compromised for packaging considerations and breadth of operating range. Therefore the base turbine rotor was reprofiled to a more "optimal" shape to give optimized efficiency for the test program with the philosophy that a more efficient turbine stage would more readily reveal any deterioration in efficiency due to increased stator losses. Figure 1 shows a meridional view of the turbine rotor with the basic dimensions.

The final rotor dimensions and the primary dimensions of the vaneless volutes were determined using a one-dimensional turbine performance prediction procedure, as detailed by Connor and Flaxington [20]. One criterion used in the 1D turbine design was achieving an optimum value of flow incidence angle at rotor inlet, which past tests at QUB (Spence and Artt [21]) and other workers have shown to lie in the range -20 to $-40°$. In this case the design value of incidence angle was $-25\pm1°$ for all turbine configurations. A second design criterion was the ratio of the rotor exit relative velocity to the radial component of velocity at rotor inlet. Rohlik [14] suggested that a moderate level of positive acceleration was desirable throughout the rotor blade passages and recommended a value of 2 for this ratio. In this investigation it was not possible to keep this value constant for each stator without changing the rotor geometry; however, the lowest value of this velocity ratio was 1.67.

Table 1 Summary of design point performance and 1D dimensions

	Stator A	Stator B	Stator C
Design point PR	1.8	2.5	3.2
Design point corrected mass flow rate (kg/s)	0.249	0.245	0.228
Design point corrected speed (rev/min)	47,348	56,766	62,893
Design point U/C	0.70	0.69	0.69
Dimensionless specific speed (rad)	0.90	0.89	0.89
Vaneless volute throat area, A (mm^2)	1703	1399	1210
Vaneless volute throat centroid radius, r (mm)	77	74	72
Vaneless volute A/r	22.1	18.9	16.8
Vaned stator throat area (mm^2)	1338	1189	1099
Rotor exducer throat area (mm^2)		2174[a]	
Rotor inlet tip diameter (mm)		86.0	
Rotor inlet blade height (mm)		9.0	
Rotor exducer tip diameter (mm)		76.0	
Rotor exducer hub diameter (mm)		29.7	
Rotor blade number		12	

[a]This value of throat area was determined from a 3D model of the modified rotor.

Three different design operating points were fixed, covering a range of practical pressure ratios, and three corresponding vaneless volutes were specified to provide optimized performance at each design point using the same turbine rotor. The specified design operating points and the 1D stator dimensions are indicated in Table 1. The mass flow and turbine speed values are corrected to standard turbine inlet conditions of 288 K and 101,325 Pa. The value for dimensionless specific speed is a function of turbine operating pressure and temperature; the values given in Table 1 were calculated using Eq. (1) based on the proposed test rig con-

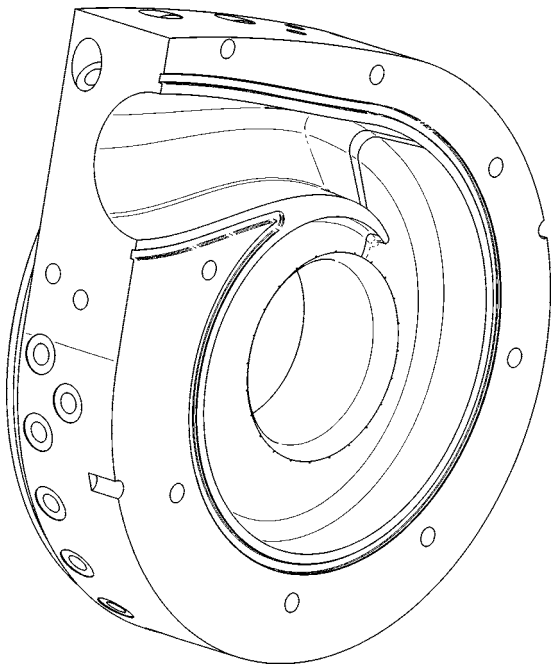

Fig. 2 Vaneless volute B

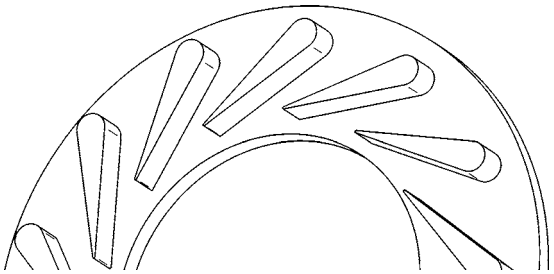

Fig. 3 Vaned stator B

ditions of an inlet temperature of 400 K and an exit pressure of 101,325 Pa, and where angular speed ω is expressed in rad/s

$$n_s = \frac{\omega\sqrt{Q_{\text{exit}}}}{\Delta h_{\text{is}}^{0.75}} \tag{1}$$

From the overall parameters listed in Table 1, detail design of the volute was undertaken using the procedure described by Chapple et al. [2]. The volute tongue angle was set at 23° to comply with the recommendations of Hussain and Bhinder [3]. The cross-sectional shape of the volute passages was a symmetrical trapezium with corner fillets. Each volute was machined in two halves from aluminum alloy to ensure a consistent and good quality internal surface finish. To assess the uniformity of the flow at rotor inlet and to support subsequent numerical analysis, 24 static pressure tappings were circumferentially spaced around the shroud surface 0.5 mm upstream of the rotor inlet. A bellmouth was incorporated at the inlet to each volute in order to achieve a relatively uniform velocity profile at inlet. One of the three volutes is illustrated in Fig. 2.

In order to achieve a direct comparison of the vaned and vaneless stators it was important that the flow capacity of each volute and its corresponding vaned stator were matched at the design point. Three vaned stators were designed using the 1D analysis, each incorporating 13 vanes and having the same leading edge and trailing edge PCDs. Details of the vaned stator are included in Table 1 and the vane shape used is shown in Fig. 3.

A large turbine housing was produced to accommodate the vaned stators, with a large internal flow path intended to deliver a uniform flow around the inlet to the stator vane row. Four static pressure tappings were included around the rotor inlet on the shroud surface. The machining process and the materials used to manufacture all the vaned and vaneless stator components were the same, and the surface finish levels were comparable.

Test Facility Description

Turbine power output was absorbed using a series of centrifugal compressors of different flow capacities in order to achieve a broad range of turbine loads. The turbine rotor blade clearance was 0.3 mm in both the radial and axial directions, and was held constant for all turbine configurations. Turbine efficiency was calculated from the measured temperature drop across the turbine stage. To avoid errors due to heat loss from the turbine, the entire turbine stage was heavily insulated and testing was conducted with a relatively low inlet temperature of 400 K. This method of efficiency measurement has been used during many turbine test programs at QUB and has demonstrated excellent repeatability

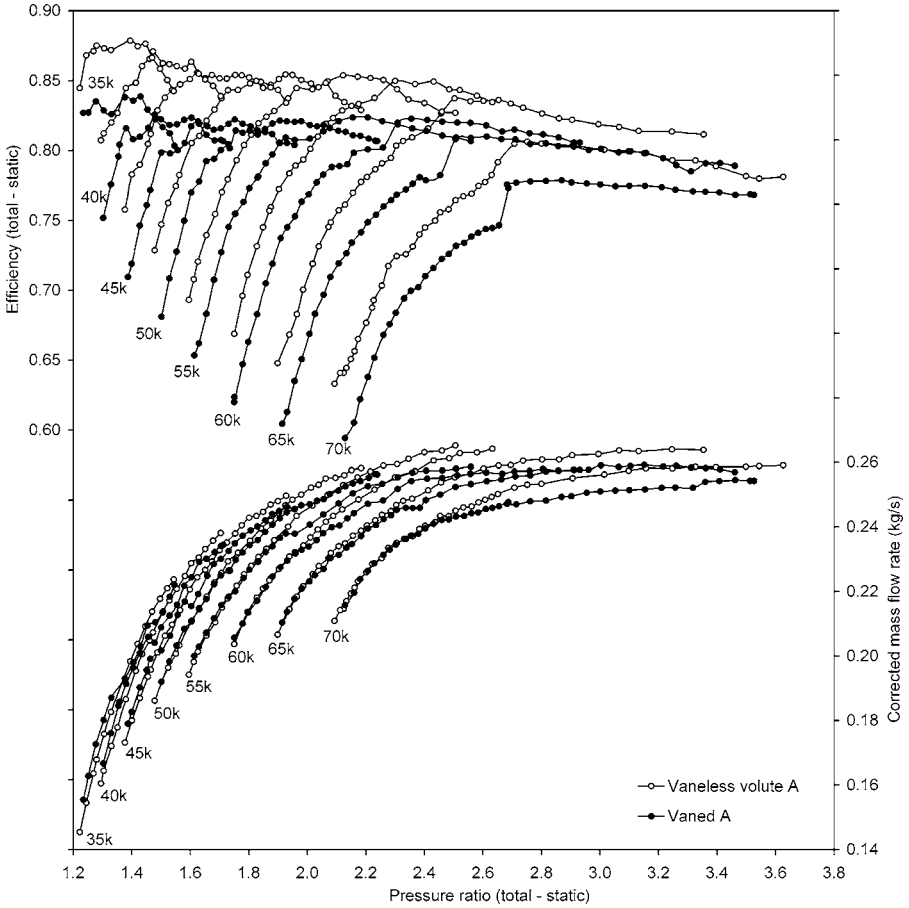

Fig. 4 Comparison of efficiency and mass flow rate for turbine A with vaned and vaneless stators

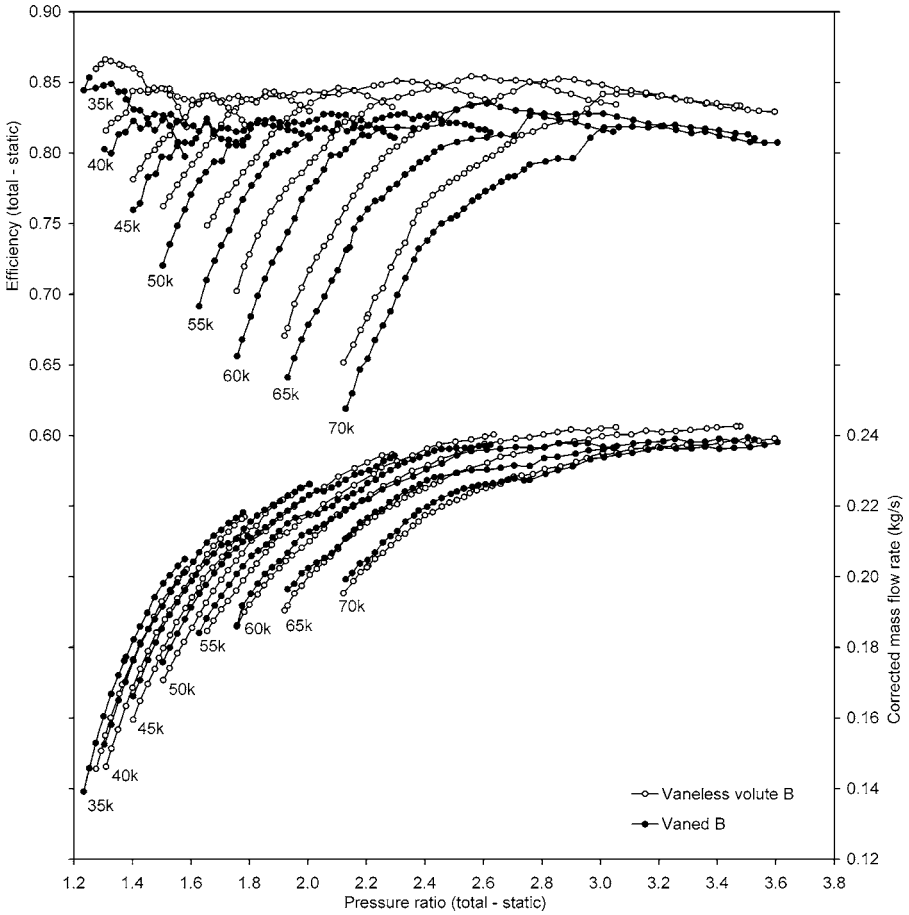

Fig. 5 Comparison of efficiency and mass flow rate for turbine B with vaned and vaneless stators

providing adequate care is taken during testing to achieve thermal equilibrium before measurements are taken. Static pressure was measured at inlet before the bellmouth and at outlet at the sudden expansion from the exducer diameter to the exhaust duct diameter. The test rig was specifically designed to provide temperature and pressure measurement points at inlet and outlet in regions of relatively low velocity where uncertainties relating to recovery of dynamic head would be minimized. The turbine exhaust pressure was approximately equivalent to atmospheric pressure. Turbine mass flow rate was measured using a number of ISO 5167 orifice plate installations to cover a broad range of flow rates. All measurements were logged on a computerized data-acquisition system. The turbine inlet air was heated in a propane combustion chamber.

When tested, the mass flow rates from the vaned stators did not adequately match the flow rates for the vaneless volutes at the chosen design points. Consequently, after brief testing, new vaned stators were manufactured with slightly modified throat areas in order to satisfactorily match the required mass flow rate for each vaneless volute.

Presentation of Results

Figure 4 presents the measured performance of the turbine fitted with the vaned stator A compared with the vaneless volute A. The total-to-static efficiency and the corrected mass flow rate are plotted against the stage total-to-static pressure ratio for a series of constant speed lines. The turbine speeds are labeled on the graph, where a label of "55k" corresponds to a speed of 55,000 rev/min. The mass flow rates and the speeds presented have been corrected to turbine inlet conditions of 101,325 Pa and 288 K using the conventional equations. Each individual turbine test point is indicated on the graph. Figures 5 and 6 present the corresponding results for the B and C stator sizes, respectively. The complete experimental program and the test results are reported in more detail by Rosborough [22].

Comparison of Turbine Performance With Vaned and Vaneless Stators

Table 2 presents the measured turbine performance for each configuration at the respective design operating points. The mass flow rates have been successfully matched at the design points of each vaned/vaneless pair within a maximum discrepancy of 1.0%. The matched mass flow rates enable direct comparison of the efficiencies, with any difference in loss levels being attributable to the choice of a vaned stator or vaneless volute. It is immediately evident from Figs. 4–6 that the vaneless volute configurations deliver better efficiency than the vaned stators at all operating conditions. This finding contrasts with measurements reported by Baines and Lavy [18], where the use of a vaned stator resulted in total-to-static efficiency values around 15 points greater than for the same turbine with a vaneless volute. One factor affecting the comparison of the present efficiency measurements with those presented by Baines and Lavy is the volute surface finish. Baines and Lavy compared machined stator vanes against a vaneless volute with a cast finish. The results reported here were based on vaned stators and vaneless volutes with machined finishes of a similar surface roughness. While the higher standard of surface finish on the vaneless volutes tested in this case undoubtedly contributed to their higher efficiency, this factor alone seems unlikely to account for such a large disparity in efficiency between the

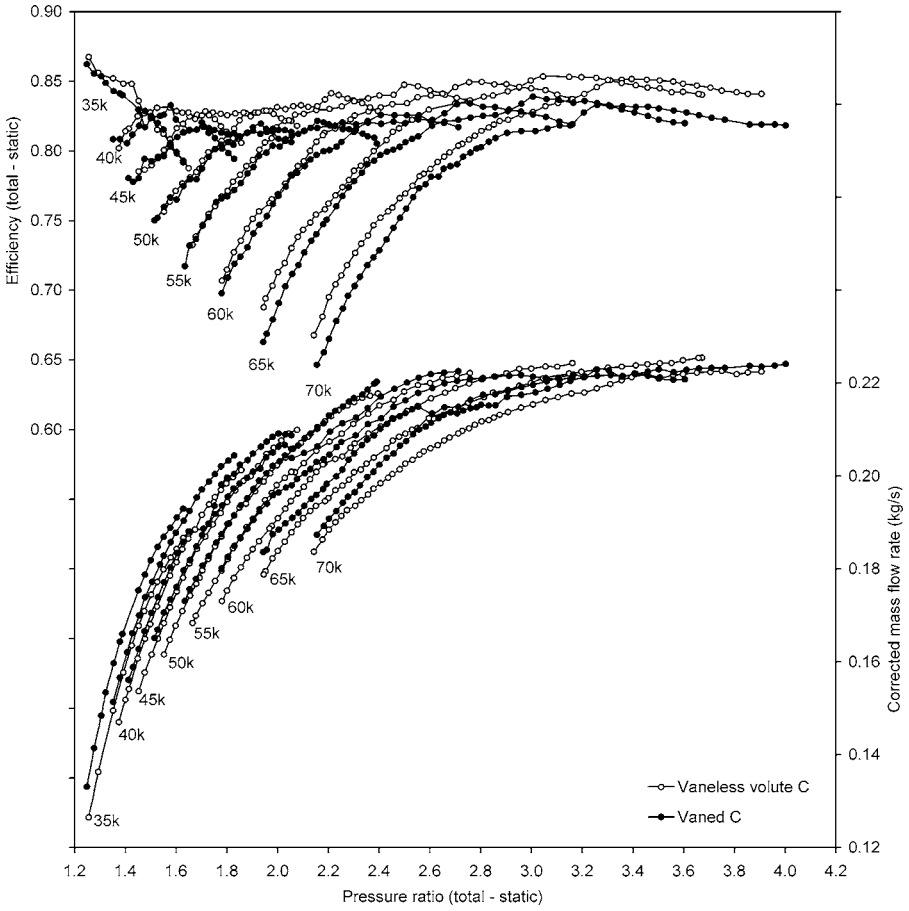

Fig. 6 Comparison of efficiency and mass flow rate for turbine C with vaned and vaneless stators

present results and those of previous workers. A further consideration would be the uniformity of flow achieved at rotor inlet by the vaneless volutes. It may be that a significant level of circumferential nonuniformity existed in the volutes used in previous work, while the volutes used in this study achieved an improved level of circumferential uniformity. It appears that a volute of good surface finish, achieving uniform circumferential conditions, is capable of matching or exceeding the efficiency of a vaned stator with its additional wetted surface area, secondary flows, and wakes.

Table 2 Measured performance at the design point for vaned stator and vaneless volute turbines

		Vaneless volute	Vaned stator
Stator A	Turbine PR	1.80	1.80
	Corrected speed (rev/min)	47,348	47,348
	Corrected mass flow rate (kg/s)	0.239	0.237
	Total-static efficiency (%)	85.0	81.6
	Total-total efficiency (%)	93.8	89.9
Stator B	Turbine PR	2.50	2.50
	Corrected speed (rev/min)	56,766	56,766
	Corrected mass flow rate (kg/s)	0.237	0.236
	Total-static efficiency (%)	84.7	82.5
	Total-total efficiency (%)	93.5	91.0
Stator C	Turbine PR	3.20	3.20
	Corrected speed (rev/min)	62,893	62,893
	Corrected mass flow rate (kg/s)	0.223	0.221
	Total-static efficiency (%)	84.7	82.9
	Total-total efficiency (%)	93.6	91.6

Baines and Lavy also found that along with higher efficiency, the vaned stator resulted in a more sharply peaked efficiency curve. However, Figs. 4–6 reveal that the same characteristic was not evident for the current comparison, in fact the shapes of the efficiency curves for the vaned and vaneless stators were very similar, although offset by several percentage points. As a consequence of the more "peaky" efficiency characteristic of the vaned stator, Baines and Lavy found the vaneless volute to be substantially more tolerant of off-design operating conditions at high values of velocity ratio. However, Fig. 7 demonstrates that in this case the variation of efficiency with velocity ratio is very similar for both the vaned stator and vaneless volute configurations of turbine B, with neither stator option demonstrating a better tolerance for off-design conditions over the range of turbine loads tested ($0.6 < U/C < 0.94$). Although not presented here, the same trend was evident for turbine configurations A and C.

Total-to-total efficiency values were calculated using a value of total pressure at rotor exit determined from a one-dimensional analysis at the exducer rms diameter. The mean relative flow velocity through the exducer throat area, which was calculated at each operating point using the measured flow rate, was used in conjunction with the exducer blade angle and blade speed at the rms diameter to calculate a value of absolute velocity at rotor exit. The exit total pressure was obtained from the calculated exit velocity and the measured exit static pressure. Total-to-total efficiency values at the design points of each configuration are included in Table 2. The values for the vaned stator turbines compare well with total-to-total efficiency values presented for equivalent turbines by NASA [12,13].

The vaneless volute is clearly the most efficient stator at all test

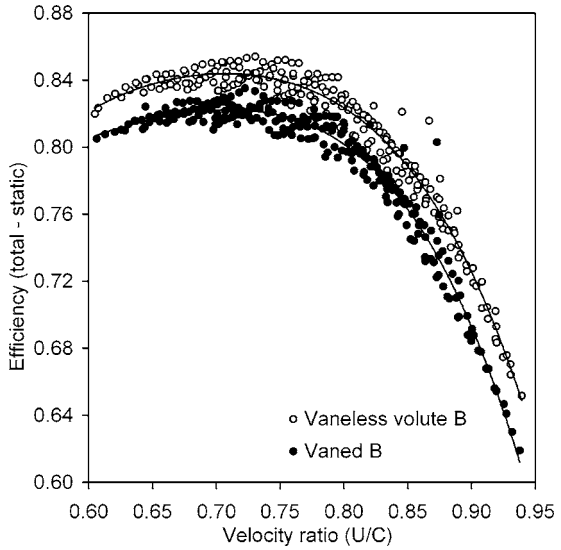

Fig. 7 Comparison of efficiency for vaned stator B and vaneless volute B, plotted against velocity ratio *U*/*C*

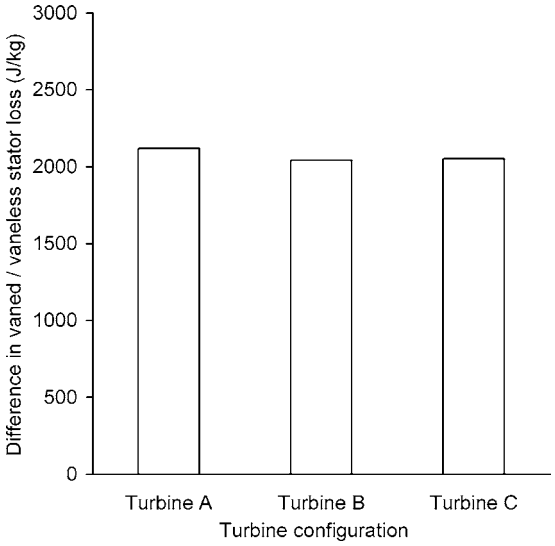

Fig. 9 Difference in vaned and vaneless stator losses for each of the turbine configurations A, B, and C

conditions, although the difference appears greatest for the turbine A configuration where the vaneless volute is around 3.5% more efficient than the vaned stator. The difference is less for turbines B and C; around 2% for turbine C. While the design point efficiency of the vaneless volute configuration remained relatively constant for the three different turbine configurations, the design point efficiency of the vaned stator configuration progressively increased through turbines A, B, and C. Figure 8 shows the envelope of the peak efficiency points for each of the three vaned configurations, and it is evident that better efficiencies are attainable at higher stage pressure ratios. However, at higher pressure ratios the efficiency achieved by the vaned C turbine is substantially better than the vaned A or B turbines. It might be suggested that the "C" vaned stator had a smaller throat area and consequently lower mass flow rate resulting in reduced rotor exit losses and a higher static efficiency. However, the differences were very similar when the total efficiencies were compared, so variation in exit loss does not appear to be the explanation. A previous publication by Spence et al. [23] highlighted the relevance of the stator/rotor throat area ratio with regard to the maximum attainable efficiency at a given pressure ratio. In that case best efficiency at a pressure ratio of 2.2 was achieved with a stator/rotor throat area ratio of 0.5, and at a pressure ratio of 2.7 with a stator/rotor throat area ratio of 0.45. In this investigation, vaned turbine C had a stator/rotor throat area ratio of 0.5 and clearly performed better at higher pressure ratios than the other two larger vaned stators. The stator/rotor throat area ratio is implicitly linked to the turbine degree of reaction, however, it was not possible to calculate the degree of reaction directly from the experimental measurements since either the stator loss or the stator exit static temperature was required.

The stator exit region of a small radial flow turbine is a difficult environment for experimental measurements and ideally a nonintrusive method such as laser Doppler anemometry would be used to survey the stator exit velocity and determine total pressure. Such measurements were not available in this investigation and consequently absolute measurements of the losses through the vaned and vaneless stators cannot be obtained. However, the difference in incurred losses between the vaned and vaneless stators was determined with confidence from the experimental measurements. Figure 9 shows the additional loss incurred by the vaned stator relative to the vaneless volute at the design point for each of the three turbine configurations. The difference in vaned and vaneless stator loss is very similar for each turbine; although these values do vary with changing turbine operating conditions. The

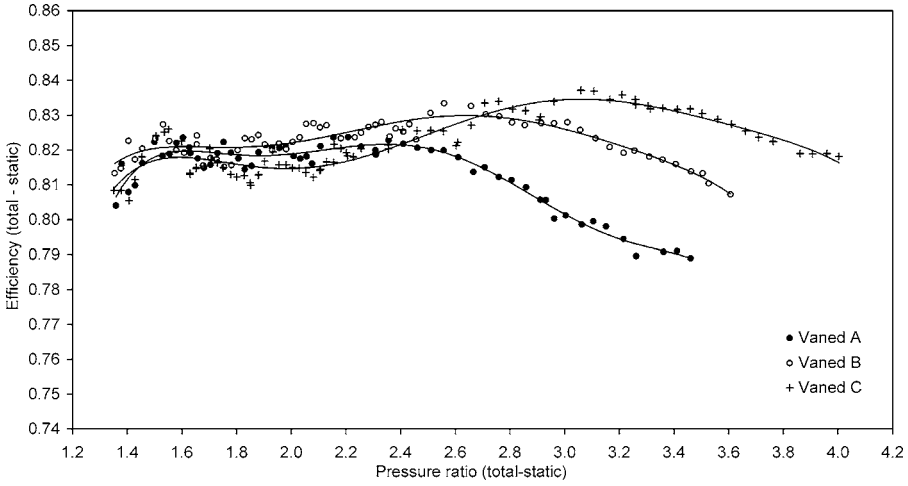

Fig. 8 Peak efficiency envelopes for the vaned stator configurations A, B, and C

Table 3 Loss coefficients used for 1D turbine performance prediction

Coefficients	Vaneless volute turbines A, B, and C	Vaned stator turbines A, B, and C
Housing exit swirl velocity factor	0.91	1
Housing total pressure loss factor	0.15	0.15
Nozzle incidence loss factor	n/a	0
Nozzle total pressure loss factor	n/a	0.4
Nozzle exit throat blockage factor	n/a	0.07
Impeller incidence loss factor	1.3	1.3
Impeller total pressure loss factor	0.25	0.25
Impeller exit throat blockage factor	0	0

stator loss is assumed to encompass all losses between the turbine inlet flange and the rotor inlet radius. In the case of the vaned stator this will include frictional and secondary flow losses in the casing that houses the stator vanes, any incidence losses at inlet to the stator vanes, frictional losses in the vane passages, mixing losses due to the trailing edge wakes from the vanes and frictional losses in the vaneless space prior to rotor inlet. Furthermore, the value presented for the difference in losses will also include any change in losses through the rotor passages as a consequence of nonuniform pressure distribution around the vaneless volute or the greater number of jets and wakes emerging from the vaned stator.

As a result of experimental modification of the geometry of each vaned stator, the mass flow rates for the vaned and vaneless stators were well matched at the design operating points. However, Figs. 4–6 show that discrepancies in mass flow have occurred at off-design conditions. For example, Fig. 4 reveals that the flow rates for the vaned and vaneless stators are well matched at the lower pressure ratio end of the performance map, but the vaned stator passes less mass flow at higher pressure ratios than the vaneless volute. This is consistent with the fact that the vaned stator is less efficient, since additional pressure losses are incurred in the stator leaving less pressure ratio across the rotor and therefore a smaller flow rate. However, why the discrepancy only occurs at higher pressure ratios is not clear. Vaned turbine A appears to choke at corrected mass flow rates of approximately 0.26 kg/s. Since the maximum achievable mass flow rate decreases with decreasing stator throat area, it is therefore apparent that it is the stator area which dictates the choked mass flow rate, not the rotor throat area. The mass flow rates for each of the three stator sizes were between 2 and 4% below the values predicted by the 1D design analysis.

1D Performance Prediction Method

The validity of the 1D performance prediction method used at the turbine design stage was evaluated by comparing the model with the measured turbine performance. The component loss models with the 1D performance prediction model, which are described in detail by Connor and Flaxington [20], were calibrated to give a good fit with the turbine B configuration. The 1D model incorporated different empirical loss models for vaned and vaneless stators, but for consistency the same loss coefficients were used for the rotor in each case. Table 3 lists the values of loss coefficients used for the 1D performance comparison. The comparison between the predicted and measured performance for vaned and vaneless turbine B at 65,000 rev/min is shown in Figs. 10 and 11. The same values of stator and rotor loss coefficients were then used to predict the performance for turbines A and C, which is also compared with the measured performance in Figs. 10 and 11. Having been calibrated against turbine B, the 1D performance model provides a good overall prediction of mass flow rate for turbines A and C, although there is a tendency to overpredict the mass flow rate at higher pressure ratios (low values of U/C). Prediction of turbine efficiency is not as good as for mass flow rate and, like the mass flow rate, is overpredicted at high pressure ratios, which suggests a weakness in the incidence loss model at positive incidence angles. The loss model adopted by Connor and Flaxington [20] was based on a model published by Futral and Wasserbauer [11], which assumed that minimum incidence loss occurred at 0° incidence. Since this is not the case, the 1D prediction procedure underestimates the losses incurred at 0° and positive values of rotor incidence. Clearly the prediction could be improved by developing the incidence loss model to give minimum loss at a specified negative value of incidence, as has been suggested by other researchers. The 1D performance prediction method provides a good means of extrapolating the performance of a particular turbine, provided there is experimental data for initial calibration of the loss models.

Conclusions

A comprehensive experimental investigation of turbine performance has been carried out providing direct comparison of turbines with vaned stators and vaneless volutes using the same rotor at identical operating conditions. Three pairs of vaned and vaneless stators were tested, covering a range of pressure ratios and flow rates.

The vaneless volutes delivered consistent and significant efficiency advantages over the vaned stators over the complete range

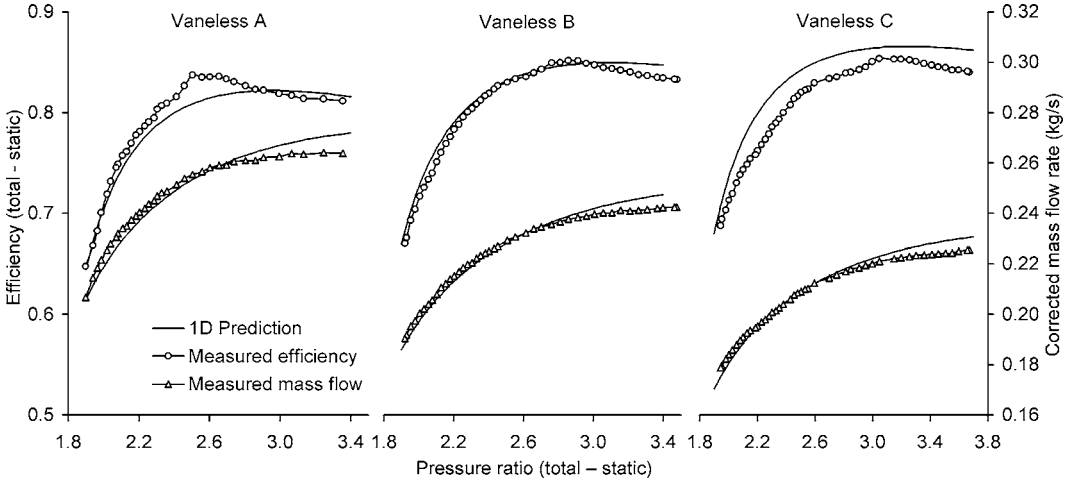

Fig. 10 Comparison of predicted and measured performance for the vaneless volute turbines at 65,000 rev/min

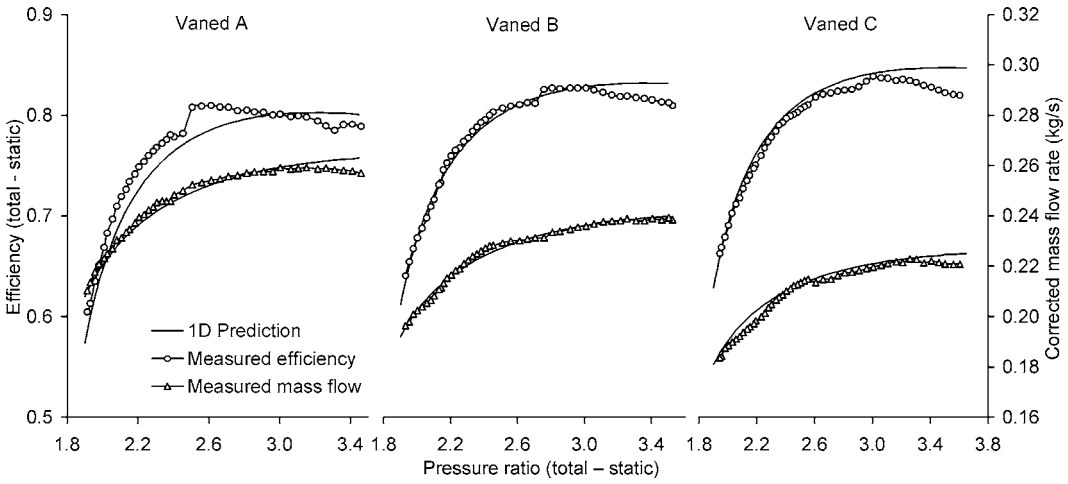

Fig. 11 Comparison of predicted and measured performance for the vaned stator turbines at 65,000 rev/min

of pressure ratios tested. At the design operating conditions, the efficiency advantage was between 2% and 3.5%. Previous comparisons have typically compared machined stator vanes with a vaneless volute having a rough cast surface finish with a high level of roughness, and found the volute to be less efficient. While these are not strictly comparable situations, the implication is that housing surface roughness is a significant factor in overall turbine efficiency. The turbines configured with vaneless volutes, while maintaining an efficiency advantage, were not found to be any more tolerant of off-design operating conditions than the vaned stator turbines.

The best achievable efficiency at a given turbine pressure ratio with a vaned stator was a function of the stator to rotor throat area ratio, with a smaller ratio giving better efficiency at higher pressure ratios. A ratio equal to 0.5 gave good efficiency at moderate pressure ratios.

A volute design method presented by Chapple et al. was used and yielded good turbine efficiency levels and mass flow rates within 4% of the design values. A 1D turbine design prediction method presented by Connor and Flaxington was used for the turbine design and was subsequently shown to be a good method of extrapolating turbine performance providing experimental data were available to calibrate the loss coefficients in the model.

Acknowledgment

The authors would like to acknowledge the financial support of EPSRC (Grant No. GR/M41865), without which this investigation would not have been possible. Thanks are also due to Holset Engineering Co. Ltd. for ongoing technical and hardware support, and particularly to Nick Sharp for his interest, enthusiasm, and generosity with his time.

Nomenclature

VGT = variable geometry turbine
EGR = exhaust gas recirculation
1D = one dimensional
U/C = turbine blade speed velocity ratio
PCD = pitch circle diameter
rms = root mean square
n_s = dimensionless specific speed (rad)
Q_{exit} = volumetric flow rate at rotor exit (m^3/s)
Δh_{is} = isentropic stage enthalpy drop (J/kg)
ω = angular speed (rad/s)

References

[1] Bhinder, F. S., 1969, "Investigation of Flow in the Nozzle-Less Spiral Casing of a Radial Inward-Flow Gas Turbine," Proc. Inst. Mech. Eng., **184**, pp. 66–71.
[2] Chapple, P. M., Flynn, P. F., and Mulloy, J. M., 1980, "Aerodynamic Design of Fixed and Variable Geometry Nozzleless Turbine Casings," Trans. ASME: J. Eng. Gas Turbines Power, **102**, pp. 141–147.
[3] Hussain, M., and Bhinder, F. S., 1984, "Experimental Study of The Performance of a Nozzleless Volute Casing for Turbocharger Turbines," SAE Paper No. 840571.
[4] Kastner, L. J., and Bhinder, F. S., 1975, "A Method for Predicting the Performance of a Centripetal Gas Turbine Fitted With a Nozzle-less Volute Casing," ASME Paper No. 75-GT-65.
[5] Chen, H., 1996, "Design Methods of Volute Casings for Turbocharger Turbine Applications," Proc. Inst. Mech. Eng., Part A, **210**, pp. 149–156.
[6] Whitfield, A., and Mohd Noor, A. B., 1994, "Design and Performance of Vaneless Volutes for Radial Inflow Turbines. 1. Non-dimensional Conceptual Design Considerations," Proc. Inst. Mech. Eng., Part A, **208**, pp. 199–211.
[7] Whitfield, A., MacGregor, S. A., and Mohd Noor, A. B., 1994, "Design and Performance of Vaneless Volutes for Radial Inflow Turbines. 2. Experimental Investigation of the Mean Line Performance-Assessment of Empirical Design Parameters," Proc. Inst. Mech. Eng., Part A, **208**, pp. 213–224.
[8] MacGregor, S. A., Whitfield, A., and Mohd Noor, A. B., 1994, "Design and Performance of Vaneless Volutes for Radial Inflow Turbines. 3. Experimental Investigation of the Internal Flow Structure," Proc. Inst. Mech. Eng., Part A, **208**, pp. 295–302.
[9] Glassman, A. T., 1976, "Computer Program for Design and Analysis of Radial Inflow Turbines," NASA/TN D-8164.
[10] Stewart, W. L., Whitney, W. J., and Wong, R. Y., 1960, "A Study of Boundary Layer Characteristics of Turbomachine Blade Rows and Their Relation to Overall Blade Loss," J. Basic Eng., **82**(3), pp. 588–592.
[11] Futural, S. M., and Wasserbauer, C. A., 1965, "Off-Design Performance Prediction With Experimental Verification for a Radial-Inflow Turbine," NASA, TN/D-2621.
[12] Kofskey, M. G., and Nusbaum, W. J., 1972, "Effects of Specific Speed on Experimental Performance of a Radial-Inflow Turbine," NASA, TN/D-6605.
[13] Kofskey, M. G., and Wasserbauer, C. A., 1966, "Experimental Performance Evaluation of a Radial-Inflow Turbine Over a Range of Specific Speeds," NASA, TN/D-3742.
[14] Rohlik, H. E., 1968, "Analytical Determination of Radial-Inflow Turbine Design Geometry for Maximum Efficiency," NASA TN/D-4384.
[15] Palmer, R. M., 1956, "D.I.G.T. Radial Inflow Turbine-Scroll and Nozzle Performance—Part II," Ricardo Internal Report No. 1368, Ricardo & Co., Sussex.
[16] Hiett, G. F., 1959, "D.I.G.T. Radial Inflow Turbine-Cold Tests on Turbine B, Turbine A and Turbine D," Ricardo Internal Report No. 1412, Ricardo & Co., Sussex.
[17] Hiett, G. F., and Johnston, I. H., 1963, "Experiments Concerning the Aerodynamic Performance of Inward Flow Radial Turbines," Proc. Inst. Mech. Eng., **178**, pp. 28–42.
[18] Baines, N. C., and Lavy, M., 1990, "Flows in Vaned and Vaneless Stators of Radial Inflow Turbocharger Turbines," Institution of Mechanical Engineers Turbochargers and Turbocharging Conference, Paper No. C405/005, pp. 7–12.

[19] Rodgers, C., 2000, "Radial Turbines-Blade Number and Reaction Effects," ASME Paper No. 2000-GT-456.
[20] Connor, W. A., and Flaxington, D., 1994, "A One-Dimensional Performance Prediction Method for Radial Inflow Turbines," Institution of Mechanical Engineers Turbochargers and Turbocharging Conference, Paper No. C484/041/94, pp. 271–282.
[21] Spence, S. W. T., and Artt, D. W., 1998, "An Experimental Assessment of Incidence Losses in a Radial Inflow Turbine Rotor," Proc. Inst. Mech. Eng., Part A, **212**, pp. 43–53.
[22] Rosborough, R. S. E., 2003, "An Experimental Assessment of Different Vaned and Vaneless Stators for a Radial Inflow Turbine," Ph.D. thesis, Queen's University of Belfast, UK.
[23] Spence, S. W. T., Doran, W. J., and Artt, D. W., 1999, "Experimental Performance Evaluation of a 99.0 mm Radial Inflow Nozzled Turbine at Larger Stator/Rotor Throat Area Ratios," Proc. Inst. Mech. Eng., Part A, **213**, pp. 205–218.

Aerodynamic Design and Testing of Three Low Solidity Steam Turbine Nozzle Cascades

Bo Song[1]
Wing F. Ng

Mechanical Engineering Department,
Virginia Polytechnic Institute
and State University,
Blacksburg, VA 24061

Joseph A. Cotroneo
Douglas C. Hofer

GE Energy,
1 River Road,
Schenectady, NY 12345

Gunnar Siden
GE Energy,
300 Garlington Road,
Greenville, SC 29602

Three sets of low solidity steam turbine nozzle cascades were designed and tested. The objective was to reduce cost through a reduction in parts count while maintaining or improving performance. The primary application is for steam turbine high pressure sections where Mach numbers are subsonic and high levels of unguided turning can be tolerated. The base line design A has a ratio of pitch to axial chord of 1.2. This is the pitch diameter section of a 50% reaction stage that has been verified by multistage testing on steam to have a high level of efficiency. Designs B and C have ratios of pitch to axial chord of 1.5 and 1.8, respectively. All three designs satisfy the same inlet and exit vector diagrams. Analytical surface Mach number distributions and boundary layer transition predictions are presented. Extensive cascade test measurements were carried out for a broad incidence range from −60 to +35 deg. At each incidence, four outlet Mach numbers were tested, ranging from 0.2 to 0.8, with the corresponding Reynolds number variation from 1.8×10^5 to 9.0×10^5. Experimental results of loss coefficient and blade surface Mach number are presented and compared for the three cascades. The experimental results have demonstrated low losses over the tested Mach number range for a wide range of incidence from −45 to 15 deg. Designs B and C have lower profile losses than design A. The associated flow physics is interpreted using the results of wake profile, blade surface Mach number distribution, and blade surface oil flow visualization, with the emphasis placed on the loss mechanisms for different flow conditions and the loss reduction mechanism with lower solidity. The effect of the higher profile loading of the lower solidity designs on increased end wall losses induced by increased secondary flow, especially on low aspect ratio designs, is the subject of ongoing studies.
[DOI: 10.1115/1.2372774]

Introduction

Low solidity airfoil designs offer advantages to steam turbines used in the power generation industry. The most obvious is reduced parts count and therefore reduced cost. Alternatively, axial chord can be reduced resulting in a shorter turbine, which is useful in tradeoffs between rotor dynamics and turbine efficiency. Efficiency is also of paramount importance so these low solidity designs must not compromise performance. In combined cycle high pressure steam turbines the blades can be small but there are minimum manufacturing and reliability limits on trailing edge thickness. A large ratio of trailing edge thickness to throat will lower turbine efficiency. Low solidity airfoils reduce these trailing edge blockage losses. Conversely, lower solidity airfoils for the same duty are more highly loaded than their higher solidity counterparts. The objective of this work is to define airfoils that have low profile losses at low solidity and to determine what levels of low solidity are attainable with high efficiency. The optimum solidity should be a good trade off for weight and efficiency [1,2]. Another issue to consider is that more highly loaded airfoils can tend to have higher endwall losses generated by increased secondary flow [3,4]. This can be a significant source of efficiency loss for low aspect ratio designs. The profile losses of the low solidity designs presented here are actually lower than the base line higher solidity design. This will help counter the increased end wall losses. The effect of low solidity designs on secondary flow in the endwall region and associated losses is the subject of ongoing studies.

Prior work on low solidity or the so-called high lift turbine blading has been carried out mostly on gas turbine low-pressure turbines, which operate at relatively low Reynolds number (up to 21,000). Solomon [5,6] found the efficiency gain by reduced solidity on a low-pressure turbine was conditional, jointly dependent on inlet turbulence, Reynolds number, and clocking effect. Howell et al. [7] further reduced solidity of high lift blading (datum profile) based on understanding of the boundary layer behavior. They achieved 15% greater lift under unsteady flow condition, with the new reduced-solidity profile losses only slightly higher than those of the datum profile. They referred to this new blading as "ultra-high lift" (UHL) concept. However, with steady inflow, they found the UHL profiles performed poorly. The following full-scale LP turbine rig test showed lower efficiencies associated with the afore-mentioned UHL blading than the datum [8]. Another effort by Howell et al. [9] detailed a study into the unsteady boundary layer behavior in two high lift and one ultrahigh lift LP turbines, showing advantage of the low solidity concept in LP turbines under unsteady flow and stage interaction. These prior studies have shown that the high lift turbines benefit from unsteady effects of upstream blade wakes, with a comprehensive summary given by Hodson [10]. The parametric effect of reduced solidity on profile losses seems not to be so certain from these studies.

The work by Gonzalez et al. [11] contributed to high lift LP turbine blading research with low-speed cascade steady and unsteady experiments. Their work demonstrated 10% profile loss reduction by redesigning pressure and suction surfaces to make thicker profiles. The cascade testing was performed with relatively low Reynolds numbers up to 30,000. Their results also support an important idea of an optimum axial position for the peak Mach

[1]Currently Sr. Product Development Engineer with Gardner Denver, Inc.

Contributed by the International Gas Turbine Institute (IGTI) of ASME for publication in the JOURNAL OF TURBOMACHINERY. Manuscript received October 1, 2003; final manuscript received March 1, 2004. IGTI Review Chair: A. J. Strazisar. Paper presented at the International Gas Turbine and Aeroengine Congress and Exhibition, Vienna, Austria, June 13–17, 2004, Paper No. 2004-GT-53329.

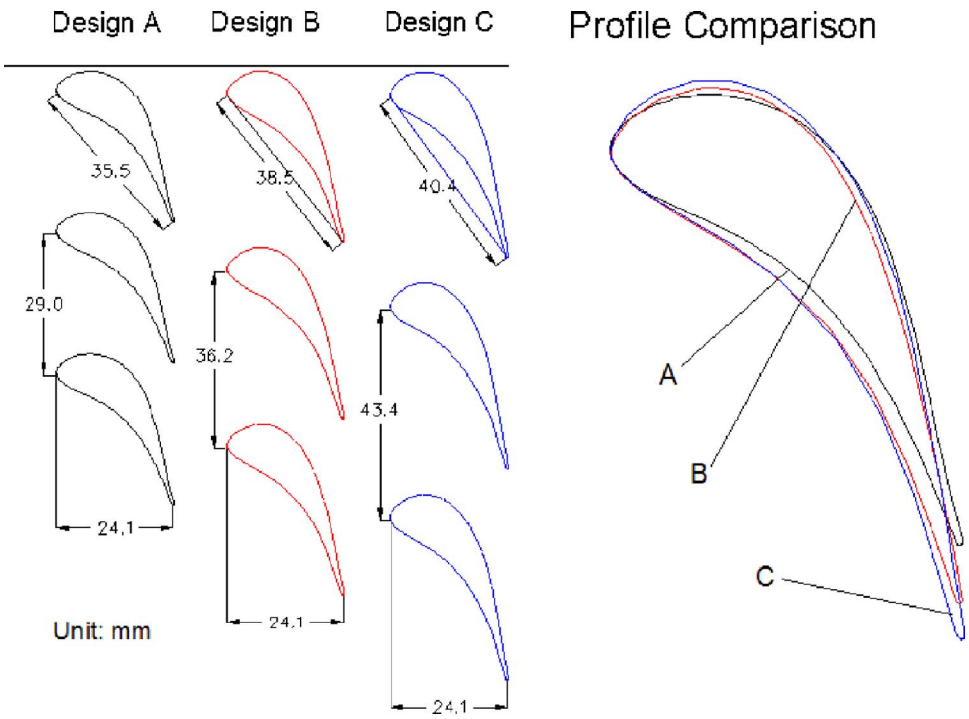

Fig. 1 Cascade profile shapes

number, or put it another way, the concept of aft loading to reduce losses is not absolute (this point is supported by the current work as will be shown in the paper). Low speed wind tunnel testing of a high lift LP turbine cascade by Houtermans et al. [12] provided more profile loss data to the open literature over an incidence range from −9 to 5 deg at Reynolds numbers of 50,000 to 200,000. The blade used was a front-loaded type with the peak velocity at 32% of the suction side length. This research also indicated the position of the peak velocity coupled with the incidence had a strong effect on the cascade performance. Cascade testing of three HP turbine blades (front loaded, midloaded, aft loaded) at relatively high Reynolds numbers (30,000–100,000) by Corriveau and Sjolander [13] also indicated important influence of loading distribution on the cascade performance and the dependence of performance gain on conditions. The effect of loading distribution on turbine blade performance was studied earlier, and again, the conclusion to favor front or aft loading is somewhat in contradiction [14–16].

The particular airfoil design addressed here is the pitch line section of a master nozzle design used in 50% reaction high pressure steam turbines for the combined cycle power generation market. The base line design A has been applied in the high pressure sections of GE's new 107FA and 109FB HEAT™ steam turbines [17,18]. Laboratory testing of a 12 stage prototype on steam has demonstrated a high level of efficiency. The next design objective is a reduced cost product that maintains this high efficiency level. Reduced solidity airfoil design optimization is one part of that effort. The design and test of the base line plus two 2D cascades with decreased solidity will be presented here. It should be noted that the current design for steam turbine application rendered a high Reynolds number (2×10^6) and the testing was extended to as wide a range of conditions as possible for sufficient experimental demonstration (incidence: −60 to +35 deg, outlet Mach number: 0.2–0.8, and Reynolds number: 1.8×10^5–9.0×10^5). The blade profiles of the reduced-solidity cascades were optimized for performance improvement. Therefore, the current work should be also of general interest with an addition of data and reference to turbine blading research with respect to effects of solidity, profile, and loading distribution.

Cascade Design/Optimization

The airfoils were designed using an in house Bezier curve blade geometry generator to allow for maximum flexibility in optimizing the profile shape. Flow analysis was performed with a 2D Euler flow solver with boundary layer and loss calculations [19]. This level of analysis is believed to be proper for designing airfoils for 2D cascade testing. It gives the advantage of quick turn around time allowing for a maximum number of design iterations. All three cascades were designed for the same duty. The design Reynolds number is approximately 2×10^6. Figure 1 gives the profile shapes of designs A, B, and C. The cascade nomenclature used in this study is illustrated in Fig. 2. Table 1 gives a summary of some relevant design parameters. The base line design A has a ratio of pitch to axial chord of 1.2 while for designs B and C the values are 1.5 and 1.8, respectively. Design A has a solidity of 1.22 while for designs B and C the values are 1.06 and 0.93, respectively.

Variations in stagger and unguided turning were investigated as part of the profile optimization process. As expected, reduced solidity leads to higher unguided turning and more tangential stagger. The higher stagger is needed to form good throat converging passage geometry. High unguided turning can be detrimental at higher Mach numbers because of increased shock losses but is not necessarily a problem at the subsonic Mach numbers of these designs. Decreased solidity causes increased loading and can lead to high diffusion on the suction surface downstream of the throat. This high diffusion can lead to increased boundary layer thickness and even flow separation. The philosophy taken here was to move some of the load forward on the lower solidity designs to control suction side diffusion and hence limit losses. It should be noted that even though some of the load was moved forward, the distributions are still closer to aft loaded than uniformly loaded. Pressure and suction surface Mach number distributions over a range of exit Mach numbers are shown in Fig. 3 for all three designs.

Reynolds numbers at nozzle exits for the 107FA high pressure turbine range from about 2×10^6 in the back end to about 5×10^6 in the front end. The Reynolds numbers for this cascade testing are lower due to rig pressure limitations and cover a range

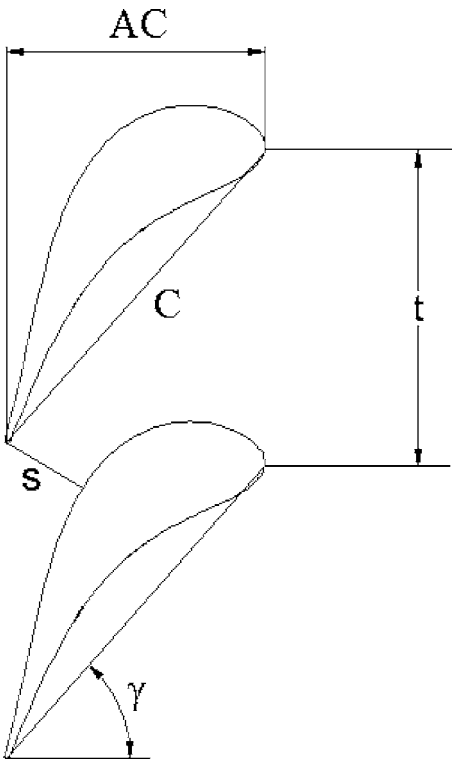

Fig. 2 Cascade nomenclature

from about 2×10^5 to 9×10^5. Figure 4 shows normalized predicted losses and boundary layer transition points versus Reynolds number for the three cascades. Turbulence levels for the predictions were set to approximate those of the cascade test (about 2%). All three designs show similar trends. The cascade test conditions are somewhat up the knee in the loss versus Reynolds number curve compared to the field conditions. The suction surface is predicted to transition from laminar to turbulent at a little less than 90% axial chord for the test conditions and between about 75% and 50% for the field conditions. The pressure surface is predicted to be laminar for both test and field Reynolds numbers. The lower Reynolds numbers of the test are expected to give somewhat higher losses than would be seen in the field. If the increased loading of the low solidity designs does not cause increased losses at the lower cascade test Reynolds numbers, it will not be a problem at the higher field Reynolds numbers.

Table 1 Cascade geometry

	Cascade		
Parameter	A	B	C
Axial chord, AC (mm)	24.1	24.1	24.1
Chord, C (mm)	35.5	38.5	40.4
Span, H (mm)	152.4	152.4	152.4
Throat, s (mm)	8.1	10.6	13.2
Pitch, t (mm)	29.0	36.2	43.4
Ratio of pitch to axial chord, t/AC	1.20	1.50	1.80
Solidity, $\sigma=C/t$	1.22	1.06	0.93
Aspect ratio, AR$=H/C$	4.3	4.0	3.8
Stagger angle, γ	47.9 deg	51.9 deg	54.0 deg
Unguided turning	17 deg	25 deg	34 deg

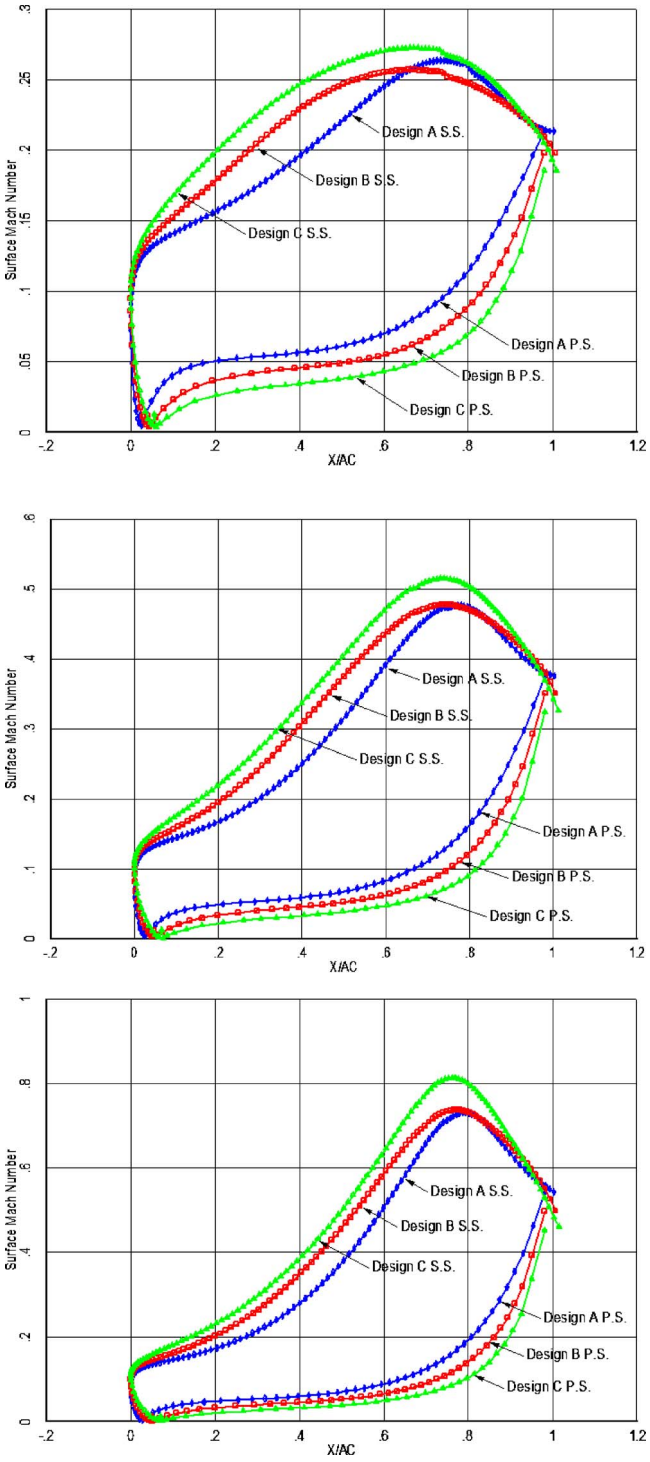

Fig. 3 Predicted blade surface Mach number distributions on steam at three different exit Mach numbers

Facility and Experimental Procedure

The experiments were conducted in the Virginia Tech High Speed Cascade Wind Tunnel. A schematic of the tunnel facility is shown in Fig. 5. The wind tunnel is a blowdown type, with the capacity to sustain high speed flow for about 10 s. During each blowdown tunnel run, the cascade inlet total pressure was maintained by a feedback control scheme to obtain the desired Mach number. High pressure air was supplied by a four-stage reciprocating compressor and accumulated in large storage tanks. Upon discharge from the storage tanks, the air passed through an

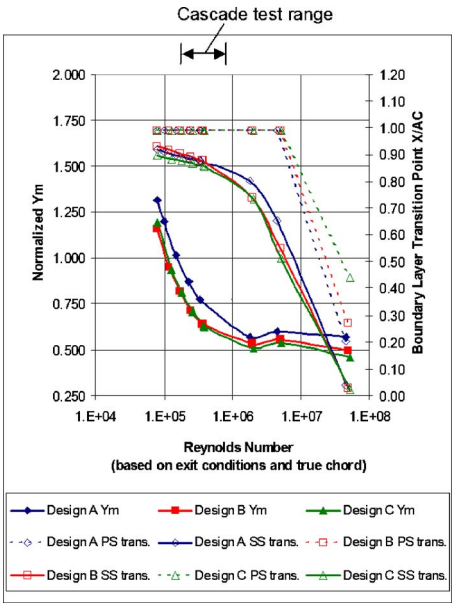

Fig. 4 Predicted losses and boundary layer transition points on steam at constant Mach number

activated-aluminum dryer for dehumidification and then proceeded through the settling chamber where a flow straightener and a screen were placed to make the flow uniform. Upstream of the test section, a turbulence grid was inserted to increase inlet free-stream turbulence to a level of about 2%. After passing through the test section, the flow was guided into the exhaust pipe, and finally discharged to the atmosphere.

The test section is better shown by an insert view in Fig. 5 and a sideview picture in Fig. 6. The cross section of the cascade inlet had dimensions of 232 mm × 152 mm (height × width). The tested cascade was mounted between a pair of Plexiglas sidewalls,

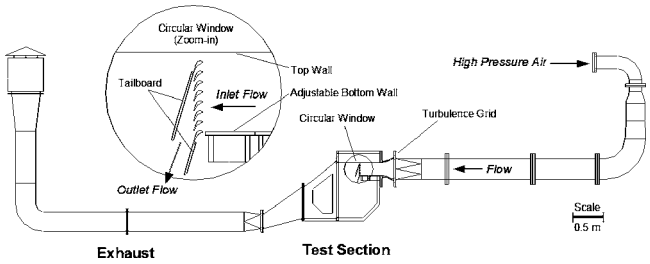

Fig. 5 Virginia Tech High Speed Cascade Wind Tunnel

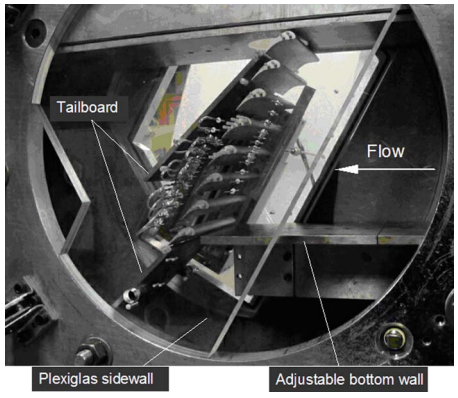

Fig. 6 Cascade test section

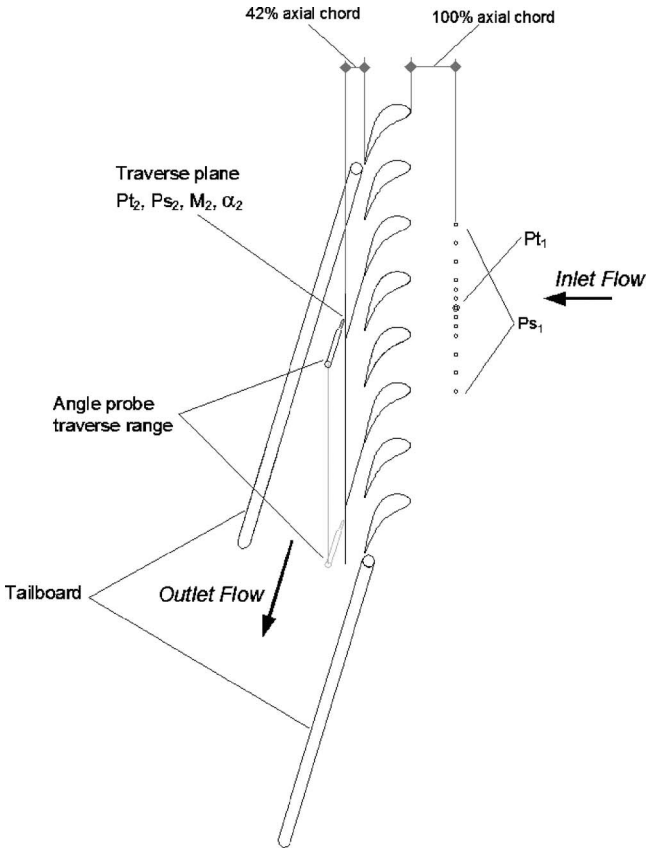

Fig. 7 Aerodynamic measurements

which allow for visual observation and optical measurements. The sidewalls fit into the circular window. By rotating the sidewall-cascade assembly, different incidence angles could be obtained for the tests. The cascade flow uniformity/periodicity was achieved by using no less than six blades and employing a pair of tailboards downstream of the cascade along with an adjustable bottom wall at the inlet. The number of blades mounted to construct the cascade depended on the available space in the test section, which was a function of the cascade solidity and different incidence angles. It turned out that 8–10 blades were used for design A, and 7–8 blades for design B, and six blades for design C. The tailboards were set parallel to the cascade design outlet flow angle. For different incidence angles, the axial length of the adjustable bottom wall was set to fit the cascade very well. Figure 6 shows one example of a negative incidence test case.

Temperature in the tunnel was measured using a type *K* thermocouple total temperature probe located upstream of the test section. The facility operated with an inlet total temperature range of 277–298 K in the current experiment. Aerodynamic measurements are illustrated in Fig. 7. All the aerodynamic measurements were performed in the midspan for a wide range of outlet Mach numbers from 0.21 to 0.80. Since the tunnel cannot control Mach number and Reynolds number independently, the corresponding Reynolds number varied from 1.8×10^5 to 9.0×10^5. Broad incidence ranges (from −45 to 30 deg for designs A and C and from −60 to 35 deg for design B) were tested for each outlet Mach number.

Inlet total pressure was measured one axial chord upstream of the cascade in the spanwise center of the middle passage using a total pressure probe. The facility operated with an inlet total pressure range of $0.97–1.81 \times 10^5$ Pa in the current experiment. Inlet flow angle was checked by traversing a three-hole angle probe 100% axial chord upstream of the cascade for selected Mach numbers and incidence angles. It was found the inlet flow was parallel

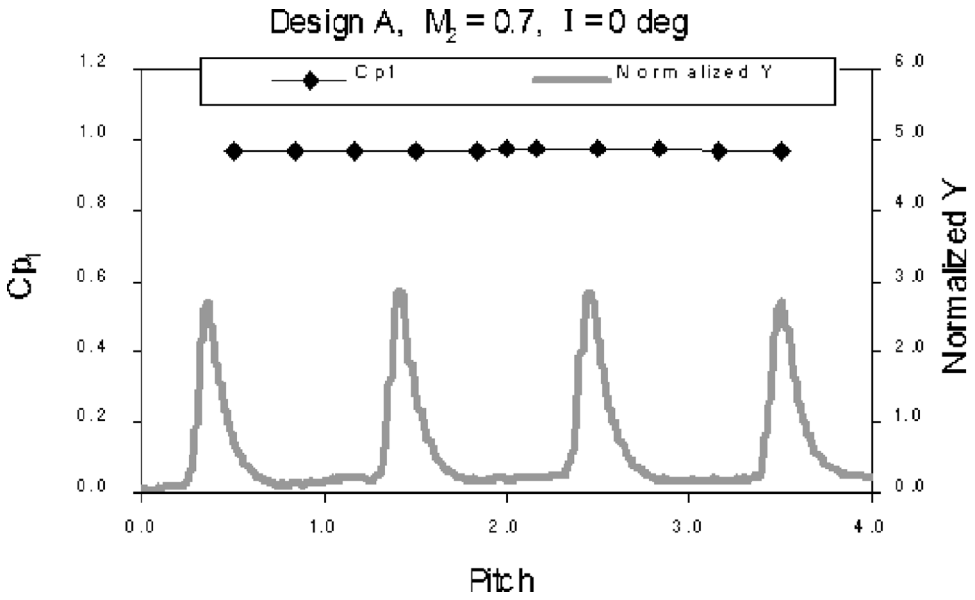

Fig. 8 Pitchwise flow uniformity and periodicity

to the top and bottom walls of the test section to within 0.5 deg deviation. Thirteen sidewall pressure taps were aligned in the pitchwise direction 100% axial chord upstream of the cascade, covering the middle three passages. The static pressures measured by these taps were used to monitor the inlet flow uniformity. The static pressures taken in the middle passage were averaged and used along with the measured total pressure to determine the inlet Mach number. At the cascade outlet, a three-hole angle probe was traversed 42% of the axial chord downstream of the blade trailing edge to measure outlet total pressure, Mach number, and flow angle. The traverse range covered the middle three passages providing good monitoring of the outlet flow periodicity. Overall aerodynamic parameters at the outlet were averaged for one pitch. This pitch was chosen such that the wake profile of the middle blade was completely included. The two blades that composed the middle passage were instrumented on the pressure surface and suction surface respectively for blade surface pressure measurement. Blade surface oil flow visualization was performed on the middle four blades for selected test cases to help understanding the flow.

Throughout the experiments, uncertainty was introduced from different sources including instrumentation, flow aperiodicity, and tunnel unsteadiness (although the latter two were relatively small). The overall uncertainty for the major measured flow quantities was estimated to have the following range: Mach number within ±5%, loss coefficient within ±5%.

Results Discussion

Flow Uniformity and Periodicity. In cascade testing, pitchwise flow uniformity/periodicity is an important requirement. Both inlet and outlet aerodynamic measurements in the current experiments showed good inlet flow uniformity and outlet flow periodicity. A representative example of the experimental results is shown in Fig. 8. The inlet flow uniformity is represented by inlet static pressure coefficient Cp_1 (normalized by the inlet total pressure). The outlet flow periodicity is represented by wake profile (quantified by local loss coefficient, normalized Y).

In 2D linear cascade testing, another important concern is the spanwise flow uniformity (3D effect from the sidewall). In turbine cascade testing, previous experience has shown that solid sidewalls are adequate, particularly for high aspect ratio cascades such as the ones used in this study. Sieverding [20] recommended minimum aspect ratios to obtain reliable 2D midspan performance data in turbine cascade tests from 1.6 to 2.2 based on different velocity ratios across the cascade. In the current tests aspect ratios greater than 3.8 were used ensuring good spanwise flow uniformity. Confirmation of the spanwise flow uniformity is provided by blade surface oil flow visualization. One example is shown in Fig. 9. The picture was taken after the tunnel run and the flow was visualized through the oil pattern left on the blade surface. In addition to showing good spanwise flow uniformity, pitchwise periodic flow was also indicated by blade surface flow visualization (see Fig. 9 for good repeatability of the oil pattern from blade to blade).

Profile Losses. The profile losses of the three cascades were tested at incidence angles of −45, −30, 0, 15, and 30 deg. At each incidence, four Mach numbers ranging from 0.21 to 0.8 were tested. The overall aerodynamic parameters for the outlet flow were averaged from the measured pitchwise local quantities using a mixing algorithm. The algorithm calculated a mixing process with the conservation of mass and momentum, through which the cascade outlet flow turned to a uniform flow. The obtained uniform total and static pressure ($P_{t_{2m}}$ and $P_{s_{2m}}$) were then used to calculate the loss coefficient Y_m.

Figure 10 shows the experimental results of the loss development with outlet Mach number at three representative incidence angles: −45, 0, and 30 deg, respectively. The corresponding variation of Reynolds number with M_2 is also plotted in the chart. As

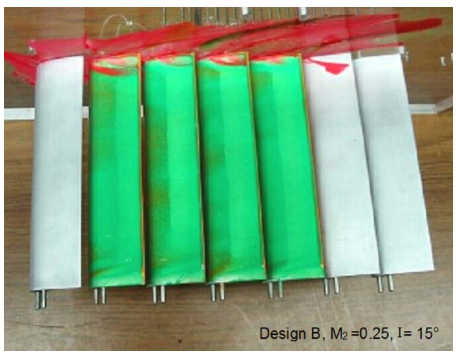

Fig. 9 Flow uniformity and periodicity confirmed by blade surface flow visualization (S.S.)

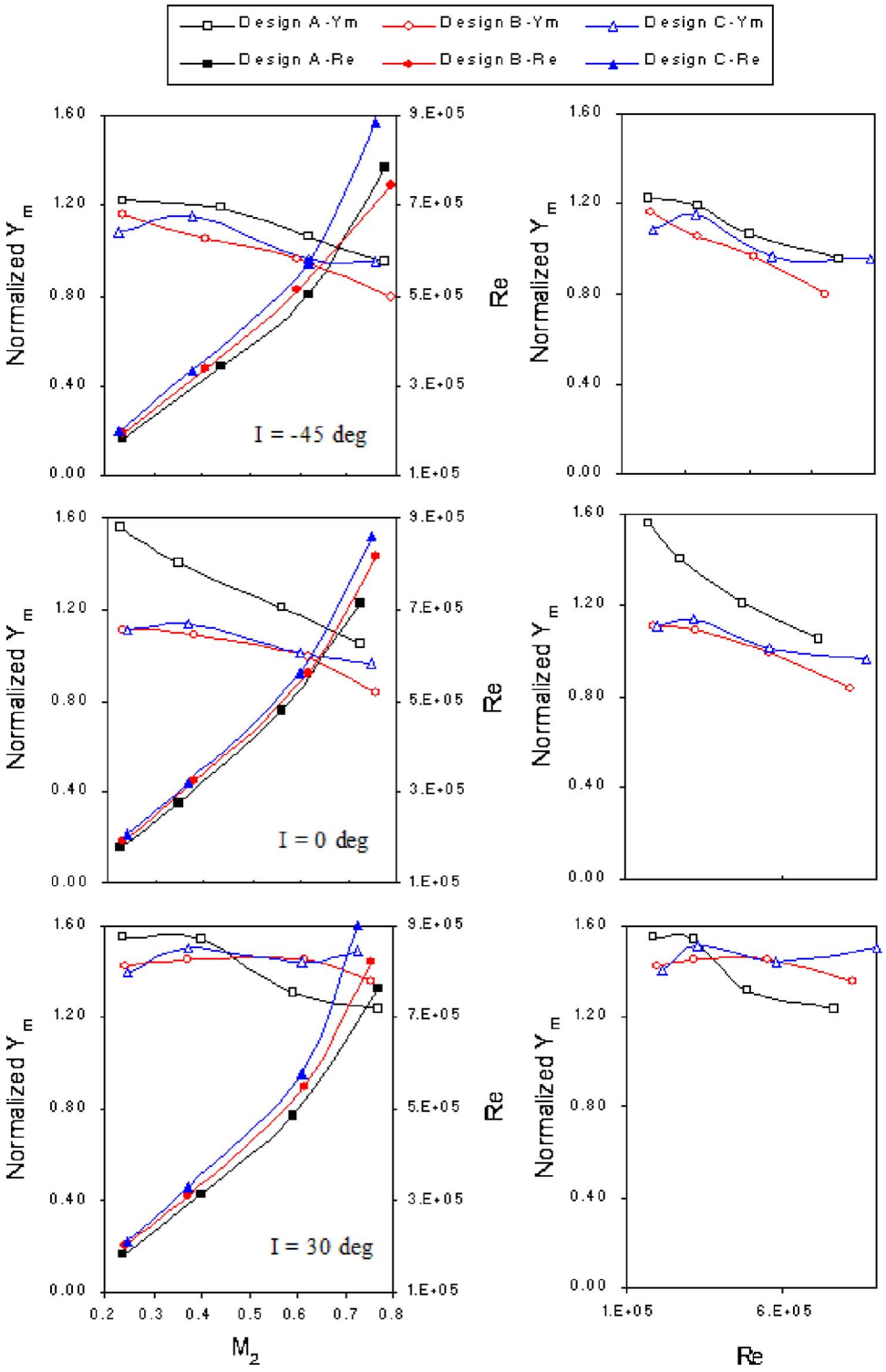

Fig. 10 Experimental loss development with M_2 and Re

shown in the figure, Reynolds number increased monotonically with increasing M_2. To better view the loss development with Reynolds number, the same experimental data of each incidence case was plotted on the right side as loss versus Reynolds number. The Reynolds number effect on the losses can also be viewed from the predicted trends (see Fig. 4).

Because the tunnel facility did not allow independent control of Mach number and Reynolds number, the loss development with M_2 seen in Fig. 10 includes the effect of Reynolds number. Probably driven primarily by Reynolds number, the losses decrease with increasing M_2 for most of the test conditions, except for designs B and C at the incidence of 30 deg. The effect of Reynolds number on turbine cascade losses, independent of Mach number, was studied by Corriveau and Sjolander [13]. Their findings supported the loss-versus-Re trend presented here. Despite the combined effects of M_2 and Re, the losses of the three cascades can be effectively evaluated by back-to-back comparison

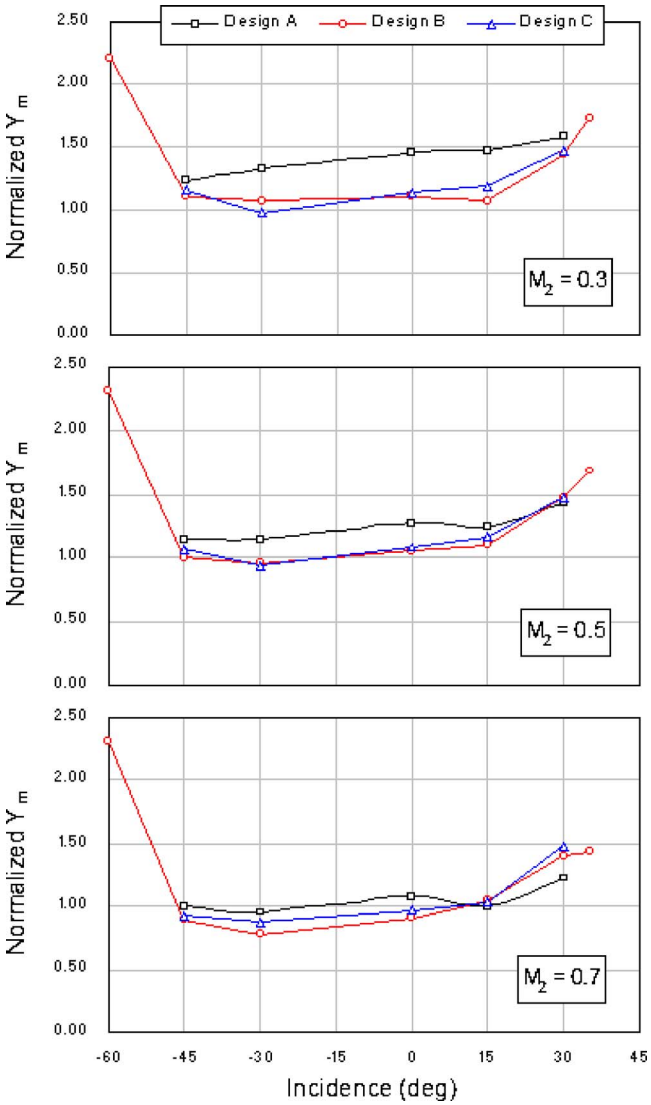

Fig. 11 Experimental loss variation with incidence

since for the same I and M_2, their Re values are very close. It is seen that designs B and C have lower losses than design A for most of the tested conditions, including the design incidence of 0 deg with the exception of high M_2 at the off-design incidence of 30 deg. The trend of loss drop with increasing M_2 and Re was also published by Jouini et al. [21] in the same M_2 range, although their cascades were designed at a supersonic exit Mach number.

Considering that no drastic increase in loss was found for the tested extreme negative and positive off-design incidences (−45 and 30 deg), further tests were carried out for design B at incidences of −60 and 35 deg in an attempt to better define the loss bucket. Again, four Mach numbers were tested for each of these two incidences. To better view the loss variation with incidence, all the tested loss data were interpolated at the same M_2 and plotted as loss versus incidence, as shown in Fig. 11. A third-order polynomial was chosen for the interpolation and the obtained trend lines fit the data well. Three charts are presented in Fig. 11, which correspond to low, intermediate, and high M_2. It is seen that all three cascades have a very large low-loss incidence range of 60 deg (from −45 to 15 deg), i.e., excellent incidence robustness. When increasing incidence from 15 to 35 deg, the losses increase modestly; decreasing incidence from −45 to −60 deg causes the losses to rise dramatically.

The experimental results as shown in Figs. 10 and 11 clearly

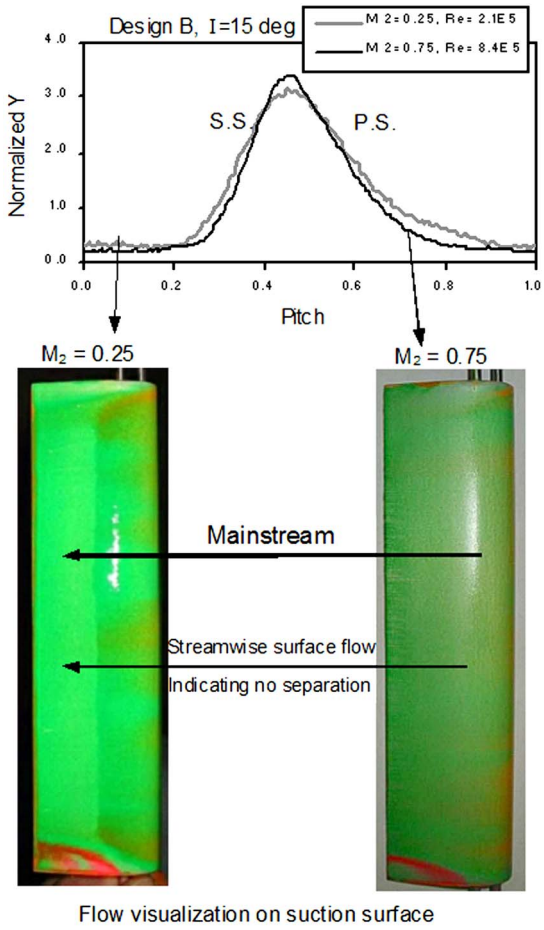

Fig. 12 Experimental wake profile and surface flow at different M_2 for design B

exhibit the superiority of designs B and C to design A. For the wide low-loss incidence range (−45 to 15 deg), approximately 20% loss reduction has been obtained. At the design incidence and low M_2, even more loss reduction has been achieved. Only at the off-design conditions, with incidence greater than 15 deg and M_2=0.7, are designs B and C inferior to design A. Therefore, the cascade tests have demonstrated the success of the cascade design/optimization, i.e., the pitch is enlarged while the losses are reduced. It is seen that the gain is for broad flow conditions. Based on design A, the pitch is increased by 1.25 times for design B and increased by 1.5 times for design C. The further increase in pitch from design B to design C hardly degrades the performance. This result provides experimental confirmation, based on 2D midspan losses, that design B is a robust design for the application.

Loss Mechanisms. As the cascade of most interest for future application, the loss mechanisms of design B are investigated, and compared with design A. For the incidence range from −45 to 15 deg, the losses of the two cascades remain low and have insignificant variation. Examination of the shape and size of the wake profiles for these conditions suggests no sign of boundary layer separation. In addition, even for a low Mach number that corresponds to a larger wake size and higher losses, blade surface oil flow visualization had confirmed no boundary layer separation on the suction and pressure surfaces. Therefore, the loss variation with M_2 of the two cascades and the loss reduction from design A to design B are due to differences in unseparated boundary layer thickness and subsequently different size of the wakes.

Experimental evidence to support the above discussion is shown in Fig. 12, including the wake profiles and blade surface

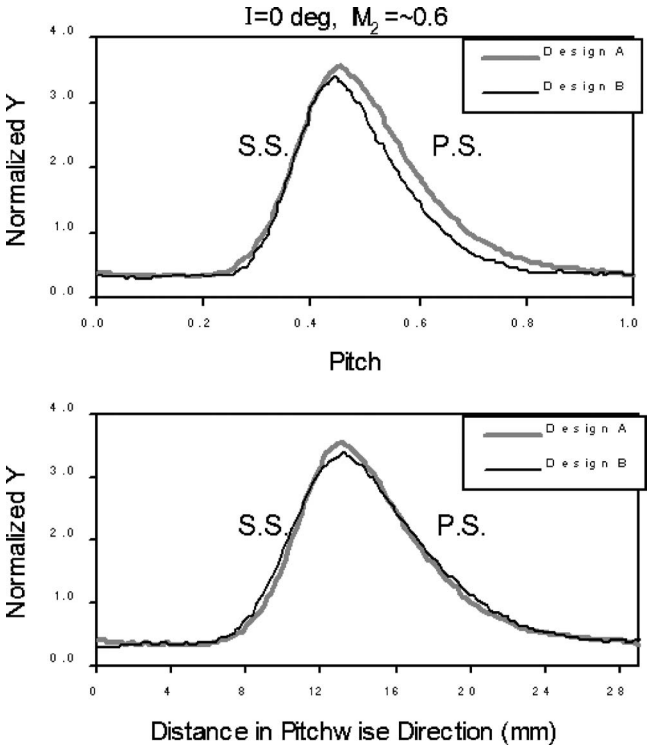

Fig. 13 Experimental wake profile comparison between design A and design B

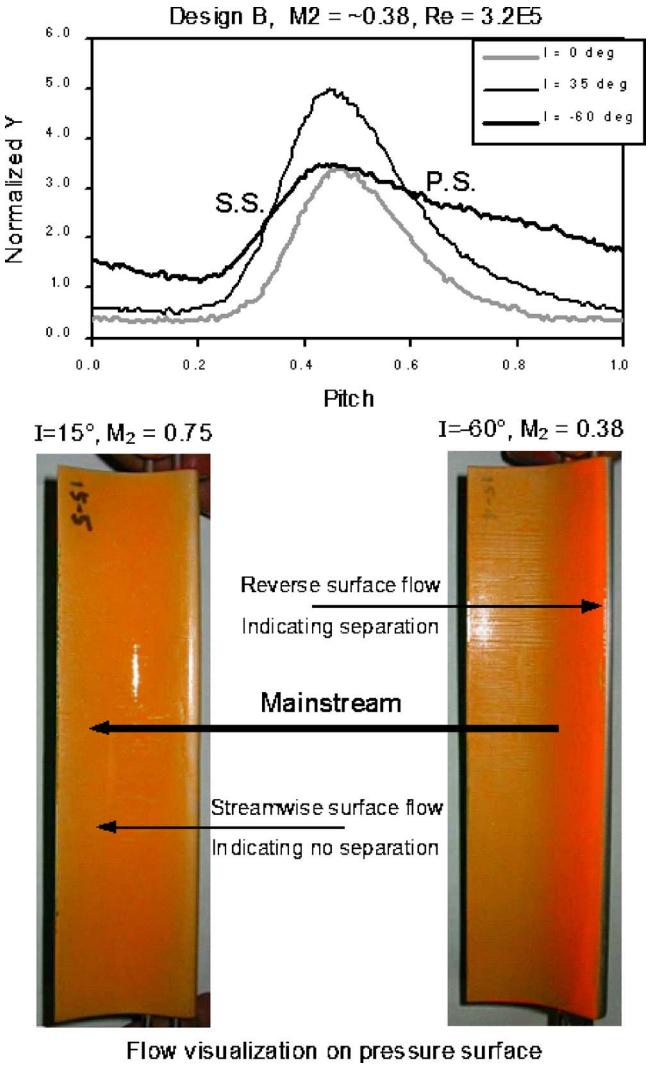

Fig. 14 Experimental wake profile and surface flow at different incidence for deign B

flow visualizations of design B at $I=15$ deg at two different M_2. It is seen that at the high M_2 of 0.75 (corresponding to a high Re of 8.4×10^5), the width of the wake is slightly smaller than that of the low M_2 of 0.25, leading to the lower losses for $M_2=0.75$. The flow visualizations at these two conditions confirmed no boundary layer separation on both S.S. and P.S. of the blade. Only S.S. flow visualization is shown here. Moreover, it is observed that there are different oil patterns on the S.S. for the two M_2. At $M_2=0.25$, more oil was left on front half chord and there was a sharp change near 50% chord, right after which more oil was removed. At $M_2=0.75$, much thinner oil was left on the surface, due to higher flow speed and the oil distribution along the entire chord was very uniform. These oil pictures may suggest different characteristics of the boundary layer development for the two M_2, which caused the difference in the wake size and loss level. Although it cannot be concluded by oil pictures alone, speculations can be reasonably made considering the effects of Reynolds number: At $M_2=0.25$ ($Re=2.1\times10^5$), transition probably occurred around 50% chord, and the boundary layer developed with relatively larger thickness than that of $M_2=0.75$, at which a fully turbulent boundary layer swept across the entire chord. Clarification of this issue relies on further study of the boundary layer characteristics in the future.

The mechanism for the loss reduction from design A to design B at the lowloss incidence range from −45 to 15 deg is presented below. As already mentioned, no boundary layer separation was present for either design over this incidence range. The back-to-back comparison for the two cascades is at the same condition (I, M_2 and Re), meaning they should have similar boundary layer development characteristics according to the above analysis. Blade surface flow visualization did show similar surface flow patterns for the two cascades. Then why does design B have 15–30% lower losses than design A? The answer has been determined by scrutinizing their wake profiles. Figure 13 gives one example at the design incidence and M_2 of about 0.6. The top plot in the figure compares the wake profiles of the two cascades plotted against the normalized pitch for one blade passage of each cascade. Apparently, the narrower wake of design B accounts for its lower losses. But this is not due to the thinner boundary layer of design B but due to the larger pitch of design B. Thus, when integrating the traverse data for one pitch, the wake of design B contributes less percentage in one entire pitch. Replotting the wake profiles of the two cascades against the absolute length of one pitch of design A (29 mm), as shown in the lower part of Fig. 13, the two wakes overlapped completely, indicating the physical sizes of wakes A and B are the same. It should be emphasized that the solidity influence on losses elucidated herein could by no means be taken as the sole reason for the loss reduction. Only increasing the pitch for a cascade with the same blade profile would not necessarily lead to loss reduction. The explanation of the loss reduction mechanism is as follows. As a new optimized cascade, design B differs from design A in terms of not only the decreased solidity, but also the blade profile. The boundary layer development characteristic due to the new cascade blade geometry is similar to that of the base line, so are the physical boundary layer thickness and wake size. When integrated over one pitch, lower overall losses are obtained on design B due to the fact that the wake of design B occupies less percentage of the entire pitch.

The rapid increase in losses at the very high incidences of −60 and 35 deg, as seen in Fig. 11, is typical in cascade tests. Figure 14 shows the wake profile comparison for design B at M_2 of about 0.38 for three incidences, 0, 35, and −60 deg. The wake sizes for

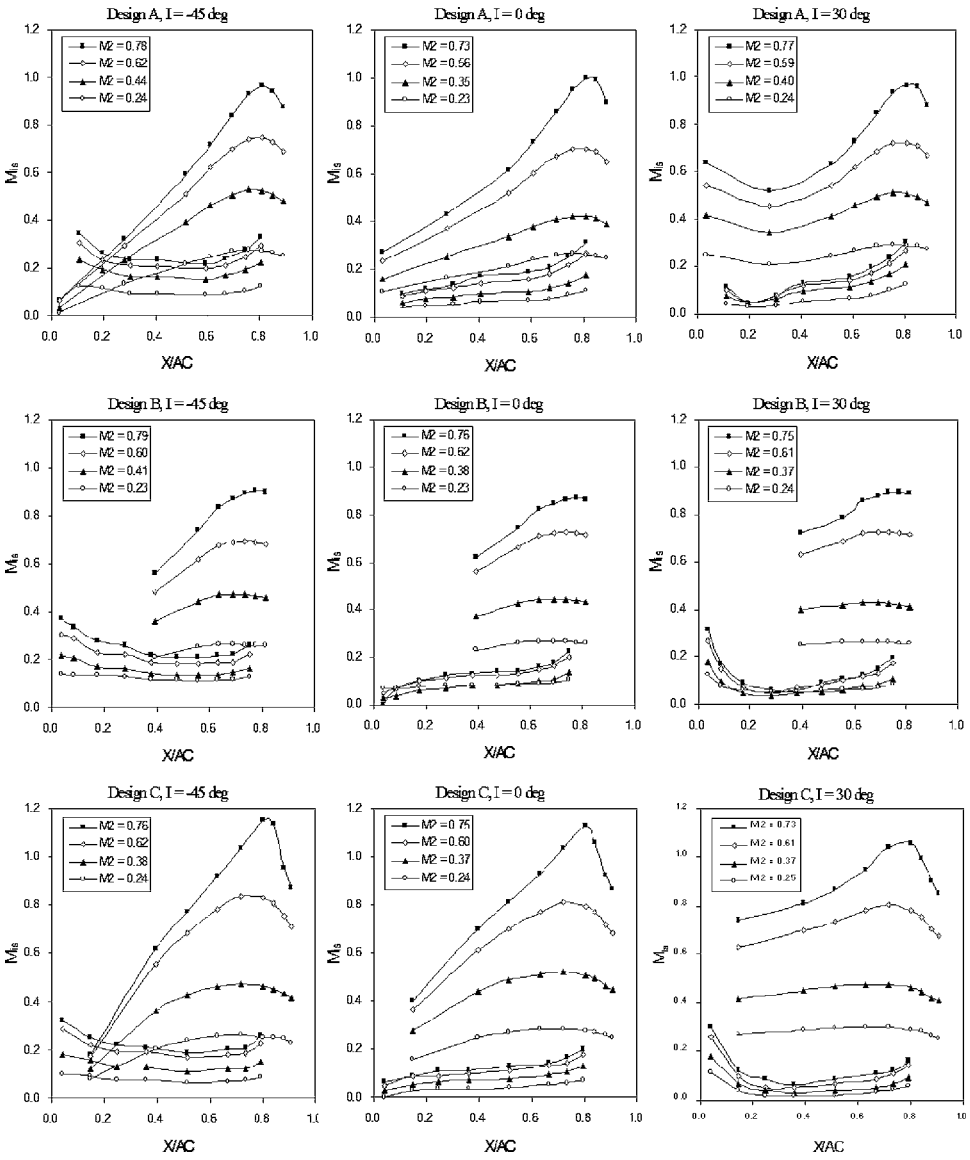

Fig. 15 Experimental blade surface isentropic Mach number

35 and −60 deg are much larger than that of 0 deg, which accounts for much higher losses. The wake shape of 35 deg is similar to that of 0 deg, only with the size enlarged, an indication of the thickening or possible separation of the boundary layer on the S.S. The case of −60 deg gives a quite different wake profile with losses raised for the entire pitch, particularly on the P.S., indicating flow separation there. This is also confirmed by blade surface oil flow visualization. Two pictures of the oil flow visualization on the pressure surface are given in Fig. 14. The right one shows an accumulation of the oil at the blade front part, caused by the reverse surface flow. The reverse surface flow was observed during the tunnel run. For comparison, the left picture shows an example of the streamwise surface flow with no boundary layer separation. In this case, the oil was simply carried away in the streamwise direction, leaving a relatively uniform oil pattern on the blade surface after the tunnel run.

Blade Surface Mach Number. As summarized in Fig. 15, experimental results of blade surface pressure provide another perspective to investigate the flow and compare the cascade performance. The values shown are blade surface isentropic Mach numbers, calculated using the blade surface static pressures and the cascade inlet total pressures. All the data points correspond to the same conditions of those in Fig. 10. The variation of flow and blade loading with outlet Mach number and incidence, as well as the comparison between the three cascades are illustrated in Fig. 15. The lack of data near the leading edge and trailing edge, particularly the front part of design B on the S.S. was unfortunately due to instrumentation constraints.

The data show the trends one would expect. Positive incidence loads up the front end and negative incidence unloads it. Higher Mach numbers load up the entire chord and shift more load aft. The flow is well behaved and there are no indications of separation over the incidence range covered in Fig. 15. The design philosophy of moving some load forward to control diffusion on the suction side downstream of the throat is evident in the lower solidity designs. As intended the distributions are still more aft loaded than uniformly loaded

Designs A and B approach sonic Mach numbers locally on the S.S. at the throat at an exit Mach number of about 0.75. Design C actually goes locally supersonic under similar conditions due to the higher loading from decreased solidity and due to the higher unguided turning. At exit Mach numbers of 0.6 all blades are comfortably subsonic.

Inspection of the Mach number distributions of Fig. 15 indi-

cates that the quality of the flow for design B is good. Further it can be seen that the quality of the flow at the lower solidity of design C indicates that design B has some margin with respect to decreased solidity. It is therefore a robust choice to pick for future applications.

Conclusion

Extensive cascade tests were carried out to determine the performance of three steam turbine nozzle cascades. The three cascades are designed for the same inlet and exit vector diagrams. They have the same axial chord, but the solidity is varied from 1.22 to 0.93. For all three cascades, experimental results have shown a wide lowloss incidence range from −45 to 15 deg at the tested outlet Mach numbers ranging from 0.2 to 0.8. At these broad conditions, the boundary layer is well controlled without separation such that the losses are low. Most importantly, a 15–30% profile loss reduction has been obtained while reducing the solidity on the new cascades. The larger improvements are at the lower Mach numbers. As the best candidate cascade for application, design B was tested at two more off-design incidences (−60 and 35 deg) to more fully document the loss bucket.

Wake profile comparison and blade surface flow visualization are successfully used in conjunction to help understand the flow and the loss reduction mechanism. It is confirmed that design B has the same boundary layer characteristics as the baseline. The wakes of designs A and B are the same size but since design B has a larger pitch and fewer blades and wakes for a given application the overall losses are lower.

Cascade design optimization led to more tangential stagger and higher unguided turning for the lower solidity cascades. The loading on the lower solidity cascades was brought forward somewhat to control the suction surface diffusion downstream of the throat to avoid separation and high losses. This strategy has proved effective in developing low loss cascades at low solidities. The low solidities allow a reduction in parts count for reduced cost at a high level of efficiency.

It is also of interest to point out that a design which is based on the use of a 2D Euler flow solver with boundary layer and loss calculations proved to be sufficient to give optimized blade shapes, as verified by the experiment.

Acknowledgment

This work was sponsored by GE Energy. Stephen Guillot and Troy Jones of Techsburg, Inc. provided significant support for the experimental work. Their help is gratefully acknowledged.

Nomenclature

AC = axial chord
AR = aspect ratio
C = true chord
C_p = pressure coefficient $= P_s / P_{t_1}$
H = blade span
I = incidence angle
M = Mach number
P.S. = pressure surface
P_s = static pressure
P_t = total pressure
Re = Reynolds number (based on true chord and outlet condition)
t = pitch
S.S. = suction surface
s = throat
Tu = free-stream turbulence intensity
X = distance in axial direction
Y = loss coefficient $= (P_{t_1} - P_{t_2}) / (P_{t_1} - P_{s_2})$
Y_m = mix-out loss coefficient $= (P_{t_1} - P_{t_{2m}}) / (P_{t_1} - P_{s_{2m}})$
γ = stagger angle
σ = solidity, $\sigma = C/t$

Subscripts

1 = cascade inlet
2 = cascade inlet
m = mix-out
is = isentropic

References

[1] Cobley, K., Coleman, N., Siden, G., and Arndt, N., 1997, "Design of New Three Stage Low Pressure Turbine for the BMW Rolls-Royce BR715 Turbofan Engine," ASME Paper No. 97-GT-419.
[2] Curtis, E. M., Hodson, H. P., Banieghbal, M. R., Denton, J. D., and Howell, R. J., 1996, "Development of Blade Profiles for Low Pressure Turbine Application," ASME Paper No. 96-GT-358.
[3] Tsujita, H., Mizuki, S., and Yamamoto, A., 2004, "Numerical Investigation of Blade Profile Effects on Aerodynamic Performance of Ultra-Highly Loaded Turbine Cascades," ASME Paper No. GT2004–53429.
[4] Moustapha, S. H., Paron, G. J., and Wade, J. H.T., 1985, "Secondary Flow in Cascade of Highly Loaded Turbine Blades," ASME Paper No. 85-GT-135.
[5] Solomon, W. J., 2000, "Effects of Turbulence and Solidity on the Boundary Layer Development in a Low Pressure Turbine," ASME Paper No. 2000-GT-273.
[6] Solomon, W. J., 2002, "Performance Characteristics of a Reduced Solidity Low Pressure Turbine," ICAS 2002 Congress, pp. 5112.1–5112.10.
[7] Howell, R. J., Ramesh, O. N., Hodson, H. P., Harvey, N. W., and Schulte, V., 2000, "High Lift and Aft Loaded Profiles for Low Pressure Turbines," ASME Paper No. 2000-GT-261.
[8] Haselbach, F., Schiffer, H., Horsman, M., Dressen, S., Harvey, N., and Read, S., 2002, "The Application of Ultra High Lift Blading in the BR715 LP Turbine," ASME J. Turbomach., **124**, pp. 45–51.
[9] Howell, R. J., Hodson, H. P., Schulte, V., Stieger, R. D., Schiffer, H., Haselbach, F., and Harvey, N. W., 2002, "Boundary Layer Development in the BR710 and BR715 LP Turbines—The Implementation of High-Lift and Ultra-High-Lift Concepts," ASME J. Turbomach., **124**, pp. 385–392.
[10] Hodson, H. P., and Howell, R. J., 2001, "High Lift Low Pressure Turbines," NASA/CP-2001-210888.
[11] Gonzalez, P., Ulizar, I., Vazquez, R., and Hodson, H. P., 2002, "Pressure and Suction Surfaces Redesign for High-Lift Low-Pressure Turbines," ASME J. Turbomach., **124**, pp. 161–166.
[12] Houtermans, R., Coton, T., and Arts, T., 2003, "Aerodynamic Performance of a Very High Lift LP Turbine Blade With Emphasis on Separation Prediction," ASME Paper No. GT2003-38802.
[13] Corriveau, D., and Sjolander, S. A., 2003, "Influence of Loading Distribution on The Performance of Transonic HP Turbine Blades," ASME Paper No. GT2003-38079.
[14] Patterson, D. J., and Hoeger, M., 1986, "The Effect of Reynolds Number and Velocity Distribution on LP Turbine Cascade Performance," ASME Paper No. 86-GT-271.
[15] Hashimoto, K., and Kimura, T., 1984, "Preliminary Study on Forward Loaded Cascades Designed With Inverse Method for Low Pressure Turbine," ASME Paper No. 84-GT-65.
[16] Hoheisel, H., Kiock, R., Lichtfuss, H. J., and Fottner, L., 1987, "Influence of Free-Stream Turbulence and Blade Pressure Gradient on Boundary Layer and Loss Behavior of Turbine Cascades," ASME J. Turbomach., **109**, pp. 210–219.
[17] Boss, M., Hofer, D., Gazzillo, C., and Jacobs, J., 2002, "Advances in Combined-Cycle Steam Turbines," Power-Gen International 2002, Orlando, FL.
[18] Boss, M., 2003, "Steam Turbine Technology Heats Up," PEi Mag., April.
[19] Drela, M., and Youngren, H., 1996, *A User's Guide to MISES 2.4*, MIT Computational Aerospace Sciences Laboratory, Cambridge, MA.
[20] Sieverding, C. H., 1993, "Subsonic-Choked (Turbine) Cascades," Advanced Methods for Cascade Testing, AGARD-AG-328, p. 23.
[21] Jouini, D. B. M., Sjolander, S. A., and Moustapha, S. H., 2001, "Midspan Flow-Field Measurements for Two Transonic Linear Turbine Cascades at Off-Design Conditions," ASME Paper No. 2001-GT-0493.

Aeroelastic Stability of Welded-in-Pair Low Pressure Turbine Rotor Blades: A Comparative Study Using Linear Methods

Roque Corral[1]
e-mail: roque.corral@itp.es

Juan Manuel Gallardo

Carlos Vasco

Technology and Methods Department,
Industria de Turbopropulsores S.A.,
28830 Madrid, Spain

The aerodynamic damping of a modern low pressure turbine bladed-disk with interlock rotor blades is compared for the first time to that obtained when the rotor blades are welded in pairs through the lateral face of the shroud. The damping is computed solving the linearized Reynolds averaged Navier-Stokes equations on a moving grid. First the basics of the stabilizing mechanism of welding the rotor blades in pairs is investigated using two-dimensional analyses and the Panovsky and Kielb method. It is concluded that the stabilizing effect is due to the suppression of unsteady perturbations in one out of the two passages providing for the first time a physical explanation to engine data. Three-dimensional effects are then studied using the actual mode shapes of two bladed disks differing solely in the shroud boundary conditions. It is concluded that the increase in the aerodynamic damping, due to the modification of the mode shapes caused by welding the rotor blades in pairs, is smaller than that due to the overall raise of the reduced frequencies of a bladed disk with an interlock design. The modification of the flutter boundaries due to mistuning effects is assessed using the reduced order model known as the Fundamental Mistuning Model. A novel extension of the critical reduced frequency stability maps accounting for mistuning effects is derived and applied for both, the freestanding and welded-in-pair airfoils. The stabilizing effect of mistuning is clearly seen in these maps. Finally, the effect of mistuning on low-pressure-turbine bladed disks is studied. It is shown that the modification on the stability limit of the interlock bladed disk is negligible, while for the welded-in-pair configuration a 0.15% increase of the damping relative to the critical damping is found. This qualitative difference between both configurations had not been reported before. [DOI: 10.1115/1.2366512]

Introduction

Flutter has been a problem traditionally associated with compressor and fan blades. However, the steady trend during the last decades to design high-lift, highly loaded low pressure turbines (LPTs), with the final aim of reducing their cost and weight, while keeping the same efficiency, has led to a reduction of the blade and disk thicknesses and an increase of the blade aspect ratio. Both factors tend to lower the stiffness of the bladed-disk assembly and therefore its natural frequencies. The decrease of the maximum relative thickness of LPT midsections during the last two decades is depicted in Fig. 1.

As a result of the aforementioned evolution, vanes and rotor blades of the latter stages of modern LPTs of large commercial turbofan engines, which may be designed with aspect ratios of up to six, may potentially flutter and undergo alternate stresses similar to those encountered in fans and compressors.

Vibration control of shrouded LPT blades may be accomplished using either cantilever, interlock or welded-in-pairs rotor blades (see Fig. 2). Flat sided shrouds may vibrate freely even for very small clearances especially for low inter blade phase angles (IBPA) and provide little control over the vibration characteristics of the bladed disk. To remedy this deficiency z-shaped shrouds (interlocks) were designed with the aim of remaining tight during the whole flight envelope. This type of design significantly modifies the vibration characteristics of cantilever blades, however, the mode shapes of a given family may significantly vary with the nodal diameter and induce bending-torsion coupling. Finally, pairs of rotor blades welded in the tip shroud were devised as a practical alternative to control the vibration characteristics of LPT bladed disks and may be seen in some modern turbofan engines. This latter configuration substantially modifies as well the mode shapes and frequencies of the base line (cantilever) and interlock solutions.

It is well known that flutter boundaries are very sensitive to blade mode shapes and that the reduced frequency plays a secondary role. A comprehensive numerical study of the influence of both parameters for LPT airfoils was performed by Panovsky and Kielb [1] and supported by experimental work [2].

The beneficial effect of grouping the airfoils in packets was first demonstrated by Whitehead and Evans [3]. Kahl [4] studied the stability of a LPT sectored vane of three airfoils and later on Chernysheva et al. [5] extended the stability studies to packets of six vanes using the Panovsky and Kielb (PK) method.

However, in an actual machine rotor blades are never exactly identical because of manufacturing imperfections, which result in slightly different natural frequencies and phase shifts of the blades. There is numerical [6–8] and experimental [2] evidence that mistuning has a strong beneficial effect on self-excited vibra-

[1]Also Associate Professor at the Department of Engine Propulsion and Fluid Dynamics of the School of Aeronautics, UPM.

Contributed by the International Gas Turbine Institute (IGTI) of ASME for publication in the JOURNAL OF TURBOMACHINERY. Manuscript received October 1, 2003; final manuscript received March 1, 2004. IGTI Review Chair: A. J. Strazisar. Paper presented at the International Gas Turbine and Aeroengine Congress and Exhibition, Vienna, Austria, June 13–17, 2004, Paper No. 2004-GT-54119.

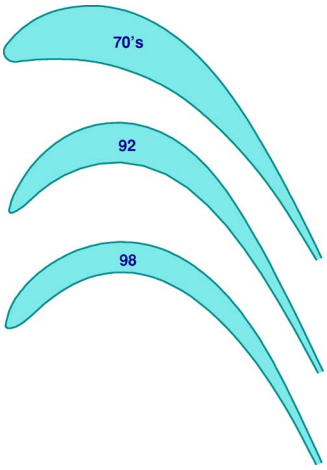

Fig. 1 Evolution of LPT mid-section airfoils during the last two decades

tions. However, the attempts to analyze [9] or devise design methods [10] retaining the effect of mistuning are scarce.

Flutter analyses are usually performed in the frequency domain making use of the hypothesis of linearity to dramatically reduce the computational cost of non-linear single-passage or whole annulus computations. Mistuned aerodynamic models make use of the hypothesis of linearity as well as precomputing the aerodynamic damping in traveling-wave form for a prescribed frequency, and deriving the damping of the mistuned case expanding the eigenmodes of the mistuned problem in traveling waves [11,10] which is several orders of magnitude less expensive than computing the whole mistuned wheel [9].

The use of welded-in-pair rotor blades in large civil turbofans dates back to the early 1990s. However, the rationale of its stabilizing effect has been poorly understood and has never been reported before. The aim of this work is to investigate, using numerical tools, the influence of pairing the rotor blades on the aerodynamic damping of a typical LPT bladed disk and compare the results with the equivalent, and more widespread, interlock configuration.

In this work, the analysis methodology is presented first. Then a typical airfoil is used to analyze the stabilizing effect of welding the airfoils in pairs from a two-dimensional point of view using simplified methods. A significant part of the article is focused on the analysis of realistic bladed disks with special emphasis in the comparison of the relative merits of interlock and welded-in-pair rotor blades. In this study we retained three-dimensional features both in the structural dynamics and aerodynamics, where viscous effects are also accounted for. Finally, the beneficial effect of mistuning on the stability is assessed, both for a standard two-dimensional airfoil and for realistic bladed disks. The use of the PK method in this part, retaining the effect of mistuning, is novel. The paper is closed deriving some final conclusions.

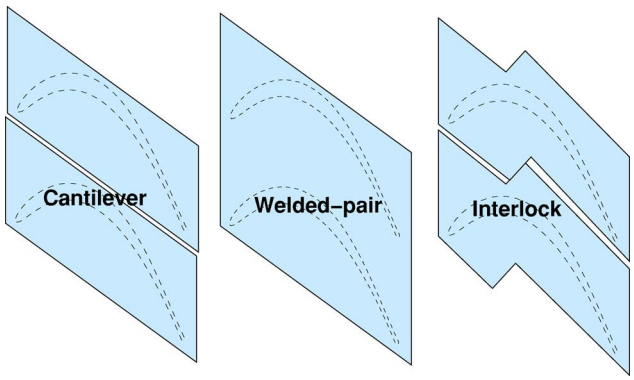

Fig. 2 Sketch of cantilever, welded-in-pair and interlock shrouds

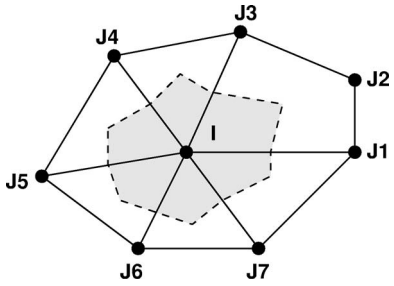

Fig. 3 Typical hybrid-cell grid and associated dual mesh

Numerical Formulation

Linearized Navier-Stokes Equations. The three-dimensional Navier-Stokes equations in conservative form for an arbitrary control volume may be written as:

$$\frac{d}{dt}\int_{\Omega}\mathbf{U}d\mathbf{\Omega}+\int_{\Sigma}(\mathbf{f}-\mathbf{U}v_x,\mathbf{g}-\mathbf{U}v_y,\mathbf{h}-\mathbf{U}v_z)\,.\,d\mathbf{A}=0 \qquad (1)$$

where $\mathbf{U}$ is the vector of conservative variables, $\mathbf{f}$, $\mathbf{g}$, and $\mathbf{h}$ the sum of the inviscid and viscous fluxes, Ω the flow domain, Σ its boundary, $d\mathbf{A}$ the differential area pointing outward to the boundary and v_x, v_y and v_z the three components of the boundary velocity. Now we may decompose the flow into two parts: a steady or mean background flow, plus a small but periodic unsteady perturbation, which in turn may be expressed as a Fourier series in time. If we retain just the first harmonic any variable may be expressed as:

$$\mathbf{U}(\mathbf{x},t)=\mathbf{U}_0(\mathbf{x})+\mathrm{Re}(\hat{\mathbf{u}}(\mathbf{x})e^{i\omega t}) \qquad (2)$$

where $\mathbf{U}_0$ represents the background flow and $\hat{\mathbf{u}}$ is the complex perturbation. The Navier-Stokes equations may then be linearized about the mean flow to obtain:

$$\left(\frac{d}{d\tau}+i\omega\right)\int_{\Omega}\hat{\mathbf{u}}d\Omega+\int_{\Sigma}\left(\frac{\partial\mathbf{f}}{\partial\mathbf{U}}\hat{\mathbf{u}},\frac{\partial\mathbf{g}}{\partial\mathbf{U}}\hat{\mathbf{u}},\frac{\partial\mathbf{h}}{\partial\mathbf{U}}\hat{\mathbf{u}}\right)\,.\,d\mathbf{A}+i\omega\int_{\Omega}\mathbf{U}_0d\mathbf{\Omega}'$$
$$+\int_{\sum}(\mathbf{f}_0,\mathbf{g}_0,\mathbf{h}_0)\,.\,d\mathbf{A}'=i\omega\int_{\Sigma}\mathbf{U}_0\mathbf{x}'\,.\,d\mathbf{A} \qquad (3)$$

which is a linear equation of complex coefficients and where the first term is an additional time derivative added to solve the equations marching in the pseudo-time τ.

Spatial Discretization. The code used here (Mu^2s^2T-L) solves the three-dimensional linearized Navier-Stokes equations in conservative form [12]. The spatial discretization is obtained linearizing the discretized equations of the non-linear version of the code Mu^2s^2T [13], from which the background solution is obtained. The spatial domain is discretized using hybrid unstructured grids that may contain cells with an arbitrary number of faces and the solution vector is stored at the vertexes of the cells. The code uses an edge-based data structure, a typical grid is discretized by connecting the median dual of the cells surrounding an internal node (Fig. 3). For the node i the semi-discrete form of Eq. (3) can be written as

$$\frac{d(\Omega_i \hat{\mathbf{u}}_i)}{d\tau} + \sum_{j=1}^{n_{\text{edges}}} \frac{1}{2} S_{ij}(\hat{\mathbf{F}}_i + \hat{\mathbf{F}}_j) - \hat{\mathbf{D}}_{ij} = \hat{\mathbf{S}}(\hat{\mathbf{u}}_i) \tag{4}$$

where S_{ij} is the area associated with the edge ij, and n_{edges} the number of edges that surround node j. The resulting numerical scheme is cell centered in the dual mesh and second-order accurate. It may be shown that for triangular grids the scheme is equivalent to a cell vertex finite volume scheme. A blend of second and fourth order artificial dissipation terms, $\hat{\mathbf{D}}_{ij}$, is added to capture shock waves and prevent the appearance of high frequency modes in smooth flow regions, respectively. The second-order terms are activated in the vicinity of shock waves by means of a pressure-based sensor and locally the scheme reverts to first order in these regions. The artificial dissipation terms can be written as

$$\hat{\mathbf{D}}_{ij} = |A_{ij}| S_{ij} [\mu_{ij}^{(2)}(\hat{\mathbf{u}}_j - \hat{\mathbf{u}}_i) - \mu_{ij}^{(4)}(L_j - L_i)] \tag{5}$$

where $\mu_{ij}^{(2)}$ and $\mu_{ij}^{(4)}$ are the average of the artificial viscosity coefficients in the nodes i and j. $|A_{ij}|$ is a 5×5 matrix that plays the role of a scaling factor. If $|A_{ij}| = (|u| + c)_{ij} I$, where I is the identity matrix, the standard scalar formulation of the numerical dissipation terms [14] is recovered. When $|A_{ij}|$ is chosen as the Roe matrix [15] the matricial form of the artificial viscosity [16] is obtained. The scalar version of the numerical diffusion terms has been used in this work since the difference between both approaches is negligible for the Mach numbers of interest [17] and is more robust.

The viscous fluxes can be evaluated in a number of ways. The gradients of the flow variables are approximated at the nodes using the divergence theorem in the same way that the convective fluxes are computed. Then an approximation of the gradients at the midpoint of the edge is obtained by a simple average,

$$\overline{\nabla U}_{ij} = \frac{1}{2}(\nabla U_i + \nabla U_j) \tag{6}$$

The Baldwin-Lomax turbulence model [18] has been used for the steady flow computations and the turbulence viscosity has been frozen in the linear version of the code.

Temporal Discretization. Equation (4) can be expressed in compact form as

$$\frac{d(\Omega_i \hat{\mathbf{u}}_i)}{d\tau} = \mathbf{R}(\hat{\mathbf{u}}) = \mathbf{C}(\hat{\mathbf{u}}) + \mathbf{H}(\hat{\mathbf{u}}) + \mathbf{S}(\hat{\mathbf{u}}) \tag{7}$$

where the residual can be split in the convective, **C**, the numerical diffusion and viscous, **H**, parts and a source term **S**. The integration in time is performed using an explicit five stage Runge-Kutta scheme, where the artificial viscosity terms are evaluated only in three stages of the Runge-Kutta.

The scheme is second-order accurate in time. Implicit residual smoothing and full coarsening multigrid may be used to increase the stability limit of the scheme and speed up its convergence. A more detailed description of the numerical scheme and details of the validation process may be found in [12].

Boundary Conditions. The exact, 2D, unsteady, non-reflecting boundary conditions [19] have been used at the inlet and outlet in a plane by plane basis. At the solid walls half volumes associated with the wall nodes are used to march in pseudo time. For inviscid simulations the unsteady fluxes are imposed at the boundaries while for viscous cases the velocity is imposed at the boundary nodes. The code uses phase-shifted boundary conditions in the periodic boundaries to simulate annular cascades of airfoils vibrating sinusoidally with a common angular frequency, ω, and common IBPA.

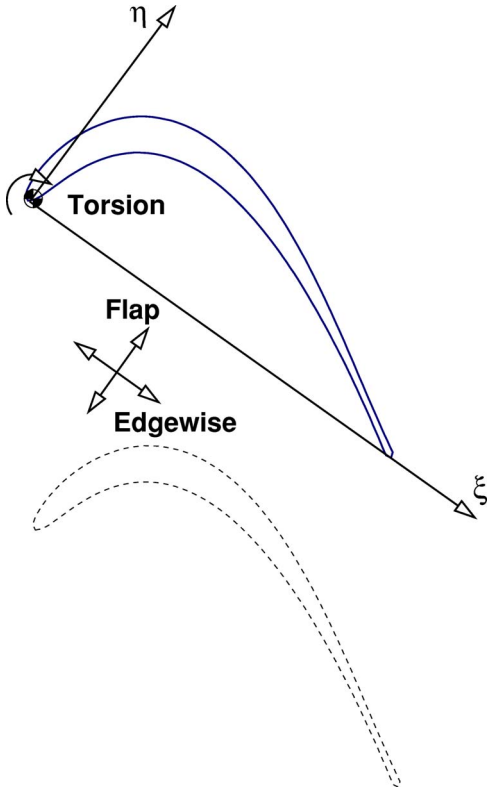

Fig. 4 Definition of fundamental mode shapes

Two-Dimensional Analysis Methodology

Description of the Method. Using flutter stability maps, Panovsky and Kielb [1] showed that the mode shape and the reduced frequency are the basic parameters that control the stability of a two-dimensional LPT section. Since one of the aims of this work was to understand the stability of welded-in-pair rotor blades, including the influence of the torsion center and reduced frequency, it was decided to adopt this simplified approach.

Following the PK approach only the unsteady pressure fields associated with two orthogonal bending directions and the torsion about a given point, P, for a reference displacement need to be computed for each IBPA (see Fig. 4). The unsteady pressure associated with the motion of the airfoil as a rigid body about an arbitrary torsion axis, O, is computed as a linear combination of the three reference solutions.

The main differences of the present method with the original approach are the systematic use of viscous simulations and the extension of the analyses to pairs of airfoils moving as a rigid body. However, instead of using an influence coefficient technique to simulate the sector as in [5], we have included pairs of airfoils vibrating as a rigid body to emulate the dynamic behavior of rotor blades welded in pairs.

Underlying Hypothesis. Although the details of the method are well known and may be found in [1], the main hypotheses of the approach are revisited here to check its validity for the present study:

1. The superposition principle holds. This is not usually a problem for LPTs with subsonic flows and small vibration amplitudes.
2. The airfoil moves as a rigid body. For elongated, high aspect ratio LPT airfoils, with a similar stiffness along the chord and without constraints at the tip, it is unusual to have local modes. Figure 5 shows the first bending (left) and first torsion (right) mode shapes of a welded-pair bladed disk on the

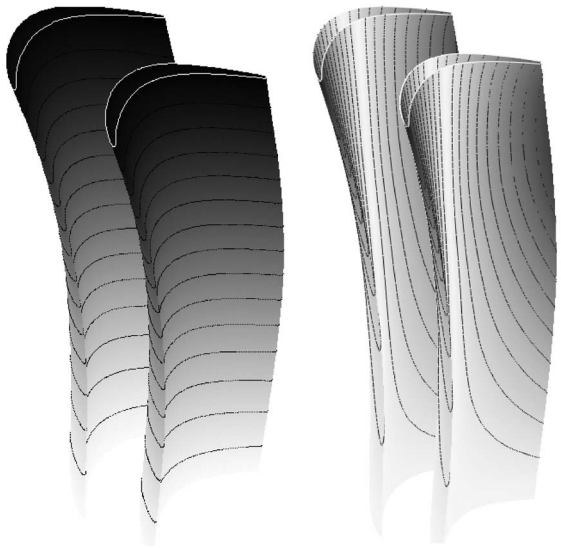

Fig. 5 Mode shapes of a welded-pair configuration. Left: flap mode. Right: 1st torsion mode.

airfoil, obtained from a bladed-disk finite element method (FEM). It may be seen that the modes are quite two-dimensional for the bending mode where the iso-displacement contours are parallel among them. The torsion mode is also quite two-dimensional except at the blade root. It may be observed in Fig. 5 that the iso-displacement contours of both blades are quite similar indicating that they, in first approximation, move as a rigid body and may be readily simulated using the PK method.

3. All the points of a given section move in phase, or in other words, the airfoil motion along a whole cycle may be described as a rotation about a fixed given point. This is sometimes referred to as a real mode. Figure 6 displays the phase of the bending (left) and torsion (right) modes at the mid-section of a welded-in-pair rotor blade. It may be seen that the differences in phase are negligible for both, the nodes located in the suction and pressure side of the same airfoil, and the two airfoils of the pair. The torsion modes exhibit a transition in phase between 0 and π indicating that both ends move in the opposite direction. The transition is smoothed out by the structural grid that is much coarser than the aerodynamic one.

The structural modes of a tuned bladed disk are traveling waves with constant IBPA. This means that the periodic boundaries of a fundamental sector need to impose a constant phase shift. On the cantilever and welded-pair configurations, the nodes with a given phase shift correspond to the disk and the contribution to the mode shape in the airfoil region is negligible. This is due to the very small displacements at the blade root. However, the situation

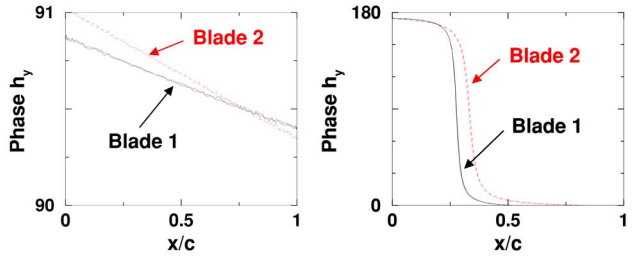

Fig. 6 Phase of the flap (left) and 1st torsion (right) mode-shapes at the mid-section

is different for interlocks where the structural coupling between fundamental sectors through phase-shifted (cyclic symmetry in structural FEM terminology) boundary conditions occurs at the region of the largest mode displacements, inducing significant phase variations in the airfoil.

Tuned Flutter Stability Maps

The fundamental mode shapes used in this work are described in Fig. 4. The edgewise and flap modes are defined as bending modes along and perpendicular to the chord. The center of torsion of the third fundamental mode is located at the l.e. of the airfoil. When pairs of blades are considered, the pair is formed by adding a new airfoil (dashed line in Fig. 4) adjacent to the pressure side of the reference airfoil and the center of torsion of the fundamental node is kept at the l.e. of the reference section. The airfoil used in all the simulations corresponds to the midsection of a representative rotor blade ($\alpha_{\text{inlet}}=37$ deg, $\alpha_{\text{exit}}=64$ deg, $M_{is}=0.76$, Re $=2.5\times10^5$). Modern LPTs may have large separation bubbles on the pressure side (p.s.) of the airfoils that may not be accounted for using inviscid simulations. They induce phase shifts in the p.s. of the airfoil whose relative importance depends on the case. Usually, the contribution to the work per cycle of the airfoil pressure side is smaller than that of the suction side. However, to avoid any further problems, all the simulations performed in the present study have retained viscous effects since its extra cost compared to that of the inviscid simulations is affordable. Pressure side bubbles are not difficult to capture in this type of airfoil, provided that the mesh resolution is high enough, because the reattachment is a nearly geometric effect and the sensitivity of the bubble size to the type of turbulence model is small.

The damping coefficient or non-dimensional work-per-cycle is defined as:

$$\Theta = \frac{W}{\pi\rho_e U_e^2 d_{\max}^2 H}$$

where W is the work per cycle over the airfoil, ρ_e and U_e are, respectively, the density and velocity at the cascade inlet, $d_{\max}$ is the maximum airfoil displacement in the reference cases, and H is the cascade span.

Figure 7 shows the damping coefficient as a function of the IBPA for the different fundamental modes previously described. In general the IBPA is defined as $\sigma=2\pi(m-1)/N_S$ where $m=1\ldots N_s$ and N_s is the number of fundamental sectors. For a free-standing airfoil the number of sectors coincides with the number of blades, and hence $N_s=N$, while for welded-pair rotor blades the number of sectors is half that of the rotor blades and hence $N_s=N/2$. It must be understood, therefore, that for a welded-pair rotor the IBPA represents the phase between each pair of blades, which constitute the basic sector of the bladed disk. The damping coefficient in the welded-pair case is defined in a per blade basis. The stabilizing effect of the reduced frequency can be seen for both, the single and welded-pair configurations. The most unstable modes of the freestanding configuration are the flap and torsion modes. The instability of the torsion mode is, however, stronger than that of the flap mode. The stabilizing effect of the welded-pair configuration may be clearly seen at the bottom of the same figure. In this case, all the fundamental modes are stable for $k\simeq0.3$. The torsion mode is highly stabilized for the welded-pair configuration and is neutrally stable for $k\simeq0.2$. The flap mode becomes the most critical one.

It may be appreciated that the damping coefficient curves of the edgewise and flap modes have a sinusoidal form specially for low reduced frequencies ($k=0.1$) while for high reduced frequencies ($k=0.4$) two spikes, corresponding to resonant conditions, are superimposed to the sine-like shape. This behavior is expected since the relative influence of the adjacent blades with respect to the reference decreases when the reduced frequency is increased (see [20], for example). The deviations from the sinusoidal are larger

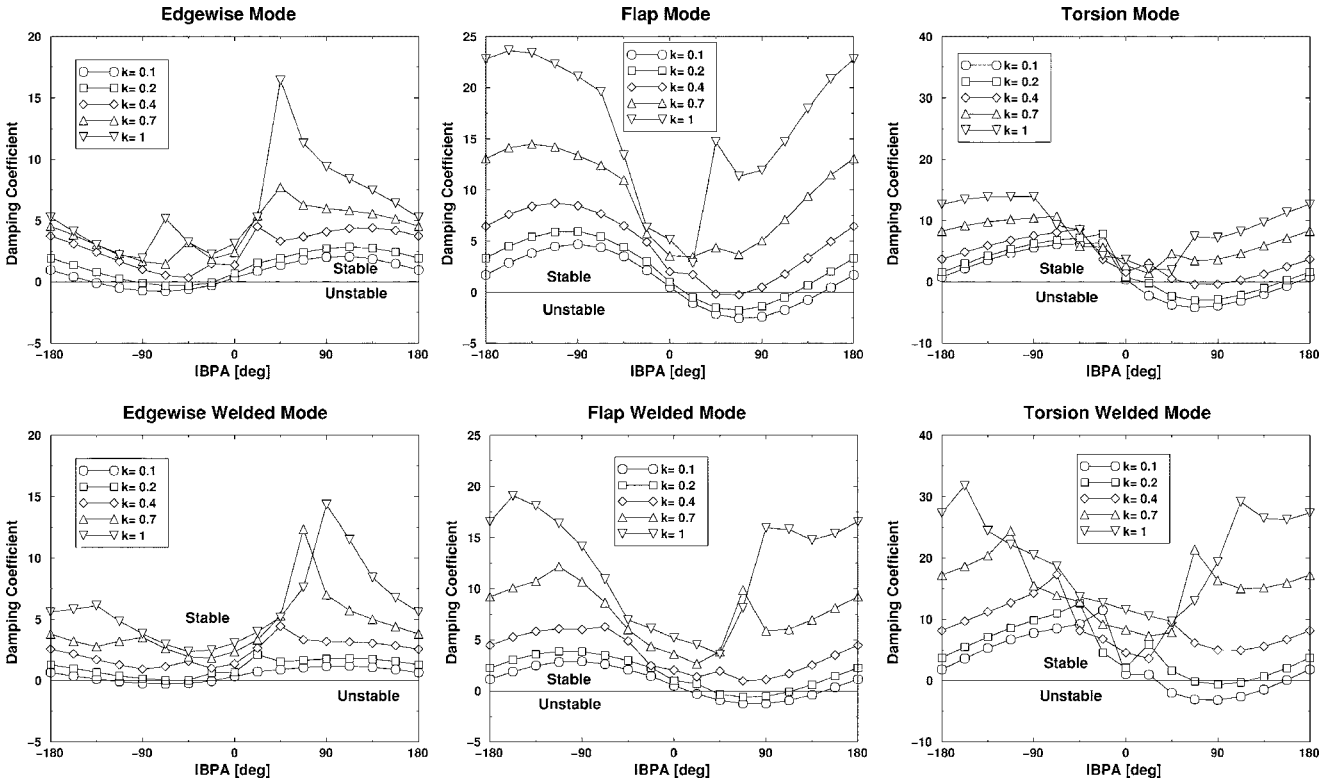

Fig. 7 Damping as a function of IBPA for the three fundamental modes. Top: freestanding airfoil. Bottom: welded-in-pair configuration.

for the torsion mode. For the welded-pair configuration, the situation is somewhat more complex and the damping curves exhibit several peaks. Due to the spiky shape of the damping curves, we have consistently computed them using 16 IBPAs.

Figure 8 (left) shows the critical reduced frequency stability map for a freestanding airfoil. The reduced frequency assigned to every point of the plot is the minimum that ensures that the vibration of the airfoil as a rigid body about this center of torsion is stable. The tie-dye plots are used computing the actual reduced frequency and torsion center for the section of interest and comparing the actual reduced frequency with that of the plot. The middle section represents the reference section. It can be seen that the airfoil is highly unstable in torsion, and increasing the reduced frequency enlarges the stable region. It is also worth noting that while the axial mode (bending in the x direction) is quite stable, the flex mode (bending in the y direction) nearly coincides with the most unstable direction. This may be inferred by realizing that a torsion axis at infinity ($y \to \infty$, for instance) generates a pure bending mode.

Figure 8 (right) shows the equivalent map for a pair of airfoils moving as a rigid body. The lower airfoil of the pair corresponds to the lower section of the figure. The increase in the aerodynamic damping in all the modes with respect the single blade configuration is clearly seen. For k=0.4, the airfoil is stable for torsion modes whose center of torsion lies in the vicinity of the welded-pair passage and in a wide range of bending directions. The most unstable direction (bending) coincides with that of the flex mode.

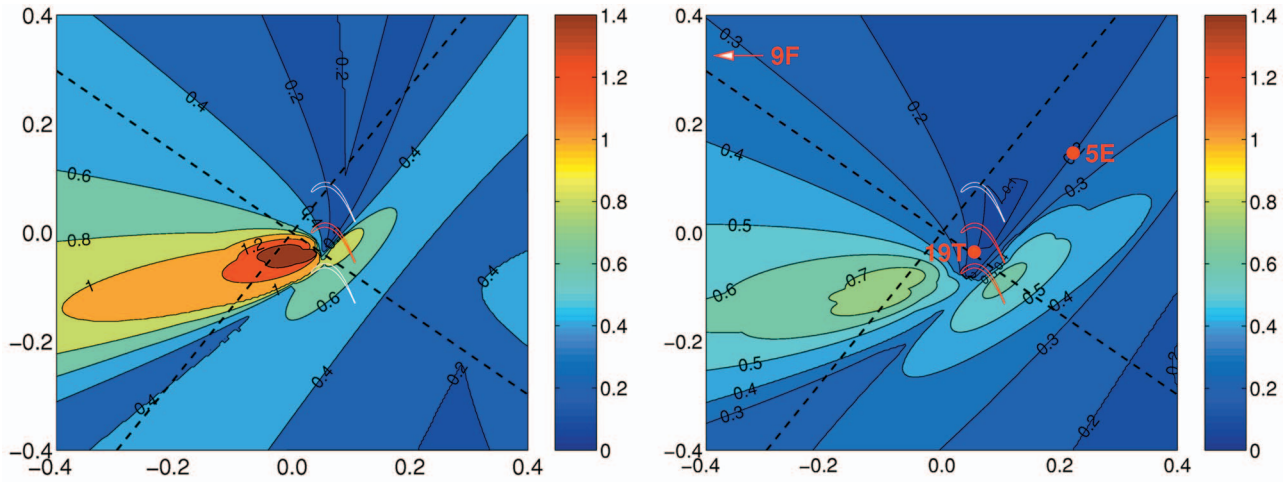

Fig. 8 Critical reduced frequency maps for the freestanding (left) and welded-in-pair (right) configurations

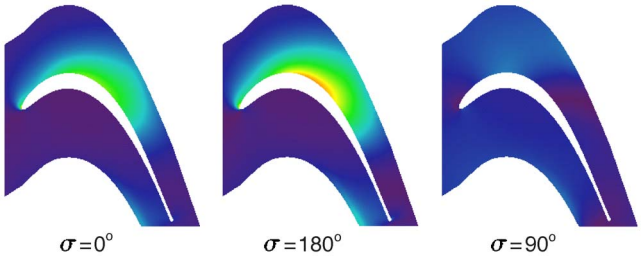

Fig. 9 Modulus of the unsteady pressure for a single airfoil vibrating in torsion about the leading edge for different IBPA

Only qualitative comparisons are possible with the results obtained by Panovsky and Kielb [1] since neither the geometry nor all the aerodynamic conditions are available. Still it may be concluded that, the basic steady aerodynamic conditions are comparable in first approximation and the stability maps of both cases are similar as well. This confirms the idea that the sensitivity to the geometry and aerodynamic conditions is low.

Physical Mechanism of Damping

It has already been shown that welding the blades in pairs is an effective mechanism to increase the damping of the system while keeping the reduced frequency constant. The simulations of the fundamental modes for a single airfoil indicate that the most unstable IBPA is around ±90°, depending on the mode, while the $\sigma=0°$ and $\sigma=180°$ are only slightly damped. This behavior may be readily understood by noting that the modulus of the unsteady pressure for the $\sigma=0°$ case is much smaller than for the $\sigma=180°$ case. This is sketched in Fig. 9 where the unsteady pressure modulus fields generated by the airfoil vibrating in torsion about the leading edge for $\sigma=0$ deg, $\sigma=90$ deg and $\sigma=180$ deg are displayed. It is clearly seen that the modulus of the unsteady pressure is very small for $\sigma=0$ deg since the relative displacement between the two airfoils in the throat region is very small compared to that obtained for $\sigma=180$ deg, where both airfoils move in antiphase. For $\sigma=90$ deg the modulus of the unsteady pressure lies in between the other two.

Since the work per cycle depends strongly on the phase between the unsteady pressure and the blade displacement this aspect is reviewed in the following lines. Figure 10 displays the unsteady pressure phase for the $\sigma=0$ deg, $\sigma=90$ deg and $\sigma=180$ deg. It is important to recall that the unsteady pressure on the suction side (filled symbols) is significantly larger than that on the pressure side (open symbols). The phase of $\sigma=0$ deg, and $\sigma=180$ deg is zero in first approximation. This means that, both modes are neutral from a stability point of view. When the blade moves closing the throat, the pressure is increased in that region, tending to damp the vibration in that part of the cycle but that energy is transmitted back to the airfoil in the second part of the cycle. The damping for $\sigma=180$ deg is dominated by the pressure side which is the only region with a non-null phase with the airfoil. The most critical IBPAs are those in which the modulus of the unsteady pressure is high and the pressure raise when the airfoil moves opening the throat (i.e., when the motion of the suction-side neighboring airfoil closing the throat leads the motion of the reference airfoil).

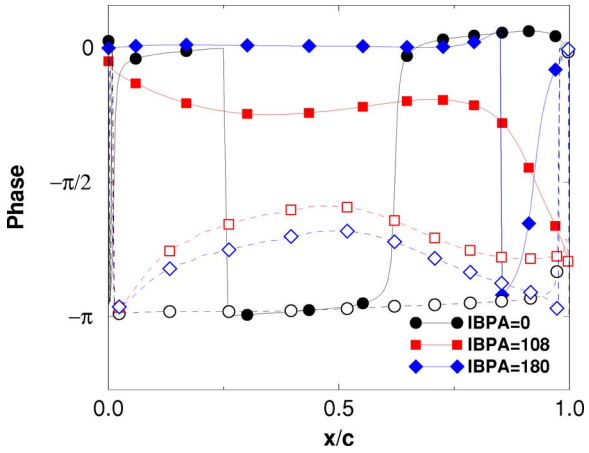

Fig. 10 Unsteady pressure phase along the blade surface. Filled symbols: suction side. Open symbols: pressure side.

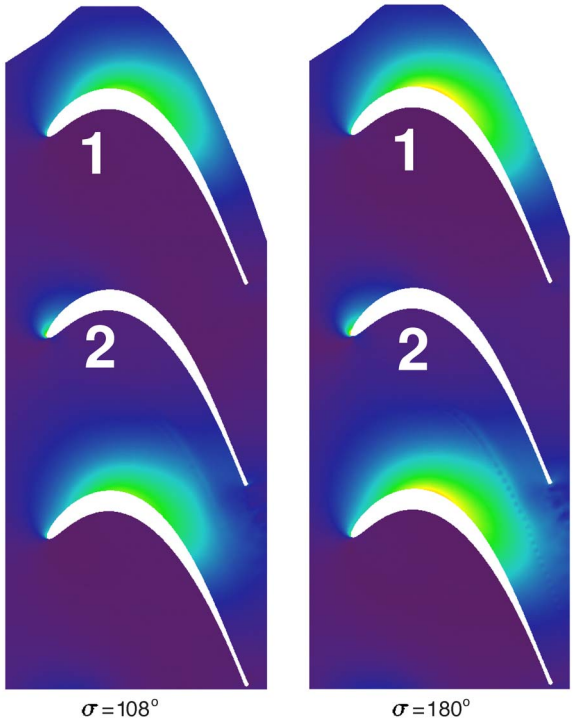

Fig. 11 Modulus of the unsteady pressure for a welded pair of airfoils vibrating in torsion about the leading edge for different IBPA

The effect of welding the airfoils in pairs is depicted in Fig. 11. Within the passage defined by the pair (passage 1) the modulus of the unsteady pressure is very small, since the relative displacement between the airfoils is null, in the same way it was for the freestanding airfoil for $\sigma=0°$. Figure 11 shows clearly that for $\sigma\approx90$ deg and 180 deg, the inner passage of the welded pair has a very low activity, while the passages that define the neighboring pairs (passage 2) have unsteady pressures very similar to those that are encountered in the freestanding airfoil, both in terms of distribution and intensity. The $\sigma=180$ deg case, actually the interpair phase angle $\sigma=180$ deg, has higher unsteady pressure than the $\sigma=90$ deg case, as could be expected. Essentially one out of every two airfoils is not contributing to the total work, halving the amplitude of the first harmonic of the damping curve.

Modal Characterization of Bladed Disks

The aim of this section is to elucidate in a qualitative manner how the previous results influence the stability of realistic bladed-disk assemblies and, in particular, to discuss the relative merits of using cantilever, interlock or welded-in-pair interlocks (see Fig. 2). Although there exists a big leap in moving from pure 2D to fully 3D mode shapes the simplicity of the approach makes the exercise still attractive.

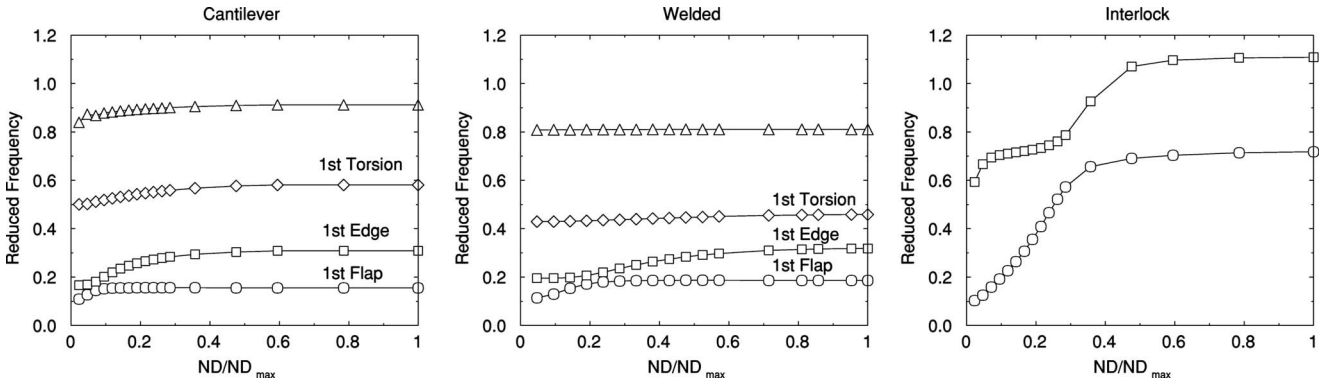

Fig. 12 Modal characteristics of the bladed-disk assembly. Left: cantilever. Middle: welded pair. Right: Interlock.

The bladed-disk assembly considered in this study is representative of the first stages of modern LPTs. The vibration characteristics of the cantilever, interlock and welded-pair configurations have been obtained with the same grid. The boundary condition in the contact nodes between the blade and the disk enforces that the displacements of these are identical in both solids. In the contact faces of the interlock, cyclic symmetry, following the structural FEM terminology, or phase-shifted boundary conditions, in the aerodynamic terminology, are used. This simplifying hypothesis is made to avoid the generation of non-linear models where the concepts of natural frequency and mode shape need to be reinterpreted. However, special care has been taken in this case to match the experimental frequencies of the rotor.

Figure 12 displays the non-dimensional frequency of the first mode families for the cantilever (left), welded-pair (middle), and interlock (right) configurations as a function of the non-dimensional nodal diameter, $ND/ND_{\max}$, where $ND_{\max}=N/2$ for the cantilever and interlock configurations and $ND_{\max}=N/4$ for welded pairs. Several conclusions may be drawn upon inspection of this figure and the mode shapes, not shown here for the sake of brevity,

1. The disk is very stiff compared to the blades. This may be seen in the mode shapes, that show very small displacements of the disk, as well as in the frequency nodal diameter diagram that displays a high number of modes with nearly the same frequency within the same family.
2. The flap and edgewise modes of the welded-pair configuration have slightly higher frequencies than the cantilever one in the high ND region, which is the relevant one from a flutter point of view.
3. The frequency of the first torsion (1T) mode of the welded-pair configuration is lower than that of the cantilever configuration in the whole range of ND.
4. The disk dominated modes of the welded-pair configuration are shifted to the right in Fig. 12 due to the rescaling with $ND_{\max}$ of the horizontal axis.
5. The interlock provides an effective means to raise the frequencies of the assembly. The highest nodal diameters of the first family corresponding to shroud dominated modes.

Application of the PK Method

The objective of this section is to apply the results obtained with the PK method to realistic bladed disks. To simplify the discussion it will be assumed that the bending direction of the flap-wise and edge-wise modes approximately coincides with that of the fundamental modes, i.e., the direction defined by the line that joins the l.e. and t.e. of the airfoil and its normal (dashed lines in Fig. 8). The rationale of this assumption is based on the fact that these directions approximately match those of the principal directions of the airfoil, which are the airfoil *natural* directions of vibration.

It is clearly seen from Fig. 8, left, that the freestanding configuration is unstable. The reduced frequency of the first flap mode is less than 0.2 (see Fig. 12, left) while the minimum reduced frequency to stabilize a flap mode is approximately 0.5. The first torsion mode is probably unstable as well. While the actual value of the reduced frequency for high ND is about 0.6, the torsion center lies in a region of the tie-dye plot of high gradients where the critical reduced frequency may raise up to 1.2. The welded-pair configuration is better from a stability point of view than the freestanding one.

Figure 8 (right) depicts the critical reduced frequency map for the welded-in-pair configuration. We have superimposed on it the location of the torsion centers of the most unstable modes of the first three family modes obtained from a 3D FEM (see Fig. 13, right) to compare the damping obtained from pure two-dimensional and three-dimensional simulations. Torsion centers are computed using a best fit to the motion of the section located at 70% span of the rotor blade. The torsion mode is stable in spite of having a lower reduced frequency, however the flap mode is still unstable.

The stability of the interlock configuration may not be discussed using the critical reduced frequency stability maps since its most unstable modes are complex. This discussion is postponed to the next section where the 3D results for the damping of the interlock bladed disk are available. It may be anticipated, however, that the interlock is marginally unstable and that the interlock is overall more stable than both, the freestanding and the welded-in-pair configuration.

Tuned Three-Dimensional Results

Interlock Configuration. The frequencies and mode shapes of the interlock version of the bladed-disk assembly, whose frequency characteristics are displayed in Fig. 12 (right), have been injected in the 3D linear viscous code. The mode-shape displacements are specified on the structural grid surface and interpolated on the aerodynamic surface grid from where the displacements of the 3D aerodynamic mesh are derived. The computed modes are complex in general and this fact is taken into account explicitly when computing the grid displacements of the aerodynamic mesh.

Figure 13 (left) displays the damping, ξ, (expressed as a fraction of the critical damping) as a function of the IBPA (solid line). Two different grid resolutions with 275,000 and 550,000 nodes per passage, approximately, were considered to assess grid sensitivity. It may be seen that the coarse grid is dense enough to obtain grid independent solutions for most of the IBPAs. Only in the region of minimum damping some differences may be appreciated, but the region of instability is essentially well predicted. The differences in the high ND region are due to the comparatively large reduced frequency of these NDs that would require a slightly finer grid.

This case corresponds to a real design of a marginally stable

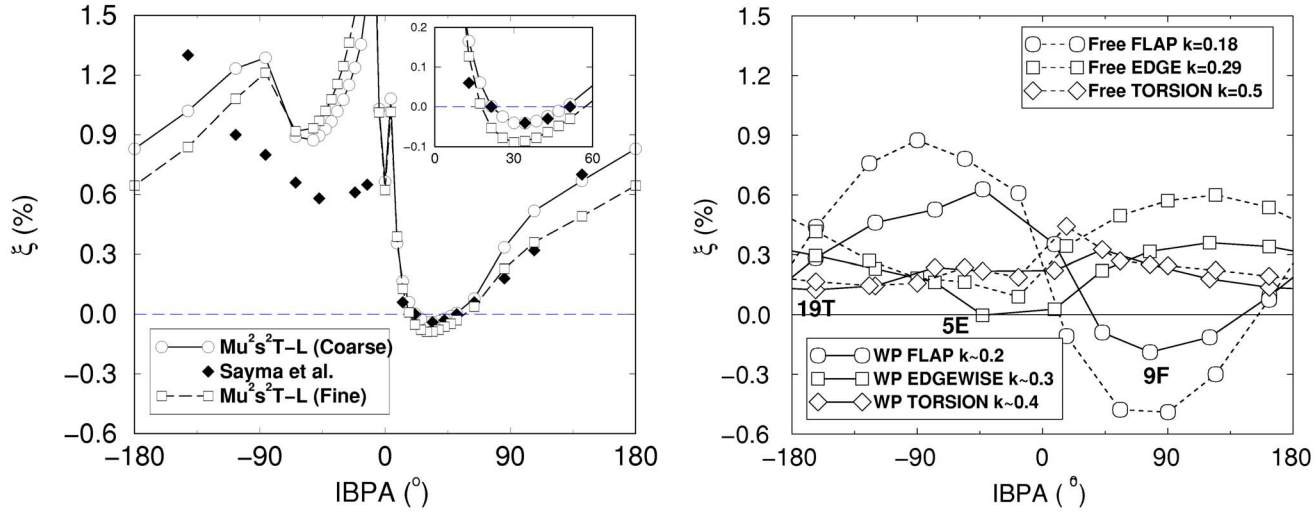

Fig. 13 Damping as a function of the inter-blade phase angle for an interlock (left) and its equivalent welded-in-pair (solid lines) and freestanding configuration (right)

LPT rotor. Experimental data are in agreement with the simulations. The symbols on the same figure were computed using a fully coupled simulation by Sayma et al. [21]. They found that the 6–12 nodal diameters, which corresponds in Fig. 12 right) to 20% of the maximum nodal diameter, were unstable confirming previous rig testing. Our results compare well with [21] except at the high nodal diameter region. It is speculated that this may be due to resolution limitations on their computations, about 500,000 nodes for the whole wheel, inherent to the use of a costly fully coupled approach.

The low nodal diameters are edgewise real modes, which are stable even for very low reduced frequencies, as may be seen in the stability maps, while high nodal diameter modes are torsion modes, whose stability is ensured because of their high reduced frequency. The instability is concentrated in the region where the edgewise modes become torsion modes (the modes are complex) and the reduced frequency is not high enough to ensure their stability.

Sensitivity to Boundary Conditions. In order to understand the differences in the aerodynamic damping between an interlock and a welded-pair configuration, the boundary conditions at the shroud of the interlock configuration were modified to obtain the corresponding natural frequencies and mode shapes of the equivalent welded pair. The grids used in both computations were identical, except for the fact that in the welded-pair case the FEM was made up by two basic sectors. The resulting frequency characteristics are displayed in Fig. 12 (middle) where it may be appreciated that the reduced frequencies of the welded-pair modes are significantly lower than those of the first family of the interlock.

The aerodynamic damping of the first three family modes, computed using linear viscous simulations, is displayed in Fig. 13 right, solid lines). The reduced frequencies assigned to the each mode in the legend correspond to the asymptotic values obtained for the highest nodal diameters and are included as a guideline, however the damping of each mode (nodal diameter) was actually computed using the corresponding natural frequencies and mode shapes obtained from a bladed-disk FE model using cyclic symmetry analysis. It may be appreciated that the flap mode is clearly unstable while the edgewise mode is marginally stable.

Figure 13 (right, dashed lines) represents the damping as a function of the IBPA of the cantilever configuration. It may be appreciated that the freestanding airfoil is significantly more unstable than both the welded-in-pair and the interlock configurations. The increase in damping of the welded in pair with respect the cantilever rotor blades is about 0.3% of the critical damping. The flap mode is the more critical one and the stabilizing effect of the welded-in-pair configuration predicted by the 2D simulations is confirmed.

These results are consistent with the critical reduced frequency of each mode derived from the 2D flutter stability maps of the freestanding and welded-pair configurations, backing the idea of their validity for preliminary design purposes. Figure 8 (right) shows the torsion centers of the most unstable modes of each family (see Fig. 13 (right)). The critical reduced frequencies of both the edge-wise and torsion modes are about 0.2. According to this observation the torsion mode should be stable while the edgewise mode should be marginally stable. This is in agreement with the 3D simulations. According to the stability map of the welded-pair configuration, the critical reduced frequency for the flap mode is about 0.35, which is much higher than the critical reduced frequency of the high nodal diameter modes obtained from the FE model (about 0.2). This result is also aligned with the 3D calculations.

It could be concluded at this stage that interlock configurations, apart from other considerations, are most effective increasing the aerodynamic damping of freestanding airfoils than welded-in-pair rotor blades. It may be claimed also that stability maps predictions are consistent with 3D simulations.

Welded in Pairs. The results of the previous subsection demonstrate that the interlock simulations are consistent with experimental evidence, but the equivalent welded-in-pair rotor does not show any improvement on the aerodynamic damping of the system, since the stabilizing effect on the aerodynamic damping associated with the welding the rotor blades in pairs is smaller than the beneficial effect of increasing the reduced frequency of the interlock.

To ensure the generality of this conclusion two more LPT bladed disks, whose rotor blades had been welded in pairs, were simulated. According to the experimental evidence, both rotors were aerodynamically unstable, being the instability is more severe in the so-called WP1 rotor than in WP2 due to its lower reduced frequency. The simulations were conducted following the same methodology outlined in the previous sections being the steady aerodynamics of both cases comparable in terms of the Mach number distribution to that of the interlock case.

Figure 14 displays the aerodynamic damping of the first three family modes (flap-wise, edge-wise and torsion) for WP1 (solid line) and WP2 (dashed line). The reduced frequency for the high ND of the family modes is also displayed in Fig. 14. The results are qualitatively very similar to those obtained in the previous

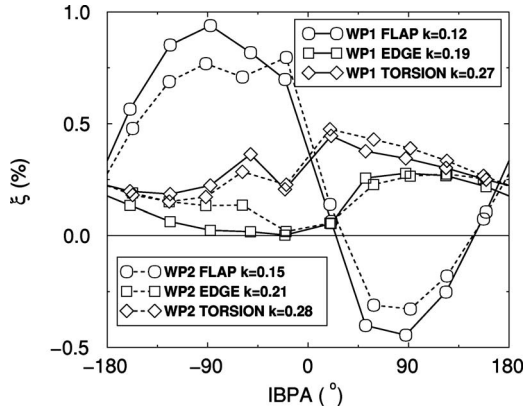

Fig. 14 Aerodynamic damping as a function of the IBPA for the WP1 (solid line) and WP2 (dashed line)

subsection. WP2 is slightly less unstable than WP1, which is consistent with engine readings, however the differences in reduced frequency are small except for the first flap mode where a 25% variation is observed

Mistuning Effects

Bladed disks used in turbine engines are nominally designed to be cyclically symmetric. However, in practice, small variations that result from the manufacturing process and wear break the symmetry, split the eigenvalue pairs, and prevent the existence of traveling-wave modes. Numerous studies have been conducted to understand mistuning effects on the dynamics of bladed-disk assemblies (see the survey paper of Srinivasan [22]). The main conclusions are that while mistuning has an undesirable effect on forced response, increasing the maximum amplitude of some blades, it has often a beneficial (stabilizing) effect on flutter [6].

The damping of a mistuned bladed disk is always larger than that of the tuned case. Let us consider a bladed disk in absence of any structural damping and for which the aerodynamic damping is positive for most of the IBPAs except for a small fraction of them that are unstable and the damping is negative. For the tuned problem the mode shapes of the aeroelastic problem are pure traveling waves and the aerodynamic damping is readily obtained from the curves $\xi = \xi(\text{IBPA})$ that are usually computed in traveling-wave form. In this case the system is unstable since there is at least one unstable traveling wave that is a mode of the system also. However, in the mistuned case the bladed-disk mode shapes are not pure traveling waves anymore and may be expressed as a linear combination of the original traveling waves. The damping, in an analogous way, is expanded as well as a linear combination of the damping associated with each traveling wave. This means that the least stable mode of the mistuned problem will be composed by an important fraction of the most unstable mode of the tuned case and a small fraction of the rest of the modes, most of them stable, and that contribute to increase the overall stability of the tuned case. As a consequence, if we assume that both the aerodynamic and the structural models of the problem, are linear, the damping of the mistuned configuration is always larger than that of the tuned problem. For a more rigorous approach see [23].

Accurate computational methods for the prediction of flutter boundaries are essential to achieve high performance and low cost turbomachinery by allowing adequate but not excessive design margins. Consequently, the mistuning stabilizing effect must be accounted for by preliminary and detailed analysis methods to obtain realistic values of the aerodynamic damping.

Most structural analysis performed on bladed disks assume cyclic symmetry. Therefore, the resulting aeroelastic modes are traveling waves, and this fact is exploited by linear aerodynamic codes to compute the aerodynamic damping efficiently. It is still possible to take advantage of the linearity of flow field to derive the damping of the mistuned problem at a small extra cost making the approach suitable for either preliminary design or detailed analyses within the time scales of a production (design) environment.

Formulation of the Mistuned Problem. The Fundamental Mistuning Model is used to model the structural dynamics. The complete details of the formulation may be found in [24], however a brief summary of the main ideas is given here for the sake of completeness. The governing equations of a linear aeroelastic system, neglecting structural damping and assuming an harmonic motion, may be written as:

$$-\omega^2[M]\{\bar{x}\} + [K]\{\bar{x}\} = C(\omega)\{\bar{x}\} \tag{8}$$

where $\{x(t)\} = \mathrm{Re}(\{\bar{x}\}e^{i\omega t})$, is the vector of the structural degrees of freedom (DOFs) and $C(\omega)$ is the matrix of aerodynamic force influence coefficients. This is an eigenvalue problem where the stability of the system is determined by the imaginary part of ω; stability is restricted to $Im(\omega) \geqslant 0$ and rigorously, $C(\omega)$ is only defined for $\omega \in \Re$.

Choosing the modal coordinates, $\{\bar{q}\}$, in the traveling wave basis of the tuned structure as the new DOFs we may write $\{\bar{x}\} = [\Phi_0]\{\bar{q}\}$, where $[\Phi_0]$ is a matrix whose columns are the tuned system modes. It may be shown that the problem may be reduced to the solution of

$$[\mathbf{\Omega}^2 + 2\mathbf{\Omega}\Delta\tilde{\Omega}\mathbf{\Omega} - \tilde{W}(\mathbf{\Omega}) - \omega^2]\{\bar{q}\} = 0 \tag{9}$$

Equation (9) is a standard eigenvalue problem where the dependence of the aerodynamics on the frequency has been removed. In practice, Ω, a diagonal matrix containing the natural frequencies of the tuned problem, and $[\Phi_0]$ are obtained from a structural FEM while $\Delta\tilde{\Omega}$, is obtained by sampling a given population and contains the mistuning pattern. $\tilde{W}$ is a complex matrix with the work coefficients calculated by the linear code. Since traveling waves with different ND are aerodynamically orthogonal, $\tilde{W}$ is a sparse matrix and if only a family of modes is kept the matrix is diagonal. One of the attractions of the FMM is that it may be regarded as an inexpensive post-processing step of the tuned solution.

Mistuned Flutter Stability Maps

The underlying hypotheses of the PK method have been outlined in a previous section and will not be repeated here, however an additional hypothesis that is usually overlooked is that the cascade is tuned, i.e., all the airfoils are identical and the system modes are traveling waves. However, it is well known that mistuning significantly increases the stability of bladed disks. In this section, modified critical reduced frequency maps that account for mistuning effects are presented.

The computations are performed using the FMM. The airfoils are assumed to be identical, mechanically decoupled, and recoupled by the aerodynamics. The mistuning problem is obtained sampling the airfoils from a normal distribution whose standard deviation is 1% of the natural frequency. Sampling is stopped when the statistical minimum damping is 2% smaller than the difference between the maximum and minimum damping of the tuned case, which for a typical case leads to approximately 300 samples, and represents about a 3σ statistical level of confidence. This criterion has been used for all the estimates of the minimum mistuned damping on this work.

Figure 15 displays the mistuned critical reduced frequency maps for the same airfoil and operating conditions used for the construction of the tuned maps (Fig. 8). The number of airfoils is assumed to be 84.

The isolines of the mistuned maps are noisy due to statistical nature of the computations, however the patterns of the equivalent

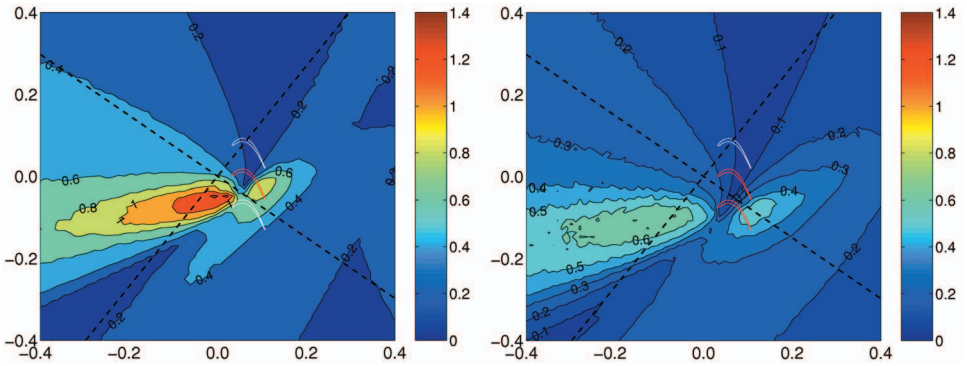

Fig. 15 Critical reduced frequency maps for mistuned freestanding (left) and welded-in-pair (right) airfoils

tuned maps (Fig. 8) are clearly recognized. The differences in the critical reduced frequency with the tuned case are about 20% for the freestanding airfoil, although this result is mode dependent.

For the welded-pair case (Fig. 15 (right)), airfoils are moved as a rigid body. The lower airfoil of the pair corresponds to the section located at the bottom of row. The increase of the aerodynamic damping in all the modes with respect to the single blade configuration is clearly seen. The pattern of both, the tuned (Fig. 8 right), and mistuned maps is similar, however in this case the effect of mistuning is much higher than in the freestanding blade with an increase of up to 30% in the reduced critical frequency for the flap modes. Certainly, this is a factor that needs to be accounted for from an engineering point of view to produce meaningful results.

Mistuned Three-Dimensional Results

The methodology described in the previous section has been applied to estimate the increase in aerodynamic damping due to mistuning in realistic bladed disks. The disk is assumed to be perfectly tuned while a normal population of blades with a standard deviation, σ, of 1% of the rotor blade natural frequency has been used to perform a Monte Carlo simulation. The number of different bladed-disk samples per standard deviation is about 400, which represents about a 3σ statistical level of confidence.

Figure 16 displays the minimum damping as a function of blade frequency mistuning of the sample for the interlock configuration (solid symbols) and its equivalent welded pair (open symbols). The horizontal lines represent the minimum damping for the tuned case. It may be seen that the minimum of the tuned case and that obtained with the Monte Carlo simulation are essentially the same for the interlock configuration, not being the mistuning an effective mechanism to increase the aerodynamic stability in this case. However, for the welded-in-pair rotor blades, the increment in damping is about 0.1%, which is comparable to the beneficial effect of welding the airfoils in pairs.

The different sensitivity of the welded-pair and interlock configurations to mistuning is due to the different form of their frequency characteristics (see Fig. 12). The minimum damping of the interlock bladed disk occurs at low nodal diameters which are separated modes and may not be effectively combined by mistuning, while the minimum damping for rotor blades welded in pairs occurs in the high nodal diameter region, where many modes have nearly the same frequency and may be effectively combined by the rotor blades' mistuning to increase the minimum damping.

Figure 17 displays the damping as a function of the mistuning amplitude in frequency for the welded-pair equivalent of the interlock bladed disk. It may be seen that damping increases almost linearly with the mistuning amplitude and then saturates for $\sigma \approx 2\%$. The lower part of the envelope, that provides the minimum damping, is the most relevant from an engineering point of view. The maximum damping saturates with the damping amplitude to a value that approximately coincides with the mean damping of the family, while the minimum damping depends essentially on the statistical confidence level.

Figure 18 shows the minimum damping as a function of the standard deviation of the sample for the welded-pair bladed disks WP1 and WP2. WP1 is more unstable than WP2, as expected, and the increase in damping due to mistuning effects is about 0.15% of the critical damping in both cases. This means that WP2 still needs about 0.2% of structural critical damping to become stable.

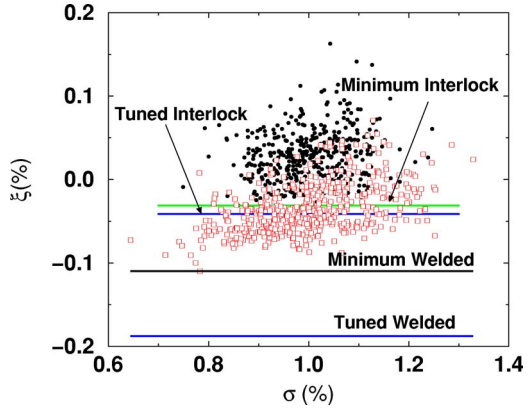

Fig. 16 Minimum damping as a function of the standard deviation of the rotor blade airfoil frequency for an interlock (solid symbols) and a welded-pair (open symbols) blade disk

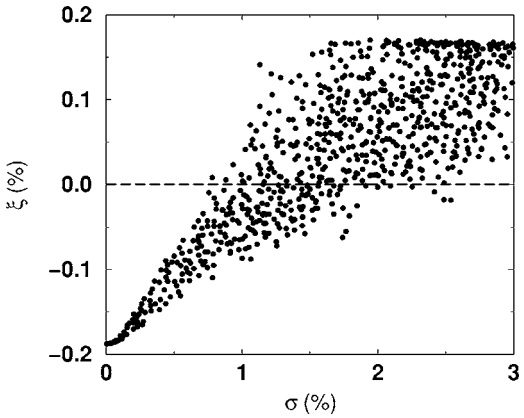

Fig. 17 Damping relative to the critical damping as a function of the rotor blade frequency standard deviation

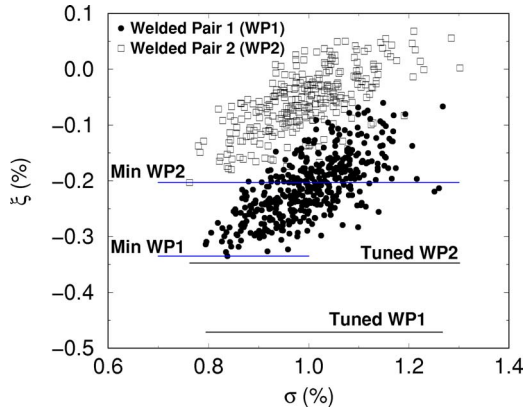

Fig. 18 Minimum damping as a function of the standard deviation of the rotor blade frequency for the WP1 (solid symbols) and the WP2 (open symbols) blade disks

It is important to notice that while paying attention to the worst case of the variational study makes sense for design applications, this is not the best choice for validation. The most logical comparison for a single sample would be to compare to the average of the population. WP1 and WP2 were tested during the development phase of an engine. Strain-gauge readings showed that the vibration amplitude associated with non-synchronous excitations of WP1 was significantly larger than that of WP2 accordingly with our predictions

Concluding Remarks

LPT blades are sometimes welded in pairs to increase their flutter margin. It has been shown by means of two-dimensional viscous linear simulations that the aerodynamic damping of welded-in-pair rotor blades is larger than that of the freestanding airfoils. This is specially true for torsion modes but for bending modes whose flapping direction is aligned with the tangential direction of the cascade the benefit is not large enough to stabilize the mode.

The frequency characteristics of three bladed disks differing just in the tip-shroud boundary conditions have been obtained. It has been observed that the natural frequencies of the welded-pair and cantilever configurations are essentially the same while the interlock dramatically changes the overall behavior of the assembly.

A direct application of the critical reduced frequency maps shows that flap modes are unstable for the reduced frequencies that are typically seen in the engine, while torsion modes become stable. The stability of the interlock is a compromise of the transition between edge-wise modes at low nodal diameters and torsion modes at high nodal diameters. These modes are known to be complex and their stability may not be derived from the critical reduced frequency maps.

To overcome the aforementioned problem, 3D detailed simulations have been performed. First, a realistic interlock has been simulated importing 3D mode shapes into a 3D linear viscous code. It has been concluded that the configuration is marginally stable which is in good agreement with engine experience. The equivalent welded pair of the same bladed disk has been shown to be aerodynamically unstable, matching the results forecast by the 2D stability maps. Two more welded-pair bladed disks, WP1 and WP2, have been simulated using the same technique. The relative stability between them is according to the experience.

Critical reduced frequency maps that retain the stabilizing effect of mistuning have been computed using the FMM. The only additional hypothesis with respect to the PK method is that all the airfoils are identical, structurally uncoupled, and recoupled by the aerodynamics. The stabilizing effect of mistuning is clearly seen, especially for rotor blades welded in pairs, and the modification of the critical reduced frequencies due to mistuning relevant from an engineering point of view.

The application of the FMM to evaluate the underestimation of the aerodynamic damping due to mistuning on realistic bladed disks shows that the effect of mistuning on interlock configurations is negligible, however retaining this effect on welded pairs is essential to a correct prediction of damping.

For the base line case the interlock seems to be superior to the welded-pair configuration from the point of view of aerodynamic damping. The three welded-pair bladed disks analyzed are unstable and require mechanical damping to become stable. Two of them were tested during an engine development phase and their relative vibration amplitudes associated with non-synchronous are aligned with their relative aerodynamic damping.

Acknowledgment

The authors wish to thank ITP for the permission to publish this paper and for its support during the project. We want to acknowledge also the ITP Mechanical Technology Department for its support in providing mechanical models and compiling the required data. Finally, we would like to thank Bob Elliott of Rolls-Royce Turbine Systems for encouraging the development of this work. This work has been partially funded by the Spanish Ministry of Science and Technology under the PTA II framework.

Nomenclature

c = speed of sound
$d_{\max}$ = maximum airfoil displacement
DOF = degree of freedom
$\mathbf{f},\mathbf{g},\mathbf{h}$ = sum of inviscid and viscous fluxes along the x, y and z directions, respectively
FEM = finite element model
IBPA = inter blade phase angle
H = cascade span
k = $\omega c/V_{\text{exit}}$ reduced frequency
$[K]$ = stiffness matrix
L = pseudo Laplacian operator
LPT = low pressure turbine
$[M]$ = mass matrix
N = number of rotor blades
ND = nodal diameter
R = vector of discretized fluxes
q = modal coordinate
Re = real part
$\hat{\mathbf{u}}$ = complex perturbation
$\mathbf{U}$ = vector of conservative variables
v_α = control volume boundary velocity components
$\mu^{(2)},\mu^{(4)}$ = artificial viscosity coefficients
$[\Phi_0]$ = matrix of the tuned system modes
σ = standard deviation of blade frequency mistuning
ξ = damping relative to the critical damping
ω = angular frequency
Θ = non-dimensional work per cycle
Ω = volume

References

[1] Panovsky, J., and Kielb, R., 2000, "A Design Method to Prevent Low Pressure Turbine Blade Flutter," ASME J. Eng. Gas Turbines Power, **122**, pp. 89–98.
[2] Nowinski, M., and Panovsky, J., 2000, "Flutter Mechanisms in Low Pressure Turbine Blades," ASME J. Eng. Gas Turbines Power, **122**, pp. 89–98.
[3] Whitehead, D. S., and Evans, D., 1992, "Flutter of Grouped Turbine Blades," ASME Paper No. 92-GT-227.
[4] Kahl, G., 1995, "Application of the Time Linearized Euler Method to Flutter and Forced Response Calculations," ASME Paper No. 95-GT-123.
[5] Chernysheva, O. V., Fransson, T. H., Kielb, R. E., and Barter, J., 2003, "Effect of Sector Mode Shape Variation on the Aerodynamic Stability of a Low-Pressure Turbine Sectored Vane," ASME Paper No. 2003-GT-38632.

[6] Kaza, K.-R. V., and Kielb, R. E., 1982, "Flutter and Response of a Mistuned Cascade in Incompressible Flow," AIAA J., **20**(8), pp. 1120–1127.
[7] Bendiksen, O. O., 1984, "Flutter of Mistuned Turbomachinery Rotors," ASME J. Eng. Gas Turbines Power, **106**, pp. 25–33.
[8] Crawley, E., 1987, *Manual on Aeroelasticity in Axial Flow Turbomachines Vol. 2, Structural Dynamics and Aeroelasticity*, Chapter on Aeroelastic Formulation of Tuned and Mistuned Rotor, pp. 19-1–19-24.
[9] Sadeghi, M., and Liu, F., 2001, "Computation of Mistuning Effects on Cascade Flutter," AIAA J., **39**(1), pp. 22–28.
[10] Seinturier, E., Dupont, C., Berthillier, M., and Dumas, M., 2002, "A New Method to Predict Flutter in Presence of Structural Mistuning With Application to a Wide Chord Fan Stage," *9th International Symposium on Unsteady Aerodynamics, Aeroacoustics and Aeroelasticity of Turbomachines*, P. Ferrand, ed., Lyon, France, September, pp. 739–749.
[11] Sommer, T. P., Stanppenbeck, F., and Schmitz, M., 2002, "Application of Probabilistic Design Methods to the Prediction of Turbomachinery Blade Flutter," *9th International Symposium on Unsteady Aerodynamics, Aeroacoustics and Aeroelasticity of Turbomachines*, P. Ferrand, ed., Lyon, France, September, pp. 387–396.
[12] Corral, R., Escribano, A., Gisbert, F., Serrano, A., and Vasco, C., 2003, "Validation of a Linear Multigrid Accelerated Unstructured Navier-Stokes Solver for the Computation of Turbine Blades on Hybrid Grids," AIAA Paper No. 2003-3326.
[13] Corral, R., Crespo, J., and Gisbert, F., 2004, "Parallel Multigrid Unstructured Method for the Solution of the Navier-Stokes Equations," AIAA Paper No. 2004-0761.
[14] Jameson, A., Schmidt, W., and Turkel, E., 1981, "Numerical Solution of the Euler Equations by Finite Volume Techniques Using Runge-Kutta Time Stepping Schemes," AIAA Paper No. 81-1259.
[15] Roe, P., 1981, "Approximate Riemman Solvers, Parameters, Vectors and Difference Schemes," J. Comput. Phys., **43**, pp. 357–372.
[16] Swanson, R. C. and Turkel, E., 1992, "On Central-Difference and Upwinding Schemes," J. Comput. Phys., **101**, pp. 292–306.
[17] Corral, R., Burgos, M. A., and Garcia, A., 2000, "Influence of the Artificial Dissipation Model on the Propagation of Acoustic and Entropy Waves," ASME Paper No. 2000-GT-563.
[18] Baldwin, B. S., and Lomax, H., 1978, "Thin Layer Approximation and Algebraic Model for Separated Flows," AIAA Paper No. 78-257.
[19] Giles, M. B., 1990, "Non-Reflecting Boundary Conditions for Euler Equation Calculations," AIAA J., **28**(12), pp. 2050–2057.
[20] Corral, R., and Gisbert, F., 2003, "A Numerical Investigation on the Influence of Lateral Boundaries in Linear Vibrating Cascades," ASME J. Turbomach., **125**, pp. 433–441.
[21] Sayma, A. I., Vahdati, M., Green, J. S., and Imregun, M., 1998, "Whole-Assembly Flutter Analysis of a Low Pressure Turbine Blade," *8th International Symposium on Unsteady Aerodynamics and Aeroelasticity of Turbomachines*, T. Fransson, ed., Stokholm, Sweden, pp. 347–359.
[22] Srinivasan, A. V., 1984, "Vibrations of Bladed-Disc Assemblies-A Selected Survey," ASME J. Vib., Acoust., Stress, Reliab. Des., **106**(2), pp. 165–168.
[23] Martel, C., Corral, R., and Llorens, J. M., 2006, "Stability Increase of Aerodynamically Unstable Rotors Using Intentional Mistuning," ASME Paper No. 2006-GT-90407.
[24] Feiner, D. M., and Griffin, J. H., 2002, "A Fundamental Model of Mistuning for a Single Family of Modes," ASME J. Turbomach., **124**, pp. 597–605.

The Effect of Work Processes on the Casing Heat Transfer of a Transonic Turbine

Steven J. Thorpe
Department of Aeronautical and Automotive Engineering,
Loughborough University,
Loughborough LE12 7TW, UK
e-mail: s.j.thorpe@lboro.ac.uk

Robert J. Miller
Whittle Laboratory,
University of Cambridge,
Cambridge CB3 0DY, UK

Shin Yoshino
Tokyo Electric Power Company,
Yokohama 230-8510, Japan

Roger W. Ainsworth
Department of Engineering Science,
University of Oxford,
Oxford OX1 3PJ, UK

Neil W. Harvey
Rolls-Royce plc,
Derby DE24 8BJ, UK

This paper considers the effect of the rotor tip on the casing heat load of a transonic axial flow turbine. The aim of the research is to understand the dominant causes of casing heat transfer. Experimental measurements were conducted at engine-representative Mach number, Reynolds number, and stage inlet to casing wall temperature ratio. Time-resolved heat-transfer coefficient and gas recovery temperature on the casing were measured using an array of heat-transfer gauges. Time-resolved static pressure on the casing wall was measured using Kulite pressure transducers. Time-resolved numerical simulations were undertaken to aid understanding of the mechanism responsible for casing heat load. The results show that between 35% and 60% axial chord the rotor tip-leakage flow is responsible for more than 50% of casing heat transfer. The effects of both gas recovery temperature and heat transfer coefficient were investigated separately and it is shown that an increased stagnation temperature in the rotor tip gap dominates casing heat transfer. In the tip gap the stagnation temperature is shown to rise above that found at stage inlet (combustor exit) by as much as 35% of stage total temperature drop. The rise in stagnation temperature is caused by an isentropic work input to the tip-leakage fluid by the rotor. The size of this mechanism is investigated by computationally tracking fluid path lines through the rotor tip gap to understand the unsteady work processes that occur. [DOI: 10.1115/1.2372772]

Winner of the Turbo Expo Heat Transfer Committee Best Paper Award

Introduction

The blade-tip region of a high-pressure turbine continues to present a challenge to gas turbine engine manufacturers due to the complex aerothermal conditions encountered in this region of the machine. High flow temperatures, unsteady blade row interactions and cooling difficulties have resulted in a situation where designers rely on expensive design phase iterations rather than an appropriate physical understanding of the flow and heat transfer [1]. There is of course a desire to increase turbine entry temperatures still further, and this means that an improved knowledge of the flow physics in this area will continue to be important for the foreseeable future. Many investigations of blade-tip aerodynamics and heat transfer have been conducted in an attempt to provide designers with a good physical understanding of how flow phenomena affect blade-tip heat transfer and tip-leakage loss. The vast majority of this work has been performed in low-speed test facilities, usually in the form of linear cascades with no relative motion between blade and casing wall. These tests have been essential in gaining an appreciation of the general features of the flow field in the region of the blade tip gap.

By comparison far less work has been reported on the aerodynamic and heat transfer aspects of the stationary overtip casing wall. This component is itself exposed to fierce convective heat transfer and requires careful cooling system design. At present, the knowledge of the relationship between the blade row aerodynamics and the casing heat transfer is poor. This paper will show that it is important to consider the turbine as an aerothermal machine, and that the transfer of work within the turbine causes spatial and temporal distributions of total temperature that are critical to understanding the origins of the heat load to which the overtip casing is subjected.

Historical Perspective

A large body of literature is available relating to the overtip leakage problem in high-pressure turbines, see, for example, Ref. [2]. Indeed, the basic physical process by which the pressure difference across the blade tip drives a leakage of fluid from pressure surface to suction surface is well understood from low-speed cascade experimentation, as is the interaction of this leakage fluid with the blade passage flow (producing the tip-leakage vortex, e.g., Ref. [3]). Detailed measurements of the effect of blade-tip treatments and tip-gap height have been reported by several workers, including Heyes et al. [4] for a low-speed cascade with tip clearance. These investigations are typically concerned with the impact of tip leakage on the aerodynamic loss in the turbine. The experimental investigation of heat transfer in the tip region has been less widely reported in the open literature, although an increase in activity has been apparent in recent years. In addition, the available literature concentrates on the heat transfer to turbine blade tips rather than overtip casing, with the work of Kim and Metzger [5], Papa et al. [6], and Srinivasan and Goldstein [7] being representative examples. The findings of these and other workers are important for establishing the effects of tip-gap height, tip geometry, and blade/casing relative motion.

Moore et al. [8] highlighted the inadequacy of low-speed facilities in simulating the true flow structure in the tip gap. This is due to the pressure ratio across a high-pressure blade tip being sufficient to accelerate the flow to supersonic Mach numbers. The published literature contains only a small quantity of experimental information that has been obtained at fully representative flow conditions for the high-speed axial turbine. The first report of overtip casing heat transfer and aerodynamics for a fully scaled transonic turbine stage was by Guenette et al. [9], who showed the

Contributed by the International Gas Turbine Institute (IGTI) of ASME for publication in the JOURNAL OF TURBOMACHINERY. Manuscript received October 1, 2004; final manuscript received February 1, 2005. IGTI Review Chair: K. C. Hall. Paper presented at the ASME Turbo Expo 2005: Land, Sea and Air, Reno, NV, June 6–9, 2005, Paper No. GT2005-68437.

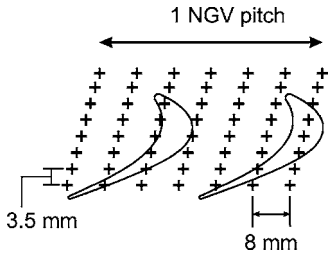

Fig. 1 Location of pressure and heat transfer measurements on the casing wall

influence of blade passing on the unsteady heat transfer to the casing wall as well as the effect of stage Reynolds number. Metzger et al. [10] reported overtip casing heat flux data for a turbine operating at flow conditions representative of those found in modern gas turbine engines. These two investigations have demonstrated the fact that the casing heat flux falls with axial distance through the rotor, but neither included the measurement of the local gas recovery temperature, with the result that a detailed interpretation of the heat transfer results was seriously impeded. The work of Thorpe et al. [11,12] addressed this issue by obtaining detailed spatial and temporal information on the casing heat transfer and aerodynamics in an engine representative turbine stage, and reporting both the time-mean and time-resolved gas recovery temperature on the overtip casing wall.

In this paper time-resolved experimental measurements of both casing heat transfer and gas recovery temperature are used in conjunction with a time-resolved computational prediction to determine the relative importance of gas temperature and heat-transfer coefficient on the total heat load experienced by the casing of a transonic turbine.

Methodology

The Turbine Test Facility. The experimental measurements described in this paper were carried out in the Oxford Rotor Facility [13,14]. This is a short duration transonic turbine stage experiment that uses an isentropic light piston tube to generate the required flow conditions. Before each run the inlet gas is isentropically compressed to raise its stagnation temperature. This ensures that a gas to wall temperature ratio of 1.18 is maintained during the 200 ms run time of the facility.

The working section of the facility contains a 0.55 m diameter shroudless high-pressure turbine stage and allows the simulation of engine representative Mach and Reynolds numbers as well as the appropriate gas-to-wall temperature ratio. The upstream row of vanes had 36 blades with an exit Mach number of 0.95 and an exit Reynolds number, based on axial chord, of 1.55×10^6. The rotor disk had 60 blades with an exit Mach number of 0.98 and the rotational speed of the rotor disk was 8910 rpm. The tip clearance on the rotor was 2.25% of the blade height. The axial gap between the upstream vane and rotor was 36% of the upstream vane axial chord. The total flow-on time is typically 200 ms, which represents approximately 30 disk revolutions.

Casing Heat Transfer Measurements. Fast-response thin-film heat transfer gauges have been used to measure the unsteady heat transfer to the overtip casing wall. In order to generate spatially detailed heat transfer data, a new fabrication technique was devised that allows miniature thin-film sensors to be etched directly onto turbine components at precisely known locations. Details of the heat transfer instrumentation are provided by Thorpe et al. [15]. The casing heat flux sensors are 1 mm by 0.08 mm in plan form and arranged in a regular 7 by 8 array across one nozzle guide vane (NGV) pitch (56 measurement positions in total). Figure 1 shows a schematic diagram of the gauge layout on the casing wall. The frequency response of the heat transfer instrumentation is from dc to 100 kHz. The heat transfer data presented here have been phase averaged to remove random unsteadiness from the signals, leaving the deterministic unsteady component associated with the blade passing events. In addition to the measurement of unsteady heat flux, the casing heat transfer instrumentation was designed in such a way as to allow the direct measurement of the local flow recovery temperature (adiabatic wall temperature). This was achieved by varying the casing wall temperature prior to each test, thereby allowing the measurement of local time-mean and time-resolved recovery temperature. Further details of this method are given in Thorpe et al. [11].

Casing Static Pressure Measurements. The unsteady static pressure was measured at the same locations on the casing wall where heat transfer data were obtained (see Fig. 1). This was achieved using Kulite fast-response pressure sensors embedded in the wall of the overtip casing. The frequency response of the Kulite sensors mounted in this way was greater than 100 kHz, and the pressure sensing area was 1 square millimeter.

Measurement Accuracy. The uncertainty in the measurements has been estimated and previously reported in Thorpe et al. [11]. At the 95% confidence limit the typical uncertainties are: 6% in heat transfer rate, 10% in heat transfer coefficient, and 2 K in adiabatic wall temperature. The temporal frequency response of the instrumentation has implications for the spatial distributions of heat flux and static pressure that are presented in this paper. In fact, the upper limit of 100 kHz implies a limitation of 2.5 mm in the spatially resolved data (this is equivalent to 6% of the blade pitch). The measurement positions on the casing wall are spaced by 8 mm in the circumferential direction (16% of the NGV pitch) as shown in Fig. 1.

Computational Technique. Numerical simulations were performed using a three-dimensional viscous time-unsteady code, Unstrest, developed by Denton [16] at Cambridge University. The code solves the Navier–Stokes equations using a thin shear layer model with the viscous terms evaluated every time step, and turned into body force terms for momentum and source terms for energy. The structured grid is formed by the rotation of points defined in two dimensions (x,r) about the turbine axis; the (x,r) points are defined by meridional (pseudostreamwise) and pseudoradial vectors. The code uses a "time-marching" solution scheme in which one blade row gradually rotates relative to the other with flow parameters being interpolated across a sliding plane between the two grids.

The mesh had 2.6 million nodes. The simulation spanned the correct 3:5 vane rotor repeat ratio. Each rotor passage contained three hundred thousand nodes. The rotor tip gap contained 9 radial nodes. The element to element expansion ratio was less than 1.18 in the axial direction and less than 1.1 in the radial and circumferential directions.

The computation does not include wall heat transfer and was used to understand the aerothermal processes within the fluid. The rotor results presented in this paper have been time averaged over the 36 time steps in one rotor passing cycle. The aim of the research is to understand the effect of isentropic work processes on the total temperature in the tip gap. It is therefore felt that a URANS solver such as Unstrest using a simple mixing length model is sufficient.

Casing Heat Load

The heat load to the casing wall is determined by the temperature difference between the local recovery temperature of the gas, the surface temperature of the wall and the heat-transfer coefficient of the boundary layer, thus

$$\frac{q}{A} = h(T_{\text{rec}} - T_w) \tag{1}$$

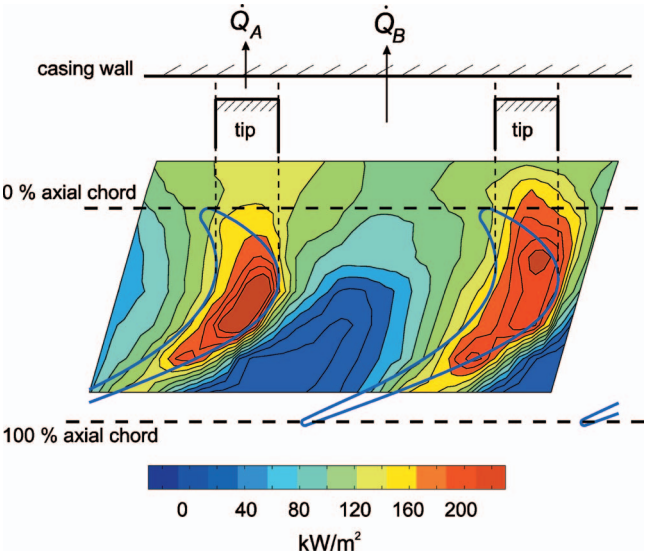

Fig. 2 Time-resolved measurements of the casing heat transfer rate

Using the stage inlet total temperature this can be rearranged to give

$$\frac{q}{T_0 A} = h\left(\frac{T_{\text{rec}}}{T_0} - \frac{T_w}{T_0}\right) \tag{2}$$

If in a particular turbine the boundary layer heat-transfer coefficient (h) and the gas recovery temperature (T_{rec}) are known then to calculate heat transfer rate (q) it is necessary to specify the stage inlet to wall temperature ratio (T_0/T_w). In an optimized gas turbine design the casing would require the minimum level of cooling possible. This would mean that its surface would be designed to run at the maximum allowable temperature of the particular material used. If the casing were covered in a thermal barrier coating, with a maximum surface temperature stipulated to be 1500 K, the casing surface temperature would be designed to be 1500 K at all axial locations. As the gas passes through the rotor work is extracted and its stagnation temperature drops. This causes the driving temperature difference ($T_{\text{rec}} - T_w$) to fall from rotor leading edge to trailing edge. The cooling on such an idealized turbine would be optimized to take advantage of this axial reduction in heat transfer, with the casing towards the trailing edge requiring less cooling air than at the leading edge.

For a modern civil aeroengine with a turbine entry temperature of 1800 K and a casing that employs a thermal barrier coating, the stage inlet to wall temperature ratio is 1.2. For the testing reported in this paper the stage inlet to wall temperature ratio was set at 1.18.

The aim of this section is to determine the spatial and temporal effect of the rotor on the casing heat load. Equation (1) will then be used to determine the relative importance of gas temperature and heat-transfer coefficient on the heat load.

Spatial Distribution of Heat Load. An instantaneous snapshot of the experimentally measured casing heat transfer rate is shown in Fig. 2. The measurements show strong spatial variations both circumferentially and axially, and very high levels of casing heat transfer are observed within the blade-tip footprint. The highest values occur in the vicinity of the crown of the blade and toward the blade suction surface. A region of elevated heat transfer is also seen axially forward of the blade tips in the vane-rotor axial gap. The pattern of casing heat load shown in Fig. 2 moves at blade speed relative to the casing wall; consequently, a fixed point on the casing wall is alternately exposed to blade passage flow and blade tip leakage flow. This can be appreciated from the schematic diagram at the top of Fig. 2.

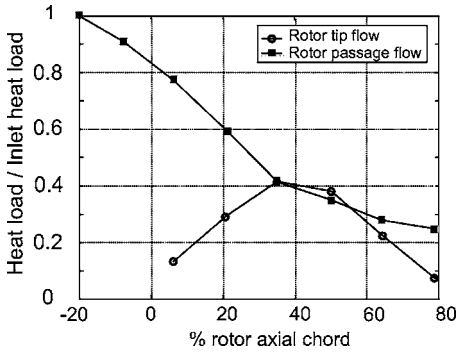

Fig. 3 Experimentally measured casing heat load caused by rotor tip and passage flows

The total heat load at any particular point on the casing wall can be divided into portions that originate from either the rotor passage flow or the rotor tip flow: these are shown as $\dot{Q}_B$ and $\dot{Q}_A$ respectively in Fig. 2. To quantify the fraction of casing heat load that is caused by the presence of an individual rotor tip the total heat transfer at each measurement point has been split into the heat transfer above a rotor tip and above the passage flow (using the time-resolved data). The axial variation of each of these components is shown in Fig. 3. The measurements show that even though the rotor-tip covers only between 10% and 24% of the casing circumference (depending on axial position) it contributes up to 50% of the total heat load to the casing. Figure 2 shows that in addition to the enhanced heat transfer above the rotor the presence of the rotor also enhances heat transfer close to the suction surface, pressure surface, and upstream of the blade. The total contribution of the rotor-tip to casing heat load can therefore be well over 50%.

Cause of High Heat Load Above the Rotor. Equation (1) shows that a high casing heat load above the rotor can be caused by: (1) an elevated gas temperature ratio (T_{rec}/T_0); (2) an elevated heat transfer coefficient (h); or (3) a combination of the two. The axial variation of gas temperature ratio and heat transfer coefficient derived from the experimental results is shown in Figs. 4 and 5 (these data represent average values for tip and passage regions).

Figure 4 shows the circumferentially and temporally averaged gas recovery temperature over the rotor tip and passage flow. The maximum difference between the passage and tip stagnation temperatures occurs at 50% axial chord and shows an 11% rise. It is interesting to note that this rise in stagnation temperature is 40%

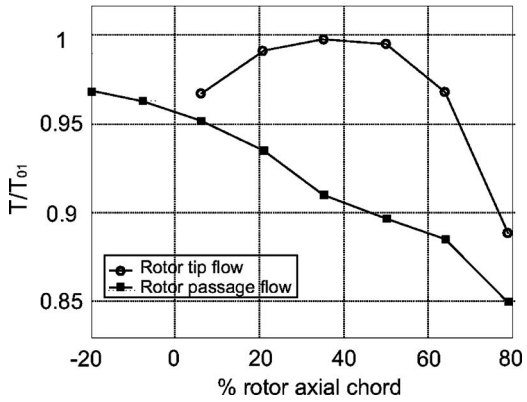

Fig. 4 Experimentally measured casing recovery temperature in the rotor tip gap and rotor passage

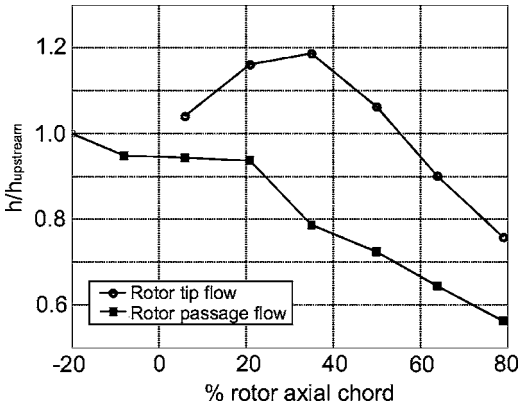

Fig. 5 Experimentally measured casing heat transfer coefficient in the rotor tip gap and rotor passage

of the total stagnation temperature drop across the stage. The increase in casing heat transfer rate caused by the temperature rise above the rotor tip can be found from Eq. (1). The stage inlet to wall stagnation temperature ratio (T_0/T_w) in the Oxford Rotor Facility is 1.18. The 11% rise in stagnation temperature thus causes a 250% rise in heat transfer.

The maximum measured difference between the passage and tip heat transfer coefficient occurs at 35% axial chord (Fig. 5). At this location the casing heat transfer coefficient in the rotor tip gap is 55% higher than in the blade passage. Table 1 shows the increase in casing heat load caused by the rotor tip flow at 50% axial chord. The results show that at a stage inlet to wall temperature ratio of 1.2 (typical of a civil aeroengine) the heat transfer rises by a factor of 2.09 compared to the case when the tip-leakage flow is not present. It is important to note that the reason the temperature variation has such a large effect on casing heat load is that the peak temperature in the tip gap was measured to be 35% of stage ΔT_0 above the stage inlet temperature. If an overtip casing is designed to have a stage inlet to wall temperature ratio (T_0/T_w) of 1.2 the driver temperature at 50% axial chord is only 15% of stage ΔT_0. Table 1 also shows the effect of raising T_0/T_w to 1.4. This is equivalent to increasing casing cooling until the wall surface temperature is limited to 1286 K. At these wall temperatures the effects of stagnation temperature and heat transfer coefficient have a comparable effect on the casing heat load.

Time-Resolved Casing Wall Temperature. Figure 6 shows the measured distribution of time-resolved gas recovery temperature for the same instant in the blade passing cycle as the heat transfer rate data shown in Fig. 2. Figure 7 shows the comparable computational results averaged over one vane passing cycle. Upstream of the blade row the recovery temperature on the casing wall is high and close to the stage inlet total temperature of 374 K. The rotor potential field causes a stagnation temperature variation upstream of the blade. Within the rotor passage the flow recovery temperature falls as work is extracted from the fluid.

Over the rotor tip the gas recovery temperatures rise above the stage inlet stagnation temperature. In both the experiment and computation the region of highest temperature rise occurs on the

Table 1 Increase in casing heat load caused by elevated levels of h and T_{rec} in the rotor tip gap at 50% axial chord (expressed as a factor relative to the no tip-leakage case)

T_0/T_w	1.2	1.4
Effect of h	1.09	1.09
Effect of T_{rec}/T_0	1.68	1.13
Total rise in Q	2.09	1.29

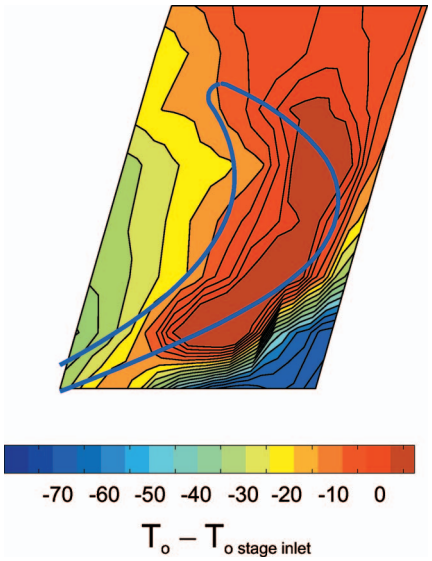

Fig. 6 Measurement of the time-resolved gas recovery temperature on the casing wall

suction side of the blade tip. The highest measured stagnation temperature was 35 K above that at stage inlet (35% stage ΔT_0). The highest computationally predicted stagnation temperature was 40 K above stage inlet.

The results in this section have shown that at engine representative stage inlet to wall temperature ratios the presence of the rotor tip leakage can double the local heat load. This rise in heat load is caused by the recovery temperature of the gas in the rotor tip gap reaching values 35% of stage ΔT_0 above stage inlet and enhanced levels of heat transfer coefficient. The following section explains the mechanism for this rise.

Effect of Work Processes

The change in the stagnation enthalpy and temperature of a fluid particle per unit time and mass, in a particular frame of reference, is given by

$$\frac{Dh_0}{Dt} = \frac{1}{\rho}\frac{\partial q_i}{\partial x_i} + \frac{1}{\rho}\frac{\partial(\tau_{ij}u_i)}{\partial x_j} + \frac{1}{\rho}\frac{\partial p}{\partial t} \tag{3}$$

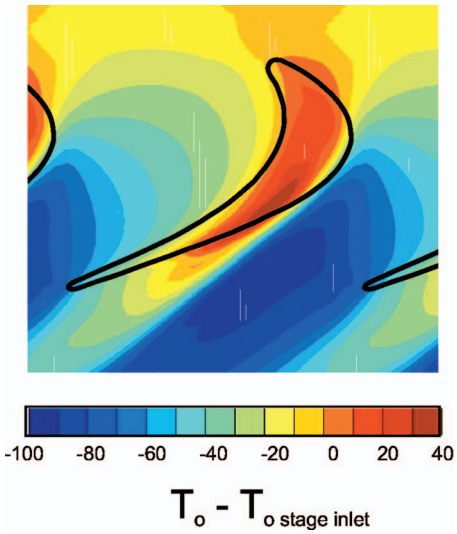

Fig. 7 Time-mean computational prediction of casing flow total temperature

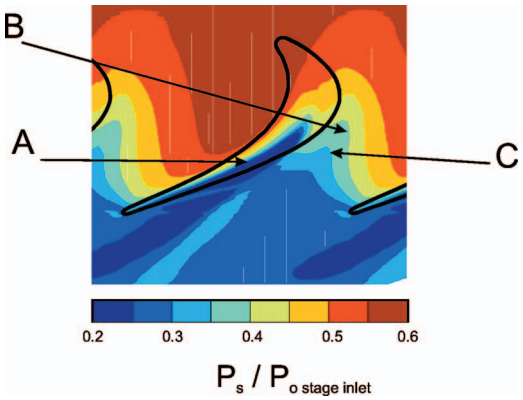

Fig. 8 Time-mean computational prediction of casing static pressure

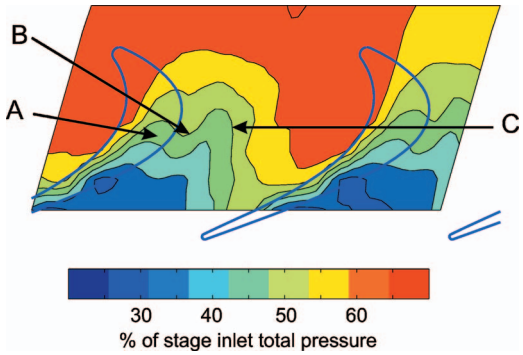

Fig. 9 Experimental measurements of the time-resolved casing static pressure

The three source terms are the heat flow into the element, the work done by viscous stresses, and the change in enthalpy caused by temporal gradients in the static pressure field. The stagnation temperature of a gas is altered by the frame of reference in which it is viewed. If the flow through the rotor gap is observed in the rotor relative frame the problem becomes steady and the third term in Eq. (3) does not occur. The heat transfer to the casing wall is driven by the stagnation temperature in the casing (stationary) frame of reference. In the stationary frame the rotor flow is unsteady and thus the third term in Eq. (3) is nonzero.

To understand the possible causes of the rise in stagnation temperature of the fluid as it passes into the rotor tip gap it is worth examining the source terms on the right of Eq. (3).

The first term represents the net heat transfer into or out of the fluid. This can be caused either by conduction of heat through the fluid or by the mixing of the fluid with a second stream of differing temperature. Heat transfer to a fluid particle can only occur from a hotter source. The temperatures in the rotor tip gap are higher than at combustor exit. Heat transfer therefore cannot be the cause of the elevated tip temperatures.

The second term represents viscous work done on or by the fluid. In the stationary frame of reference the casing wall is not moving and therefore cannot do viscous work on the fluid. The rotor tip moves in the direction of fluid motion with a velocity less than that of the fluid. This results in the rotor tip applying a viscous drag to the fluid. The rotor's viscous drag extracts work from the fluid causing a drop in its stagnation enthalpy.

The third term shows that in an isentropic fluid the stagnation enthalpy can only be changed by the presence of a temporal variation in static pressure at a stationary point in the chosen frame of Ref. [17]. It should be noted that the drop in stagnation temperature of the core fluid as it moves through the rotor (isentropic work extraction) is as a result of the movement of the rotor static pressure field relative to the stationary frame. For the stagnation enthalpy in the casing frame of reference to rise as a fluid particle enters the tip gap the fluid must therefore experience a positive temporal static pressure gradient.

Casing Static Pressure. The unsteady pressure field at a fixed point in space is the result of the movement of the rotor pressure field at blade speed. The computationally predicted and experimentally measured static pressure fields on the casing wall are shown in Figs. 8 and 9. The computational and experimental results exhibit a number of similar features. A band of low static pressure stretches from around 50% axial chord to the trailing edge on the suction side of the gap (marker A). This is caused by the overexpansion of fluid to supersonic Mach numbers in the tip gap. The casing passage boundary layer migrates under the influence both of the relative wall motion and the cross-passage pressure gradient towards the rotor suction surface. Where the casing boundary layer meets the rotor tip-leakage jet the flow separates from the casing wall and the tip-leakage flow rolls up into a vortical type structure ("tip-leakage vortex"). This causes the static pressure close to the rotor suction surface first to rise (marker B) then to fall (marker C). The structure of the static pressure field described above is characteristic of shroudless transonic turbines. The temporal static pressure gradient in the stationary frame of reference is obtained by moving the static pressure field (Fig. 8) at the blade speed and at each point differentiating with respect to time. The temporal static pressure gradient is shown in Fig. 10. A number of distinct regions are observed. Marker D shows the negative temporal pressure gradient in the rotor passage causing

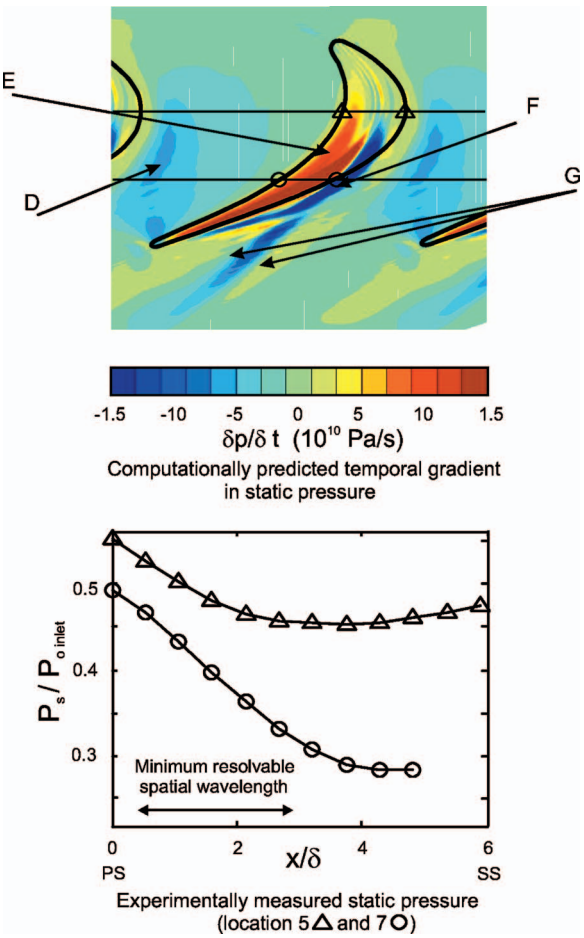

Fig. 10 Computationally predicted temporal gradient in static pressure and experimentally measured pressure

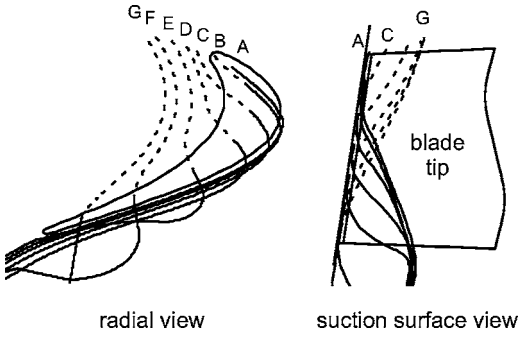

Fig. 11 Fluid path lines through the rotor tip gap

work extraction in the main passage. Marker E shows the acceleration of fluid through the tip gap causing a positive temporal pressure gradient and thus work addition. Marker F shows that as the fluid leaves the tip gap it experiences a negative temporal pressure gradient and thus a work extraction. Marker G shows that the tip leakage vortex results in work extraction and addition downstream of the blade trailing edge.

The bottom half of Fig. 10 shows the experimentally measured static pressure at locations 5 and 7. The gauges show the two distinct regions of the tip flow. Upstream of 50% Cax (gauge 5) the pressure on the casing wall first rises then is observed to fall. This indicates that the flow accelerates in to the gap then starts to mix within the gap. It should be noted that the temporal bandwidth of the pressure measurements is 100 kHz and this limits the minimum measurable spatial frequency (Fig. 10). This makes observation of small flow structures such as the pressure surface separation bubble impossible. Downstream of 50% Cax (gauge 7) the pressure on the casing wall drops throughout the gap. This indicates that the flow continues to accelerate to the exit of the gap.

Enthalpy Change Along Rotor Relative Path Lines. To determine the effect of temporal pressure gradients on the stagnation enthalpy of the tip flow it is necessary to track fluid particles as they travel along path lines through the rotor tip gap. Fluid path lines are frame independent and represent the path along which the fluid particles travel. Figure 11 shows seven path lines that pass through the rotor tip gap. For simplicity the path lines were started at time zero at points located at the midradius and midcircumference of the tip gap. The axial locations of the points were equispaced between the rotor leading edge and trailing edge. The path lines were then tracked for both positive and negative time until they left the domain. It should be noted that path-lines and streamlines coincide in steady flow. Figure 11 can thus be interpreted as streamlines in the rotor-relative frame.

The stagnation temperature variation along the seven path lines is shown in Fig. 12. The path lines are plotted above each other with the stage inlet stagnation temperature for each, plotted as a dotted line (Note that the stage inlet stagnation condition is the same for all path lines.). The time at which the path line enters and leaves the tip gap are marked with circles.

The change in swirl velocity of a fluid particle in an inviscid flow is given by

$$\frac{Dr\nu_\theta}{Dt} = -\frac{r}{\rho}\frac{\partial p}{r\partial\theta}$$

If the flow in the rotor is considered steady in the rotor-relative frame then the spatial pressure gradient in the rotor can be related to the temporal pressure gradient such that

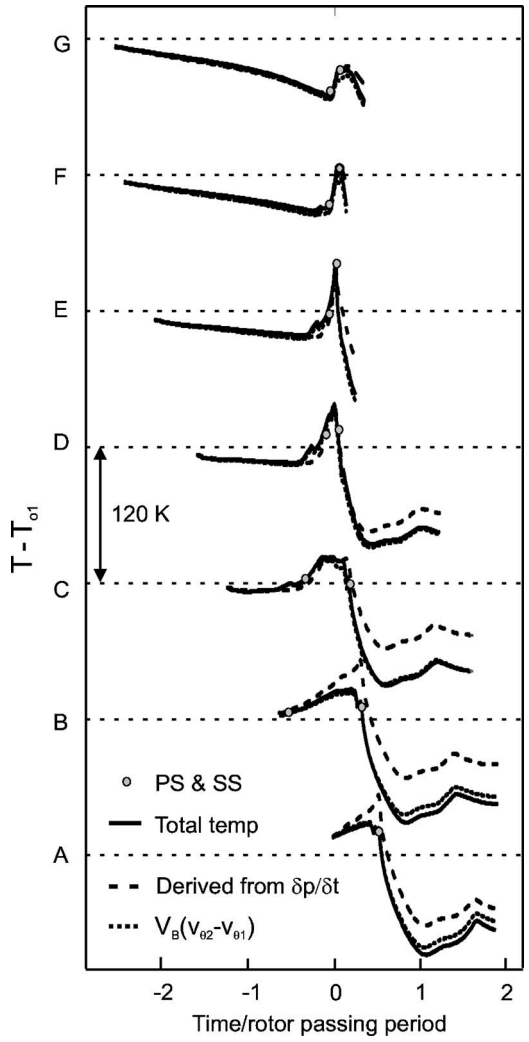

Fig. 12 Computationally predicted stagnation temperature variations along seven path lines (these path lines are shown in Fig. 11)

$$\frac{Dr\nu_\theta}{Dt} = -\frac{1}{\rho}\frac{\partial p}{\partial\theta} = \frac{1}{\rho\omega}\frac{\partial p}{\partial t}$$

Combining the above with the isentropic form of Eq. (3) and integrating from a point at rotor inlet to a point on the same path line gives

$$\Delta h_{ois} = \int_1^2 \frac{1}{\rho}\frac{\partial p}{\partial t}dt = u_2\nu_{\theta 2} - u_1\nu_{\theta 1} \tag{4}$$

The above equation shows that the change in isentropic stagnation temperature of a fluid particle travelling through the rotor can either be obtained by integrating the temporal pressure gradient along a path line or from the Euler work equation. Both methods of calculating the stagnation temperature along a path line are shown in Fig. 12.

The total temperature calculated from the Euler work equation for a particle is shown as a dotted line in Fig. 12. It should be noted that a constant radius was assumed in the calculation of the blade velocity. This causes a small error downstream of the rotor tip gap. It should also be noted that the total temperature predicted by the Euler equation agrees closely with that predicted by the viscous computation. The derivation of the Euler equation for a

particle, given above, is for an isentropic flow. Figure 12 indicates that it accurately predicts the total temperature variation in the viscous flow.

The total temperature change derived by integration of the temporal pressure field agrees well with the numerical prediction up to the exit of the tip gap. Downstream of the exit of the gap the total temperature is over estimated. Equation (4) shows that the integral of the temporal pressure gradient gives only the isentropic change in total enthalpy. The difference between the two temperatures is a result both of viscous processes in the rotor relative frame and of the limited accuracy of the path-line tracking around the core of the tip vortex.

The seven path lines fall into two groups. The first group located downstream of 50% Cax (path lines E, F, G) have a low gap length to height ratio (between 4 and 1). As shown in Fig. 10 this results in acceleration of the fluid throughout the gap and thus a work addition throughout. This shows that the stagnation temperature is raised by up to 80 K by work addition. The second group located upstream of 50% Cax (path lines A, B, C, and D) has a high gap length to height ratio (between 12 and 5). In this region the tip-leakage flow experiences both a positive temporal pressure gradient as it accelerates into the gap and a negative temporal pressure gradient as it mixes within the gap. On path lines A and B the isentropic work addition over predicts the total temperature within the gap. This is likely to be caused by the viscous processes in the rotor relative frame.

The above discussion shows that the majority of the rise in stagnation temperature over the tip gap results from isentropic work input from the rotor. In this way the rotor tip gap can be viewed as a super high-pressure compressor stage.

Design Implications

The area of the casing wall affected by the highest stagnation temperature is dependent on the geometry of the rotor tips. If a single squealer tip as used on the suction surface then the stagnation temperature rise would only occur for a very small percentage of the circumference, lowering the total casing heat load. This is because as soon as the fluid re-entered the mainstream work extraction occurs and the casing boundary layer would cause the tip-leakage fluid to leave the casing wall. If a single squealer tip was used on the pressure surface the opposite would occur and the region of stagnation temperature would be maximized raising the total casing heat load.

It should be noted that low-speed testing does not correctly simulate the magnitude of the work processes in the rotor. This means that in a low-speed test the gas temperature through the rotor tip gap will remain constant and the casing heat load will be underestimated. The results from low-speed tests should therefore be compensated for variations of gas temperature caused by work processes.

Conclusions

The experimental results show the presence of the rotor tip causes large spatial and temporal variations in instantaneous heat flux to the overtip casing wall. Analysis of the time resolved data has shown that over half of the local heat load to the casing wall can be attributed to the tip-leakage fluid. The experimental results allow the individual effects of gas recovery temperature and heat transfer coefficient to be investigated. For an axial turbine with a stage inlet to wall temperature ratio of 1.2 the rise in stagnation temperature caused by the rotor tip leakage flow results in a 68% increase in the heat load at 50% axial chord. The rise in heat load due to increased heat transfer coefficient at the same location is 9%.

The computation and experiment show the stagnation temperature in the tip gap rising by 40% and 35% of stage ΔT_0. The majority of this change is caused by an isentropic work addition to the flow within the tip gap. The maximum calculated stagnation temperature rise was found to be 80 K. On leaving the tip gap work extraction was found to occur. The regions of highest heat load were found to be occur in the same regions as the maximum gas stagnation temperatures. This was found be close to the suction side of the rotor between 20% and 60% axial chord.

Acknowledgment

The authors would like to acknowledge the support of Rolls-Royce plc and the UK government Department of Trade and Industry. Important improvements to the operation of the test facility were made by Dr. Nick Atkins, to whom the authors are indebted. The authors would also like to acknowledge the generous support provided to Shin Yoshino by the Tokyo Electric Power Company (TEPCO).

Nomenclature

h = heat transfer coefficient
p = pressure
q = heat addition per unit mass
q_i = component of heat flux vector
t = time
u = blade velocity
v = velocity
x_{ij} = Cartesian coordinates
ρ = density
τ_{ij} = shear stress
∂ = partial derivative
A = area
D = substantial derivative
T_{rec} = gas recovery temperature
T_0 = stage inlet temperature
T_w = casing wall temperature

Subscripts

1 = rotor inlet
2 = position along a path-line
θ = circumferential

References

[1] Bunker, R. S., 2001, "A Review of Turbine Blade Tip Heat Transfer," Ann. N.Y. Acad. Sci., **934**, pp. 64–79.
[2] Arts, T., ed., 2004, "Turbine Blade Tip Design and Tip Clearance Treatment," von Karman Institute for Fluid Dynamics Lecture Series 2004-02.
[3] Yamamoto, A., 1988, "Endwall Flow/Loss Mechanisms in a Linear Turbine Cascade With Blade Tip-clearance," ASME Paper No. 88-GT-235.
[4] Heyes, F. J. G., Hodson, H. P., and Dailey, G. M., 1992, "The Effect of Blade Tip Geometry on the Tip Leakage Flow in Axial Turbine Cascades," ASME J. Turbomach., **114**(3), pp. 643–651.
[5] Kim, Y. W., and Metzger, D. E., 1995, "Heat Transfer and Effectiveness on Film Cooled Turbine Blade Tip Models," ASME J. Turbomach., **117**(1), pp. 12–21.
[6] Papa, M., Goldstein, R. J., and Gori, F., 2003, "Effects of Tip Geometry and Tip Clearance on the Mass/Heat Transfer From a Large-Scale Gas Turbine Blade," ASME J. Turbomach., **125**(1), pp. 90–96.
[7] Srinivasan, V., and Goldstein, R. J., 2003, "Effect of Endwall Motion on Blade Tip Heat Transfer," ASME J. Turbomach., **125**(2), pp. 267–273.
[8] Moore, J., Moore, J. G., Henry, G. S., and Chaudhry, U., 1988, "Flow and Heat Transfer in Turbine Tip Gaps," ASME Paper No. 88-GT-188.
[9] Guenette, G. R., Epstein, A. H., Norton, R. J. G., and Yuzhang, C., 1985, "Time Resolved Measurements of a Turbine Rotor Stationary Tip Casing Pressure and Heat Transfer Field," AIAA Paper No. 85-1220.
[10] Metzger, D. E., Dunn, M. G., and Hah, C., 1991, "Turbine Tip and Shroud Heat Transfer," ASME J. Turbomach., **113**, pp. 502–507.
[11] Thorpe, S. J., Yoshino, S., Ainsworth, R. W., and Harvey, N. W., 2004, "An Investigation of the Heat Transfer and Static Pressure on the Over-Tip Casing Wall of an Axial Turbine Operating at Engine Representative Flow Conditions (I) Time-Mean Results," Int. J. Heat Mass Transfer, **25**(6), pp. 933–944.
[12] Thorpe, S. J., Yoshino, S., Ainsworth, R. W., and Harvey, N. W., 2004, "An Investigation of the Heat Transfer and Static Pressure on the Over-Tip Casing Wall of an Axial Turbine Operating at Engine Representative Flow Conditions (II) Time-Resolved Results," Int. J. Heat Mass Transfer, **25**(6), pp. 945–960.

[13] Ainsworth, R. W., Schultz, D. L., Davies, M. R. D., Forth, C. J. P., Hilditch, M. A., Oldfield, M. L. G., and Sheard, A. G., 1988, "A Transient Flow Facility for the Study of the Thermofluid-Dynamics of a Full Stage Turbine Under Engine Representative Conditions," ASME Paper No. 88-GT-144.
[14] Miller, R. J., Moss, R. W., Ainsworth, R. W., and Horwood, C. K., 2003, "Time-Resolved Vane-Rotor Interaction in a High-pressure Turbine Stage," ASME J. Turbomach., **125**(1), pp. 1–13.
[15] Thorpe, S. J., Yoshino, S., Ainsworth, R. W., and Harvey, N. W., 2004, "Improved Fast Response Heat Transfer Instrumentation for Short Duration Wind Tunnels," Meas. Sci. Technol., **15**(9), pp. 1897–1909.
[16] Denton, J. D., 1990, "The Calculation of Three Dimensional Viscous Flow Through Multistage Turbomachines," ASME Paper No. 90-GT-19.
[17] Dean, R. C., 1959, "On the Necessity of Unsteady Flow in Fluid Machines," ASME J. Basic Eng., **81**(1), pp. 24–28.

Effect of Reynolds Number and Periodic Unsteady Wake Flow Condition on Boundary Layer Development, Separation, and Intermittency Behavior Along the Suction Surface of a Low Pressure Turbine Blade

M. T. Schobeiri

B. Öztürk

Turbomachinery Performance and
Flow Research Laboratory (TPFL),
Texas A&M University,
College Station, TX 77843-3123

David E. Ashpis

National Aeronautics and Space Administration,
John H. Glenn Research Center at Lewis Field,
Cleveland, OH 44135

The paper experimentally studies the effects of periodic unsteady wake flow and Reynolds number on boundary layer development, separation, reattachment, and the intermittency behavior along the suction surface of a low pressure turbine blade. Extensive unsteady boundary layer experiments were carried out at Reynolds numbers of 110,000 and 150,000 based on suction surface length and exit velocity. One steady and two different unsteady inlet flow conditions with the corresponding passing frequencies, wake velocities, and turbulence intensities were investigated. The analysis of the experimental data reveals details of boundary layer separation dynamics which is essential for understanding the physics of the separation phenomenon under periodic unsteady wake flow and different Reynolds numbers. To provide a complete picture of the transition process and separation dynamics, extensive intermittency analysis was conducted. Ensemble-averaged maximum and minimum intermittency functions were determined, leading to the relative intermittency function. In addition, the detailed intermittency analysis was aimed at answering the question as to whether the relative intermittency of a separated flow fulfills the universality criterion. [DOI: 10.1115/1.2219762]

Introduction

In recent years, gas turbine engine aerodynamicists have focused their attention on improving the efficiency and performance of the low pressure turbine (LPT) component. Research performed by the industry, research centers, and academia has shown that a reduction of the blade number can be achieved without substantially sacrificing the efficiency of the LPT blading. This reduction contributes to an increase in thrust/weight ratio, thus reducing the fuel consumption. Unlike the high pressure turbine that operates in a relatively high Reynolds number environment, the LPT of large commercial engines operates at Reynolds numbers ranging from 75,000 to 400,000. Since the major portion of the boundary layer, particularly along the suction surface, is laminar, the low Reynolds number, in conjunction with the local adverse pressure gradient, makes it susceptible to flow separation, thus increasing the complexity of the LPT boundary layer aerodynamics. The periodic unsteady nature of the incoming flow associated with wakes that originate from upstream blades substantially influences the boundary layer development, including the onset of the laminar separation, the extent of the separation bubble and its turbulent reattachment. Of particular relevance in the context of LPT aerodynamics is the interaction of the wake flow with the suction surface separation bubble. While the phenomenon of the unsteady boundary layer development and transition in the absence of the separation bubbles has been the subject of intensive research, the multiple effects of mutually interacting parameters on the LPT boundary layer separation and their physics still requires more research for full understanding.

The significance of the unsteady flow effect on efficiency and performance of compressor and turbine stages was recognized in the early seventies by several researchers. Fundamental research by Pfeil and Herbst [1], Pfeil et al. [2], and Orth [3], studied and quantified the effect of unsteady wake flow on the boundary layer transition along flat plates. Schobeiri and his coworkers [4–7] experimentally investigated the effects of the periodic unsteady wake flow and pressure gradient on boundary layer transition and heat transfer along the concave surface of a constant curvature plate. The measurements were systematically performed under different pressure gradients and unsteady wake frequencies using a squirrel cage type wake generator positioned upstream of the curved plate. Liu and Rodi [8] carried out the boundary layer and heat transfer measurements on a turbine cascade, which was installed downstream of a squirrel cage type wake generator, mentioned previously.

Analyzing the velocity and the turbulence structure of the impinging wakes and their interaction with the boundary layer, Chakka and Schobeiri [7] developed an intermittency-based unsteady boundary layer transition model. The analysis revealed a universal pattern for the relative intermittency function for all the frequencies and pressure gradients investigated. However, the above investigations were not sufficient to draw any conclusion with regard to an eventual universal character of the relative intermittency function. Further detailed investigations of the unsteady boundary layer on a high Reynolds number turbine cascade

Contributed by the International Gas Turbine Institute (IGTI) of ASME for publication in the JOURNAL OF TURBOMACHINERY. Manuscript received October 1, 2004; final manuscript received February 1, 2005. IGTI Review Chair: K. C. Hall. Paper presented at the ASME Turbo Expo 2005: Land, Sea and Air, Reno, NV, June 6–9, 2005, Paper No. GT2005-68600.

by Schobeiri et al. [9,10] and its subsequent analysis [11,12] verified the universal character of the relative intermittency function. For this purpose, Schobeiri et al. [9] utilized a conceptually different type wake generator, which is also used for the investigation presented in this paper. Fottner and his coworkers [13,14] and Schulte and Hodson [15] used the same wake generating concept for the investigations on the influence of the unsteady wake flow on the LPT-boundary layer. Kaszeta, Simon, and Ashpis [16] experimentally investigated the laminar-turbulent transition within a channel with the two curved walls resembling the suction and pressure surfaces of an LPT-blade using a retractable wake generator. Lou and Hourmouziadis [17] investigated the effect of oscillating inlet flow conditions on laminar boundary layer separation along a flat plate under LPT-pressure conditions. This was emulated by contouring the test section top wall. They studied the Reynolds number effect on the transition region. Their results showed that the higher Reynolds numbers cause an earlier transition and reduction of the transition length, while the separation point does not change its location.

Using the surface-mounted hot film measurement technique, Fottner and his coworkers [13,14], Schröder [18], and Haueisen, Hennecke, and Schröder [19] documented strong interaction between the wakes and the suction surface separation bubble on the LPT blades, both in the wind tunnel cascade tests and in a turbine rig. Furthermore, they investigated the boundary layer transition under the influence of the periodic wakes along the LPT surface and found that the interaction of the wake with the boundary layer greatly affects the loss generation. The investigations by Halstead et al. [20] on a large scale LP turbine use surface-mounted hot films to acquire detailed information about the quasi-shear stress directly on the blade surface. Investigations by Cardamone et al. [14] and Schröder [18] indicate that the benefit of the wake-boundary layer interaction can be used for the design procedure of modern gas turbine engines with a reduced LPT blade number, without altering the stage efficiency.

Most of the studies mentioned above on LP turbine cascade aerodynamics have largely concentrated on the measurement of the signals stemming from hot films mounted on the suction and pressure surfaces of the blades under investigation. Although this technique is qualitatively reflecting the interaction of the unsteady wake with the boundary layer, because of the lack of an appropriate calibration method, it is not capable of quantifying the surface properties such as the wall shear stress. The few boundary layer measurements are not comprehensive enough to provide any conclusive evidence for interpretation of the boundary layer transition and separation processes and their direct impact on profile loss, which is a critical parameter for blade design. Furthermore, the numerical simulation of the unsteady LPT blade aerodynamics, using conventional turbulence and transition models, fails if it is applied to low Reynolds number cases. Recent work presented by Cardamone et al. [14] shows that in the steady state case at Re =60,000 the separation is captured, however, for the unsteady case the separation bubble is not reproduced.

A recent experimental study by Schobeiri and Öztürk [21,22] investigated the physics of the inception, onset and extent of the separation bubble along a low pressure turbine blade, which was the first part of a series of investigations carried out at TPFL. A detailed experimental study on the behavior of the separation bubble on the suction surface of a highly loaded LPT blade under a periodic unsteady wake flow was presented in Ref. [21]. Surface pressure measurements were performed at Re=50,000, 75,000, 100,000, and 125,000. Increasing the Reynolds number has resulted in no major changes to the surface pressure distribution. They concluded that the unsteady wake flow, with its highly turbulent vortical core over the separation region, caused a periodic contraction and expansion of the separation bubble. It was proposed that, in conjunction with the pressure gradient and periodic wakes, the temporal gradient of the turbulence fluctuation, or more precisely the fluctuation acceleration $\partial \nu_{\mathrm{rms}}/\partial t$, provides a higher momentum and energy transfer into the boundary layer, energizing the separation bubble and causing it to partially or entirely disappear. They found that for $\partial \nu_{\mathrm{rms}}/\partial t > 0$ the separation bubble starts to contract, whereas for $\partial \nu_{\mathrm{rms}}/\partial t < 0$ it gradually assumes the shape before the contraction. They argued that not only the existence of higher turbulence fluctuations expressed in terms of higher turbulence intensity influences the flow separation, but also its gradient is of crucial importance in suppressing or preventing the onset and the extent of the separation bubble. They stated that the fluctuation gradient is an inherent feature of the incoming periodic wake flow, and does not exist in a statistically steady flow that might have a high turbulence intensity. They also stated that unsteady wake flow, with its highly turbulent vortical core passing over the separation region, caused a periodic contraction and expansion of the separation bubble and a reduction of the separation bubble height. Increasing the passing frequency associated with a higher turbulence intensity further reduced the separation bubble height [21].

The objective of the present study, dealing with the specific issues of the LPT boundary layer aerodynamics, is to provide detailed unsteady boundary layer flow information to understand the underlying physics of the inception, onset, and extension of the separation bubble for different Reynolds numbers. Furthermore, the unsteady boundary layer data from the present and planned experimental investigations will serve to extend the intermittency unsteady boundary layer transition model developed by Schobeiri and his coworkers [7,11,12] to the LPT cases, where a separation occurs on the suction surface at a low Reynolds number at the design and off-design incidence. The experimental results are also intended to serve as benchmark data for a comparison with numerical computation using DNS or RANS codes.

It is well known that the boundary layer measurement is one of the most time consuming aerodynamic measurements. Any attempt to increase the number of parameters to be studied would inevitably result in a substantial increase of the measurement time. Considering this fact, the research facility described in Refs. [9,10], with state-of-the-art instrumentation, has been substantially modified to systematically and efficiently study the influence of the periodic unsteady and highly turbulent flow on the LPT cascade aerodynamics at the design and off-design incidence angles, where the Reynolds number, wake impingement frequency, free-stream turbulence, and the blade solidity can be varied independently.

Experimental Research Facility

To investigate the effect of unsteady wake flow on turbine and compressor cascade aerodynamics, particularly on unsteady boundary layer transition, a multipurpose, large-scale subsonic research facility was designed and has been taken into operation since 1993. Since the facility in its original configuration is described in Refs. [9,10,21], only a brief description of the modifications and the main components is given below. The research facility consists of a large centrifugal compressor, a diffuser, a settling chamber, a nozzle, an unsteady wake generator, and a turbine cascade test section as shown in Fig. 1. The compressor, with a volumetric flow rate of 15 m^3/s, is capable of generating a maximum mean velocity of 100 m/s at the test section inlet. The settling chamber consists of five screens and one honeycomb flow straightener to control the uniformity of the flow.

Two-dimensional periodic unsteady inlet flow is simulated by the translational motion of a wake generator (see Fig. 1), with a series of cylindrical rods attached to two parallel operating timing belts driven by an electric motor. To simulate the wake width and spacing that stem from the trailing edge of rotor blades, the diameter and number of rods can be varied. The rod diameter, its distance from the LPT blade leading edge, the wake width and the corresponding drag coefficient are chosen according to the criteria outlined by Schobeiri et al. [23]. The belt-pulley system is driven by an electric motor and a frequency controller. The wake-passing

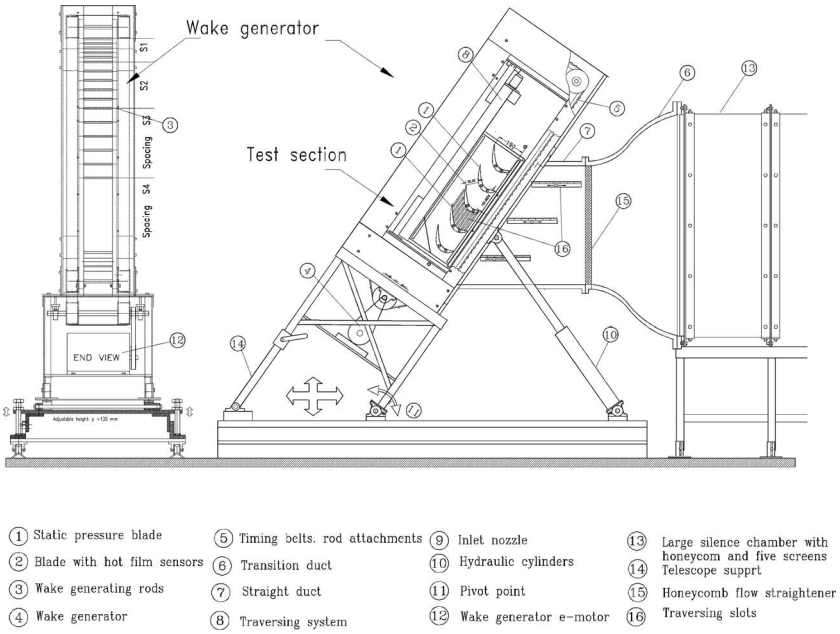

Fig. 1 Turbine cascade research facility with the components and the adjustable test section

frequency is monitored by a fiber-optic sensor. The sensor also serves as the triggering mechanism for data transfer and its initialization, which is required for ensemble-averaging. This type of wake generator produces clean, two-dimensional wakes, whose turbulence structure, decay and development are, to a great extent, predictable [23]. The unsteady boundary layer transition and heat transfer investigations [9–12] performed on this facility serve as the benchmark data for validation of turbulence models, transition models and general code assessments.

To account for a high flow deflection of the LPT cascade, the entire wake generator and test section unit, including the traversing system, was modified to allow a precise angle adjustment of the cascade relative to the incoming flow. This is done by a hydraulic platform, which simultaneously lifts and rotates the wake generator and test section unit. The unit is then attached to the tunnel exit nozzle with an angular accuracy less than 0.05 deg, which is measured electronically.

The special design of the facility and the length of the belts (L_{belt}=4960 mm) enable a considerable reduction of the measurement time. For the present investigation, two clusters of rods with constant diameters of d=2 mm are attached to the belts as shown in Fig. 2. The two clusters, with spacings S_R=160 mm and S_R =80 mm, are separated by a distance which does not have any rods, thus simulating steady state case (S_R=∞). Thus, it is possible to measure sequentially the effect of three different spacings at a single boundary layer point. To clearly define the influence domain of each individual cluster with the other one, the clusters are arranged with a certain distance between each other. Using the triggering system mentioned above and a continuous data acquisition, the buffer zones between the data clusters are clearly visible.

The data analysis program cuts the buffer zones and evaluates the data pertaining to each cluster. Comprehensive preliminary measurements were carried out to make sure that the data were exactly identical to those when the entire belt length was attached with rods of constant spacing, which corresponded to each individual cluster spacing. The cascade test section shown in Fig. 1, located downstream of the wake generator, includes five LPT blades with a height of 200.0 mm and the chord of 203.44 mm. For boundary layer investigations, five identical "Pak B" airfoils designed by Pratt & Whitney were implemented and whose cascade geometry is given in Table 1.

The blade geometry resembles the essential feature, such as the laminar boundary layer separation, that is inherent to typical LPT blades. The blade geometry was made available to NASA researchers and academia to study the specific problems of LPT flow separation, its passive and active control and its prevention. As shown in Ref. [9], this blade number is necessary and sufficient to secure a spatial periodicity for the cascade flow. Identical pressure distributions taken from blade Nos. 2 and 4 (counted from the test section bottom, Fig. 1) demonstrate the required periodicity. These blades were specially manufactured for measurement of pressure and showed identical pressure distributions.

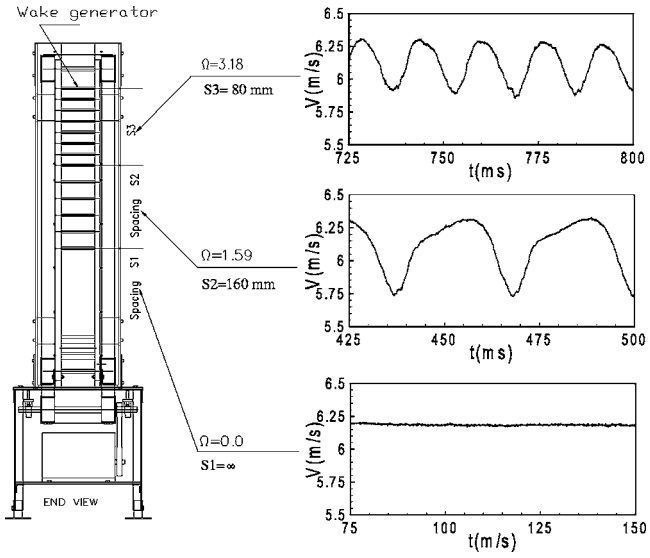

Fig. 2 Wake generator

Table 1 Parameters of turbine cascade test section

Parameters	Values	Parameters	Values
Inlet velocity	V_{in}=4 m/s	Inlet turbulence intensity	Tu_{in}=1.9%
Rod translational speed	U=5.0 m/s	Blade Re number	Re=110,000
Nozzle width	W=200.0 mm	Blade height	h_B=200 mm
Blade chord	c=203.44 mm	Cascade solidity	σ=1.248
Blade axial chord	c_{ax}=182.85 mm	Zweifel coefficient	Ψ_A=1.254
Blade suction surface length	L_{SS}=270.32 mm	Cascade angle	γ=55 deg
Cascade flow coefficient	ϕ=0.80	Cascade spacing	S_B=163 mm
Inlet air angle to the cascade	α_1=0 deg	Exit air angle from the cascade	α_2=90 deg
Rod diameter	D_R=2.0 mm	Rod distance to lead. edge	L_R=122 mm
Cluster 1 (no rod, steady)	S_R=4 ∞	Ω— parameter steady case	Ω=0.0
Cluster 2 rod spacing	S_R=160.0 mm	Ω— parameter for cluster 1	Ω=1.59
Cluster 3 rod spacing	S_R=80.0 mm	Ω— parameter for cluster 2	Ω=3.18

A computer-controlled three-axes traversing system (Fig. 3) is used to measure the inlet velocities, turbulence intensity, and the entire boundary layer distribution on suction and pressure surfaces. The traversing system was added very recently to the test section to allow the probe to reach all streamwise positions along the suction and pressure surfaces, with a positioning accuracy of 1 μm. The three-axis system is vertically mounted on the plexiglass side wall. Each axis is connected to a direct current-stepper motor with an encoder and decoder. The optical encoder provides a continuous feedback to the stepper motor for accurate positioning of the probes. The x- and y-axis of the system are capable of traversing along the suction and pressure surfaces in small steps up to 1 μm. The third axis rotates the probe holder with an angular accuracy less then $\Delta\Theta$=0.05 deg, which is specifically required for boundary layer investigations where the measurement of the laminar sublayer is of particular interest.

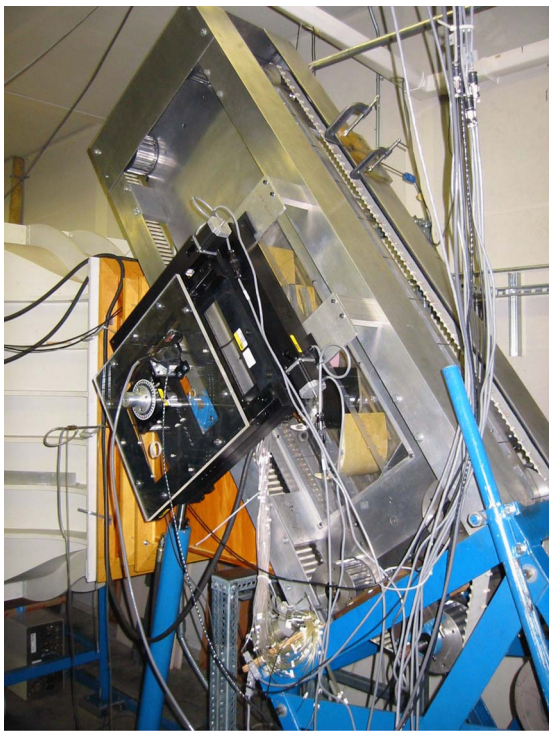

Fig. 3 Turbine cascade research facility with three-axis traversing system

Instrumentation, Data Acquisition, and Data Reduction

The data acquisition system is controlled by a personal computer that includes a 16-channel, 12-bit analog-digital (A/D) board. Time-dependent velocity signals are obtained by using a commercial three-channel, constant temperature hot wire anemometer system that has a signal conditioner with a variable low pass filter and adjustable gain. A hot wire probe placed upstream of the diffuser monitors the reference velocity at a fixed location. The pneumatic probes are connected to high precision differential pressure transducers for digital readout. Several calibrated thermocouples are placed downstream of the test section to constantly monitor the flow temperature. The wake generator speed and the passing frequency signals of the rods are transmitted by a fiber-optic trigger sensor. The passage signals of the rods are detected by the sensor using a silver-coated reflective paint on one of the belts. This sensor gives an accurate readout of the speed of the wake generator and the passing frequency of the rods. The signals of the pressure transducers, thermocouples and trigger sensors are transmitted to the A/D board and are sampled by the computer. To ensure the cascade periodicity, the second and fourth blades are each instrumented with 48 static pressure taps. Two adjacent blades are used for boundary layer measurement. The taps are connected to a scanivalve, which sequentially transfers the pressure signals to one of the transducers connected to the A/D board.

The unsteady data are taken by calibrated, custom designed miniature single hot wire probes. At each boundary layer position, samples were taken at a rate of 20 kHz for each 100 revolutions of the wake generator. The data were ensemble averaged with respect to the rotational period of the wake generator. Before final data were taken, the number of samples per revolution and the total number of revolutions were varied to determine the optimum settings for convergence of the ensemble average.

For the steady state case, the instantaneous velocity components are calculated from the temperature-compensated instantaneous voltages by using the calibration coefficients. The instantaneous velocity can be represented in the following form:

$$V = \bar{V} + \nu \tag{1}$$

where $\bar{V}$ is the mean (time-averaged) velocity and ν is the turbulent fluctuation component. The mean velocity, also known as the time average, is given by

$$\bar{V} = \frac{1}{M}\sum_{j=1}^{M} V_j \tag{2}$$

where M is the total number of samples at one boundary layer location. The root mean square value of the turbulent velocity fluctuation is

$$\nu = \sqrt{\frac{1}{M}\sum_{j=1}^{M}(V_j - \bar{V})^2} \tag{3}$$

and the local turbulence intensity is defined as:

$$\mathrm{Tu}_{\mathrm{luc}} = \frac{\nu}{\bar{V}} \times 100 = \frac{1}{\bar{V}}\sqrt{\frac{1}{M}\sum_{j=1}^{M}(V_j - \bar{V})^2} \times 100 \tag{4}$$

For unsteady cases, the ensemble-averaged velocity, fluctuation velocity, and the turbulence intensity were calculated from the instantaneous velocity samples by:

$$V_i(t_i) \equiv \langle V_i(t_i)\rangle = \frac{1}{N}\sum_{j=1}^{N} V_{ij}(t_i) \tag{5}$$

$$\nu_i(t_i) \equiv \langle \nu_i(t_i)\rangle = \sqrt{\frac{1}{N}\sum_{j=1}^{N}[V_{ij}(t_i) - \langle V_i(t_i)\rangle]^2} \tag{6}$$

$$\mathrm{Tu}_i(t_i) \equiv \langle \mathrm{Tu}_i(t_i)\rangle = \frac{\langle \nu_i(t_i)\rangle}{\langle V_i(t_i)\rangle} \times 100 \tag{7}$$

where $N=100$ is the total number of wake generator periods and M is the number of samples taken per period. $\langle V_i(t_i)\rangle$ is the ensemble-averaged velocity for the particular boundary layer traverse.

Experimental Results and Discussion

Detailed surface pressure and boundary layer measurements were performed at Reynolds numbers of 110,000 and 150,000. These Reynolds numbers, which pertain to a typical cruise operation, exhibit a representative value within LPT operating range between 75,000 and 400,000, as discussed by Hourmouziadis [24]. Furthermore, it produces separation bubbles that can be accurately measured by miniature hot wire probes. For the Reynolds numbers of 110,000 and 150,000, three different reduced frequencies were examined. To generate unsteady wakes, cylindrical rods with the diameter $d_R=2$ mm were chosen to fulfill the similar criterion that requires the generation of a drag coefficient, C_D, that is approximately equal to the C_D of the turbine blade with the chord and spacing given in Table 1 (for details we refer to the studies in Refs. [23,25]). Furthermore, we define a reduced frequency Ω that includes the cascade solidity σ, the flow coefficient φ, the blade spacing S_B, and the rod spacing S_R. The reduced frequency Ω is an extension of Strouhal number, in the sense that it incorporates the rod spacing S_R and the blade spacing S_B in addition to the inlet velocity and wake generator speed. For surface pressure measurement, rods with uniform spacing as specified in Table 1 were attached over the entire belt length. For boundary layer measurement, however, clusters of rods were attached, as mentioned previously.

Surface Pressure Distributions. Detailed pneumatic surface pressure measurements were taken at Re=110,000 and 150,000. For each Reynolds number, three different reduced frequencies, namely $\Omega=0.0$, 1.59, and 3.18, are applied that correspond to the rod spacings $S_R=\infty$ (no rod), 160, and 80 mm. The pressure distributions in Fig. 4 show the results of the steady case and two unsteady cases. The pressure signals inherently signify the time-averaged pressure, because of the internal pneumatic damping effect of the connecting pipes to the transducer. The noticeable deviation in pressure distribution between the steady and unsteady cases, especially on the suction surface, is due to the drag forces caused by the moving rods. The drag forces are imposed on the main stream and cause momentum deficiency that leads to a reduction of the total and static pressure. The time-averaged pressure coefficients along the pressure and suction surfaces are plotted in Fig. 4. The suction surface (upper portion) exhibits a strong

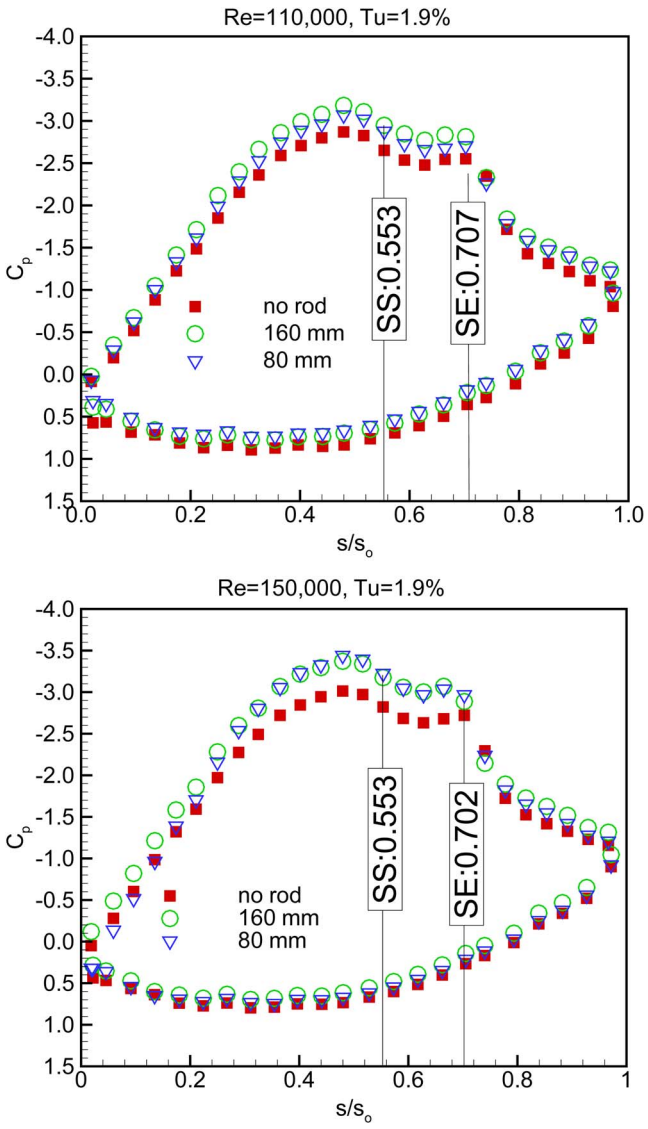

Fig. 4 Static pressure distributions at two different Re numbers and reduced frequencies $\Omega=0$, 1.59, 3.18 (no rod, 160, 80 mm), SS=separation start, SE=separation end

negative pressure gradient. The flow accelerates at a relatively steep rate and reaches its maximum surface velocity that corresponds to the minimum $C_p=-3.5$ at $s/s_0=0.42$. Passing through the minimum pressure, the fluid particles within the boundary layer encounter a positive pressure gradient that causes a sharp deceleration up to $s/s_0=0.55$. This point signifies the beginning of the laminar boundary layer separation and the onset of a separation bubble. As seen in the subsequent boundary layer discussion, the separation bubble characterized by a constant C_p plateau extends up to $s/s_0\approx0.74$, thus occupying more than 19% of the suction surface and constituting a large separation. Passing the plateau, the flow first experiences a second sharp deceleration indicative of a process of reattachment, followed by a further deceleration at a moderate rate. On the pressure surface, the flow accelerates at a very slow rate, reaches a minimum pressure coefficient at $s/s_0=0.42$, and continues to accelerate until the trailing edge has been reached. Unlike the suction surface, the pressure surface boundary layer does not encounter any adverse positive pressure gradient that triggers separation. However, close to the leading edge, a small plateau extending from $s/s_0=0.08-0.16$ indicates the existence of a small size separation bubble that might be attributed to a minor inlet flow incidence angle.

Considering the unsteady case with the reduced frequency $\Omega=1.59$ corresponding to a rod spacing of $S_R=160$ mm, Fig. 4 exhibits a slight difference in the pressure distribution between the steady and unsteady cases. As mentioned above, this deviation is attributed to the momentum deficiency that leads to a reduction of the total and static pressure. For Re=110,000, the wakes have a reducing impact on the streamwise extent of the separation plateau. As seen in Fig. 4(*a*), the trailing edge of the plateau has shifted from $s/s_0=0.74$ to $s/s_0=0.702$. This shift reduced the streamwise extent of the separation plateau from 19% to 15% of the suction surface length which is, in this particular case, 21% of reduction in streamwise extent of the separation. Increasing the reduced frequency to $\Omega=3.18$ by reducing the rod spacing to $S_R=80$ mm causes a slight shift of the C_p distribution compared with $\Omega=1.59$ case. One should bear in mind that pneumatically measured surface pressure distribution represents a time integral of the pressure events only.

Increasing the Reynolds number to Re=150,000 has not brought major changes in steady state C_p distribution. However, the combination of higher Reynolds number with unsteady wakes reveals the noticeable deviation on the streamwise extent of the separation plateau. As seen in Fig. 4(*b*), the trailing edge of the plateau has shifted from $s/s_0=0.74$ to $s/s_0=0.702$ for Reynolds number of 150,000. The combination of higher Reynolds number with high unsteady wakes introduce fluctuation kinetic energy into the boundary layer which tends to inhibit the separation tendency. C_p distribution clearly shows that the wake impingement with higher Reynolds number shortens the streamwise extent of the separation zone compared to the steady case.

Detailed information regarding the structure of the separation bubble is delivered by means of a detailed unsteady boundary layer measurement using hot wire probes, as will be discussed in the subsequent sections.

Time Averaged Velocity and Fluctuation Distributions. Following the surface pressure investigations that mainly addressed the onset and extent of the separation zone discussed previously, comprehensive boundary layer measurements were performed to identify the streamwise and normal extent, as well as the deformation of the separation zone under unsteady wake flow. The steady state case serves as the reference configuration.

Consistent with the surface pressure distribution above, the effect of the wake frequency on the time-averaged velocity profiles and fluctuation velocity distribution are presented for one steady and two unsteady inlet flow conditions on the suction surface along 31 streamwise locations for the Reynolds number of 110,000, and 41 streamwise locations for the Reynolds number of 150,000. After completing the velocity measurements, the boundary layer coordinates were transformed into a blade orthogonal coordinate system. Velocities at blade normal positions were obtained by interpolating their transformed values. The results showed almost no difference between the interpolated and noninterpolated velocity data. Experimental investigations were performed for three different values of $\Omega=0.0$, 1.59, and 3.18. These values cover the reduced frequency range encountered in LPT design and off-design operation conditions.

The effect of wake frequency on time-averaged velocity and velocity fluctuation distributions is shown in Figs. 5–8 at six representative streamwise locations for Re=110,000 and Re=150,000. Among 31 streamwise positions measured along the suction surface, Figs. 5 and 6 display the velocity and fluctuation distributions at one streamwise position upstream, three positions within and two positions downstream of the separation bubble. The diagrams include the steady state data for reference purposes, $\Omega=0.0$ ($S_R=\infty$), unsteady data for $\Omega=1.59$ ($S_R=160$ mm) and $\Omega=3.18$ ($S_R=80$ mm).

As Fig. 5 indicates, in the upstream region of the separation bubble the flow is fully attached. At $s/s_0=0.49$, the velocity distributions inside and outside the boundary layer experience a hardly noticeable decrease with increasing the reduced frequency. At the same positions, however, the time-averaged velocity fluctuations shown in Fig. 6 exhibit substantial changes within the

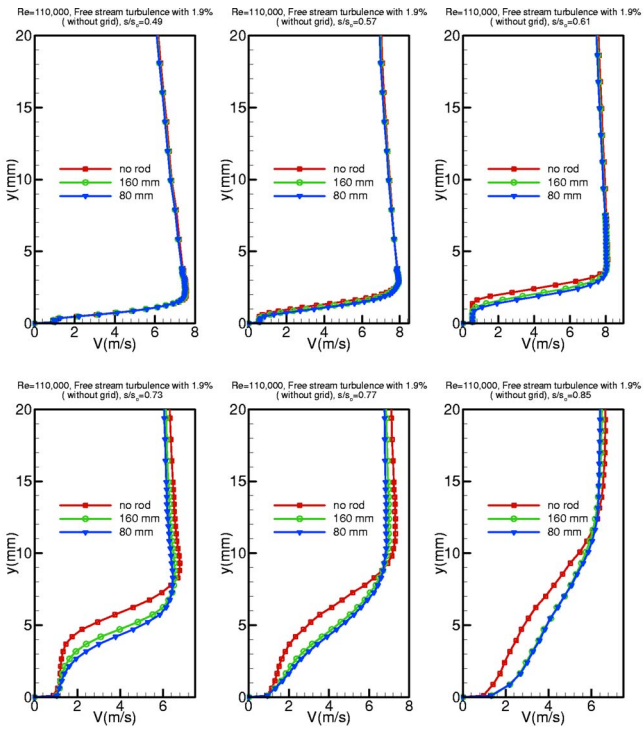

Fig. 5 Distribution of time-averaged velocities along the suction surface for steady case $\Omega=0$ ($S_R=\infty$) and unsteady cases $\Omega=1.59$ ($S_R=160$ mm) and $\Omega=3.18$ ($S_R=80$ mm) at Re=110,000

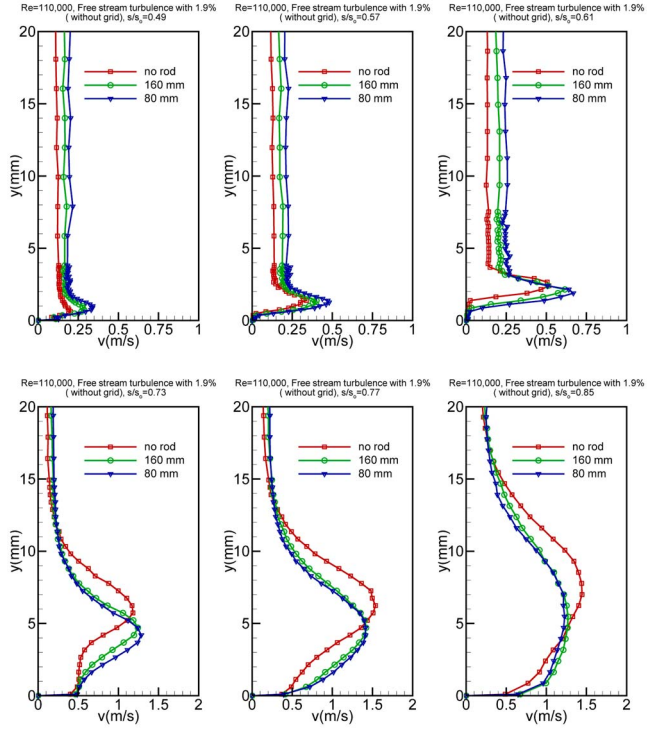

Fig. 6 Distribution of time-averaged velocity fluctuations along the suction surface for steady case $\Omega=0$ ($S_R=\infty$) and unsteady cases $\Omega=1.59$ ($S_R=160$ mm) and $\Omega=3.18$ ($S_R=80$ mm) at Re=110,000

boundary layer, as well as outside it. The introduction of the periodic unsteady wakes with highly turbulent vortical cores and the subsequent mixing has systematically increased the free-stream turbulence level from 1.9% in steady case to almost 3% for $\Omega=3.18$ ($S_R=80$ mm). Comparing the unsteady cases, $\Omega=1.59$ and 3.18, with the steady reference case, $\Omega=0.0$, indicates that with increasing Ω the lateral position of the maximum velocity fluctuation shifts away from the wall. This is due to the periodic disturbance of the stable laminar boundary layer upstream of the separation bubble.

As Fig. 6 shows, a substantial influence of the wake frequency is observed inside the separation bubble at $s/s_0=0.57$, $s/s_0=0.61$, and $s/s_0=0.73$. The wake impingement introduces fluctuation kinetic energy stemming from its vortical core into the boundary layer, trying to energize it and to reverse the separation tendency. As seen from the velocity profiles, the wake frequency effect shortens the bubble height and reduces its streamwise extent. Compared to the steady case, however, the onset of the separation bubble has not changed substantially. This shows that, although the impingement of the vortical wake core periodically reduces the separation bubble height, it does not have sufficient momentum to completely suppress it. Figure 6 displays the details of the turbulence fluctuation activities in and outside of the separation bubble at $s/s_o=0.57$, $s/s_o=0.61$, and $s/s_o=0.73$. Strong turbulent activities are measured within the separation bubble that extends to the shear layer. Outside the separation bubble, the turbulence activities rapidly decrease, approaching the free-stream levels that correspond to the individual unsteady frequency discussed above. A comparison of the unsteady cases, $\Omega=1.59$ and 3.18, with the steady reference case, $\Omega=0.0$, indicates that with increasing Ω the lateral position of the maximum fluctuation shifts toward the wall. This is the consequence of the overall decrease of the lateral extension of the separation bubble as a result of wake impingement.

Close to the bubble trailing edge at $s/s_o=0.73$ and $s/s_o=0.77$, Fig. 5 shows that the undisturbed flow, $\Omega=0$ ($S_R=\infty$), still has its inflectional pattern. The perturbation by impinging the wakes causes the velocity profile to become fully turbulent and attached. Once the profile becomes fully turbulent, increasing the reduced frequency from $\Omega=1.59$ ($S_R=160$ mm) to $\Omega=3.18$ ($S_R=80$ mm) does not substantially change the velocity distribution pattern. Figure 6 displays the details of the velocity fluctuation activities inside and outside of the reattached boundary layer at $s/s_o=0.77$ and $s/s_o=0.85$. As in Fig. 5, once the velocity profile has become fully turbulent, its corresponding fluctuation distribution remains almost unchanged.

In the context of transitional and turbulent boundary layer flow investigations, it is worth noting the different behavior of these boundary layer types. According to the previous investigations by Schobeiri et al. [10–12] in a HP-turbine cascade with transitional boundary layer throughout, an increased wake frequency causes turbulence fluctuations to rise inside and outside the boundary layer. However, in the LPT case with the boundary layer separation, once the boundary layer is reattached and the velocity distribution assumes a fully turbulent profile, no major changes are observed either in the velocity or in the fluctuation velocity distribution.

For Re=150,000, Figs. 7 and 8 display the velocity and velocity fluctuation distributions at the same streamwise locations as discussed above. Likewise, the diagrams include the steady state, $\Omega=0.0$, data for reference purposes and the unsteady data for $\Omega=1.59$ and $\Omega=3.18$. Although the results for Re=150,000 show very similar velocity and fluctuation patterns, it is observed that the starting point of the separation bubble and its reattachment point have moved slightly further downstream. This is clearly visible in Fig. 7, at $s/s_o=0.73$ and $s/s_o=0.77$, where the inflectional pattern of the velocity profiles indicates that the above streamwise positions are located close to the trailing edge within the separation bubble. Increasing the frequency from $\Omega=0$ ($S_R=\infty$) to $\Omega=3.18$ ($S_R=80$ mm) brings the profiles closer to the fully turbulent pattern, without collapsing. The same statement is true for the turbulence fluctuations, Fig. 8, at $s/s_o=0.73$ and $s/s_o=0.77$. Also,

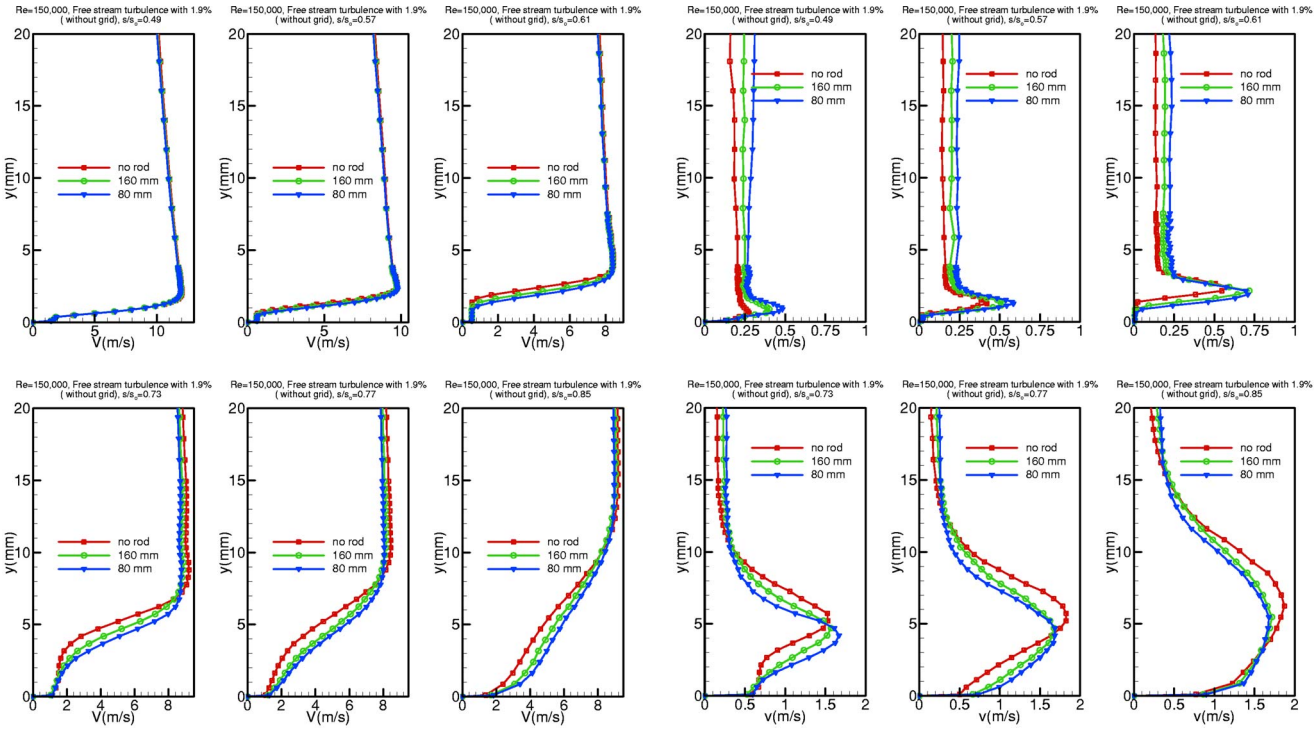

Fig. 7 Distribution of time-averaged velocity distributions along the suction surface for steady case $\Omega=0$ ($S_R=\infty$) and unsteady cases $\Omega=1.59$ ($S_R=160$ mm) and $\Omega=3.18$ ($S_R=80$ mm) at Re=150,000

Fig. 8 Distribution of time-averaged fluctuation velocities along the suction surface for steady case $\Omega=0$ ($S_R=\infty$) and unsteady cases $\Omega=1.59$ ($S_R=160$ mm) and $\Omega=3.18$ ($S_R=80$ mm) at Re=150,000

the size of the separation bubble is smaller when compared to that for Re=110,000. To achieve a noticeable impact of the Reynolds number on the onset and extent of the bubble, the Reynolds number needed to increase above 150,000.

Temporal Behavior of the Separation Zone Under Periodic Unsteady Wake Flow. Velocity distributions on the suction surface with time as the parameter are plotted in Figs. 9–12 for Re =110,000, 150,000 for rod spacings S_R=80 mm and S_R =160 mm that correspond to Ω=1.59 and 3.18. The nondimensional time (t/τ) values are chosen that they represent the temporal states within one full period of wake passing. For Re =110,000, Figs. 9(*a*)–9(*f*) show the velocity distributions, inside and outside the boundary layer at fixed s/s_o locations, experience moderate to pronounced changes. Figure 9(*a*) represents the instantaneous velocity distribution upstream of the separation zone, followed by Figs. 9(*b*)–9(*f*) which represent the velocity distributions inside the separation zone. In discussing the following results, we simultaneously refer to the wake distribution as well as the turbulence fluctuation results.

Figure 9(*a*) exhibits the velocity distribution on the suction surface at s/s_o=0.49. At this streamwise position, the laminar boundary layer is subjected to a strong negative pressure gradient. The velocity distributions at different (t/τ) experience changes in magnitude that reflect the corresponding changes of the impinging periodic wake velocity. It is worth noting that, despite the injection of turbulence kinetic energy by the impinging wakes, no local instantaneous boundary layer transition occurs. This is because of the strong negative pressure gradient that prevents the boundary layer from becoming instantaneously transitional. Instantaneous velocity distributions inside the separation zone are shown in Figs. 9(*b*)–9(*f*).

As a representative case, we discuss the results plotted in Fig. 9(*e*) at s/s_o=0.65. During the time interval from t/τ close to 0.5 (1.5, 2.5, etc.) to about t/τ=0.75 (1.75, 2.75, etc.), the separation zone is exposed to the wake external flow with relatively lower turbulence level. This flow does not have the capability to suppress the separation zone. Thus, the separation region is clearly shown by the velocity distributions at t/τ=0.5 and t/τ=0.75. As the wake passes over the blade at s/s_o=0.65 introducing high turbulence kinetic energy into the boundary layer, the boundary layer is energized, causing the separation zone to partially reduce. To emphasize this statement, the steady state velocity distribution at the same streamwise position is also plotted in Fig. 9(*e*) using full circles. It shows clearly the separated nature of the boundary layer which coincides with the instantaneous velocity profile at t/τ=0.75. Intermediate times reflect the gradual change between different t/τ states as the flow is undergoing the influence of the oncoming wake. Moving to the trailing edge of the separation zone, at s/s_o=0.73, Fig. 9(*f*), a partial reduction in boundary layer thickness as the result of wake impingement is visible, however, the separation zone does not seem to disappear.

Figures 10(*a*)–10(*f*) show that the velocity distributions outside the boundary layer at fixed s/s_o locations experience noticeable changes at Ω=3.18 (S_R=80 mm). Increasing the wake passing frequency causes the wake turbulence kinetic energy to increase, resulting in a stronger suppression compared with the Ω=1.59 (S_R=160 mm) case. As seen in Figs. 11 and 12, increasing the Reynolds number to 150,000 causes the leading and trailing edges of the separation bubble to move further downstream. It is also observed that increasing the Reynolds number reduces the size of the separation bubble.

The effect of the periodic unsteady wakes on the onset and extent of the separation bubble is shown in Figs. 13–16 for Re =110,000 and 150,000, and for two different frequencies, namely Ω=1.59 and Ω=3.18. These figures display the full extent of the separation bubble and its behavior under a periodic wake flow impingement at different t/τ. The wake propagation for Ω=1.59 and Ω=3.18 is analyzed and the value of t/τ corresponds to the point in the cycle at which the data acquisition system is triggered. During a rod passing period, the wake flow and the separation bubble undergo a sequence of flow states which are not noticeably

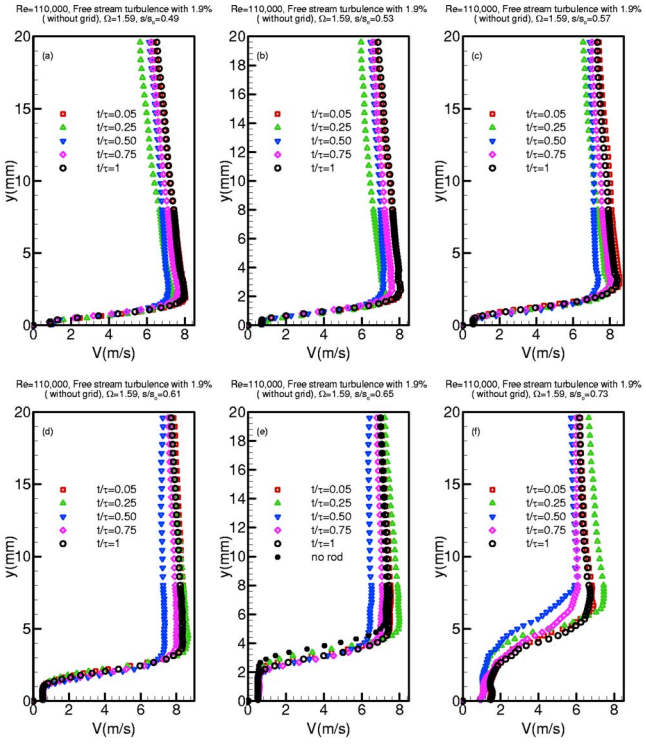

Fig. 9 Distribution of the ensemble-averaged velocity development along the suction surface for different s/s_0 with time t/τ as parameter for Ω=1.59 (S_R=160 mm) and Re=110,000

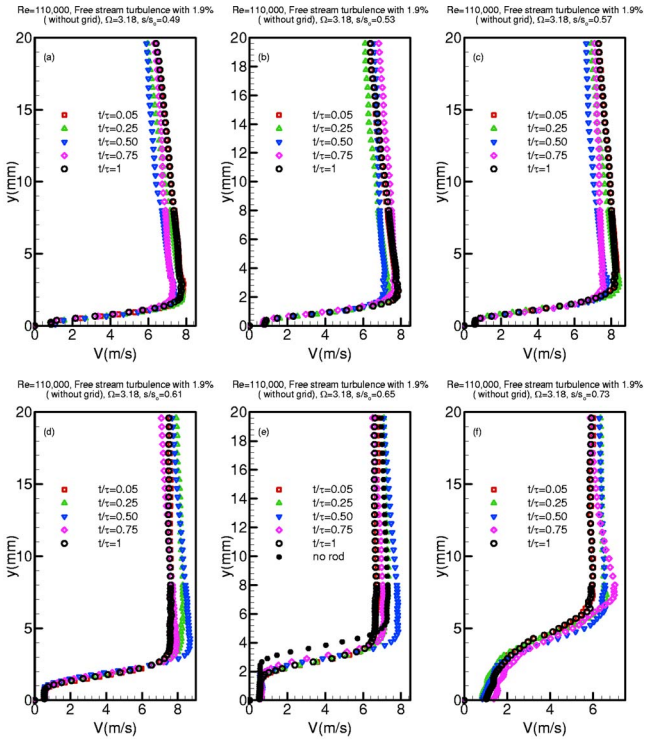

Fig. 10 Distribution of the ensemble-averaged velocity development along the suction surface for different s/s_0 with time t/τ as parameter for Ω=3.18 (S_R=80 mm) and Re=110,000

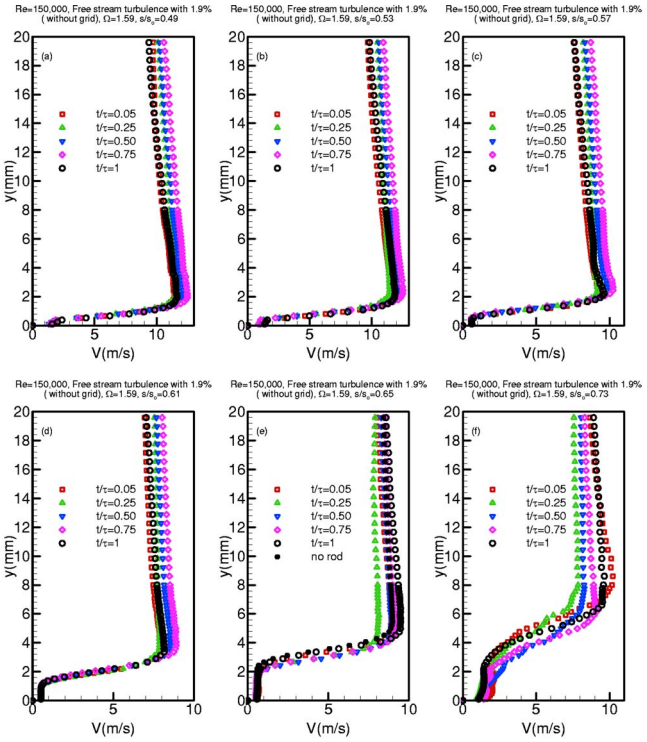

Fig. 11 Distribution of the ensemble-averaged velocity development along the suction surface for different s/s_0 with time t/τ as parameter for $\Omega=1.59$ ($S_R=160$ mm) and Re=150,000

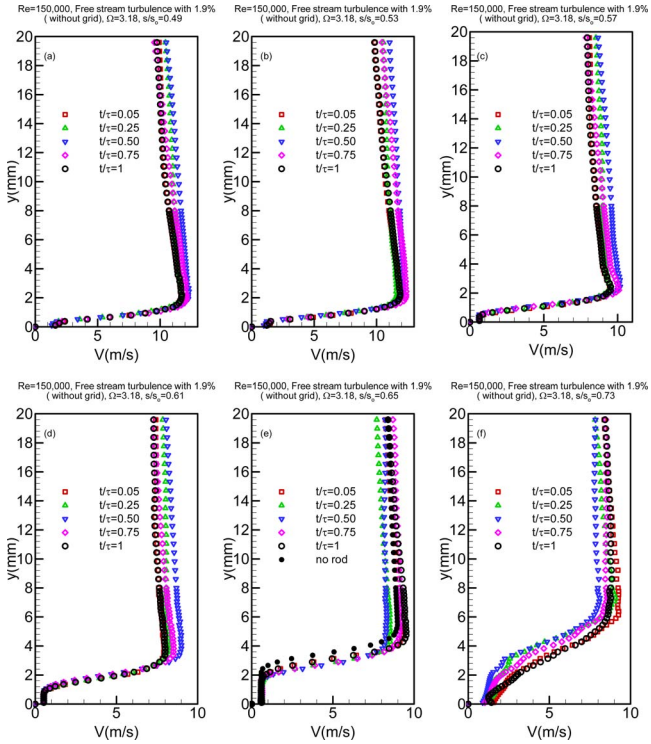

Fig. 12 Distribution of the ensemble-averaged velocity development along the suction surface for different s/s_0 with time t/τ as parameter for $\Omega=3.18$ ($S_R=80$ mm) and Re=150,000

different when the unsteady data are time averaged.

Starting with Re=100,000 and $\Omega=1.59$, Fig. 13(*a*) exhibits the separation bubble in its full size at $t/\tau=0.25$. At this instant of time, the incoming wakes have not reached the separation bubble. At $t/\tau=0.5$, the wake, with its highly turbulent vortical core, passes over the blade and generates high turbulence kinetic energy. At this point, the wake turbulence penetrates into the bubble causing a strong mass, momentum, and energy exchange between the wake flow and the fluid contained within the bubble. This exchange causes a dynamic suppression and a subsequent contraction of the bubble. As the wake travels over the bubble, the size of the bubble continues to contract at $t/\tau=0.75$ and reaches its minimum size at $t/\tau=1.0$. At $t/\tau=1$, the full effect of the wake on the boundary layer can be seen before another wake appears and the bubble moves back to the original position. Similar results are observed when operating at the same Reynolds number, Re =110,000, but at a higher reduced frequency, $\Omega=3.18$, Figs. 14(*a*)–14(*d*). A comparison of Figs. 14(*a*)–14(*d*) with Figs. 12(*a*)–12(*d*) illustrates the pronounced influence of higher reduced frequency which causes more frequent penetration of wake turbulence into the separation bubble, causing a stronger suppression and subsequent contraction of the bubble.

Figures 15 and 16 display the behavior of the separation bubble under higher Reynolds number, Re=150,000, and reduced frequencies, $\Omega=1.59$ and $\Omega=3.18$. While the higher Reynolds number moves the separation bubble further downstream. Similar contracting effects as discussed above are observed at $\Omega=1.59$. However, doubling the reduced frequency and increasing the Reynolds number is associated with the higher turbulence intensity that leads to stronger suppression of the separation bubble, as shown in Figs. 15 and 16.

Intermittency Analysis

Intermittency distribution, which identifies whether the flow is laminar or turbulent inside the boundary layer, is calculated following the method of Hedley and Keffer [26]. Instantaneous velocity is sensitized to increase its discriminatory capabilities between turbulent and nonturbulent parts of the signal. For this purpose, the multiplication of the first derivative of the velocity signal and the velocity signal is used for further analysis. This is called the detector function, $S(t)$, defined as

$$S(t) = \left| u \frac{\partial u}{\partial t} \right| \tag{8}$$

The above detector function is used by many researchers, including Antonia and Bradshaw [27], Kovasznay et al. [28], Bradshaw and Murlis [29], and Schobeiri and his coworkers [7,12]. A very recent paper by Schobeiri [30] extensively discusses different issues relative to intermittency based transition modeling. Though sensitized detector function separates the turbulent and nonturbulent zones of the fluid, there is still some overlap between the two near the origins. The discrimination between the two zones of the flow will be ideal when the overlap between the two distributions is minimal or zero. To eliminate the disturbing effects of the velocity signal peaks, a smoothing procedure is applied to the $S(t)$ signal. The mean value of ten consecutive $S(t)$ values is calculated and the ten values are substituted by their mean value of $S_{\text{sm}}(t)$. After smoothing the detector function, a threshold level C is then applied to the smoothed detector function to distinguish between true turbulence and the signal *noise*. It is defined as

$$I(t) = \begin{cases} 1 \text{ when } S_{\text{sm}}(t) \geqslant C \\ 0 \text{ when } S_{\text{sm}}(t) < C \end{cases} \tag{9}$$

Once the threshold level is applied to the detector function $S(t)$, the result is a random square wave called the indicator function I, with 0's representing the nonturbulent case and 1's indicating the turbulent behavior of the boundary layer. A threshold level, C, of 1.2 is used for all the data on the suction surface. In the absence of length scales, this value is chosen from visual observations. Several other values of C are tested and little qualitative difference is seen in the intermittency distribution during transition. Though the

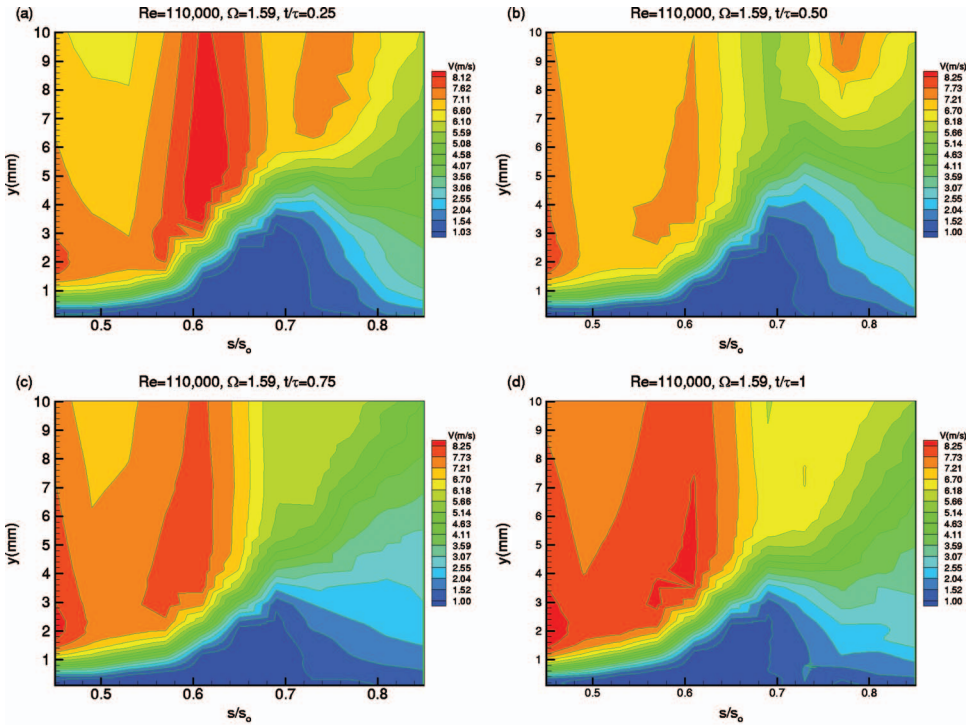

Fig. 13 Ensemble-averaged velocity contours along the suction surface for different s/s_0 with time t/τ as parameter for $\Omega=1.59$ ($S_R=160$ mm), Re=110,000

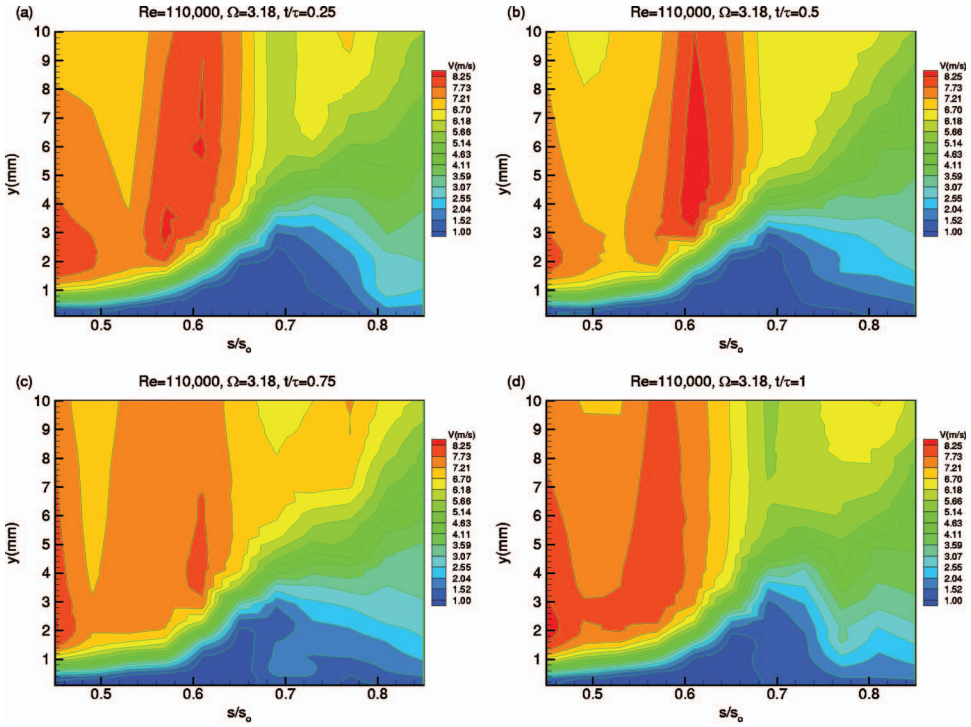

Fig. 14 Ensemble-averaged velocity contours along the suction surface for different s/s_0 with time t/τ as parameter for $\Omega=3.18$ ($S_R=80$ mm), Re=110,000

intermittency values vary with different values of C, the important parameters like start and end of transition are not affected by C. The resulting square wave after applying the threshold is ensemble averaged to get the ensemble-averaged intermittency as follows

$$\langle \gamma_i(t_i) \rangle = \frac{1}{N} \sum_{j=1}^{N} I_{ij}(t_i) \tag{10}$$

where N is the number of revolutions of the wake generator for which the data are collected. For time-averaged intermittency,

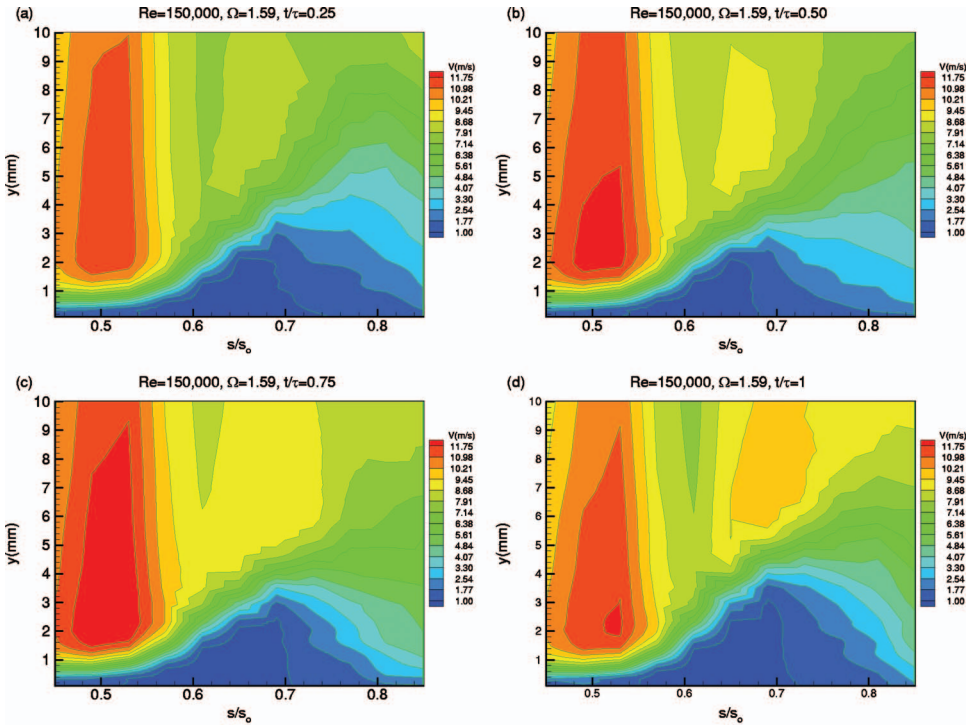

Fig. 15 Ensemble-averaged velocity contours along the suction surface for different s/s_0 with time t/τ as parameter for $\Omega=1.59$ ($S_R=160$ mm), Re=150,000

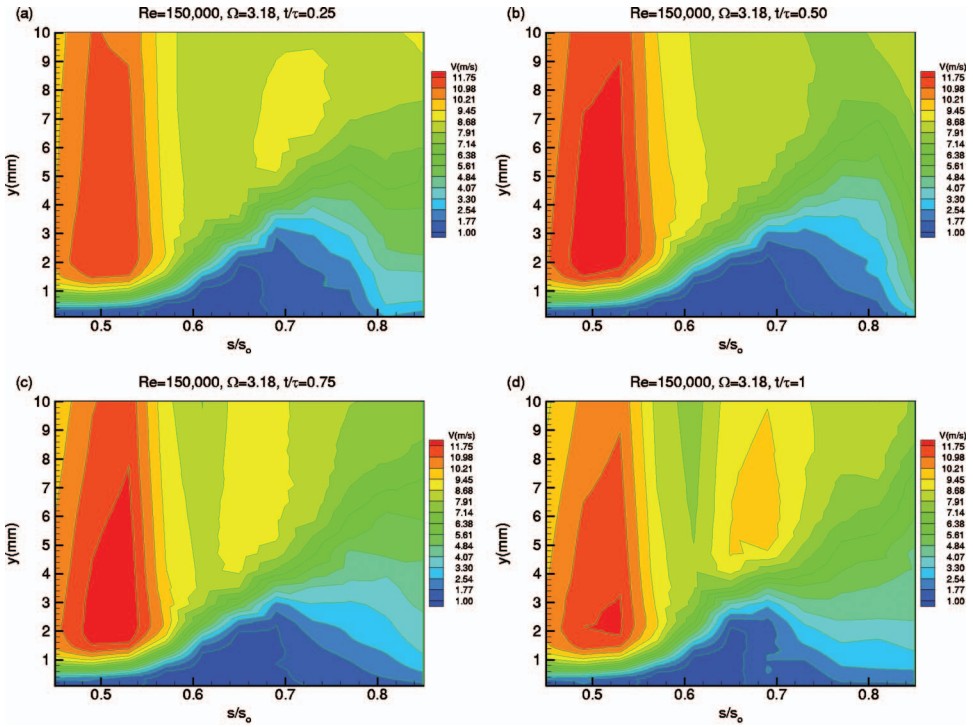

Fig. 16 Ensemble-averaged velocity contours along the suction surface for different s/s_0 with time t/τ as parameter for $\Omega=3.18$ ($S_R=80$ mm), Re=150,000

$\langle \gamma_i(t_i) \rangle$ is integrated with respect to time to arrive at

$$\bar{\gamma} = \frac{1}{T}\int_{t=0}^{T} \langle \gamma_i(t_i) \rangle dt \tag{11}$$

Figure 17 shows the processing of instantaneous velocities.

Ensemble-Averaged Intermittency Distribution. Figure 18 presents the temporal-spatial contours of the ensemble-averaged intermittency distribution at three different lateral positions above the blade suction surface, $y=1.341$, 1.755, and 6.10 mm, for two reduced frequencies, $\Omega=1.59$ and $\Omega=3.18$. For better comparison of the effects of the impinging wake frequency, Fig. 18 exhibits

only the first three wakes. In this figure, the wakes with the highly vortical cores display intermittency values close to 0.6 indicating the transitional character of the boundary layer at the particular instant of time of wake impingement on the surface. Intermittency is approximately equal to zero outside the wake region near the leading edge, showing the nonturbulent behavior of the flow.

The wakes represented by narrow green strips pass through the turbine blade channel and periodically switch the boundary layer from laminar to turbulent and vice versa. Upstream of the separation bubble a pretransitional strip with an ensemble-averaged intermittency of $\gamma(t) \approx 0.5$ starting at $s/s_0 \approx 0.43$ and ending at $s/s_0 \approx 0.52$ separates the attached boundary layer from the bubble leading edge. At $s/s_0 \approx 0.52$, the visibility of the wake vanishes due to the interaction with the separation bubble. As Fig. 18 shows, the separation bubble starts at $s/s_0 \approx 0.52$ and extends up to $s/s_0 \approx 0.75$, thus occupying more than 24% of the suction surface and forming a large separation zone. At $s/s_0 \approx 0.75$, the intermittency field in Figure 18(*a*) displays an abrupt change in intermittency level, which indicates the start of a reattachment process. Once the wake passes over the separation zone, its signature reappears again as spots, with higher intermittency level (red) associated with becalmed zones (blue). Increasing Ω to 3.18, Fig. 18(*b*), causes an earlier mixing of the impinging wakes which results in widening the areas occupied by the wake vortical core, thus reducing the wake external region. Figure 18(*b*) suggests that further increase of Ω may lead to a complete degeneration of the deterministic periodic wake flow into a stochastic turbulence. Figures 18(*c*)–18(*f*) display the intermittency distributions at higher normal position from the blade surface. They are quite identical with Figs. 18(*a*) and 18(*b*) discussed above.

The intermittency distributions in Fig. 18 clearly show the unsteady nature of the boundary layer transition. In this form, however, they cannot quantitatively describe the complex unsteady transition, separation and reattachment process. To establish the basic relations essential for a quantitative description of the unsteady boundary layer transition, we resort to the fundamental study by Schobeiri and his coworkers [23] that deals with the physics of steady and unsteady wake development in a curved environment. The study clearly shows that the turbulence structure of the steady and unsteady wake flow is determined by the wake defect, which is a Gaussian function. Following the above study, we define a dimensionless parameter

$$\zeta = \frac{tU_w}{b} = \frac{ts_R}{\tau b} = \frac{\xi_2}{b} \text{ with } b = \frac{1}{\sqrt{\pi}} \int_{-\infty}^{+\infty} \Gamma d\xi_2 \tag{12}$$

Equation (12) relates the wake passing time t with the wake passing velocity in the lateral direction U_w, and the intermittency width b, with ξ_2 as the lateral distance from the wake center [23]. The intermittency width b is directly related to the wake width introduced by Schobeiri and his coworkers [7,12,23]. In an analogous way to find the defect function, we define the relative intermittency, Γ, as

$$\Gamma = \frac{\langle \gamma_i(t_i) \rangle - \langle \gamma_i(t_i) \rangle_{\min}}{\langle \gamma_i(t_i) \rangle_{\max} - \langle \gamma_i(t_i) \rangle_{\min}} \tag{13}$$

In the above equation, $\langle \gamma_i(t_i) \rangle$ is the time dependent ensemble-averaged intermittency function, which determines the transitional nature of an unsteady boundary layer. The intermittency $\langle \gamma_i(t_i) \rangle_{\max}$ exhibits the maximum intermittency value inside the wake vortical core. Finally, $\langle \gamma_i(t_i) \rangle_{\min}$ represents the minimum ensemble-averaged intermittency values outside the wake vortical core.

A representative relative intermittency function, Γ, is shown in Figs. 19(*a*)–19(*d*) for a frequency value of $\Omega = 1.59$ at lateral distances from the blade surface of $y = 0.858$, 0.996, 5.3, and 9.3 mm, with the dimensionless longitudinal distance s/s_0 as a parameter. The above distances are representative for intermittency distributions before, inside and outside the separation bubble over the entire suction surface. The symbols represent the experimental data. As seen for the reduced frequency of $\Omega = 1.59$, the measured relative intermittency functions follow very closely a Gaussian distribution, given by

$$\Gamma = e^{-\zeta^2} \tag{14}$$

with ζ as the nondimensionalized lateral length scale defined in Eq. (12). The slight deviation within and after the separation zone is due to a difficulty associated with capturing the maximum and minimum intermittencies. Using Eq. (14) as a generally valid intermittency relationship for unsteady wake flows, the intermittency function $\langle \gamma_i(t_i) \rangle$ is completely determined if additional information about the intermittency functions $\langle \gamma_i(t_i) \rangle_{\max}$ and $\langle \gamma_i(t_i) \rangle_{\min}$ are available. The distribution of $\langle \gamma_i(t_i) \rangle_{\max}$ and $\langle \gamma_i(t_i) \rangle_{\min}$ in the streamwise direction are plotted in Fig. 20 for Ω values of 1.59 and 3.18 on the suction surface. The distribution of $\langle \gamma_i(t_i)_{\max} \rangle$ corresponds to the condition when the wake, with its high turbulence intensity core, impinges on the plate surface. Once the wake has passed over the surface, the same streamwise location is exposed to a low turbulence intensity flow regime with an intermittency state of $\langle \gamma_i(t_i) \rangle_{\min}$, where no wake is present.

Figure 20 displays the striking features of $\langle \gamma(t) \rangle_{\max}$ and $\langle \gamma(t) \rangle_{\min}$. While for zero and moderate pressure gradients, the minimum intermittency $\langle \gamma_i(t_i) \rangle_{\min}$ distribution reveals a certain

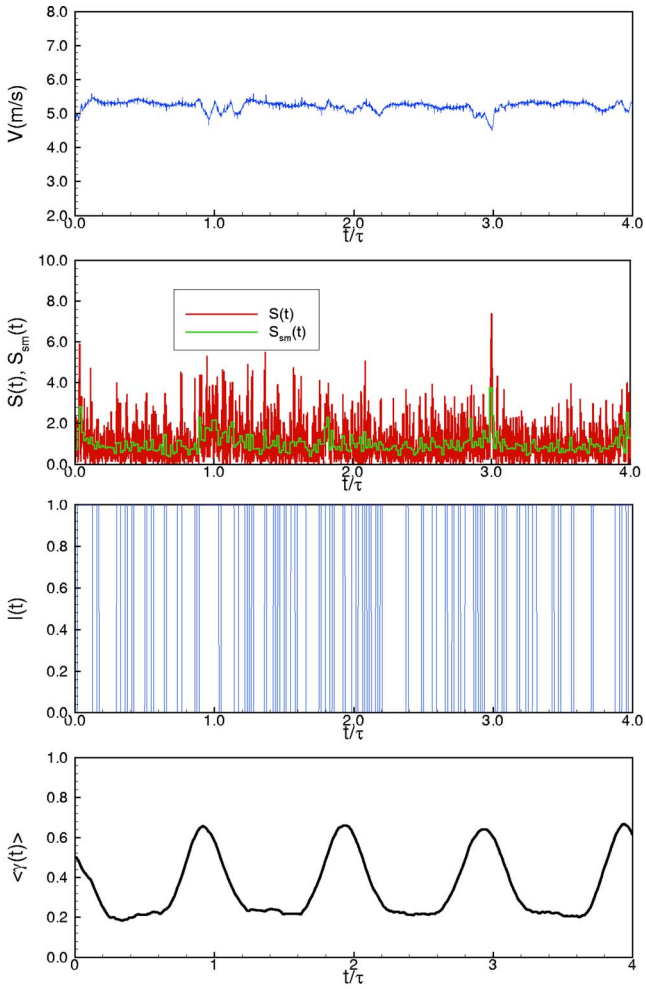

Fig. 17 Calculation of ensemble-averaged intermittency function from instantaneous velocities for $\Omega = 1.725$ at $y = 0.720$ mm

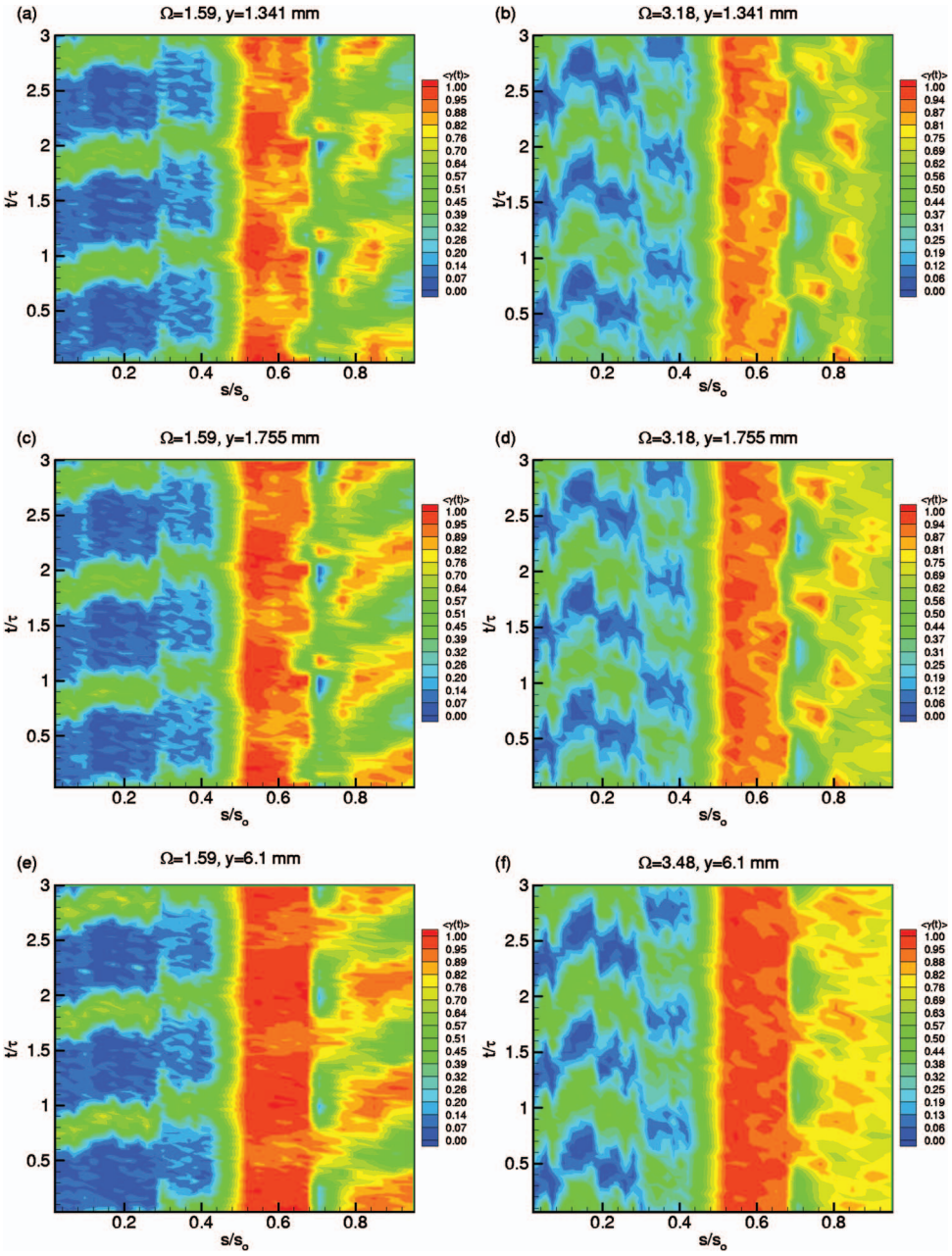

Fig. 18 Ensemble-averaged intermittency factor in the temporal-spatial domain at different *y* positions for $\Omega=1.59$ ($S_R=160$ mm) and $\Omega=3.18$ ($S_R=80$ mm)

similarity to the one described by the Emmons-Narasimha transition model [31], the present LPT-flow case with a strong negative pressure gradient associated with separation, $\langle\gamma_i(t_i)\rangle_{\min}$ exhibits a remarkably different course that occurs systematically and reproducibly for all Ω cases at all y positions over the blade surface. Upstream of the separation bubble, the course of $\langle\gamma(t)\rangle_{\min}$ with the value close to zero indicates a stable *nonturbulent* character of the boundary layer. A sharp increase in intermittency indicates the separation begins shortly before the pressure minimum (Fig. 4) has been reached. It is followed by a high intermittency region that covers the separation plateau (Fig. 4) and a steep decrease that is indicative of reattachment. The streamwise location of the intermittency minimum at $s/s_0\approx0.7$ coincides with the end of the separation plateau. The following increase in intermittency is due to the steep positive pressure gradient that follows the constant pressure plateau. On the other hand, $\langle\gamma_i(t_i)\rangle_{\max}$ reveals a fundamentally different behavior. As Fig. 20 shows, the wake flow with an intermittency of $\langle\gamma_i(t_i)\rangle_{\max}\approx0.8-0.9$ impinges on the blade surface. By convecting downstream, because of an extremely thin boundary layer, the wake turbulent fluctuations do not undergo a strong damping by the wall shear stress forces, as was observed in zero and moderate pressure gradient cases reported in Refs. [7,12].

Utilizing $\langle\gamma(t)\rangle_{\max}$ and $\langle\gamma(t)\rangle_{\min}$, the relative intermittency Γ is found to be described by a Gaussian distribution. This observation is in accord with the findings reported in Refs. [7,12], and very recently in Ref. [30] confirming the universal character of Γ. Considering the intermittency results of the current investigations and those reported above, it can be concluded that, in general, $\langle\gamma_i(t_i)\rangle_{\max}$ and $\langle\gamma_i(t_i)\rangle_{\min}$ are not only functions of reduced frequency, but they are also strongly influenced by the pressure gra-

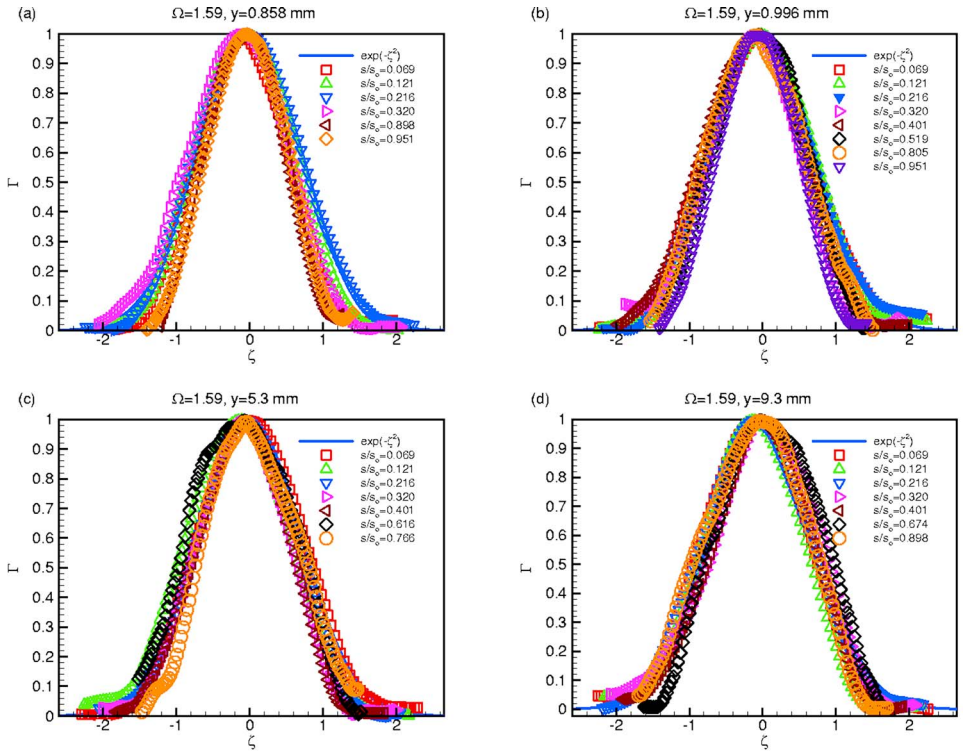

Fig. 19 Relative intermittency as a function of s/s_0 for unsteady frequency of $\Omega=1.59$ ($S_R=160$ mm) at (*a*) $y=0.858$ mm, (*b*) $y=0.996$ mm, (*c*) $y=5.3$ mm, and (*d*) $y=9.3$ mm at Re =110,000

dient, turbulence intensity, Reynolds—and possibly Mach number, and surface roughness. This implies that neither $\langle\gamma_i(t_i)\rangle_{\min}$ nor $\langle\gamma_i(t_i)\rangle_{\max}$ have universal character.

Uncertainty Analysis

The Kline and McClintock [32] uncertainty analysis method was used to determine the uncertainty in the velocity after calibration and data reduction for the single-wire probe. The Kline and McClintock method determines the uncertainty with a 95% confidence level. The uncertainty in the velocity for the single-wire probe after the data reduction is given in Table 2. As shown, the uncertainty in the velocity increases as the flow velocity decreases. This is due to the pneumatic pressure transducer having a large uncertainty during calibration.

Conclusions

A detailed experimental study on the behavior of the separation bubble along the suction surface of a highly loaded LPT blade under periodic unsteady wake flow was presented. Varying the Reynolds number, one steady and two different unsteady inlet wake flow conditions with the corresponding passing frequencies, the wake velocity and the turbulence intensities were investigated by utilizing a large-scale, subsonic research facility. Periodic unsteady wake flow was established by translational motion of two parallel moving timing belts on which cylindrical rods were attached. The following conclusions were drawn.

Table 2 Uncertainty in velocity measurement for hot-wire probe

$\overline{V}$ (m/s)	3	5	12
$\omega\overline{V}/\overline{V}_0(\%)$	5.78	2.41	1.40

(1) Slight changes of the pressure distribution occurred, while operating at the unsteady flow conditions. Increasing the Reynolds number from Re=110,000 to Re=150,000 has not brought major changes in steady state C_p distribution. However, the combination of higher Reynolds number with higher unsteady wake frequency introduced higher fluctuation kinetic energy into the boundary layer, which tends to reverse the separation tendency. C_p distribution clearly shows that the wake impingement with higher Reynolds number shortens the streamwise extent of the separation zone compared to the steady case.

(2) Detailed unsteady boundary layer measurement identified the onset and extent of the separation bubble as well as its behavior under the unsteady wake flow. Passing the wake flow with its highly turbulent vortical core over the separation region caused a periodic contraction and expansion of the separation bubble and a reduction of the separation bubble height. Increasing the passing frequency associated with a higher turbulence intensity further reduced the separation bubble height. It was observed that, by increasing the Reynolds number to 150,000, the leading edge and trailing edge of the separation bubble and, thus, the re-attachment point, moved further downstream to $s/s_0=0.56$ and $s/s_0=0.788$, respectively. Also, the size of the separation bubble was further reduced.

(3) Intermittency analysis of the current boundary layer experimental data with the flow separation determined the minimum, maximum, and the relative intermittency functions, $\langle\gamma_{\min}\rangle$, $-\langle\gamma_{\max}\rangle$, and Γ. The minimum intermittency function, $\langle\gamma_{\min}\rangle$, represented the boundary layer behavior when it is exposed to the wake external region (region between the turbulent wake strips). On the other hand, $\langle\gamma_{\max}\rangle$ describes the state of the boundary layer when it is subjected to the wake vortical core with its high turbulence level.

(4) The relative intermittency factor followed a Gaussian distribution confirming the universal character of the relative intermittency function. In contrast to the relative intermittency function Γ,

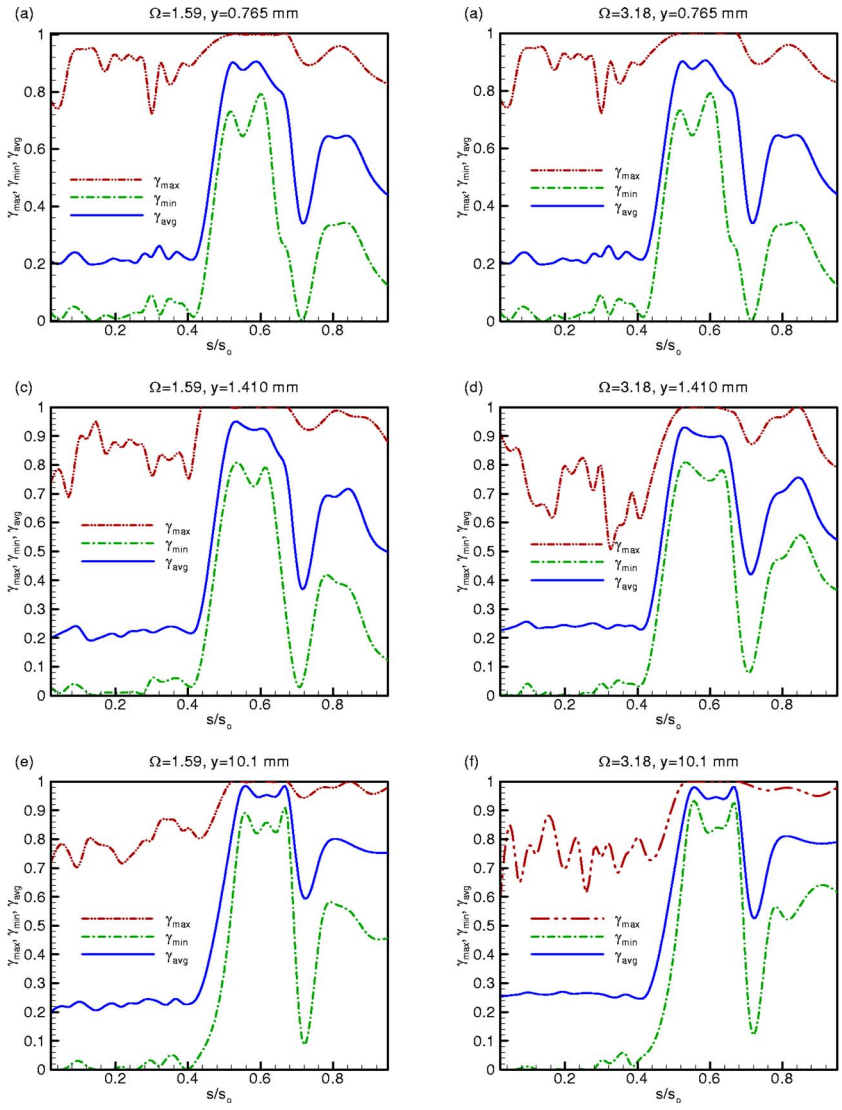

Fig. 20 Maximum, minimum, and time-averaged intermittency as a function of s/s_0 at different lateral positions for steady case $\Omega=0$ ($S_R=\infty$) and unsteady cases $\Omega=1.59$ ($S_R=160$ mm) and $\Omega=3.18$ ($S_R=80$ mm) at Re=110,000

the minimum as well as the maximum intermittency do not suggest to have a universal character. Several parameters, such as free-stream turbulence intensity, reduced frequency, surface roughness, Re number, and pressure gradient, are instrumental in affecting the pattern of these two intermittencies. Future studies need to incorporate these parameters.

Acknowledgment

The study presented is a part of an ongoing LPT-aerodynamics project executed by the NASA Glenn Research Center. The first two authors were supported by NASA Cooperative Agreement NCC3-793 monitored by Dr. David Ashpis. The support and the permission for publication are gratefully acknowledged. The authors also gratefully acknowledge Pratt & Whitney for providing the research community with the blade coordinates.

Nomenclature

b = intermittency wake width
c = blade chord
c_{ax} = axial chord
C_p = pressure coefficient, $C_p=(p_i-p_s)/(p_t-p_s)_{inl}$
C = threshold level
d_R = rod diameter
H_{12} = shape factor, $H_{12}=\delta_1/\delta_2$
h_m = maximum separation bubble height
$I(\mathbf{x},t)$ = indicator function
L_{SS} = suction surface length
M = number of samples
N = number of wake cycles
p_i = static pressure taps $i=1,\ldots,48$
p_s, p_t = static, total pressure
Re_{LSS} = suction surface Reynolds number $\mathrm{Re}=L_{ss}V_{exit}/\nu$
s = streamwise distance from the leading edge of the blade
s_{md} = streamwise location of maximum separation bubble height
s_o = streamwise distance from the leading edge to the trailing edge of the blade
s_r = re-attachment point of the separation bubble from blade leading edge
s_s = start of the separation bubble at a streamwise distance from blade leading edge
$S(\mathbf{x},t)$ = criterion function

S_B = blade spacing
S_R = rod spacing
t = time
Tu = reference turbulence intensity
$\langle \mathrm{Tu} \rangle$ = ensemble-averaged turbulence intensity
U = belt translational velocity
v = fluctuation velocity
V = velocity
V_{ax} = axial velocity
V_{exit} = exit velocity
$\mathbf{x}$ = position vector
y = lateral distance from plate surface
$\alpha_{1,2}$ = cascade inlet, exit flow angles
γ = cascade stagger angle
$\bar{\gamma}$ = time-averaged intermittency
$\langle (\gamma) \rangle$ = ensemble-averaged intermittency
$\langle (\gamma) \rangle_{\max}$ = maximum ensemble-averaged intermittency
$\langle (\gamma) \rangle_{\min}$ = minimum ensemble-averaged intermittency
Γ = relative turbulence intermittency
ζ = nondimensional coordinate, y/b
ν = kinematic viscosity
ξ_2 = lateral distance from wake center
ρ = density of air
σ = cascade solidity, $\sigma = c/S_B$
τ = one wake-passing period
φ = flow coefficient, $\varphi = V_{\mathrm{ax}}/U$
ψ_A = Zweifel coefficient
$\psi_A = 2\sin^2 \alpha_2 (\cot \alpha_2 - \cot \alpha_1) S_B / c_{\mathrm{ax}}$
Ω = reduced frequency $\Omega = (c/S_R)(U/V_{\mathrm{ax}})$
$= (\sigma/\varphi)(S_B/S_R)$

References

[1] Pfeil, H., and Herbst, R., 1979, "Transition Procedure of Instationary Boundary Layers," ASME Paper No. 79-GT-128.
[2] Pfeil, H., Herbst, R., and Schröder, T., 1983, "Investigation of the Laminar Turbulent Transition of Boundary Layers Disturbed by Wakes," ASME J. Eng. Power, **105**, pp. 130–137.
[3] Orth, U., 1992, "Unsteady Boundary-Layer Transition in Flow Periodically Disturbed by Wakes," ASME Paper No. 92-GT-283.
[4] Schobeiri, M. T., and Radke, R. E., 1994, "Effects of Periodic Unsteady Wake Flow and Pressure Gradient on Boundary Layer Transition Along the Concave Surface of a Curved Plate," ASME Paper No. 94-GT-327.
[5] Schobeiri, M. T., Read, K., and Lewalle, J., 2003, "Effect of Unsteady Wake Passing Frequency on Boundary Layer Transition, Experimental Investigation and Wavelet Analysis," ASME J. Fluids Eng., **125**, pp. 251–266.
[6] Wright, L., and Schobeiri, M. T., 1999, "The Effect of Periodic Unsteady Flow on Boundary Layer and Heat Transfer on a Curved Surface," ASME J. Heat Transfer, **120**, pp. 22–33.
[7] Chakka, P., and Schobeiri, M. T., 1999, "Modeling of Unsteady Boundary Layer Transition on a Curved Plate under Periodic Unsteady Flow Condition: Aerodynamic and Heat Transfer Investigations," ASME J. Turbomach., **121**, pp. 88–97.
[8] Liu, X., and Rodi, W., 1991, "Experiments on Transitional Boundary Layers with Wake-Induced Unsteadiness," J. Fluid Mech., **231**, pp. 229–256.
[9] Schobeiri, M. T., Pappu, K., and Wright, L., 1995, "Experimental Study of the Unsteady Boundary Layer Behavior on a Turbine Cascade," ASME Paper No. 95-GT-435.
[10] Schobeiri, M. T., John, J., and Pappu, K., 1997, "Experimental Study on the Effect of Unsteadiness on Boundary Layer Development on a Linear Turbine Cascade," Exp. Fluids, **23**, pp. 303–316.
[11] Schobeiri, M. T., and Wright, L., 2003, "Advances in Unsteady Boundary layer Transition Research: Part I and II," Int. J. Rotating Mach., **9**(1), pp. 1–22.
[12] Schobeiri, M. T., and Chakka, P., 2002, "Prediction of Turbine Blade Heat Transfer and Aerodynamics Using Unsteady Boundary Layer Transition Model," Int. J. Heat Mass Transfer, **45**, pp. 815–829.
[13] Brunner, S., Fottner, L., and Schiffer, H.-P., 2000, "Comparison of Two Highly Loaded Turbine Cascade Under the Influence of Wake-Induced Transition," ASME Paper No. 2000-GT-268.
[14] Cardamone, P., Stadtmüller, P., Fottner, L., and Schiffer, H.-P., 2000, "Numerical Investigation of the Wake-Boundary Layer Interaction on a Highly Loaded LP Turbine Cascade Blade," ASME Paper No. 2002-GT-30367.
[15] Schulte, V., and Hodson, H. P., 1996, "Unsteady Wake-Induced Boundary Layer Transition in High Lift LP Turbines," ASME Paper No. 96-GT-486.
[16] Kaszeta, R., Simon, T. W., and Ashpis, D. E., 2001, "Experimental Investigation of Transition to Turbulence as Affected by Passing Wakes," ASME Paper No. 2001-GT-0195.
[17] Lou, W., and Hourmouziadis, J., 2000, "Separation Bubbles Under Steady and Periodic Unsteady Main Flow Conditions," ASME Paper No. 200-GT-270.
[18] Schröder, Th., 1989, "Measurements With Hot-Film Probes and Surface Mounted Hot Film Gages in a Multi-Stage Low Pressure Turbine," European Propulsion Forum, Bath, UK.
[19] Haueisen, V., Hennecke, D. K., and Schröder, T., 1997, "Measurements With Surface Mounted Hot Film Sensors on Boundary Layer Transition in Wake Disturbed Flow," AGARD-CP-598.
[20] Halstead, D. E., Wisler, D. C., Okiishi, T. H., Walker, G. J., Hodson, H. P., and Shin, H.-W., 1997, "Boundary Layer Development in Axial Compressors and Turbines: Part 3 of 4," ASME J. Turbomach., **119**, pp. 225–237.
[21] Schobeiri, M. T., and Öztürk, B., 2003, "On the Physics of the Flow Separation Along a Low Pressure Turbine Blade Under Unsteady Flow Conditions," ASME Paper No. 2003-GT-38917, ASME J. Fluids Eng., **127**, pp. 503–513.
[22] Schobeiri, M. T., and Öztürk, B., 2004, "Experimental Study of the Effect of the Periodic Unsteady Wake Flow on Boundary Layer Development, Separation, and Re-Attachment Along the Surface of a Low Pressure Turbine Blade," ASME J. Turbomach., **126**(4), pp. 663–676.
[23] Schobeiri, M. T., John, J., and Pappu, K., 1996, "Development of Two-Dimensional Wakes Within Curved Channels, Theoretical Framework and Experimental Investigation," ASME J. Turbomach., **118**, pp. 506–518.
[24] Hourmouziadis, J., 1989, "Blading Design for Axial Turbomachines," AGARD, Lecture Series LS-167.
[25] Eifler, J., 1975, "Zur Frage der freien turbulenten Strömungen, insbesondere hinter Ruhenden und bewegten Zylindern," Dissertation D-17, Technische Hochschule Darmstadt, Germany.
[26] Hedley, B. T., and Keffer, F. J., 1974, "Turbulent/Non-Turbulent Decisions in an Intermittent Flow," J. Fluid Mech., **64**, pp. 625–644.
[27] Antonia, R. A., and Bradshaw, P., 1971, Imp. College Aero. Rep. No. 71–04.
[28] Kovasznay, L. S. G., Kibens, V., and Blackwelder, R. F., 1970, J. Fluid Mech., **41**, p. 283.
[29] Bradshaw, P., and Murlis, J., 1973, Imp. College Aero. Tech. Note, No. 73–108.
[30] Schobeiri, M. T., 2005, "Intermittency Based Unsteady Boundary Layer Transition Modeling, Implementation Into Navier-Stokes Equations," ASME Paper No. GT2005–68375.
[31] Dhawan, S., and Narasimha, R., 1958, "Some Properties of Boundary Layer Flow During The Transition From Laminar to Turbulent Motion," J. Fluid Mech., **3**, pp. 418–436.
[32] Kline, S. J., and McKlintock, F. A., 1953, "Describing Uncertainties in Single-Sample Experiments," Mech. Eng. (Am. Soc. Mech. Eng.), **75**, pp. 3–8.

Improving Aerodynamic Matching of Axial Compressor Blading Using a Three-Dimensional Multistage Inverse Design Method

M. P. C. van Rooij[1]

T. Q. Dang

Syracuse University,
Syracuse, NY 13244

L. M. Larosiliere[2]
U.S. Army Research Laboratory,
NASA Glenn Research Center,
Cleveland, OH 44135

Current turbomachinery design systems increasingly rely on multistage CFD as a means to diagnose designs and assess performance potential. However, design weaknesses attributed to improper stage matching are addressed using often ineffective strategies involving a costly iterative loop between blading modification, revision of design intent, and further evaluation of aerodynamic performance. A scheme is proposed herein which greatly simplifies the design point blade row matching process. It is based on a three-dimensional viscous inverse method that has been extended to allow blading analysis and design in a multi-blade row environment. For computational expediency, blade row coupling is achieved through an averaging-plane approximation. To limit computational time, the inverse method was parallelized. The proposed method allows improvement of design point blade row matching by direct regulation of the circulation capacity of the blading within a multistage environment. During the design calculation, blade shapes are adjusted to account for inflow and outflow conditions while producing a prescribed pressure loading. Thus, it is computationally ensured that the intended pressure-loading distribution is consistent with the derived blading geometry operating in a multiblade row environment that accounts for certain blade row interactions. The viability of the method is demonstrated in design exercises involving the rotors of a 2.5 stage, highly loaded compressor. Individually redesigned rotors display mismatching when run in the 2.5 stage, evident as a deviation from design intent. However, simultaneous redesign of the rotors in their multistage environment produces the design intent, indicating that aerodynamic matching has been achieved. [DOI: 10.1115/1.2372773]

Keywords: inverse aerodynamic shape design, multistage turbomachinery CFD, compressor stage matching

Introduction

Turbomachinery computational fluid dynamics (CFD), in support of aerodynamic design, has evolved from isolated blade row methods to hierarchical multistage analysis encompassing various blade row coupling schemes. Three main approaches to blade row coupling exist: steady averaging plane, time mean average passage, and unsteady time periodic. The foundations of these approaches are discussed in Refs. [1,2]. Currently, multistage CFD methods are primarily suited for diagnosing design shortcomings originating from strong blade row interactions that adversely impact performance and operability. Typically, simulation results are used to revise aerodynamic matching conditions for individual blade rows and stages. The term aerodynamic matching is loosely understood to involve the compatibility of the inlet flow requirements of a stage to the outlet flow of upstream stages.

In the title of this paper, the word "matching" denotes a critical function of the multi-blade row design process, where the individual blade row shapes are simultaneously tailored in such a way as to produce a desired design intent while accounting for blade row interactions that would lead to deviations from this design intent. The "design intent" implies a physically realizable axisymmetric-averaged pressure field that is compatible with overall design point performance and off-design operability. For a given overall pressure rise, mismatching is manifested as a disruption of the design equilibrium among the circulation capacity of the blading, entropy production, and accumulation of aerodynamic blockage. Naturally, an appropriate choice of design intent can limit strong blade row interactions.

There are two key elements in the blade row matching problem. First, there is the establishment of accurate and physically realizable design intent and, second, when necessary, an efficient means for tailoring blade shapes so that design equilibrium is restored among blading circulation capacity, entropy production, and accumulation of aerodynamic blockage. Transforming overall functional requirements into credible aerodynamic design intent is an inherently iterative process guided by past experience. Note that this is compatible with the traditional model for turbomachinery aerodynamic design, as described by Marble [3], whereby the flow is conceptually decomposed into two parts: that which is due to the gross influence of all blade rows and that which is associated with local details of blade shape.

A contemporary aerodynamic design system, incorporating multistage CFD analysis, is noted in Fig. 1(*a*). This system allows two broad functions: design synthesis, and design diagnostics and development. Both of these functions can be iteratively executed to arrive at credible design intent and a blading revision strategy

[1]Present address: Siemens Power Generation Industrial Applications.
[2]Present address: Concepts NREC.

Contributed by the International Gas Turbine Institute (IGTI) of ASME for publication in the JOURNAL OF TURBOMACHINERY. Manuscript received October 1, 2004; final manuscript received February 1, 2005. IGTI Review Chair K. C. Hall. Paper presented at the ASME Turbo Expo 2005: Land, Sea and Air, Reno, NV, June 6–9, 2005, Paper No. GT2005-68271.

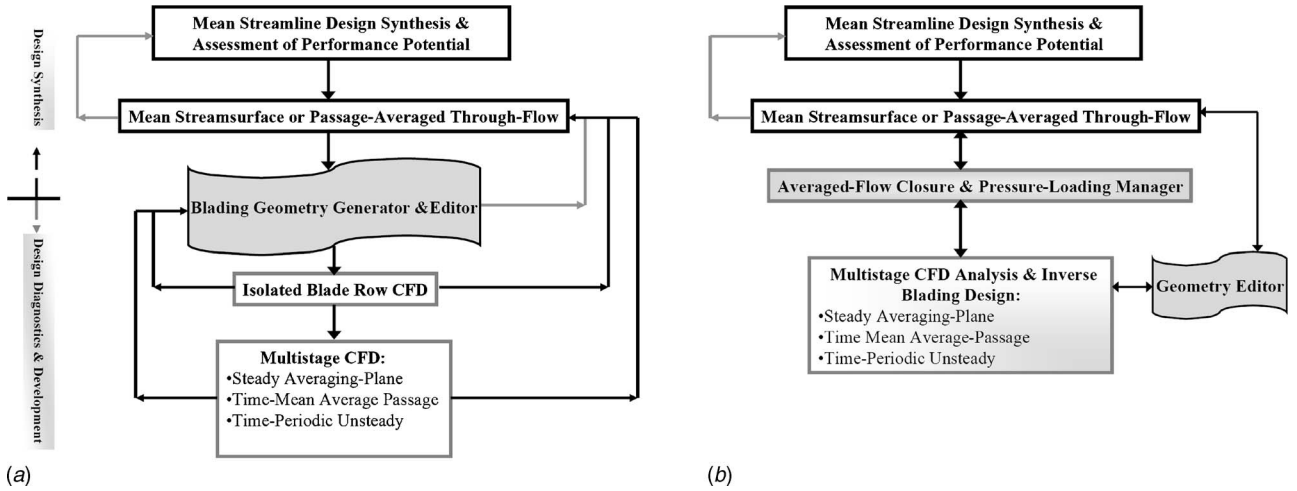

Fig. 1 (*a*) Current design system and (*b*) proposed design system incorporating 3D inverse blading design

to meet this intent. For advanced designs, this system can become very costly and ineffective due to the need for many revisions that are sometimes formulated in an ad-hoc fashion. Thus, enhancements to this process would be beneficial in terms of reductions in design cycle cost and time. Figure 1(*b*) shows a proposed enhancement to the contemporary aerodesign system. This enhancement is made possible by the following two developments: (1) incorporation of an inverse blade-design procedure into the multistage CFD, and (2) improved consistency between the passage-averaged throughflow model, the multistage CFD analysis, and inverse blade design. Note that the enhanced design system involves automatic exchange of appropriate information between 3D viscous multistage analysis, inverse blade design, and passage-averaged throughflow. This is achieved by a so called averaged-flow closure and pressure-loading manager which regulates the design intent, thereby reducing and perhaps eliminating the need for circuitous and possibly ad-hoc design revision strategies. Work on the pressure-loading manager, possibly involving neural networks, is in its infancy and will be forthcoming.

In this paper, a three-dimensional viscous inverse blade design method with multirow analysis and indirect geometric sculpting capabilities is presented. Currently, blade row coupling is done via an averaging plane, mainly for computational expediency. Thus, the major axisymmetric blade row interactions are captured while the nonaxisymmetric coupling effects involving deterministic unsteadiness are neglected. Debate still continues as to the impact of the unsteady deterministic flow on time-mean performance, especially near design point conditions. Does one need to accurately predict the consequences of mismatching in order to diagnose the existence of improperly matched blade rows? No attempt is made to resolve this issue here; instead, ultimate model selection is left up to the designer. Suffice it to say that the current inverse design method can be incorporated into higher-fidelity blade row coupling schemes. The usefulness of this approach for improving design point blade row matching by direct regulation of the circulation capacity of the blading within a multistage environment is illustrated via a redesign of supersonic rotors for a highly loaded 2.5-stage compressor.

Development of Methodology

The goal of blading design is to effectively realize an intended velocity diagram with minimal loss and the widest possible operating range. This is achieved by tailoring the blade pressure loading distribution as is reflected in the angular momentum-force balance relationship for a quasi-3D blade element

$$\int_{\mathrm{LE}}^{\mathrm{TE}} r\Delta p dA_\theta \approx \dot{m}[(r\bar{V}_\theta)_{\mathrm{TE}} - (r\bar{V}_\theta)_{\mathrm{LE}}]$$

In the above relation, Δp (i.e., blade pressure loading) is the difference between the blade upper and lower surface pressures at fixed axial locations; the subscripts LE and TE denote leading and trailing edges; $\dot{m}$ is the mass flow rate; A_θ is the projected surface area in the tangential direction; and $r\bar{V}_\theta$ is the mass-averaged swirl velocity. Thus, the overall blading design strategy can be described as pressure-loading tailoring to attain local aerodynamic control while satisfying certain global constraints such as net circulation, mass flow rate, and blade count.

The current multistage inverse design method is an extension of the code INV3D, which has been reported in previous papers by Dang [4], Qiu [5], Damle et al. [6], Qiu and Dang [7], Dang et al. [8], and Medd [9]. Note that INV3D can be used for both design and analysis. In the inverse mode, the primary prescribed quantities are the blade axis definition in terms of its axial grid-line location i_{ba} and tangential orientation along the camber surface $f_{\mathrm{ba}}(r)$, the blade thickness distribution $T(r,z)$, and the pressure loading distribution $\Delta p(r,z)$. Note that the blade axis gives a reference for locating the various spanwise blade sections in space and thus must be compatible with the spanwise distribution of Δp. For a given set of inputs, the 3D inverse method computes the corresponding wrap angle $f(r,z)$. Thus, this is a semi-inverse procedure in the sense that the full geometry is not evolved and only the mean camber surface, $f(r,z)$, is updated via the flow-tangency condition along the blade surfaces. Clearly, the blade geometry corresponding to prescribed values for $[i_{\mathrm{ba}}, f_{\mathrm{ba}}, T, \Delta p]$ and operating in a particular inflow/outflow environment may not satisfy certain geometric smoothness criteria and is not guaranteed to have optimum performance nor be aeromechanically acceptable. The challenge is to pick these quantities to arrive at a satisfactory design.

The computational method is based on the solution of the three-dimensional Reynolds-averaged Navier–Stokes (RANS) equations on a simple sheared H grid using the robust finite-volume time-marching cell-centered scheme of Jameson et al. [10]. All boundary layers are assumed turbulent and viscous effects are modeled using wall functions with an adaptation of the Baldwin–Lomax turbulence closure. Normally, INV3D employs a "slip" velocity on the blade surface, since the inverse scheme requires a finite velocity to trace the surface (tangency condition), as discussed earlier. In this case, the viscous sublayer is neglected subject to the condition that the first cell next to a solid boundary lies in the loga-

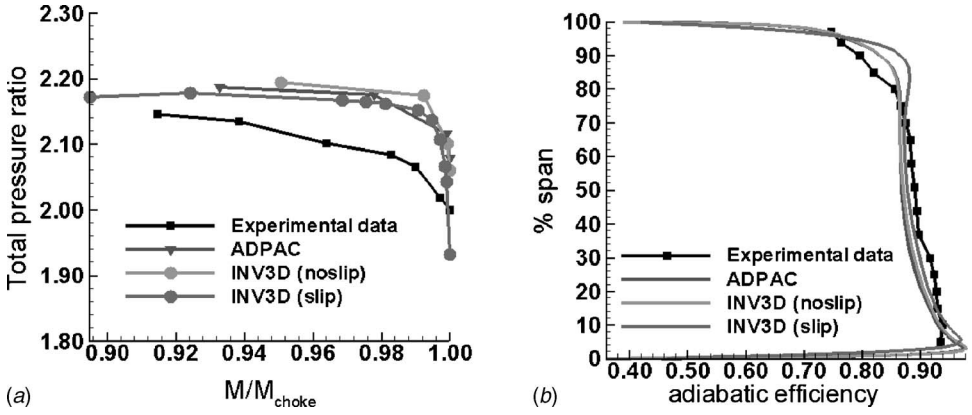

Fig. 2 Comparison between measured data and CFD simulations of NASA rotor 37 using INV3D and ADPAC: (*a*) performance map of total pressure ratio versus mass flow and (*b*) exit spanwise profile of total-to-total adiabatic efficiency at nominal operation

rithmic region and hence the existence of a slip velocity [11]. Typical viscous calculations using INV3D employ near-wall $y+$ on the order of 30–150. Leakage flows are approximated by assuming periodicity across the extended blade surfaces in the clearance gap.

In order to transform the original research code into a practical tool, several modifications were made to the basic methodology described by Dang [4] and Dang et al. [8]. The two most critical modifications are: (1) the solution method for the camber surface generator, and (2) a hybrid inverse/analysis scheme to handle the blade leading and trailing edges.

In the original method, the camber surface is developed by enforcing the condition of zero-normal velocity on the blade surface. The resulting equation for the camber wrap angle $f(r,z)$ is a convective equation, the so-called camber generator equation. It is basically a stream surface tracer, the stream surface being the blade surface. In the original method, the camber generator equation is solved using the implicit Crank–Nicholson scheme. This approach was demonstrated to work very well for inviscid flows [8], but it is not robust for practical problems involving significant viscous effects and leakage flows. In the latter case, the streamline in the clearance region is highly three dimensional, resulting in the blade shape being exceedingly distorted during the iterative process.

Rather than solving the camber generator "exactly" with a conventional implicit numerical method as in the original methodology described in Dang et al. [8], the camber generator equation is satisfied by minimization in the least squares sense, with the spanwise variation of the camber defined in terms of a NURBS curve [9]. In essence, the camber is generated by fitting the blade as best as possible to the velocity field. This is done in the spanwise direction at each axial location of the grid, followed by a geometrical smoothing in the chordwise direction. The originally specified blade axis is maintained. This method is very robust, and makes it possible to obtain smooth blade geometries and good convergence in the presence of strong clearance leakage flow.

As this is a minimization process, it cannot be guaranteed that the local normal velocity be driven to zero during convergence of the design calculation. This again implies that the specified loading distribution may not be strictly enforced. However, this is outweighed by the advantages of increased robustness and geometrically smoother blade shapes. To obtain a satisfactory balance between smoothness and accuracy, the number of NURBS control points used in the spanwise and chordwise directions can be varied. The more points used, the closer the normal velocity is driven to zero and the more strictly the specified loading is enforced, but at a cost of smoothness and possibly convergence (e.g., in the presence of strong leakage flow).

Another important modification to the original method is the implementation of a hybrid inverse/analysis technique to handle the blade leading and trailing edges. Experience with application of the inverse method to the design of highly loaded transonic blades, revealed the need for the inverse method to preserve the blade leading-edge detailed geometry in order to capture important local flow structures. For example, the grid must be clustered near the leading edge so that the incoming flow sees the blade leading edge as blunt rather than sharp. However, highly clustered sheared H grids near the leading edge can result in convergence difficulties initiated by possible distortion of the blade leading edge shape. This is due to the fact that near the leading edge, grid skewness, and dispersion errors can create a locally distorted velocity field, and since the blade shape is traced from this velocity field, it too will be distorted. Thus, in order to maintain geometrically accurate leading and trailing edge shapes during the design process, a hybrid inverse technique is used [9]. Here, the leading and trailing edge geometries are created by extrapolation of the blade camber surface from the interior using a NURBS curve. The meridional envelope of the blade is maintained. Analysis boundary conditions are specified in these regions, which typically encompass 1–5% of the blade chord. Apart from geometric fidelity, this method also increases robustness of the camber generator in the presence of exceedingly high swirl angles that are typical of multistage end wall flows at the design point. It may not be desirable to sustain high local gradients in the blade edge angles, and the 3D relief phenomenon discussed in Wadia and Beacher [12] tends to accommodate smooth blades.

The INV3D solver is able to predict the static pressure field with reasonable accuracy along with adequate resolution of most critical flow structures responsible for relative changes in the entropy production mechanisms (e.g., when massive flow separation is not present). Figure 2 shows overall total pressure ratio characteristics and axisymmetric-averaged spanwise profiles of adiabatic efficiency for NASA rotor 37 [13] comparing results from INV3D both with and without wall slip against measurements [14]. Also indicated, are results using the NASA developed multiblock RANS code, ADPAC [15]. Both INV3D and ADPAC show good agreement with the spanwise distribution of efficiency inferred from measurements. The absolute level of total pressure is not well predicted and could be improved with better viscous and/or turbulence modeling. Overall, the agreement with measurements is adequate in the sense that INV3D does identify critical flow structures responsible for relative changes in performance.

INV3D was extended to multistage by adding a blade row coupling scheme and parallelization. Currently, blade row coupling for multistage calculations is achieved by a steady averaging-plane approximation. Two versions have been implemented. The

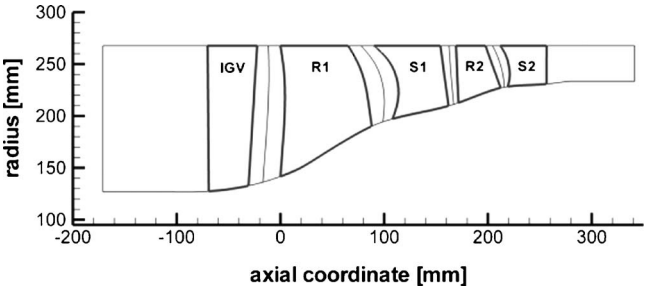

Fig. 3 Meridional flow path for the 2.5-stage compressor used in the design examples: Inlet guide vane (IGV), rotor 1 (R1), stator 1(S1), rotor 2 (R2) and stator 2 (S2); rotor 1: 26 blades, average solidity=2.16, aspect ratio=0.83; rotor 2: 56 blades, average solidity=1.96, aspect ratio=0.86. Also indicated, are multistage computational averaging planes.

first involves direct exchange of circumferentially averaged density, momentum and pressure across the averaging-plane [11,16]. The second, considered to be numerically superior, is an adaptation of the nonreflecting averaging plane presented by Chima [17], which is based on characteristic boundary conditions derived by Giles [18]. It is recognized that the steady averaging-plane coupling ignores much, if not all, of the physics associated with deterministic unsteadiness inherent to multistage turbomachinery flows. However, it does provide spanwise consistency in the conservative variables along with global mass conservation thereby allowing first-order axisymmetric blade row interactions to be captured. Due to ease of implementation and computational convenience, as a first step, the averaging-plane blade row coupling was therefore chosen for exploring the potential of blade inverse design in a multistage environment.

Because of the extensive computational demand of a multistage calculation, the ability to exploit parallel processing computing capability has been added to the code in the form of MPICH [19,20]. For a parallel run, each blade row is assigned to a slave process on a separate processor, while a master process handles all the input and output. A cluster of 5 AMD XP2400+ PCs running Windows 2000 has been used for all calculations presented here.

Aerodynamic Matching Study

A meridional cross section of the 2.5-stage advanced compressor used to illustrate the viability of blade inverse design for improving blade row matching in a multistage environment is shown in Fig. 3. The design philosophy of this compressor is given in Larosiliere et al. [21]; however, the current blading set is a variant of that described in the reference. Design features include variable inlet guide vane, cantilevered stators, and 3D blading. The compressor can be characterized as generally high Mach number, high reaction, and highly loaded. Rotor 2 has supersonic relative inlet Mach numbers along its entire span, thus exacerbating the stage-matching problem. The aerodynamic design requirements for this compressor are a corrected mass flow of 31.8 kg/s (70 lbm/s), an overall total compression ratio of 4.65:1 (at shroud backpressure of 4.0), a total pressure ratio of 2.42:1 across rotor 1 with a corrected tip speed of 450.2 m/s (1477 ft/s), and a rotor 2 total pressure ratio of 2.0:1 at a corrected tip speed of 393.2 m/s (1290 ft/s).

This compressor was originally designed using a contemporary design system similar to that noted in Fig. 1(*a*). An earlier isolated blade row version of INV3D (i.e., rudimentary viscous model, low mesh resolution, and basic inverse scheme), with aerodynamic matching conditions extracted from a design point throughflow model, was used to refine the rotor blade shapes in an attempt to better manage the passage shock structure and strength (see Ref. [21] for details). Note that the credibility of the design-intent axisymmetric-averaged pressure field from the design point throughflow model is debatable and indicates the need for establishing consistency among the various mathematical formulations and physical model closures. Overall, the blading design objective was to achieve efficient design point operation at very high aerodynamic loading levels (i.e., average Lieblein D-factors ~0.55).

The computational mesh used in the present study consisted of 51 cells in the axial direction along the blade surface (for each blade row), 45 cells in the radial direction, and 35 cells in the pitchwise direction. Three cells were placed in the rotor tip and stator hub gaps (clearances ranging from 0.5% to 1% local chord). In the analysis mode, this mesh size requires approximately 1 h for 1500 time steps using 5 AMD XP2400+ processors (one processor for each blade row). A single blade row calculation takes about 2000 iterations to convergence. A multistage calculation typically requires more iterations, since errors propagate through multiple blade rows and the blade row coupling itself affects overall convergence. For the 2.5-stage geometry presented here, about 6000 iterations were needed to reach convergence, corresponding to a computational time of 4 h. Compared to the analysis mode, the inverse mode takes about 10% longer per iteration. For all cases presented, the same profiles of total pressure, total temperature, and radial and absolute tangential flow angles were prescribed at the inlet of the computational domain. A design point backpressure of 4.00 (normalized to inlet total pressure at midspan) was specified at the casing, and simple radial equilibrium was used to construct the spanwise exit static pressure profile. The standard averaging-plane approach [11,16] was used for steady blade row coupling.

Diagnosis of Original Blading Geometry. The complete 2.5 stage with the original blading geometry was analyzed at the design-intent backpressure and speed using INV3D in the analysis mode. Diagnostic plots of results for the original geometry are shown in Figs. 4–6, which are described in the following. Figure 4 shows contours of relative Mach number at 3%, 50%, and 100% span. Three important conclusions can be made by inspection: (1) generation of significant aero blockage by strong leakage/shock interaction near the casing end wall of both rotors, (2) existence of a strong quasi-normal passage shock at the mouth of rotor 2 extending from hub to near midspan, and (3) evolution of separated suction-side corner flow near rotor 2 hub inducing increased aero blockage production in the downstream stator (S2) hub clearance region. Thus, based on INV3D analysis at the design-intent backpressure, the original blading set is forced into an off-design operation due to aerodynamic mismatching.

Further insight into the nature of the design point mismatching can be gleaned from the predicted pressure-loading distributions for R1 (Fig. 5) and R2 (Fig. 6). These figures show three plots each. The first plot indicates the pressure-loading distribution, $\Delta p(r,z)$, for the original blading resulting from a multistage analysis at the design backpressure; the second plot is for an isolated analysis of each rotor using inflow/outflow conditions from the design point throughflow model; and the third plot is the design-intent pressure-loading distribution to be discussed shortly. A comparison of the multistage and isolated analysis results given in Fig. 5 indicates that R1 does not experience significant multistage design point mismatching effects; rather there exists a strong tip leakage/shock interaction resulting in larger aero blockage than intended. A similar comparison for R2, shown in Fig. 6, indicates significant multistage design point mismatch. The hub corner separation appears to be eliminated or greatly reduced for the isolated analysis of R2, which can be discerned by a comparison of the two loading distributions (i.e., Fig. 6(*a*) versus Fig. 6(*b*) with low Δp implying separation) along the hub section. It is evident that the passage shock for R2 is close to being spilled. Indeed, throttling the 2.5 stage to a higher backpressure of 4.02 leads to the passage shock of R2 being spilled completely, shortly followed by a numerical stall of the 2.5 stage.

To explore the viability of the inverse method for facilitating

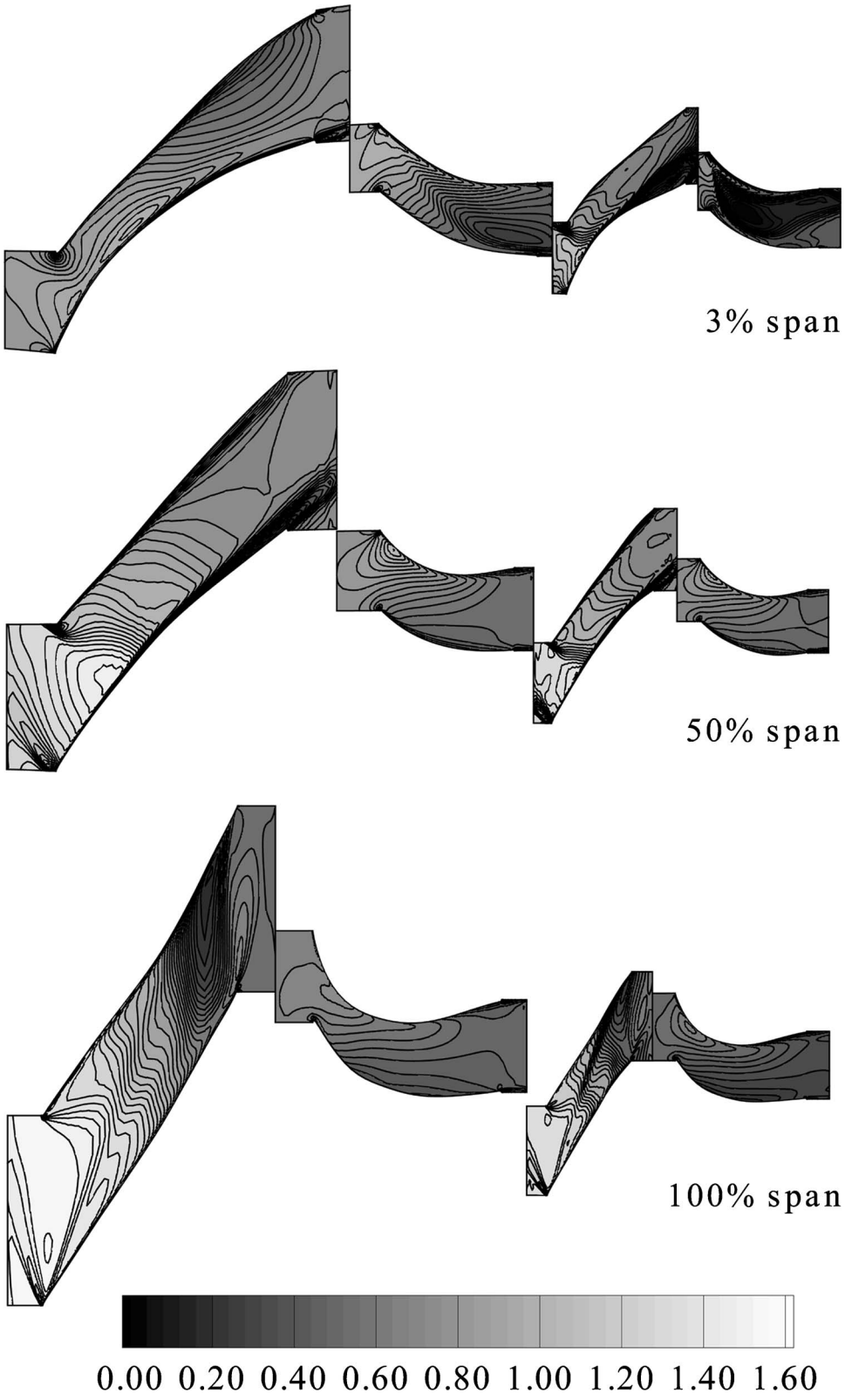

Fig. 4 Diagnosis (multistage analysis) of flow structure induced by original geometry at design point in terms of contours of relative Mach number at 3%, 50%, and 100% (rotor blade tip) span. IGV and exit region are not shown for clarity.

and improving design point matching, two design exercises have been executed. In the first, R1 and R2 are redesigned in isolation using the latest improved version of INV3D. Inflow and outflow conditions are specified in accordance with a design point throughflow model of the original design. The second involves the redesign of both rotors simultaneously within the multistage environment. Both cases employ exactly the same pressure-loading distributions. Design-intent pressure-loading distributions for the

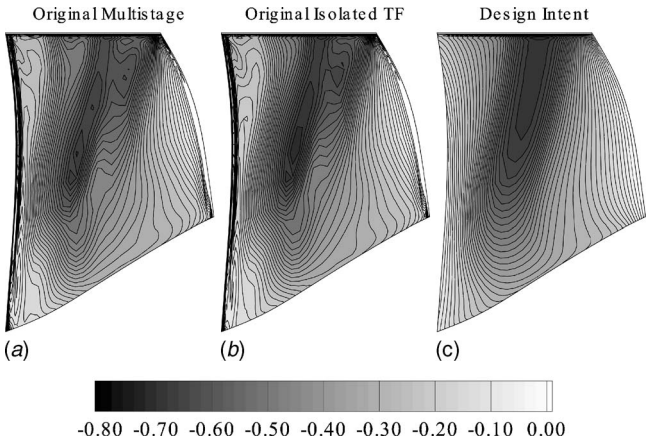

Fig. 5 Predicted pressure-loading distribution for original R1 at design point: (*a*) multistage analysis of original design, (*b*) isolated analysis of original R1 with throughflow conditions, and (*c*) prescribed design intent for redesign exercise

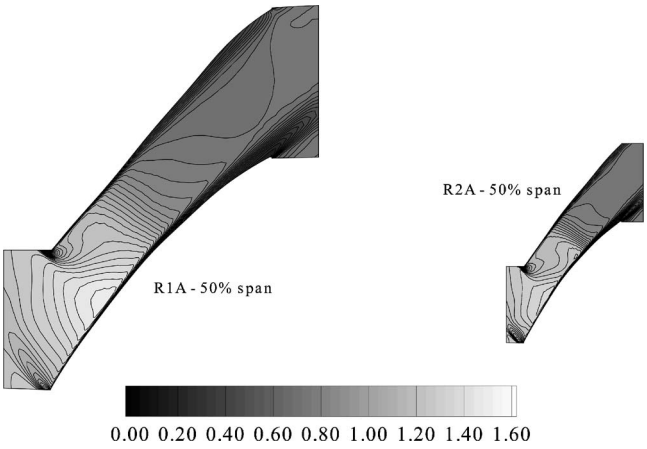

Fig. 7 Isolated analysis of R1 and R2 (case A) at design point in terms of midspan contours of relative Mach number

redesigns are shown in Figs. 5 and 6, respectively, for R1 and R2. The objective is for both rotors to have a single swallowed passage shock, positioned such that the shock extends from near the trailing edge at the blade tip to the leading edge at around 25% span, where the shock weakens as it enters a region of low-supersonic or subsonic flow at lower spanwise positions. These loading distributions, derived from numerical experiments, are chosen for the purpose of achieving reduced tip leakage/shock interaction, and to enable larger design-speed throttling range. A detailed explanation of the rationale behind these loading distributions is given in Refs. [9,22]. Furthermore, the separation region near the hub of R2 is to be removed, which should not only improve overall throttling capability but also provide better matching with Stator 2.

For the design-intent pressure-loading distribution of R1, the spanwise loading area distribution was taken directly from the analysis result of the original 2.5 stage at design backpressure. For R2, the spanwise distribution of loading area was altered slightly, increasing the loading near the hub and decreasing it elsewhere, while maintaining the total loading volume and therefore work done by the rotor. This was done to counter the separation region close to the hub. The loading area distributions used here are not directly tied to any "optimized" design-intent pressure field, especially considering that the passage shock for the original R2 is nearly spilled. However, the aim here is not to obtain a "best" axisymmetric-averaged design-intent pressure field, but to demonstrate the feasibility of the multistage design method to enforce a prescribed design-intent pressure-loading distribution and thus facilitate design point blade row matching. Note that the proposed pressure-loading manager indicated in Fig. 1(*b*) would attempt to manipulate the loading area in order to achieve design-intent averaged static pressure distributions consistent with other prescribed quantities. For both rotors, the axial position of the blade axis was set at about 20% axial chord.

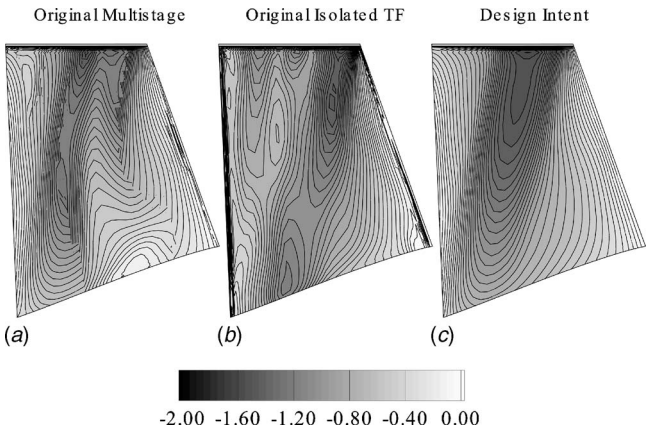

Fig. 6 Predicted pressure-loading distribution for original R2 at design point: (*a*) multistage analysis of original design, (*b*) isolated analysis of original R2 with throughflow conditions, and (*c*) prescribed design intent for redesign exercise

Design Case A: Rotors 1 and 2 Redesigned in Isolation. Both rotors were redesigned in isolation. Axisymmetric-averaged profiles of total pressure, total temperature and flow angles, obtained from the design point throughflow model, were specified as inflow conditions. Backpressures, also obtained from the throughflow model, of 1.645 for R1 and 3.48 for R2 were specified at the shroud, with radial equilibrium used to compute the spanwise distribution of static pressure. The newly obtained geometries, denoted as R1A and R2A, were then analyzed in isolation, with the same "throughflow" boundary conditions used for the redesign. Predicted relative Mach number distributions at midspan are shown in Fig. 7 for later comparison.

Figure 8 gives a design point (p_b=4.00) diagnosis of the flow structure as predicted by a multistage analysis of the 2.5 stage incorporating the newly designed R1A and R2A. For both rotors, the design-intent pressure-loading distribution along with its implied shock structure is *nearly* realized. However, closer inspection of Figs. 7 and 8 reveal the existence of aerodynamic mismatching manifested by the relative changes in shock structure between isolated and multistage operations. The passage shock for R2A (Fig. 8) is situated further upstream in the multistage environment than intended (Fig. 7). Similarly, R1A is throttled lower than intended in the multistage environment. Both rotors exhibit reduced tip leakage/shock interaction resulting in a much cleaner casing endwall flow than that of the original design. The suction-side hub corner separation is subdued and a significantly reduced level of aero blockage is generated in the hub clearance region of Stator 2 (Fig. 4 versus Fig. 8).

The changes in flow field (and therefore pressure-loading) from "intent" imply some sort of mismatching of the rotors to their surroundings. Noting the changes in Mach number levels that have occurred within the 2.5 stage, this in itself is not surprising. It does raise many questions, one of which is whether the observed changes could have been predicted and accounted for in the redesign. A simpler question to be answered, which is attempted here, is the following: if a blade is redesigned within its multistage environment, will the design adapt to this (possibly

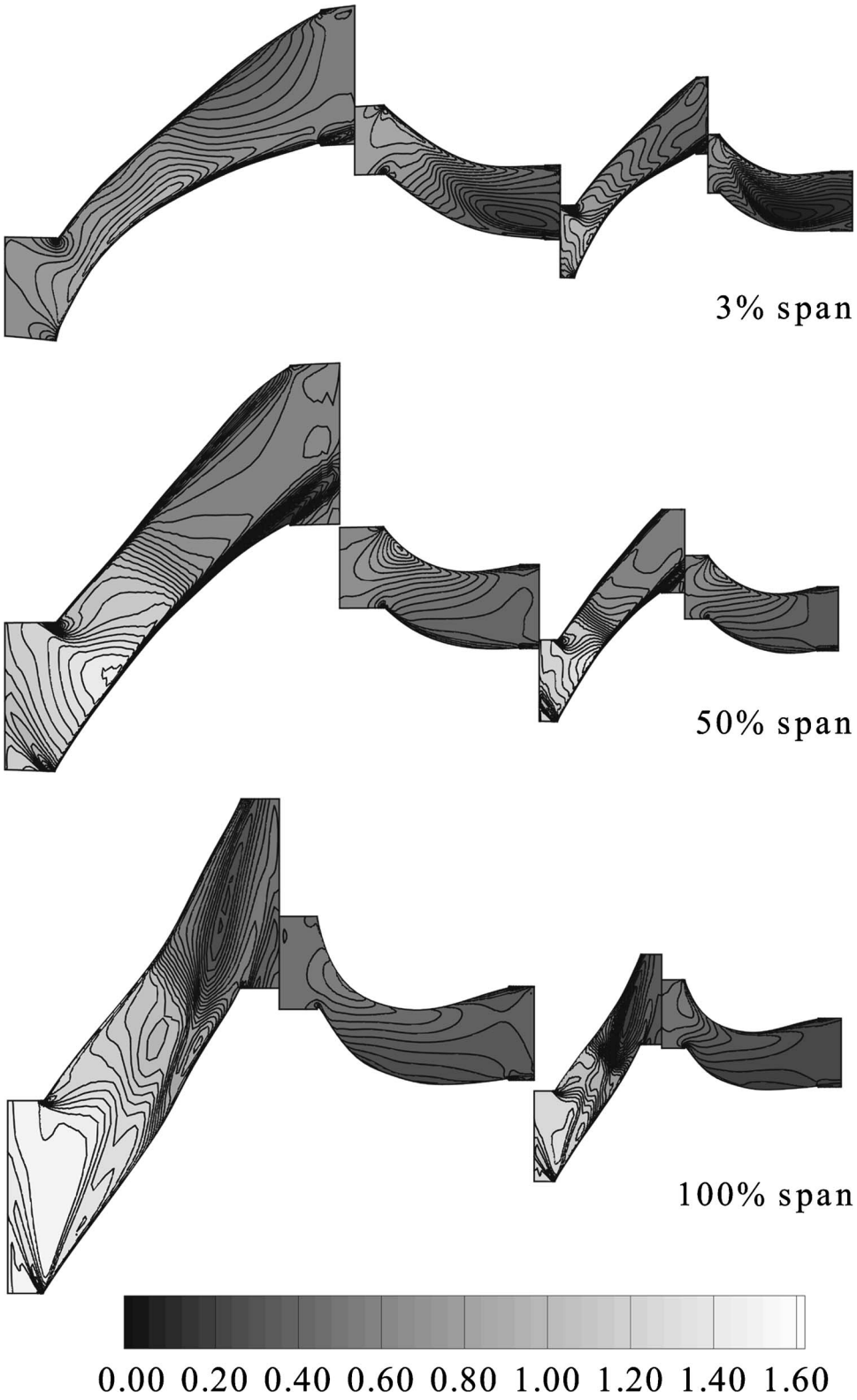

Fig. 8 Diagnosis of flow structure induced by design case A geometry at design point in terms of contours of relative Mach number at 3%, 50%, and 100% (rotor blade tip) span. IGV and exit region are not shown for clarity.

changing) environment in order to produce the desired intent in the form of specified pressure-loading distribution? To this end, design case B was performed.

Design Case B: Rotors 1 and 2 Redesigned in 2.5 stage. Here, both rotor 1 and rotor 2 were redesigned *simultaneously* within the 2.5 stage. The redesign calculation was restarted from the multistage analysis calculation of R1A and R2A. The exact same loading shapes and loading area distributions were used as

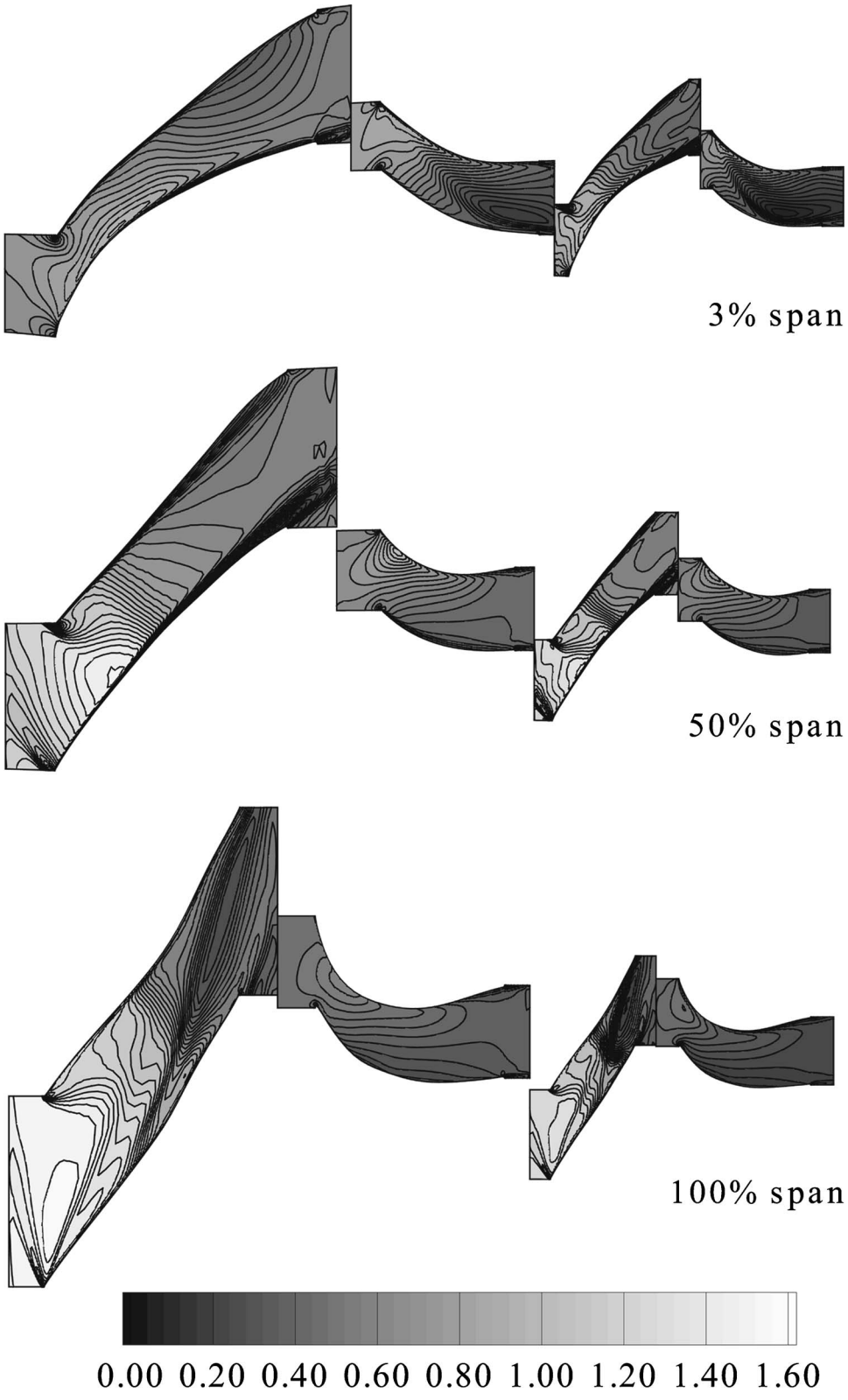

Fig. 9 Diagnosis of flow structure induced by design case B geometry at design point in terms of contours of relative Mach number at 3%, 50%, and 100% (rotor blade tip) span. IGV and exit region are not shown for clarity.

in design case A. The convergence rate in camber during the design calculation was lower than in the isolated designs. This was expected, because the blades have to adapt to changing inlet and exit conditions during the design calculation. However, the same level of convergence was ultimately reached as in the isolated designs. The rotor geometries obtained here are denoted as R1B and R2B.

Results of the subsequent design point multistage analysis with

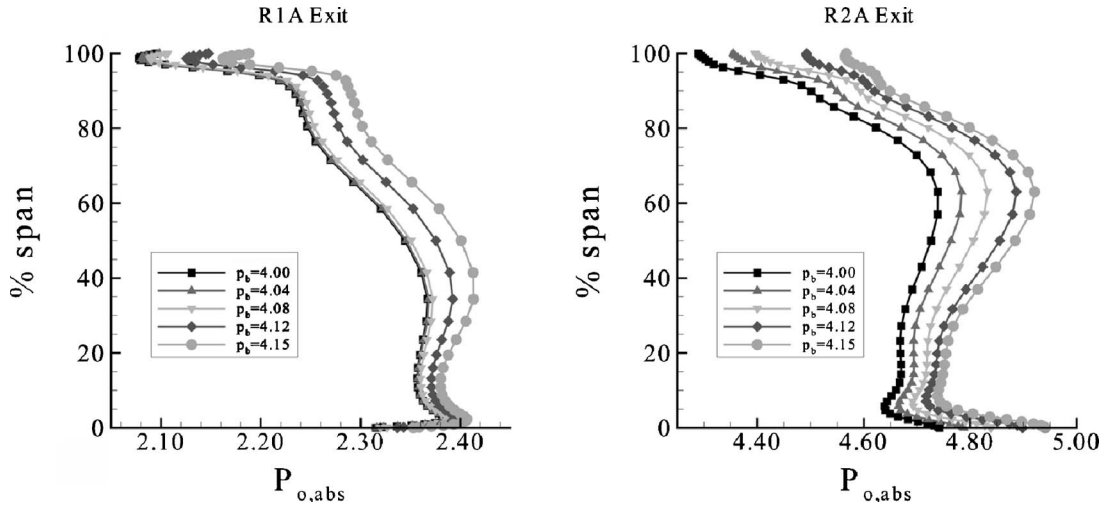

Fig. 10 Multistage analysis of design speed throttling (varying backpressure, p_b) for case A in terms of spanwise profiles of axisymmetric-averaged rotor exit cumulative total pressure

R1B and R2B are shown in Fig. 9. From the contours of relative Mach number in Fig. 9, it can be seen that both rotors now produce the implied flow structure of the design-intent pressure loading. Both rotors have passage shocks in their intended locations. In particular, the passage shock positions in both R1B and R2B are much closer to those shown in Fig. 7 than the case of R1A and R2A shown in Fig. 8. The flow field near the hub of stator 2 has improved somewhat relative to that of the isolated design (Fig. 8 versus Fig. 9).

Compressor Performance at Design Speed. Next, a design-speed multistage analysis of the redesigned rotors was performed at various backpressures from design to near stall (p_b =4.0–4.15). Note that the original design shown in Fig. 4 has very limited range; rotor 1 shock spills at a backpressure of around p_b=4.05. Results for case A (isolated blade design) and case B (multistage design) are shown in Figs. 10 and 11, respectively. Indicated, are plots of spanwise profiles of axisymmetric-averaged (mass weighted) rotor exit total pressure. It can be seen that case B has a superior throttling characteristic relative to that of case A. In particular, with respect to the second rotor, R2A is hub weak as the machine is throttled (Fig. 10), while the spanwise total pressure profile of R2B is relatively uniform (Fig. 11). With respect to the first rotor, R1B is completely insensitive to the compressor backpressure variations (Fig. 11), while R1A is insensitive to compressor throttling up to p_b=4.10.

Figure 12 shows comparison of the Mach number contours at the midspan station between case A (plots on left side) and case B (plots on right side). Inspection of these Mach number contours shows that above the backpressure value of p_b=4.10, the passage shock in R2A spills while it is still well inside the blade passage in R2B. It is also observed that the passage shock in R1B is much weaker than in R1A over the throttling range.

The differences in design-speed performance characteristic between case A and case B are further illustrated in Fig. 13 in terms of rotor total pressure ratio and adiabatic efficiency variations with compressor backpressure. This performance variation is strongly dictated by the passage area distribution of each rotor. Both rotors have a certain amount of internal contraction resulting from the prescribed pressure-loading distribution, which is intended to reduce the passage shock strength at design speed with possible negative effects on part-speed performance. It is clear that R1B remains choked throughout the throttling range as is evident by the nearly constant performance characteristic with varying backpressure. The rates of change of pressure ratio and

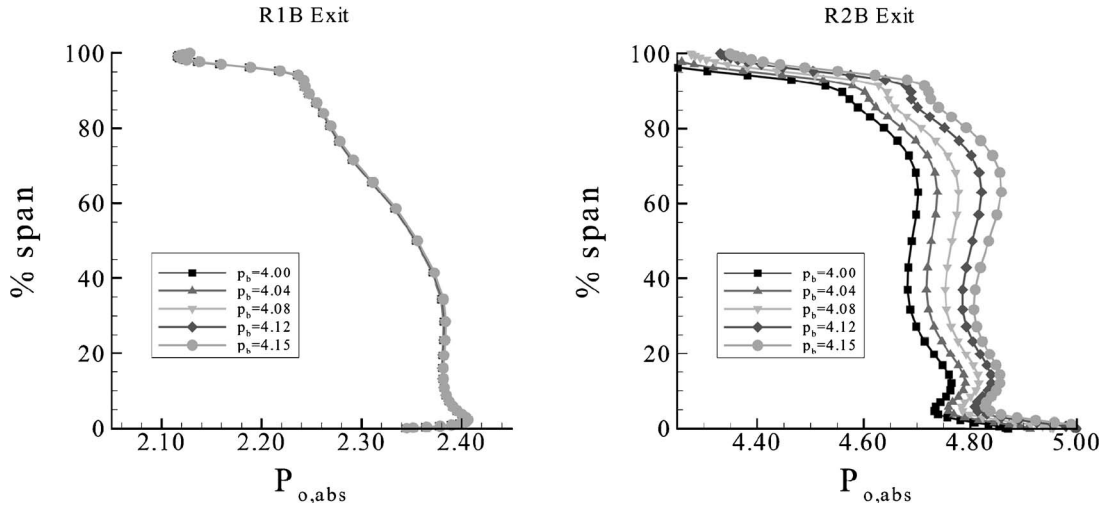

Fig. 11 Multistage analysis of design speed throttling for case B in terms of spanwise profiles of axisymmetric-averaged rotor exit cumulative total pressure

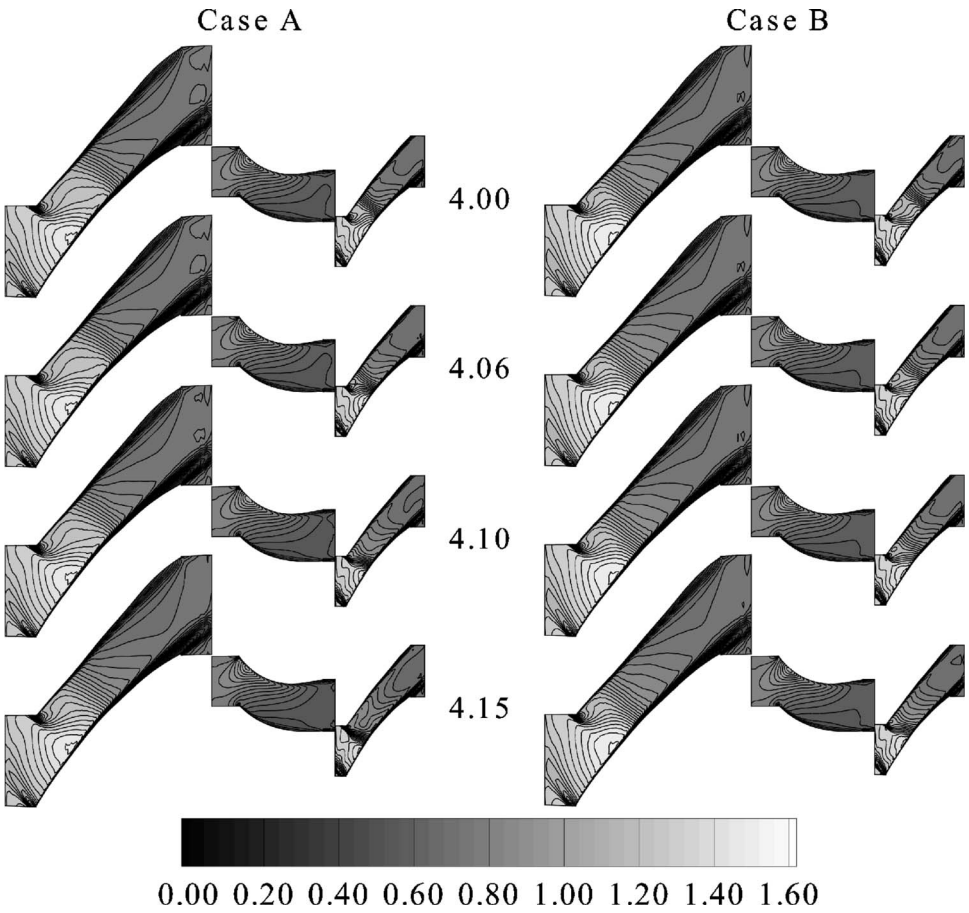

Fig. 12 Multistage analysis of design speed throttling for case A (left) and case B (right) in terms of relative Mach number contour at midspan for different backpressures

efficiency with backpressure for the two cases are very different indicating a superior design point blade row matching potential for case B. Assessment of the aero-stability of the 2.5 stage is computationally difficult and is subject to many uncertainties that are beyond the scope of this analysis. Heuristically, it would seem that R2B has a lager peak pressure rise potential than R2A, which does not necessarily imply a more favorable compressor in terms of ultimate throttling range. Finally, Fig. 14 shows that case B also exhibits a slight increase in adiabatic efficiency over the applied design-speed throttling range when compared to case A, on the order of 0.3%. Figure 14 indicates that for both case A and case B, the design requirement of an overall compression ratio of 4.65:1 at a backpressure of 4.0 is nearly satisfied.

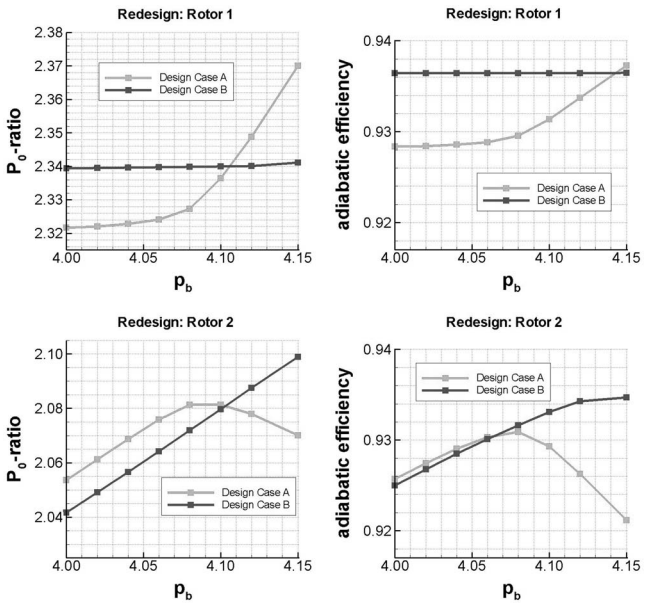

Fig. 13 Multistage analysis of design speed throttling for cases A and B. Shown are throttling characteristics of the respective rotors 1 and rotors 2 within the 2.5 stage.

In summary, this exercise shows that by using the newly implemented multistage inverse method, the resulting rotor blade designs (design case B) produce pressure-loading distributions closer to design-intent than when using the isolated blade row inverse method (design case A). The rotor blades designed using the multistage method also exhibit a more desirable design-speed throttling characteristic. Whether or not this leads to a more favorable aerostability characteristic requires further careful investigation.

Conclusions

An existing three-dimensional inverse blading design code, INV3D, has been successfully extended to handle multistage blading design and analysis via a steady averaging-plane blade row coupling scheme. The extended code has been successfully applied to redesign exercises involving a highly loaded 2.5-stage axial compressor.

It has been shown that multiple blades can be redesigned simultaneously in their mutually interacting environments with a modest increase in computational cost. Furthermore, the viability of

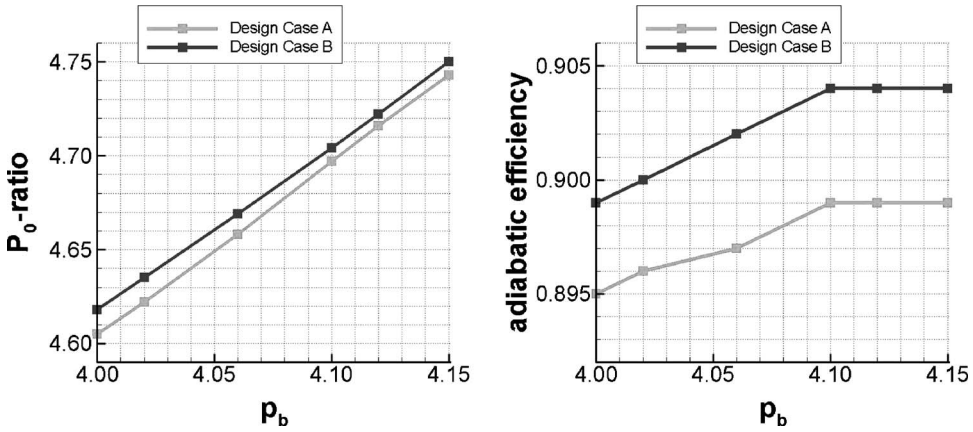

Fig. 14 Multistage analysis of design speed throttling for cases A and B. Shown are the throttling characteristics of the complete 2.5 stages.

inverse blading design for the purpose of enhanced design point aeromatching of multistage compressors has been demonstrated. This has the potential to greatly facilitate the process of blade row matching during design iterations, and is a significant improvement over existing approaches used to address design point aerodynamic matching.

Many more issues need to be addressed before this inverse design scheme can be successfully deployed in the future design system proposed herein. Noteworthy, is the need for a pressure-loading regulation scheme that automatically adjusts the pressure-loading distribution and magnitude in order to meet the required axisymmetric-averaged design intent static pressure field. It is hoped that the present investigation will serve to motivate further research.

Acknowledgment

This work was partially funded by NASA Glenn Research Center for whose support the authors are grateful.

References

[1] Adamczyk, J. J., 2000, "Aerodynamic Analysis of Multistage Turbomachinery Flows in Support of Aerodynamic Design," ASME J. Turbomach., **122**, pp. 189–217.
[2] Gallimore, S. J., 1999, "Axial Flow Compressor Design," *Developments in Turbomachinery Design*, J. Denton, ed., American Institution of Mechanical Engineers.
[3] Marble, F. E., 1964, "Three-Dimensional Flow in Turbomachines," *High Speed Aerodynamics and Jet Propulsion, Vol. X, Aerodynamics of Turbines and Compressors*, W. R. Hawthorne, ed., Princeton University Press, Princeton, NJ, pp. 83–165.
[4] Dang, T. Q., 1995, ' 'Inverse Method for Turbomachine Blades Using Shock-Capturing Techniques," AIAA Paper No. 95-2465.
[5] Qiu, X., 1999, "Improved Algorithm for Three-Dimensional Inverse Method," Ph.D. dissertation, Department of Mechanical Engineering, Syracuse University, Syracuse, NY.
[6] Damle, S., Dang, T., Stringham, J., and Razinsky, E., 1999, "Practical Use of a 3D Viscous Inverse Method for the Design of Compressor Blade," ASME J. Turbomach., **121**(2), pp. 321–325.
[7] Qiu, X., and Dang, T., 2000, "3D Inverse Method for Turbomachine Blading With Splitter Blades," ASME Paper No. 2000-GT-526.
[8] Dang, T., Damle, S., and Qiu, X., 2000, "Euler-Based Inverse Method for Turbomachine Blades: Part II—Three Dimensions," AIAA J., **38**(11), pp. 2007–2013.
[9] Medd, A. J., 2002, "Enhanced Inverse Design Code and Development of Design Strategies for Transonic Compressor Blading," Ph.D. dissertation, Department of Mechanical Engineering, Syracuse University, Syracuse, NY.
[10] Jameson, A., Schmidt, W., and Turkel, E., 1981, "Numerical Solution of the Euler Equations by Finite Volume Methods Using Runge-Kutta Time-Stepping Schemes," AIAA Paper No. 81-1259.
[11] Denton, J. D., 1992, "The Calculation of Three Dimensional Viscous Flow Through Multistage Turbomachines," ASME J. Turbomach., **114**, pp. 18–26.
[12] Wadia, A. R., and Beacher, B. F., 1990, "Three-Dimensional Relief in Turbomachinery Blading," ASME J. Turbomach., **112**, pp. 587–598.
[13] Reid, L., and Moore, R. D., 1978, "Design and Overall Performance of Four Highly-Loaded, High-Speed Inlet Stages for an Advanced, High-Pressure-Ratio Core Compressor," NASA TP-1337.
[14] Reid, L., and Moore, R. D., 1980, "Experimental Study of Low Aspect Ratio Compressor Blading," ASME Paper No. 80-GT-6.
[15] Hall, E. J., and Delaney, R. A., 1995, "Investigation of Advanced Counterrotation Blade Configuration Concepts for High Speed Turboprop Systems: Task VII-ADPAC User's Manual," NASA CR-195472.
[16] Dawes, W. N., 1992, "Toward Improved Throughflow Capability: The Use of Three-Dimensional Viscous Flow Solvers in a Multistage Environment," ASME J. Turbomach., **114**, pp. 8–17.
[17] Chima, R. V., 1998, "Calculation of Multistage Turbomachinery Using Steady Characteristic Boundary Conditions," NASA Technical Memorandum, No. 206613.
[18] Giles, M. B., 1990, "Nonreflecting Boundary Conditions for Euler Equation Calculations," AIAA J., **28**, pp. 2050–2058.
[19] Gropp, W., Lusk, E., Doss, N., and Skjellum, A., 1996, "A High-Performance, Portable Implementation of the MPI Message Passing Interface Standard," Parallel Comput., **22**, pp. 789–828.
[20] Gropp, W. D., and Lusk, E., 1996, "Guide for a Portable Implementation of MPI," ANL-96/6, Mathematics and Computer Science Division, Argonne National Laboratory.
[21] Larosiliere, L. M., Wood, J. R., Hathaway, M. D., Medd, A. J., and Dang, T. Q., 2002, "Aerodynamic Design Study of an Advanced Multistage Axial Compressor," NASA TP-211568.
[22] Medd, A. J., Dang, T. Q., and Larosiliere, L. M., 2003, "3D Inverse Design Loading Strategy for Transonic Axial Compressor Blading," ASME Paper No. 2003-GT-38501.

Elisabet Syverud
Department of Energy and Process Engineering,
NTNU,
Norwegian University of Science and Technology,
Trondheim, Norway

Olaf Brekke
Royal Norwegian Navy,
Bergen, Norway

Lars E. Bakken
Department of Energy and Process Engineering,
NTNU,
Norwegian University of Science and Technology,
Trondheim, Norway

Axial Compressor Deterioration Caused by Saltwater Ingestion

Gas turbine performance deterioration can be a major economic factor. An example is within offshore installations where a degradation of gas turbine performance can mean a reduction of oil and gas production. This paper describes the test results from a series of accelerated deterioration tests on a General Electric J85-13 jet engine. The axial compressor was deteriorated by spraying atomized droplets of saltwater into the engine intake. The paper presents the overall engine performance deterioration as well as deteriorated stage characteristics. The results of laboratory analysis of the salt deposits are presented, providing insight into the increased surface roughness and the deposit thickness and distribution. The test data show good agreement with published stage characteristics and give valuable information regarding stage-by-stage performance deterioration. [DOI: 10.1115/1.2219763]

Introduction

Compressor fouling causes 70–85% of the performance loss due to deterioration in gas turbines [1]. The degradation rate will be affected by site-specific conditions of the fouling and by engine operating conditions. A thorough review of engine performance deterioration mechanisms and modeling is given by Kurz and Brun [2].

From operating experience and literature the first stages of an axial compressor are expected to be the ones most heavily fouled. Deposits will have different characteristics depending on the nature of the fouling. Dry particles in dry atmospheres are likely to deposit in different areas compared to sticky matters and oily compounds. At high inlet humidity, the drop in static pressure during acceleration will increase the dust adhesion on the blades [3,4].

To understand and reveal the degradation and restoration mechanisms related to recoverable compressor deterioration, a systematic test campaign has been performed on a General Electric (GE) J85-13 jet engine. The overall performance of the gas turbine and compressor stage characteristics were analyzed in detail. The tests reflect actual performance deterioration as found in offshore applications and provide valuable information regarding overall and stage-by-stage compressor performance deterioration in a real engine.

The tests were part of a larger online water wash test program. The results from this program are reported in a different paper [5] which should be seen in context with the present work.

Test Facilities and Engine Description

The GE J85-13 engine has been a successful engine in different applications since it first entered service in 1960. More than 6000 of these engines are still in service worldwide. The Royal Norwegian Air Force (RNoAF) F-5 Freedom Fighters have two GE J85-13 engines for propulsion. Because these aircrafts have been replaced by the F-16 aircraft, one GE J85-13 engine has been made available to the Norwegian University of Science and Technology for use in this project. Engine testing was carried out at the RNoAF's test facilities at Kjeller, Norway. Kjeller is located inland, ~25 km east of Oslo at an altitude of 119 m above sea level.

The GE J85-13 is a compact, light-weight, single-spool turbojet engine. It has an eight-stage axial-flow compressor that is directly coupled to a two-stage turbine. The exhaust nozzle has a variable throat area, and the engine is equipped with an afterburner. The GE J85-13 is rated to deliver a minimum thrust of 2720 lb (12.1 kN) at 100% shaft speed without the afterburner and a minimum thrust of 4080 lb (18.1 kN) with full afterburner.

The eight-stage compressor has a pressure ratio of 6.5:1. First- and second-stage rotor blades are coated for corrosion protection. To handle off-design operation, the compressor has variable inlet guide vanes (IGV) and bleed-off-valves at stages 3–5, as well as a variable exhaust nozzle. The variable geometry is controlled by the throttle angle, but the timing is ambient temperature biased. At ISO conditions, IGV will be at maximum deflection and bleed-off-valves will be fully open below ~81% corrected speed and fully closed at >96% corrected speed. At ambient temperatures above ISO conditions, the bleed-off-valves will close at lower speed settings. The nozzle is controlled by the throttle as long as the engine is running below the exhaust temperature limit. When the maximum exhaust temperature is reached, the exhaust nozzle will open to increase the exhaust flow. This reversal in the exhaust nozzle schedule occurs close to the maximum throttle angle.

Bleed air is also used for internal cooling of the afterburner actuators, combustor liner, and turbine guide vanes. Bleed air for anti-ice is taken at the compressor discharge. The anti-ice air valve was kept closed during all tests associated with this project.

Engine Model Data. Detailed knowledge of compressor stage geometry is available through several sources providing a good basis for developing engine simulation models.

NASA carried out several tests on the GE J85-13 in the late 1960s and throughout the 1970s, and reported compressor stage temperature and pressure profiles [6], individual compressor stage characteristics [7,8] as well as gas path geometry [9].

Initial Engine Condition. The engine used in this test program was preserved and stored after serving ~300 h onboard an aircraft. The engine was not overhauled prior to testing.

To avoid disturbances to the airflow attributable to loose coating, the coating on the second-stage rotor blades was removed by hand prior to the testing, using emery paper grade 320. The compressor inlet, inlet guide vanes, first-stage rotor, and stator were cleaned by hand using solvent, while the upper half of the casing, including stator vanes from stages 1 to 7 were cleaned using an ultrasonic cleaning bath. In addition, online compressor cleaning was performed prior to the testing using water at a flow of 13.2 l/min, for a 30 second period at idle, 70%, 90%, 95%, and 100% corrected engine speed. Details of the online water wash system are given in a different paper [5].

Contributed by the International Gas Turbine Institute (IGTI) of ASME for publication in the JOURNAL OF TURBOMACHINERY. Manuscript received October 1, 2004; final manuscript received February 1, 2005. IGTI Review Chair: K. C. Hall. Paper presented at the ASME Turbo Expo 2005: Land, Sea and Air, Reno, NV, June 6–9, 2005, Paper No. GT2005-68701.

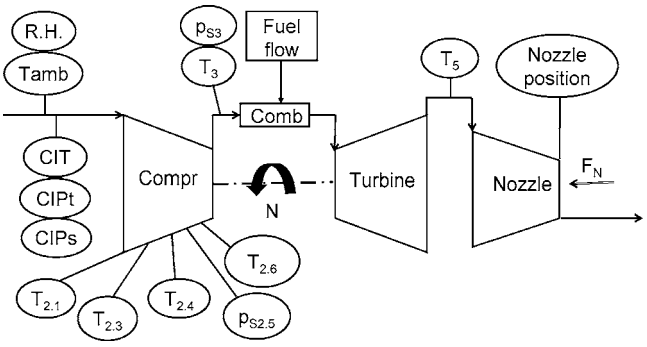

Fig. 1 GE J85-13 engine instrumentation

Engine Instrumentation

Additional sensors were installed to provide more information than is available from standard, test-cell instrumentation. The engine instrumentation is shown in Fig. 1.

The temperatures at stages 1, 3, 4, 6, and 8 were measured using a single resistance temperature detector (RTD) at each stator row. The entire 15 mm sensor length was immersed into the airflow, giving a representative measure of the gas path bulk average temperature. Because the sensors are unshielded, the velocity error will be significant in the temperature reading. The velocity error was calculated with a temperature recovery factor of 0.65 [10].

The static pressures at stage 5 and at compressor discharge were measured at a single point on the circumference. The stage 5 static pressure was measured in the bleed channel.

Engine throttle and nozzle position were recorded manually at each setting. Relative humidity and ambient temperature were recorded manually throughout the testing and measured at the same location outside of the test-cell intake. Due to test-cell recirculation, the recorded compressor inlet total temperature (CIT) was slightly higher than the measured ambient temperature. The CIT was measured using four sensors located at the engine inlet screen.

All instruments were calibrated prior to the test program, and the measurement uncertainties were calculated based on methods given in the ASME performance test codes [11,12].

To reduce the data scatter, a minimum of 60 data points (2 Hz sampling rate) were collected at each setting. The average of these readings was taken as the steady-state data point.

Engine Degradation Method and Equipment

Accelerated engine deterioration was done through the ingestion of atomized saltwater. A similar method has been used by the United States Navy [13]. The saltwater ingestion system is illustrated in Fig. 2. Saltwater was atomized in front of the compressor inlet using four atomizing nozzles installed on a bracket on the online water wash manifold positioned 0.77 m in front of the compressor inlet. This ensures complete atomization of the saltwater prior to the inlet guide vanes. The saltwater was gravity fed from a storage tank while air pressure was taken from the pressurized air supply in the test cell.

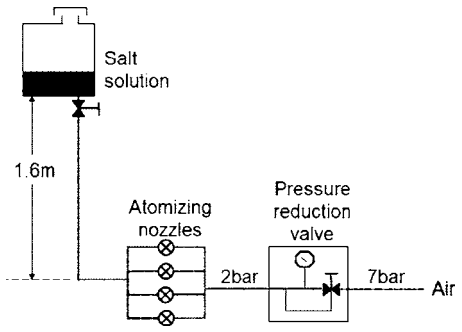

Fig. 2 Salt ingestion system

The droplet diameter of the saltwater spray was measured as 23 μm volume median diameter (VMD) in still air using a Malvern laser diffraction spray analyzer and applying the ASTM Standard for calculating spray characteristics [14]. The measurements were taken at the center of the fully developed spray at a distance of 44 cm from the nozzles. The 23 μm_{VMD} is higher than the <8 μm droplet size indicated as typical values after the intake filters of marine gas turbine units [15].

For all salt-deterioration tests, 3 l of saltwater were ingested at a flow rate of 0.2 l/min. The salt concentrations in the initial tests were 0.2% and 0.4% (by weight). For the accelerated deterioration tests associated with the online water wash trials, 3 l of saltwater was ingested with a salt concentration of 1% (by weight). The salt used in the tests constituted (by weight) 99.83% sodium chloride, 0.04% calcium, 0.03% magnesium, and 0.1% sulphione.

Test Procedure

The engine base lines were established for steady-state operation at 12 operating points from 60% corrected speed to full load. Prior to establishing each baseline, the engine was run for 5 min at full load. Engine speed was then reduced to idle before being increased to the initial throttle setting. At each throttle setting, the engine was allowed to stabilize for 1 min before reading 60 data points. To prevent impact of hysteresis from the instrument or control system, all throttle settings were established at increasing engine speeds. Engine base lines were recorded prior to degradation, after salt degradation, and after each online water wash.

All salt degradation trials were run at 10 deg throttle angle (equivalent to 97.5% engine shaft speed) at constant nozzle position and with closed bleed-off-valves and fully open IGV.

To completely clean the compressor of salt deposits, a 5 min online water wash was done at engine speeds varying from full speed to idle for two complete cycles using 17.6 l of water per minute (droplet size of 200 μm_{VMD}).

Salt Deposits

The salt deposits on the axial compressor were analyzed nondestructively. Deposits on the stator vanes were analyzed at a laboratory. The deposits on the rotor blades were visually evaluated, because the rotor assembly could not be moved to the laboratory within the available timeframe.

Location of Deposits. The salt deposits were mainly found along the leading edge of the first four stages and on the pressure side of the stator vanes along the hub. The heaviest deposits were found along the first-stage annulus, at the leading edge of the second-stage stator vanes and along the hub at the pressure side of the second-and third-stage blades and vanes.

Compared to the stator vane deposits, the deposits on the rotor blades were significantly smaller. The rotor blade deposits were mainly on stages 2–4. Deposits of a coarse structure were found along the hub, while deposits of a finer structure were found along the annulus. These deposits covered 35% of the second-stage pressure side and 20% of the third-stage pressure side.

For the fourth stage, the deposits were different from the previous stages, occurring as a shimmering layer covering the entire pressure side surface, except for the 20% closest to the hub. Suction-side deposits were virtually nonexisting, except for some traces found along the separation line on the first- and second-stage blades. Leading-edge deposits were found on stages 2–4.

Only immeasurable traces of salt (streaks) were found on the suction side of the fifth- and sixth-stage stator vanes and along the leading edge of the fifth-stage rotor blades. The spanwise distance between the streaks varied from 0.11 mm on the fifth-stage suc-

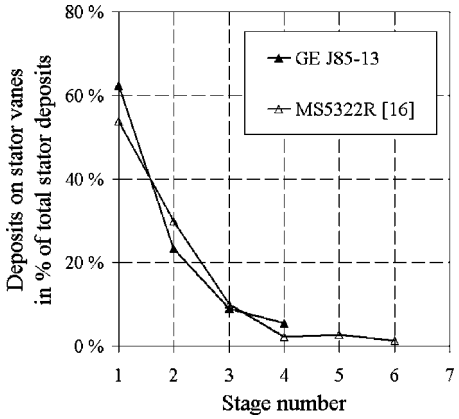

Fig. 3 Deposit distribution on stator vanes

tion side to 0.17 and 0.88 mm on the sixth-stage suction and pressure sides, respectively. No salt deposits were found on the sixth-stage rotor or on stages 7 and 8.

The salt deposits on the stator vanes at the top half of the compressor were measured by dissolving the salt in water and measuring conductivity and chloride content. The salt content measured by conductivity correlated well with the salt content measured by chloride content. Chloride content was transformed to a distribution of the salt deposits on the stator vanes as shown in Fig. 3.

In Fig. 3, the data are compared to results of an investigation of compressor blade contamination carried out on the 16-stage compressor of the Nuevo Pignone MS5322R [16]. The deposits are given as a percentage distribution to outbalance differences in the number of vanes measured. The salt deposits measured for the GE J85-13 include the deposits along the annulus; this is not the case for the data obtained for the MS5322R.

In the MS5322R, the rotor and stator blades of the first stage had more deposits on the suction side. The deposited masses on the blades aft of the first stage were approximately equal for the two sides. More deposits were found on the stator blades than on the rotor blades. It is suggested that this is due to a certain cleaning effect on rotor blades from the influence of centrifugal forces on the dirt particles [16]. The findings for the MS5322R correspond to the findings of this project, except that the salt deposits in the present study were mainly on the pressure side of the stator vanes.

Deposit Thickness. The salt deposits were analyzed using laboratory electron microscopes. Figure 4 shows the leading-edge deposits close to the hub on the second-stage stator vanes. The heavy leading-edge deposits are probably caused by the constant shaft speed during salt ingestion. The buildup is strong enough to withstand the increased turbulence due to changing incidence at lower speed settings, since only parts of the deposits were broken off by the airflow although the engine has been run at several speeds after salt deterioration. The leading-edge deposits were measured using the microscope and the results are given in Table 1.

Table 1 Leading-edge deposit thickness

Stator stage No.	Leading-edge salt deposits
1	No deposits at leading edge
2	500 μm at hub, 25 μm at annulus
3	200 μm at hub, no deposits along annulus
4	125 μm at hub, 25 μm at annulus
5–8	No deposits

Mean Line Salt Crystal Characteristics. The grain size and surface structure of the salt crystals along the mean line of the first three stators were analyzed from Struers replicas. Struers replicas enable three-dimensional replicas of material microstructure with a resolution as low as 0.1 μm [17]. In addition, the replicas collect loose surface particles that can be further analyzed with a microscope.

Figure 5 shows the salt grains found on a 330×240 μm surface on the pressure side of the first-stage stator. In general, the suction side had smaller, more homogenous grain sizes. The salt crystals on the pressure side were larger and more distributed; for stages 2 and 3 they were caught in a thin film of liquid salt flowing in the direction of the air flow.

The technical roughness is influenced both by the size and shape of the salt crystals as well as by the distribution of salt crystals along the blade. The authors are fully aware of the difficulties involved when measuring technical roughness. The estimation of a technical roughness level from the two-dimensional view given in Fig. 5 will only be approximate.

For all stages, the arithmetic mean diameter of the salt grains in the sample is considered a measure of the grain size, k. The average distance between the salt crystals is calculated based on the number of crystals found in the sample. The associated equivalent sand roughness, k_s, is estimated based on the average distance between the salt grains and by comparing the ratio of grain size to grain spacing with the associated equivalent sand roughness for regularly arranged spheres [18,19]. The relative roughness is the ratio of equivalent sand roughness to the blade chord length. The results are given in Table 2. As expected, the largest relative roughness is found on the pressure side.

The small chord lengths of the GE J85-13 compressor make the engine sensitive to small grain sizes (in terms of relative roughness). The equivalent sand roughness levels given in Table 2 imply less roughness than from a surface of emery grade 320 [20].

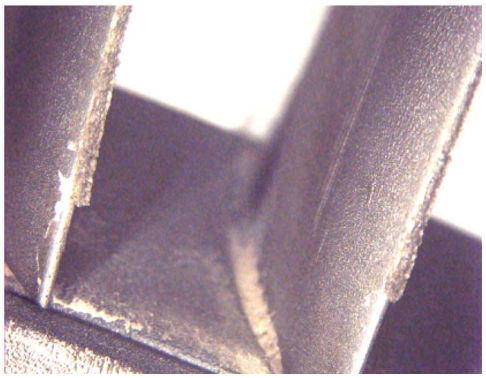

Fig. 4 Salt deposits at the leading edge of the second-stage stator vanes (at 6.5× magnification)

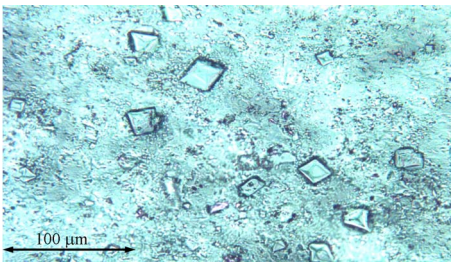

Fig. 5 Salt grains on first-stage stator vane pressure side along mean line (330×240 μm picture)

Table 2 Salt crystal grain size and distribution at mean line

Stator vane	Mean grain size, k (μm)	Mean grain distance (μm)	Equivalent sand roughness, k_s (μm)	Relative roughness, k_s/chord
1 PS	22	88	25	11*E*-4
1 SS	14	88	10	4*E*-4
2 PS	16	62	20	11*E*-4
2 SS	8	25	15	8*E*-4
3 PS	15	65	15	10*E*-4
3 SS	5	40	2	0.6*E*-4

Significance of Salt Deposits on Compressor Performance Characteristics

The effect of Reynolds number on compressor performance is well known for compressors in new and clean conditions. The ASME test code on compressors [21] does not give any attention to testing in deteriorated conditions. A study of Reynolds number effects in centrifugal compressors shows how efficiency can be correlated to increases in the friction factor with increased surface roughness [22]. Some research exists on the effect of increased roughness in axial compressors: A study of profile loss due to surface roughness on NACA 65-12(06) profiles showed a 2% increase in the profile losses at a relative roughness (k_s/chord) of 3*E*-4 and a 10% increase at 50*E*-4 [2]. Another study showed a 9% reduction in the static pressure ratio at a relative roughness of 10*E*-4, but the static pressure ratio is a strong function of the volume flow and blade velocity [20]. The effect of surface roughness on blade profile loss is quantified through a momentum thickness correlation [23]. Additional insight is given into the boundary layer characterization of rough surfaces, although applied to new and clean surfaces [19].

The critical roughness Reynolds number, defined in Eq. (1) [19], is independent of the characteristic length of the compressor

$$\mathrm{Re}_{\mathrm{critical}} = \frac{k_s V}{\nu} \tag{1}$$

When the critical Reynolds number is above 90, the flow can be assumed hydrodynamically rough with turbulent attached flow (i.e., with the salt crystals protruding into the laminar sublayer). For these cases, the associated blade profile loss will depend solely on the surface roughness to chord level, and not on the chord Reynolds number [19].

Applying Eq. (1) to the GE J85-13, a critical Reynolds number of 90 implies a maximum equivalent sand roughness of 5 μm. Table 2 shows the salt crystals have equivalent sand roughness levels above 5 μm for all stages except the suction side of stage three stator vanes. This implies that the blade loss, hence, the efficiency, of the deteriorated engine will be dependent on the roughness level and not on the chord Reynolds number. The change in stage efficiency should therefore be possible to calculate based on the correlation for momentum thickness with surface roughness [23].

Another aspect of the increased surface roughness is the change in deviation angle due to the thickening of the blade boundary layer. A correlation for changes in the deviation angle due to surface roughness is found from tests of a helicopter engine after 1500 h of flight [24]. The relative roughness levels reported were in the range of 10.9*E*-3 in the first stage to $0.7 \times 10E$-3 in the last stage and at Reynolds numbers of 240,000. Typical Reynolds numbers in the GE J85-13 are 200,000 to 600,000; however, the relative roughness level given in Table 2 is only one tenth of the level reported for the helicopter engine [24]. Therefore, changes to the deviation angle due to deterioration are considered negligible for the salt-deteriorated GE J85-13.

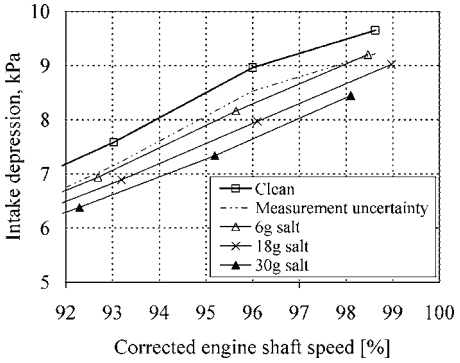

Fig. 6 Deterioration of intake depression

Engine Performance Deterioration

The engine deterioration due to salt deposits is analyzed in the following section. All overall engine performance parameters presented are corrected to ISO reference conditions [25]. Variations in humidity were not accounted for in the calculations. Data points measured at low speed settings were not included, because these include large unaccounted bleed flows.

Initial Salt Deterioration Trials. Figure 6 shows the results from the initial salt-deterioration testing, where salt was injected in three separate tests without water wash in between. The figure shows the total mass of salt ingested in the tests. The overall engine performance deterioration is shown for intake depression, which is defined as the difference between the total and static pressure in the bellmouth throat. The intake depression deteriorates rapidly and is outside of the measurement uncertainty tolerance even after 6 g of salt ingestion. The intake depression was the most sensitive parameter to compressor deterioration and was found to be the best method for condition monitoring of the engine, because it is less dependent of the engine control mode.

Overall Engine Performance Deterioration. The engine performance deterioration with 30 g of salt ingested is shown in Figs. 7–10. For simplicity in the presentation of data, only two representative cases are shown. These cases were recorded on the same day at identical compressor variable geometry and nozzle positions. Because the testing was done at ambient temperatures above the ISO reference condition, the 100% corrected speed setting was never reached. At these high ambient temperatures, the bleed-off valves are fully closed above 95% corrected speed.

Figure 7 shows the engine performance deterioration in terms of changes on the compressor equilibrium operating line. The static-to-total compressor pressure ratio is given at stage 5 (station 2.5) and at compressor discharge (station 3); both parameters are

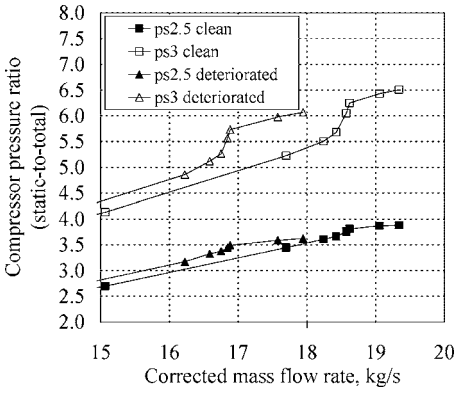

Fig. 7 Effect of deterioration on compressor operating line

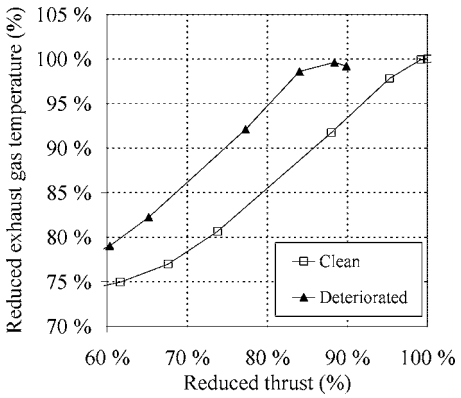

Fig. 8 Change in exhaust gas temperature with thrust

related to the total inlet pressure. Deterioration shifts the compressor operating line to a lower flow rate and a lower pressure ratio. Similar percentage changes to the compressor pressure ratio are found at both stations, indicating that the pressure deterioration was at the front end of the compressor. Front stage fouling is known to cause larger changes in the flow rate than in the pressure capability [3], and the results of Fig. 7 are in agreement with this.

The surge line is not known for the engine; however, surge was not encountered at any time during the test.

Figure 8 shows the change in exhaust gas temperature with thrust. The exhaust gas temperature is approximately nine percentage points higher for the deteriorated engine. The flattening of the deteriorated engine curve at the high end is due to exhaust gas temperature limitations in the engine control.

The variation in compressor isentropic efficiency with corrected engine shaft speed is shown in Fig. 9. This figure shows that

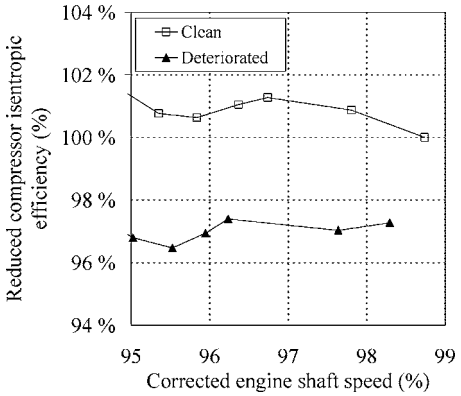

Fig. 9 Deterioration of compressor isentropic efficiency

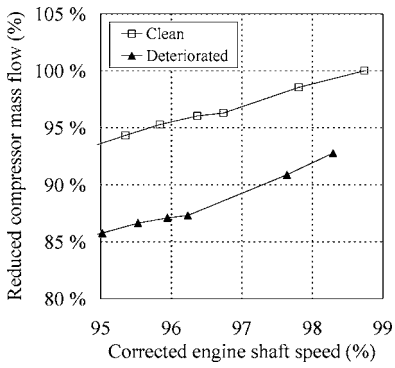

Fig. 10 Deterioration of compressor mass flow

deterioration reduces the isentropic efficiency by approximately three percentage points along the operating line, and reduces the engine operating speed. In addition, the isentropic efficiency curve is flattened when the maximum exhaust gas temperature is reached.

The variation in compressor mass flow rate with engine shaft speed is shown in Fig. 10. This figure shows the significant reduction in air flow rate for the deteriorated engine. Again, the deteriorated engine performance is shifted to a lower shaft speed; however, the mass flow rate is only slightly affected by the exhaust gas temperature limitation. Mass flow rate is directly related to the intake depression which was found as the best parameter for engine condition monitoring in the initial salt deterioration trials.

Stage Work Coefficient Deterioration

The compressor temperature measurements allow for a close look at the stage work coefficient during salt deterioration. The presented test data are limited to engine operation above 95% engine shaft speed where the engine bleed-off-valves were closed and the IGV fully open.

The following assumptions are made when analyzing the test data:

- The temperatures were measured at stages 1, 3, 4, 6, and 8, and a linear temperature distribution was used for the remaining stages. The stage temperatures were measured in the stator; however, the measurements were assumed to be valid at the stator outlet plane.
- The temperature dependence of the specific heat at constant pressure and the ratio of specific heats are defined by a fifth-order polynomial correlation for dry air [26] and a seventh-order polynomial for water vapor [25]. These polynomial correlations fit original data within 0.1% at the temperature range applicable to the GE J85-13.
- Air is assumed to be a thermally perfect gas, but with humidity included in the calculation of R, c_p, and γ as described in Appendix A. With an engine pressure ratio of 6.5:1, this implies a 0.3% error compared to the results using the Redlich-Kwong correlation for humid air mixtures [27] in the range of temperatures and pressures applicable to the GE J85-13 axial compressor.
- The axial velocity is assumed constant from rotor inlet to rotor outlet in a stage.
- The stage pressure rise is found from the measured polytropic efficiency.
- The stator deviation angle is assumed constant independent of incidence angle or corrected speed [9]. Increased deviation due to surface roughness is neglected as discussed above.
- The discharge coefficient of the bellmouth is assumed to be 0.98.
- The pressure loss in the IGV is assumed negligible. For the data presented, the fully open IGV will not cause any turning of the flow.
- Deterioration is assumed to increase the sidewall boundary layers due to deposits on the first-stage annulus. The resulting decrease in effective flow area is modeled through a blockage factor defined as the ratio of true flow area to geometrical flow area. Assuming no deviation of the eight-stage flow coefficient for the deteriorated engine compared to clean conditions, the deteriorated engine blockage factor was found to be 0.96. The blockage factor is assumed constant for all stages.
- The equations used to calculate stage performance are given in Appendix B.

The test data are compared to the theoretical work coefficient based on the engine geometry and the stage work coefficient found in literature [7].

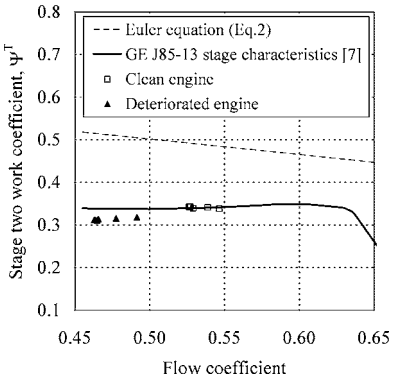

Fig. 11 Stage 2 work coefficient

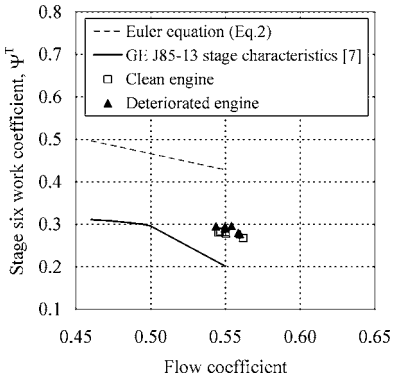

Fig. 14 Stage 6 work coefficient

The theoretical work coefficient is defined from the Euler turbine equation, Eq. (2) [28]

$$\Psi^T_{\text{theoretical}} = 1 - \Phi[\tan(\alpha_1) + \tan(\beta_2)] \tag{2}$$

where α_1 is the exit angle from the preceding stator and β_2 is the exit blade angle (relative) from the rotor.

The data published on the stage work coefficients are calculated based on constant values for c_p (1.005 kJ/kg K) and γ (1.4) [7]. In this paper, these gas properties are dependent on gas temperature and humidity. The difference will be largest in the aft stages where the gas temperatures are at the highest. Still, the published data gives a good indication of the GE J85-13 stage performance for a large range of flow coefficients.

Figures 11–14 show the change in the stage work coefficient with engine deterioration for stages 2–4 and 6. For stages 2–4, deterioration reduces both the stage work coefficient and the flow coefficient. This was expected for a degraded stage. For stage 6, the data for deteriorated engine and clean engine overlay each other. The same trend is found in all stages 5–8, indicating zero fouling in the aft stages. This agrees well with the observation of only minor traces of salt deposits in stages 5 and 6 and no salt deposits in stages 7 or 8.

The measurements are in good agreement with the published data [7] for stages 2–4. However, for stage 6, the measured stage work coefficient is higher than the published data. Because the current analysis is based on the difference between the clean and deteriorated condition, this deviation from expected stage work coefficient is of no consequence. The bellmouth discharge coefficient and the temperature recovery factor will influence on the stage work and flow coefficients. These factors are kept constant in the analysis.

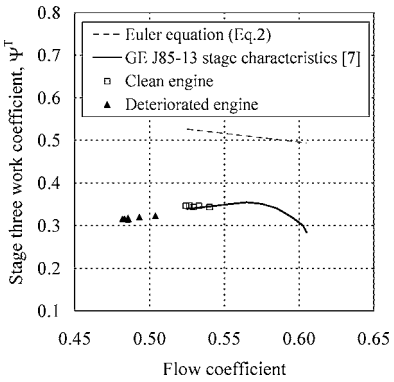

Fig. 12 Stage 3 work coefficient

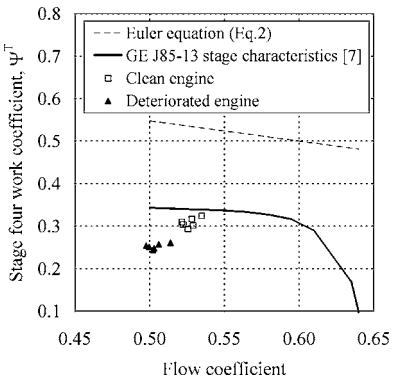

Fig. 13 Stage 4 work coefficient

Conclusions

The test results presented in this paper show deteriorated performance of the GE J85-13 jet engine after accelerated salt-deterioration tests undertaken at the test facilities of the Royal Norwegian Air Force. Accelerated salt testing was found to be an effective method to systematically deteriorate gas turbine compressor performance.

Deposited matter in an engine will depend on the nature of the deposits (i.e., the material, the particle size, and the adhesive capability of the deposits). With the present testing, the salt deposits were found mainly in the front stages of the compressor, and the stators were found to have more deposits than the rotor blades. The surface roughness levels and applicable Reynolds numbers were found to give added profile losses but no significant increases in the stator deviation angle.

The overall engine performance shows the difficulties involved in condition monitoring of deteriorated engines, because the deterioration causes a nonlinear shift in the degraded performance. This hampers the comparison of deterioration trends based on the calculation of percentage deviation at constant corrected engine speed.

Intake depression was found to be the parameter most sensitive to compressor deterioration. In addition, intake depression was less influenced by the engine control mode.

The test data show good agreement with published data on incremental stage work and give valuable information of stage-by-stage engine performance deterioration. The salt deterioration caused an increase in the sidewall boundary layers and significant deterioration in the stage characteristics of the first four stages.

This paper provides valuable information on stage performance deterioration used in the evaluation of test data from online water wash tests [5].

Acknowledgment

The project has been supported by Statoil ASA, Dresser-Rand Norwegian Operations and the Royal Norwegian Navy. The Royal

Norwegian Air Force is acknowledged for allowing access to their test facilities and for allowing us to borrow a GE J85-13 for test purposes. Without the help of Hans K. Henriksen, a retired test-cell operator of the RNoAF, this project would never have come to fruition.

Nomenclature

A = effective flow area (m^2)
c_p = specific heat at constant pressure (kJ/kg K)
C = absolute air velocity (m/s)
CIT = compressor inlet temperature (K)
CIP = compressor inlet pressure (kPa)
Comb = combustor (Fig. 1)
Compr = compressor (Fig. 1)
EGT = exhaust gas temperature (Fig. 1)
GE = General Electric
IGV = inlet guide vanes
ISO = International Organization for Standardization[1]
k = grain size of salt crystals (μm)
k_s = equivalent sand roughness (μm)
$\dot{m}$ = mass flow rate (kg/s)
MW = molecular weight (kg/kmole)
N = shaft speed (rpm)
NACA = National Advisory Committee for Aeronautics
NASA = National Aeronautics and Space Administration
p = pressure (kPa)
PS = pressure side (concave) of blades/ vanes
R = gas constant (kJ/kg K)
r = radius (m)
R_0 = universal gas constant (kJ/kg K)
Re = Reynolds number
R.H. = relative humidity (%)
RNoAF = Royal Norwegian Air Force
RTD = resistance temperature detector
SS = suction side (convex) of blades and vanes
Stg = stage
T = temperature (K)
U = blade velocity (m/s)
V = relative air velocity (m/s)
VMD = volume median diameter
war = Specific humidity (kg H_2O/kg dry air)
x = molar fraction of component

Greek Symbols

α = absolute air angle (deg)
β = relative air angle (deg)
ρ = air density (kg/m^3)
η = efficiency
ν = kinematic viscosity (m^2/s)
τ = temperature recovery factor
γ = ratio of specific heats
$\Psi^T = c_p \Delta T_t / U_{tip}^2$ = stage work coefficient
$\Phi = C_a / U_{tip}$ = flow coefficient

Subscripts

a = axial velocity component
amb = ambient condition
mix = mixture (humid air)
poly = polytropic
s = static condition
t = total condition
tip = tip
VMD = volume median diameter
w = tangential velocity component
2.1, 2.2,…, 2.7 = Compressor stage 1, 2,…, to stage 7
3 = Compressor discharge
5 = Turbine discharge

[1]ISO reference conditions assume an ambient temperature of 288.15 K, a barometric pressure of 101.325 kPa and a relative humidity of 60%.

Appendix A: Gas Properties for Humid Air

Gas properties for humid air are calculated from the following correlations [25]

$$c_{p\_mix} = \mathrm{war}_{molar} c_{p\_H_2O} + (1 - \mathrm{war}_{molar} c_{p\_dry\ air})$$

$$\gamma_{mix} = \mathrm{war}_{molar} \gamma_{H_2O} + (1 - \mathrm{war}_{molar} \gamma_{dry\ air})$$

$$R_{mix} = \frac{R_0}{MW_{mix}}$$

$$MW_{mix} = x_{H_2O} MW_{H_2O} + x_{dry\ air} MW_{dry\ air}$$

where $\mathrm{war}_{molar} = \mathrm{war}(28.96/18.015)$.

Appendix B: Stage Performance Calculations

Consider a stage where the rotor inlet, rotor outlet, and stator outlet are designated as stations 1, 2, and 3, respectively. The performance of a single stage is calculated using the following iterative sequence. The same sequence is used on all compressor stages.

(1) The following parameters are known at the rotor inlet: p_{t1}, p_{s1}, T_{t1}, T_{s1}, c_{p1}, γ_1, and $\dot{m}$.

(2) From the principle of conservation of mass and the assumption of a thermally perfect gas, the following parameters are calculated at the rotor inlet

$$\rho_1 = \frac{p_{s1}}{R_{mix} T_{s1}} \quad , \quad C_{a1} = \frac{\dot{m}}{\rho_1 A_1}$$

(3) The definition of total condition gives the absolute air velocity at the inlet

$$C_1 = \sqrt{2 c_{p\_mix\_1} (T_{t1} - T_{s1})} \quad , \quad C_{w1} = \sqrt{C_1^2 - C_{a1}^2}$$

(4) The blade velocities at rotor inlet and outlet are given by the shaft rotation, where the radius, r, is the mean line radius for calculation of velocity diagrams and the tip radius for calculation of stage work coefficient

$$U_1 = 2\pi r_1 \frac{N}{60} \quad , \quad U_2 = 2\pi r_2 \frac{N}{60}$$

(5) To start the calculation loop, the static temperature at the stator outlet, T_{s3}, is given an initial value.

(6) The total temperature is calculated from the temperature recovery factor and the measured temperature, T_m

$$\tau = \frac{T_m - T_s}{T_t - T_s} \Rightarrow T_t = \frac{1/\tau (T_m - T_s) + T_s}{1 - \tau}$$

(7) All stage work is applied in the rotor row, hence, the total temperature will not change across the stator row

$$C_{w2} = \frac{c_{p\_mix\_1} (T_{t2} - T_{t1}) + C_{w1} U_1}{U_2}$$

$$C_2 = \sqrt{C_{w2}^2 + C_{a2}^2}$$

$$T_{s2} = T_{t2} - \frac{C_2^2}{2 c_{p\_mix\_1}}$$

(8) Assuming constant axial velocity across the rotor row, $C_{a2} = C_{a1}$

$$\rho_2 = \frac{\dot{m}}{C_{a1}A_2}$$

$$p_{s2} = \rho_2 R_{\text{mix}} T_{s2}$$

$$p_{t2} = p_{s2}\left(\frac{T_{t2}}{T_{s2}}\right)^{\gamma_{\text{mix}}/(\gamma_{\text{mix}}-1)}$$

(9) The stage pressure rise is found from the measured polytropic efficiency and assumed constant in all stages

$$p_{t3} = p_{t1}\left(\frac{T_{t3}}{T_{t1}}\right)^{\eta_{\text{poly}}\gamma_{\text{mix}}/(\gamma_{\text{mix}}-1)}$$

$$p_{s3} = p_{t3}\left(\frac{T_{s3}}{T_{t3}}\right)^{\gamma_{\text{mix}}/(\gamma_{\text{mix}}-1)}$$

$$\rho_3 = \frac{p_{s3}}{R_{\text{mix}} T_{s3}}$$

(10) The stator exit velocity is found assuming zero deviation in the stator blade exit angle, $\beta_3 = 0$

$$C_{a3} = \frac{\dot{m}}{\rho_3 A_3}$$

$$C_3 = C_{a3}\cos(\alpha_3)$$

(11) Then, the value for c_{p_mix} at the stator outlet is updated based on T_{s3} and a new value for static temperature at the stator outlet is calculated

$$T_{s3} = T_{t3} - \frac{C_3^2}{2c_{p\_\text{mix}\_3}}$$

(12) The calculations are repeated from step 6 and on using the value for T_{s3} found in step 11, and the whole sequence is repeated until T_{s3} converges.

References

[1] Diakunchak, I. S., 1992, "Performance Degradation in Industrial Gas Turbines," ASME J. Eng. Gas Turbines Power, **114**, pp. 161–168.

[2] Kurz, R., and Brun, K., 2001, "Degradation in Gas Turbine Systems," ASME J. Eng. Gas Turbines Power, **123**, pp. 70–77.

[3] Zaba, T., 1980, "Losses in Gas Turbines Due to Deposits on the Blading," Brown Boveri Rev., **67**(12), pp. 715–722.

[4] Meher-Homji, C. B., Chaker, M. A., and Motiwala, H., 2001, "Gas Turbine Performance Deterioration," *Proceedings From the 30th Turbomachinery Symposium*, Texas A&M, College Station, TX.

[5] Syverud, E., and Bakken, L. E., 2007, "Online Water Wash Test of GE J85-13," ASME J. Turbomach., **129**(1), pp. 136–142.

[6] Hager, R. D., 1977, "Analysis of Internal Flow of J85-13 Multistage Compressor," NASA TM X-3513.

[7] Milner, E. J., and Wenzel, L. M., 1975, "Performance of a J85-13 Compressor With Clean and Distorted Inlet Flow," NASA TM X-3304.

[8] Willoh, R. G., and Seldner, K., 1969, "Multistage Compressor Simulation Applied to the Prediction of Axial Flow Instabilities," NASA TM X-1880.

[9] Tesch, W. A., and Steenken, W. G., 1976, "Blade Row Dynamic Digital Compressor Program: Volume 1 J85 Clean Inlet Flow and Parallel Compressor Models," NASA CR-134978.

[10] AGARD, 1990, "Recommended Practices for Measurement of Gas Path Pressures and Temperatures for Performance Assessment of Aircraft Turbine Engines and Components," AGARD Advisory Report AR-245, H. I. H. Saravanamuttoo, ed., AGARD, Neuilly Sur Seine, France.

[11] ASME, 1997, *Performance Test Code on Gas Turbines*, ASME PTC 22-1997, ASME, New York.

[12] ASME, 1998, *Test Uncertainty*, ASME PTC 19.1-1998, ASME, New York.

[13] Caguiat, D. E., Zipkin, D. M., and Patterson, J. S., 2002, "Compressor Fouling Testing on Rolls Royce/Allison 501-K17 and General Electric LM2500 Gas Turbine Engines," ASME Paper No. GT2002-30262.

[14] ASTM, 1992, *Standard Practice for Determining Data Criteria and Processing for Liquid Drop Size Analysis*, ASTM E 799-92, ASTM International, West Conshohocken, PA.

[15] Caguiat, D. E., Connor, J., Duckless, E., and DeCorso, R. J., 2004, "Inlet Air Salt Concentration Detection on U.S. Navy Ship Service Gas Turbine Generator Sets," ASME Paper No. GT2004-53984.

[16] Tarabrin, W. P., Schurovsky, V. A., Bodrov, A. I., and Stalder, J.-P., 1998, "Influence of Axial Compressor Fouling on Gas Turbine Unit Performance Based on Different Schemes and With Different Initial Parameters," ASME Paper No. 98-GT-416.

[17] Struers RepliSet System, Struers A/S, Ballerup, Denmark, http://www.struers.com

[18] Schlichting, H., 1979, *Boundary-Layer Theory*, 7th ed., Mc Graw-Hill, New York.

[19] Schäffler, A., 1980, "Experimental and Analytical Investigation of the Effects of Reynolds Number and Blade Surface Roughness on Multistage Axial Flow Compressors," ASME J. Eng. Power, **102**, pp. 5–13.

[20] Bammert, K., and Woelk, G. U., 1979, "The Influence of the Blading Surface Roughness on the Aerodynamic Behavior and Characteristic of an Axial Compressor," ASME Paper No. 79-GT-102.

[21] ASME, 1997, *ASME Performance Test Code on Compressors and Exhausters*, ASME PTC 10, ASME, New York.

[22] International Compressed Air and Allied Machinery Committee, 1987, "Influence of the Reynolds Number on the Performance of Centrifugal Compressors," ASME Paper No. 87-GT-10.

[23] Koch, C. C., and Smith, L. H., 1979, "Loss Sources and Magnitudes in Axial-Flow Compressors," ASME J. Eng. Power, **98**, pp. 411–424.

[24] Mal'tsev, Yu. N., and Shakov, V. G., 1989, "Influence of Roughness of Deposits in Compressor Cascade on Flow Lag Angle (English Translation)," Izvestiya VUZ, Aviatsionnaya Tekhnika, **32**, pp. 80–82.

[25] Walsh, P. P., and Fletcher, P., 1998, *Gas Turbine Performance*, Blackwell Science, Oxford.

[26] Keenan, J. H., Chao, J., and Kaye, J., 1983, *Gas Tables International Version, SI Units*, 2nd ed., Wiley, New York.

[27] Aungier, R. H., 2003, "A Fast, Accurate Real Gas Equation of State for Fluid Dynamic Analysis Applications," ASME J. Fluids Eng., **177**, pp. 277–281.

[28] Saravanamuttoo, H. I. H., Rogers, G. F. C., and Cohen, H., 2001, *Gas Turbine Theory*, 5th ed., Prentice-Hall, Englewood Cliffs, NJ.

Matthew D. Langford
Techsburg, Inc.,
2901 Prosperity Road,
Blacksburg, VA 24060
e-mail: mlangford@techsburg.com

Andrew Breeze-Stringfellow
GE Aircraft Engines,
1 Neumann Way,
Cincinnati, OH 45215
e-mail: andy.breeze-stringfellow@ae.ge.com

Stephen A. Guillot
Techsburg, Inc.,
2901 Prosperity Road,
Blacksburg, VA 24060
e-mail: sguillot@techsburg.com

William Solomon
GE Aircraft Engines,
1 Neumann Way,
Cincinnati, OH 45215
e-mail: william.solomon@ae.ge.com

Wing F. Ng
Mechanical Engineering Department,
Virginia Tech,
Blacksburg, VA 24060
e-mail: wng@vt.edu

Jordi Estevadeordal
Innovative Scientific Solutions, Inc.,
2766 Indian Ripple Road,
Dayton, OH 45440
e-mail: jordi@innssi.com

Experimental Investigation of the Effects of a Moving Shock Wave on Compressor Stator Flow

Linear cascade testing was performed to simulate the flow conditions experienced by stator blades in an axial compressor with supersonic relative Mach numbers at the inlet to the downstream embedded rotors. Experiments were conducted in a transonic blow-down wind tunnel with a nominal inlet Mach number of 0.65. A single moving normal shock introduced at the exit of the stator cascade simulated the bow shock from a downstream rotor. The shock was generated using a shock tube external to the wind tunnel. Pressure measurements indicated that the stator matched its design intent loading, turning, and loss under steady flow conditions. Effects of the passing shock on the stator flowfield were investigated using shadowgraph photography and digital particle image velocimetry (DPIV). Measurements were taken with three different shock strengths. In each case, the passing shock induced a vortex around the trailing edge of the stator. The size and strength of these vortices were directly related to the shock strength. A suction side separation on the trailing edge of the stator was observed and found to correlate with the vortex blockage. [DOI: 10.1115/1.2370745]

Introduction

The trend toward higher stage loadings in axial compressors is driving the designer to include embedded rotor stages with leading edge relative Mach numbers in excess of unity over most of the rotor span. Under these conditions the rotor will have either a weak attached bow shock or possibly a strong detached shock upstream of the leading edge, depending on its design and operating condition. At the design rotational speed, it is desirable for maximum rotor efficiency to position a normal shock structure near the minimum flow area region of the rotor passage, with an additional weak oblique bow shock attached to the rotor leading edge, as seen in Fig. 1(*a*). The relatively small stagnation pressure loss due to these shocks is generally acceptable when compared with the increased mass flow rate and pressure ratio afforded by transonic rotor operation. At compressor operating points below the design rotational speed or when experiencing an elevated back-pressure, the shock structure detaches and is pushed entirely upstream of the rotor leading edge, as seen in Fig. 1(*b*) [1–3]. Unlike the weak bow shock present at the design condition, the strong bow shock, which occurs under off-design operation, extends relatively far upstream from the rotor leading edge. If the axial spacing between the upstream stator and the embedded transonic rotor is consistent with normal compressor design practice, the rotor bow shocks will impact the stator trailing edge.

The issue of transonic rotor-stator interactions has been a topic of both experimental and analytical research recently. The general consensus among these researchers is that the losses in transonic compressors increase rapidly as axial spacing between stages is reduced. Prasad [4] developed a numerical simulation of the upstream-propagating shock waves from the isolated compressor designated NASA Rotor-35. Prasad compared viscous numerical results to a semi-analytical acoustic model and concluded that the shock wave evolution is primarily an inviscid phenomenon. The shock-induced circumferential pressure distortion near the stator trailing edge for an isolated rotor was compared to results for the same rotor imbedded in a time-accurate multi-stage simulation, leading Prasad to conclude "…that one may use the induced pressure distortion generated by an isolated rotor to obtain conservative preliminary estimates for the distortion experienced by the upstream stator trailing edge flow in a multi-stage environment." In addition, it was shown that to maintain a given level of induced pressure distortion, the axial spacing required between a transonic/supersonic rotor and its upstream stator must be nearly twice that required for a subsonic compressor.

Gorrell et al. [5,6] conducted an experimental investigation of the effect of blade-row spacing on the performance of a transonic compressor using the U.S. Air Force Research Laboratory's Stage Matching Investigation (SMI) rig. Mass flow rate, pressure ratio,

Contributed by the International Gas Turbine Institute (IGTI) of ASME for publication in the JOURNAL OF TURBOMACHINERY. Manuscript received October 1, 2004; final manuscript received February 1, 2005. IGTI Review Chair: K. C. Hall. Paper presented at the ASME Turbo Expo 2005: Land, Sea and Air, Reno, NV, June 6–9, 2005, Paper No. GT2005-58722.

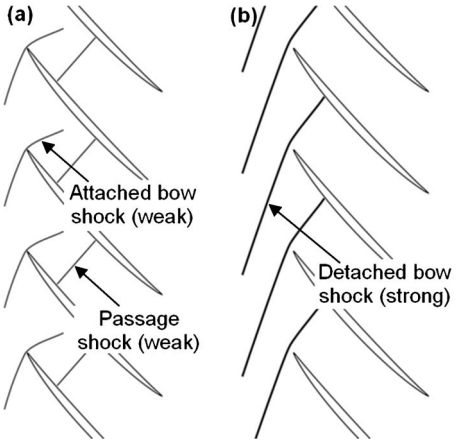

Fig. 1 Schematic of transonic rotor shock structure under (a) design and (b) off-design operation [1–3]

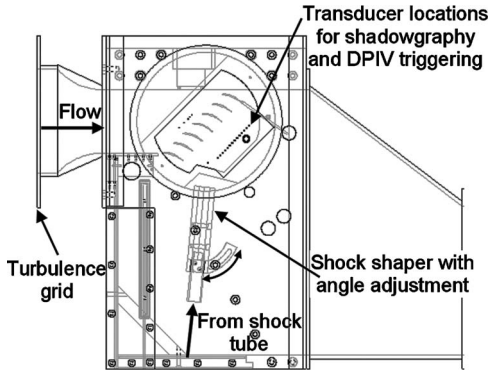

Fig. 2 CAD drawing of the cascade test section in the Virginia Tech Transonic Cascade Wind Tunnel

and efficiency all decreased as the axial spacing between the upstream wake generator and the transonic rotor was reduced. At close spacing, an additional loss beyond mixing losses was present. Part 2 of the paper presents CFD results for the same wake generator/transonic rotor system used in the experiment. At far axial spacing between the wake generator row and the rotor row, the rotor bow shock has degenerated into a weak pressure wave by the time it reaches the wake generator surface and is simply blocked. At close axial spacing, however, the shock turns normal to the wake generator surface as it passes the trailing edge and propagates upstream. The wake generator flow is supersonic relative to this moving wave, and thus Gorrell et al. conclude that it acts like a normal shock, causing significant entropy generation and total pressure loss.

Estevadeordal et al. [7] documented the flow field within a transonic compressor using DPIV. This experimental study also took place at the AFRL SMI rig. Data were gathered for two span-wise locations, two different wake generator counts, and two axial spacings between wake generator and rotor. The wake generators (WGs) in this test had blunt trailing edges, which led to vortex shedding in the wake. These vortices were found to grow as they convected downstream. For the largest axial spacing tested, the vortices are estimated to be 30% larger than the WG thickness. The vortex shedding frequency was largely dictated by the rotor blade passing frequency. Flow patterns such as the number and location of the vortices were always similar for a given rotor blade passing frequency. The rotor bow shocks provided a strong periodic pressure fluctuation that forced the synchronization of the vortex shedding to the shock-passing frequency.

Sanders et al. [8] performed an experimental investigation of rotor-IGV interactions in a transonic compressor using the Purdue transonic multistage axial compressor research facility. At purely subsonic rotor operating speeds, the upstream IGV flow field experienced only mild variations throughout the rotor blade-passing cycle, mostly due to slight back pressure variations. However, under transonic rotor operation, a complex time-dependent shock wave pattern propagated upstream through the IGV passage, causing large fluctuations in the location of the trailing edge stagnation point.

Zachcial and Nurnberger [9] numerically investigated the effects of axial spacing in subsonic and transonic stages (using a two-dimensional computational domain representative of the flowfield near the tip). They documented the computation of vortex shedding from the stator trailing edges in the case of a transonic rotor with a detached bow shock and concluded that the vortex structure was due to unsteady flow separation on the stator. They computed that for a transonic stage, the stage efficiency increased with reduced spacing. This initially seems counter to Gorrell et al.'s results; however, Zachcial and Nurnberger focused on only the radial location near the tip, a region that Gorrell et al. found to exhibit reduced losses with decreasing stage spacing (despite an increase in the net losses for the entire stage).

In the current work, the stator flow environment within a close-stage-spacing embedded transonic compressor was simulated by a linear cascade of loaded stator blades. The steady performance of the stator cascade was measured to provide a baseline to which cases involving the moving shock could be compared. A moving shock wave was then introduced into the stator cascade to simulate the detached bow shock from a downstream transonic rotor operating at off-design conditions. The effects of this passing shock on the stator flow field were explored qualitatively using shadowgraph photography and quantitatively using digital particle image velocimetry (DPIV).

Experimental Setup

The experiments took place at the Transonic Cascade Wind Tunnel at Virginia Tech. It is a blow-down-type tunnel, providing up to 20 s of usable run time for the inlet Mach number of 0.65 used in these tests. A four-stage Ingersoll-Rand type H reciprocating compressor provides the air supply for the tunnel. Before entering the tunnel, the air is filtered, cooled, dried, and stored in outdoor tanks. The tunnel is run by a computer-controlled main valve and simple feedback electronics, which maintain a specified stagnation pressure downstream of the control valve. A turbulence grid was mounted upstream of the test section, generating a turbulence intensity of about 1.6%, with a length scale of 1.7 cm [10]. Figure 2 is a CAD drawing of the cascade test section in the wind tunnel.

Although the blade profile of stators in actual transonic compressors varies extensively in the radial direction, a typical midspan blade profile was chosen for the cascade tests. Table 1 describes the key parameters for the cascade. The cascade stators have a 0.76 mm endwall clearance from 50% chord to the trailing edge. This clearance allows a small amount of leakage flow from the pressure surface to the suction surface, helping to prevent

Table 1 Cascade parameters

Blade chord, cm (in.)	7.62 (3.00)
Blade span, cm (in.)	15.24 (6.00)
Blade pitch, cm (in.)	5.04 (1.98)
Solidity	1.512
Blade turning angle	35 deg
Stagger angle	23.5 deg
Inlet Mach number	0.65
No. of blades	7
Blade trailing edge thickness, mm (in.)	0.89 (0.035)
Stator Reynolds no.	1.05×10^6

corner separation that would otherwise damage the two-dimensional nature of the experiment. The blades are mounted to the acrylic test section windows using four 3.175 mm diameter pins.

The moving shock was generated by rupturing a Mylar diaphragm within a pressurized shock tube and transferring the resulting shock into the test section. The shock tube consists of two sections of 3 in. nominal diameter steel pipe separated by the diaphragm. The shock strength, measured as the static pressure ratio across the shock front, is directly proportional the diaphragm thickness. To initiate the shock, the driver section was rapidly compressed with helium until the diaphragm ruptured. Helium was used as the driver gas because a greater shock static pressure ratio may be achieved at a lower driver pressure when the ratio of fluid acoustic velocities between the driver and driven sections is increased [11]; the acoustic velocity of helium is roughly three times greater than air.

After the shock was fully developed within the driven section of the shock tube, it was transmitted through flexible reinforced tubing into the test section. Before being introduced into the cascade, the shock was passed through a shock shaper apparatus. The purpose of the shock shaper was to expand the shock in such a way that the wave becomes purely cylindrical (i.e., 2-D), rather than spherical, as it passed the stator blades. The design of the shock shaper was based on a similar apparatus developed by Doughty [12] for the purpose of turbine shock research. After consulting literature on the subject [13–15], Doughty chose to use a tapered shock shaper with a divergence angle of 24 deg. This angle minimized side-wall reflections and other disturbances behind the shock. It was also necessary that the exit plane of the shock shaper be nearly the same width as the test section span, to minimize wall reflections as the shock propagated through the test section.

Steady downstream data were gathered using a traverse-mounted three-hole probe. The head of this probe was located approximately 45% chord downstream from the stator trailing edge. These pressure measurements were reduced to determine the flow angle distribution along the traverse axis. Stagnation pressure losses in the stator wakes were also quantified by directly measuring the pressure differential between a Kiel-type stagnation pressure probe at the cascade inlet and the center port on the three-hole probe.

The center blade in the cascade was machined to have 12 static pressure taps distributed along the suction surface at mid-span. The next blade up in the cascade had 12 taps distributed along the pressure surface at mid-span. These static pressure taps allowed the blade surface static pressure distribution to be measured for a single passage in the cascade.

For cases involving the moving shock, the static pressure rise across the shock at the trailing edge of the center blade in the cascade was measured using wall-mounted Kulite high-bandwidth pressure transducers. The pressure data were sampled at 1 MHz using a 12-bit LeCroy 6810 A/D converter. Kulites were also used to trigger the spark light source for the shadowgraph images, in addition to triggering the laser pulses for the DPIV measurements.

The DPIV capabilities for these tests were provided by Innovative Scientific Solutions, Inc. The system involved seeding the flow with small particles and then illuminating a two-dimensional slice of the particle flow path using Nd:YAG laser sheets pulsed in rapid succession (2 μs apart in this case). The two resulting images were captured using an ES1.0 Kodak CCD camera. Processing the image pair allowed the instantaneous 2-D velocity vector field for the area of interest to be calculated.

The laser sheet delivery system consisted of an optical probe designed with light-sheet-forming optics similar to that used in compressor applications [7], but designed for transonic cascade investigations. The probe (12.7 mm OD) was placed in the flow path inside a glass rod (19.1 mm OD, 3.2 mm thick) for protection and to hold it transverse to the mean flow direction. To allow illumination of various flow regions, several downstream locations were available for positioning the probe. The laser sheet could also be traversed in the spanwise direction and rotated. The location of the glass protecting the probe was selected as far downstream as possible to assure minimal flow interference and to allow orientations that prevent the seed from depositing in the face of the optics. The cascade endwalls were machine from 31.8 mm thick acrylic to allow optical access for the cameras. One instantaneous double exposure was taken for every blow-down run, and the relative location of the shock in the images was varied by changing the location of the wall-mounted pressure transducer used to trigger the exposures. The cameras were mounted in an automated traversing system for accurate positioning. The magnification for the data presented in this paper was $\sim$35.6 pixels/mm, which corresponds to a viewing width of $\sim$28 mm. The lens was a 105 mm macro and F# was typically 5.6. The vectors fields presented in the paper were generated with algorithms using two and three subgrid iterations with interrogations cells sizes from 128 to 32 pixels and cell overlapping of 75%. This yielded grid resolutions of 0.44 and 0.22 mm, respectively, allowing precise calculations of streamlines and vortex circulation.

For successful DPIV measurements, the selection and implementation of the proper seeding strategy is a major factor. The seeding particles must be extremely small and have specific gravity close to air to faithfully follow the flow by avoiding the influence of viscous and inertia forces that can produce particle lag. The seeding particles must also efficiently scatter light to ensure that exposure of the recording media occurs. The choice of particles and the mechanism for their introduction in the fluid flow must be carefully considered to minimize particle agglomeration and ensure uniform distribution. For the present experiments, high-purity submicron sized ($\sim$0.5 μm) alumina dioxide white particles were used. Although their specific gravity is 3.06 and they are nonspherical (plates), numerous studies have shown that they can be used for seeding low-speed, transonic, and some higher Mach number flows [16]. The seeding particles were injected into the flow far upstream, close to the turbulence grid using a 12.7 mm diameter perforated tube inserted vertically at mid-span. The seeder was a cyclone-type fluidized bed driven by pressurized air that was regulated to control the rate of seed injection.

The velocity U (m/s) was computed using the formula $U = \Delta x / \Delta t / M$, where Δx is the displacement (pixels) of each interrogation region during Δt (s), the time interval between the two exposures, and M is the magnification of the digital image relative to the object (pixels/m). The displacement in pixels was obtained by using peak locator algorithms (centroid) that find the location of the peak on the correlation map obtained from cross-correlating the two images and correct for various biases [17], yielding subpixel accuracy ($<$0.1 pixels). The Δt was adjusted to allow typical displacements of $>$10 pixels, yielding an uncertainty of $<$1%. Values in the lower velocity regions, however, may have higher uncertainties due to the lower Δx. The maximum uncertainty in the Δt was calculated from the time interval between the two laser pulses. It was found that this uncertainty increases with lower laser power and with lower Δt. A conservative uncertainty value for typical DPIV experiments using a Δt of 2 μs and powers around 20 mJ was found to be 1%. The magnification was measured using images of targets located in the laser sheet plane and it was read to better than 1%. Combining these three conservative uncertainty values for typical displacements yields a maximum error of $<$2%. A more detailed discussion of the DPIV system may be found in [7].

With only main-flow seeding, seeding in separated regions and vortex centers can only be achieved with leftover seed from previous runs and through mixing. With the magnification and resolution of the views presented in this paper, this was sufficient for generating vectors in some areas of the separation regions and in

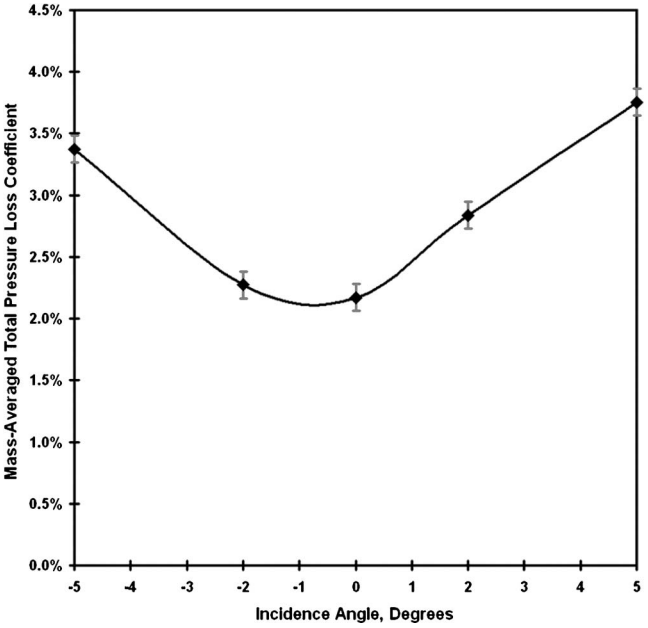

Fig. 3 Mass-averaged total pressure loss coefficient versus incidence angle

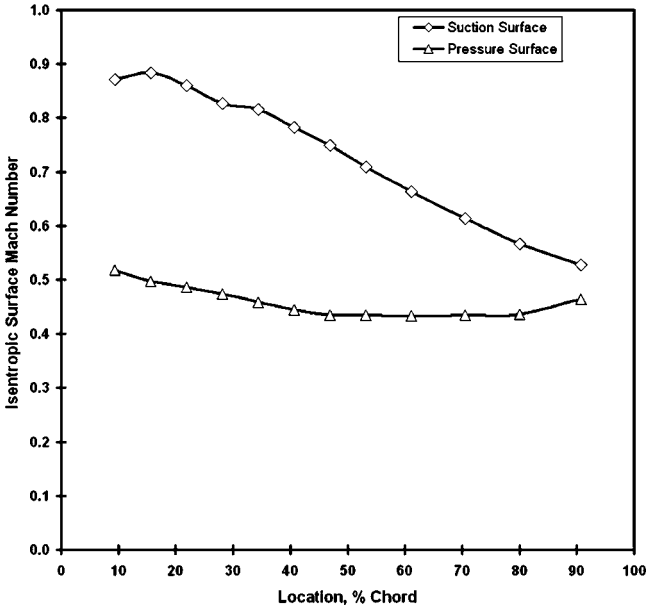

Fig. 4 Isentropic Mach number distribution along the blade surface at design incidence

most of the vortex regions. Areas of insufficient seed can be discerned as blue contours (0 level) in the velocity field plots.

Steady Results

The steady performance of this stator cascade was not the primary focus of this work, although it was necessary to verify that the stator cascade was operating under design intent loading (since the steady loading on the stator could have an impact on the unsteady results). The stator operated at a Reynolds number of 1.05 million based on inlet conditions and chord length. This value was selected to be representative of the stator Reynolds numbers experienced in a typical compressor environment. The steady performance was quantified in three ways: the wake stagnation pressure losses, exit flow angle, and blade surface static pressure distribution. The stagnation pressure deficit in the stator wake is nondimensionalized using the total pressure loss coefficient, ω, defined as

$$\omega = \frac{P_{0\mathrm{Up}} - P_{0\mathrm{Down}}}{P_{0\mathrm{Up}} - P_{\mathrm{Up}}} \tag{1}$$

The stagnation pressure losses (weighted by the local fluid velocity) were integrated over one blade pitch to yield the mass-averaged total pressure loss coefficient, plotted for the five different incidence angles in Fig. 3. The lowest losses occurred near design incidence, and the overall level of the losses was small for all incidence angles between −5 and +5 deg. The uncertainty of the loss coefficient measurements is depicted by the error bars and is approximately 0.1%.

In an axial compressor, the stator rows serve two primary functions: to provide diffusion and to turn the flow so that it enters the downstream rotor row at the correct angle. Therefore, the exit flow angle from the stator row is of primary importance in determining whether the cascade is operating properly. Reduction of three-hole probe data showed that the exit flow deviated less than 3 deg from the stator exit metal angle for all incidence angles between −5 and +5 deg.

The blade surface static pressure distribution was the final measure of steady cascade performance that was investigated. Figure 4 shows the blade surface isentropic Mach number distribution at design incidence. The blade surface isentropic Mach number is a representation of the surface static pressure in terms of the ideal Mach number immediately outside of the boundary layer along a vector normal to the blade surface at each static tap location. It is calculated as:

$$M_s = \sqrt{\left(\frac{2}{\gamma - 1}\right)\left[\left(\frac{P_{0\mathrm{Up}}}{P_s}\right)^{(\gamma-1)/\gamma} - 1\right]} \tag{2}$$

On both the pressure and suction surfaces, the static pressure distribution was smooth and continuous. The isentropic Mach number remained subsonic along the entire suction surface, which indicated that there were no losses due to stationary shocks. The uncertainty of the surface isentropic Mach number values is less than 0.0015. The dip in the suction surface Mach number at 25% chord is very likely due to the transition of the suction surface boundary layer. This phenomenon has been predicted numerically by a coupled inviscid/integral boundary layer cascade solver (MISES).

Unsteady Results

With the design intent operation of the stator cascade verified, experiments incorporating the passing shock were then conducted (all at the design incidence angle of 0 deg). First, shadowgraphs of the shock-passing event were captured for the nominal shock strength (defined as the static pressure ratio across the shock as it passes the stator trailing edge) of 1.76. The shadowgraph images of Fig. 5 were taken from different runs (due to limitations with the photography equipment), but each photograph was taken at a different shock location by varying the placement of the triggering pressure transducer on the wall. The trigger locations were spaced 1/2 in. apart and formed a line parallel to the stagger axis. This line of trigger locations was placed just far enough downstream from the trailing edge to not appear in the shadowgraph images, and may be seen in the test section window of Fig. 6. Although the trigger locations were equally spaced, the shock propagation speed (and strength) decreased the further the shock was from the shock shaper exit, so the actual time delay between each successive image in Fig. 6 increased slightly and was difficult to identify precisely. However, the time delay between each successive shadowgraph image was estimated to be 35 ± 5 μs.

The most significant flow feature present in Fig. 7 is the vortex that forms as the shock passes the stator trailing edge in image 4. This vortex grows as the shock propagates upstream (reaching its

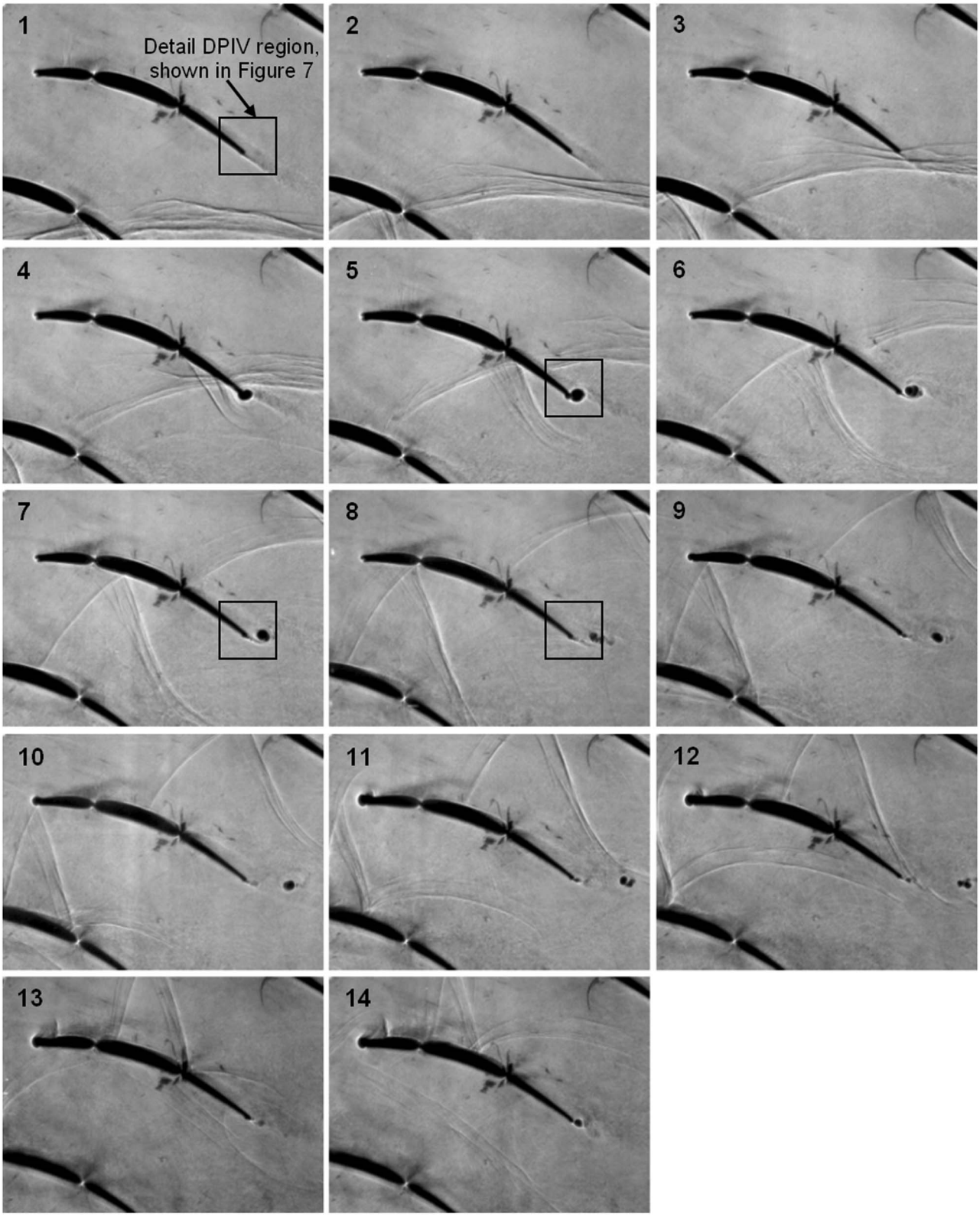

Fig. 5 Shadowgraph images of shock progression for 1.76 shock strength

peak size in image 6) and is still intact as it leaves the image region. The shadowgraph images also show that the vortex caused the blade wake to shift upwards. The direction of vortex propagation is also of interest; rather than traveling tangent to the stator exit camber line (the design flow direction), the vortex seemed to propagate along a line about 30 deg above the design exit flow direction. There are also indications in the shadowgraphs that the presence of the shock and/or vortex may have caused a suction side boundary layer separation on the stator.

Shadowgraphs from this experiment support the phenomenon that Gorrell et al. [5] observed whereby the rotor bow shock turns as it passes the stator trailing edge and propagates upstream nor-

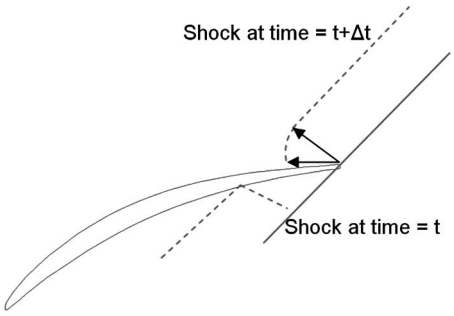

Fig. 6 Schematic of the shock turning phenomenon

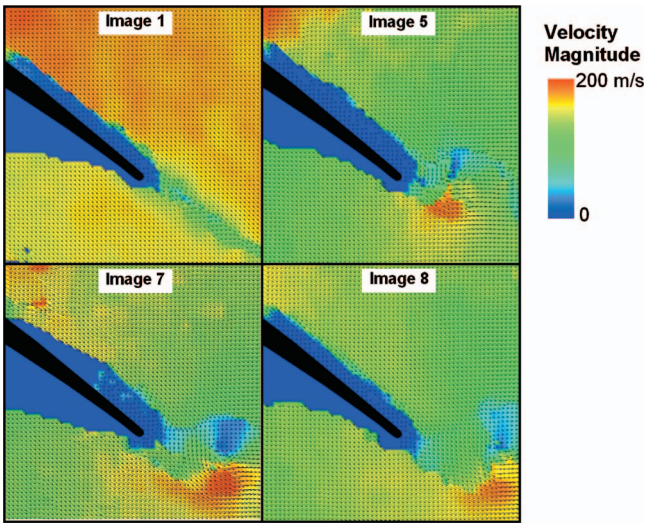

Fig. 7 DPIV velocity fields of the trailing edge vortex created by the moving shock (shock strength=1.76), with the corresponding shadowgraph image number from Fig. 5

mal to the blade surface. The shock has an angle relative to the blade suction surface of about 27 deg as it is passing the trailing edge in image 4, but has turned to be nearly 90 deg from the blade surface by image 10. An explanation for the mechanism that causes this apparent turning of the shock is illustrated in Fig. 7. The figure shows the shock at time t and then diagrams the shock front geometry as it advances from the stator trailing edge for time Δt. The shock propagation velocity is shown as if it were constant in all directions (which was not the case in the experiment), but the concept remains valid. Although it is true that the shock is normal to the blade surface in some shadowgraph images, it is incorrect to conclude that this results in a higher static pressure ratio or increased entropy rise relative to instances where the shock is oblique relative to the blade surface. In fact, the portion of the shock near the blade surface will be weaker than the oblique portion of the shock. If the shock were responsible for the observed suction surface separation, a modification of the shock geometry near the suction surface would result, a trend that was not evident in the shadowgraph images.

To provide more quantitative detail on the trailing edge vortex from Fig. 5, four DPIV velocity vector fields are presented in Fig. 7. These DPIV images are centered on the stator trailing edge and are approximately 2.5 cm by 2.5 cm.

There are several important flow features present in Fig. 7: First, note the overall reduction in freestream velocity magnitude due to the shock-passing event. This drop in velocity magnitude is due to the superposition of the induced velocity field behind the moving shock with the unperturbed velocity field. The immediate nature of the velocity reduction across the moving shock may be seen in the DPIV image 5. The shock appears in the upper left corner of this image as a distinct velocity magnitude discontinuity.

DPIV also provides significantly more detail about the vortex flow field than the shadowgraphs, which merely show the vortex size. It is clear from examining the velocity vectors in Fig. 7 that the vortex rotates in the opposite direction of the flow circulation around the stator. The vortex is analogous to a starting vortex as it was shed in response to the unsteady increase in circulation on the stator that was induced by the shock. The result of superimposing the counter-clockwise rotating vortex with the freestream flow is increased velocity on the lower side of the vortex but stagnated flow on the upper side, thus leading to blockage. As the shadowgraphs also showed, the DPIV images illustrate the vortex growing in size as it propagates downstream.

The trailing edge velocity field after the shock-passing event was also captured for three different shock strengths. While a vortex clearly formed in each case, the size of the vortex proved to increase directly with shock strength. Figure 8 shows the trailing edge velocity vector fields for the three different shock strengths at roughly the same time in the shock-passing cycle.

There are several significant trends visible in the images of Fig. 8. Primarily, the magnitudes of the velocities in the vortex relative to the freestream velocity increased with greater shock strength. Using the DPIV data, the size and strength of the vortex were deduced. Figure 9 shows the distribution of tangential velocity in the vortex for the 1.76 shock strength case. The circulation can be computed from the DPIV data as either the line integral of the velocity at a given radius or the area integral of the vorticity. Both methods give similar results. Figure 9 also compares the measured vortex tangential velocity with a Rankine vortex and a Newman [18] vortex. The Newman vortex is derived from laminar viscous assumptions and agrees well with the measurements. The multiple lines in Fig. 10 represent results computed using different as-

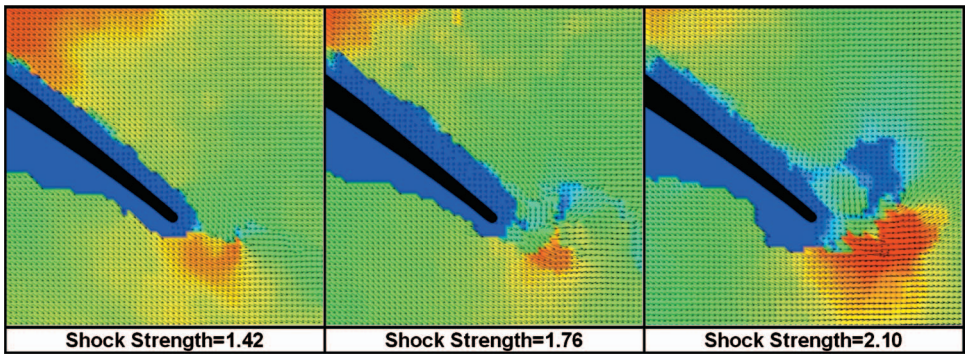

Fig. 8 Trailing edge velocity vector fields for three different shock strengths

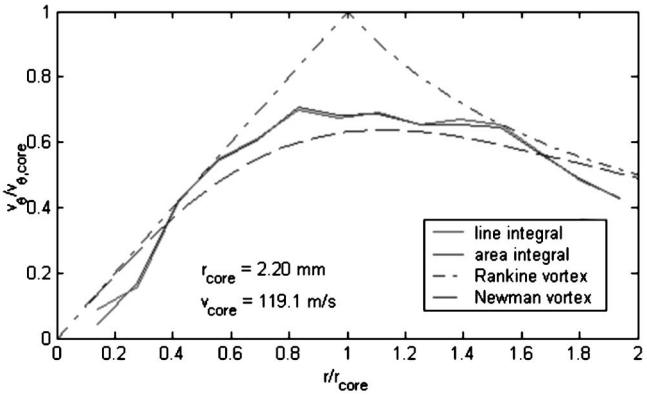

Fig. 9 DPIV measured vortex tangential velocity versus radial location within vortex and comparison to theory (shock strength=1.76)

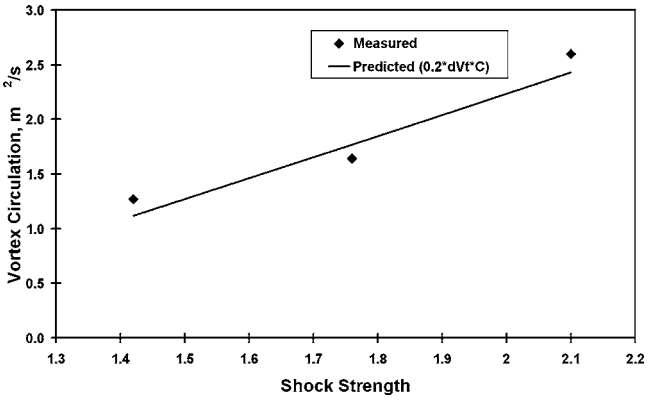

Fig. 11 Vortex circulation versus shock strength, measured and predicted

sumed centers for the integration areas. The measured vortex strength is relatively insensitive to precise identification of the vortex center.

The properties of the vortices generated by the three different shock strengths investigated are presented in Table 2. The measured vortex circulation is divided by the maximum angular velocity (Ω) in the vortex to calculate a vortex radius R. The Mach numbers upstream and downstream relative to the shock are also presented. It is desirable to have a simple model that gives a guide to the induced vortex strength. The shock induces a velocity in the flowfield (dV), and it is the component in the flowfield perpendicular to the trailing edge mean camber line (dVt) that drives the vortex formation. This perpendicular velocity, when multiplied by 20% of the stator chord, gives a good correlation with the measured vortex circulation, as plotted in Fig. 11. The 20% chord value was arrived at as an arbitrary constant, but it is significant that it is approximately representative of the length of the stator subjected to the unsteady loading induced by the shock when the vortex detaches from the trailing edge of the stator as in image 5 from Fig. 5.

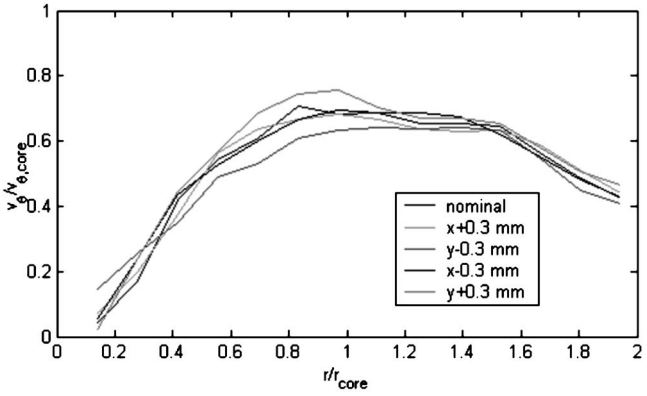

Fig. 10 Sensitivity of DPIV measured tangential velocity to error in locating vortex center (shock strength=1.76)

Table 2 Vortex parameters

Parameter	Units	Shock strength 1.42	1.76	2.10
$\Gamma_{Measured}$	m^2/s	1.27	1.64	2.60
Ω	rad/s	2432	2457	2984
R	mm	1.71	2.19	2.87
$\Omega^* R$	m/s	118	119	145
M_1		1.17	1.28	1.40
M_2		0.86	0.80	0.74
$dVt=dV^* \cos(\theta)$	m/s	73.2	115.8	159.3
$\Gamma_{Predicted}$ $0.2^* dVt^* C$	m^2/s	1.11	1.77	2.43

Since flow velocity was the only parameter that was measured in the vortex region, it would be difficult to calculate the stagnation pressure loss due to the shed vortices. Even if stagnation pressure measurements were available in the region, the results would be difficult to interpret since the shock itself added energy to the flowfield. Even an accurate means of directly measuring the unsteady cascade losses would be of limited value since this cascade test was not truly representative of the full repeating conditions that occur in an actual compressor. However, Crocco's theorem gives a relationship that could be used to estimate the entropy in the vortex:

$$2\Omega = 1/V(\partial h_0/\partial r - T\,\partial s/\partial r) \tag{3}$$

It is noted that vorticity requires gradients of entropy, stagnation enthalpy, or both in the fluid. Analytical attempts to estimate the entropy in the vortex have proved difficult, so loss estimates have relied heavily on CFD simulation of the test configuration. Further loss will occur as the vortex core mixes out as it propagates downstream, and this can be estimated by assuming the vortex loses all its kinetic energy in the mixing process. The resultant losses in the vortex fluid may be high, but only affect the relatively small percentage of mass flow contained within the vortex core. A representative rotor passing frequency to this stator in an operating compressor would be 5500 Hz, and so each stator would shed 5500 primary vortices per second. The mass flow contained in these vortices compared to the mass flow in the freestream would be relatively small, approximately 1% for the 1.76 pressure ratio shock, so that the resultant mass-averaged loss in the vortex is expected to be small. However, the effects of the vortex and its blockage, which can be considerable at some instances in time, on the downstream transonic rotor may also result in a significant loss for an operating compressor stage.

The vortex in Fig. 11 travels approximately 6.5 mm in about 100 μs, which corresponds to a propagation velocity of about 65 m/s. This means the vortex travels downstream at roughly half the local freestream velocity, forcing the freestream flow to bypass the slower-moving vortex. In this manner, the vortex acts as a passage blockage.

The best way to visualize the effects of the passage blockage due to the vortex is to plot streamlines for the DPIV velocity fields. The unsteady nature of the trailing edge flowfield means that the calculated streamlines are instantaneous and do not represent *pathlines* that a specific particle would take through the flow during the unsteady vortex-formation event. However, they

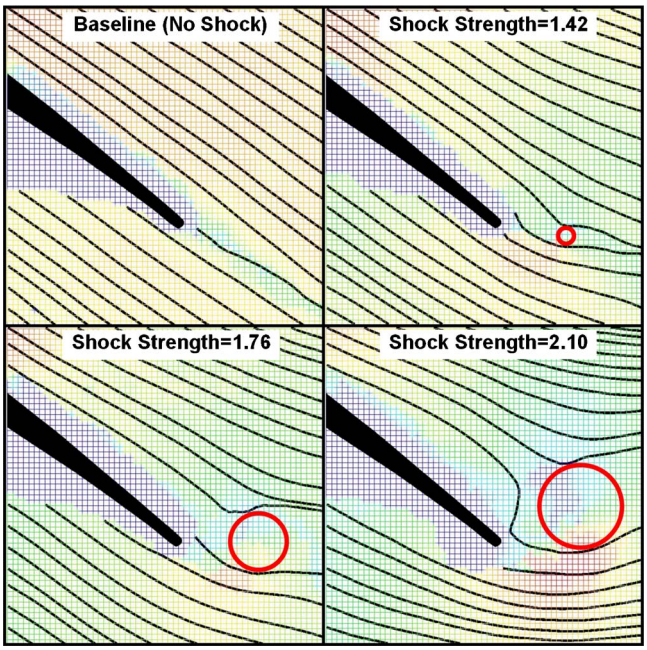

Fig. 12 Instantaneous streamlines for steady flow and three different shock strengths, with corresponding effective blockage

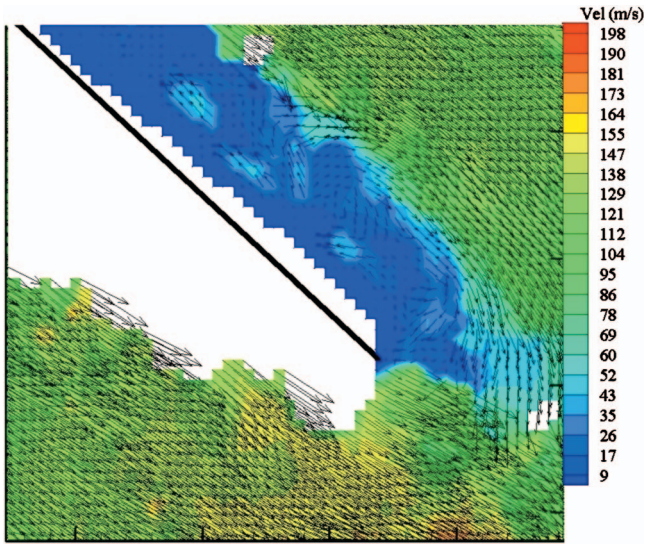

Fig. 13 Trailing edge DPIV velocity vectors of stator suction surface separation due the vortex blockage (shock strength=1.76)

do provide a suitable representation of the flowfield at a specific instant in time. Figure 12 shows a set of streamlines near the blade trailing edge for four cases; steady flow and the unsteady flowfield at approximately the same time in the shock-passing cycle for each of the three shock strengths. The streamlines were used to approximate an effective blockage size, which is represented by a red circle through which no streamlines would pass. The estimated blockage as a percentage of the cascade pitch is shown in Table 3. Note the direct relationship between shock strength and passage blockage due to the vortex.

The shadowgraph results indicated that there may have been a stator suction surface separation created by the passing of the shock and/or the formation of the resultant vortex. DPIV measurements supported this observation. As depicted in Fig. 13, there are clear signs of the turbulent eddies of a flow separation near the suction surface. This separation is considered to be a result of the vortex blockage and not a direct result of the shock influence on the suction surface boundary layer. The best evidence for this is that CFD analysis was unable to predict the separation when the CFD time step resolution was too coarse to adequately resolve the vortex. An in-depth review of the numerical work conducted to match the experimental results has been presented in a follow-on paper [19].

Figure 14 shows a PIV image pair overlay taken later in time after the shock-induced vortex has moved well downstream of the stator trailing edge. In the stator wake that follows the shock-induced vortex, the Von Karman vortex sheet of the conventional stator wake can be clearly seen. At a Strouhal number of 0.2, the distance between shed Von Karman vortices ought to be 5 trailing edge diameters, and this is consistent with the structure depicted in the image. This image is shown to demonstrate that the particle images from PIV can also serve an additional purpose beyond velocimetry measurements: qualitative visualization of unsteady flow phenomena.

Table 3 Effective vortex blockage versus shock strength

Shock strength	Effective vortex blockage, % Pitch
1.42	2.9
1.76	10.0
2.10	14.3

Conclusions

The rotor bow shock/stator interactions present in modern embedded transonic compressors were experimentally simulated using a subsonic linear stator cascade and a single moving shock wave from a shock tube. The shock generated a vortex structure as it passed the stator trailing edge, and this vortex remained in the stator flow field throughout what would be the rotor blade-passing period in an actual compressor. Three shock strengths were tested, with a vortex forming in each case. The size of the vortex-induced blockage ranged from 2.9% of the stator pitch for the weakest shock to 14.3% of the stator pitch for the strongest shock wave.

The stator trailing edge vortex structure bears a striking resemblance to the flowfields observed in experiments on impulsively

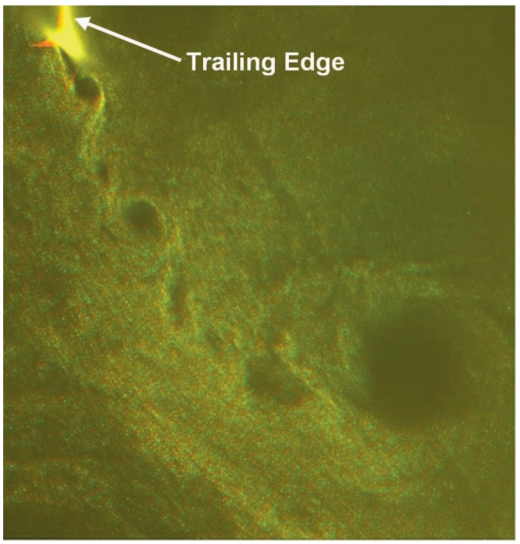

Fig. 14 PIV flow visualization of Von Karman vortex street following the shock-induced vortex

started bodies [20–22]. This observation is the basis of the simple correlation presented that relates the vortex circulation to the shock-induced velocity and the stator chord length. An estimate of the loss incurred by the formation and mixing of the vortex structure indicated that the loss potential in the vortex system itself was small. DPIV measurements also indicated the onset of suction surface boundary layer separation due to the vortex blockage in some cases, but the lack of resolution in this region hampered attempts to quantify the losses due to this separation.

It is worth noting that the shock in the current work varies somewhat from the rotor leading edge shock structure in actual transonic compressors. The leading edge shocks from actual transonic rotors produce the same rapid rise in static pressure, but they are followed by an expansion wave, which lowers the static pressure and turns the flow in order to maintain circumferential periodicity [23]. The rapid static pressure increase of the shock in the current work is followed only by a gradual decay in static pressure. How a successive expansion wave would affect the vortex structure is beyond the scope of this work, but poses an interesting topic for future research and is discussed in the follow-on paper [19].

Acknowledgment

The authors would like to thank GE Aircraft Engines for providing the funding for this project and allowing the work to be published.

Nomenclature

C = stator chord length
dV = shock-induced velocity
dVt = shock-induced velocity component normal to trailing edge camber line
h_0 = stagnation enthalpy
M_1 = relative Mach number upstream of shock
M_2 = relative Mach number downstream of shock
M_s = blade surface isentropic Mach number
P_{0Down} = cascade downstream total pressure
P_{0Up} = cascade upstream total pressure
P_{Up} = cascade upstream static pressure
P_s = blade surface static pressure
r = radial location within vortex
R = vortex radius
s = entropy
T = temperature
V = vortex circumferential velocity
γ = specific heat ratio
$\Gamma_{Measured}$ = vortex circulation measured with DPIV
$\Gamma_{Predicted}$ = predicted vortex circulation
ω = local total pressure loss coefficient
Ω = vortex angular velocity

References

[1] Denton, J. D., and Xu, L., 2002, "The Effects of Lean and Sweep on Transonic Fan Performance," ASME Paper No. GT-2002-30327.
[2] Kerrebrock, J. L., 1981, "Flow in Transonic Compressors," AIAA J., **19**, pp. 4–19.
[3] Lakshminarayana, B., 1996, *Fluid Dynamics and Heat Transfer of Turbomachinery*, Wiley, New York, pp. 99–107.
[4] Prasad, A., 2003, "Evolution of Upstream Propagating Shock Waves From a Transonic Compressor Rotor," ASME J. Turbomach., **125**, pp. 133–140.
[5] Gorrell, S. E., Okiishi, T. H., and Copenhaver, W. W., 2003, "Stator-Rotor Interactions in a Transonic Compressor—Part I: Effect of Blade-Row Spacing on Performance," ASME J. Turbomach., **125**, pp. 328–335.
[6] Gorrell, S. E., Okiishi, T. H., and Copenhaver, W. W., 2003, "Stator-Rotor Interactions in a Transonic Compressor—Part II: Description of a Loss Producing Mechanism," ASME J. Turbomach., **125**, pp. 336–345.
[7] Estevadeordal, J., Gogineni, S., Goss, L., Copenhaver, W., and Gorrell, S., 2002, "Study of Wake-Blade Interactions in a Transonic Compressor Using Flow Visualization and DPIV," ASME J. Fluids Eng., **124**, pp. 166–175.
[8] Sanders, A. J., Papalia, J., and Fleeter, S., 2002, "A PIV Investigation of Rotor-IGV Interactions in a Transonic Compressor," J. Propul. Power, **18**(5), pp. 969–977.
[9] Zachcial, A., and Nurnberger, D., 2000, "A Numerical Study on the Influence of Vane-Blade Spacing on a Compressor Stage at Sub and Transonic Operating Conditions," ASME Paper No. GT2003-38020.
[10] Douglas, J. W., 2001, "Effects of Free Stream Turbulence on Compressor Cascade Performance," M.S. thesis, Virginia Polytechnic Institute and State University, Blacksburg, VA.
[11] Anderson, J. D., 1982, *Modern Compressible Flow*, McGraw-Hill, New York, pp. 202–203.
[12] Doughty, R. L., 1994, "Effects of Multiple Incident Shock Waves on the Flow in a Transonic Turbine Cascade," Ph.D. dissertation, Virginia Polytechnic Institute and State University, Blacksburg, VA.
[13] Chester, W., 1960, "The Propagation of Shock Waves Along Ducts of Varying Cross Section," Adv. Appl. Mech., **VI**, pp. 119–152.
[14] Nettleton, M. A., 1973, "Shock Attenuation in a Gradual Area Expansion," J. Fluid Mech., **60**, pp. 209–223.
[15] Sloan, S. A., and Nettleton, M. A., 1975, "A Model for the Axial Decay of a Shock Wave in a Large Abrupt Area Change," J. Fluid Mech., **71**, pp. 769–785.
[16] Melling, A., 1997, "Tracer Particles and Seeding for Particle Image Velocimetry," Meas. Sci. Technol., **8**, pp. 1406–1416.
[17] Westerweel, J., 1997, "Fundamentals of Digital Particle Image Velocimetry," Meas. Sci. Technol., **8**, pp. 1379–1392.
[18] Newman, B. G., 1958, "Flow in a Viscous Trailing Vortex," Aeronaut. Q., **10**(2), pp. 149–162.
[19] van de Wall, A., Breeze-Stringfellow, A., and Dailey, L., 2006, "Computational Investigation of Unsteady Flow Mechanisms in Compressors With Embedded Supersonic Rotors," ASME Paper No. GT2006-90633.
[20] Pullin, D. I., and Perry, A. E., 1980, "Some Flow Visualization Experiments on the Starting Vortex," J. Fluid Mech., **97**(2), pp. 239–255.
[21] Auerbach, D., 1987, "Experiments on the Trajectory and Circulation of the Starting Vortex," J. Fluid Mech., **183**, pp. 185–198.
[22] Lian, Q. X., and Huang, Z., 1989, "Starting Flow and Structures of the Starting Vortex Behind Bluff Bodies with Sharp Edges," Exp. Fluids, **8**, pp. 95–103.
[23] Kerrebrock, J. L., 1977, *Aircraft Engines and Gas Turbines*, MIT, Cambridge, MA, pp. 135–138.

Online Water Wash Tests of GE J85-13

Elisabet Syverud

Lars E. Bakken

Department of Energy and Process Engineering,
NTNU,
Norwegian University of Science and Technology,
Trondheim, Norway

This paper reports the results of a series of online water wash tests of a GE J85-13 jet engine at the test facilities of the Royal Norwegian Air Force. The engine performance was deteriorated by injecting atomized saltwater at the engine inlet. The engine was then online washed with water injected at three different droplet sizes (25, 75, and 200 μm*) and at water-to-air ratios ranging from 0.4% to 3% by mass. Engine performance was measured using standard on-engine instrumentation. Extra temperature and pressure sensors in the compressor section provided additional information of the propagation of deposits in the aft stages. The measurements were supported by visual observations. The overall engine performance improved rapidly with online wash. The buildup of deposits in the aft stages was influenced both by the droplet size and the water-to-air ratio. The water-to-air ratio was the most important parameter to achieve effective online washing.* [DOI: 10.1115/1.2372768]

Keywords: compressor cleaning, axial compressor, stage characteristics, GE J85-13

Introduction

Online water washing has become increasingly important with operators of industrial gas turbines due to the potential for reduced degradation rate and increased operating intervals. Successful online washing requires close attention to the gas turbine flow path geometry, the operating profile, and the nature of the airborne fouling at the compressor inlet (after filtration).

Several manufacturers offer online washing equipment and many patents exist relating to gas turbine water wash. There is currently no consensus on a recommended method for effective online water washing. System properties like droplet size, droplet velocity, and fluid injection rate vary from one system to another. This makes it difficult for operators to select the best online water wash system for their application. Two recent publications give a historical review of online washing systems and a classification of available systems [1,2].

Today's online washing equipment for aeroderivative engines can be categorized in two main pressure ranges: Fluid pressures up to 10 bar are considered low pressure systems, while high pressure systems have fluid pressures above 50 bar. The atomized droplets produced by high pressure systems have a droplet diameter typically less than 150 μm and resemble the water occurring naturally in clouds and fog. Low pressure systems will have larger, drizzle-like droplets with diameter ranging from 100 to 500 μm and larger. Low pressure systems with air assisted nozzles will generate smaller droplet sizes, resembling the droplets of the high pressure systems. Large droplets may cause blade erosion in the compressor [2–5].

The fluid injection rate (water-to-air ratio) has an impact on the internal surface wetting of the compressor. Due to possible control instabilities, flame-out, or blade erosion the water-to-air ratio has generally been kept low. A typical online washing system for aeroderivative engines has fluid injection in the range from 0.2% to 0.8% (mass based) [2–5].

The flow field within an axial compressor subject to water injection is complex to predict due to the two-phase nature of the flow. The motion of water droplets inside axial compressors has been studied for droplets smaller than 70 μm [6]. Experimental work on a six stage axial compressor gives data for droplets of 90 and 600 μm and at water injection rates up to 15% (by mass) [7]. Several papers offer theoretical approaches to wet compression [8–10]. These studies are related to tiny droplets, less than 15 μm, with no velocity slip between the droplet and air. A study of the effects on gas turbines of naturally occurring water in the atmosphere gives additional insight into the operating limitations of gas turbine engines [11].

To understand and reveal the mechanisms related to online water washing, a systematic test campaign was performed on a GE J85-13 jet engine. The engine performance was deteriorated by injecting atomized saltwater at the engine inlet and the engine performance was restored using online water washing. The water was injected at three different droplet sizes (25, 75, and 200 μm) at water-to-air ratios from 0.4% to 3% by mass. The cleaning effectiveness was measured in terms of improved engine performance using standard on-engine instrumentation. Further, extra temperature and pressure sensors installed in the compressor section provided additional information on the propagation of the deposits into the engine. The measurements were supported by visual observations through the borescope and by laboratory analysis of the stator vane deposits. The results of the axial compressor deterioration are reported in a different publication [12], and that paper should be seen in context with the present work. The test facilities, the GE J85-13 engine and its initial condition, the engine instrumentation, and the deterioration method is described in the present paper only when required for completeness.

Test Facilities and Engine Description

Engine testing was carried out at the Royal Norwegian Air Force (RNoAF) test facilities at Kjeller, Norway.

The General Electric J85-13 engine is a compact, light weight, single-spool turbojet engine. It has an eight-stage axial-flow compressor with bleed-off valves, adjustable inlet guide vanes and a variable exhaust nozzle. The compressor pressure ratio is 6.5:1. The variable geometry is controlled by the throttle angle, but the timing is ambient temperature biased. At International Organization for Standardization (ISO) conditions, inlet guide vanes (IGV) will be at maximum deflection and bleed-off-valves will be fully open below $\sim$81% corrected speed and fully closed at $>$96% corrected speed. At ambient temperatures above ISO conditions, the bleed-off-valves will close at lower speed settings. The nozzle is controlled by the throttle when the engine is running below the exhaust temperature limit. When the maximum exhaust tempera-

Contributed by the International Gas Turbine Institute (IGTI) of ASME for publication in the JOURNAL OF TURBOMACHINERY. Manuscript received October 1, 2004; final manuscript received February 1, 2005. IGTI Review Chair: K. C. Hall. Paper presented at the ASME Turbo Expo 2005: Land, Sea and Air, Reno, NV, June 6–9, 2005, Paper No. GT2005-68702.

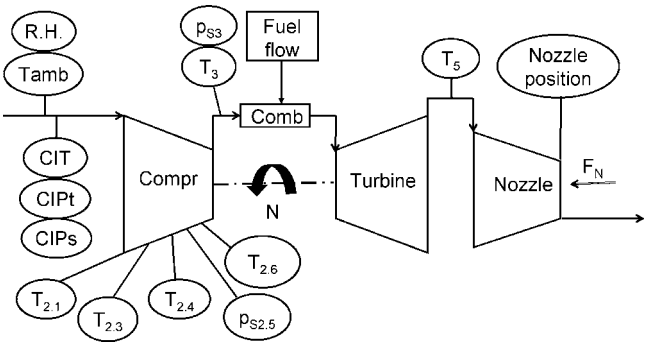

Fig. 1 GE J85-13 engine instrumentation

ture is reached, the exhaust nozzle will increase the flow. This reversal in the exhaust nozzle schedule occurs close to the maximum throttle angle.

Open literature provide information on GE J85-13 compressor geometry [13] and compressor stage characteristics [14].

Engine Instrumentation

Additional sensors were installed to provide more information than available from standard test-cell instrumentation. The engine instrumentation is shown in Fig. 1.

The temperatures at stages 1, 3, 4, 6, and 8 were measured using a single resistance temperature detector (RTD) at each stator row. The entire 15 mm sensor length was immersed into the airflow, giving a representative measure of the bulk average gas path temperature. Because the sensors are unshielded, the velocity error will be significant in the temperature reading. The velocity error was calculated with a temperature recovery factor of 0.65 [15].

The static pressures at stage 5 and at compressor discharge were measured at a single point on the circumference. The stage 5 static pressure was measured in the bleed channel.

Engine throttle and nozzle position were recorded manually at each setting. Relative humidity and ambient temperature were recorded manually throughout the testing and were measured at the same location outside of the test-cell intake. Due to test-cell recirculation, the recorded compressor inlet total temperature (CIT) was slightly higher than the measured ambient temperature. CIT was measured using four sensors located at the engine inlet screen.

All instruments were calibrated prior to the test program and the measurement uncertainties were calculated based on methods given in the ASME Performance Test Codes [16,17].

Engine Online Water Wash Equipment

Accelerated engine deterioration was done through the ingestion of atomized saltwater [18]. Further details of the deterioration method, equipment and results are given in a different paper [12].

The online water wash system consisted of a water manifold with nozzles positioned 0.77 m in front of the compressor IGV. Two different manifolds were used, one with 12 air assisted, flat spray nozzles with a droplet size of 25 μm_{VMD}, the other with provisions for up to 18 full cone spray nozzle tips with a droplet size of 75 or 200 μm_{VMD}. The number of nozzles in each test was selected to give comparable flow rates for the different cases. The pictures in Figs. 2 and 3 show the two water manifolds with comparable water flow rates. Both water wash manifolds provide good coverage of the droplets across the annulus, and the injection direction and closeness to the engine bellmouth allows for good control of the droplet sizes at the compressor face. The injection velocity is greatest for the larger droplets (75 and 200 μm).

The droplet sizes were measured using a Malvern laser diffraction spray analyzer in still air and applying the ASTM Standard E799-92 for calculating spray characteristics [19]. The measurements were taken at the center of the fully developed spray at a distance of 44 cm from the nozzles. As the nozzles were closely separated and tilted towards the centerline, the droplet size changed slightly depending on the number of nozzles used. The droplet size could not be measured in the largest flow rates due to multiple scattering of the laser beam. The measured droplet size is reported in Table 1 together with the droplet size data provided by the manufacturer. In the following, the water nozzles are referred to using the droplet sizes provided by the manufacturer.

Fig. 2 Water wash manifold with 12 nozzles giving 25 μm_{VMD} droplets at 4.4 l/min

The water was supplied at 24 bar pressure. Water flow rates were compared using a turbine flow meter. Figure 4 shows the schematics of the water wash system with air assisted nozzles given in Fig. 2. The manifold shown in Fig. 3 is run at full water pressure from the pump, and with no air assistance.

Tap water with no additives or detergents was used in all tests. The results from water analysis are given in Table 2. For field online washing, the water quality must conform to the requirements of the gas turbine manufacturer.

Fig. 3 Water wash manifold with eight nozzles giving 75 μm_{VMD} droplets at 4.3 l/min

Table 1 Test matrix

Test number	Droplet size (μm_{VMD}) From manufacturer	Droplet size (μm_{VMD}) Measured	Water flow rate (l/min)	Water-to-air ratio (%)
1	200	—	30.9	3.0
2	200	—	17.6	1.7
3	200	131	8.8	0.87
4	200	139	4.4	0.43
5	75	83	9.1	0.89
6	75	93	4.3	0.42
7	25	39	4.4	0.43

Test Procedure

The engine base lines were established for steady-state operation at 12 operating points from 60% corrected speed to full load. Prior to establishing each base line, the engine was run for 5 min at full load. Engine speed was then reduced to idle before being increased to the initial throttle setting. At each throttle setting, the engine was allowed to stabilize for 1 min before reading 60 data points. To prevent impact of hysteresis from the instrument or control system, all throttle settings were established at increasing engine speeds. Engine base lines were recorded prior to degradation, after salt degradation, and after each online water wash.

All salt degradation trials and online water wash tests were run at 10 deg throttle angle (equivalent to 97.5% engine shaft speed) at constant nozzle position and with closed bleed-off-valves and fully open IGV.

To completely clean the compressor of salt deposits, a 5 min online water wash was done at engine speeds varying from full speed to idle for two complete cycles using 17.6 l of water per minute (droplet size of 200 μm).

Seven online water wash tests were completed. The test matrix is given in Table 1. Engine performance was measured after 30, 60, 90 s, 4 min, and 10 min online water wash.

Results

The engine performance deterioration and restoration was analyzed through changes in the intake depression and in the compressor stage work coefficient. Intake depression is defined as the deviation between the total and static pressure at engine inlet. Detailed background on the stage performance calculations is given in a different publication [12], and will not be repeated here, since the only difference is the blockage factor which is set to 1.0 for all cases presented in this paper.

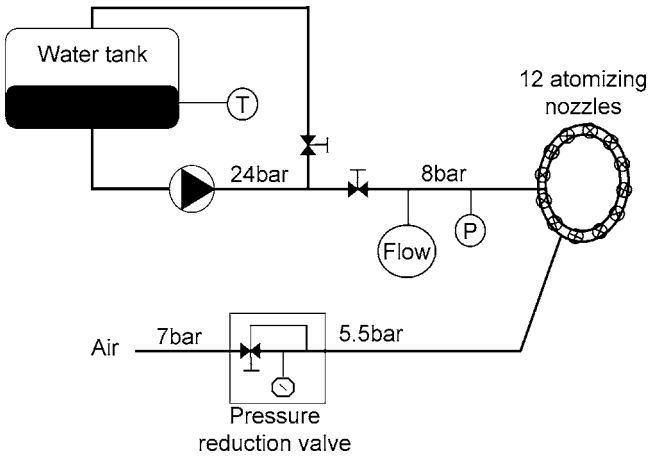

Fig. 4 Water wash system schematics (air assisted nozzles)

Table 2 Analysis of water used for online water wash

Parameter	Value
Total matter	<1 mg/l
*p*H	7.52
Sodium	2.1 ppm by weight
Potassium	0.63 ppm by weight
Chloride	1.7 ppm by weight

The presented test data are limited to engine operation above 95% engine shaft speed where the engine bleed-off valves were closed and the IGV were fully open.

The test data are compared to the stage work coefficient [14]. Those data are based on constant values for c_p (1005 J/kg K) and γ (1.4), while here the gas properties are dependent on gas temperature and humidity. The difference will be largest in the aft stages where the gas temperatures are at the highest. Nonetheless, the published data give a good indication of the GE J85-13 stage performance for a large range of flow coefficients.

Water-to-Air Ratio. The GE J85-13 was operated without stability or structural problems at water injection rates of 40 l/min at all speeds from 70% to full speed. This represents mass based water-to-air ratios above 3% at full speed and 7% at 70% speed. However, these very high water-to-air ratios may cause excessive blade loads and potential erosion damage and are not recommended for online water washing.

Figure 5 shows the change in intake depression as a function of corrected engine shaft speed for three different water-to-air ratios with 200 μm droplet size and 1 min water injection time.

Figures 6 and 7 show the change in stage work coefficient for the same cases as given in Fig. 5. Stage four performance is not restored with the smallest water-to-air ratio of 0.43%. The remaining salt deposits reduce the effective flow area and cause a reduction in the stage six flow coefficient. With a 3% water-to-air ratio sixth stage performance is restored.

The tests clearly document the impact of increased water-to-air ratio on the compressor performance recovery. At low water-to-air ratios, performance recovery is limited.

Water Injection Time. Increasing the water injection time of online water wash is expected to improve performance recovery when the engine is fouled with water soluble components such as salt [1].

Figure 8 compares the change in intake depression for three

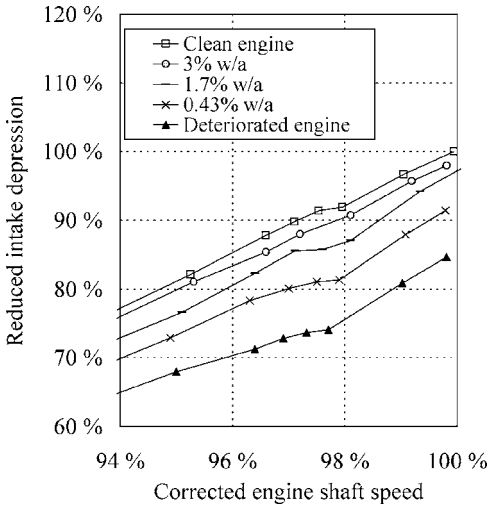

Fig. 5 Intake depression recovery after 60 s water wash with 200 μm droplets

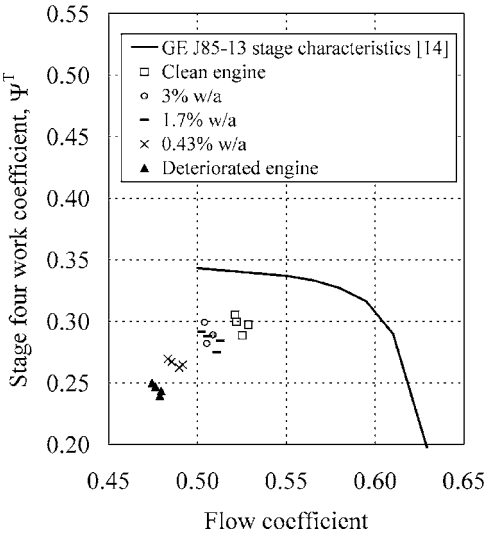

Fig. 6 Stage 4 work coefficient after 60 s water wash with 200 μm droplets

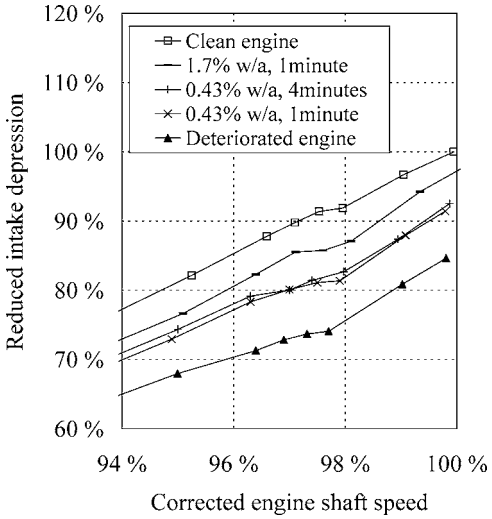

Fig. 8 Intake depression recovery at different water injection times with 200 μm droplets

different cases with 200 μm droplet size. The total water injected in the 4 min water wash at 0.43% water-to-air ratio is equivalent to the total water injected during the 1 min water wash at 1.7% water-to-air ratio. The 0.43% 1 min water wash case is included for reference. The impact on stage four and six work coefficients are given in Figs. 9 and 10, respectively.

Although an equivalent mass of water is used in the 1.7% 1 min wash and the 0.43% 4 min wash, the increased water injection time at lower flow rate fails to recover engine performance. With the low water-to-air ratio of 0.43%, the water seems to evaporate in stage four and the expected benefit from increased soaking time is therefore not apparent.

The tests show that water injection time is only an issue in the front stages where the wash fluid is not evaporated. For aft stage performance recovery, it is better to inject the water in a shorter time, hence, at a higher water-to-air ratio.

Droplet Size. Droplet size is considered important for performance recovery in the aft compressor stages. Water flow path, surface wetting, evaporation rate, and erosion are all affected by the droplet size.

Figures 11–13 compare the intake depression restoration and the stage four and six work coefficient recovery after 1 min online water wash at a water-to-air ratio of 0.4% and with various droplet sizes.

The 75 μm droplets are the most effective in recovering the overall engine performance, and in cleaning the fourth stage; however, the smaller droplets seem to redeposit the fouling in the sixth stage and cause increased sixth stage deterioration. The 25 μm droplets cause heavy deposits in the sixth stage and are the least effective in restoring the overall engine performance.

The tests show that small droplets increase the fouling in the aft stages.

Salt Distribution After Water Wash. Further evidence of the movement of salt from the front stages to the aft stator vanes is given in Fig. 14. The figure compares the salt deposits on the stator vanes after degradation to the salt distribution after a 1 min water wash with 75 μm droplets and 0.42% water-to-air ratio. The salt deposits were measured as chlorine content and converted to

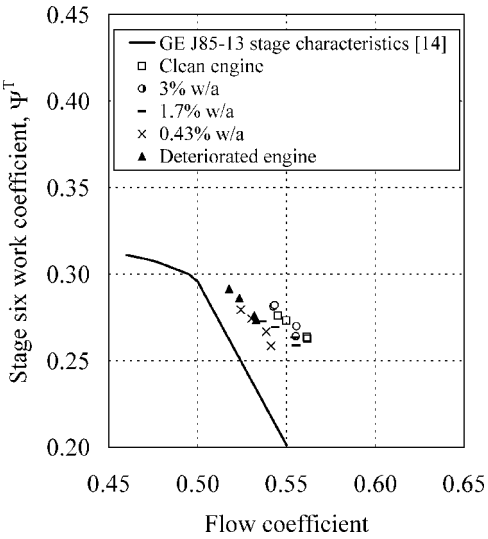

Fig. 7 Stage 6 work coefficient after 1 min water wash with 200 μm droplets

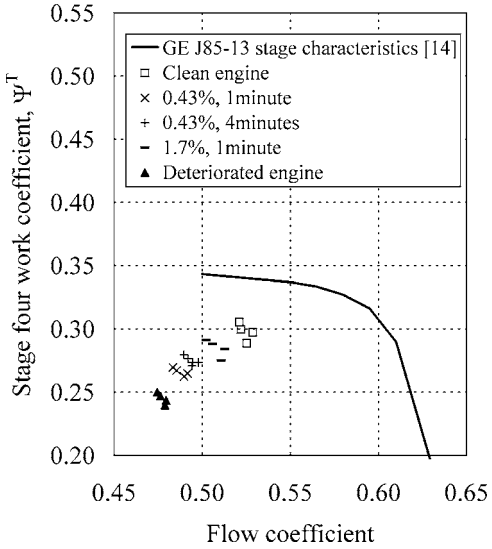

Fig. 9 Stage 4 work coefficient after water wash with 200 μm droplets at different water injection times

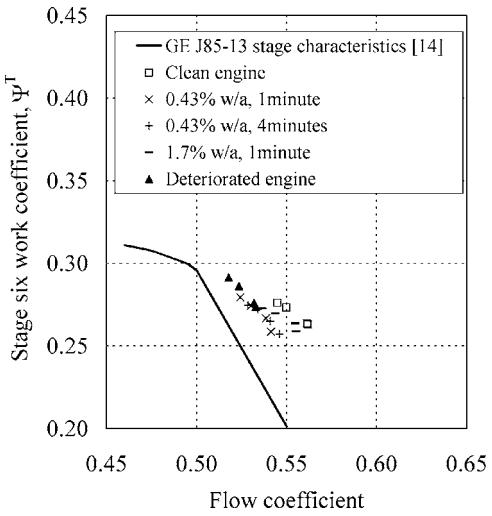

Fig. 10 Stage 6 work coefficient after water wash with 200 μm droplets at different water injection times

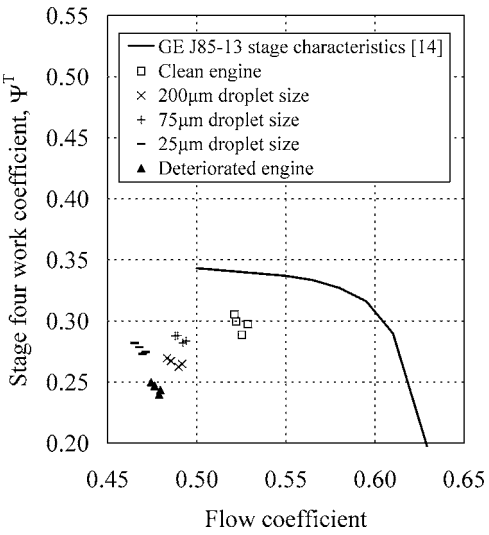

Fig. 12 Stage 4 work coefficient after 1 min water wash at 0.4% *w/a*

weight distribution of salt (sodium chloride).

After degradation, immeasurably small traces of salt were found on the aft stages. However, after the water wash, the salt had moved from the front stages and aft, redepositing on all stages from stage four.

Rotor deposits were not possible to measure due to practical limitations; however, from visual observation, the salt deposits after water wash were found to be heaviest on the suction side of stages 3, 4, and 6 and on the pressure side of stage 5.

Velocity Triangles. As a visualization of the change in stage loading with deterioration and online water wash, the velocity triangles for stage 4 in the clean, deteriorated and washed conditions are shown in Fig. 15. The data are for the 98% operating point, where the engine shaft speed varied from 16,204 to 16,162 and 16,208 rpm for clean, deteriorated, and washed conditions, respectively. This change in blade speed was negligible when comparing the velocity triangles. The water wash data are for 75 μm droplets, 0.42% water-to-air ratio, and 1 min water injection time. The data are calculated based on the assumptions above for the calculation of stage work [12]. As discussed above, the

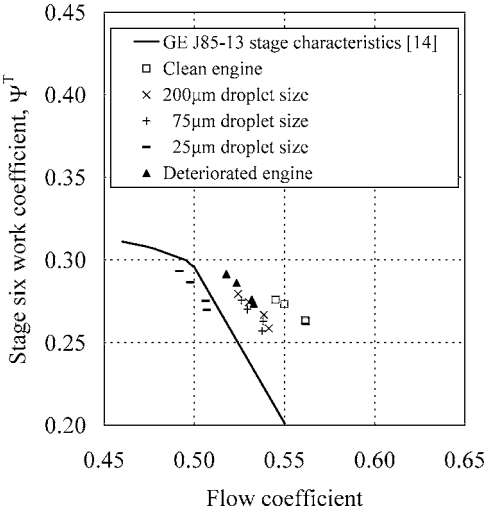

Fig. 13 Stage 6 work coefficient after 1 min water wash at 0.4% *w/a*

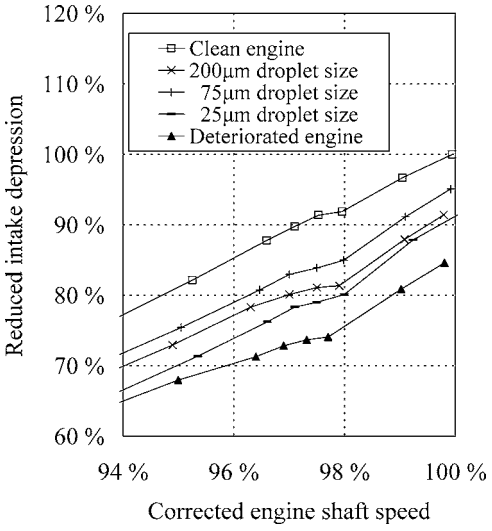

Fig. 11 Intake depression recovery after 1 min water wash with various droplet sizes at 0.4 % *w/a*

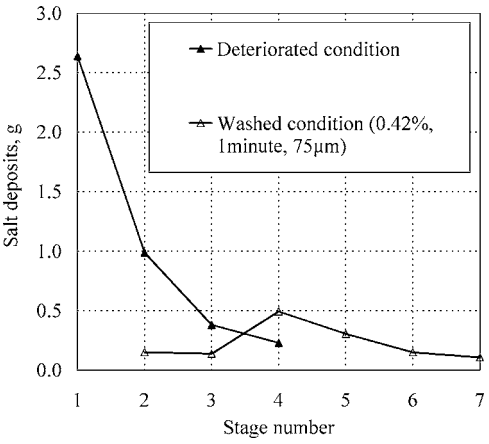

Fig. 14 Weight distribution of salt deposits on stator rows

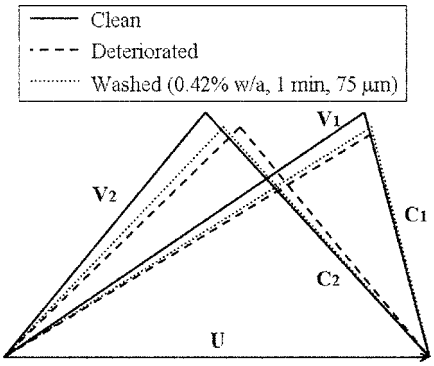

Fig. 15 Stage 4 velocity triangles at 98% shaft speed

deviation angles are assumed constant for the clean and deteriorated cases. Equations for the calculations of velocity triangles are given in the Appendix.

The velocity triangles show that the deterioration causes a reduction in the flow coefficient and a change in the stage work coefficient.

Conclusions

Online water washing has become increasingly important with operators of industrial gas turbines due to the potential for reduced degradation rate, increased operating intervals, and high overall performance.

To reveal the compressor performance deterioration and restoration mechanisms, an in-depth test campaign has been performed on a GE J85-13 engine. Based on test results and performance analyses the main mechanisms are:

- High water flow rate is the most significant parameter for effective online water wash.
- Low flow rates cause redeposition of the fouling in the aft stages.
- Increased water injection time cannot compensate for low flow rates.
- Smaller droplets increase the fouling in the aft stages.

For effective water washing of the entire compressor section, the recommended water-to-air ratio is between 0.8% to 2%. Droplet diameters up to 200 μm have been tested. The maximum droplet size and water-to-air ratio should be determined with close attention to blade erosion and other long term mechanical and structural problems.

The present achievements will be followed by field tests on a Rolls-Royce RB 211 in an offshore application.

Acknowledgment

The project has been supported by Statoil ASA, Dresser-Rand Norwegian Operations, and the Royal Norwegian Navy. The Royal Norwegian Air Force is acknowledged for allowing access to their test facilities and for allowing the authors to borrow a GE J85-13 for test purposes. Without the help of Hans K. Henriksen, a retired test-cell operator of the RNoAF, this project would never have come to fruition.

Nomenclature

A = flow area (m^2)
c_p = specific heat at constant pressure (kJ/kgK)
C = absolute air velocity (m/s)
CIT = compressor inlet temperature (K)
CIP = compressor inlet pressure (kPa)
GE = General Electric
IGV = inlet guide vanes
ISO = International Organization for Standardization[1]
$\dot{m}$ = mass flow rate (kg/s)
N = shaft speed (rpm)
NASA = National Aeronautics and Space Administration
p = pressure (kPa)
r = blade radius (m)
R = gas constant (kJ/kg K)
R.H. = relative humidity (%)
RNoAF = Royal Norwegian Air Force
RTD = resistance temperature detector
T = temperature (K)
U = blade velocity (m/s)
V = relative air velocity (m/s)
w/a = water-to-air ratio (kg H_2O/kg air)

Greek Symbols

α = absolute air angle (deg)
β = relative air angle (deg)
ρ = air density (kg/m^3)
γ = ratio of specific heats
$\Psi^T = c_p \Delta T_t / U_{tip}^2$ = stage work coefficient
$\Phi = C_a / U_{tip}$ = flow coefficient

Subscripts

a = axial velocity component
amb = ambient condition
mix = mixture (humid air)
s = static condition
t = total condition
tip = tip
VMD = volume median diameter
w = tangential velocity component
2.1,2.2,…,2.7 = compressor stage 1,2,…, to stage 7
3 = compressor discharge
5 = turbine discharge

Appendix: Equations for Calculations of Velocity Diagram

Data for the velocity diagram are readily available from the iterative calculation of stage performance [12].

Consider a stage where the rotor inlet, rotor outlet, and stator outlet are designated as stations 1, 2, and 3, respectively.

1 The absolute air velocities and the blade velocity are known from the stage performance calculations at the rotor inlet: C_{a1}, C_1, C_{w1}, U_1

2 The relative velocity at rotor inlet is calculated from

$$V_{w1} = U_1 - C_{w1}, \quad V_1 = \sqrt{V_{w1}^2 + C_{a1}^2}$$

3 The tangential blade velocity at rotor outlet is given by

$$U_2 = 2\pi r_2 \frac{N}{60}$$

4 The tangential component of the absolute velocity at rotor outlet is given by the change in work input

$$C_{w2} = \frac{c_{p1}(T_{t2} - T_{t1}) + C_{w1}U_1}{U_2}$$

5 Consequently, the absolute velocity at rotor outlet is

$$C_2 = \sqrt{C_{w2}^2 + C_{a2}^2}$$

6 And the relative velocity at rotor outlet is given by

[1]ISO reference conditions assume an ambient temperature of 288.15 K, a barometric pressure of 101.325 kPa, and a relative humidity of 60%.

$$V_{w2} = U_2 - C_{w2}, \quad V_2 = \sqrt{V_{w2}^2 + C_{a2}^2}$$

7. Knowing the velocity vectors, the absolute and relative air angles at rotor inlet and outlet are given from geometry

$$\alpha = \arctan\left(\frac{C_w}{C_a}\right), \quad \beta = \arctan\left(\frac{V_w}{C_a}\right)$$

8. The stator exit velocity is found from assuming zero deviation in the stator blade exit angle: $C_{a3} = \dot{m}/\rho_3 A_3$, $C_3 = C_{a3}/\cos(\alpha_3)$.

References

[1] Stalder, J.-P., 2001, "Gas Turbine Compressor Washing State of the Art: Field Experiences," ASME J. Eng. Gas Turbines Power, **123**, pp. 363–370.

[2] Mund, F., and Pilidis, P., 2004, "A Review of Online Washing Systems," ASME Paper No. GT2004–53224.

[3] Asplund, P., 1997, "Gas Turbine Cleaning Upgrade (Compressor Wash)," ASME Paper No. 97-AA-135.

[4] Asplund, P., and Hjerpe, C. J., 2004, "A Method for Cleaning a Stationary Gas Turbine Unit During Operation," World Patent No. WO2004/055334.

[5] Faddegon, C. J., 1999, "Effective Compressor Cleaning as a Result of Scientific Testing and Field Experience," FP Turbomachinery Consultants GmbH, Spinzalaan 177-C, 2273 XG Voorburg, The Netherlands.

[6] Marchik, A., 1965, "Motion of Condensed Phase in the Blade Passages of an Axial Gas Turbine Stage," Teploenergetika, pp. 51–57.

[7] Tsuchiya, T., and Murthy, S. N. B., 1982, "Water Ingestion Into Jet Engine Axial Compressors," AIAA Paper No. 82–0196.

[8] Horlock, J. H., 2001, "Compressor Performance With Water Injection," *Proceedings of ASME Turbo Expo 2001*, June 4–7, New Orleans, LA.

[9] Young, J. B., 1995, "The Fundamental Equations of Gas-Droplet Multiphase Flow," Int. J. Multiphase Flow, **21**(2), pp. 175–191.

[10] Meacock, A. J., and White, A. J., 2006, "The Effect of Water Injection on Multispool Gas Turbine Behavior," ASME Paper No. GT2004–53320.

[11] Garwood, K. R., 1995, "Recommended Practices for the Assessment of the Effects of Atmospheric Water Ingestion on the Performance and Operability of Gas Turbine Engines," AGARD Advisory Report AGARD AR-332.

[12] Syverud, E., Brekke, O., and Bakken, L. E., 2007, "Axial Compressor Deterioration Caused by Saltwater Ingestion," ASME J. Turbomach., **129**(1), pp. 119–126.

[13] Tesch W. A., and Steenken, W. G., 1976, "Blade Row Dynamic Digital Compressor Program Volume 1 J85 Clean Inlet Flow and Parallel Compressor Models," NASA CR-134978.

[14] Milner, E. J., and Wenzel, L. M., 1975, "Performance of a J85–13 Compressor With Clean and Distorted Inlet Flow," NASA TM X-3304.

[15] Saravanamuttoo, H. I. H., ed., 1990, "Recommended Practices for Measurement of Gas Path Pressures and Temperatures for Performance Assessment of Aircraft Turbine Engines and Components," AGARD Advisory Report AGARD AR-245.

[16] ASME, 1997, *Performance Test Code on Gas Turbines*, ASME PTC-22, ASME, New York.

[17] ASME, 1998, *Test Uncertainty*, ASME PTC-19.1, ASME, New York.

[18] Caguiat, D. E., Zipkin, D. M., and Patterson, J. S., 2002, "Compressor Fouling Testing on Rolls Royce/Allison 501-K17 and General Electric LM 2500 Gas Turbine Engines," ASME Paper No. GT2002–30262.

[19] ASTM Standard E 799–92, 1992, "Standard Practice for Determining Data Criteria and Processing for Liquid Drop Size Analysis," ASTM International, West Conshohocken, PA.

Advanced Modeling of Underplatform Friction Dampers for Analysis of Bladed Disk Vibration

E. P. Petrov

D. J. Ewins

Mechanical Engineering Department,
Centre of Vibration Engineering,
Imperial College London,
South Kensington Campus,
London SW7 2AZ, UK

Advanced structural dynamic models for both wedge and split underplatform dampers have been developed. The new damper models take into account inertia forces and the effects of normal load variation on stick-slip transitions at the contact interfaces. The damper models are formulated for the general case of multiharmonic forced response analysis. An approach for using the new damper models in the dynamic analysis of large-scale finite element models of bladed disks is proposed and realized. Numerical investigations of bladed disks are performed to demonstrate the capabilities of the new models and an analysis of the influence of the damper parameters on the forced response of bladed disks is made. [DOI: 10.1115/1.2372775]

Introduction

Due to the high density of natural frequencies of realistic bladed disks and of the broad spectrum of aerodynamic excitation forces, the complete avoidance of all resonance regimes is not generally possible. Thus, the use of special devices that dissipate vibration energy and, hence, reduce the resonance amplitudes to acceptable levels is usually essential. One of the most effective types of damping device is the underplatform friction damper (UPD) that is generally a small piece of metal which frequently has a wedge-like or other shape, and which is usually located underneath the blade platforms. Damping of the blade vibration is achieved by friction forces acting at the contact interfaces between blades and dampers. Dissipation of vibration energy into thermal starts when blade displacements reach a certain level. This level, and the effectiveness of reducing forced response levels by using underplatform dampers, is highly dependent on the choice of the damper parameters. Optimal selection of these parameters can only be made efficiently when accurate modeling and analysis tools are available to provide capabilities for reliable prediction of the forced response levels for bladed discs with the dampers.

There is more than 30 years of history of development of models for dynamic analysis of bladed disks with friction dampers. The simplest model which was applied initially for analysis of a blade-damper system was a classical single-degree-of-freedom (SDOF) oscillator with Coulomb friction. The first engineering friction damper models were investigated and experimentally validated in Refs. [1,2]. These models, while still applied to the SDOF blade model, were essentially spring-slider models, which included not only friction but also the flexibility effect introduced by the damper. Development of these models for cases of multiharmonic forced response is considered in Refs. [3,4]. Multibody model for a two-bladed system with a damper was proposed in Ref. [5] where a 2DOF model was used for each of two blades and 3DOF model for a friction damper with two contact interfaces. Coulomb-style friction damper models are also applied for multiharmonic forced response analysis in Refs. [6,7].

In real conditions underplatform friction dampers have at least two interfaces at which they interact with adjacent blades. In order to obtain a more accurate prediction of the forced response in conjunction with multidegree-of-freedom blade models, several "kinematic" models were developed in Refs. [8–11]. These models are based on some kinematic hypothesis about the relative motion of a wedge-shape damper and blade platform. The damper and blade platforms are considered as some kind of mechanism obeying this kinematic hypothesis and hence the damper's dynamics are ignored and inertia forces are neglected. As a result, the friction forces are expressed in these models ultimately through motion of the blade platforms. In order to describe microslip at the contact interfaces two approaches were explored: (*i*) representation of friction contact by an array of spring-slider elements with different parameters (see Ref. [8]) and (*ii*) use of an analytical solution for friction forces between a bar and a foundation supporting this bar (see Refs. [9,10]). Underplatform dampers of semi-cylindrical and wedge shapes were studied in Ref. [12] with accounting for damper inertia forces due to rigid body motion. The idea of using two-piece dampers, so-called "split dampers" (SD) for increase of energy dissipation and first kinematic-hypothesis-based models for split dampers were proposed in Ref. [13].

Friction contact modeling capabilities and multiharmonic analysis code developed in Ref. [14] were applied in Ref. [15] to explore possibilities of forced response analysis of flexible finite element damper models using a two-blade system.

However, all engineering damper models require information about friction coefficient and damper stiffness to be supplied. The problem of determining contact stiffness for dampers and its role in forced response prediction was studied in Ref. [16] using detailed finite element models for contact areas.

Damper models need to be further improved to allow more accurate and reliable quantitative predictions of forced response. Among the phenomena which are still not included in existing models are the effects of variation of the normal load on stick-slip transitions at damper contact interfaces (see some of these effects in Ref. [17]). Moreover, in the majority of damper models existed to date only monoharmonic forced response is considered. There are dampers of such designs that still do not have fully consistent, not-contradictory models. One of those damper designs is a damper consisting from two or more separate parts.

In this paper, new models for underplatform dampers of different designs are developed. The models are aimed at multiharmonic forced response analysis of large-scale realistic finite ele-

Contributed by the International Gas Turbine Institute (IGTI) of ASME for publication in the JOURNAL OF TURBOMACHINERY. Manuscript received October 1, 2005; final manuscript received February 1, 2006. IGTI Review Chair: R. S. Abhari. Paper presented at the ASME Turbo Expo 2006, Barcelona, Spain, May 8–11, 2006, Paper No. GT2006-90146.

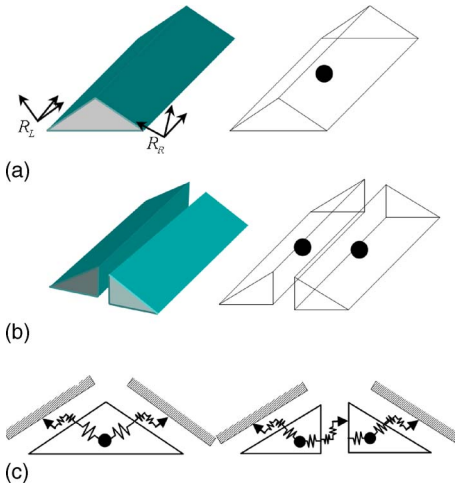

Fig. 1 Underplatform damper models: (*a*) cottage-roof dampers, (*b*) split dampers inertial model allowing for rigid body motion, and (*c*) interaction of dampers and blade platforms

ment models of bladed disks with underplatform dampers. Models for dampers consisting a single piece of metal, so-called "cottage roof damper" (CRDs) and for split dampers (SD) are developed. CRDs and SDs of symmetric and asymmetric geometry shapes are considered. The dynamic damper models are developed which take into account here damper inertia properties. The flexibility of the underplatform dampers, together with the elasticity or stiffness properties of a layer of microasperities which is due to the roughness of contact surfaces is considered. Forces at contact interfaces are described by advanced friction contact models previously developed by the authors in Refs. [17,18]. The friction models include all the effects of variation of normal load on friction forces, including its influence on slip-stick transitions, and allow for temporary separation of the contact surfaces. Numerical investigations of bladed disks are performed to demonstrate and to validate the capabilities of the new models. Realistic large-scale finite element models of bladed disks are used in the calculations. An analysis of the influence of parameters of the dampers on the forced response of bladed disks is carried out.

Modeling of Bladed Disks With Dampers

Bladed Disk Modeling. For analysis of the steady-state nonlinear forced response of bladed disks, large-scale finite element models are used. The models can frequently comprise millions of DOFs, which scale has become customary in industrial applications in order to achieve high-fidelity models describing realistic geometric shapes and dynamic properties of all components of bladed disks. Tuned and mistuned bladed disks can be considered. For the case of a tuned assembly a single sector model is used for forced response calculations. A method for analysis of nonlinear dynamics of structures with cyclic symmetry previously reported in Ref. [19] is used for this case, and allows significant reduction of computational expense while ensuring completeness and accuracy of calculations even for highly nonlinear structures. For a mistuned assembly, the dynamic properties of each sector can differ from the others and a method developed in paper [20] is applied.

Underplatform Friction Damper Modeling. There is a variety in underplatform damper designs used by different companies for different types of practical bladed disks, including: cottage-roof dampers (Fig. 1(*a*)), split dampers (Fig. 1(*b*)), cylindrical dampers (see Ref. [12]), and others.

The widely used massless damper models relate to kinematic models of damper motion. Such models are developed for a single-piece damper and require the introduction of assumptions on the character of motion which are not universally valid. When the validity of these assumptions is violated, these models can produce significant errors in predictive analysis of forced response. For example, in most such models, relative motion of the damper along normal-to-the-damper contact surface is assumed to be negligible, although there are conditions under which such motion is significant and can even lead to separation of the damper and blade platforms.

Moreover, for some of damper designs (e.g., dampers consisting of several unconnected parts, such as split dampers) there is no available consistent approach to describe their motion simply from kinematics, i.e., without inertia forces included into modeling.

In the models developed here every part of the damper is considered as an elastic body with mass lumped in the center of the inertia of this body (Figs. 1(*a*) and 1(*b*), on the right). The case of rigid body can be considered as a particular case of the model. Three-dimensional translational motion of all parts of underplatform dampers is determined as a result of calculation of the dynamics of UPDs in a coupled system: bladed disk—UPDs.

Modeling of Blade-Damper Contact Interfaces. Interaction of the UPD with the blade platform is modeled by friction contact interface elements developed in Refs. [18,21]. The contact interface elements include interaction due to friction forces which are tangential to the contact surface, and interaction forces that are normal to a contact surface. Parameters of the contact surface which are used in the friction contact interaction model are: (*i*) friction coefficient, μ; (*ii*) contact tangential stiffness coefficient, k_t; (*iii*) contact normal stiffness coefficient, k_n; and (*iv*) static normal load, N. It should be noted that, similar to the friction coefficient, the tangential and normal stiffness coefficients result from the interaction of a multitude of microasperities of the rough contacting surfaces and are essentially characteristics of surface roughness included in the friction model.

The friction model implemented in these friction contact elements allows for the effects of variable normal load on the friction forces and on stick-slip transitions. An arbitrary high range of normal displacements can be considered, including cases with temporary separation of the contact surfaces. Unilateral character of the interaction forces acting along a direction normal to the contact interface is accounted for. The unilateral interaction results from the impossibility of transfer tensile stresses from one side of the contact interface to another one and is another source of nonlinearity in the bladed disk-UPDs system, in addition to the essentially nonlinear character of friction forces.

Expressions for the friction and normal forces, and for stiffness matrices of a contact interface, are derived analytically for the general case of steady-state multiharmonic vibrations as explicit functions of the relative motion of adjoining contact surfaces. These expressions are reported in Refs. [18,21]. The analytical expressions ensure both high accuracy and a rapid convergence rate of the iterative solution process for the nonlinear equation of motion. This analytical derivation has allowed us to overcome difficulties in the numerical analysis of structures having abrupt changes of contact conditions (such as contact—absence of contact; slip—stick, etc.). Such difficulties have been common in the past, often leading to a loss of convergence and failure in the search for steady-state solutions.

To use these elements for blade-damper interaction modeling we have to express the contact interaction forces and stiffness matrices in terms of motion of the nodes of the finite element (FE) model created for the blade platforms and motion of the UPD mass center. Moreover, a local coordinate system has to be used for each contact interface in order to evaluate friction and normal forces at pairing contact surfaces. Each CRD and each of the two parts of a SD has two contact interfaces: (*i*) left and (*ii*) right. Hence, vectors of relative motion between the UPD's mass cen-

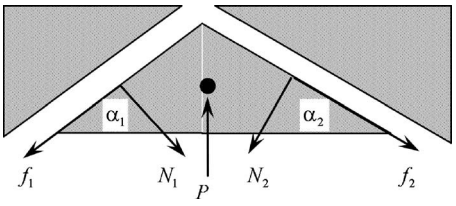

Fig. 2 Forces applied to an asymmetric CRD

ter(s) and contact nodes at left and right blade platforms can be expressed in local coordinate systems of contact interfaces:

- for the two contact interfaces of the CRD

$$\boldsymbol{u}_L^* = \boldsymbol{R}_L(\boldsymbol{u}^{\mathrm{CRD}} - \boldsymbol{u}_L^B); \quad \boldsymbol{u}_R^* = \boldsymbol{R}_R(\boldsymbol{u}^{\mathrm{CRD}} - \boldsymbol{u}_R^B) \tag{1}$$

- for the three contact interfaces of the SD

$$\boldsymbol{u}_L^* = \boldsymbol{R}_L(\boldsymbol{u}_1^{\mathrm{SD}} - \boldsymbol{u}_L^B);\ \boldsymbol{u}_m^* = \boldsymbol{R}_m(\boldsymbol{u}_2^{\mathrm{SD}} - \boldsymbol{u}_1^{\mathrm{SD}});\ \boldsymbol{u}_R^* = \boldsymbol{R}_R(\boldsymbol{u}_2^{\mathrm{SD}} - \boldsymbol{u}_R^B) \tag{2}$$

where $\boldsymbol{u}^{\mathrm{CRD}}$, $\boldsymbol{u}_1^{\mathrm{SD}}$, and $\boldsymbol{u}_2^{\mathrm{SD}}$ are vectors of displacements for CRD and parts of SD mass centers; $\boldsymbol{u}_L^B$ and $\boldsymbol{u}_R^B$ are vectors of displacement of nodes on left and right blade platforms accordingly; $\boldsymbol{u}_L^*$, $\boldsymbol{u}_R^*$, and $\boldsymbol{u}_m^*$ are vectors of relative displacements in local coordinate systems of left, right blade platform and of middle contact surface of SD; $\boldsymbol{R}_L$, $\boldsymbol{R}_R$, and $\boldsymbol{R}_m$ are matrices of the local coordinate systems for all contact interfaces.

For the case of a UPD rigid body model the relative displacements at pairing surfaces will coincide with the relative displacement between the UPD's mass center and the blade contact nodes. For the case of an elastic UPD body, the expressions given by Eq. (1) allow evaluation of the interaction forces with the friction contact elements. To include damper elasticity, the stiffness coefficients k_t and k_n have to be updated. For a simple case when the UPD deformations in different directions are weakly coupled, new values for the contact stiffness coefficients can be obtained from $k_{t,n}^* = k_{t,n} k_{t,n}^{\mathrm{UDP}} / (k_{t,n} + k_{t,n}^{\mathrm{UDP}})$, where $k_{t,n}^{\mathrm{UDP}}$ are stiffness coefficients of the UPD body along tangential and normal directions to the contact surface.

The friction interface elements allow calculation of the contact interaction forces, $\boldsymbol{f}_L^*$, $\boldsymbol{f}_R^*$, and $\boldsymbol{f}_m^*$, and stiffness matrices, $\boldsymbol{K}_L^*$, $\boldsymbol{K}_R^*$, and $\boldsymbol{K}_m^*$, in the local coordinate systems of the left and right contact interfaces

$$\boldsymbol{f}_\gamma^* = \boldsymbol{f}_\gamma^*(\boldsymbol{u}_\gamma^*); \quad \boldsymbol{K}_\gamma^* = \boldsymbol{K}_\gamma^*(\boldsymbol{u}_\gamma^*); \quad \gamma = L,R,m \tag{3}$$

In order to apply these forces and stiffness matrices in calculation of the whole bladed-disk-UPDs system they are transformed into the global coordinate system which is used for construction of the FE model for the bladed disk

$$\boldsymbol{f}_\gamma = \boldsymbol{R}_\gamma^T \boldsymbol{f}_\gamma^*; \quad \boldsymbol{K}_\gamma = \boldsymbol{R}_\gamma^T \boldsymbol{K}_\gamma^* \boldsymbol{R}_\gamma; \quad \gamma = L,R,m \tag{4}$$

The friction interface element proposed in Ref. [18] describes the interaction of the contacting surfaces at one node. The area contact element developed in Ref. [21] allows for contact interaction distributed over some area covered by the friction contact element. For the UPD model introduced in this paper, both types of friction interface elements can be applied at blade-damper and damper-damper interfaces, depending on the level of detail required for blade-damper interaction description.

Static Component of the Normal Load. The friction contact element allows description of dynamic normal and tangential interaction forces acting at contact interfaces. One of the parameters defining friction interaction forces, and which is required as input data for application of the friction contact elements, is a value for the static normal load. Expressions for the normal load values are derived here from equations of equilibrium of the centrifugal, friction, and normal forces applied to the UPD without accounting for elastic deformation of the damper and blade platforms.

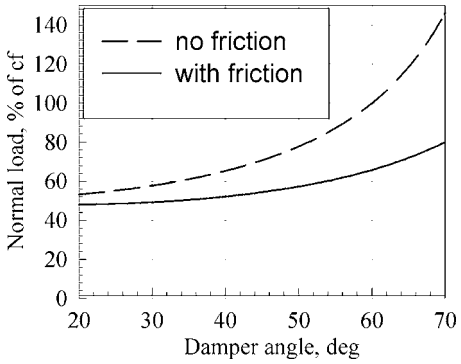

Fig. 3 Normal load obtained with and without accounting for friction forces: a case of symmetric CRD

Cottage-Roof Damper. The general case considered here is of an asymmetric CRD which can have different inclination angles, α_1 and α_2, for its two contact surfaces (Fig. 2).

A centrifugal force, P, is applied to the center of inertia of the CRD. It is determined by damper mass, m_{CRD}, rotation speed, Ω, and distance from the rotation axis, r_{CRD}, i.e., $P = m_{\mathrm{CRD}} r_{\mathrm{CRD}} \Omega^2$. Equilibrium conditions of all forces for the CRD take the form

$$N_1 \cos\alpha_1 + N_2 \cos\alpha_2 + f_1 \sin\alpha_1 + f_2 \sin\alpha_2 = P$$

$$N_1 \sin\alpha_1 - N_2 \sin\alpha_2 - f_1 \cos\alpha_1 + f_2 \cos\alpha_2 = 0 \tag{5}$$

For a case when both damper angles satisfy to the slip condition, i.e.: $\alpha_1 > \alpha_2 > \tan(\mu)$ we can assume

$$f_1 = \mu N_1 \quad \text{and} \quad f_2 = \mu N_2 \tag{6}$$

Equations (5) and (6) give the following expression for the normal load applied at both contact surfaces of the asymmetric CRD:

$$N_1 = \frac{-(\sin\alpha_2 - \mu\cos\alpha_2)}{\sin(\alpha_1+\alpha_2)(\mu^2-1) + 2\cos(\alpha_1+\alpha_2)\mu} P \tag{7}$$

$$N_2 = \frac{-(\sin\alpha_1 - \mu\cos\alpha_1)}{\sin(\alpha_1+\alpha_2)(\mu^2-1) + 2\cos(\alpha_1+\alpha_2)\mu} P \tag{8}$$

For a case of symmetric CRD, $\alpha_1 = \alpha_2 = \alpha$, the following expression can be derived:

$$N_1 = N_2 = \frac{1}{2}\frac{P}{\cos\alpha + \mu\sin\alpha} \tag{9}$$

It should be noted that the expressions for the normal load obtained without friction forces, $N = P/(2\cos\alpha)$ frequently used in UPD modeling, can give excessively large values (see Fig. 3).

Split Damper. For an asymmetric split damper (Fig. 4) the equilibrium conditions formulated for each of two parts of the SD take the form

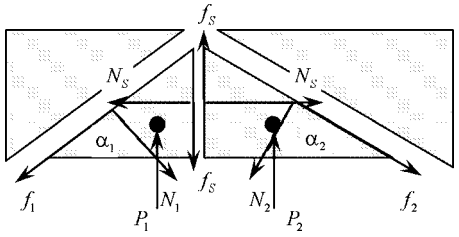

Fig. 4 Forces applied to an asymmetric SD

- left part

$$N_1 \cos\alpha_1 + f_1 \sin\alpha_1 + f_s = P_1$$

$$N_1 \sin\alpha_1 - f_1 \cos\alpha_1 - N_s = 0 \tag{10}$$

- right part

$$N_2 \cos\alpha_2 + f_2 \sin\alpha_2 - f_s = P_2$$

$$-N_2 \sin\alpha_2 + f_2 \cos\alpha_2 + N_s = 0 \tag{11}$$

where P_1 and P_2 are the centrifugal forces applied to the two parts of the damper. Additional constraints on tangential forces should be applied in the form of the following inequalities:

$$|f_1| \le \mu N_1, \quad |f_2| \le \mu N_2, \quad |f_s| \le \mu N_s \tag{12}$$

One can see that the system of equations thus produced is underdetermined since there are six unknowns in four equations and, hence, it does not generally have a unique solution. For the general case of an asymmetric SD, these linear equations have to be solved numerically together with the constraints imposed on the friction forces. Assuming that the masses of both parts of the damper are proportional to the area of the damper cross section (which is displayed by two triangles in Fig. 4) and that both the damper angles satisfy to the slip condition: $\alpha_1 > \alpha_2 > \tan(\mu)$; we can obtain the following expressions for the normal load at the middle contact surfaces:

- for an asymmetric split damper

$$N_s = \frac{1}{2} P \frac{\cos(\alpha_1+\alpha_2)(1-\mu^2) - \cos(\alpha_1-\alpha_2)(1+\mu^2) + 2\sin(\alpha_1+\alpha_2)\mu}{\sin(\alpha_1+\alpha_2)(\mu^2-1) + 2\cos(\alpha_1+\alpha_2)\mu} \tag{13}$$

- for a symmetric split damper

$$N_s = \frac{1}{2} \frac{P(\sin\alpha - \mu\cos\alpha)}{\cos\alpha + \mu\sin\alpha} \tag{14}$$

where $P = P_1 + P_2$ is a total centrifugal force produced by the SD. Expressions for the normal loads at the other two contact surfaces are given for an asymmetric SD by Eqs. (7) and (8), and for the symmetric SD by Eq. (9).

Method for Forced Response Analysis

A bladed disk with UPDs is essentially a nonlinear structure. For a search of the steady-state periodic nonlinear forced response, the time variation of all DOFs in the model of a bladed disk with UPDs is represented by a restricted Fourier series

$$\boldsymbol{q}(t) = \boldsymbol{Q}_0 + \sum_{j=1}^{n} (\boldsymbol{Q}_j^{(c)} \cos m_j \omega t + \boldsymbol{Q}_j^{(s)} \sin m_j \omega t) \tag{15}$$

where $\boldsymbol{q}(t)$ is a vector comprising time variation of DOFs; $\boldsymbol{Q}_j^{(c)}$ and $\boldsymbol{Q}_j^{(s)}$ $(j=1,\ldots,n)$ are vectors of cosine and sine harmonic coefficients for system DOFs, marked by superscripts $^{(c)}$ and $^{(s)}$ accordingly; $\boldsymbol{Q}_0$ is a vector of constant components of the displacements; m_j are specific numbers of harmonics that are kept in the displacement expansion.

Application of the multiharmonic balance method and condensation techniques described in Refs. [19,20] gives an equation of motion in the frequency domain with respect to the harmonic coefficients of a multiharmonic expansion in the form

$$\boldsymbol{R}(\boldsymbol{Q},\omega,\lambda) = \boldsymbol{Q} + \boldsymbol{A}(\omega)(\boldsymbol{F}(\boldsymbol{Q},\boldsymbol{b}(\lambda)) - \boldsymbol{P}(\lambda)) = \boldsymbol{0} \tag{16}$$

where $\boldsymbol{Q} = \{\boldsymbol{Q}_0, \boldsymbol{Q}_1^{(c)}, \boldsymbol{Q}_1^{(s)}, \ldots, \boldsymbol{Q}_n^{(s)}\}^T$ is a vector of harmonic coefficients of displacements; $\boldsymbol{P} = \{\boldsymbol{P}_0, \boldsymbol{P}_1^{(c)}, \boldsymbol{P}_1^{(s)}, \ldots, \boldsymbol{P}_n^{(s)}\}^T$ is a vector of harmonic components of the excitation forces; $\boldsymbol{F}(\boldsymbol{Q},\boldsymbol{b}(\lambda)) = \{\boldsymbol{F}_0, \boldsymbol{F}_1^{(c)}, \boldsymbol{F}_1^{(s)}, \ldots, \boldsymbol{F}_n^{(s)}\}^T$ is a vector of harmonic components of nonlinear forces applied at contact interfaces, and $\boldsymbol{A}(\omega)$ is a multiharmonic FRF matrix of the linear part of the system, i.e.,

$$\boldsymbol{A}(\omega) = \mathrm{diag}[\boldsymbol{A}_0, \boldsymbol{A}_1(\omega), \ldots, \boldsymbol{A}_n(\omega)] \tag{17}$$

where FRF matrices for each harmonic, $\boldsymbol{A}_j(\omega)$, can be generated from mode shapes and natural frequencies obtained for a linear structure without contact interactions. The solution of nonlinear Eq. (16) and the tracing of solutions when rotation speed, excitation frequency, or UPD's parameters are varied is performed using methods reported in Refs. [19,20,22].

Test Case Studies

A blisk of 24 blades, which is analyzed here, was manufactured for a test rig built at Imperial College London in the framework of the EU project "Aeroelastic Design of Turbine Blades II" (ADTurbII) (see Ref. [23]). A finite element model of this blisk is shown in Fig. 5.

Two types of UPD are analyzed: (*i*) cottage-roof dampers and (*ii*) split dampers. The case of a tuned blisc is analyzed here and identical UPDs are applied to all sectors of the bladed disk. A FE model of one sector of the blisk used in calculation contains 21,555 DOFs. The natural frequencies—nodal diameters diagram for this bladed disk are given in Ref. [24]. The background damping due to damping in the blisk material is assumed to be low: $\eta = 7.5e-05$. Dissipation of vibration energy due to friction forces produced by UPDs is calculated together with the forced response calculation. A traveling wave excitation pattern of 19th engine order is applied to the blisk in the forced response calculations. Five harmonics, which are the first five odd multiples of the 19th engine order (i.e., 19, 57, 95, 133, and 171), are used in the multiharmonic expansion of displacements for the calculations performed here.

Cottage-Roof Dampers. Numerical investigations were performed for the case of a symmetric CRD of prismatic shape (Fig. 5(*b*)). The CRD was inserted into the specially machined slots underneath the blade platforms. The slots are inclined to the rotation axis by approximately 30 deg. The effects of parameters of

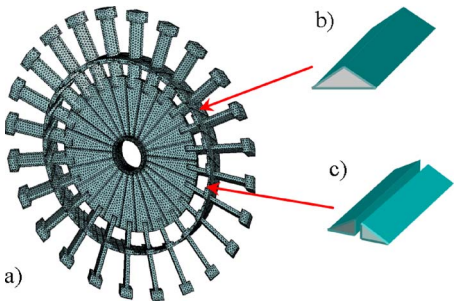

Fig. 5 FE model of a blisc and UPD's models studied

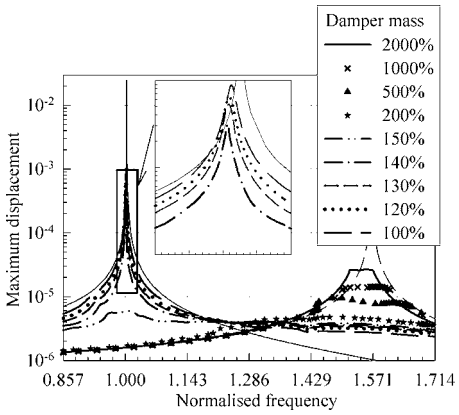

Fig. 6 Cottage-roof damper response levels: effect of damper mass

the CRD damper on the forced response were analyzed, namely: (*i*) damper mass, (*ii*) damper angles, and (*iii*) friction coefficient value. Moreover, the influence of the excitation level on reduction of the forced response by CRDs is estimated. Values of parameters of initial CRD designs and nominal excitation levels were selected as reference values. The reference damper angle is 30 deg, the friction coefficient is 0.3, and the initial damper mass is referred to as "100%." Variation of the centrifugal forces applied to UPDs with changes in the rotation speed and excitation frequency is accounted for in the calculations.

Effects of CRD Parameters and Excitation Level. In Fig. 6 the levels of forced response determined at the blade tips over a frequency range including the first resonance peak are plotted for different values of damper mass.

The damper mass variation affected the centrifugal forces applied to the CRD and also its inertia properties. Forced response characteristics obtained for the case of a blisk without UPDs and with fully stuck UPDs are plotted here and in the figures below by thin solid and dashed black lines accordingly. As expected, resonance response levels and resonance frequencies were significantly affected by the damper mass. One can see that for relatively light dampers, the resonance frequencies are close to those of the blisk without dampers and for heavy dampers, the system has resonance frequencies which are close to the resonance frequency of the blisk with stuck dampers. Nevertheless, even 2000% damper mass did not make the dampers fully stuck. For very low or high mass values one can also observe small decrease of the resonance frequency when damper mass is increased which is due to additional inertia added to the system considered.

Trajectories of the motion of the damper inertia center at resonance peaks are shown in Fig. 7. One can see that for light dampers the trajectory is close to elliptical, while for 150% damper mass, and especially for 2000%, the trajectories have more complex shapes for which influence of higher harmonics is evident.

Motion of the CRD and blade platforms over a period of vibration is illustrated in Fig. 8 for the case of resonance vibrations of a blisc with dampers of 100% mass. Positions of the CRD and blade platform are displayed for four different time values over a vibration period, $T=2\pi/(m_1^*\omega)$. A trajectory of motion of the underplatform damper inertia center is also plotted in this figure. Levels of vibration of the CRD and blade platforms are too small to show the damper geometry shape and its displacements to the same scale, and, therefore, the displacements are magnified here. One can see noticeable relative CRD-blade displacement along the normal direction of the right platform while the CRD makes sliding motion over left blade platform.

The effects of friction coefficient on forced response levels are demonstrated in Fig. 9. One can see that the friction coefficient

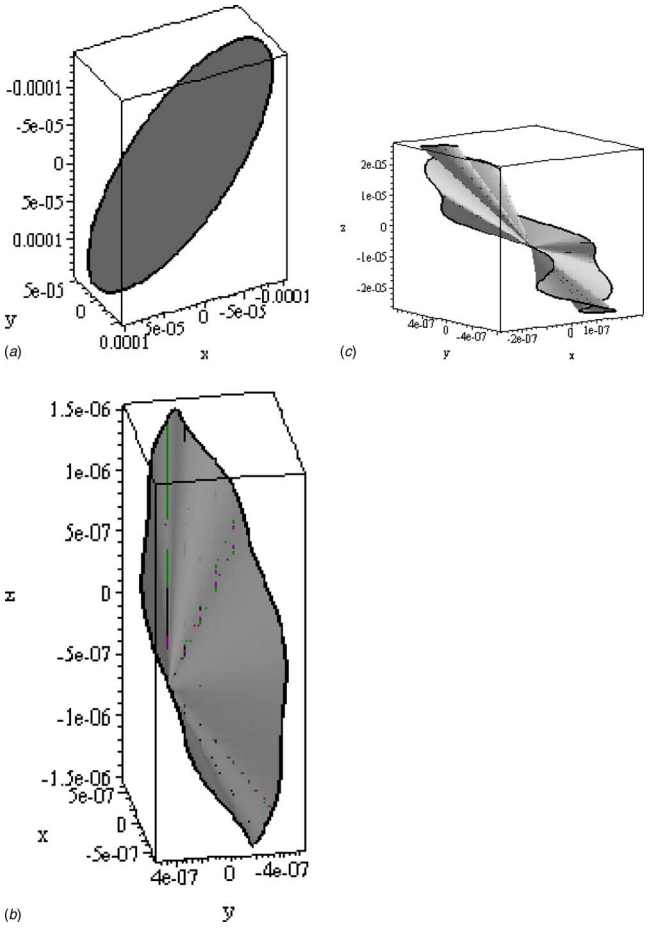

Fig. 7 3D trajectory of CR motion at a resonance: (*a*) mass =100%, (*b*) mass=150%, and (c) mass=2000%

can change the resonance response levels for the structure considered by two orders of magnitude. It also affects the shape of the forced response curves in near-resonance frequency ranges and the resonance peaks are much suppressed for higher values of friction coefficient.

The influence of the damper angle is shown in Fig. 10 for the case of a damper with 150% mass. Decreasing the damper angle from 40 to 20 deg significantly increases the resonance response. A damper with 15 deg produces forced response characteristics almost coinciding with those of a 20-deg damper.

A bladed disk with CRDs of 200% mass was chosen in order to explore whether the parameters of CRDs which are optimized for a selected excitation level are effective for other levels of excita-

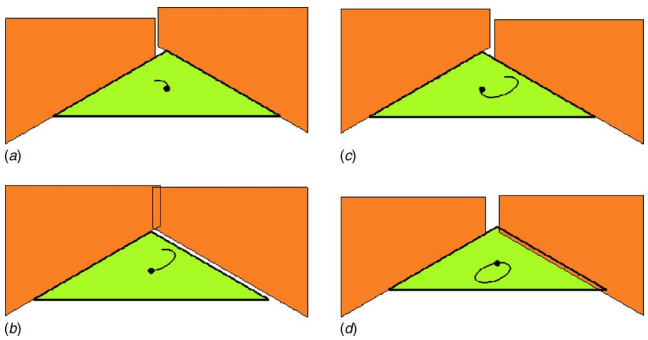

Fig. 8 Motion of the cottage-roof damper and blade platforms over vibration period

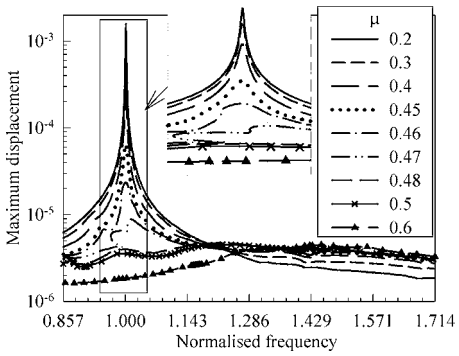

Fig. 9 Cottage-roof damper response levels: effect of friction coefficient (mass=100%, angle=30 deg)

tion. The 200% damper mass value was chosen because it produced the lowest level of the forced response for 100% excitation level (see Fig. 6). In Fig. 11 the forced response levels are plotted for a blisk with such CRDs for several different levels of excitation from 100% to 200%. One can see that although the damper is optimal for the excitation level of 100%, for higher levels of excitation the forced response curve becomes similar to the cases of lighter dampers under 100% excitation and the damper mass is not already optimal for this excitation level.

The effects of UPD parameters and the excitation level on the resonance forced response level are summarized in Fig. 12, which shows a high sensitivity of the resonance peak responses to the parameter values and helps in the choice of the optimal parameter values.

Multiharmonic Spectrum of the Forced Response. Due to the nonlinear character of the blade-UPD interactions, the forced response spectrum is essentially multiharmonic, even when mono-

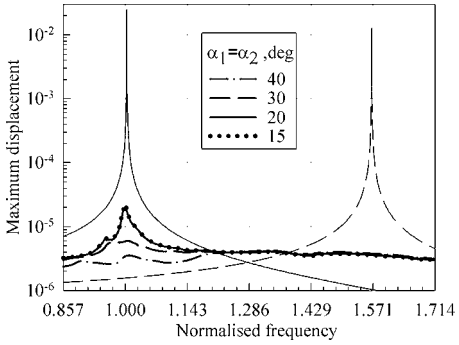

Fig. 10 Cottage-roof damper response levels: effect of damper angle (mass=150%)

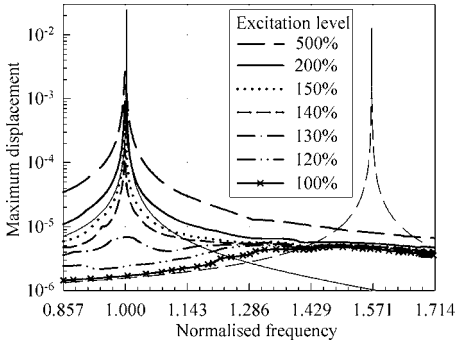

Fig. 11 Cottage-roof damper response levels: effect of excitation level (mass=200%, angle=30 deg)

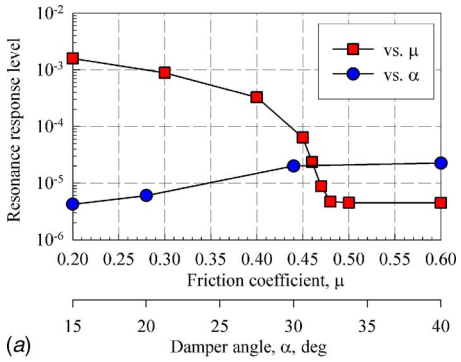

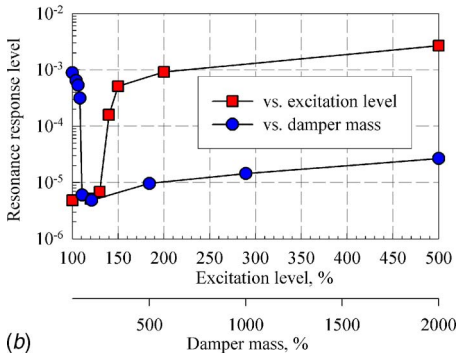

Fig. 12 Cottage-roof damper: resonance peak levels as functions of the damper parameters

harmonic excitation forces are applied. Spectra of the forced response calculated over the whole frequency range analyzed are shown in Figs. 13 and 14. The forced response spectra are plotted for two differently located nodes: (*i*) at the blade tip and (*ii*) at the

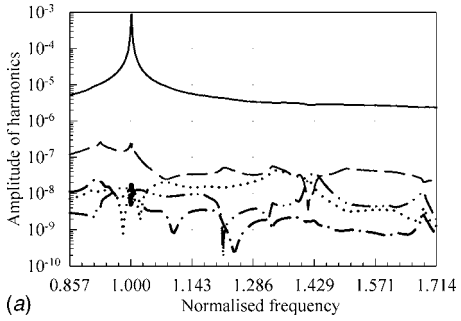

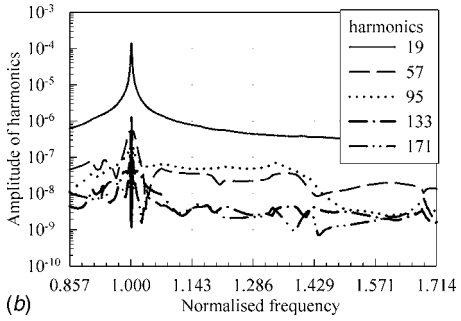

Fig. 13 Amplitudes of harmonics of the multiharmonic forced response (mass=100%): (*a*) at the blade tip and (*b*) for CR damper motion

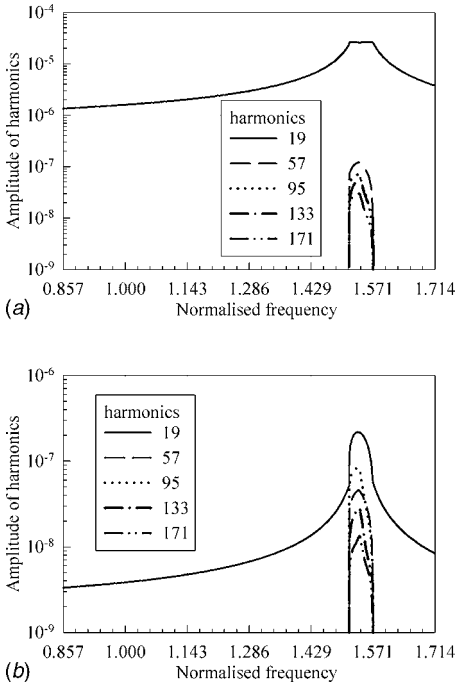

Fig. 14 Amplitudes of harmonics of the multiharmonic forced response (mass=2000%): (*a*) at the blade tip and (*b*) for CR damper motion

UPD inertia center.

Two cases are considered: (*i*) the case of a light UPD (mass =100%, Fig. 13) and (*ii*) the case of heavy damper (mass =2000%, Fig. 14). One can see that for a blade tip displacement, the first harmonic is dominant for both cases displayed here. For the UPD displacement, the contributions of higher harmonics are significant. For the case of a heavy damper, the higher harmonic

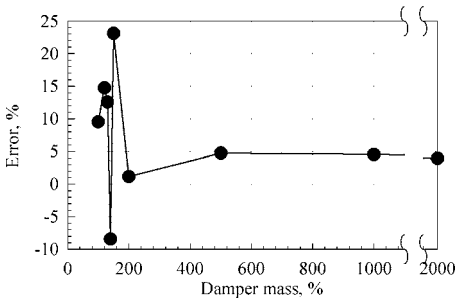

Fig. 15 Error in prediction of the resonance response levels when only one harmonic is allowed for

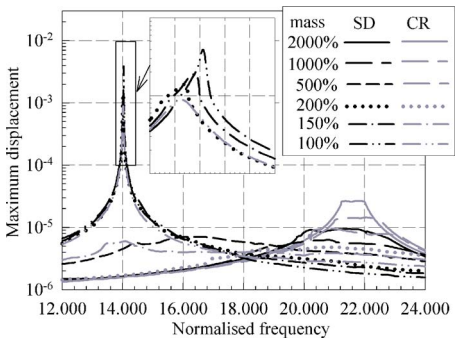

Fig. 16 Comparison of response levels for a blisk with CRD and SD for different damper mass values

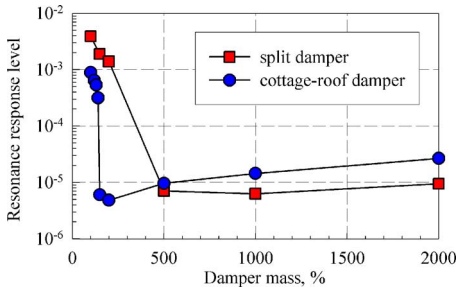

Fig. 17 Resonance peak response for a blisk with CRD and SD for different damper mass values

amplitudes are close to that of the first harmonic.

Since contact interface interactions are determined by motion of the UPD and the blade platforms accounting for these higher harmonics is essential to determine accurately the forces at UPD contact interfaces. When higher harmonics are significant, the trajectory of UPD motion has a complex shape (see Figs. 7(*b*) and 7(*c*)) which is different from conventional ellipsoidal shape inherent for monoharmonic motion. Errors in predictions of resonance peak forced response when monoharmonic forced response representation is used are shown in Fig. 15 where results of the multiharmonic analysis are used for reference values.

Split Damper. Forced responses of a blisk with split dampers are shown in Fig. 16 for different values of damper mass. For comparison, forced response levels of the blisc with CRDs are plotted there, also. One can see that the SD is more efficient in reducing the response levels for heavy dampers and less efficient

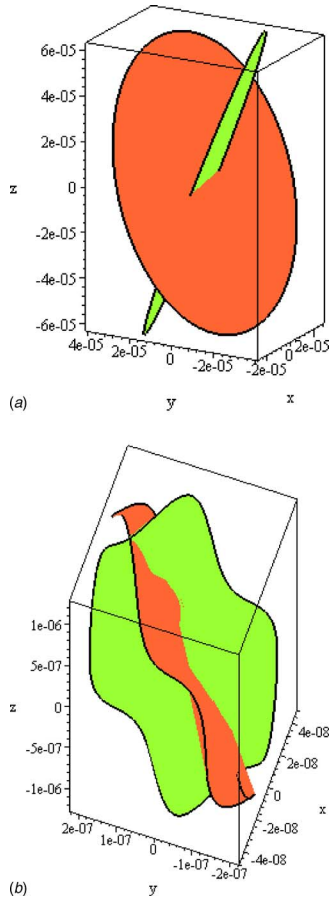

Fig. 18 3D trajectories of motion for two parts of the split damper: (*a*) mass=100%, (*b*) mass=2000%

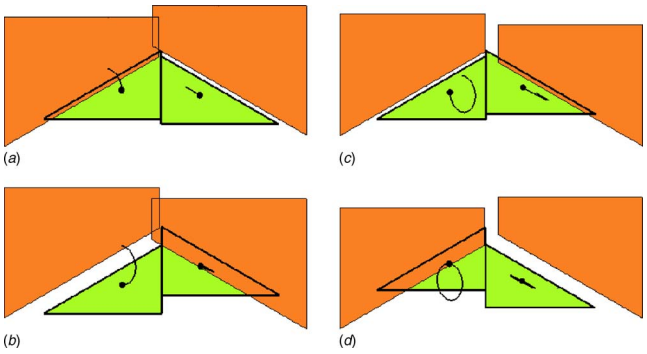

Fig. 19 Motion of the split damper and blade platforms over vibration period

when the damper mass is small. This difference is due to the additional contact interface between the two parts of the SD where static normal load is smaller than at the contact surfaces adjacent to blade platforms.

Comparison of the forced response levels at the resonance peaks for a blisk with CRDs and SDs obtained for different damper values is shown Fig. 17. One can see there that the SDs produce resonance forced response levels which are significantly lower than CRDs with mass value varying from 500% to 2000% and these levels are not sensitive to damper mass variation. The lowest resonance response level for the blisc with CRDs (achieved when the damper mass is 200%) is 30% lower than that for the blisk with SDs (achieved when the damper mass is 1000%). However, resonance levels for the blisc with CRDs fitted are significantly more sensitive to the damper mass value than the blisk with SDs and small variation of the damper mass or excitation level (see Fig. 12(*b*)) can give higher response levels than those for the blisk with SDs.

Trajectories of motion of the inertia centers are shown in Fig. 18 for both SD parts. Similar to a case of the CRD, for the SD one can observe elliptical trajectories for light dampers and more complex trajectories for heavy dampers.

Positions of the SD and the blade platforms at several time instants selected over a complete period of vibration are shown in Fig. 19 together with the trajectories of motion for both split damper parts. A case of resonance vibrations of a blisk with 100% damper mass is considered here. It is evident that significant slip occurs over the middle SD interface and significant normal component of SD motion at the contact interfaces adjacent to blade platform. It should be also noted that significant differences in motion of the left and right parts of the SD occur although the damper is symmetrical.

Conclusions

New models for two types of underplatform dampers have been developed and described here: (*i*) a cottage-roof, single-piece damper and (*ii*) a split, two-piece, damper.

The damper models take into account the effect of the normal load variation on stick-slip transitions and on friction force variation. The damper models also allow for inclusion of the inertia forces which occur due to damper vibrations and are capable of describing blade-damper interaction under temporal separation of damper and blade platforms.

The damper models are formulated for the general case of multiharmonic expansion of forced response.

An approach for inclusion of the new damper models in forced response analysis of large-scale finite element models of bladed disks is proposed and realized. Numerical investigations of bladed disks have been performed to demonstrate the capabilities of the new models. Realistic large-scale finite element models of bladed disks are used in the calculations. Analysis of the influence of damper parameters on the forced response of bladed disks is carried out.

For split dampers, a pioneering study on modeling and damping capabilities has been made.

Comparative analysis of the capabilities of cottage-roof dampers and split dampers to reduce forced response levels and analysis of optimal values of damper parameters have been carried out.

Acknowledgment

The authors are grateful to Rolls-Royce plc. for providing the financial support for this project.

References

[1] Griffin, J. H., 1980, "Friction Damping of Resonant Stresses in Gas Turbine Engine Airfoils," ASME J. Eng. Power, **102**, pp. 329–333.
[2] Cameron, T. M., Griffin, J. F., Kielb, R. E., and Hoosac, T. M., 1990, "An Integrated Friction Damper Design," ASME J. Vibr. Acoust., **112**, pp. 175–182.
[3] Cameron, T. M., and Griffin, J. H., 1989, "An Alternating Frequency/Time Domain Method for Calculating Steady Response of Nonlinear Dynamic Systems," ASME J. Appl. Mech., **56**, pp. 149–154.
[4] Wang, Y., and Chen, W. K., 1993, "Investigation of the Vibration of a Blade With Friction Damper by HBM," Trans. ASME: J. Eng. Gas Turbines Power, **115**, pp. 294–299.
[5] Pfeifer, F., and Hajek, M., 1992, "Stick-Slip Motion of Turbine Blade Dampers," Philos. Trans. R. Soc. London, Ser. A, **338**, pp. 503–517.
[6] Pierre, C., Ferri, A. A., and Dowel, E. H., 1985, "Multi-Harmonic Analysis of Dry Friction Damped Systems Using an Incremental Harmonic Balance Method," ASME J. Appl. Mech., **52**, pp. 958–964.
[7] Berthillier, M., Dupont, C., Mondal, R., and Barrau, R. R., 1998, "Blades Forced Response Analysis With Friction Dampers," ASME J. Appl. Mech., **120**, pp. 468–474.
[8] Sanliturk, K. Y., Ewins, D. J., and Stanbridge, A. B., 2001, "Underplatform Dampers for Turbine Blades: Theoretical Modelling, Analysis and Comparison With Experimental Data," Trans. ASME: J. Eng. Gas Turbines Power, **123**, pp. 919–929.
[9] Csaba, G., 1998, "Forced Response Analysis in Time and Frequency Domains of a Tuned Bladed Disk With Friction Dampers," J. Sound Vib., **214**(3), pp. 395–412.
[10] Jareland, M. H., 2001, "A Parametric Study of a Cottage Roof Damper and Comparison With Experimental Results," ASME Paper No. 2001-GT-0275.
[11] Yang, B.-D., and Menq, C.-H., 1998, "Characterization of Contact Kinematics and Application to Design of Wedge Dampers in Turbomachinery Blading," Trans. ASME: J. Eng. Gas Turbines Power, **119**, pp. 410–423.
[12] Panning, L., Sextro, W., and Popp, K., 2003, "Spatial Dynamics of Tuned and Mistuned Bladed Disks With Cylindrical and Wedge-Shaped Friction Dampers," Int. J. Rotating Mach., **9**(3), pp. 219–228.
[13] Sanliturk, K. Y., 1998, "Dual Operation Split Damper: Theoretical Modelling and Preliminary Studies," VUTC Report D-98023, Imperial College, London, p. 25.
[14] Petrov, E. P., and Ewins, D. J., 2004, "State-of-the-Art Dynamic Analysis for Nonlinear Gas Turbine Structures," J. Aerosp. Eng., **218**(G3), pp. 199–211.
[15] Yeo, S., and Kielb, J., 2002, "The Application of a Numerical Code to the Optimisation of Inter-Platform Damping Technology," *Proc. 7th HCF Conference*, Florida, May 14–17, p. 16.
[16] Szwedowicz, J., Kissel, M., Ravindra, B., and Kellerer, R., 2001, "Estimation of Contact Stiffness and Its Role in the Design of a Friction Damper," ASME Paper No. 2001-GT-0290.
[17] Petrov, E. P., and Ewins, D. J., 2004, "Generic Friction Models for Time-Domain Vibration Analysis of Bladed Discs," ASME J. Turbomach., **126**, pp. 184–192.
[18] Petrov, E. P., and Ewins, D. J., 2003, "Analytical Formulation of Friction Interface Elements for Analysis of Nonlinear Multi-Harmonic Vibrations of Bladed Discs," ASME J. Turbomach., **125**, pp. 364–371.
[19] Petrov, E. P., 2003, "A Method for Use of Cyclic Symmetry Properties in Analysis of Nonlinear Multiharmonic Vibrations of Bladed Discs," ASME Paper No. GT-2003-38480.
[20] Petrov, E. P., and Ewins, D. J., 2005, "Method for Analysis of Nonlinear Multiharmonic Vibrations of Mistuned Bladed Discs With Scatter of Contact Interface Characteristics," ASME J. Turbomach., **127**, pp. 128–136.
[21] Petrov, E. P., and Ewins, D. J., 2005, "Effects of Damping and Varying Contact Area at Blade-Disc Joints in Forced Response Analysis of Bladed Disc Assemblies," Paper No. GT2005-68936.
[22] Petrov, E. P., 2004, "Method for Direct Parametric Analysis of Nonlinear Forced Response of Bladed Discs With Friction Contact Interfaces," ASME J. Turbomach., **126**, pp. 654–662.
[23] Elliott, R., Green, J. S., and Seinturier, E., 2005, "Aeroelastic Design of Turbine Blades—ADTurB II Overview," AMP-105_01/62, 6th European Turbomachinery Conference, Lille, France, March 7–11.
[24] Petrov, E. P., and Ewins, D. J., 2005, "Mistuning Effects on Forced Response of Bladed Discs With Friction Dampers," *Proc. of NATO Symposium: Evaluation, Control and Prevention of High Cycle Fatigue in Gas Turbine Engines for Land, Sea and Air Vehicles*, Granada, Spain, Oct. 3–5, Paper No. 38–1.

Effect of Tip and Pressure Side Coolant Injection on Heat Transfer Distributions for a Plane and Recessed Tip

Hasan Nasir

Srinath V. Ekkad[1]
Professor
Mem. ASME
e-mail: ekkad@me.lsu.edu

Mechanical Engineering Department,
Louisiana State University,
Baton Rouge, LA 70803

Ronald S. Bunker
General Electric Global R&D Center,
Schenectady, NY

The present study investigates the effects of coolant injection on adiabatic film effectiveness and heat transfer coefficients from a plane and recessed tip of a high pressure turbine first stage rotor blade. Three cases where coolant is injected from (a) five orthogonal holes located along the camber line, (b) seven angled holes located near the blade tip along the pressure side, and (c) combination cases when coolant is injected from both tip and pressure side holes were studied. The pressure ratio (inlet total pressure to exit static pressure for the cascade) across the blade row was 1.2, and the experiments were run in a blow-down test rig with a four-blade linear cascade. The Reynolds number based on cascade exit velocity and axial chord length was 8.61×10^5 *and the inlet and exit Mach numbers were 0.16 and 0.55, respectively. A transient infrared technique was used to measure adiabatic film effectiveness and heat transfer coefficient simultaneously for three blowing ratios of 1.0, 2.0, and 3.0. For all the cases, gap-to-blade span ratio of 1% was used. The depth-to-blade span ratio of 0.0416 was used for the recessed tip. Pressure measurements on the shroud were also taken to characterize the leakage flow and understand the heat transfer distributions. For tip injection, when blowing ratio increases from 1.0 to 2.0, film effectiveness increases for both plane and recessed tip and heat transfer coefficient decreases for both plane and recessed tip. At blowing ratio 3.0, lift-off is observed for both cases. In case of pressure side coolant injection and for plane tip, lift-off is observed at blowing ratio 2.0 and reattachments of jets are observed at blowing ratio 3.0. But, almost no effectiveness is observed for squealer tip at all blowing ratios with pressure side injection with reduced heat transfer coefficient along the pressure side. For combination case, very high effectiveness is observed at blowing ratio 3.0 for both plane and recessed blade tip. It appears that for this high blowing ratio, coolant jets from the tip hit the shroud first and then reattach back onto the blade tip with very high heat transfer coefficients for both plane and recessed blade tip.*
[DOI: 10.1115/1.2366540]

Introduction

Modern turbine blades are exposed to increasingly high inlet temperatures. The high pressure turbine (HPT) first stage blade is subject to extremely harsh environments. Most failures in blades occur at the turbine tip region due to over-temperature and cooling problems. The tip region through exposure to hot leakage gases leads to loss of performance and life through oxidation, erosion, rubbing against stationary outer casing, and high local thermal stresses.

The cause for tip failures is fairly well understood and can be explained as follows. A clearance gap between the rotating blade tip and stationary shroud is necessary to allow for the blade's mechanical and thermal growth during operation. Unfortunately, the gap allows for leakage flow from the pressure side to the suction side of the blade surface. The gas accelerates as it passes through the small gap. This leads to enhanced heat load to the blade tip region. Leakage flow, or clearance flow, also leads to undesirable aerodynamic losses. In fact, one third of the aerodynamic losses through the turbine section can be attributed to leakage flow. The effects of leakage flow are increased thermal loading and reduced aerodynamic performance, which affects durability and life of the component. At these elevated temperatures, the turbine blades are also at risk of undergoing oxidation, thermal barrier coating (TBC) spallation, thermal fatigue, and creep. Tip region is difficult to cool with conventional internal cooling because of the difficulty of producing high internal heat transfer coefficients to effectively reduce tip region thermal loading. Typically, coolant is injected into the tip gap to reduce the heat loading by reducing overall leakage flow temperature. Also, coolant is injected along the pressure side surface of the blade close to the tip gap. However, the lack of flow field knowledge and accurate local thermal distribution on the tip region results in ineffective cooling. This study looks at heat transfer measurements on cooled tips with typical cooling hole placements as seen in an in-service engine blade.

An overview of the tip heat transfer through different sealing mechanisms is presented in detail by Nasir et al. [1]. Several different geometries such as trip strips and recessed cavity geometry were examined for reducing leakage flow and associated heat transfer. However, film cooling of the tips still remains a major need as tip temperatures are significant. Film injection on the tip surface has been primarily through dust/purge holes in conventional designs. These are metered holes that release some coolant to the tip to remove collection of dust inside the internal passages of the blades. However, with increased problems in the tip region, tip holes were also used to deliver coolant to the tip gap region to reduce the leakage flow and provide cooling. Recently, there have

[1]Corresponding author.
Contributed by the International Gas Turbine Institute (IGTI) of ASME for publication in the JOURNAL OF TURBOMACHINERY. Manuscript received October 1, 2004; final manuscript received February 1, 2005. IGTI Review Chair: K. C. Hall. Paper presented at the ASME Turbo Expo 2005: Land, Sea and Air, Reno, NV, June 6–9, 2005, Paper No. GT2005-68595.

been a few studies that have investigated tip cooling designs. Kim et al. [2] studied various tip film cooling geometries on 2D tip models. They presented heat transfer coefficient and film effectiveness results for several hole locations on the tip itself and on the pressure side just underneath the tip gap. They indicated that the tip region cooling is affected by the right placement of holes inside the gap or on the pressure side just upstream of the gap. Although the results presented in this study provided some interesting validations, the flow field was not typical of realistic leakage flows. Kwak and Han [3] studied coolant blowing effects on tip heat transfer coefficients and film effectiveness over a real blade tip in a blowdown test. They indicated that higher blowing ratios increase film effectiveness and decrease heat transfer coefficients. They found that static pressure on the shroud and film-cooling effectiveness increased as the blowing ratio increased, whereas heat transfer coefficient decreased slightly with increasing blowing ratio. They concluded that these effects might be due to blockage effect of the injected coolant into the tip gap. Hohlfeld et al. [4] presented predictions of cooling from tip purge holes. They predicted local film effectiveness distributions on the tip and the shroud. They increased coolant blowing from a mass flux ratio of 0.9–7.4. Both the holes are located in the "sweet spot" region closer to the leading edge region of the tip where the heat transfer coefficient is lowest on the tip surface. Larger blowing ratios showed higher effectiveness on the shroud and no effectiveness on the tip itself. However, the study does not provide detailed heat transfer coefficients on the tip. Ahn et al. [5] studied the effects of the presence of recess/squealer rim, the location of the film cooling holes, and the tip gap clearance on the film cooling effectiveness in comparison to plane tip. They used pressure sensitive paint technique. Film cooling holes were located along the camber line on the tip and along the span of the pressure side. All measurements were made at three different tip gap clearances of 1%, 1.5%, and 2.5% of blade span. They found that for plane tip cases, the film-cooling effectiveness on blade tip is higher for the case with pressure side injection as compared to only tip and combination (both tip and pressure side injection). Also, squealer blade tip showed negligible film effectiveness for pressure side injection, whereas the plane tip showed significant film effectiveness. Christophel et al. [6,7] performed experiments in a linear cascade to measure adiabatic effectiveness and heat transfer for blowing from the tip of a turbine blade for two tip gap heights over a range of blowing ratios. They found that the dirt purge jets provided a significant amount of cooling for the leading edge area particularly for the small tip gap case. Also, increased blowing resulted in a larger cooling benefit for the large tip gap as compared with small tip gap. However, their study did not simulate an actual pressure drive flow that exists on a HPT blade tip. This may have caused their results to show very high film effectiveness. Polanka et al. [8] compared the experimental data taken in the tip region of a fully rotating turbine blade rotor with true predictions of the flow field made with a 3D Reynolds averaged Navier-Stokes solver. The results showed that the clearance has more of an effect with downstream distance for the tip, particularly after the throat of the blade passage. Yang et al. [9] predicted film cooling effectiveness and heat transfer coefficient for three types of film-hole arrangements: (1) the holes located on the mid-camber line of the tips, (2) the holes located upstream of the tip leakage flow and high heat transfer region, (3) combined arrangements of camber and upstream holes. They found that upstream film hole arrangements provided better film cooling performance than camber arrangements.

In the present study, both tip injection and pressure side injection along the tip are investigated. Initially, the two schemes are considered individually and then a combination of both tip and pressure side injection is studied. Film effectiveness and heat transfer coefficients are measured simultaneously using a transient IR technique.

Theory

In film cooling situations, the solution for 1D semi-infinite solid with transient conduction at the wall is modified to include the film temperature (T_f) based on the definition of the local heat flux [1]. The equation becomes:

$$\frac{T_w - T_i}{T_f - T_i} = 1 - \exp\left(\frac{h^2 \alpha t}{k^2}\right) \operatorname{erfc}\left(\frac{h\sqrt{\alpha t}}{k}\right) \tag{1}$$

where T_f is the local film temperature and is a function of the local mixing between the mainstream and coolant jet near the surface.

Vedula and Metzger [10] presented a method wherein two color change times can be obtained from a single transient test at every location. If during the transient, the liquid crystal coating indicates one surface temperature (T_{w1}) at time, t_1 and another surface temperature (T_{w2}) at time, t_2. Basically, two events are measured at every point leading to the solution of both h and T_f from the simultaneous solution of the two equations:

$$\frac{T_{w1} - T_i}{T_f - T_i} = 1 - \exp\left(\frac{h^2 \alpha t_1}{k^2}\right) \operatorname{erfc}\left(\frac{h\sqrt{\alpha t_1}}{k}\right)$$

$$\frac{T_{w2} - T_i}{T_f - T_i} = 1 - \exp\left(\frac{h^2 \alpha t_2}{k^2}\right) \operatorname{erfc}\left(\frac{h\sqrt{\alpha t_2}}{k}\right) \tag{2}$$

Also, they defined film effectiveness (η) as

$$\eta = \frac{T_m - T_f}{T_m - T_c} \tag{3}$$

where T_f represents the film temperature which is the same as adiabatic wall temperature as there is no heat transfer through the wall during the transient test. Several studies have used this technique to obtain film cooling measurements for different surface geometries. Ekkad et al. [11] and Du et al. [12] used a transient cooling technique to eliminate the use of superposition integration for the mainstream and coolant temperatures but they still needed two different tests to obtain both heat transfer coefficient and film effectiveness at every point on the surface.

In the present study, a transient infrared thermography technique is described for obtaining both heat transfer coefficient and film effectiveness from a single test. The transient infrared (IR) technique is based on the two equation, single test proposed by Vedula and Metzger [10] but similar to that used by Ekkad et al. [13]. In this test, two images with surface temperature distributions are captured at two different times during the transient test. The two temperatures at two different instants are used in the two equations (Eq. (2)) shown above to calculate both heat transfer coefficient and film temperature. The test is typical of a transient liquid crystal technique experiment wherein the heated test surface is suddenly exposed to a cold mainstream and hot coolant jet. The surface temperature response is captured by the IR camera at different time instants during the transient test. The distribution of initial temperature on the surface is also obtained using the IR camera. A variant of this technique is presented in another paper by Ekkad et al. [14]. A finite element analysis using ANSYS software of the test blade was conducted and results are presented on the effects of lateral conduction and associated uncertainty in the previous study by Nasir et al. [1]. It is to be noted that both the 3 s settling time for the mainstream flow and the slow rise in coolant temperature are accounted for in the heat transfer coefficient and film effectiveness calculation by using Duhamel's superposition integration scheme [15].

Major uncertainty in the calculation comes from measurement of initial, mainstream, and coolant temperatures. Estimated uncertainty in initial and wall temperature (ΔT_i) is $\pm 1.0^\circ$C, mainstream temperature (ΔT_∞) is $\pm 0.2^\circ$C, and coolant temperature (ΔT_c) is $\pm 0.2^\circ$C. The camera frame rate is 60 Hz resulting in a time error of $\pm 1.6\%$ and the test surface property uncertainty is estimated at $\pm 3\%$. The resulting average uncertainty using the methodology

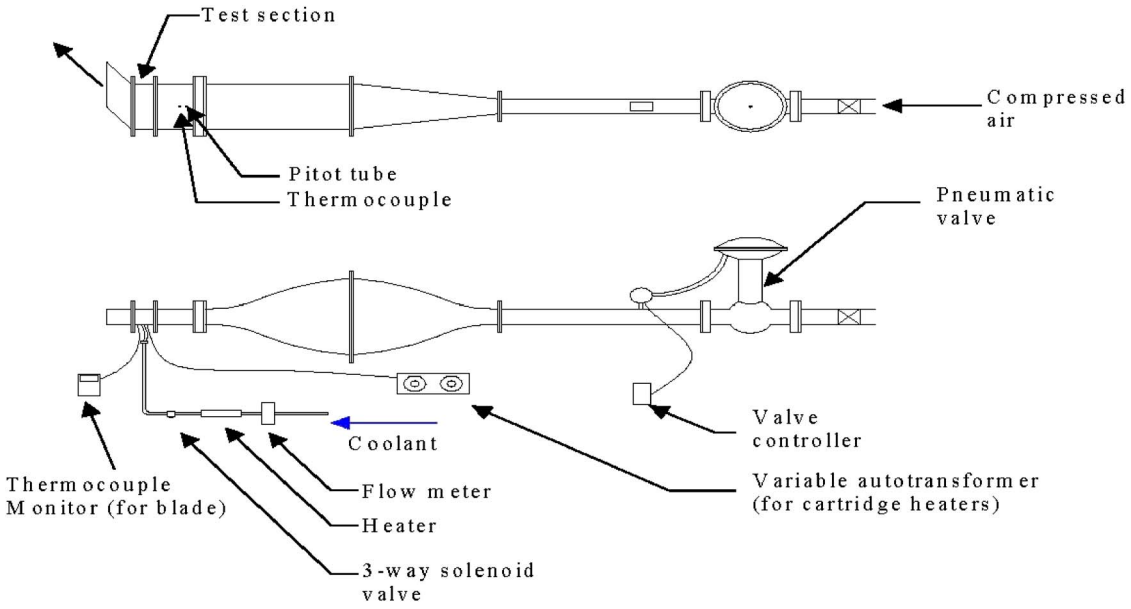

Fig. 1 Illustration of the blowdown experimental setup

proposed by Kline and McClintock [16] for heat transfer coefficient is ±9.7%. Edge effects can be severe causing high uncertainty along the pressure and suction side edges of the tip surface and hole corners. This uncertainty can be as high as ±15%. Uncertainty for local film effectiveness depends on the local value. Uncertainty for effectiveness measurements is ±0.0. Because of the low effectiveness values obtained on the tip, the levels of uncertainty could be as high as ±20–30 %.

Test Facility

This experiment uses a blow-down test rig as illustrated in Fig. 1. The test rig was designed to produce the required pressure ratio across the blade for a short duration. An air compressor supplies dry air to a large tank capable of holding 8 m^3 of high pressure air at 20 atm. This system is capable of generating a steady flow rate of 0.5 kg/s. The test section uses an open loop blow-down test rig as illustrated in Fig. 1. A gate valve isolates the entire wind tunnel from the supply tank. Downstream from that valve is a large pneumatically actuated control valve. A programmable controller regulates the pneumatic valve. The controller allows one to set the valve and maintain a specified valve opening and/or operating pressure in the test section. Air then passes through a rectangular diverging-converging section. This section is placed directly upstream from the test section. Its purpose is to settle the flow and make it more uniform before entering the test section. Boundary layer bleeds (slotted openings) along the test section inlet ensure the formation of a new boundary layer before the air enters the four-blade linear cascade test section. The exhaust area of the cascade is fitted with two tailboards. One tailboard is aligned with the pressure blade trailing edge and the other is aligned with the heat transfer blade. The movable tailboards can be used to back pressurize some passages and adjust the flow in all three passages. The tailboards are adjustable to help equalize pressure distribution in the passages adjacent to each blade and ensure periodic flow in all passages. The coolant loop provides cooling flow to the tip from below the blade into a cavity inside the blade. The coolant flow is diverted away from the test blade before the test and a three-way valve is used to switch the flow into and out of the blade. A heater is used to heat the coolant flow for the test.

The test section is a stationary linear cascade with four, two-dimensional blades with the tip section profile. The blade profile was taken from the tip section of a General Electric HPT blade. Each blade is made of aluminum using an EDM machine, and bolted to a steel base plate that can easily be removed from the test section. The blade spacing (S) is 95.25 mm, and the axial chord (C) is 60.02 mm. The two outer blades guide airflow around the inner blades. Inner blades are used for pressure and heat transfer measurements. Tip gap-to-blade span ratio of 1.0% is maintained for both pressure and heat transfer blade but film injection was implemented for heat transfer blade only. All blades have a span height from root to tip (H) of 76.2 mm. Figure 2 shows the four-blade linear cascade.

Pressure measurements are made on the blade surface in order to map the surface distribution and ensure that the flow conditions during heat transfer tests are correct. The "pressure blade" (Fig. 3(a)) outer surface is lined with small tubes, extending from root to tip, that are set in recesses. The blade is then covered by a thin, strong tape to provide a smooth surface. Small tap holes are drilled in the tubes at the specified locations for the purpose of making static pressure measurements, 33.3, 86.7, and 100% of the span from hub to tip (one hole per tube). The 100% span tap holes are exposed to the tip gap as shown in Fig. 3(a), whereas the other two span locations measure the blade surface pressure distributions. Each alternate hole has a different span wise location. A total of 96 taps are distributed among the three span locations. Pressure measurements are also made on the shroud for each of the recessed tips and the plane tip cases as indicated in Fig. 3(b). A special top plate with holes 6.35 mm away from the suction

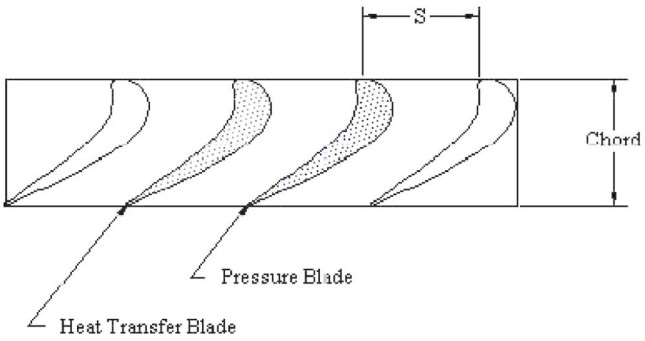

Fig. 2 Cascade geometry

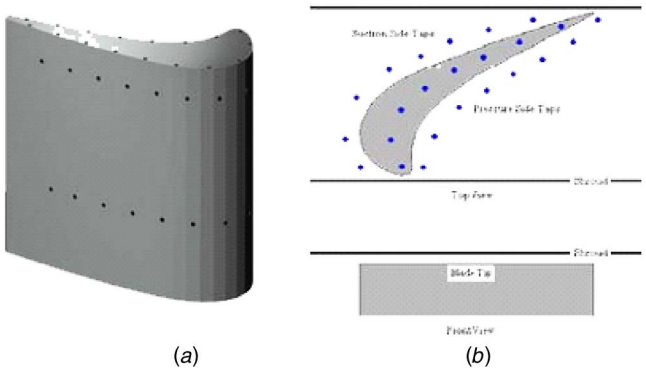

(*a*) (*b*)

Fig. 3 (*a*) Pressure test blade and (*b*) shroud plate with pressure taps

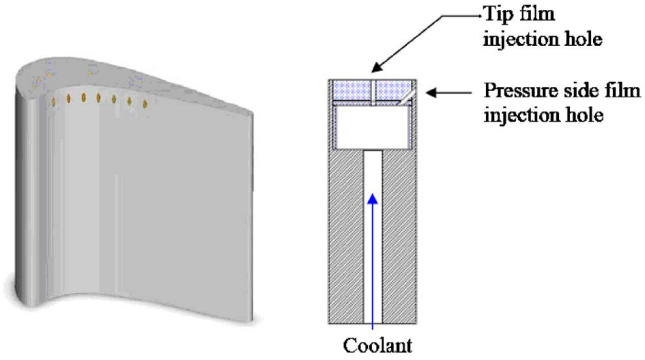

Fig. 5 Pressure side and tip injection holes

side, 6.35 mm from the pressure side, and along the camber line, allows for static pressure measurements on the stationary shroud.

Figure 4 presents the film cooling blade geometry for tip injection. The blade is primarily made of aluminum. Two cartridge heaters heat the aluminum blade through direct contact. The heat is conducted to the Plexiglas piece. There is a cavity with a hole feeding the cavity for the film cooling air supply through the aluminum core. The coolant flow collects in the cavity and is then discharged out through the tip gap from the five film holes. The holes are angled 90 deg or orthogonal to the leakage flow. The diameter of each hole is 0.79 mm. The holes are located at axial chord locations of 17, 25, 35, 55, and 74%, respectively along the camber line.

Coolant injection from pressure side holes and combined cooling when coolant is injected from both tip and pressure side holes will be studied also. Figure 5 shows 3D model and cut away view of the blade. There are seven holes located along the pressure side of the airfoil surface. The diameter of each hole is 1.524 mm and the center-to-center distance between each hole is 6.35 mm The first hole is located 17% of axial chord. The center of each hole is 5.08 mm down from the tip and each hole is oriented at each location with an angle of 20 deg to the surface (70 deg to surface normal). The angle is steep so that the coolant stays attached to the surface and also to allow drilling into the internal cooling passages. For recessed tip blade, coolant coming out through these holes also helps to cool the squealer rim.

The gap between the tip and the shroud is 1.0% of the blade span (7.62 cm). The recessed tip has a recess depth-to-blade span ratio of 4.16%. The holes are placed at the bottom of the recess cavity at the same locations along the camberline as for the plain tip.

The infrared thermography system used is a FLIR systems ThermaCAM SC 500. The camera offers a high quality, nonintrusive method for obtaining thermal data through a commercially available software package for data analysis. The camera has a range of $-40-500\,^{\circ}\mathrm{C}$. The ThermaCAM 500 utilizes uncooled microbolometer long-wave detectors to sense IR radiation. This makes them ideal for general thermal measurement applications. The SC 500 system features real time 14 bit digital output, a 320×240 pixel detector, precision temperature measurement, internal data storage, and outstanding thermal sensitivity. The camera has the following specifications: the field of view and minimum focus distance are 240×180 and 0.5 m respectively, the spectral range is 7.5–13 mμ and accuracy is ±2% or $2\,^{\circ}\mathrm{C}$ of the measured temperature.

Procedure

During a blow-down test the supply tank, which provides air to the test rig, empties into the test section. Therefore, the inlet total pressure does not remain constant. A test was performed to determine the total pressure variation during the blow-down operation. Inlet total pressure is measured with a pitot probe (located 23 cm upstream of the test blades at midspan) and the NetScanner system.

Heat Transfer Tests. Figure 6 shows the camera, IR window arrangement over the blade tip. The blade tip was painted with flat black paint first. When the paint dried, the blade was heated up for one and a half hours so that the Plexiglas reaches the steady state temperature. During the heating, the Plexiglas temperature was checked every 15 min. Then a reference point was selected and its temperature was measured using a 32 gauge thermocouple. The

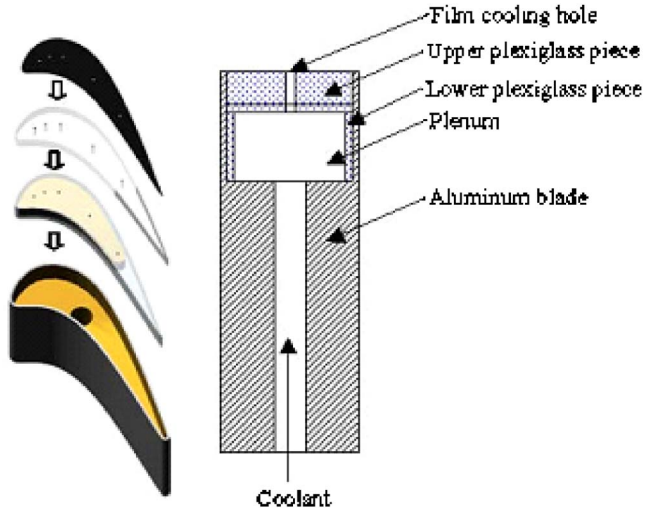

Fig. 4 Film cooled blade geometry

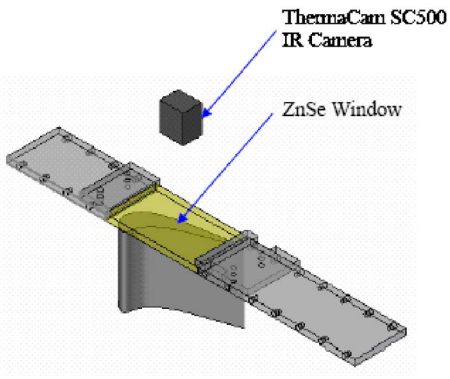

Fig. 6 Infrared camera arrangement

thermocouple was calibrated using an ice bath and boiling water bath. The analog/digital system was adjusted to convert the voltage to the right temperature. This ensured a better accuracy of the results. The IR camera is calibrated using the thermocouple placed on the surface with a high conductive aluminum tape to ensure proper contact on the surface. The tape is spray painted black to ensure high emissivity. After that the emissivity was altered until the temperature measured by the camera agrees with the thermocouple reading. This is the emissivity value of the reference object. However, the temperature of the reference object must not be too close to the ambient temperature for this to work. During the emissivity calculation, zinc-selenide window was not used. So, the transmissivity value used was 1. The emissivity calibration provided an emissivity for the black painted surface to be 0.95. The measured transmissivity pf the zinc-selenide window found by the calibration technique and the transmissivity value of the window supplied by the manufacturer matches exactly. The transmissivity of the window is 0.75.

The heat transfer blade is coated black and is heated for 2 h to ensure that its temperature reaches steady state before testing. During heating, the surface temperature is monitored by the IR camera. The inside temperature of the Plexiglas piece is monitored using thermocouples. These thermocouples are checked every 5 min. Once the blade temperature reaches steady state, the coolant flow is set to bypass and heated to about the same temperature as the test blade. The blade heaters are switched off, the IR camera is set to take images at periodic intervals, the coolant flow is switched into the test blade, and the pneumatic valve is then opened so that compressed air may enter the test rig. Coolant flow temperature is measured in the cavity before the air enters the film hole. The images are recorded and saved as data files. The digitized temperature values at initial condition, 5 s into the test, and 35 s into the test are provided as input into a Fortran program to calculate h and η simultaneously from Equation set (2). The equations are solved for every pixel location on the Plexiglas tip where T_i is the initial heated blade temperature before the transient is initiated; T_m is the oncoming mainstream recovery temperature; T_c is the coolant temperature; T_w is the wall temperature or the reference temperature during the transient test; α and k are the thermal diffusivity and thermal conductivity of the Plexiglas surface; and t is the time at which the frames are recorded. All the above values are either known or measured during the test and the local heat transfer coefficient (h) and film effectiveness (η) are calculated at every pixel location

Pressure Tests. Pressure measurements were made using a KPSI 32-channel system that acquires data at 100 Hz frequency at each port. Static pressure measurements are made on the shroud for each blade tip configuration. Measurements are also made on the pressure blade suction and pressure surfaces. Before each pressure test, moisture is blown from the pressure system data ports using the supply pressure. The data ports are calibrated and reset to zero, when necessary, to ensure accuracy. The pneumatic valve is then opened and air enters the test rig. The duration of all pressure tests matched that of the heat transfer tests. The pressure system reads surface gauge static pressures. Pressure ratios are computed based on the measured inlet total pressure at that instant. Nasir et al. [1] provide more details on the test rig, basic pressure distributions for the cascade, and flow verification for the system.

Local Blowing Ratio Calculations. The set blowing ratio is called global blowing ratio because it is based on velocity of the mainstream at the inlet of the cascade. But actual or local blowing ratio for each hole is more than likely to be different than the global blowing ratio. The reason is that the amount of coolant coming out from each hole depends on the difference between plenum pressure and local static pressure. If pressure difference is higher, more coolant will come out, i.e., higher blowing ratio and vice versa. Local blowing ratio is an important parameter because it gives us the local picture of coolant and leakage flow interaction. The equation used to calculate actual mass flow rate of coolant coming out through each hole [17] is

$$\dot{\mathbf{m}} = \mathbf{C_D P_{tc}}\left(\frac{\mathbf{P_m}}{\mathbf{P_{tc}}}\right)\sqrt{\frac{2\boldsymbol{\gamma}}{(\boldsymbol{\gamma}-1)\mathbf{R T_{tc}}}\left(\left(\frac{\mathbf{P_{tc}}}{\mathbf{P_m}}\right)^{(\gamma-1)/\gamma}-1\right)}\left(\frac{\boldsymbol{\pi}}{\mathbf{4}}\mathbf{d}^2\right)$$

where $\dot{\mathbf{m}}$ is the actual mass flow rate of coolant, C_D is the discharge coefficient or the ratio of actual mass flow rate to ideal mass flow rate through the film cooling hole; P_{tc} is the total pressure of coolant inside plenum; P_m is the static pressure of mainstream at the hole location based on the measured shroud pressures with injection; γ is the specific heat ratio; R is the gas constant; T_{tc} is the total temperature of coolant inside plenum; and d is the diameter of film cooling hole. The above equation assumes an isentropic one-dimensional expansion from the total pressure in the coolant loop to the static pressure in the primary or mainstream. For present study, static pressure measured on the floor of the plenum is used as the total pressure of coolant. It can be safely assumed in our case that static and total pressures inside the plenum are the same because plenum acts as a reservoir. Static pressure inside the plenum is measured at two places on the floor and no significant difference in pressure readings was found. It shows that coolant flow equalizes well inside the plenum. The discharge coefficient for the hole was measured with a simple flow test and the value obtained from experiment was 0.64, 0.62, 0.58 for the three blowing ratios. The value of 0.6 was used for all conditions.

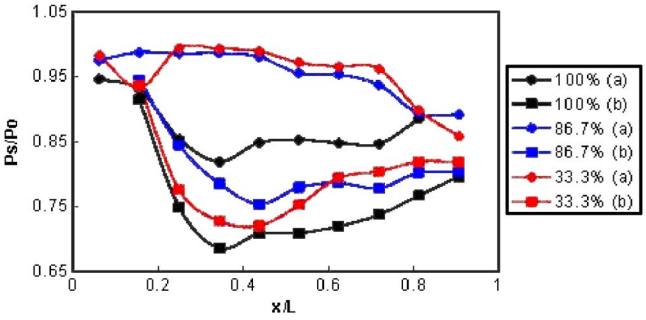

Fig. 7 Surface pressure distributions on the blade surface and tip gap with 1% clearance gap (*a*) pressure surface (*b*) suction surface

Results and Discussion

The test flow conditions at inlet to cascade were measured using hot wire anemometry. The flow inlet velocity at cascade inlet was 60 m/s, which represents a cascade inlet Mach number of Ma=0.16. The exit velocity to the cascade was 188 m/s, which is a Mach number of Ma=0.54. The Reynolds number based on cascade exit velocity and blade axial chord is 861,000. The engine condition is simulated at entrance but the blade exit is dependent on the pressure ratio resulting in lower than engine condition of Ma=0.8. The coolant to mainstream density ratio is 0.95 and is much lower than the engine conditions which is typically in the order of 1.7–2.0.

Figure 7 presents the blade pressure distribution at three different span locations for a tip gap of 1.0% of blade span plotted against normalized length along the pressure and suction surfaces (x/L). The measurement locations for hub to tip are at locations along 33.3, 86.7, and 100% of the blade span. The local static pressure is normalized by the cascade inlet total pressure ($P_s/P_{o,\text{inlet}}$). In the figure, curve (a) represents the pressure side and curve (b) represents the suction side. At 33.3% blade height from the hub, there is a large pressure differential between the pressure and suction surface which is the main driving potential for the leakage flow. Also just downstream of the leading edge,

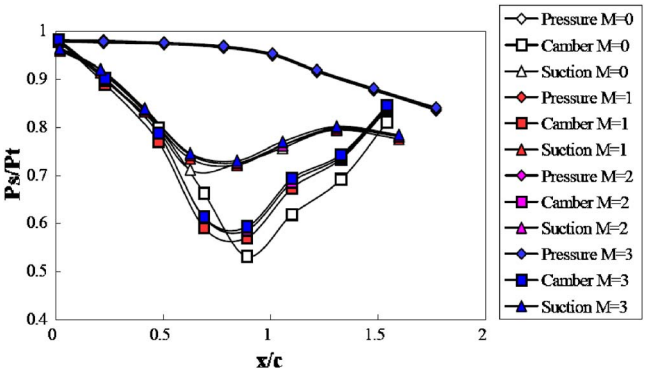

Fig. 8 Effect of blowing ratio on shroud pressure distributions for a plane tip with tip injection only

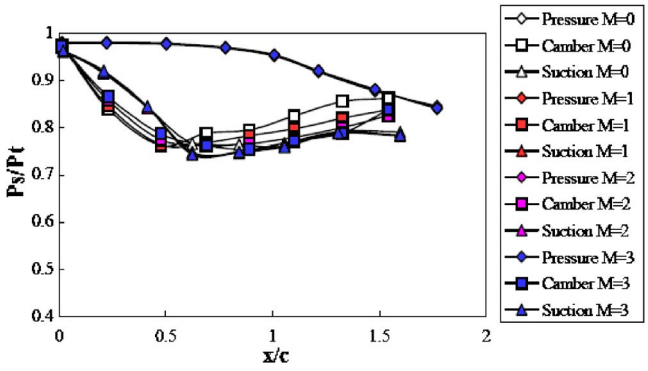

Fig. 9 Effect of blowing ratio on shroud pressure distributions for a recessed tip with tip injection only

the static pressure on the pressure side is actually lower than that for the suction side at 33% height. This is consistent with the design data provided during rig characterization. At 86.7% of blade span closer to the tip gap, the pressure side distribution seems unaffected by the span location. However, the suction side static pressures are higher than for 33.3% span location. The pressure distributions in the tip gap along the blade edges are shown by the 100% case and are significantly affected by the leakage flow. In this case, the static pressure on the pressure side drops significantly from the 86.7% location values as the flow accelerates through the gap. The suction side pressure is not as significantly affected as the pressure side.

Tip Injection Only. Figure 8 shows the effect of blowing ratio on pressure distributions for a plane tip film injection. Static pressures on the shroud (Ps) are normalized by the inlet total pressure (Pt) and the distance along the blade profile (x) is normalized by the axial chord (C) for all the graphs. The diamond, square, and triangle legends represent values for pressure taps located pressure side, camber line, and suction side, respectively. Different color is used for different blowing ratios. The lower value of pressure ratio indicates higher velocity and vice versa. As expected, we see acceleration of flow from pressure side to the camber line. Due to sudden acceleration, static pressure along the camber line is lowest and as the fluid expands out of the tip, static pressure along the suction side line increases. This is expected due to the presence of pressure driven accelerated flow through the tip gap. The first noticeable effect of coolant injection is the shift of lowest value for camber line between no coolant injection ($M=0$) and all coolant injection tip injection hole cases. Also, as the blowing ratio increases, the pressure ratio does not seem affected.

Local blowing ratios for plane blade tip with tip only injection cases are shown in Table 1. The local blowing ratios are calculated using the equation and procedure described earlier. Hole number starts with the first hole from the leading edge. As seen, local blowing ratios for the first three holes are lower than global blowing ratios for all three global blowing ratios. Whereas the last two holes show higher local blowing ratios than the global blowing ratio and the 4th hole has the highest local blowing ratio. As mainstream static pressure is higher near the leading edge, coolant mass flow rate coming out through the first three holes is lower. Conversely, mainstream static pressure along the middle to near trailing edge is lower which results in higher coolant mass flow rate or higher blowing ratio.

Table 1 Local blowing ratios for plane tip with tip injection only

Plane tip with tip injection						
Hole	Global M	Local M	Global M	Local M	Global M	Local M
1	1.0	0.2511	2.0	0.9758	3.0	1.8433
2		0.6237		1.3742		2.2846
3		0.9729		1.8706		2.8605
4		1.9737		3.4473		4.7490
5		1.2087		2.3112		3.2845

The addition of film injection at the tip, on the pressure side or a combination of both, does not alter the pressure distributions on the shroud surface. The effect of blowing on the static pressure is limited to a small region on the middle of the tip region resulting in maybe a slight alteration of the pressure relating leakage flow. The pressure distributions will not be shown for the other two injection configurations.

Figure 9 shows the effects of coolant injection from the tip on pressure distributions for recessed blade tip. One obvious difference between the plane tip and the recessed tip is the magnitude of pressure ratio for camber line values. For the recessed tip, the ratio is much higher than the plane tip. So, we can expect lower values of heat transfer coefficient for the recessed tip. Also, one interesting observation is that for the plane tip, camber line values almost collapse with suction line values near leading edge ($x/c < 0.5$), whereas, for the recessed tip, camber line values are lower than suction line values. This indicates that flow is accelerating near the leading edge for recessed tip due to larger pressure difference near to the leading edge and the opposite is true for the plane tip. So, higher heat transfer region for recessed tip near the leading edge region and lower heat transfer region for the plane tip can be expected as shown by [1]. For effects of blowing ratio, it is noticed that as the blowing ratio increases, a decrease in pressure ratio near leading edge is observed. An increase in pressure ratio with an increase in blowing ratio is observed for middle to trailing edge region. So, a decrease and an increase in heat transfer coefficient for near leading edge and trailing edge, respectively, are expected. But we will see from our heat transfer results that flow over recessed tip is too complex to explain from shroud pressure distribution. We will try to present a possible explanation in the heat transfer results section.

Local blowing ratios for recessed tip with tip only injection cases are shown in Table 2. It is observed that local blowing ratios are much more even between holes and the values are closer to global blowing ratios. This shows that an even pressure distribution is present on the recessed blade tip than plane blade tip. It also seems that flow is decelerating or pressure is high near the trailing edge, which results in lower blowing ratio for the 5th hole.

Figure 10(i) shows the detailed film effectiveness distributions for the plane tip with tip hole injection only. No film effectiveness is observed for almost the entire blade tip except small regions just after the holes. Because of the difference in local blowing ratio between holes, different jet widths are observed for different holes. An increase in film effectiveness is noticed as blowing ratio

Table 2 Local blowing ratios for recessed tips with tip injection only

Recessed tip with tip injection						
Hole	Global M	Local M	Global M	Local M	Global M	Local M
1	1.0	1.0953	2.0	2.0341	3.0	2.9969
2		1.0804		2.0758		3.0891
3		1.0529		2.0825		3.1305
4		0.9361		2.0100		3.1008
5		0.8567		1.7582		2.6970

increases from 1 to 2. But a decrease in value is noticed for the blowing ratio, $M=3$. As seen in Table 1, the local blowing ratios for each hole are pretty high, which indicates high momentum jets. Due to high momentum, the coolant jet maintains a cylindrical structure and detaches from the injection surface and dissipates into the mainstream without adhering to the primary surface as seen for hole numbers 1 and 3. Sometimes, the jet may reattach itself to the tip surface after interacting with the opposite shroud surface, which results in high effectiveness as seen for hole numbers 2, 4, and 5.

Figure 10(ii) shows the detailed film effectiveness distributions for the squealer tip with tip hole injection only. Highest film effectiveness is observed for blowing ratio, $M=2$. The directions of high effectiveness streaks are along the camber line. The first four holes have similar local blowing ratios and they also exhibit similar film effectiveness. Interestingly, the 5th hole has lowest effectiveness for all three blowing ratios. It is may be due to the fact that it has the lowest local blowing ratio as noticed in Table 2. For blowing ratio, $M=3$, almost no effectiveness is observed for the whole tip. This may be due to complete detachment of the coolant jet from the injection surface.

Figure 11(i) shows the detailed heat transfer coefficient distributions for the plane tip with tip hole injection only. For no coolant injection case ($M=0$), a low heat transfer coefficient region is observed near the leading edge. This is referred to as sweet spot. In this region, suction and camber line pressures collapse, meaning that there is little pressure difference to drive leakage flow. Very high heat transfer coefficient region is observed along the pressure side from middle of the blade towards trailing edge. This is due to the pressure side entry loss vortex. The heat transfer coefficient distribution observed is typical for plane blade tip and observed by many previous researchers. The obvious effect of coolant injection is a reduction in heat transfer coefficient, especially along the pressure side region. Also, horseshoe vortex is clearly visible ahead of each hole. For blowing ratio, $M=1$, from the direction of horseshoe vortex, it is clearly seen that leakage flow is directing from pressure side leading edge towards suction side trailing edge. A region of very low heat transfer coefficient region is also observed just after the holes. Due to acceleration of flow in between holes, higher heat transfer coefficient regions are observed there. Due to blockage effect, heat transfer coefficient decreases as blowing ratio increases. It is also seen that the region of small heat transfer coefficient near the trailing region diminishes as blowing ratio increases.

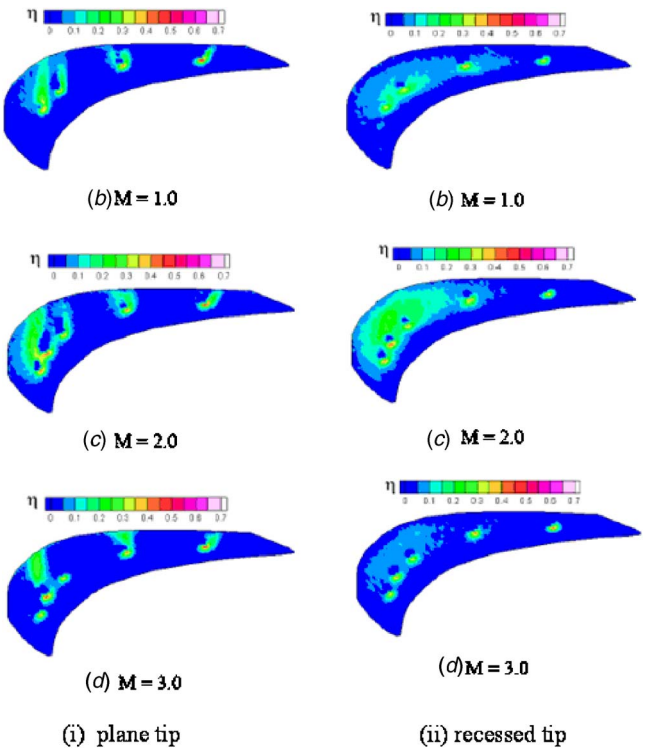

Fig. 10 Detailed film effectiveness distributions with tip injection only

Figure 11(ii) shows the detailed heat transfer coefficient distributions for the squealer tip with tip hole injection only. Reverse trend is observed for recessed tip than plane tip. A high heat transfer coefficient region is noticed near the leading edge region and lower values are noticed for the trailing edge region. This opposite trend is actually beneficial to the blade because the cross section is the widest near the leading edge due to which it can better withstand higher heat load than thin trailing edge. It appears that as the blowing ratio increases, heat transfer coefficient decreases, at least near the leading edge, though the decrease is not as obvious as a plane tip. Also, there is a low heat transfer region near the pressure side of the trailing edge region. Thickness of this region is smallest for the highest blowing ratio. It seems like that for bowing ratio, $M=1$ and $M=2$, leakage flow enters the recessed tip near the leading edge and goes out of the tip near the suction side of the trailing edge region. For blowing ratio, $M=3$, possibly the interaction between jet and leakage flow is minimum due to higher momentum of the jet. As a result, leakage flow expands more and reduces the low heat transfer region.

Pressure Side Injection Only. Local blowing ratios for plane tip with pressure side only coolant injection are presented in Table 3. Surface pressure on the 86.7% span of the pressure side of the blade (Fig. 6) is used as reference data. So, the values presented here are just estimated values. The first observation is that local blowing ratio for all holes is almost equal. This is due to the fact that static pressure on the pressure surface of the blade remains almost constant and does not decrease sharply as compared to suction surface. Also, local blowing ratio values are closer to global blowing ratios.

Table 4 shows local blowing ratios for recessed tip with pressure side injection only case. Not much of a difference is observed between plane and recessed blade tip cases. Though similar local blowing ratios are observed between plane and recessed blade tip, it will be observed later that heat transfer coefficient and film effectiveness distributions between the two blade tips are entirely different. This is due to the two completely different flow patterns present between the two blade tips.

Figure 12(i) shows the detailed film effectiveness distributions for the plane tip with pressure side hole injection only. Low effectiveness values are observed for all blowing ratios. Coolant jet streaks are visible for blowing ratio $M=1$, along the pressure side. But for blowing ratio $M=2$, those jet streaks are not present. It appears that all the jets detach from the tip surface and they do not reattach themselves on the tip surface. For blowing ratio, $M=3$, we see the reattachment of the jets along the suction side after the jets hit the shroud surface.

Figure 12(ii) shows the detailed film effectiveness distributions

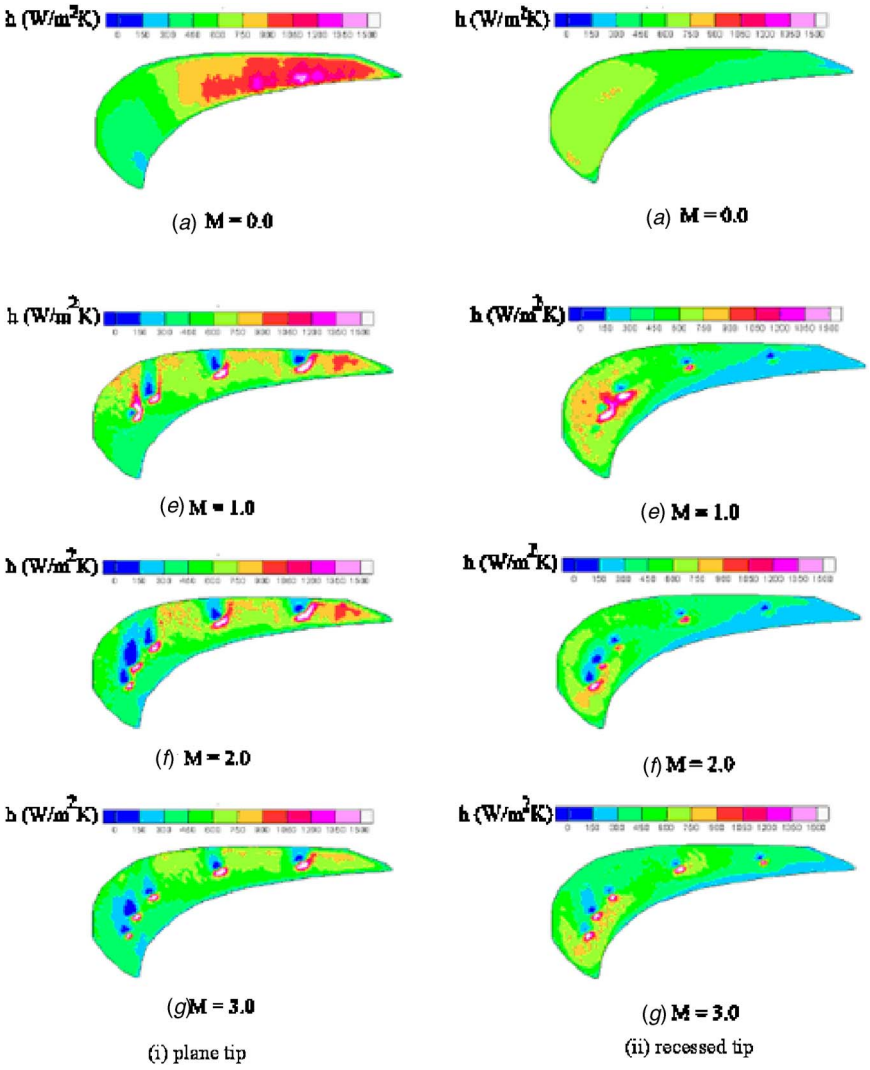

Fig. 11 Detailed heat transfer coefficient distributions with tip injection only

for the recessed tip with pressure side hole injection only. No film effectiveness (all blue) is observed for all blowing ratios except a faint trace for blowing ratio, $M=3$. Overall, it appears that pressure side coolant injection is totally ineffective for recessed tip case. This may be due to high pressure present inside the squealer cavity. As seen in Fig. 9, pressure ratios along the camber line for recessed tip are much higher than the plane tip. This high pressure possibly prevents coolant jets from getting into the cavity, which results in no effectiveness for the recessed blade tip.

Figure 13(i) shows the detailed heat transfer coefficient distributions for the plane tip with pressure side hole injection only. One obvious effect of pressure side coolant injection is the reduction in heat transfer coefficient along the pressure side that is observed for no injection or $M=0$ case. It appears that separation entry vortices are no longer present for all the coolant injection cases. It has also been noticed that high heat transfer coefficient regions are present along the suction side for blowing ratio $M=1$ case. These regions diminish as blowing ratio increases to 2. The high heat transfer coefficient regions for blowing ratio M

Table 3 Local blowing ratios for plane tip with pressure side injection

Plane tip with pressure side injection						
Hole	Global M	Local M	Global M	Local M	Global M	Local M
1	1.0	1.0462	2.0	2.0573	3.0	3.0517
2		0.9691		1.9513		2.9544
3		0.9803		1.9666		2.9684
4		0.9900		1.9799		2.9805
5		0.9870		1.9758		2.9767
6		1.0013		19953		2.9945
7		1.0314		2.0368		3.0328

Table 4 Local blowing ratios for recessed tip with pressure side injection

Recessed tip with pressure side injection						
Hole	Global M	Local M	Global M	Local M	Global M	Local M
1	1.0	1.0307	2.0	2.0527	3.0	3.0484
2		0.9666		1.9662		2.9688
3		0.9759		1.9785		2.9802
4		0.9839		1.9894		2.9900
5		0.9814		1.9860		2.9870
6		0.9933		2.0019		3.0016
7		1.0184		2.0359		3.0329

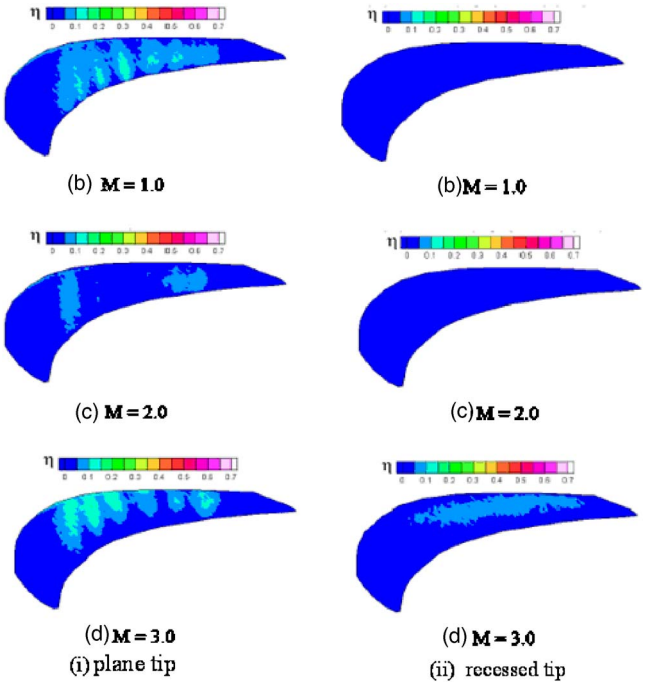

Fig. 12 Detailed film effectiveness distributions with pressure side injection only

=3 are due to reattachment of coolant jets along the suction side region of the tip surface. Also, streaks of jets marked by low heat transfer regions are visible along the pressure side of the blade tip.

Figure 13(ii) shows the detailed heat transfer coefficient distributions for the recessed tip with pressure side hole injection only. No injection case and blowing ratio $M=1$ cases are almost identical except the low heat transfer coefficient region located near the pressure side trailing edge for $M=1$ case. This low heat transfer region is present for all blowing ratio cases. As blowing ratio increases, the high heat transfer coefficient region near the leading edge continues to decrease in size.

Combined Pressure Side and Tip Hole Injection. Local blowing ratios for plane tip with combination injection cases are shown in Table 5. It is observed that local blowing ratios for tip coolant holes are higher than pressure side holes. In fact, local blowing ratios for tip coolant holes are higher than global blowing ratios. This is due to the fact that pressure side surface has higher pressure than blade tip especially the camber line where the tip coolant holes are located. This high pressure is causing less coolant to come out through the pressure side holes in comparison to the tip holes. Again, the 4th tip hole has the highest value. If local blowing ratios for tip holes in Table 1 (tip only injection) are compared to local blowing ratios for tip holes in Table 5 (combination injection), a significant increase in local blowing ratios for combination cases is observed for all the holes, especially for the first hole. As will be seen later, this increase in blowing ratio for tip holes causes substantial impact between coolant and mainstream interaction, particularly for blowing ratio, $M=3.0$.

Local blowing ratios for recessed tip with combination coolant injection are shown in Table 6. Again, tip holes have higher local blowing ratios than pressure side holes. But the tip holes for recessed tip have lower local blowing ratios than plane tip and the opposite is true for pressure side holes. This is due to higher static pressure on the recessed blade tip than plane tip. Also, the tip holes have almost equal local blowing ratios and the values are higher than global blowing ratios.

Figure 14(i) shows the effect of blowing ratio on detailed film effectiveness for plane tip pressure distribution for combined coolant injection. For blowing ratio, $M=1$ and $M=2$, coolant jets are much wider than tip only and pressure side injection only cases. This is obviously due to the combined injection and higher blowing ratios. Also, small effectiveness values are observed in between holes because of the injection from pressure side holes. For blowing ratio, $M=3$, high film effectiveness value of around 0.5 is observed for holes 2, 4, and 5. It appears that for a high blowing ratio of $M=3$, coolant jet from the tip hits the shroud first and then adheres back onto the blade tip resulting in higher film effectiveness. This was not observed for tip only and pressure side injection only cases because in combination cases the pressure side injection jets are creating a barrier for the tip injection jets. In addition, the tip holes have higher blowing ratios and this higher momentum of the jets causes minimum interaction between leakage flow and tip injection jet. As a result, the tip jets shoot up and then reattach back onto the tip. Also, some reattachments of pressure side injection jets are observed for this case. High effectiveness values are observed in regions between holes. This is due to the reattachments of jets coming out of the pressure side holes.

Figure 14(ii) presents the effect of blowing ratio on detailed film effectiveness distributions for combined injection on a recessed tip. Blowing ratio, $M=1$ and $M=2$, shows the almost same level of effectiveness. The high effectiveness regions are around holes 2, and 3. Though all the tip holes have similar local blowing ratios, holes 1, 3, and 5 are not showing lesser effectiveness. This is possibly due to the fact that effectiveness not only depends on local blowing ratios but also it depends on how the jet is interacting with leakage flow locally. It appears that leakage flow is pushed along the camber line from the leading edge towards the trailing edge and does not cross from pressure side to suction side as is the case without film injection. As expected, high film effectiveness values are observed for blowing ratio, $M=3$ case. But the level of effectiveness is lower than the plane tip case.

Ahn et al. [5] also shows similar film effectiveness results for a different blade where they considered tip and pressure side injection. They also showed film effectiveness distributions on the pressure side edge where coolant is injected. However, the levels of film effectiveness obtained in this study and their study are in good correlation. The main focus of the present study is to indicate the effects for a different blade with different pressure distributions are similar. However, locally, the effects are clearly dependent on the pressure distributions that drive the tip leakage flow.

Figure 15(i) shows the effect of blowing ratio on detailed heat transfer coefficient distributions for plane tip with combined coolant injection. Coolant injection decreases the heat transfer coefficient compared to the no injection case. For blowing ratio, $M=2$, streaks of jets from pressure side holes are visible along the pressure side of the blade. These streaks are not visible for the blowing ratio 1 case. For blowing ratio, $M=3$, very high heat transfer coefficient regions are observed around holes 2, 4, and 5. These butterfly-shaped regions are extended from the middle of the blade towards the suction side. It appears that for this high blowing ratio, coolant jet from the tip hits the shroud first and then bounces back onto the blade tip. This was not observed for tip only and pressure side injection only cases because in combination cases, the pressure side injection jets are creating a barrier for the tip injection jets. In addition, the tip holes have higher blowing ratios and this higher momentum of the jets causes minimum interaction between leakage flow and tip injection jet. As a result, the tip jets shoot up and then reattach back on to the tip. Also, some reattachments of pressure side injection jets are observed for this case.

Figure 15(ii) presents the effect of blowing ratio on detailed heat transfer coefficient distributions for combined injection on a recessed tip. It has been observed that the high heat transfer coefficient region that is present in no injection case is absent for blowing ratio, $M=1$ case. For tip only and pressure side injection only cases, this high heat transfer coefficient region was present

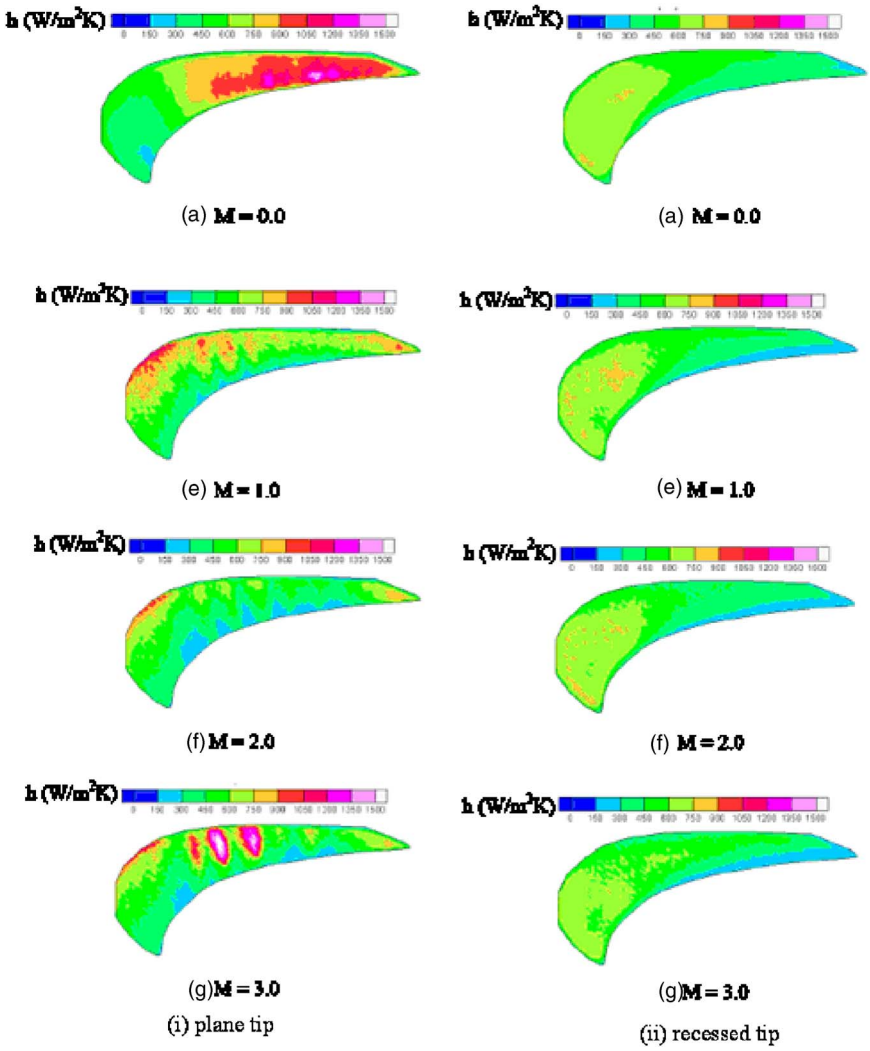

Fig. 13 Detailed heat transfer coefficient distributions with pressure side injection only

for blowing ratio, $M=1$ case. Typical low heat transfer coefficient region located along the pressure side trailing edge region is also present for all blowing ratio cases. This region increases in size as blowing ratio increases. Like the plane tip, very high heat transfer coefficient regions around holes 2, 3, and 4 are present for blowing ratio, $M=3$. This may be due to the same reason as explained in the plane tip case.

Heat Flux Ratio Distributions. Heat flux ratios (q''/q_0'') for all

Table 5 Local blowing ratios for combined injection for a plane tip

Plane tip with combination injection							
	Hole	Global M	Local M	Global M	Local M	Global M	Local M
Tip holes	1	1.0	1.1003	2.0	2.8557	3.0	2.9457
	2		1.3949		3.2801		3.3229
	3		1.6726		3.5392		3.6003
	4		2.5463		3.1916		4.4880
	5		1.4541		2.3274		3.5239
Pressure side holes	1	1.0	0.5800	2.0	1.2983	3.0	2.6385
	2		0.5232		1.2349		2.5805
	3		0.5316		1.2441		2.5888
	4		0.5388		1.2520		2.5960
	5		0.5366		1.2495		2.5937
	6		0.5471		1.2612		2.6044
	7		0.5693		1.2861		2.6272

Table 6 Local blowing ratios for combined injection for a recessed tip

Recessed tip with combination injection							
	Hole	Global M	Local M	Global M	Local M	Global M	Local M
Tip holes	1	1.0	1.4369	2.0	2.5513	3.0	3.1272
	2		1.4413		2.5790		3.3547
	3		1.4468		2.5926		3.4449
	4		1.4446		2.5963		3.5424
	5		1.4760		2.6491		3.4557
Pressure side holes	1	1.0	0.7013	2.0	1.6129	3.0	2.7585
	2		0.6427		1.5468		2.7053
	3		0.6513		1.5563		2.7129
	4		0.6587		1.5645		2.7195
	5		0.6564		1.5620		2.7174
	6		0.6673		1.5741		2.7271
	7		0.6902		1.6001		2.7481

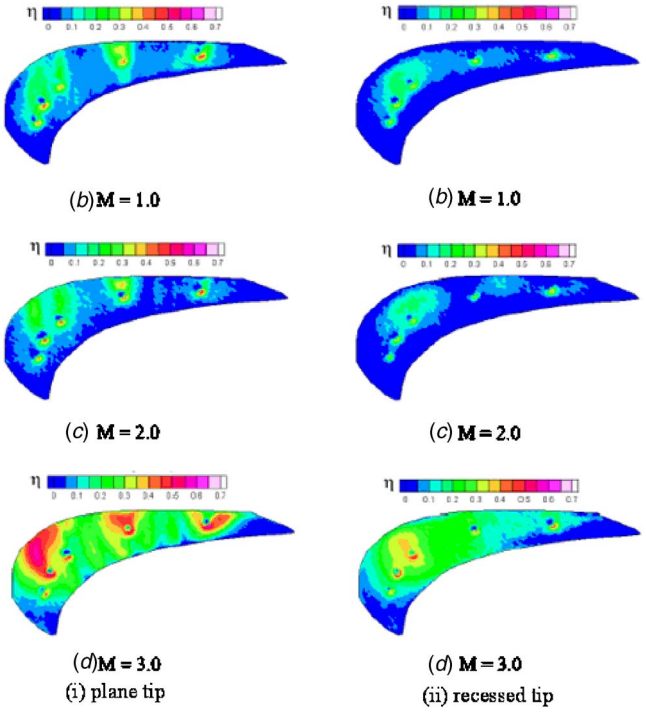

Fig. 14 Detailed film effectiveness distributions with combined injection

the cases takes into account the effect of both heat transfer coefficient and film effectiveness values. The heat flux ratio is calculated based on the formulation presented by Mehendale et al. [18]. The heat transfer ratio with and without film injection (h/h_0) and the local film effectiveness are used to calculate the local heat flux ratio.

$$\frac{q''}{q''_0} = \frac{h}{h_0}\left(1 - \frac{\eta}{\phi}\right)$$

The term ϕ is the overall cooling effectiveness and ranges between 0.5 and 0.7 for typical blade cooling systems. In this study, a typical value of 0.6 is chosen. The areas where the ratio is less than one show benefit from film cooling.

Figure 16 shows the detailed heat flux ratios on a plane and recessed tip with tip injection only. This takes into account the combined effect of film effectiveness and heat transfer coefficient. For plane tip cases, a decrease in net heat flux ratio value for entire tip is observed as blowing ratio increases. Values of more than 1 are observed near the leading edge region. This is due to the fact that, the no-coolant case has a very low heat transfer coefficient region, whereas coolant injection actually increases heat transfer coefficient in that region and film effectiveness values are not high enough to make up for the increase in heat transfer coefficient. Also, just after the holes, very low values are observed. This is because of high film effectiveness and low heat transfer coefficient values. Also, a thin region of higher net flux ratio region is observed along the suction side region. For recessed tip blade, as blowing ratio increases from 1 to 2, we see a decrease in net heat flux ratio values. The high value region near the leading edge for blowing ratio, $M=1$, is due to the high heat transfer region observed in the detailed heat transfer coefficient distributions in Fig. 11. For blowing ratio, $M=3$, small areas of high neat flux ratio are observed near the trailing edge. They are located along the jet direction. It seems that the jet increased the heat transfer coefficient in those areas without producing any cooling effectiveness.

Figure 17 shows the detailed heat flux ratios on a plane and squealer tip with pressure side injection only. For plane tip cases, a high value region is observed near the leading edge. The value decreases as blowing ratio increases. It appears that pressure side coolant injection redirected the leakage flow for the plane tip. Low value regions can be seen along the pressure side. This is a direct effect of the coolant jets. For recessed tip blade, the value of net heat flux ratio is close to 1 for almost all the tip region. This indicates that pressure side coolant injection for the recessed tip blade is not beneficial at least for the tip. It may, however, help in cooling the thin squealer rim.

Figure 18 shows the detailed heat flux ratios on a plane and squealer tip with combined tip and pressure side injection. For the plane tip, the values are lower than 1 for most of the blade tip. Blowing ratio, $M=2$, shows low net heat flux ratio regions along pressure side of the blade tip. A small high value region near leading edge is observed for blowing ratio, $M=3$. Recessed tip shows even distribution of net heat flux ratio except a few small areas for blowing ratio, $M=1$ and $M=2$. For blowing ratio 3, the high value region is present near leading edge, which extends to the middle of the blade.

Conclusions

Detailed film effectiveness measurements were made on a high pressure turbine blade tip with an inlet total-to-outlet static pressure ratio of 1.2. A transient infrared thermography technique was used to obtain both heat transfer coefficient and film effectiveness in a single test. The heat transfer coefficients and heat flux reduction analysis are presented in the companion paper. The effects of coolant injection on plane and recessed blade tip were studied for blowing ratios of $M=1.0$, 2.0, and 3.0. Three cases studied for this case were: (1) coolant injection from holes located on the blade tip, (2) coolant injection from holes located near the tip along the pressure side and, (3) combination cases when coolant is injected both from tip holes and pressure side holes. For tip injection cases, it was found that as blowing ratio increases, film effectiveness changed slightly for both plane and recessed tip blade. Also, at highest blowing ratio, lift-off of jets is observed for both blade tips. Injection of coolant from pressure side holes was found to be less effective than tip injection. It appears to be good for plane tip in reducing heat load along the pressure side. But no film effectiveness is observed for the recessed tip case. Combined cooling was found to be the best among the three cases. For this case, a high value of film effectiveness is observed for most of the blade tip. It is observed that local blowing ratio is an important parameter to understand flow behavior and, particularly for plane tip, local blowing ratios are much more different than global blowing ratios.

For tip injection cases, it was found that as blowing ratio increases, heat transfer coefficient decreases for both plane and recessed tip blade. Also, at highest blowing ratio, lift-off of jets is observed for both blade tips. Injection of coolant from pressure side holes was found to be less effective than tip injection. It appears to be good for plane tip in reducing heat load along the pressure side. At highest blowing ratio, $M=3$, very high values of heat transfer coefficient are observed. It appears that for this high blowing ratio, coolant jet from the tip hits the shroud first and then bounces back onto the blade tip. It is observed that local blowing ratio is an important parameter to understand flow behavior and, particularly for plane tip, local blowing ratios are much more different than global blowing ratios. Overall, high blowing ratios produce high heat flux ratios resulting in increased heat transfer on the tip surface for squealer tips.

Overall, it appears that the pressure side injection reduces leakage flow into the tip gap and helps improve protection of the tip surface with the tip injection. However, pressure side injection may also protect the pressure side edge of the tip surface which is prone to erosion. This study did not have any results on the pressure side and suction side edges. For recessed tips, pressure side injection may also help protect the rim of the squealer cavity.

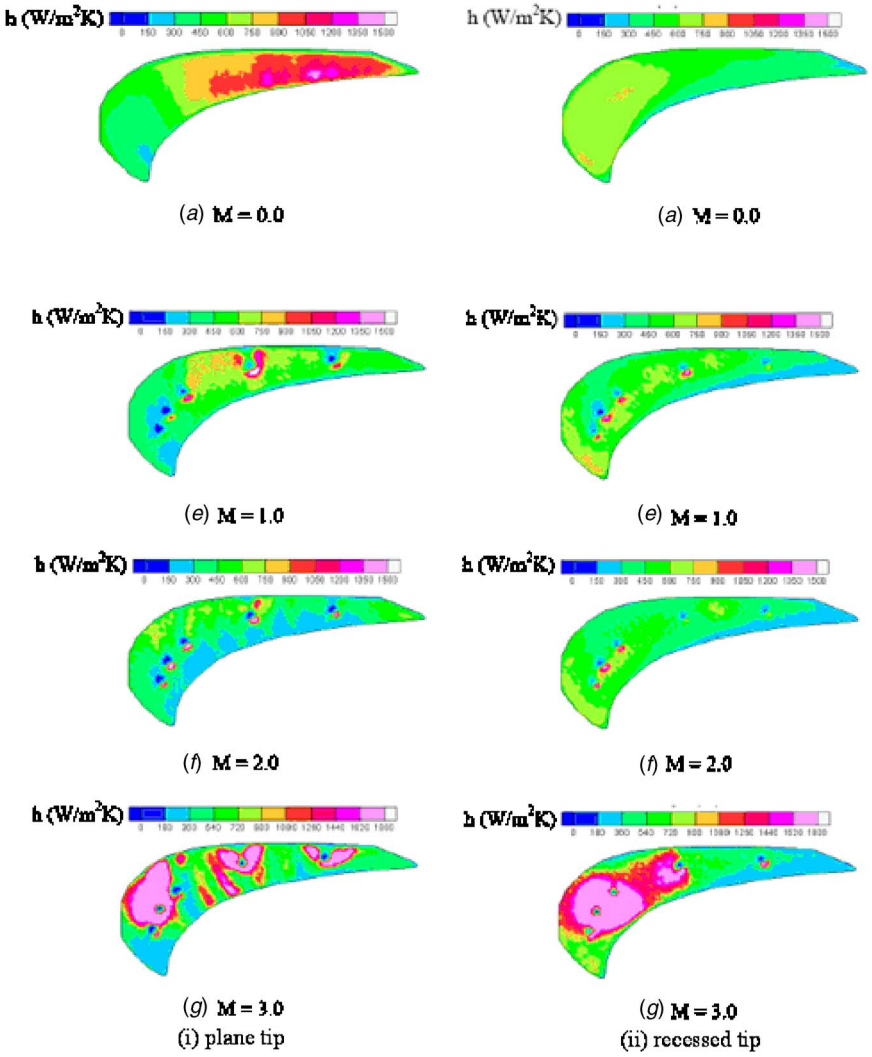

Fig. 15 Detailed heat transfer coefficient distributions with combined injection

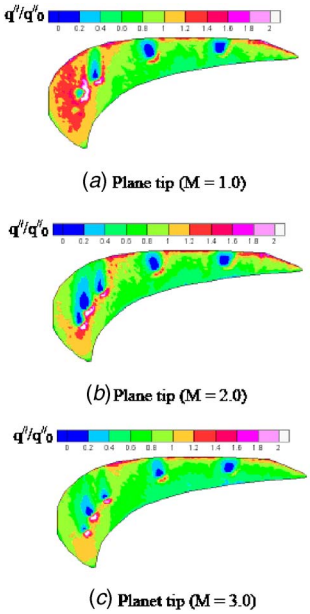

Fig. 16 Detailed heat flux ratio distributions for plane and squealer tips with tip injection only

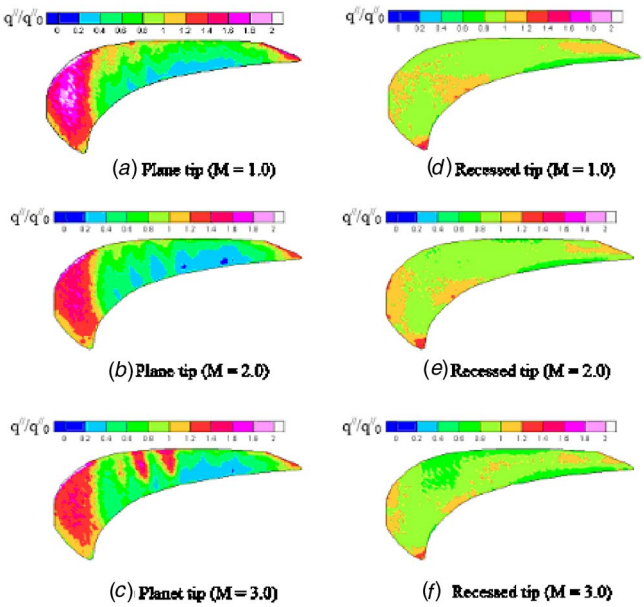

Fig. 17 Detailed heat flux ratio distributions for plane and squealer tips with pressure side injection only

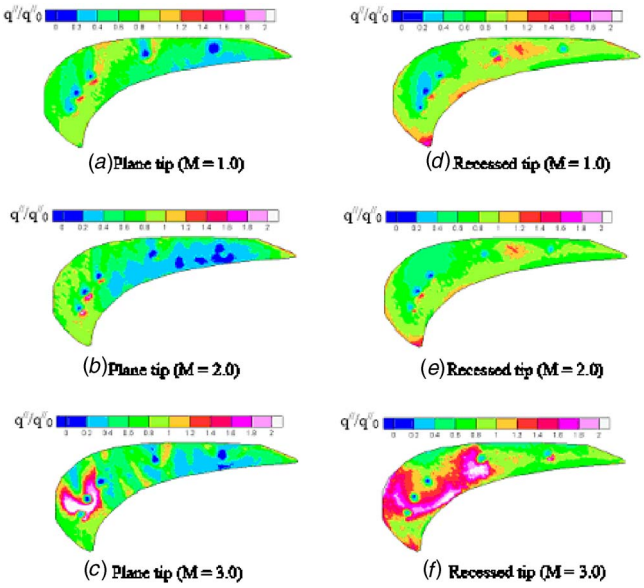

Fig. 18 Detailed heat flux ratio distributions for plane and squealer tips with combined tip and pressure side injection

Acknowledgment

This work was supported through a grant from NSF under the GOALI program. Acknowledgment is due to the program managers Dr. A. Emery, Dr. S. Thynell, and Dr. R. Smith. Acknowledgment is also due to the industrial partners, General Electric Co., for their support of the project and to Dr. Huitao Yang, Ryan Hebert, and Eric Esposito for their help during this work.

Nomenclature

C = axial chord length of the blade
d = diameter of film cooling hole
D = recess depth
H = height of test blade
h = heat transfer coefficient with film injection
h_0 = heat transfer coefficient without holes
k = thermal conductivity of Plexiglas test surface
L = pressure side or suction side length
M = blowing ratio, $\rho_c U_c / \rho_m U_m$
$\dot{m}$ = mass flow rate
PR = pressure ratio
P_m = static pressure of mainstream
P_s = static pressure
P_t = total pressure
Re = free stream Reynolds number, $\rho UC/\mu$
S = blade spacing
t = time of color change or the time when the IR image was taken after the test was initiated.
T_c = coolant temperature
T_f = film temperature
T_i = initial temperature
T_m = mainstream temperature
T_w = measured wall temperature
Tu = free stream turbulence
U_c = coolant velocity
U_m = mainstream velocity
x = axial distance

Greek Symbols

α = thermal diffusivity of Plexiglas material
γ = specific heat ratio
ρ = density of air
η = film effectiveness, $\eta = T_m - T_f / T_m - T_c$
φ = overall cooling effectiveness, $\varphi = T_m - T_w / T_m - T_c$
μ = viscosity of air

References

[1] Nasir, H., Ekkad, S. V., Kontrovitz, D., Bunker, R. S., and Prakash, C., 2003, "Effect of Tip Gap and Squealer Geometry on Detailed Heat Transfer Measurements over a HPT Rotor Blade Tip," ASME Paper No. IMECE2003–41294.

[2] Kim, Y. W., Downs, J. P., Soechting, F. O., Abdel-Messeh, W., Steuber, G. D., and Tanrikut, S., 1995, "A Summary of the Cooled Turbine Blade Tip Heat Transfer and Film Effectiveness Investigations Performed by Dr. D. E. Metzger," ASME J. Turbomach., **117**, pp. 1–10.

[3] Kwak, J. S., and Han, J. C., 2002, "Heat Transfer Coefficient and Film-Cooling Effectiveness on a Gas Turbine Blade Tip," ASME Paper No. GT-2002-30194.

[4] Hohlfeld, E. M., Christophel, J. R., Couch, E. L., and Thole, K. A., 2003, "Predictions of Cooling From Dirt Purge Holes Along the Tip of the Turbine Blade," ASME Paper No. GT2003-38251.

[5] Ahn, J., Mhetras, S., and Han, J. C., 2004, "Film-Cooling Effectiveness on a Gas Turbine Blade Tip Using Pressure Sensitive Paint," ASME Paper No. GT2004-53249.

[6] Christophel, J. R., Thole, K. A., and Cunha, F. J., 2004, "Cooling the Tip of a Turbine Blade Using Pressure Side Holes. Part 1: Adiabatic Effectiveness Measurements," ASME Paper No. GT2004-53251.

[7] Christophel, J. R., Thole, K. A., and Cunha, F. J., 2004, "Cooling the Tip of a Turbine Blade Using Pressure Side Holes—Part 2: Heat Transfer Measurements," ASME Paper No. GT2004-53254.

[8] Polanka, M. D., Clark, J. P., White, A. L., Meininger, M., and Praisner, T. J., 2003, "Turbine Tip and Shroud Heat Transfer and Loading—Part II: Comparisons Between Prediction and Experiment Including Unsteady Effects," ASME Paper No. GT-2003-38916.

[9] Yang, H., Chen, H. C., and Han, J. C., 2004, "Numerical Prediction of Film Cooling and Heat Transfer With Different Film-Hole Arrangements on the Plane and Squealer Tip of a Gas Turbine Blade," ASME Paper No. GT2004-53199.

[10] Vedula, R. J., and Metzger, D. E., 1991, "A Method for the Simultaneous Determination of Local Effectiveness and Heat Transfer Distributions in Three Temperature Convective Situations," ASME Paper No. GT-345.

[11] Ekkad, S. V., Du, H., and Han, J. C., 1998, "Detailed Film Cooling Measurements on a Cylindrical Leading Edge Model: Effect of Free-Stream Turbulence and Density Ratio," ASME J. Turbomach., **120**, pp. 779–807.

[12] Du, H., Han, J. C., and Ekkad, S. V., 1998, "Effect of Unsteady Wake on Detailed Heat Transfer Coefficient and Film Effectiveness Distributions for a Gas Turbine Blade," ASME J. Turbomach., **120**, pp. 799–807.

[13] Ekkad, S. V., Ou, S., and Rivir, R. B., 2004, "A Transient Infrared Thermography Method for Simultaneous Film Cooling Effectiveness and Heat Transfer Coefficient Measurements From a Single Test," ASME J. Turbomach., **126**. pp. 546–553.

[14] Nasir, H., Ekkad, S. V., Bunker, R. S., and Prakash, C., 2004, "Effects of Tip Gap Film Injection From Plain and Squealer Blade Tips," ASME Paper No. GT2004-53455.

[15] Ekkad, S. V., and Han, J. C., 2000, "A Transient Liquid Crystal Thermography Technique for Gas Turbine Heat Transfer Measurements," Meas. Sci. Technol., Special Edition on Gas Turbine Measurements, Vol. **11**, pp. 957–968.

[16] Kline, S. J., and McClintock, F. A., 1953, "Describing Uncertainties in Single Sample Experiments," Mech. Eng. (Am. Soc. Mech. Eng.), **75**, pp. 3–8.

[17] Gritsch, M., Schulz, A., and Witting, S., 1998, "Discharge Coefficient Measurements of Film-Cooling Holes With Expanded Exits," ASME J. Turbomach., **120**, pp. 557–563.

[18] Mehendale, A. B., Han, J. C., Ou, S., and Lee, C.-P., 1994, "Unsteady Wake Over a Linear Turbine Blade Cascade With Air and CO_2 Film Injection, Part II: Effect on Film Effectiveness and Heat Transfer Distributions," ASME J. Turbomach., **116**, pp. 730–737.

Making Use of Labyrinth Interaction Flow

A. Pfau

A. I. Kalfas

R. S. Abhari

Turbomachinery Laboratory,
Swiss Federal Institute of Technology,
8092 Zurich, Switzerland

It is the aim of this publication to attract the designers attention to the end wall flow interactions of shrouded high pressure turbines. One of the key issues for designing better turbines is the understanding of the flow interactions set up by the presence of labyrinth seals. Those interaction flows are carefully examined in this publication using the control volume analysis and the radial equilibrium of forces acting on streamlines. The consequences on secondary flow development and mixing losses are discussed and quantified. Out of this insight, design recommendations are derived, which attempt to make use of the nature of the labyrinth interaction flow. The open labyrinth cavities are classified in a systematic way. The aim of this approach is to work out the characteristic differences between hub and tip cavities and those having a leakage jet or sucking main flow fluid into the labyrinth. The influence on the main flow is discussed in terms of the incidence flow angle of downstream blade rows and the associated loss production mechanisms. The design strategies presented in this paper follow two paths: (a) Optimization of the mixing losses of the leakage jets at hub and tip is estimated to result in an efficiency increase of up to 0.2%. (b) The nonaxisymmetric shaping of the labyrinth interaction flow path aims at the secondary flow control in downstream blade rows. This approach might contribute in the same magnitude of order as reduction in the mixing losses.
[DOI: 10.1115/1.2218571]

Introduction

Labyrinth leakage flow in shrouded turbines is looked upon as an inherently detrimental effect and something which the designer cannot avoid. One design recommendation is to minimize the leakage flow through designing better labyrinth seals and to reduce the gap widths as much as possible. If heat transfer is an issue as in a gas turbine the gap must allow enough leakage mass flow in order to cool the turbine shrouds. The inlet to a labyrinth and the exit including the leakage jet alter the flow field in turbine end wall regions. This is of special significance in low aspect ratio turbine stages where secondary flows are strong. The labyrinth seal can be optimized for itself including mechanical limits and through flow coefficients.

The subject of cavity interactions in turbines was initially addressed by Denton and Johnson [1]. However, it is only in recent years that this subject attracted the attention of the turbomachinery research community. Peters et al. [2] examined the effect of gap size on the steady interaction between the leakage flow and the secondary flow field of a subsequent stator in a 1.5 stage, shrouded axial turbine. Hunter and Manwaring [3] reported about two extra vortices generated in a downstream stator blade row. Wallis et al. [4] observed that strong interactions are present in open cavities of shrouded turbine blades. The following blade rows were found to receive the tip flow at a negative incidence. Cao et al. [5] report about an unsteady, incompressible flow phenomenon affecting the interaction between the rim seal and main annulus flows and not being related to the blade passing frequency. Anker and Mayer [6] numerically investigated the leakage interaction with the main flow and found that the tip leakage flow is not uniform in the pitch-wise direction. Schlienger et al. [7] changed the geometry of the labyrinth exit cavities by introducing inserts and compared the effects on the main flow as well as on the efficiency. These studies have focused mainly on the interaction occurring in the main flow and following blade passages.

Contributed by the International Gas Turbine Institute (IGTI) of ASME for publication in the JOURNAL OF TURBOMACHINERY. Manuscript received October 1, 2003; final manuscript received March 1, 2004. IGTI Review Chair: A. J. Strazisar. Paper presented at the International Gas Turbine and Aeroengine Congress and Exhibition, Vienna, Austria, June 13–17, 2004, Paper No. 2004-GT-53797.

However, as the origins of these interactions are open cavities, an increased emphasis should be placed on the associated steady and unsteady flow interactions within these cavities. From these considerations the question arises: Is there any potential in improving the overall performance of low aspect ratio, shrouded turbines by looking at the combined system of main flow duct and labyrinth seal? In that respect, the present publication attempts to conclusively summarize and complete the work which already has been published in [8,9]. It is the aim of this publication to give an overview of labyrinth interaction effects occurring in shrouded turbines with large inlet and exit cavities. Additionally, all open cavities are treated in a systematic way and effects on the main flow are discussed and quantified. Based on the detailed flow understanding, which was experimentally gained in a two stage, shrouded, low speed turbine, new design features are derived for a range of open cavities. With this step, design modifications are proposed, which actually make use of the labyrinth interaction flows.

Test Rig, Measurement Technology, and Data Set

The cavity interaction flow was investigated in the two-stage low speed axial turbine "LISA." The test rig is described in detail in Sell et al. [10]. The main characteristics of the turbine are summarized in Table 1.

The constant annulus of the turbine and the four blade rows are depicted in Fig. 1. The stepped shrouds on the blades together with three sealing fins form the labyrinth seal. The geometry under investigation is similar to steam turbine applications, where large inlet and exit cavities allow for axial displacement of the rotor shaft due to thermal expansion of the rotor. Consequently, the blade profiles are of a medium loaded type with 50% reaction and leaned stator blades. The cylindrical coordinate system used in this publication is indicated in Fig. 1. The results are presented looking upstream as the observer indicates. The cavities are numbered for an easier identification in later discussions.

The measurement technology applied was a miniature five-hole probe of 0.9 mm head diameter and a virtual four sensor probe of 0.84 mm head diameter. The accuracy of the five-hole probe readings is discussed in detail in [11]. The corresponding error bars are

Table 1 Main characteristics of the test turbine

Pressure ratio	1.32	Mass flow	9.86 kg/s
Max power	400 kW	Turbine speed	2700 rpm
T_{inlet}	40°C	p_{exit}	Ambient
Mach	0.1–0.4	Re_{Cax}	10^5
n (rotor/stator)	42	Tip diameter	800 mm
Blade passing	1890 Hz	Blade aspect ratio	1.8

given in the diagrams. In [12] the virtual four sensor probe is described in detail. The advantages of this measurement technology are:

(1) Very small head, minimizing blockage.
(2) Three-dimensional flow vector.
(3) Unsteady total and static pressure field.
(4) Temporal resolution of the flow field up to 25 kHz.

The results gained with the five-hole probe are considered to be the time averaged picture. A comparison to the virtual four sensor probe showed that this is a justifiable assumption ([12]).

A seal gap variation was performed covering two aspects:

(a) The first gap variation of 1% blade height is close to the range found in real applications and a realistic flow field in terms of leakage jet strength and mixing can be expected.
(b) As a second case, a smaller gap width of 0.3% blade height was chosen to investigate the pure main flow to cavity interaction in a more controlled approach.

The experiments were performed at a rotational speed of 2700 rpm and a mass flow of 9.86 kg/s. In real steam turbines the fluid dynamic conditions are $Re=3\times10^6$ and $M=0.3$ with a suction peak velocity of around $M=0.8$. Therefore, compressibility as well as viscous effects are not fully modeled in this turbine. However, as the velocity triangles and reduced frequencies match to an actual stage, unsteady effects like vortex or potential field interactions are comparable.

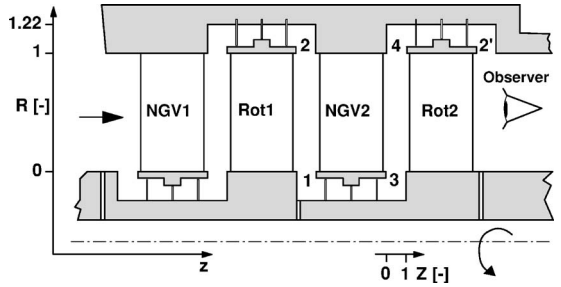

Fig. 1 Meridional cut of the test section

Table 2 Number of axial measurement planes: 1+*1*, 1 plane time averaged, *1* plane time resolved

Cavity	1	2	3	4	2′
1% gap	⋯	1+*1*	1+*0*	1+*1*	1+*1*
0.3% gap	⋯	1+*1*	1+*1*	6+5	1+*1*

In Table 2 the number of axial measurement planes in each cavity measured with the five-hole probe (time averaged) and measured with the virtual four sensor probe (time resolved) are listed. Most cavities are resolved with one measurement plane containing roughly 350 measurement points. The single plane was positioned in mid-axial gap position ($Z=0.5$). Cavity 4 was resolved with six time averaged and five time resolved measurement planes in the 0.3% gap case having an average spacing of $\Delta Z=0.15$.

Experimental Results and Discussion

Cavity 2 (Outlet, Tip)

Pitch-Wise Mass Averaged Results. First, a short comparison between the velocity fields of the 0.3% and 1% gap case of the seal gap variation is given in Fig. 2. The diagram shows the pitch-wise mass averaged tangential and axial velocity components. The black bars indicate the errors of the five-hole probe measurement chain. The error bars vary with radial height, since the error depends on the flow angle and the Mach number. For the 0.3% gap case the influence of the leakage jet onto the flow field at this location is negligible. The weak jet mixes out quickly downstream of the last seal and is not detected in the velocity profiles. In contrast, the leakage jet in the 1% gap case alters considerably the flow field due to its stronger mass and momentum flux. The leakage fluid can be localized in a radial band from $R=1.03$ to $R=1.07$. For further investigations in this section the authors concentrate on the 1% gap case, where mixing and interaction flows are more realistic than in the 0.3% gap case.

Rotor Relative, Time Averaged Results. The unsteady data sets taken in cavity 2 are postprocessed to the time-averaged picture in the relative frame of reference. The static pressure (3), the relative Mach number (4), and the radial velocity component (5) were chosen for display and discussion. The arrows indicate the sense of rotation of the relative coordinate system. The curved dashed line indicates the tip radius of the turbine blades. The shroud trailing edge reaches from $R=1$ to $R=1.06$. The discussions of the results within this section happen in the relative frame, if not

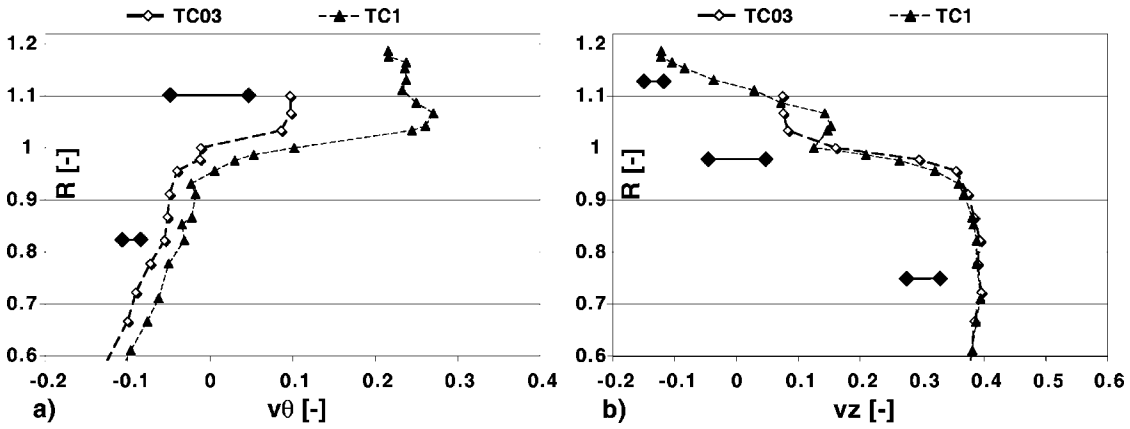

Fig. 2 Pitch-wise mass averaged velocity profiles, cavity 2, $Z=0.5$: (*a*) tangential, (*b*) axial

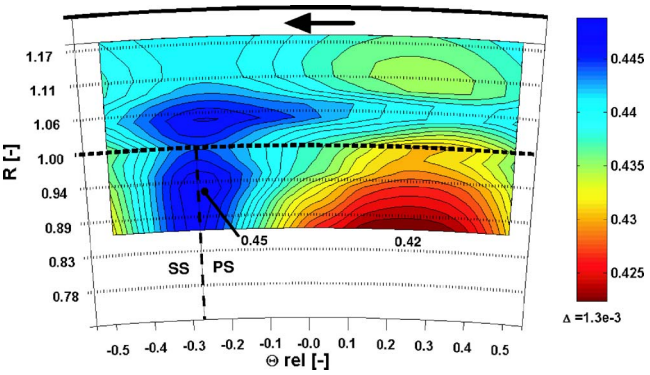

Fig. 3 Nondimensional static pressure C_{p_s} time averaged, rotor relative frame, $Z=0.5$

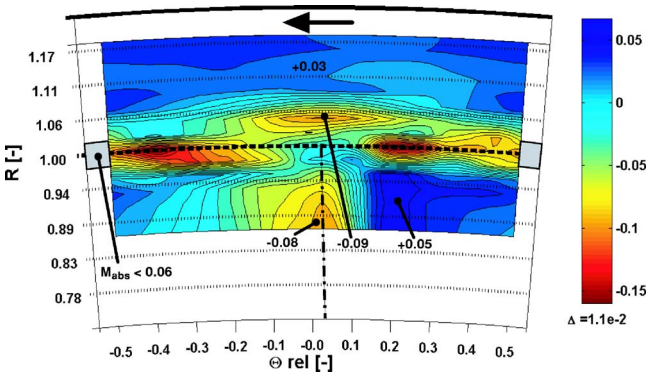

Fig. 5 Nondimensional radial velocity component, time averaged, rotor relative frame, $Z=0.5$

stated otherwise.

The static pressure distribution (Fig. 3) reveals the trailing edge position of the rotor blade at $\Theta_{rel}=-0.3$ (dashed line), where a high static pressure is induced. The circumferential pressure variation from high to low pressure at $\Theta_{rel}=0.3$ in the main flow region is also seen in the cavity. A stripe of higher static pressure at the radial position of the leakage jet ($R=1.06$) is found. The circumferential variation at $R=1.06$ is such that a low pressure region occurs at $\Theta_{rel}=0.38$. In addition, the level of static pressure within the cavity is on average $\Delta Cp_s=0.01$ higher than in the main flow. The circumferential static pressure distribution is imposed onto the cavity flow by the blade to blade pressure field.

The M_{rel} distribution (Fig. 4) shows the rotor wake at $\Theta_{rel}=0.05$ (dash-dotted line). The wake is convected into tangential direction by $\Delta\Theta_{rel}=0.35$ from the location of the trailing edge. On the pressure side of the wake, a higher M_{rel} is detected than on the suction side. Assuming a constant relative total pressure of the rotor exit flow, this effect is induced by the static pressure field.

Closer to the tip radius the wake becomes wider. A band of lower M_{rel} is found between $R=1.03$ and $R=1.07$, which corresponds to the leakage jet position observed in Fig. 2. In a region having its center at $\Theta_{rel}=0.2$ and $R=1.05$, M_{rel} reaches a local minimum of 0.24. The relative total pressure in the cavity is set up by the leakage jet and distributed such that the local minimum in velocity is found on the pressure side of the rotor wake. For this circumferential distribution of the leakage fluid two reasons can be provided: first, the momentum and kinetic energy distribution of the leakage jet at the exit of the last seal and, second, the static pressure field set up by the flow field in the main annulus including the trailing edge pressure field.

Discussing the radial velocity component given in Fig. 5, additional details of the leakage interaction are found. The rotor wake is indicated with the dashed line. The regions of large negative radial velocities $v_r=-0.15$ (red) are not considered for discussion. The reason for this is the fact that the error in the results for the virtual four sensor probe rapidly rises for absolute Mach numbers lower than 0.06. The gray shaded symbols at $R=1$ indicate a band of radial positions where the absolute Mach number falls from 0.1 to below 0.06. This deficit of absolute velocity corresponds to the wake of the shroud. The radial velocity is negative within the region of the leakage jet ($R=1.06$) having a minimum radial velocity of $v_r=-0.09$ at the circumferential position of the wake. This value is of the same order of magnitude as the radial velocity within the wake itself ($v_r=-0.08$). The leakage fluid moves out of the cavity mainly below the wake position, filling up the area of lower relative kinetic energy of the wake.

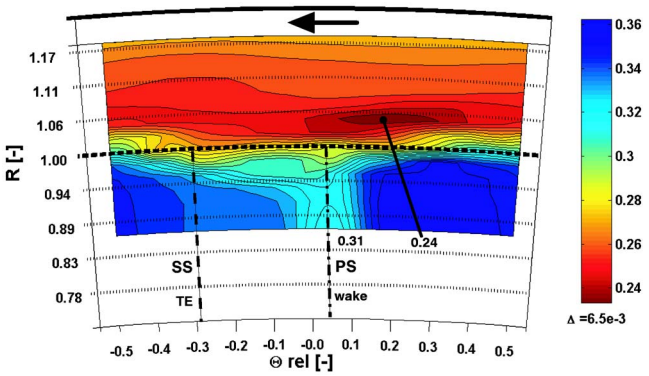

Fig. 4 Relative Mach number M_{rel}, time averaged, rotor relative frame; $Z=0.5$

Leakage to Main Flow Interaction. The basic components of the leakage jet to main flow interaction found in the 1% gap case in cavity 2 comprise three points:

(1) Leakage fluid migrates into the rotor wake causing the leakage streamlines to contract into the wake area. The radial migration of the leakage fluid leads to a broadening of the wake in the vicinity of the blade tip. The wake seems to attract low kinetic energy fluid.
(2) The potential field of the rotor trailing edge divides the leakage sheet into distinct jets. Figure 6(*a*) shows the time averaged relative velocity triangles within the relative frame of reference for the first rotor exit flow field (cavity 2). It represents the velocity vectors found with two cuts in 4, one at $R=0.91$ and the other at $R=1.06$. The upper vectors represent the leakage jet ($R=1.06$) and the lower one the main flow at $R=0.91$. Note that the base of the velocity vector is representing the location of the circumferential coordinate. The arrow represents 100% of the shroud rim speed. The circles point out the base of velocity vectors, which are facing the trailing edge position of the rotor $\Theta_{rel}=-0.25$. The leakage mass flow is redistributed from a homogeneous distribution within the last gap. A maximum of leakage mass flow is found in the mid position between the trailing edges where it forms a distinct jet (see the dotted ellipse). The main flow is much less affected by the trailing edge pressure field than the leakage jet. The main flow vectors reveal the wake of the rotor blade.
(3) The potential field of the stator leading edge three-dimensionally redistributes the flow field in the absolute frame of reference. This effect is visualized in Fig. 6(*b*), which presents the circumferential distribution of the absolute velocity triangles in the stator frame of reference for the 1% gap case. The diagram depicts the velocity vectors of the leakage fluid in the upper part and the velocity vectors of the main flow at $R=0.9$ in the lower part. The ve-

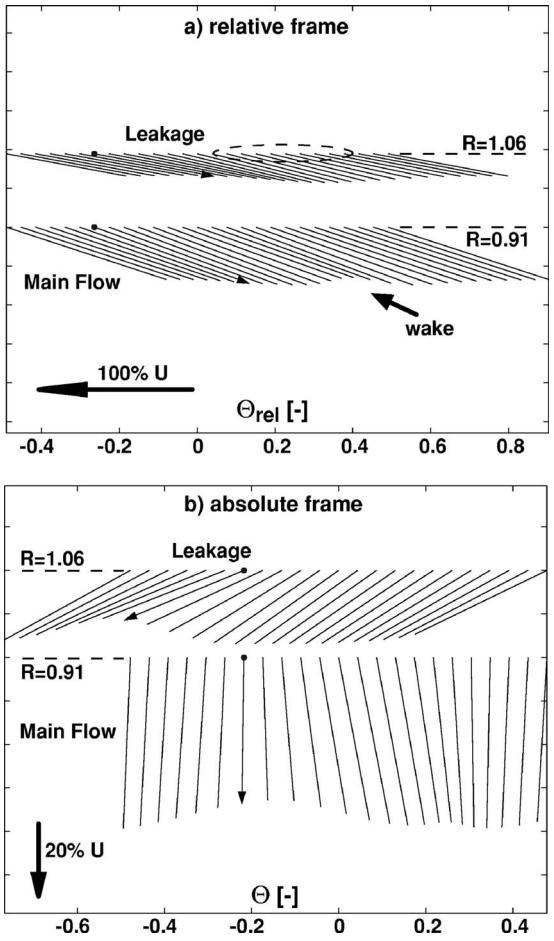

Fig. 6 Time averaged velocity triangles, cavity 2: (*a*) relative frame, (*b*) absolute frame

locity arrow represents 20% of the shroud rotational speed. The leading edge position of the stator is obvious in the downstream flow field of the first rotor (cavity 2), where it causes a deviation of streamlines. The circles point out the base of velocity vectors, which are facing the leading edge position of the stator at $\Theta_{rel}=-0.22$. Downstream of the second rotor (cavity 2′) this effect is not present and the velocity vectors of the leakage jet are constant around the circumference (not shown in a diagram).

These observations are brought together in a descriptive flow model given in Fig. 7(*a*). The arrows indicate the rotor passage vortex, the radial migration within the wake, and the tangential redistribution of the leakage mass flow (red) due to the rotor trailing edge pressure field. The gray shaded area corresponds to the higher leakage mass flow and the blue ellipse marks the area of the radial movement of the leakage fluid out of the cavity into the wake.

Mixing Calculation. At this stage of investigation it is of interest to know the losses generated by the leakage jet mixing with the main flow. Since the mixing is a three-dimensional process, the authors propose a two-step mixing approach in order to capture pitch-periodic effects. From the experimental results, it is known that the radial movement of the leakage fluid (Fig. 5) out of the cavity occurs prior to the full mixing of the two streams. In this radial movement different flow qualities do interfere due to the fact that the flow is nonaxisymmetric (wake, leakage mass distribution). Therefore, the mixing process is modeled in two steps as indicated in Figs. 7(*b*)–7(*d*):

(1) The idealized flow field shown in Fig. 7(*b*) is describing the situation depicted in Fig. 7(*a*). Two areas represent the leakage and main flow each having its proper tangential variation in velocity triangles. The first mixing step is performed under constant area for each of the 20 circumferential sections of the blade pitch (Figs. 7(*b*) and 7(*c*)).
(2) The second step is performed mixing all 20 stripes to the final mixed out situation (Figs. 7(*c*) and 7(*d*)).

The boundary conditions for this mixing calculation are given in Table 3. The inner radius of the mixing domain R_i was set to 0.72 such that the loss core of the stator is covered. This implies that the mixing of the leakage jet with the main flow will be restricted to the end wall region rather than mixing with fluid at the hub. The outer radius R_o was adjusted to the leakage to main mass flow ratio. From the measurement with FRAP probes one

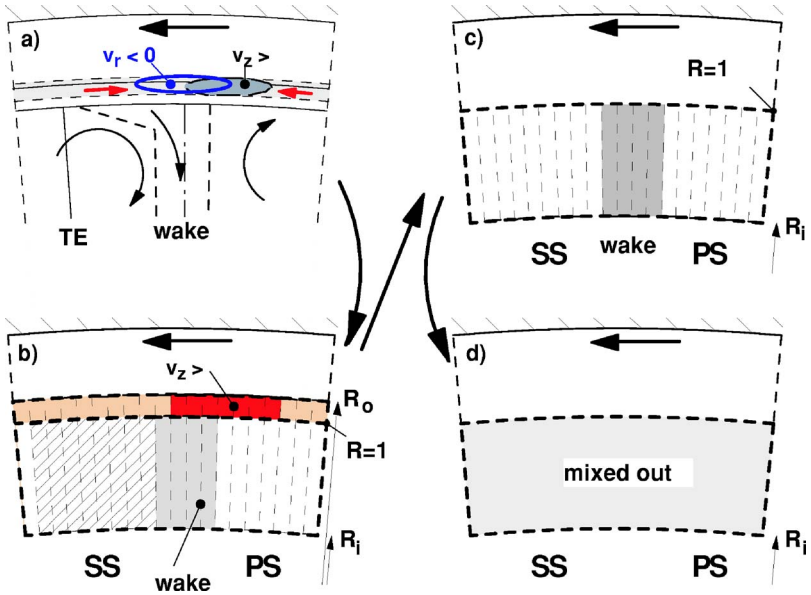

Fig. 7 (*a*) Rotor relative descriptive flow model, (*b*)–(*d*) two-step mixing calculation of leakage and main flow

Table 3 Boundary conditions for mixing calculation

R_0-R [-]	T^v_{rel} [°C]	p [kPa]	$\dot{m}_L/\dot{m}$ [%]
0.028	Jet: 34.7 Main: 33.3	11.0	1.39

also gains the time averaged total temperature of main and cavity flow. The leakage jet was found to have a 1.4°C higher relative total temperature than the main flow.

The mixing losses are expressed in terms of entropy rise as calculated with the entropy equation

$$\Delta s = c_p \ln \frac{\overline{T_0}}{T_2} - R \ln \frac{\overline{p_0}}{p_2} \tag{1}$$

The indices refer to the stagnation values of temperature and pressure at the inlet and exit of the stage. The values of entropy are nondimensionalized using the stage losses as derived from the performance measurements (see Table 4). The mixing of the leakage jet downstream of the first stage generated 6.7% of the stage losses, where on average 22% of the loss is contributed by the mixing of different total temperature streams.

Cavity 3 (Outlet, Hub). In Fig. 8 the pitch-wise mass averaged results are presented and a comparison of the 0.3% and 1% gap case is given. The velocity components are made nondimensional with the rotor hub speed. The total pressure of the cavity flow depends strongly on the gap width. A larger gap decreases the total pressure which is in conjunction with a lower tangential velocity component. A reason for this could be that the higher leakage mass flow in the 1% gap case has not fully adjusted to the circumferential speed of the rotor hub cavities. In the 0.3% gap case the tangential velocity in the cavity is much closer to the hub velocity. The axial velocity component (Fig. 8(*b*)) shows a mass deficit around $R=0.05$ in the 1% gap case and a higher axial velocity at $R=-0.08$. The first is caused by the higher mass flow being sucked into the inlet cavity, the latter is due to the stronger leakage mass flow. The point of zero through flow $v_z=0$ is located at $R=-0.12$.

Surprisingly, the radial velocity components (Fig. 8(*d*)) show mostly negative values. The radial migration of flow under the radial static pressure gradient is one explanation for the main flow region. However, the leakage mass flow was expected to show on average positive radial velocity components since the leakage mass flow has to leave the cavity at some point. In the circumferential mass averaged diagram this seems to happen further downstream, e.g., at $Z=0.8$. A stronger outflow between $Z=0.8$ and 1 would also explain the difference in radial velocity component at $R=0.05$ between the two gap cases. The main flow streamlines at this point ($Z=0.5$, $R=0.05$) would see a greater blockage at the rotor hub, causing the streamlines to bend into the main flow again ($\Delta v_r>0$).

The velocity triangles of the leakage ($R=-0.08$) and the main flow ($R=0.2$) for both gaps are compared in Fig. 9. From this, the rotor hub region can expect a negative incidence around $\Delta\beta=-70$ deg. This large value might decrease, if the leakage flow passes the exit corner of the cavity, where the fluid is accelerated and deviated into stream-wise direction.

Figure 10 presents the total pressure and the radial velocity component distribution at $Z=0.5$ of the 1% gap case. The thick dashed line represents the hub radius of the blades. The thin

Table 4 Mixing losses of cavity 2, contribution of temperature term to entropy generation

	P_{mix} [% stage loss]	$\Delta S_T/\Delta S$ [%]
1% gap	6.7	22

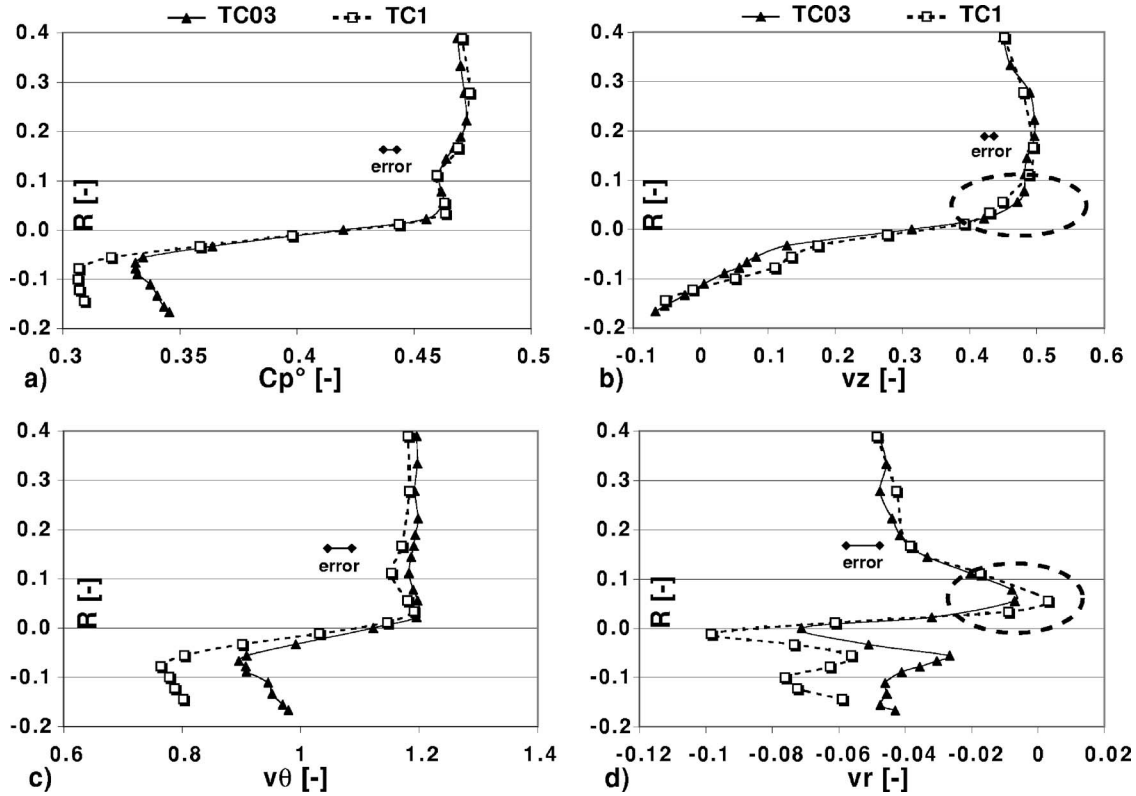

Fig. 8 Pitch-wise mass-averaged, $Z=0.5$: (*a*) total pressure, (*b*) axial, (*c*) tangential, (*d*) radial velocity components

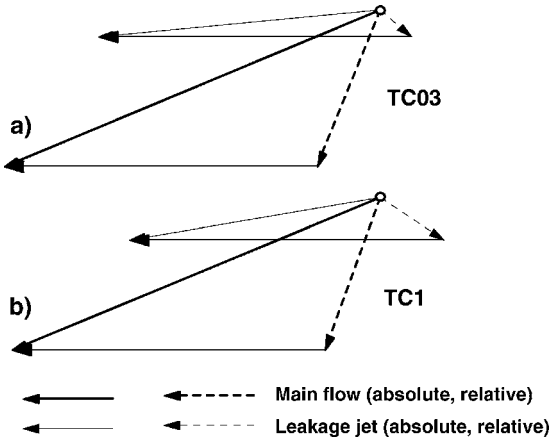

Fig. 9 Pitch-wise mass-averaged velocity triangles, Z=0.5: (*a*) 0.3% gap, (*b*) 1% gap

dashed lines are indicating the stator trailing edges which also go along with a high static pressure region. The dash dotted line highlights the position of the wake. The loss core is small since the incoming boundary layer is sucked away at the hub inlet cavity. The wavy flow structure between the main and the cavity flow is showing a distinct inflow jet on the pressure side of the wake similar to what was found for cavity 4 in [9]. Below the wake position (Θ=0.25) the radial velocity becomes positive. This is also the region where most of the leakage flow will leave the cavity further downstream.

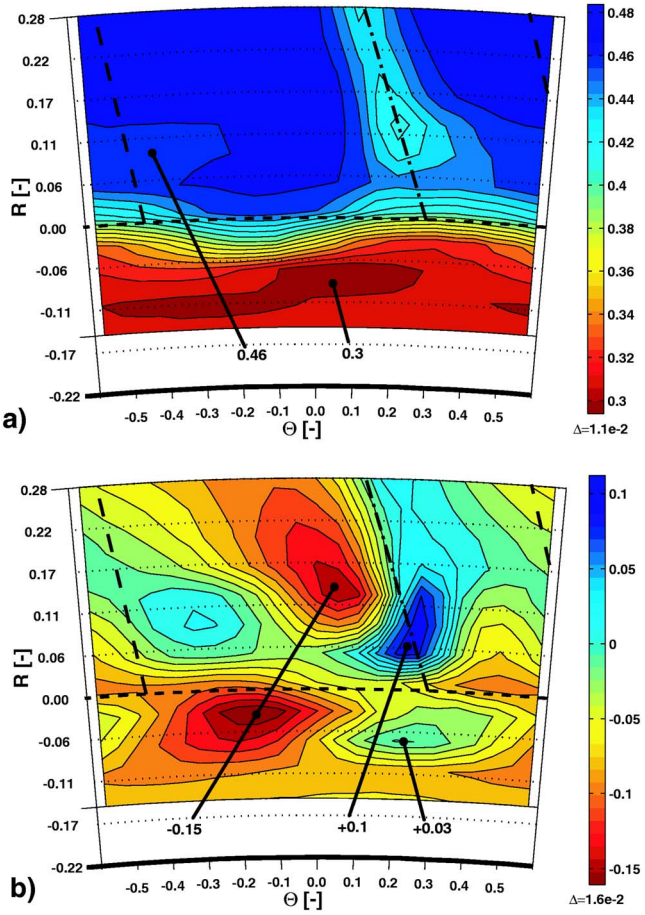

Fig. 10 Downstream stator 2, 1% gap case, Z=0.5: (*a*) total pressure, (*b*) radial velocity component

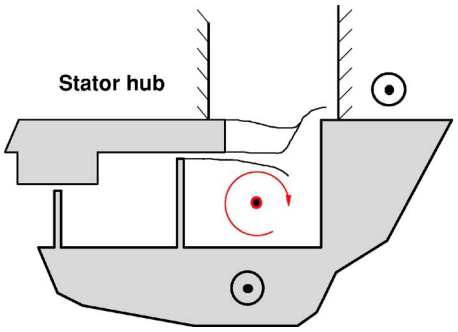

Fig. 11 Flow model for cavity 3

From these observations a short descriptive flow model can be given for this cavity (Fig. 11). The thin lines indicate dividing stream lines. The static pressure field set up by the high swirl and the stator trailing edges is expanding into the cavity. This has two consequences:

(1) The leakage flow is rather pushed into the cavity rolling up into a toroidal vortex, than moving out of the cavity immediately at Z=0.1. The outflow happens further downstream around Z=0.9.
(2) The three-dimensional pressure field redistributes the leakage mass flow such that most of it will leave the cavity at a certain circumferential position relative to the stator leading edge. Due to the convection of the wake into tangential direction both locations (wake and outflow) might coincide (e.g., at Θ=0).

Cavity 4 (Inlet, Tip). In an earlier publication, Pfau et al. [9] described the vortical flow structure in the inlet cavity (cavity 4) as in- and outflows set up by the stator flow field. A toroidal vortex was observed moving at high tangential velocity (83% of rotor speed). This toroidal vortex was discovered to be subject to unsteady vortex stretching. In this publication further details and quantification of the flow are presented.

Results on the Interface Surface. The interface surface between the cavity and the main flow is defined as a cylindrical surface with R=1. In the absolute frame of reference the radial velocity distribution shows the location of in- and outflows set up by the stator flow field as presented in Fig. 12(*a*). At the axial position Z=0.5 a comparison between the two gap cases is given in Fig.

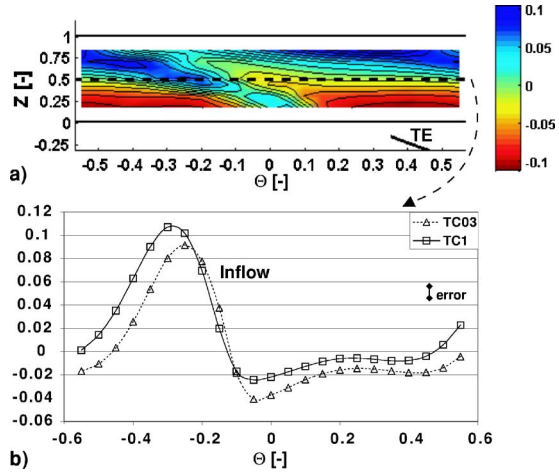

Fig. 12 Radial velocity component, absolute frame: (*a*) interface surface, R=1, 0.3% gap, (*b*) Z=0.5, 0.3% and 1% gap

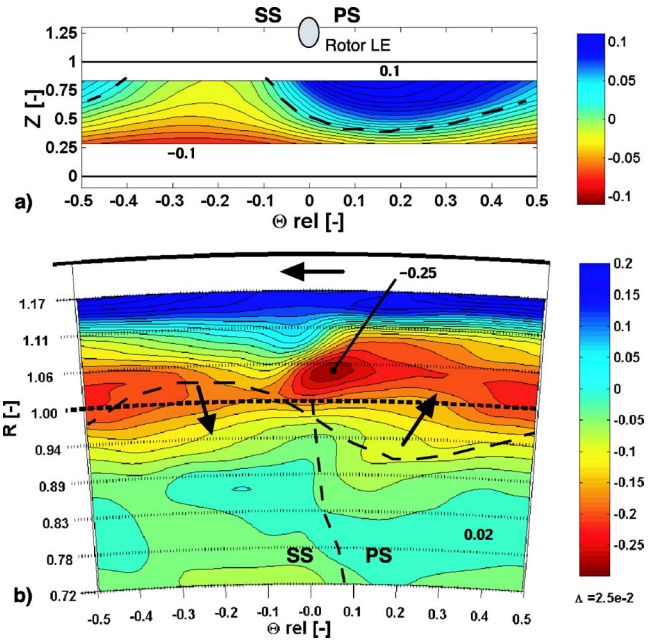

Fig. 13 Relative frame: (*a*) Radial velocity component, 0.3% gap, $R=1$, (*b*) relative stream-wise vorticity, $Z=0.83$

12(*b*). The shape of the circumferential distribution of the radial velocity component is the same, but the level is shifted according to the bigger leakage mass flow being sucked into the cavity for the 1% gap case. The inflow region with positive radial velocity component is obvious. The corresponding fluid stems from the pressure side corner of the stator passage, as described in [9].

Within the relative frame the radial velocity distribution given in Fig. 13(*a*) shows the upstream effect of the rotor passage. The isoline of zero radial velocity is indicated with a dashed line. On the pressure side of the rotor passage fluid is pushed into the cavity, while it is sucked out on the suction side. This interaction process is an additional contributor to the torque balance of the cavity, which will be discussed in the following section. Furthermore, it alters the inflow condition to the rotor end wall region considerably. For the discussion of this effect Fig. 13(*b*) shows the relative stream-wise vorticity distribution time averaged in the rotor relative frame of reference. The dashed line indicates the zero radial velocity isoline. The arrows indicate that negative stream-wise vorticity is sucked into the rotor passage on the suction side. This fluid has the same rotational direction as the rotor passage vortex which develops further downstream in the passage.

Mass and Momentum Exchange

Time averaged (absolute frame). The mass and momentum exchange due to the interaction of the main flow with the open inlet cavity is investigated using the control volume as shown in Fig. 14(*a*) and an integration tool. The integration tool uses linear interpolation within the measurement grid. Each time step is evaluated in a quasisteady way. Nonslip conditions at the stationary and rotating walls are applied. The region between the nearest measurement point to the point on the wall is linearly interpolated. The integration can be performed on surfaces of constant radii, constant axial, or circumferential position. In circumferential direction, pitch-periodic conditions are assumed. The boundary conditions on the inlet and exit axial plane $Z=0$ and $Z=1$ are set to the measurement values of the closest measurement plane.

The outer surface at $R=1$ represents the interface between main and cavity flow. The inner surface was chosen to $R=0.91$. At this radial location the area integration of constant radius delivers a net radial mass flow of approximately 0. For $R>0.91$ this integration

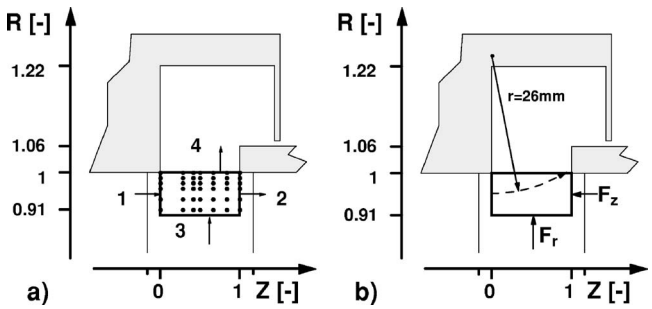

Fig. 14 Control volume for mass and momentum integration: (*a*) measurement grid, (*b*) external forces on control volume F_r, F_z; radius of average streamline curvature

becomes positive, for $R<0.91$ negative. Therefore, $R=0.91$ is interpreted as a dividing stream surface: Below $R=0.91$, the negative radial migration of the main flow dominates, above $R=0.91$ the flow field is affected by sucking mass into the cavity.

The results of the integration are given in Table 5 representing the full annulus. Fluxes out of the control volume are counted positive and external forces on the control volume are calculated. In tangential direction the momentum flux is expressed as torque.

Considering first the sum of mass flows and fluxes in the last row of Table 5, continuity is preserved within 11 g/s, which is 0.1% of the main mass flow. The sum of the momentum fluxes is positive in radial and negative in axial direction. Sucking mass flow into the cavity reduces the axial momentum in the end wall region, since some of the incoming axial momentum is transformed into radial momentum. In tangential direction, the sum is close to 0, since no external forces act in this direction. The components of the external force acting on the control volume are depicted in Fig. 14(*b*).

The mass flow passing through the control volume amounts to 6% of the main mass flow. The assumption $\dot{m}_3=0$ is met to within 0.02% of the main mass flow. The net mass flow at surface 4 compares well to the leakage mass flow, which was evaluated to 37 g/s. Associated to the inflow into the cavity at surface 4 is the transport of a torque of 1.8 Nm.

The local radial pressure gradient across this control volume is not sufficient to keep the flow on a constant radius. Streamlines from the stator pressure side corner enter the cavity. This effect arises from the presence of a sudden area increase due to the cavity and from the sucking of the leakage mass flow. The radial equilibrium of forces acting on a circular motion is given by

$$v_z \frac{\partial v_z}{\partial z} \sin\gamma + \frac{v_z^2}{r_z} \cos\gamma - \frac{v_\Theta^2}{r} = -\frac{1}{\rho}\frac{\partial p}{\partial r} + \frac{F_r}{\rho V} \qquad (2)$$

where r_z denotes the radius of the streamline in the meridian plane. The first term describes the radial acceleration along the streamline. The second term is the radial component of the centripetal acceleration due to the meridian curvature. The third term on the left-hand side represents the centripetal acceleration directed radially inward due to the main swirling flow. These three terms are balanced by the radial pressure gradient and the radial

Table 5 Control volume integration according to Fig. 14(*a*): mass flow and momentum fluxes on the full annulus

Surface i	$\dot{m}_i$ [g/s]	F_{ir} [N]	T_i [Nm]	F_{iz} [N]
1 (in)	606	0.5	−24.2	−17.1
2 (out)	−562	1.8	22.3	14.2
3 (in)	2	0.4	−0.2	−0.2
4 (out)	−35	0.4	1.8	0.6
Sum	11	3.1	−0.3	−2.4

Table 6 Mass and momentum fluxes across surface 4, absolute frame

Surface i	$\dot{m}_i$ [g/s]	F_{ir} [N]	T_i [Nm]	F_{iz} [N]
4 (in, $v_r>0$)	127	0.9	5.1	1.5
4 (out, $v_r<0$)	−92	−0.5	−3.3	−0.9
Sum	35	0.4	1.8	0.6

Table 7 Mass and momentum fluxes across surface 4, rotor relative

Surface i	$\dot{m}_i$ [g/s]	F_{ir} [N]	T_i [Nm]	F_{iz} [N]
4 (in, $v_r>0$)	148	1.6	1.1	1.4
4 (out, $v_r<0$)	−110	−0.6	−1.3	−0.9
Sum	38	1.0	−0.2	0.5

external force. In this case, Eq. (2) can be simplified with the help of the experimentally based assumption that the pitch angle of the initial streamlines in surface 1 of Fig. 14(*a*) is approximately zero which leads to

$$\frac{v_z^2}{r_z}\frac{v_\Theta^2}{r} = -\frac{1}{\rho}\frac{\partial p}{\partial r} + \frac{F_r}{\rho V_{CV}} \tag{3}$$

The unknown in this equation is r_z. All other terms can be derived out of the measurement volume. The second term on the left-hand side is evaluated in taking the arithmetic average of all values within the control volume according to

$$\frac{v_\Theta^2}{r} = \frac{\overline{v_{\Theta ijk}^2}}{r_{ijk}} \tag{4}$$

A representative radial pressure gradient is found in taking the pressure difference of each opposing pair of grid points, which lay on surfaces 3 and 4. These local pressure differences are arithmetically averaged. The external radial force is taken from Table 5. An average v_z on surface 1 can be given to 19% of shroud rim speed. From this approach a representative streamline with an average meridian radius of $r_z=26$ mm is calculated. The streamline is included in Fig. 14(*b*) as a dotted circular arc starting at mid-radial height of surface 1 with an assumed pitch angle $\gamma=0$. The inflow of surface 1 connects well to the area around $Z=0.8$ of surface 4, where most of the inflow to the cavity happens (see also Fig. 12(*a*)).

The axial component of the external force F_z (Table 5) is the result of a static pressure increase across the cavity. To verify this assumption a pressure force integration was performed taking the measured static pressure at surfaces 1 and 2. The force calculated with the pressure difference becomes −2.6 N, which compares well to the control volume integration. Across the cavity opening a positive axial pressure gradient is observed. The same procedure applied to the main flow region ($R<0.91$) results in a negative axial pressure gradient as expected.

Additional insight could be gained by observing the quantities associated to the in- and outflows across surface 4, which are summarized in Table 6. As much as four times of the leakage mass flow enters the cavity and convects up to 5 Nm of torque, 0.9 N of radial momentum flux, and 1.5 N of axial momentum flux. The outflow of roughly three times the leakage mass flow conveys less momentum in all three components. However, the major contribution to the radial and axial momentum balance of the control volume are found in surfaces 1 and 2.

Time averaged (rotor relative frame). The associated fluxes to the in- and outflow generated by the rotor pressure field are discussed in this section. To do so, the surface integration of surface 4 in Fig. 14 was performed in the relative frame of reference. The radial velocity distribution of this surface is presented in Fig. 13(*a*). In comparison to Fig. 12(*a*), the results are restricted to five axial positions, which reduces the area covered by experimental results. The integration results are shown in Table 7. The mass flow integration compares well to the results in Table 6 because the time averaged radial velocity components were adjusted to the five-hole probe results. The radial component of momentum fluxes is larger than in the stator relative flow field. The axial component of the momentum fluxes compares well to the results in the absolute frame of reference. The important result here is that the rotor in time average extracts torque from the cavity, since the sum of in- and outflows is negative.

Systematic Classification of Open Cavities

Characteristics of Open Cavities. There are three characteristics in which the open cavities differ (see also Table 8):

(I) The strength of the radial pressure gradient at the interface surface due to the swirling main flow: Downstream of the stator the swirl angle is constantly high inducing a much stronger radial pressure gradient ($dCp_s/dR=0.02$) than downstream of the rotor ($dCp_s/dR=0.004$). The exit flow of the rotor depends on the power extraction in which the stage is working. In the case of medium loaded stages the exit swirl of the rotor is small.

(II) The location at hub or tip: Radial pressure gradients are pointing either out of the cavity as is the case at the tip or pointing into the cavity as at the hub. Low kinetic energy fluid migrates on lower radii according to the pressure gradient than fluid of higher kinetic energy. Therefore, the leakage fluid in cavity 3 under the influence of the radial pressure gradient set up in the main flow region moves closer to the hub with negative radial velocity, thus forming the toroidal vortex there. The center of the vortex is found at $R=-0.12$. At the tip, the low kinetic energy fluid within the cavity is sucked out of the cavity, such that the center of the toroidal vortex in cavity 4 moves toward lower radii ($R=1.06$) and the vortical flow is observed at the interface surface ($R=1$).

(III) The leakage jet: The leakage jet in the exit cavities adds fluxes of axial and tangential momentum to the cavity flow. In addition, the mixing of the jet is a loss production mechanism. The leakage mass flow does no work to the rotor. This causes a higher total temperature of the leakage flow than the main flow downstream of the rotor. Downstream of the stator the total temperature of both fluxes is the same. Within the inlet cavities no jet is present, but end wall fluid is sucked into the labyrinth seal. Thus, the inlet cavity acts as a sink of axial and tangential momentum.

Table 8 Characteristics of open cavities in turbines

No.	Swirl I	Position II	Jet III	Incidence a)	Loss production b)
1	−	Hub	−	$\Delta\alpha=0$ deg sucking	Sucking of BL at hub, smaller hub loss core and secondary flows in rotor passage
2		Tip	$T_j^o>T_m^o$	$\Delta\alpha=-30$ deg	Mixing of the jet with cavity and main flow Jet increases. BL-thickness
3	++	Hub	$T_j^o=T_m^o$	$\Delta\beta=-70$ deg	Mixing of the jet with cavity and main flow Secondary flow development in rotor passage
4	++	Tip	−	$\Delta\beta=-7$ deg sucking	Vortex stretching, wall friction in cavity Secondary flow development in rotor

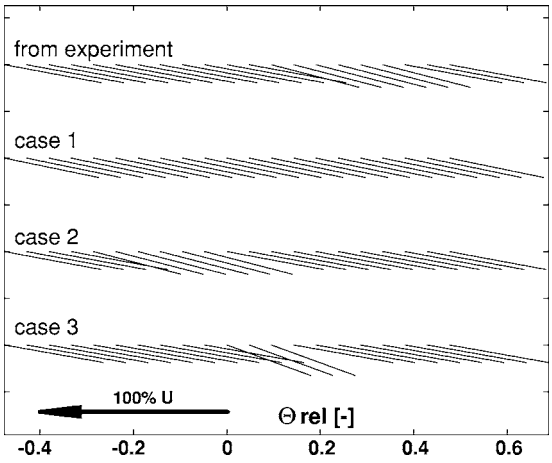

Fig. 15 Rotor relative descriptive flow model and two-step mixing calculation of leakage and main flow

Influence on Main Flow and Performance. Each of the open cavities differs in their influence on the main flow and the performance of the machine. The effects discussed here are the change of incidence and the loss production mechanisms induced by the corresponding cavity (Table 8).

(a) Incidence angle to the end wall regions of downstream blade rows: The leakage jet in cavities 2 and 3 causes a negative incidence due to the mismatch of the velocity triangles. At the inlet to the downstream blade row the incidence angles at the end wall regions are of the order of −30 deg and −70 deg. Cavity 4 induces negative incidence via sucking of circumferential momentum. Evaluating the flow with the help of a control volume analysis and further modeling the flow predicts an incidence angle of −7 deg for the 1% gap case. Cavity 1 is estimated to induce no incidence since the exit flow of the rotor, which is sucked into the hub labyrinth, has no circumferential momentum.

(b) Loss production mechanisms: Sucking of boundary layer fluid at cavity 1 can be beneficial, since a thinner boundary layer enters the stator hub and thus less secondary flow is generated. In cavity 4 the effect of sucking may be less beneficial since the cavity is pressure loaded and interaction mass flows of up to four times the leakage mass flow do leave the cavity again. These interaction outflows then enter into the rotor tip region enhancing the secondary flow development with a sheet of positive streamwise vorticity at the suction side of the rotor passage (see Fig. 13(*b*)). In addition cavity 4 contributes to the loss production via vortex stretching and enhanced wall friction due to the toroidal vortex system. In cavities 2 and 3 the leakage jet mixes with the cavity and main flow in addition to generating strong negative incidences to the downstream blade rows.

Design Proposals

In this section the gained flow understanding is used to propose design changes and to quantify a beneficial effect if possible.

Cavity 2. The approach for cavity 2 is to optimize the leakage mixing process. As reported in the previous section, 6.7% of the stage losses are attributable to the mixing. In a further step of investigation the mixing calculation model was used to investigate three cases of leakage mass distribution. The cases are visualized in Fig. 15. The upper distribution of velocity vectors belongs to the experimentally found situation.

Case 1: Homogeneous distribution of velocity vectors.

Case 2: Mirrored at $\Theta_{rel}=0$.

Case 3: Most of the leakage mass flow into the rotor wake.

By varying the leakage vector distribution the leakage mass flow as well as the momentum fluxes were kept constant. From this approach, an improvement of 0.1% in efficiency is predicted

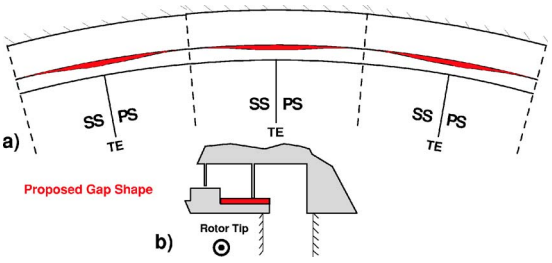

Fig. 16 Nonaxisymmetric shroud design in cavity 2: (*a*) upstream view of the last sealing gap, (*b*) side view

for cases 1 and 3 in comparison to the experiment. Case 2 does not show improvements. In case 1, downstream blade rows receive a more homogeneous inflow, which is in accordance to Dawes' comment about design goals in end wall regions [13]. Case 3 seems to be beneficial, since feeding the leakage flow into the wake reduces nonuniformity in the main flow and therefore reduces the mixing contribution in step 2 of the mixing model. Despite the rough assumptions applied to the mixing model, the results do indicate possible improvements.

In order to achieve a leakage jet distribution similar to case 3, a design modification for a nonaxisymmetric shroud contour is proposed, as shown in Fig. 16. The gap variation around the circumference varies between completely closed at mid-pitch and open at the rotor trailing edge position. The gap area is kept the same as in the 1% gap case. The leakage mass flow passing through the seal gap below the trailing edge will end up mixing with the rotor wake, when the leakage fluid leaves the cavity. Thus the leakage flow is used to reduce nonuniformities in the end wall region of the turbine.

The design of the nonaxisymmetric gap depends on the re-entry behavior of the leakage flow. A simple model is proposed to describe the circumferential position of the maximum gap relative to the rotor trailing edge ($\Delta\Theta_{relG}$) as depicted in Fig. 17. The model uses three parameters:

(1) The characteristic length scale of the problem is the axial gap width of the exit cavity z_{cav}.
(2) The average relative flow angle of the leakage flow from last seal gap to the re-entry into main flow β_L.
(3) The relative flow angle of the main flow at the rotor tip β_T.

In addition, the designer has to define the location along the convective path of the wake, where it is desirable to let the leakage flow interact with the wake (wake window). These parameters combine to the nondimensional circumferential position of the maximum gap of

$$\Theta_{relG} = \frac{z_{cav}}{p}(\tan\beta_T - 1.3\tan\beta_L) \tag{5}$$

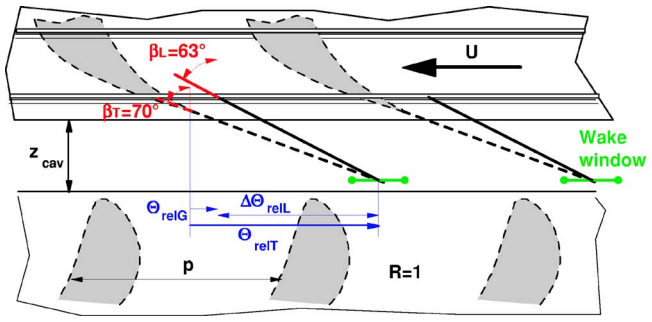

Fig. 17 Simple model for shroud design

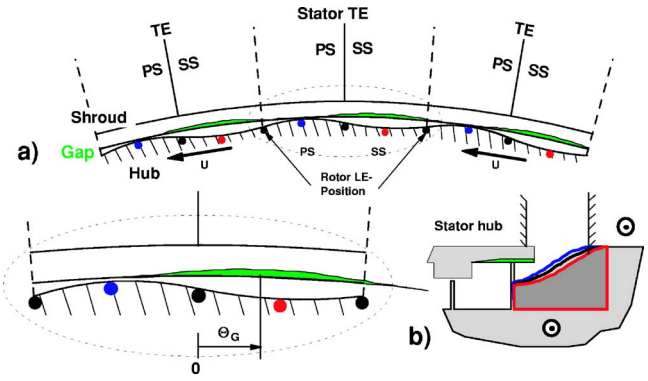

Fig. 18 Nonaxisymmetric shroud and cavity design, cavity 3: (*a*) upstream view, *Z*=0.5, (*b*) side view with nonaxisymmetric insert

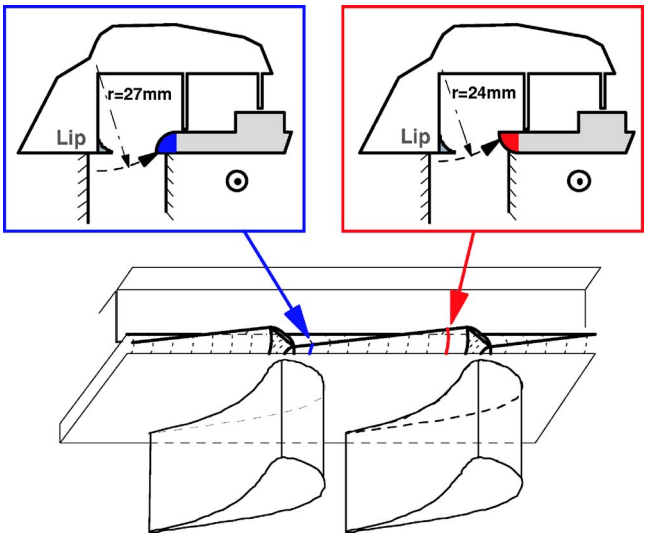

Fig. 19 Shroud leading edge design for reduced rotor passage to cavity flow interaction

The local blade pitch is denoted with p. The factor 1.3 describes the geometric fact of this configuration, that the leakage jet starts at a more upstream axial position than the wake (seal gap position versus trailing edge position). For this test case and cavity the position for the maximum gap results in $\Theta_{relG}=0.05$, which is very close to the trailing edge position.

Cavity 3. In cavity 3, the same principal as described above for cavity 2 can be applied. Thus a more uniform flow distribution would be generated at the inlet to the rotor hub and the leakage mixing losses would be reduced. As reported in [7], inserts into the exit cavities were investigated preventing the toroidal vortex to develop and guiding the leakage flow back into the main flow. The upstream effect of the rotor passage onto the leakage flow and distribution on the incoming vorticity field has been shown in the experimental results for cavity 4. In order to control the mixing and the re-entry of the leakage flow at the hub the authors propose to extend the idea of nonaxisymmetric end wall contouring as described, e.g., in [14] or in [15] into the exit cavity and combine it with the nonaxisymmetric design of the shroud trailing edge and last seal gap. The resulting design is depicted in Fig. 18. The gap shape is highlighted in green. The maximum gap is shifted to the suction side of the stator passage. Thus the leakage flow can be expected to reenter into the main duct at the circumferential position of the stator wake.

Using the approach presented for cavity 2, an equation for the hub exit cavity can be given

$$\Theta_G = \frac{z_{cav}}{p}(1.3 \tan \alpha_L - \tan \alpha_H) \tag{6}$$

Taking an average flow angle of the leakage fluid of $\alpha_L=75$ deg and the swirl angle at the hub $\alpha_H=67.5$ deg, this results in a circumferential position of the maximum gap of $\Theta_G=0.8$, relative to the stator trailing edge position. The underlying assumption is that the average flow angle of the leakage α_L remains the same with the inserts. The beneficial effect will be of the same order as in cavity 2, i.e., around 0.1% absolute turbine efficiency.

The nonaxisymmetric insert is designed such that the leakage flow is guided into the rotor passage in a favorable way. The design shifts the incoming leakage fluid onto the suction side of the rotor passage. This aims at two effects:

(1) The leakage fluid is found on the suction side, thus the secondary flow development in the passage due to the movement of the low kinetic energy fluid in the cross passage pressure gradient is reduced. Wall shear stresses at the end wall due to the development of a new boundary layer could be reduced.
(2) The distribution of the leakage fluid to the suction side reduces the likelihood of a separation bubble at the pressure side of the rotor leading edge due to the strong negative incidence of the leakage flow. Instead of leakage fluid, a thin boundary layer of main flow fluid is hitting the rotor leading edge at the correct angle of attack.

Cavity 4. The inlet cavity to the rotor tip labyrinth seal is subject to large in- and outflows as described in detail in [9]. Three approaches will be discussed, which are considered to be favorable in terms of loss production and reduction of unsteady interaction and secondary flows.

(1) Nonaxisymmetric end wall contouring in the stator passage is a promising tool to reduce secondary losses as reported in [16]. This approach has the potential to reduce the inflow and outflow due to the end wall curvature. Applied to the inlet cavity this would mean that the end wall on the pressure side would have to be convex. The induced static pressure drop would provide the fluid in the pressure side corner with additional kinetic energy. Thus the fluid particles tend to penetrate less into the cavity. The same target can be followed by introducing a local lean to the stator trailing edge, which would cause a local load increase. The pressure side corner fluid then would experience an additional radial force due to the imposed local static pressure gradient. A larger radius of streamline curvature is resulting from this and less amount of fluid is penetrating into the cavity.

(2) The lip on the stator side of the cavity, as depicted in Fig. 19, is designed to reduce the circumferential wake as found in [9] and to turn the fluid at the edge of the toroidal vortex into axial direction. The static pressure gradients originating from the stator trailing edge and acting on the interaction zone are reduced due to the potential field decay.

(3) The shroud leading edge depicted in Fig. 19 is designed to reduce the interaction flow across the cavity-to-main flow interface. One expected effect would be that the radial velocity distribution as presented in Fig. 13(*a*) is more homogeneous and the peak radial velocities are reduced. On the pressure side of the rotor passage the shroud leading edge is positioned at a higher radius than on the suction side. The effect of this is that streamlines of a lower curvature are entering on the pressure side. Less fluid is pushed into the cavity at this point. On the suction side, the cavity fluid has to reach lower radii in order to be sucked into the rotor passage. In terms of streamline curvature, more fluid is pushed into the cavity at the suction side than on the pressure side.

The design modification described above with the help of Fig. 19 can be inverted, i.e., it is the goal to enhance the interaction flow such that the inlet stream-wise vorticity distribution as found

in Fig. 13(*b*) would show a higher value at the suction side to the rotor tip inlet. Consequently, the rotor passage vortex would increase its strength and change position. At first glance, this might not be a beneficial effect. But considering a designer's need to increase the rotor tip passage vortex in order to compensate incoming or downstream vorticity of the opposite sign (vortex interaction), this might be the correct approach.

Conclusions

Detailed flow understanding is the key issue to further push the edge of the aerodynamic performance of state-of-the-art turbines. This paper presented a systematic investigation and description of the influence of large open cavities on the end wall flow region of shrouded axial turbines. This is of particular interest to low aspect ratio, high pressure stages, where secondary flows are significant. From the flow understanding design modifications have been deduced. Based on the quantitative prediction of the beneficial effect for one design modification, an optimum design suggests a potential of 0.2%–0.5% on the overall turbine efficiency. This gain can be made through applying and optimizing all the above-described design modifications. The basic idea is to introduce a new degree of freedom into the shroud and cavity design: the nonaxisymmetric shape. These modifications make use of the nature of the labyrinth interaction flows. Secondary flow development in downstream blade rows can be actively changed and the leakage fluid can be actively distributed. Secondary flow development within the blade rows as well as mixing losses should be optimized with the leakage flow development aiming at better turbine efficiency.

Acknowledgment

The flow measurements in the turbine were supported by the German Federal Ministry of Economy (BMWI) under File Nos. 0327060D and 0327060F. The authors gratefully acknowledge AG Turbo, Alstom Power, and Rolls-Royce Germany for their support and permission to publish this paper.

Nomenclature

r, θ, z = cylindrical coordinate system
g = radial gap width in % of blade height
h = blade height, 90 mm
z_{cav} = axial cavity width, 15 mm
n = numbers of blades, 42
f_{blade} = blade passing frequency
M = Mach number
p, p^0 = static, total pressure
p = local blade pitch, $2\pi r/42$
P = mixing loss in % of stage loss
R = nondimensional radial height $r-r_{Hub}/r_{Tip}-r_{Hub}$
Re = Reynolds number
s = specific entropy
T = blade passing period $1/f_{blade}$
T, T^0 = static, total temperature
U = local blade speed
V = volume
Z = nondimensional axial distance z/z_{cav}
v = nondimensional velocity u_{loc}/U
C_p = nondimensional pressure
$C_p=p_{local}-p_{stat,out}/p_{total,in}-p_{stat,out}$
α = absolute yaw angle
β = relative flow angle
γ = pitch angle
Ω = nondimensional vorticity $\omega/(4\pi f_{blade})$
Θ = nondimensional circumferential position θ/p

Indices

G = maximum gap position
H = hub
i = inner
L = leakage jet
o = outer
rel = relative system
r, θ, z = corresponding components in the coordinate system
T = tip
0,2 = inlet, exit condition of the turbine

Abbreviations

TC03 = 0.3% seal gap case ($g=0.3\%$)
TC1 = 1% gap case ($g=1\%$)
FRAP = fast response aerodynamic probe

References

[1] Denton, J. D., and Johnson, C. G., 1976, "An Experimental Study of the Tip Leakage Flow Around Shrouded Turbine Blades," CEGB Research Report No. CEGB-R/M/N848.
[2] Peters, P., Breisig, V., Giboni, A., Lerner, C., and Pfost, H., 2000, "The Influence of the Clearance of Shrouded Rotor Blades on the Development of the Flow Field and Losses in the Subsequent Stator," ASME Paper No. 2000-GT-478.
[3] Hunter, S. D., and Manwaring, S. R., 2000, "Endwall Cavity Flow Effects on Gaspath Aerodynamics in an Axial Flow Turbine. 1. Experimental and Numerical Investigation," ASME Paper No. 2000-GT-651.
[4] Wallis, A. M., Denton, J. D., and Demargne, A. A. J., 2001, "The Control of Shroud Leakage Flows to Reduce Aerodynamic Losses in a Low Aspect Ratio, Shrouded Axial Flow Turbine," J. Turbomach., **23**, pp. 334–341.
[5] Cao, C., Chew, J. W., Millington, P. R., and Hogg, S. I., 2003, "Interaction of Rim Seal and Annulus Flows in an Axial Flow Turbine," ASME Paper No. GT-2003-38368.
[6] Anker, J. E., and Mayer, J. F., 2002, "Simulation of the Interaction of Labyrinth Seal Leakage Flow and Main Flow in an Axial Turbine," ASME Paper No. GT2002-30348.
[7] Schlienger, J., Pfau, A., Kalfas, A. I., and Abhari, R. S., 2003, "Effects of Labyrinth Seal Variation on Multistage Axial Turbine Flow," ASME Paper No. GT2003-38128.
[8] Pfau, A., Treiber, M., Sell, M., and Gyarmathy, G., 2001, "Flow Interaction From the Exit Cavity of an Axial Turbine Blade Row Labyrinth Seal," J. Turbomach., **123**, pp. 342–352.
[9] Pfau, A., Schlienger, J., Rusch, D., Kalfas, A. I., and Abhari, R. S., 2003, "Unsteady Flow Interactions Within the Inlet Cavity of a Turbine Rotor Tip Labyrinth Seal," ASME Paper No. GT2003-38128.
[10] Sell, M., Schlienger, J., Pfau, A., Treiber, M., and Abhari, R. S., 2001, "The 2-Stage Axial Turbine Test Facility LISA," ASME Paper No. 2001-GT-492.
[11] Treiber, M., Kupferschmied, P., and Gyarmathy, G., 1998, "Analysis of the Error Propagation Arising From Measurements With a Miniature Pneumatic 5-Hole Probe," *Proceedings of the 13th Symposium on Measuring Techniques in Cascades and Turbomachines*, Limerick, Ireland.
[12] Pfau, A., Schlienger, J., Kalfas, A. I., and Abhari, R. S., 2003, "Unsteady, 3-Dimensional Flow Measurement Using a Miniature Virtual 4 Sensor Fast Response Aerodynamic Probe (FRAP)," ASME Paper No. GT2003-38128.
[13] Dawes, W. N., 1998, "Blade Row Interference Effects in Axial Turbomachinery Stages: Simulation of Unsteady Blade Row Interaction With CFD: Background," VKI Lecture Series, February 9–12.
[14] Gregory-Smith, D. G., Ingram, G., Jayaraman, P., Harvey, N. W., and Rose, M. G., 2001, "Non-Axisymmetric Turbine End Wall Profiling," Proc. Inst. Mech. Eng., Part A, **215**(A6), pp. 721–734.
[15] Havakechian, S., and Greim, R., 1999, "Aerodynamic Design of 50 Per Cent Reaction Steam Turbines," *Development of Turbomachinery Design*, J. Denton, ed., IMechE, Professional Engineering Publishing, London.
[16] Harvey, N. W., Brennan, G., Newman, D. A., and Rose, M. G., 2002. "Improving Turbine Efficiency Using Non-Axisymmetric End Walls: Validation in the Multi-Row Environment and With Low Aspect Ratio Blading," ASME Paper No. GT-2002–30337.

On a Novel Annular Sector Cascade Technique

T. Povey

T. V. Jones

M. L. G. Oldfield

Department of Engineering Science,
University of Oxford,
Parks Road,
Oxford OX1 3PJ, UK

An advanced technique for establishing pressure boundary conditions in annular sector cascade experiments has been developed. This novel technique represents an improvement over previous methods and provides the first means by which annular sector boundary conditions that are representative of those which develop in an annular cascade can be established with a high degree of satisfaction. The technique will enable cascade designers to exploit the obvious advantages of annular sector cascade testing: the reduced cost of both facility manufacture and facility operation and the use of engine parts in place of two-dimensional counterparts. By employing an annular sector of deswirl vanes downstream of the annular sector of test vanes, the radial pressure gradient established in the swirling flow downstream of the test vanes is not disturbed. The deswirl vane exit flow—which has zero swirl velocity—can be exhausted without unsteadiness, and without the risk of separation, into a plenum at constant pressure. The pressure ratio across the annular sector of test vanes can be tuned by adjusting the throat area at the deswirl vane exit plane. Flow conditioning systems which utilize the Oxford deswirl vane technology have previously been used to set pressure boundary conditions downstream of fully annular cascades in both model and engine scale (the Isentropic Light Piston Facility at Farnborough) experimental research facilities (Povey, T., Chana, K. S., Oldfield, M. L. G., Jones, T. V., and Owen, A. K., 2001, Proceedings of the ImechE Advances in Fluid Machinery Design Seminar, London, June 13; Povey, T., Chana, K. S., Jones, T. V., and Oldfield, M. L. G., 2003, Advances of CFD in Fluid Machinery Design, ImechE Professional Engineering, London, pp. 65–94). The deswirl vane is particularly suited to the control of highly whirling transonic flows. It has been demonstrated by direct comparison of aerodynamic measurements from fully annular and annular sector experiments that the use of a deswirl vane sector for flow conditioning at the exit of an annular sector cascade represents an attractive novel solution to the boundary condition problem. The annular sector technique is now described. [DOI: 10.1115/1.2372766]

Introduction

In the annular cascade experiment, the nature of secondary flow development depends upon both inlet and exit-flow conditions. Where a nozzle guide vane row is tested in isolation—in a stationary cascade—engine-representative pressure boundary conditions are often difficult to achieve. Radial pressure gradients, established in regions of swirling flow, affect the growth of secondary flows and, indeed, the spanwise velocity distribution at the vane exit plane. Several methods have been developed to establish the correct radial pressure gradient at the exit of annular cascade facilities, although many of these are somewhat unsatisfactory—a common problem is that of unsteady flow separation downstream of the test vane.

An alternative to annular cascade testing is the use of a fixed linear cascade of vanes, a technique that is attractive because testing is possible at lower mass flow rates—a smaller number of test vanes can be used at the same chord size. In the linear cascade, radial pressure gradients are not established, and secondary flows do not develop as they would in a working engine. This means that radial distributions of total pressure loss and whirl angle are unrepresentative of engine conditions. In addition, surface heat-transfer rate distributions, which are strongly influenced by the secondary flow structure, are nonrepresentative of engine conditions. An additional shortcoming is that only geometrically simplified (usually two dimensional) designs can be tested, whereas in annular cascade experiments the exact three-dimensional vane profiles, even engine parts, can be used. Another difficulty is that of establishing truly periodic inlet and exit-flow conditions, which, being established automatically in the annular facility, can be achieved in a linear cascade only when a very large number of vanes is used.

The sidewalls of the inflow and exit ducts of a linear cascade exert a strong influence on the streamline pattern within the cascade, and techniques such as variable wall suction and flexible sidewalls have been employed to *tune* the inlet and exit-flow conditions. Achieving even approximately periodic conditions is generally problematic, however. A very comprehensive review of advanced techniques applicable to both linear and annular cascade testing has been published by AGARD [1].

Annular sector cascade testing is a technique that combines the advantages of both the annular and linear cascade testing methods. Actual engine components can be tested, and the radial pressure gradients established in regions of swirling flow ensure secondary flows develop as they would in an operating engine. Model and testing costs for annular sector cascades are considerably lower than for their fully annular equivalents. Annular sector cascade testing is, however, relatively uncommon, as the designer is faced with the dual challenges of establishing vane-to-vane periodicity, and of maintaining the radial pressure gradient in the sector cascade exit flow. To date, these problems have not been satisfactorily resolved, and, consequently, the potential advantages of annular sector testing have so far not been fully enjoyed.

Annular Sector Facilities

Because the annular sector technique is little used, there is very little literature concerning the methods of designing and operating such facilities. Over the years, however, a few annular sector facilities have been developed, primarily for studies of cooling flow

Contributed by the International Gas Turbine Institute (IGTI) of ASME for publication in the JOURNAL OF TURBOMACHINERY. Manuscript received October 1, 2003; final manuscript received March 1, 2004. IGTI Review Chair: A. J. Strazisar. Paper presented at the International Gas Turbine and Aeroengine Congress and Exhibition, Vienna, Austria, June 13–17, 2004, Paper No. 2004-GT-53904.

effectiveness and for measurements of vane surface heat transfer coefficient. An early example is the NASA Lewis Research Centre Hot Section Facility [2], a 23 deg annular sector cascade in which engine components were used.

More recently, a high-pressure high-temperature annular sector facility was commissioned at ABB STAL—Sweden [3]. The initial configuration was a four-passage, 40 deg, annular sector of high-pressure nozzle guide vanes operated without film cooling. A large compressor unit was used, capable of delivering 10 kg s^{-1} at a pressure of 20 bar and a temperature of 200°C. The mainstream flow was heated in a combustion chamber—oil-fired burner—to temperatures of up to 800°C. The designers took considerable care in establishing engine-representative inlet boundary conditions, and, by introducing cooler air though the hub and the case platforms upstream of the test vanes, the radial temperature gradients that are present at the exit of a combustor were modeled. By using the technique of hot-wire anemometry, the freestream turbulence intensity was characterized—4–5%. The test vanes were instrumented with thermocouples. An infrared camera was also used to conduct temperature measurements. By operating the experiment in several different *modes*, it was possible to calculate the cooling effectiveness, and the internal and external heat transfer coefficients. A short exit duct with an abrupt expansion was used downstream of the test vanes.

An interesting annular sector study was conducted by Wiers and Fransson [4], who investigated the influence on cross-sector periodicity of various tailboard and diffuser geometries. The facility that was used for the study was a five-passage annular sector, with two—smaller—bypass channels. The facility could operate continuously, with air supplied by 1 MW compressor at up to 4.7 kg s^{-1} at a pressure of 4 bar. The inlet temperature could be varied between 30 and 180°C. An adjustable valve was used to set the downstream pressure. Very detailed measurements were conducted of the distributions of vane surface pressure, and end wall pressure. To quantify the degree to which periodicity had been achieved across the sector, measurements of the circumferential pressure distribution were conducted on the hub and case walls at axial distances from the trailing edge equal to 35% and 9% of the vane axial chord, respectively. Measurements were conducted only across the center two passages of the cascade. Tests were conducted with a diffuser with a 12 deg flare angle, with an abrupt expansion, and with various combinations of right-hand and left-hand tailboards. The diffusers were in both cases situated at axial distances equal to 190% of the axial chord downstream of the test vanes.

Interestingly, after extensive experimentation, the authors found that the best periodicity was obtained when the flow was allowed to exhaust as a free jet into the downstream plenum, with no flow conditioning whatsoever. For the two passages for which measurements were taken, the peak isentropic Mach numbers at hub were 0.87 and 0.84. The corresponding Mach numbers at the case were 0.81 and 0.80. The experiments demonstrate that reasonably periodic flow can be obtained across at least a limited part of an annular sector, by using the free-jet approach. The Wiers and Fransson [4] investigation is probably the most comprehensive aerodynamic survey in an annular sector to date.

At the Royal Institute of Technology in Sweden, an annular sector facility has been developed for studies of the aeroelastic behaviour of low-pressure rotor blades when subject to forcing [5]. To allow some control over the periodicity of the flow-field downstream of the (nine passage) annular sector of rotor blades, semi-flexible—polyurethane—sidewalls were employed. To mitigate the problems associated with exhausting swirling flow into a constant pressure plenum, a long exit duct was used.

A new technique of using an annular sector of half-impulse (see below) type deswirl vanes to condition the exit flow of an annular sector cascade has been developed. This has been shown to achieve excellent vane-to-vane periodicity for even a small number of test vane passages—five—while maintaining the radial

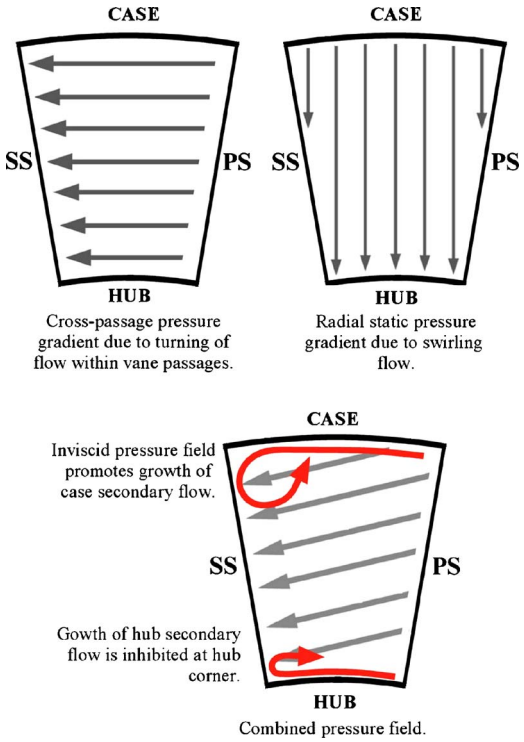

Fig. 1 Development of secondary flows in an annular cascade

pressure field established in the swirling flow downstream of the test vanes. In addition, the technique eliminates the need for an extended exit duct downstream of the test vanes: the flow can be exhausted without unsteadiness to a plenum at constant pressure.

Pressure Gradients and Secondary Flow Development

The radial pressure gradient established in regions of swirling flow contributes to the overall inviscid pressure field in such a way as to promote growth of the case secondary flow but to inhibit growth of the hub secondary flow. This is shown diagrammatically in Fig. 1—arrows point from higher to lower pressure. Although radial pressure gradients arise naturally in swirling flow, annular cascade experiments normally include only isolated turbine stages—or part stages—and the designer is therefore faced with the challenge of establishing representative conditions at inlet and exit of the cascade—the conditions that would exist in a working engine—which, in general, will be different from those conditions that would be achieved in the experiment in the absence of additional flow conditioning.

Cascade Inlet Conditions. In the working engine environment, there are radial and circumferential gradients in the combustor exit flow of total temperature, total pressure and free stream turbulence. In general, however, there is little swirl at combustor exit, and high-pressure nozzle guide vanes are usually designed for axial inlet flow. There have been very few experiments to date in which spatial variations in inlet flow properties have been simulated. In principle, it would be possible to establish a radial total pressure gradient upstream of a turbine stage by using gauzes with varying porosity, a technique that has been applied in studies of compressors but so far not of turbines. Similarly, if required, an inlet swirl angle distribution could be generated using inlet guide vanes, although wakes and secondary flows would present problems for the designer of such a system. In experiments in which heat transfer rates are to be measured, the importance is recognized of establishing the correct free stream turbulence intensity, and it is relatively common to include a turbulence grid upstream

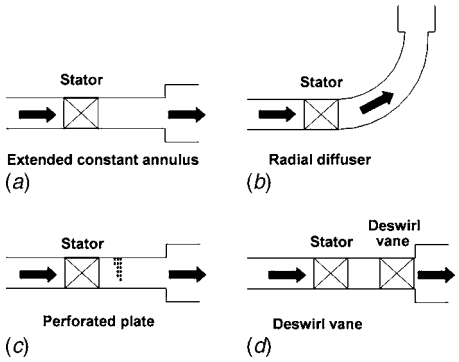

Fig. 2 Methods of setting annular cascade exit conditions: (*a*) extended constant annulus, (*b*) radial diffuser, (*c*) perforated plate, and (*d*) deswirl vane

of (or within) the cascade inlet contraction. Turbulence grids are generally designed to generate uniform turbulence across the inlet plane.

Cascade Exit Conditions. The radial static pressure gradient at the exit of an annular cascade will affect both the performance of the stage and measurements made downstream of the stage. Although it may not be necessary to employ a rotor at the exit of a stationary cascade, some means of setting the boundary conditions is normally required. Perhaps the simplest means of flow conditioning, and consequently, a commonly employed technique, is to allow the exit flow to develop though an extended annulus of constant radius, and then to exhaust as a free jet to a plenum at constant pressure. This is shown diagrammatically in Fig. 2(*a*). In this scheme, it is usually the case that the vane exit static pressure at midspan is close to the pressure of the downstream plenum. For swirling exit flow therefore, in which a radial pressure gradient is established, the hub end wall boundary layer is subject to an adverse pressure gradient towards the exit of the annulus. This can lead to flow separation. In the case of highly swirling exit flow, the blockage and unsteadiness associated with separation can lead to disturbances in the upstream flow field. Two problems in particular have been identified. First, fluctuations in vane aerodynamics associated with unsteadiness, which are known to markedly affect even time-mean heat transfer rate distributions, and, second, deviation of the upstream flow induced by gross separation, and the associated possibility of redistribution of the vane exit radial velocity (and pressure) field. Under certain conditions of flow therefore, the extended constant annulus may be an inadequate solution to the flow-conditioning problem.

Several techniques have been developed to establish the correct exit boundary conditions in cascades with highly swirling exit flow. The Whittle Laboratory transonic annular cascade [6] employs a radial diffuser, as shown Fig. 2(*b*). By increasing the mean radius of the flow path, by conservation of fluid angular momentum, the whirl velocity of the flow is reduced. This results in a small enough pressure difference between the hub and case boundary layers that the flow can be exhausted to a constant pressure plenum without flow separation. It is worth noting, however, that only by very careful design can separation be avoided in the diffusive flow along the duct. Squire et al. [7] employed perforated plates downstream of a test vane cascade. The plates had spanwise variations in on open area, allowing a radial pressure gradient to be established. The scheme is shown diagramatically in Fig. 2(*c*).

The Oxford *deswirl system* [8,9], shown diagramatically in Fig. 2(*d*), consists of a novel impulse-type vane (designed to turn flow towards the axial direction) and a downstream choke mechanism. Using this system, the radial pressure gradient established in the swirling flow downstream of the annular cascade of test vanes is undisturbed (in the region upstream of the deswirl vanes). The deswirl vane exit flow is axial and can be exhausted without unsteadiness to a downstream plenum at constant pressure. The system is also very compact and mechanically robust.

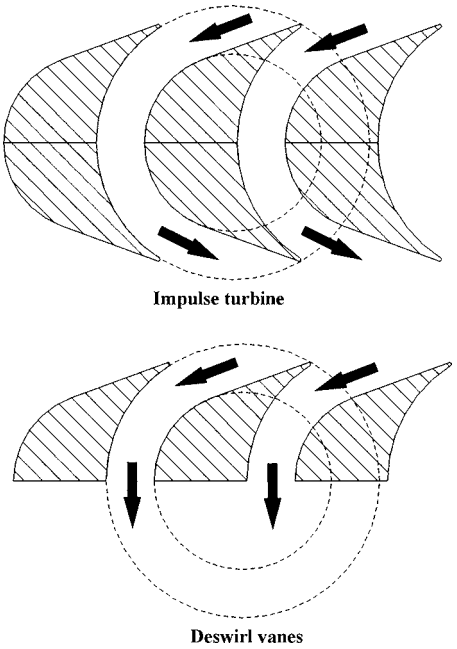

Fig. 3 An impulse turbine blade design and the corresponding impulse-type deswirl vane

The Deswirl Vane Concept. The deswirl vane is shown schematically in Fig. 3. The concept is that of an impulse-type vane truncated at half chord, where the flow direction is axial. The vane passage is of constant area (in a plane perpendicular to the streamwise direction) and therefore, if boundary layer growth is neglected, there is no static enthalpy change or static pressure drop within the passage. In transonic flows it is desirable to maintain constant flow velocity, as acceleration of the flow can lead to shocks, while diffusion can result in boundary layer separation. In reality, the effect of boundary layer growth within the deswirl vane passage is to cause the mean streamwise velocity to increase slightly. It would be a simple matter to design the vane passage to be mildly diffusive to offset the effects on the velocity field of boundary layer growth, although this is not necessary. Experimental and computational studies demonstrate that for high subsonic deswirl vane inlet flow velocities ($M>0.7$) areas of supersonic flow can develop within the vane passage, as the flow is accelerated over the suction surface. For deswirl vane inlet conditions from $M=0.1$ to $M=0.8$, separation within the passage was not observed in either computational or experimental studies, however. The relatively sharp leading edge, aligned with the inlet flow, was designed to minimize leading edge shock formation. A computer aided design (CAD) model of an annular cascade of deswirl vanes, is shown in Fig. 4.

Experimental Facility

Experiments were conducted in a blow-down—atmospheric to vacuum—test facility at the University of Oxford. The annular facility, which was modular in design, is pictured in Fig. 5. It consists of a curved inlet duct, an annular cascade of intermediate pressure (IP) guide vanes, an extended IP vane exit duct, an annular cascade of deswirl vanes, and a choke mechanism. The operation of the test vane (IP vane) was first characterized in the fully annular environment. The annular facility was then modified, with the introduction of sidewalls (the designs of which are critical to the sector performance and are discussed below), and a comparative study performed.

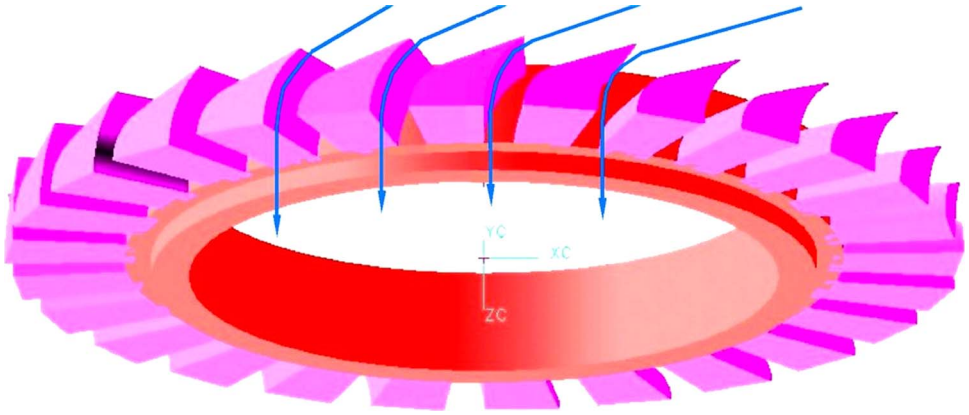

Fig. 4 Annular cascade of deswirl vanes

The IP vane count was 26 (0.270 engine scale), and 26 deswirl vanes were used for downstream flow conditioning. Both annuli of vanes were constructed from resin using the technique of stereolithography. The predicted area-mean IP vane exit-flow angle was 71.9 deg, and the area-mean exit Mach number was 0.76.

The design details and operating conditions of the facility are summarized in Table 1, below. The predicted deswirl vane inlet flow conditions were based on the results of a computational simulation conducted using the Rolls-Royce code JA63. The IP vane, IP vane exit duct, and deswirl system, were all included in the computational model.

The annular deswirl vane cascade and rotatable choke mechanism have been shown by experiment [8,9] to reproduce the radial pressure gradients downstream of an annular cascade of test vanes that exist in the working engine environment—in which the IP vane operates as part of an IP stage.

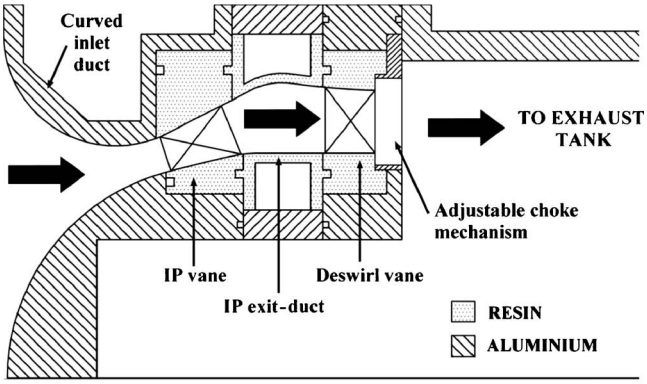

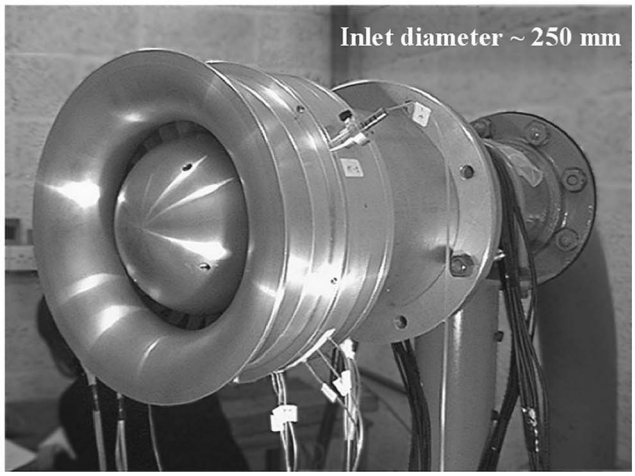

Fig. 5 The working section of the test facility

This paper presents experiments which demonstrate the usefulness of the deswirl system, not only in the fully annular environment, but also in the annular sector environment. The fully annular model test facility was modified with the introduction of shaped sidewalls so that the flow in a five-passage annular sector could be studied. If the deswirl system is used for flow conditioning downstream of a test vane, the problem of achieving engine representative flow conditions in the annular sector environment reduces to the problem of establishing periodicity. The degree of periodicity that is achieved is highly dependent on the sidewall design.

The influence of sidewall profile on the sector flow field and on the periodicity at the IP vane exit-plane within the sector was assessed by comparing measurements conducted in sectors with different sidewall designs to measurements conducted in the fully annular facility. Two sector designs were investigated. Each included five passages (six IP vanes and six deswirl vanes) and subtended an angle of 69.2 deg at the facility axis. Sector sidewalls were designed and manufactured (stereolithography hardened resin) so that they could be attached within the annular exit duct of the test facility, thereby partitioning a sector of vanes. Thus, the same instrumentation could be used for both fully annular and annular sector tests. A CAD drawing of a four-passage sector (IP vanes removed) is presented in Fig. 6 (a five-passage sector was used for experiments reported in this paper).

The angular displacement between the IP vane sector and the deswirl vane sector was dependent on the angle of the sidewalls

Table 1 Facility design details and operating conditions

Parameter	Target
IP vane inlet total pressure, bar	1.00
IP vane inlet total temperature (K)	291
Inlet Mach number	0.45
Inlet whirl angle	0°
IP vane axial chord (midspan) (mm)	23.0
Linear scale factor	0.270
IP vane throat area (m^2)	3.565×10^{-3}
Deswirl vane throat area (m^2)	3.967×10^{-3}
Re based on IP vane axial chord (at $M=0.76$)	2.88×10^5
Mass flow rate (at $M=1.0$) (kg s^{-1})	0.853
Predicted deswirl vane inlet Mach number	0.76
Predicted deswirl vane inlet whirl (deg)	71.9
Deswirl vane LE metal angle (deg)	63.1
Design incidence angle (deg)	8.8
Deswirl vane hub/case chord, mm	15.48/15.48
Deswirl vane hub/case pitch (mm)	18.34/23.49

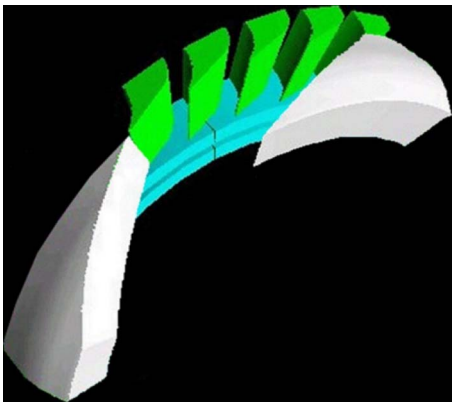

Fig. 6 A four-passage annular sector of deswirl vanes

relative to the axis. The annuli of vanes could be rotated relative to each other to ensure exact periodicity with sector sidewall designs of different angles.

Sidewall Design Philosophy. The principal objective in the design of an annular sector cascade is to reproduce the flow of the equivalent fully annular facility. It is desirable therefore for the sidewalls to have the minimum influence on the natural development of the flow streamlines downstream of the test vane cascade; that is, the streamlines should be allowed to develop as they would in the equivalent fully annular facility. The sidewall designs must necessarily be constrained, however, by the requirements of starting at the trailing edge line of the test vane and terminating at the leading edge line of the deswirl vane. In general, the test vane might have both axial and tangential lean and may also be swept. A swept vane, for example, would dictate sidewall designs that, at least on the upstream side of the sector, were convex on one side of the sector and concave on the other, so as to ensure smooth flow paths at the trailing edges of the left-hand and right-hand test vanes, at the vane-sidewall join. The general shape of the sector is determined by the sidewall angles, however, and the variation of these angles in both the radial and axial directions.

Consider a vane cascade for which the downstream streamline pattern is well characterized by either measurement or CFD modeling. In general, there will exist both radial and circumferential variations in velocity, whirl angle, and yaw angle, at the exit plane of the cascade, and in the downstream flow field. For this complex flow field, an obvious starting point in the sidewall design process might be to match the angle of both sidewalls to the pitchwise mean flow angle calculated at each radial height and at each axial plane: clearly the mean whirl angle is a more fundamental design parameter than the angle of the streamline emanating from the test vane trailing edge. For some test vanes, however, the development of (even pitchwise mean) streamlines downstream of the test cascade would be such that the hub and case streamlines would become out of step; streamlines initially distributed along a radial line would migrate such that at some later axial location they would lie on a line with tangential lean. If sidewalls were designed to follow such a streamline pattern, the shape of annular sector would become progressively more distorted (higher tangential lean) in the streamwise direction. An annular sector with high tangential lean at the deswirl vane inlet plane would require deswirl vanes with the same lean. This would give rise to unsatisfactory design complications. This problem is easily avoided, however, by defining the sidewall angle at midspan (based on the pitchwise mean exit flow angle at midspan, the area-mean exit flow angle, or any other method) at a given axial location, and by calculating sidewall angles at all other radial heights to give constant tangential lean along the exit duct. Notwithstanding small corrections to the sidewalls profiles to account for any differences in axial and tangential lean that may exist between the test vane and the deswirl vane, the above design methodology results in sidewalls which (at a given axial location) have higher wall angle at the case (and lower at the hub) than at midspan.

The annular sector designs described in this paper (and used in the experimental investigations) had sidewalls that were parallel throughout the exit duct; that is, the left-hand and right-hand walls had the same angles at a given radial height and axial location. It is not the case that parallel sidewalls limit the designer to an exit duct that is either of constant width or (independently) area. If both the endwalls (hub and case) and the sidewalls of an annular sector are parallel, however, then turning of the flow towards the axial direction (a decrease in wall angle) results in overall diffusion of the flow (an increase in downstream pressure is expected) and vice versa if the flow is turned away from the axial. Perhaps more importantly, if the flow is caused to turn in either direction by the sidewalls, a cross-sector pressure gradient is established. This is most analogous to the cross-passage pressure gradient established within a guide vane passage. It is clear therefore, that correct choice of sidewall angle, and variation of this angle with axial distance, is essential for achieving good periodicity in an annular sector. Only if it is required that parallel exit-duct endwalls be employed, and when independent control over both the cross-sector pressure gradient and the passage area are necessary, would it be necessary to consider a design with nonparallel sidewalls. In all other circumstances, a considerable degree of flexibility is afforded to the designer of such a system.

Small differences in axial and tangential lean between the test vane and the deswirl vane may have to be accommodated. The design philosophy adopted in the current investigation was to have linear variation with axial distance along the exit duct of both axial and tangential sidewall lean, with both values matched at the test vane exit plane and at the deswirl vane inlet plane.

For a given sidewall design, the minimum pressure downstream of the test vanes is determined by the ratio of the effective throat areas of the deswirl vane and the test vane (small corrections for aerodynamic loss may also be necessary). Higher-than-minimum downstream pressures are effected by adjusting the downstream choke mechanism (by increasing the blockage). The choke-plate blockage is increased until the desired operating point is reached. It is good practice to design the annular sector of deswirl vanes with a throat area approximately 5% greater than the theoretical minimum calculated based on area ratio and total pressure loss alone, to ensure the possibility of fine adjustment either side of the operating point. If it is not possible to achieve low enough downstream pressure (high enough Mach number) the sidewall profile or the deswirl vane must be redesigned. This problem is illustrated by Fig. 10: higher than predicted total pressure loss associated with the first of the two tested sidewall designs (see Fig. 8) resulted in higher than acceptable minimum downstream pressure. As a result it was not possible to operate the test vane at the design operating point. The problem was easily overcome by modifying the sidewall design (see Fig. 11).

The behaviors of the two sidewall designs were investigated, the design details of which are now summarized.

Sidewall Design 1. The hub and case profiles of sidewall design 1 are shown in Fig. 7, and the hub profile is compared to that of sidewall design 2 in Fig. 8. Both figures show the unwrapped profiles—cross sections at constant radius. Sidewall design 1 diffuses the flow by turning it towards the axial direction. The wall angles were chosen to approximately match the metal angles at the IP vane trailing edge and at the deswirl vane leading edge.

The sidewall design was based on the midspan wall profile (as discussed above), and therefore only small changes in tangential lean with axial distance were required (to match the tangential lean of the IP vane trailing edge and deswirl vane leading edge). At the IP vane trailing edge and deswirl vane leading edge the sidewall angles were 67 and 58 deg, respectively: the flow was turned towards the axial (diffused) by 9 deg within the sector

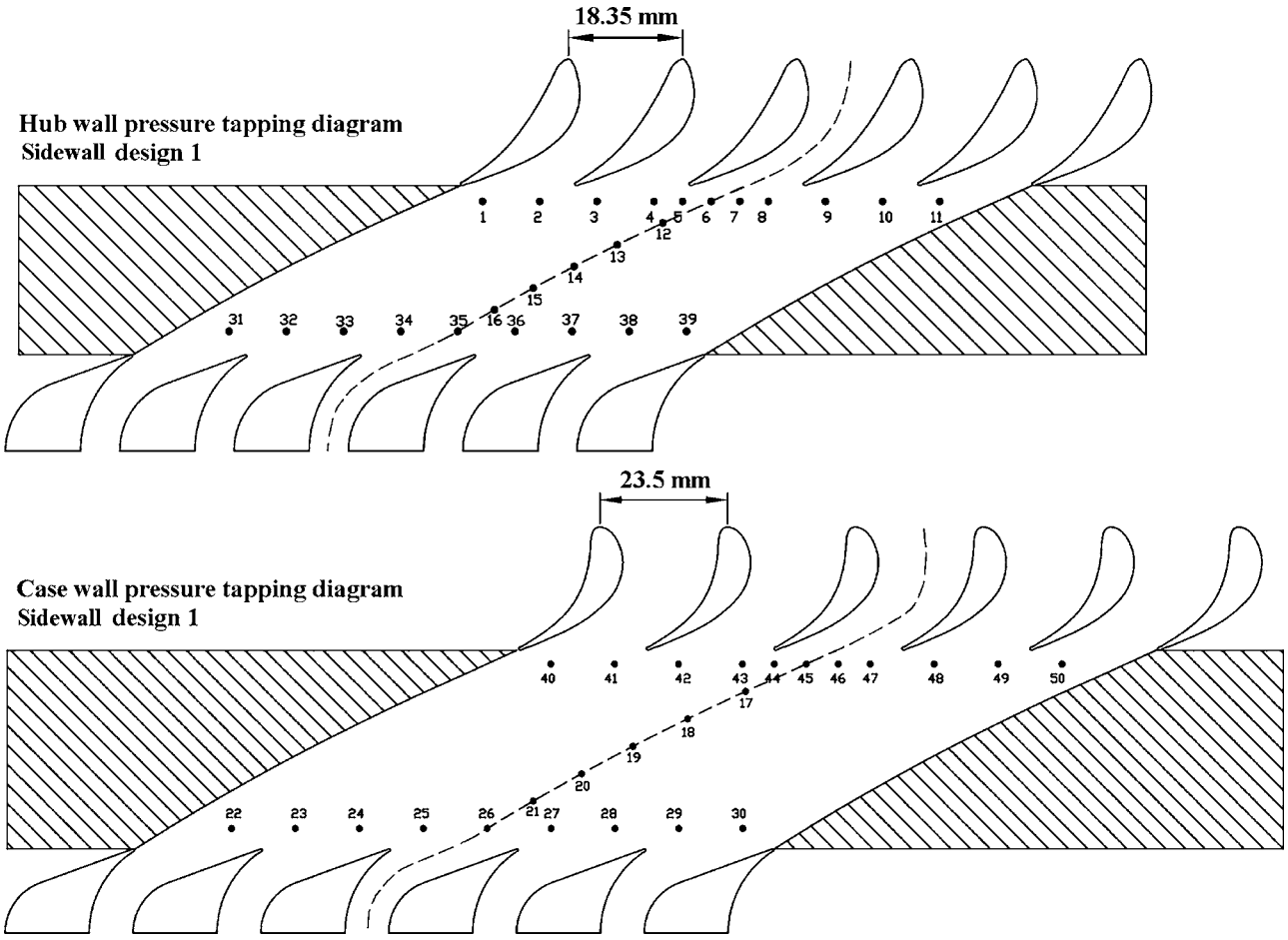

Fig. 7 Pressure tapping diagram at hub and case walls for sidewall design 1 (the wall has been unwrapped)

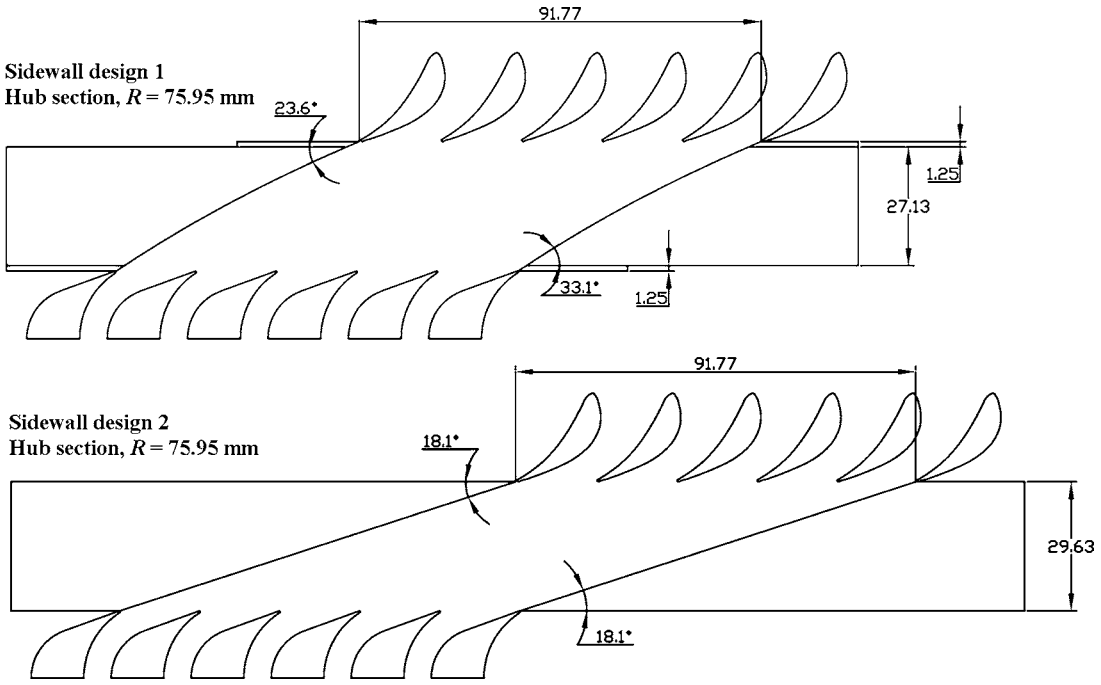

Fig. 8 Comparison of sidewall designs 1 and 2

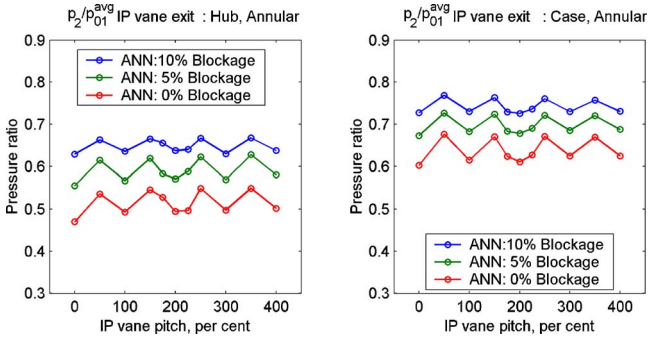

Fig. 9 Circumferential pressure distributions at the IP vane exit plane hub and case walls: fully annular cascade

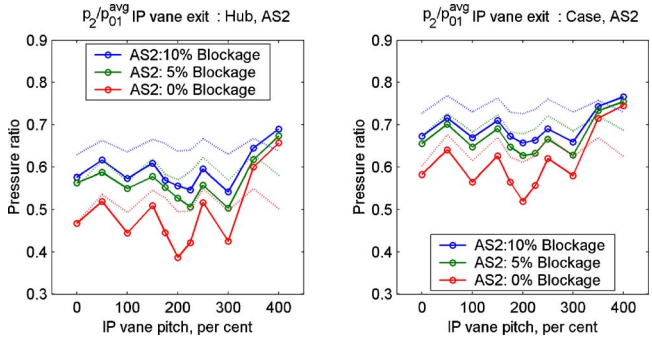

Fig. 11 Circumferential pressure distribution at the IP vane exit plane hub and case walls: annular design 2

passage. The IP vane midspan trailing edge mean metal angle was 65.7 deg, with a wedge angle of 7.96 deg, and the deswirl vane pressure surface metal angle was 58 deg, with a wedge angle of 13.8 deg. The axial and tangential leans of the sidewalls were matched at both IP vane exit and deswirl vane inlet to the vane profiles: axial lean was 22.0 and 0.0 deg for the IP and deswirl vanes, respectively, while tangential lean was 3.8 and 6.7 deg, respectively.

Sidewall Design 2. The hub profile of sidewall design 2 is compared to that of sidewall design 1 in Fig. 8. The principal difference is that the wall angle of sidewall design 2 is constant, so the flow is not diffused in the axial direction. The wall angle was higher than sidewall design 1. At midspan the wall angle was constant at 71.9 deg, matched to the mean predicted whirl angle (for the case of fully annular flow) at the deswirl vane inlet plane. Axial and tangential sidewall leans were the same as for the first sidewall design.

Instrumentation and Processing

Hub and case cross sections (at constant radial height) of the five-passage annular sector (sidewall design 1) are shown in Fig. 7. Static pressure was measured at the positions marked. Particular emphasis was placed on measuring the circumferential distributions of static pressure at the IP vane exit plane and at the deswirl vane inlet plane, so that the degree of (vane-to-vane) periodicity at these locations could be quantified. Measurements were also conducted along the hub and case walls at midsector. The midsector tappings and the deswirl vane inlet tappings were different for tests of the second annular sector design, in accordance with the position of the sidewalls, but the IP vane exit-plane tappings were the same for all tests. The spanwise distributions of static and total pressure were not measured, as the detrimental effects of probe blockage (at small scale) on the overall performance of the sector would likely have outweighed the increased understanding gained through additional measurements. It is common practice (and acceptable practice in the opinion of the authors) to characterize the operating point of a test vane in terms of the upstream total pressure and the downstream static pressure distributions at hub and case.

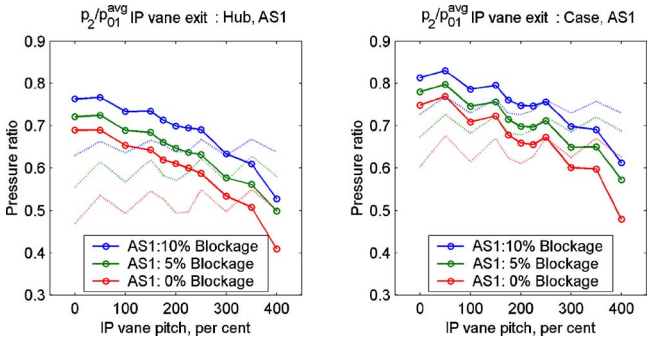

Fig. 10 Circumferential pressure distributions at the IP vane exit plane hub and case walls: annular sector design 1

Experimental Results

As we have noted, the principal objective in the aerodynamic design of an annular sector cascade is to reproduce exactly the flow conditions that would exist in the equivalent fully annular facility. It may reasonably be assumed that if inlet and exit flow boundary conditions identical to those measured in the equivalent fully annular cascade are established across all or part of an annular sector cascade, then across this part of the annular sector cascade the flow conditions will be identical to those in the fully annular facility. This will be assumed in the following discussion. Although measurements were conducted throughout the sector, for brevity, only selected pressure distributions are presented.

The measured circumferential pressure distributions at the IP vane exit plane for the case of fully annular flow are presented in Fig. 9, at the hub and the case walls, at a range of downstream blockages. The blockages, expressed as a percentage of the total deswirl vane throat area, were 0%, 5%, and 10%. The pressures have been nondimensionalized by dividing by the inlet total pressure and are plotted against IP vane pitch, positively increasing from the suction to pressure surface of the vane—that is, measurements take the same left to right positioning as the tappings in Fig. 10. Small pitch-to-pitch differences in measured pressure arise because of the slight aperiodicity of the pressure tappings—the minimum spacing was only 4.5 mm. In general, the flow was highly periodic, as expected: the IP and deswirl vane counts were the same, ensuring pitch-to-pitch flow path similarity.

Measurements conducted in the annular sector with sidewall design 1 are presented in Fig. 10, and are compared to measurements from the fully annular facility. The downstream blockage was the same for both tests. It should be noted, however, that it is possible to smoothly increase the downstream blockage, and so achieve any intermediate pressure ratio. Periodicity was markedly poor: a strong cross-sector pressure gradient (caused by turning the flow towards the axial direction, from 67 to 58 deg) influenced all of the vane passages. Under the action of this pressure gradient the flow on the left-hand side of the passage was strongly diffused, while that on the right-hand side of the passage was strongly accelerated. When the downstream blockage was increased, the effect was to raise the pressure uniformly across the sector—the strong aperiodic nature of the distribution was unchanged.

Measurements conducted in the annular sector with sidewall design 2 are presented in Fig. 11. The same downstream blockage conditions were used as for the fully annular tests. Excellent periodicity was obtained across the left-hand four passages of the sector (minimal cross-sector pressure gradients). Considering the

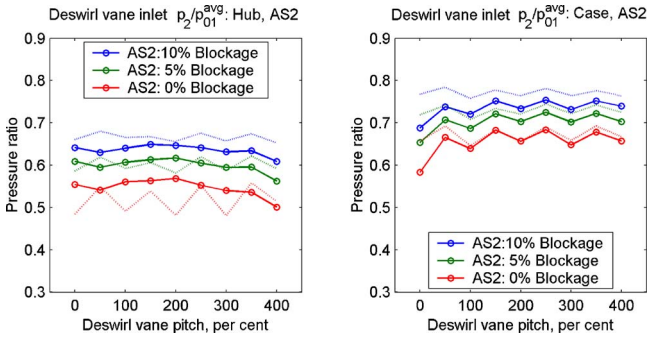

Fig. 12 Circumferential pressure distributions at the deswirl vane inlet plane hub and case walls: annular sector design 2

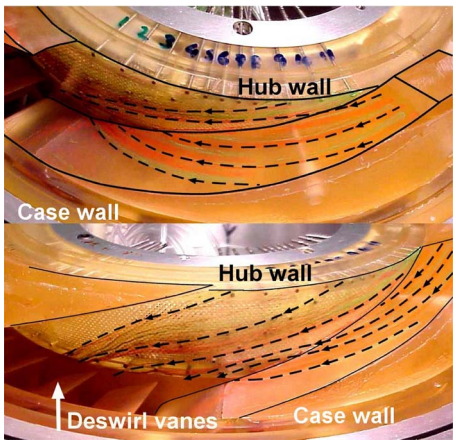

Fig. 13 Flow visualization on sector sidewalls and hub surface—sidewall design 2. Surface streamlines are highlighted.

results obtained in the annular sector for 10% blockage: at the hub, the variation in midpassage pressure ratio between the four passages was between 0.540 and 0.570, corresponding to a Mach number range between 0.98 and 0.94; at the case, the variation in midpassage pressure ratio between the four passages was 0.660–0.675, corresponding to a Mach number range of 0.79–0.77. In addition, across the four left-hand passages, the form of the measured distributions agreed very well with the measurements conducted in the fully annular environment.

The results demonstrate the suitability of the deswirl vane for setting annular sector boundary conditions. For heat transfer or aerodynamic studies in which only a single passage with representative flow is required, this degree of periodicity would be highly satisfactory. When the central passage (for example) is exactly matched to the target operating point of the vane, by adjusting the downstream blockage, adjacent passages would be matched in terms of pressure ratio to within 1.9% at the hub and to within 0.8% at the case. It is worth noting that because the flow was accelerated slightly by turning it away from the axial direction, the measured pressures were lower in the annular sector than for fully annular flow. Greater blockage was therefore required to achieve the same test vane pressure ratio.

For the annular sector with sidewall design 2 (see Figs. 8 and 11), measurements revealed a region of significantly elevated pressure in the right-hand passage (tapping locations 10, 11, 49, and 50). For 10% blockage, the midpassage pressure ratio at the case (tapping 50) was 0.76, and the pressure ratio at the hub (tapping 11) was 0.68. The corresponding measurements in passage 4 were approximately 0.66 and 0.54. There are two causes of this region of elevated pressure. Because the sidewall angle (71.9 deg) is greater than the IP vane pressure surface metal angle (69.7 deg) the location of the throat of the right-hand passage is moved from the trailing edge (of the far right-hand vane) to the trailing edge of the adjacent vane. Thus, with this sidewall in place, tapping numbers 11 and 50 are upstream of the throat. The high measured pressure is therefore expected. The high pressures measured at tapping locations 10 and 49 are caused by overturning of the IP vane exit flow. The mean metal angle is 65.7 deg, while the sidewall angle is 71.9 deg. The flow is therefore turned away from the axial by approximately 6.2 deg. The general modus operandi of the annular sector technique (or indeed the linear cascade) is to achieve representative conditions in a single passage of the cascade. A local region of elevated pressure, such as that observed, is therefore of little concern to the designer of the annular sector cascade.

The measured circumferential pressure distributions at the deswirl vane inlet plane hub and case walls for the annular sector with sidewall design 2 are presented in Fig. 12. The measurements are compared to measurements conducted in the fully annular facility. There are slight differences in form between the two sets of measurements because different (similarly positioned) tappings were used for the two tests. At the hub, the pressure profile is not characteristic stepped, as was expected, because of slight misalignment of the pressure tappings. Tappings were spaced at half-pitch intervals, so a significant shift in mean level was not expected. Excellent periodicity was achieved across most of the sector, with small differences only in the near-sidewall regions (regions of secondary flow). Most importantly, the results clearly demonstrate that the flow downstream of the test vanes, at inlet to the deswirl vanes, was periodic. Also, the strong radial pressure gradient associated with swirling flow was not disturbed.

Flow Visualization Experiments

Flow-visualization experiments (using an oil-paint technique) were conducted (in the annular sector with sidewall design 2) to determine the near-wall streamline pattern. Photographs of the right-hand wall of the sector, and the hub endwall, are presented in Fig. 13. The lower photograph was taken of the same oil streamlines, but from a position to the left of, and lower than, the upper photograph. For clarity, arrows have been added to the photographs.

Significant radial flow migration was observed on both of the sidewalls. Streamlines initially parallel to the hub and case walls were turned rapidly towards the hub wall, hence, they migrated towards the center of the sector. This observed flow migration was driven principally by the radial pressure gradient established in the swirling exit-duct flow. Lower momentum fluid in the near-wall region, being subject to the same strong radial pressure gradient as the midsector fluid, is overturned towards the hub. This fluid, migrating on to the hub surface, displaces the streamlines at both sides of the sector towards the center passages.

The experiments confirmed that the flow within the exit duct was well behaved, and that there were no separations. The analogy between secondary flow development within an annular sector and a single nozzle guide vane passage was also demonstrated.

Conclusions

A direct aerodynamic comparison has been conducted of the flow in an annular cascade facility, and in an annular sector facility of five vane passages.

In the fully annular cascade, engine representative pressure boundary conditions for a test vane cascade were established by using deswirl vanes, which allow even highly whirling transonic flow to be exhausted without unsteadiness to a plenum at constant pressure. The deswirl vane concept has previously been demonstrated at engine scale in the Isentropic Light Piston Facility at Farnborough [8,9].

By partitioning a five-passage sector of test vanes, and by using a sector of deswirl vanes for downstream flow conditioning, the

applicability of the deswirl technology to the annular sector boundary condition problem was investigated. Excellent periodicity was obtained across most of the sector, and it was demonstrated that by using the deswirl vane technology, the radial pressure gradient downstream of the test vanes (established in the swirling exit flow) was not disturbed. The technique represents a significant improvement over previous methods, and it is the first time that correct annular sector boundary conditions have been achieved to such satisfaction. Using the deswirl system, it is also possible to tune the mean downstream pressure, and thus, the operating point of the test vane. The technique is equally suited to the testing of highly three-dimensional vane profiles. If large spanwise variations in exit whirl angle exist, these can be removed gradually by correct sidewall contouring. The deswirl system therefore presents a means by which the problems associated with establishing annular sector boundary conditions may be resolved, allowing designers to exploit the obvious advantages of the annular sector cascade technique: the reduced cost of both facility manufacture and operation, and the use of engine parts in place of two-dimensional counterparts.

For investigations of surface heat transfer rate on modern high-pressure turbine vanes/blades, components that are, in general, highly three-dimensional and which have very complicated cooling systems, it is becoming unsatisfactory to use anything but the actual engine components. For these critical components, the geometry, film-cooling flows, and pressure gradients must all be simultaneously correct for the results of experimental studies to be regarded as truly engine representative. Despite their importance, relatively few such investigations are performed. This is because the costs are prohibitively high. The new annular sector technique presented in this paper provides a means by which engine-representative flow conditions can be established using only a small number of vanes and at a cost commensurate with the research environment.

References

[1] Hirsch, H., ed., 1993, "Advance Methods for Cascade Testing," AGARD-AG-328.

[2] Gladden, H. J., and Gauntner, J. W., 1975, "Experimental Verification of Film-Cooling Concepts on a Turbine Vane," ASME Paper No. 75-WA/GT-21.

[3] Radeklint, U. R., and Hjalmarsson, C. S., 1998, "A New Test Facility for Testing of Cooled Gas Turbine Components," ASME Paper No. 98-GT-557.

[4] Wiers, S. H., and Fransson, T. H., 2000, "Experimental Investigation of the Periodicity in a Sector of an Annular Turbine Cascade," 15th Bi-Annular Symposium on Measuring Techniques in Transonic and Supersonic Flow in Cascades and Turbomachines, Firenze, Italy, 21–22.

[5] Vogt, D. M., and Fransson, T. H., 2002, "A New Turbine Cascade for Aeromechanical Testing," Presented at the 16th Symposium on Measuring Techniques in Transonic and Supersonic Flow in Cascades and Turbomachines, Cambridge, UK, September.

[6] Hodson, H. P., and Dominy, R. G., 1993, "Annular and Rotating Cascades," Chap. 3, AGARD-AG-328.

[7] Squire, L. C., 1986, "Effects of Probe Supports on Measurements in Steam Turbines," ASME Paper No. 86-GT-213.

[8] Povey, T., Chana, K. S., Oldfield, M. L. G., Jones, T. V., and Owen, A. K., 2001, "The Design and Performance of a Transonic Flow Deswirling System," *Proceedings of the IMechE Advances of CFD in Fluid Machinery Design Seminar*, London, June 13.

[9] Povey, T., Chana, K. S., Jones, T. V., and Oldfield, M. L. G., 2003, "The Design and Performance of a Transonic Flow Deswirling System—An Application of Current CFD Design Techniques Tested Against Model and Full-Scale Experiments," *Advances of CFD in Fluid Machinery Design*, R. L. Elder, A. Tourlidakis, and M. K. Yates, eds., IMechE Professional Engineering, London, pp. 65–94.

Preliminary Fan Design for a Silent Aircraft

Daniel Crichton

Liping Xu

Cesare A. Hall

Whittle Laboratory,
Department of Engineering,
Madingley Road,
Cambridge, CB3 0DY, United Kingdom

Preliminary fan design for a functionally silent aircraft has been performed with noise reduction as the primary goal. For such an aircraft the fan design must, in addition to delivering low cruise fuel burn, enable low jet and fan source noise during takeoff. This requires the fan to be operating at low pressure ratio and high efficiency during takeoff and, for conditions where the relative tip Mach number onto the fan is supersonic, ensuring the primary shock structure is ingested into the blade passage. To meet these requirements, flyover and cruise flow coefficients are matched using a variable area nozzle at the same time as delivering low takeoff FPR. This places the sideline operating point near the shoulder of the characteristic and fixes the top of climb and cruise fan pressure ratios. For a 4-engine, 250 pax, 4000 nm *silent aircraft this approach leads to a top of climb FPR of 1.45, requiring a 39% increase in nozzle area at takeoff. A fan rotor has been designed for this cycle with 20 blades, low tip loading during takeoff, and a* 350 m/s *top of climb tip speed.* [DOI: 10.1115/1.2372779]

Introduction

While noise from civil aircraft has reduced significantly over the last 20 years, the downward trend is levelling off and, within the UK, predicted increases in aircraft movements are expected to lead to increasing aircraft noise exposure around airports in the future [1,2]. The ACARE2020 goals [3] that include efficiency and emissions targets in addition to a 50% reduction in perceived noise relative to 2000 technology levels are proving to be extremely challenging. It has been argued that meeting these targets will require revolution rather than evolution in airframe and engine concepts [4].

The Silent Aircraft Initiative 2025 goal of a reduction in airframe and engine noise sources to a point where they are imperceptible outside of the airport boundary in an urban environment (see Fig. 1) is considerably more challenging than the ACARE noise target. By taking noise reduction as the *primary* design driver alongside mission requirements and fuel burn, the intention is to explore innovative solutions applicable within the ACARE-2020 time frame and beyond. To this end, in this paper, noise reduction requirements drive the selection of key design values.

For the purposes of this study the SAI noise goal has been expressed as a peak dBA value that should not be exceeded outside of a typical airport boundary. A peak dBA value was used as it can be linked to both World Health Organization guidelines on community noise and data on average traffic noise levels in a typical urban area [5,6]. In addition, unlike DNL or EPNdB it does not require prior knowledge of flight profiles and (for DNL) traffic patterns.

Previous work on the installation and configuration of engines for a silent aircraft has pointed to an embedded engine configuration on top of an all-lifting body aircraft as a promising concept for ultralow noise [7]. Embedding the engines shields a large amount of forward propagating noise and enables longer ducting for acoustic treatment [8]. Ingesting and reenergizing some of the suction surface boundary layer has the potential to reduce aircraft drag enabling, for an ultralow noise aircraft, lower takeoff jet velocity. From a system perspective, increases in fan diameter do not require increases in landing gear length. In addition, the relationship between fan diameter and nacelle drag is altered, leading to the point at which minimum fuel burn is reached occurring at a larger fan diameter and lower jet stagnation pressure [7]. The installation does though introduce a range of problems not found, or less critical, in traditional underwing designs. Even without boundary layer ingestion, pressure recovery of the inlet is likely to be lower and distortion at the fan face higher compared to podded engines. Adding boundary layer ingestion to this can lead to significant inlet distortion at the fan face during cruise [9]. Safety and certification concerns including survival of turbine disk failure and impact of an engine out on airframe and adjacent engine performance require further consideration during the design process.

While previous work on quiet engine design has tended to be less far-reaching in terms of noise target and more constrained in that standard installation and flight operations were specified, several conclusions are applicable to the silent aircraft project. With a lower fan pressure ratio (FPR) leading to lower jet noise and generally lower source noise, the tradeoff between noise reduction and increasing fuel burn is critical. Gliebe and Janardan [10] investigated direct drive and geared fans for large twin engine aircraft with the aim of achieving 5–10 EPN dB reduction relative to FAR36 stage 3 at each measuring station. They concluded that top of climb FPR in the range 1.4 to 1.55 was optimal for low noise with acceptable weight and direct operating cost (DOC) penalties. More recent work by Daggett et al. [11] with a 2015 time frame aimed for ultrahigh efficiency with a noise level 20 EPNdB cumulative below stage 3. For a single (geared) fan it was found that a FPR of 1.45 was optimal in terms of DOC with lower FPR designs leading to increased weight and drag offsetting SFC improvements. As an ultralow noise concept, Dittmar has proposed a two stage fan of design overall pressure ratio 1.15 [12,13]. This gives low jet and fan noise but at the expense of a very large installation requirement leading to poor cruise performance.

To meet the silent aircraft noise target and have competitive fuel burn, a turbofan engine concept needs to operate with a fan pressure ratio in the range proposed by Dittmar at takeoff for low jet noise and in the range proposed by Gliebe and Daggett at top of climb for low fuel consumption. This requires a variable cycle engine design as described in Ref. [7]. Furthermore, low fan source noise is required at takeoff and in this paper we demonstrate how this can also be achieved with the use of a variable area exhaust nozzle. A design approach is presented that determines the fan rotor design parameters and the off-design operation needed to satisfy all the noise requirements while maintaining high effi-

Contributed by the International Gas Turbine Institute (IGTI) of ASME for publication in the JOURNAL OF TURBOMACHINERY. Manuscript received October 1, 2005; final manuscript received February 1, 2006. IGTI Review Chair: R. S. Abhari. Paper presented at the ASME Turbo Expo 2006: Barcelona, Spain, May 8–11, 2006, Paper No. GT2006-90564.

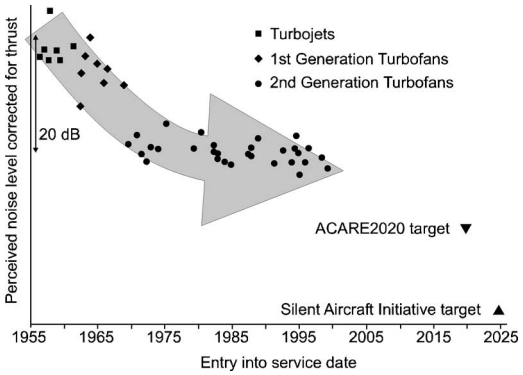

Fig. 1 Reduction in thrust corrected aircraft noise level over time

ciency. A rotor design and the corresponding characteristic are presented and the resulting requirements on future outlet guide vanes are discussed. With the aerothermal and acoustic implications of using a variable area nozzle worthy of detailed attention, the mechanical design of such a nozzle, while critical, has been left to a later stage.

Engine Cycle

While a considerable volume of work has been published in recent years on lowering jet noise through lobes, tabs, or other forms of jet shaping, a significant reduction in jet noise while maintaining thrust requires an increased jet area and reduced jet velocity. To avoid suboptimal cruise performance through increased engine weight and drag, it is desirable to minimize any required jet velocity reductions during takeoff relative to current trends. To this end, optimization of the aircraft takeoff profile to minimize the required jet area at takeoff has been performed by the authors [14] using the Stone jet noise model [15] and ESDU atmospheric corrections [16,17] to predict noise on the ground.

For a specified jet area the aircraft accelerates until rotation speed is reached and then climbs as steeply as possible at constant speed without exceeding the jet noise target outside of the airport boundary at any time. The jet area is then iteratively modified and the takeoff reflown until all operating requirements are met.

Figure 2 shows resulting takeoff profiles for a 4-engine 250 pax, 4000 nm aircraft (described further in Table 1) achieved from the baseline SAI airport under sea level ISA+12 K conditions. The runway length used was 10 000 ft and the airport boundary was set at a sideline distance of 450 m and a flyover distance of 1000 m from the runway. The sideline distance matches the ICAO certification value, but the flyover position

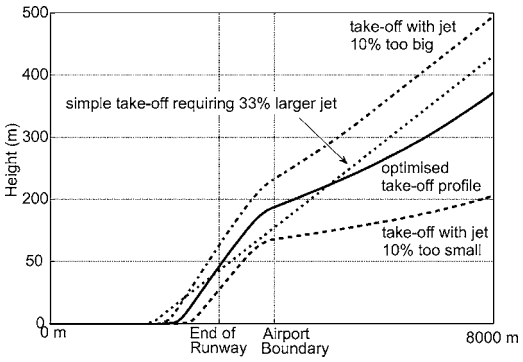

Fig. 2 Takeoff profile optimization for jet noise outside airport boundary (10 000 ft runway, airport boundary 450 m at the sideline and 1000 m from the end of the runway at flyover, sea level ISA+12 K conditions)

Table 1 250 pax, 400 nm aircraft parameters for 2 engine podded and 4 engine embedded variants

	Variant	Sideline	Flyover	Top of climb	Start of cruise
Altitude	-	190 m	210 m	12 192 m	12 192 m
Conditions	-	ISA+12 K		ISA+10 K	ISA
Velocity	-	85 m/s		Mach 0.8	Mach 0.8
Angle of climb	2 eng	7.5 deg	4.1 deg	0.33 deg	0 deg
	4 eng		1.9 deg		
PR_{IN}	2 eng	0.995			
	4 eng	0.98		0.96	
PR_{OUT}	2 eng	1.0			
	4 eng	0.98			
η_p	-	92%			
Net thrust	2 eng	304.0 kN	230.4 kN	75.2 kN	66.8 kN
	4 eng		173.2 kN		

used here is different from the certification flyover position (4048 rather than 6500 m after brakes off) [18] so as to be more closely aligned to the SAI goal. Airport and atmospheric parameters were selected to be more arduous than the majority of conditions a silent aircraft would be required to operate under with the atmospheric conditions covering 99% of operating hours at London Heathrow and the runway relatively short. A range of takeoff conditions likely to only be experienced rarely or at noise unconstrained airports have been considered during the design and can be achieved by relaxing the noise target.

Within Fig. 2, four different departure profiles are shown. The solid line is the optimized departure that meets all takeoff requirements with the minimum jet area. If the area is decreased by 10% and the same noise target met, then the lower dashed departure profiles is achieved. The reduced jet area leads to reduced thrust limiting the acceleration and climb rate. As the aircraft nears the airport boundary, the angle of climb has to reduce below that required to comply with engine-out safety requirements in order to not exceed the noise target. Conversely, if the area is increased 10% then all operational requirements are met, but achieving the top of climb performance will be harder. The dotted line represents a successful takeoff without allowing the angle of climb to reduce as the aircraft crosses the airport boundary. This simple departure profile requires a 33% increase in jet area relative to the optimized profile in order to meet the same noise target. The minimum regulated cutback height of 800 ft [19,20] is not enforced as the entire takeoff profile is low noise optimized with a continuous variation in thrust.

Fig. 3 shows how the required jet area varies with noise target

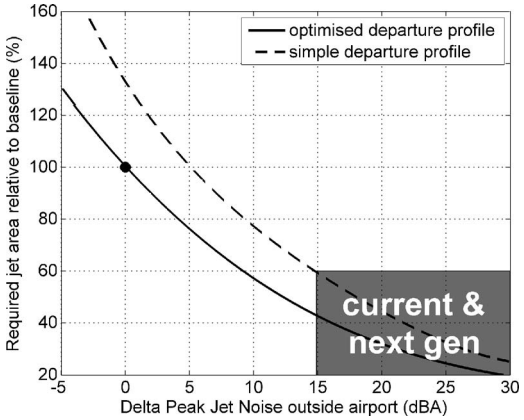

Fig. 3 Reduction in the required jet area achieved through optimization of the takeoff profile for different peak jet noise requirements

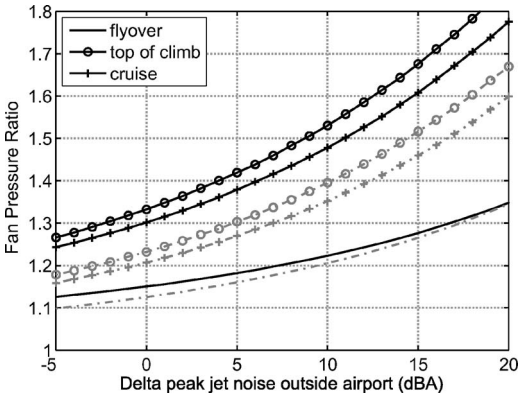

Fig. 4 FPR for a fixed nozzle engine at key operating points for a 250 pax, 4000 nm aircraft. Four-engine embedded variant =solid black lines, two-engine podded variant=dashed grey lines. (*This distinction between the two aircraft variants is followed in the remaining plots.*)

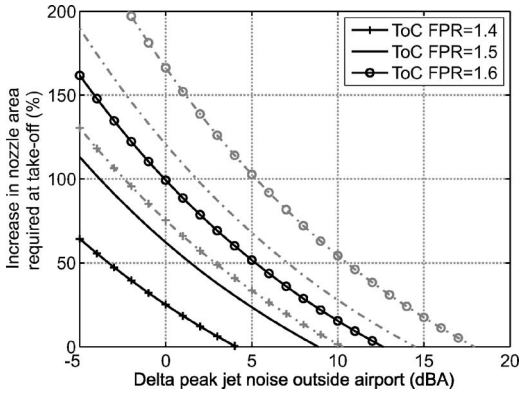

Fig. 5 Required nozzle variation to meet both top of climb FPR and takeoff jet noise requirements for two aircraft variants

for both the optimized and simple departure profiles described above. The x axis shows the takeoff noise experienced outside the airport boundary relative to the jet noise goal of the silent aircraft with positive values indicating an increase in noise. For example, if the SAI noise target was relaxed by 9 dBA, then the required takeoff jet area could be reduced by 40%. The challenge of the SAI target can be seen by comparing the required jet area at takeoff to that of current and next generation aircraft.

For an ultrahigh bypass ratio engine, the majority of the thrust comes from the bypass airflow. Neglecting the impact of the core flow on thrust leads to the following three equations that can be solved to give required fan pressure ratio for specified net thrust, nozzle area, and free-stream conditions. Equation (1) considers the pressure rise from inlet to exhaust matching static pressure at the two conditions, Eq. (2) looks at the produced thrust and Eq. (3) covers nozzle choking:

$$\mathrm{FPR} = \frac{1}{\mathrm{PR_{in}PR_{out}}}\left(\frac{1+\frac{\gamma-1}{2}M_{\mathrm{jet}}^2}{1+\frac{\gamma-1}{2}M_{\infty}^2}\right)^{\gamma/(\gamma-1)} \tag{1}$$

$$\frac{T_N}{A_{\mathrm{jet}}} = \gamma p_{\infty} M_{\mathrm{jet}}^2\left[1-\mathrm{FPR}^{(1-\gamma)/2\gamma}\eta_p\frac{M_{\infty}}{M_{\mathrm{jet}}}\left(\frac{1+\frac{\gamma-1}{2}M_{\infty}^2}{1+\frac{\gamma-1}{2}M_{\mathrm{jet}}^2}\right)^{-1/2}\right] \tag{2}$$

$$\frac{A_{\mathrm{noz}}}{A_{\mathrm{jet}}} = \max[1,M_{\mathrm{jet}}]\left(\frac{2}{\gamma+1}\left(1+\frac{\gamma-1}{2}\max[1,M_{\mathrm{jet}}]^2\right)\right)^{-\frac{1}{2}[(\gamma+1)/(\gamma-1)]} \tag{3}$$

Linking these equations to the noise optimized takeoff enables fan pressure ratio as a function of noise outside the airport to be calculated. Figure 4 presents this for a 250 pax 4000 nm aircraft utilizing a fixed nozzle at various flight conditions. It is worth noting that as jet noise is only one of several noise sources during takeoff, the jet noise target needs to be set lower than the overall noise target. The nozzle area is fixed by the noise requirement during takeoff, leading to specified fan pressure ratios at top of climb and cruise. Two aircraft variants are presented: one for a typical two engine podded aircraft and one for a four-engine embedded aircraft. Values used in the creation of this and following figures can be found in Table 1. In the current study, the boundary layer airflow is diverted around the engine for the four-engine embedded variant although the increased ducting and more complex geometry still gives rise to reduced pressure recovery. The two-engine variant is shown to see the impact of the same noise reduction requirements on a more conventional engine and airframe configuration. The differences in results between the two aircraft variants primarily arise from two sources. First, the lower pressure recovery of the four engine embedded variant impacts Eq. (1). Second, the minimum climb angle during takeoff required for engine-out situations impacts the flyover thrust requirement in Eq. (2). Both these factors lead to a higher fan pressure ratio for the same noise level being achievable with the four-engine embedded variant at takeoff. This leads to a higher top of climb and cruise fan pressure ratio.

Even for the embedded engine variant, the top of climb fan pressure ratio is very low at the required noise limit and therefore a variable cycle design must be employed as discussed by Hall and Crichton to reduce installation size, weight, and drag [7]. A variable area nozzle approach is developed here as, in addition to enabling low noise during takeoff, it can be used to minimize fuel burn during cruise and increase the surge margin. Opening the nozzle during takeoff reduces jet noise by moving the fan operating point to higher capacity and a lower fan pressure ratio. Figure 5 shows the increase in the nozzle area required relative to top of climb values to meet the design fan pressure ratio and takeoff jet noise levels.

As the required top of climb fan pressure ratio is increased, a larger variable area nozzle ratio is required to meet the same noise level at takeoff. In determining what the top of climb fan pressure ratio should be, a range of factors needs to be considered. For non-noise critical aircraft minimizing mission fuel burn is the primary driver but, for an ultralow noise aircraft, the impact on the takeoff fan source and jet noise is also critical. Therefore, in order to select the top of climb fan pressure ratio and other fan design parameters, an understanding of fan source noise generation mechanisms and mitigation is required. The impact on cruise fuel burn when selecting a fan pressure ratio for a silent aircraft is considered in more detail by Hall and Crichton [21].

Low Noise Fan Design

At a conceptual level, designing for low fan source noise is considerably more complicated than designing for low jet noise. Jet noise prediction is relatively accurate and limited variables drive one toward low jet velocity. When designing for a specified noise level, as is the case with the silent aircraft, a specified jet noise requirement translates directly into a specified jet area during takeoff. This is not the case with fan source noise. Multiple generation mechanisms exist, both tonal and broadband, including self noise, rotor-stator interaction, and multiple pure tone (buzzsaw) generation. A complex propagation path, the use of liners for attenuation and, for the current silent aircraft design,

shielding of forward propagating noise from the airframe, further complicate the problem. Publicly available noise prediction capabilities are less mature, especially in relation to broadband noise making designing for an absolute noise level hard. This is especially true for an engine using a variable area nozzle as the fan operating line during takeoff is markedly different from conventional civil engines on which current correlations are based.

For a preliminary fan design, the authors have therefore used available results, predictions, and correlations to guide the process and have not attempted to design for a specified noise level at this stage. Complementary work on the tradeoffs in liner length and inlet design for embedded engines is currently being undertaken within the silent aircraft project. Once the result of this work is available, state of the art methods to predict source noise and resulting noise on the ground will be used. While in the current work only rotor design is performed, the impact of this design on stator generated noise is considered.

Previous research has shown that increased nozzle area can lead to reduced fan noise for a given thrust. In the 1970s Woodward and Lucas [22] tested a 1.25 pressure ratio fan with area increases up to 20% of the design area. Reductions in noise level at all operating speeds were witnessed alongside increases in efficiency. Ginder and Newby [23] developed a broadband noise prediction model based on this and other work that correlated fan noise to inflow incidence. More recently, Hughes et al. [24] have shown that small increases in nozzle area (up to 12.9%) can give thrust increases and reduced broadband noise with modern wide chord fan designs. Work on the same rig [25] with two rotor designs has shown, at subsonic fan tip speeds, a link between noise generation and wake severity.

Correlations such as those based on the work of Heidmann [26], although not suitable for the direct application to engines working well away from normal working lines, provide further insight into suitable approaches to noise reduction. The ESDU fan and compressor prediction code [27] based on Heidmann presents broadband and tonal noise sources in the form of Eq. (4) with some variation for the different sources. RSS is the rotor-stator spacing and BPF the blade passing frequency.

$$\mathrm{SPL}(f) = 20\log_{10}(\Delta T_0) + 10\log_{10}(\dot{m}) + F_1(M_{\mathrm{rel}}) + F_2(\mathrm{RSS}) + F_3(\theta) + F_4(f/\mathrm{BPF}) + C \quad (4)$$

In terms of cycle and fan rotor preliminary design, the variables that can be targeted are the temperature rise across the fan, the mass flow rate, and the relative flow Mach number. With fan pressure ratio and mass flow rate set by the requirement for low jet noise, high fan efficiency is required to minimize the temperature rise. This correlates well with the work of Ginder and Newby as efficiency is closely linked to the incidence angle onto the rotor and, for a normal engine working line during takeoff, reduced incidence equals increased efficiency.

While the traditional 50 log(tip speed) correlation, used in [23] for example, would suggest reducing fan tip speed to reduce noise, this is not always the case. A second fan design as part of the NASA Advance Subsonic Technology project was found to be louder than its predecessor, despite having a reduced tip speed. Topol et al. [28] found this to be primarily due to increased broadband noise from increased fan tip turbulence impacting the stator. Included within this work is a simple formulation covering broadband noise generation (Eq. (5)) in which C is the absolute velocity onto the stator, V_0 is the turbulent velocity, and N_V is the number of Outlet Guide Vanes (OGVs).

$$\text{Sound Power} \propto 10\log[C^3 V_0^2 N_V] \quad (5)$$

Reducing rotor loading and the absolute flow velocity onto the OGVs, especially at the tip, is therefore required during takeoff. While increasing, the nozzle area will increase fan tip speed for the same thrust; the high cruise altitude and low design point fan pressure ratio lead to excess thrust at a low flight speed (reducing the fan pressure ratio increases the cruise ram drag more than the takeoff ram drag). In addition a four-engine design requires a reduced climb angle compared to a two-engine design. The fan can therefore operate at part speed during takeoff, resulting in low rotor loading at the tip and lower flow velocity onto the OGVs.

With the rapid onset of multiple pure tone noise at supersonic relative tip Mach numbers, maintaining subsonic tip velocity at all times during takeoff is desirable. As discussed later, achieving this for the entire takeoff leads to reduced cruise performance and therefore alternative mitigation strategies must be considered. As the nozzle area is increased the fan backpressure is reduced, and, for a fan operating with supersonic relative inlet flow, the primary shock structure is ingested into the blade passage, leading to choking. A weaker bow shock detached from the leading edge still propagates upstream, but a considerable reduction in MPT noise is predicted for this situation [29]. For fans working with a fixed nozzle area, this effect is generally only seen at high fan speed, where the shock is just ingested at the tip for peak efficiency. This may explain the more rapid than expected reduction in MPT noise at higher Mach numbers seen by Prasad and Prasad [30], who compared their results to the analysis of Morfey and Fisher [31]. In their analysis, Morfey and Fisher modeled the flow as having detached normal shocks for all conditions.

To summarize, for low fan source noise while maintaining low jet noise, high efficiency and low tip loading is required during the entire takeoff procedure. To minimize multiple pure tone generation, when the flow onto the rotor tip is supersonic the primary shock structure should be ingested into the blade passage. These requirements are now considered in the selection of fan rotor design parameters.

Selection of Fan Rotor Design Parameters

A variable area nozzle enables the fan to be operated at any position on its characteristic for a specified thrust. During cruise the nozzle can be set for minimum fuel burn, for hot and high operations the nozzle can be closed to increase available thrust and, during takeoff the nozzle can be set to minimize noise.

With the nozzle setting impacting both fan and jet noise the same nozzle position needs to meet the requirements of both sources. This requires the fan pressure ratio being at a specified level for low jet noise and the fan operating at an efficient position for low fan noise. The aircraft is as close as it gets to ground outside the airport boundary at the flyover position and, as jet noise reduces more rapidly than fan noise when the engine is throttled back, this position is critical. As discussed later in this section, the relative tip flow can be set to below unity Mach number at this position and therefore high fan efficiency is the main requirement. At the sideline position the subsonic tip Mach number cannot be maintained and therefore while high efficiency is still important, any primary shock structures must be ingested to minimize MPT noise. This requires operating near the shoulder of the fan characteristic.

For a typical fan design, a locus of constant flow coefficient, φ, tracks peak efficiency well, so ensuring both the cruise and flyover points are at the same flow coefficient will ensure they are both at, or close to, peak efficiency. If the nozzle is operated at a fixed area during takeoff (as is assumed in the current takeoff optimization work), the sideline point on the fan characteristic is at a higher flow coefficient than flyover and on a higher thrust line. Setting the flyover flow coefficient to match cruise will also therefore place the sideline point near the fan shoulder. Performing this calculation requires the use of a sample characteristic because the flow coefficient is a function of blade speed (see Eq. (6)). If a realistic fan map is not available, similar results can be obtained by fixing the stage loading divided by the flow coefficient squared, ψ/φ^2. This is independent of blade speed but diverges from peak efficiency at higher Mach numbers (Eq. (7)).

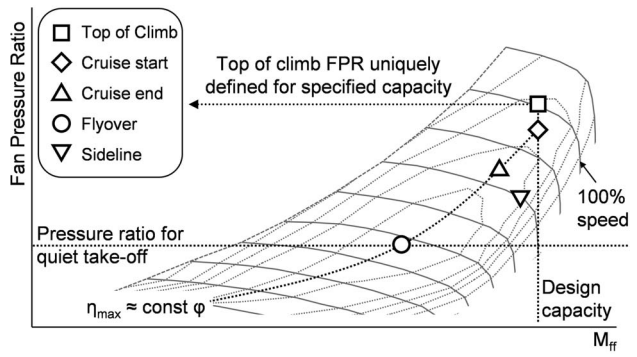

Fig. 6 Top of climb FPR uniquely defined by specifying flyover FPR, fan capacity, and matching flow coefficient at flyover and cruise

$$\varphi = \frac{V_x}{U} \propto \frac{M_{\mathrm{ff}}\left(1 + \frac{\gamma-1}{2}M_{\mathrm{ff}}^2\right)^{-1/2}}{U} \tag{6}$$

$$\frac{\psi}{\varphi^2} = \frac{\Delta h_0}{V_x^2} = \left(\frac{1}{(\gamma-1)M_{\mathrm{ff}}^2} + \frac{1}{2}\right)\left(\mathrm{FPR}^{\frac{\gamma-1}{\eta_p \gamma}} - 1\right) \tag{7}$$

To reduce the fan diameter and installed weight, the mass averaged fan face Mach number should be as high as possible without leading to excessive shock losses. A design value of 0.66 for the top of climb conditions is representative of modern designs. In choosing the top of climb fan pressure ratio the following procedure has therefore been followed:

(i) Set the top of climb and start of cruise fan face Mach numbers to meet specified capacity;
(ii) place the flyover operating point at the same flow coefficient, φ, as the start of cruise operating point for high efficiency at takeoff;
(iii) set the flyover fan pressure ratio to the level required for an ultralow noise takeoff.

This approach is demonstrated on the fan characteristic in Fig. 6. Fan face area is fixed by matching jet and fan face mass flow rates (Eq. (8)) and meeting thrust requirements at both the flyover and cruise positions. This gives a unique fan pressure ratio at the top of climb condition.

$$\frac{A_{jet}}{A_{ff}} = \frac{\mathrm{FPR}^{\left(\frac{\gamma-1}{2\gamma\eta_p}-1\right)}}{\mathrm{PR}_{\mathrm{out}}} \frac{M_{\mathrm{ff}}}{M_{\mathrm{jet}}} \left(\frac{1 + \frac{\gamma-1}{2}M_{ff}^2}{1 + \frac{\gamma-1}{2}M_{\mathrm{jet}}^2}\right)^{-\frac{1}{2}[(\gamma+1)/(\gamma-1)]} \tag{8}$$

Figure 7 shows the result of matching the flow coefficient at flyover and cruise for the two aircraft engine variants previously discussed. As fan efficiency plateaus near peak values, especially at part speed, there is some tolerance in the flow coefficient at flyover while still maintaining high efficiency. Figure 7 shows bounds of FPR at $\varphi_{\mathrm{flyover}} = (1 \pm 0.05)\varphi_{\mathrm{cruise}}$ with a reduced flow coefficient at flyover leading to a reduced fan pressure ratio at top of climb. This tolerance can be utilized to assist in ensuring any shock structures formed on the blade tip at or around the sideline position are ingested. The fan characteristic shown in Fig. 6, which is representative of a high bypass ratio low pressure ratio transonic design, has been used in the creation of this plot to track the flow coefficient.

From Fig. 7 it can be seen that to meet the target jet noise level of the silent aircraft and operate at the same flow coefficient during flyover and cruise requires a top of climb fan pressure ratio of approximately 1.45 and an increase in nozzle area of 39% between top of climb and flyover. The equivalent numbers for the podded engine variant are a fan pressure ratio at the top of climb of approximately 1.3 and a nozzle area increase of 33%. With the fan pressure ratio now selected, tip speed at the design point needs to be specified.

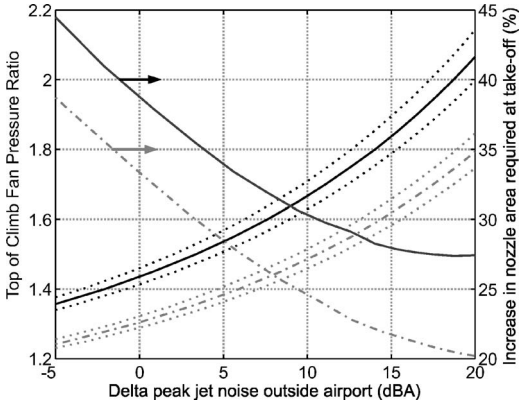

Fig. 7 Required top of climb FPR and nozzle opening at take-off relative to top of climb to match φ at flyover and cruise conditions for two aircraft variants

As previously discussed, by ensuring subsonic relative flow onto the fan tip during takeoff, multiple pure tone (buzzsaw) noise can be removed. The resulting design point blade speed can be calculated by setting the flyover or sideline relative tip Mach number to one to get the flyover/sideline blade speed (Eq. (9)). A representative fan characteristic can then be used to find the design point tip speed.

$$\left.\frac{U_{\mathrm{tip}}}{\sqrt{\theta}}\right|_{\mathrm{takeoff}} = a_{0,\mathrm{ref}} \sqrt{\frac{1 - M_{\mathrm{ff}}^2}{1 + \frac{\gamma-1}{2}M_{\mathrm{ff}}^2}} \tag{9}$$

Figure 8 shows the maximum top of climb blade speed possible for $\varphi_{\mathrm{flyover}} = \varphi_{\mathrm{cruise}}$ to meet subsonic relative flow for the whole take-off (where the sideline point is the limiting condition) or for just the flyover position.

To ensure subsonic relative tip flow during the entire takeoff leads to a requirement for a very low tip speed if the fan face Mach number is maintained. With a hub-tip ratio of 0.25, the four-engine variant gives a design point stage loading close to 0.75 at equal area radius. This would require increased rotor solidity for the same diffusion factor [32], impact efficiency, and possibly increase broadband noise [28]. For the current fan design, tip speed at top of climb conditions (40 000 ft ISA+10 K)

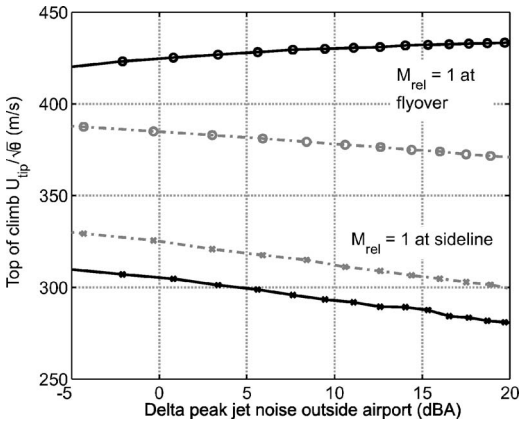

Fig. 8 Required top of climb fan blade speed to meet $M_{\mathrm{rel@tip}} = 1$ at specified conditions for two aircraft variants

Table 2 Fan rotor design point values

	r_1	χ_1	χ_2	σ	$M_{1,rel}$@DP
Hub	0.276 m	25.0 deg	−26.0 deg	3.26	0.63
Mid	0.689 m	45.0 deg	26.0 deg	1.45	1.01
Tip	1.103 m	59.0 deg	56.5 deg	1.13	1.28

has been set to 350 m/s (1150 ft/s), which is equivalent to a corrected speed of 371 m/s. This is low enough to comfortably ensure subsonic tip flow at flyover, where the aircraft is closest to the ground but not at the sideline position. The stage loading is reduced to 0.48 for a hub-tip ratio of 0.25, in line with current trends. Fan aerodynamic design is now required, using a 20 blade rotor, to confirm that flyover is at or close to peak efficiency and to see if the tip shock is ingested at the sideline position.

Fan Rotor Aerodynamic Design

The fan aerodynamic design was performed using MULTIP, a highly developed three-dimensional viscous solver widely used in industry and described in more detail by Denton and Xu [33]. Tip clearance was set to a constant value of 0.25% of span. Blade sections were stacked through their centroid without sweep or lean. Table 2 presents key details of the blade geometry and the inlet relative Mach number at the top of climb condition.

When predicting performance at off-design conditions untwist due to centrifugal and pressure forces was accounted for. Blades were modeled as solid titanium Ti6Al4V and deformation predicted for different rotational speeds. Pressure distribution at approximate peak efficiency for the speed in question was used and the deformation assumed constant for a given speed. Generation of the solid blade mesh from the CFD mesh was performed in Patran and Abaqus was used for finite element modeling. The resulting deformation at a given speed was translated to a rotation about a fixed point for each of the design stream surfaces and used as input to the CFD code. At design speed two degrees of untwist at the tip (included within the values shown in Table 2) was predicted.

Figure 9 shows the resulting fan rotor only characteristic with contours of polytropic efficiency. Key design points are marked on the figure. No attempt has been made to specify the exact position of the surge/stall line.

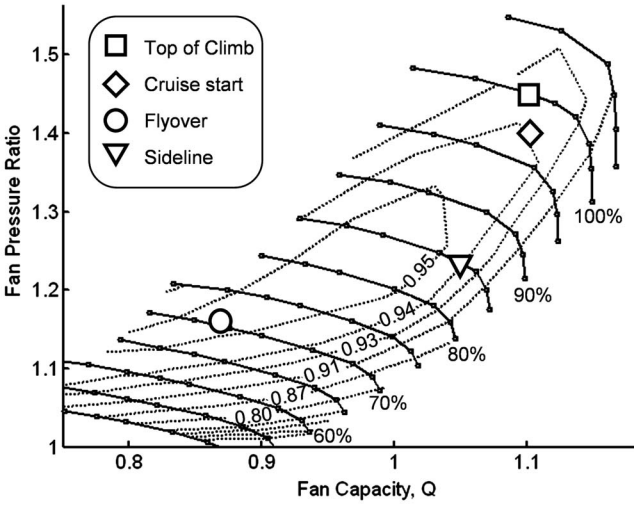

Fig. 9 Fan characteristic showing lines of fan speed relative to the design point and contours of rotor only polytropic efficiency

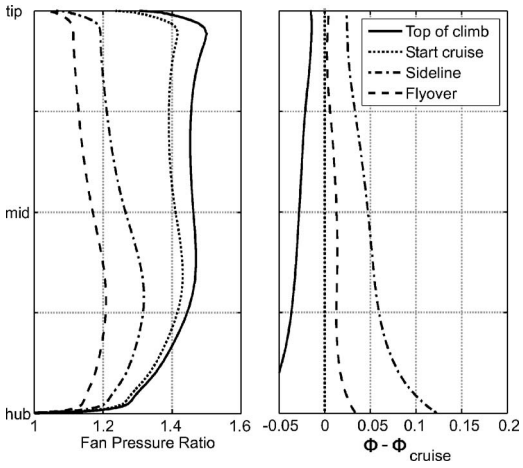

Fig. 10 Radial variations in fan pressure ratio and inlet flow coefficient for key operating conditions

Figure 10 shows the radial variation of fan pressure ratio and flow coefficient for key operating points. Blade loading is biased slightly toward the hub giving an approximate constant pressure rise at the start of cruise point. This leads to reduced tip loading during takeoff, which is required for low fan source noise. The flyover flow coefficient is very close to the cruise flow coefficient as designed, with sideline at higher and the top of climb at lower values as expected.

Figure 11 shows contours of relative Mach number at 95% and 75% span when operating at the sideline position. As required for low MPT noise the primary shock is ingested into the blade passage at the tip leaving a bow shock that is rapidly weakened by expansion waves from the rotor suction surface. At lower span positions the shock remains ingested until the inlet relative Mach number drops low enough for it to disappear completely. If this had not been the case then the design could have been repeated with a flyover position set to a slightly higher flow coefficient leading to a small increase in top of climb fan pressure ratio. Alternatively, the nozzle area can be temporarily opened a little as the sideline point is approached to move the operating line down and ensure the tip shock structure is ingested at all times.

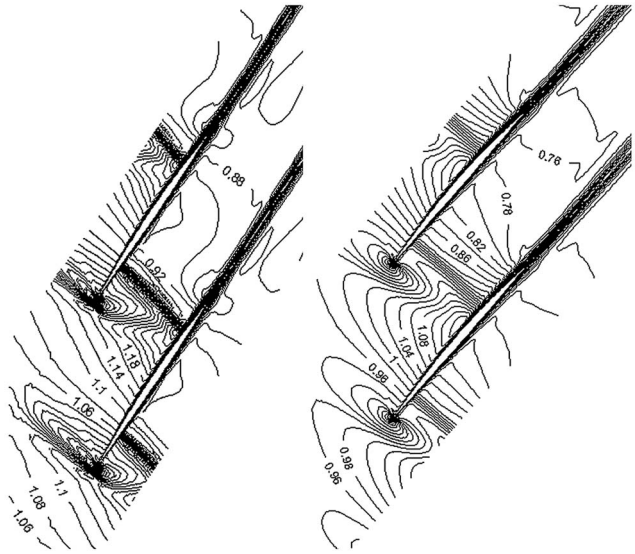

Fig. 11 Contours of the relative Mach number at 95% and 75% span when operating at the sideline position

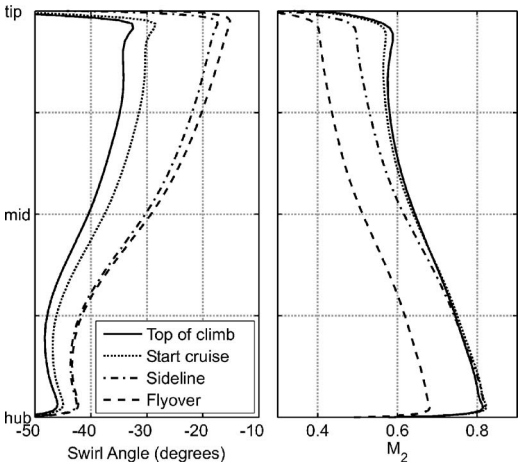

Fig. 12 Swirl and absolute Mach number onto OGVs at key operating points

Velocity and Incidence on to OGVS

While a variable area nozzle can be used to optimize the incidence onto the fan rotor at off-design conditions, the incidence onto the exit guide vanes moves away from optimum. Opening the nozzle increases the axial velocity and reduces the loading, especially at the tip, resulting in reduced swirl onto the stator, as shown in Fig. 12. To cover conditions from top of climb to flyover, the stator needs to support approximately 18 deg of swirl angle variation in the tip region with low loss. This range of required incidence is challenging, but, with a low Mach number at the tip (see Fig. 12), just within limits of the useful incidence range for controlled diffusion airfoils [34]. Variable pitch stators could be employed to support the operating range but this would be at the expense of additional weight and complexity.

Conclusions and Further Work

A functionally silent aircraft requires considerable jet noise reduction relative to conventional designs leading to a large increase in required jet area at takeoff, even when the departure profile is optimized for low noise. This leads to a low fan pressure ratio during takeoff and, to avoid low FPR at cruise that would lead to higher than optimum fuel burn, a variable area nozzle is employed.

This variable area nozzle, in addition to delivering the required FPR at cruise and takeoff, must also deliver high efficiency at both conditions. This is because high efficiency at takeoff equates with low fan source noise through reduced self noise and minimal wake severity onto the fan OGVs. Ingesting the primary shock structure is required to minimize MPT noise when operating with supersonic flow onto the fan tips. These requirements are achieved by matching the flow coefficient at flyover to that at cruise. This maximizes flyover efficiency and places the sideline position, where the relative tip Mach number exceeds unity, close to the shoulder of the fan characteristic. For a given capacity, the fan design parameters are then fully constrained and top of climb and cruise fan pressure ratios fixed.

For the current 4-engine, 250 pax, 4000 nm silent aircraft concept, this process sets the design top of climb FPR to 1.45, requiring a 39% increase in nozzle area at takeoff. The FPR selected is expected to give low fuel burn, as shown in [7] and [21].

A 20 blade fan rotor with a hub tip ratio of 0.25 had been designed with the required top of climb FPR and a design blade tip speed of 350 m/s. Rotor alone efficiency is high during takeoff, especially at flyover and, as required for low MPT noise, the primary shock structure on the blades is ingested at the sideline position. The fan rotor tip is lightly loaded during takeoff, which is desirable for low fan source noise.

The change in incidence onto the OGVs between top of climb and flyover is considerable, especially at the tip. While literature indicates that this is within the range of useful incidence for the flow Mach number, future work is required in this area. The OGV design will need to ensure low fan-stator interaction noise at takeoff without impacting cruise efficiency.

Allowing the nozzle area to vary during the noise critical portion of the takeoff may further assist in meeting the design requirements and requires further investigation. This will require the noise optimized takeoff profile development to be linked to a specified fan operating line rather than a specified jet area. This operating line can be designed to minimize incidence variation onto the OGVs and to ensure that any shock structures on the blades during takeoff are ingested.

Finally, to support the ingestion and reenergizing of airframe boundary layer airflow, further research on the design of low pressure ratio fans to support steady inlet distortion both from an aerodynamic and noise perspective is required.

Acknowledgment

The authors would like to thank members of the Silent Aircraft Initiative and Rolls Royce plc. for providing consultation and advice. They would also like to acknowledge the Cambridge-MIT Institute for the financial support of this work.

Nomenclature

Latin

a	=	speed of sound
A	=	area
dB	=	decibels
dBA	=	a-weighted decibels
DNL	=	day night level
EPN	=	effective perceived noise
h	=	enthalpy
M	=	Mach number
$\dot{m}$	=	mass flow rate
p	=	pressure
PR	=	pressure recovery
r	=	radius
T	=	temperature
T_N	=	net thrust
U	=	blade speed
V	=	velocity

Greek

γ	=	ratio of specific heat capacities
η	=	fan efficiency
θ	=	temperature correction, T_0/T_{0ref}
σ	=	solidity
ϕ	=	flow coefficient
χ	=	metal angle
ψ	=	stage loading

Subscripts

0	=	stagnation conditions
1	=	rotor leading edge
2	=	rotor trailing edge
ff	=	fan face
in	=	inlet (free stream to fan face)
jet	=	fully expanded jet
noz	=	nozzle
out	=	exhaust (fan exit to fully expanded)
p	=	polytropic
ref	=	reference=ISA sea level
x	=	axial
∞	=	freestream

References

[1] "Air Travel—Greener by Design: The Technology Challenge," Greener by Design 2001.
[2] "The Future of Air Transport," Department for Transport, UK Government 2003.
[3] ACARE, 2000, "European Aeronautics: A Vision for 2020," Advisory Council for Aeronautics Research in Europe 2000.
[4] Smith, C. P., 2005, "The Environmental Challenge—Bringing Technology to Market," ISABE-2005–1008.
[5] Berglund, B., Lindvall, T., and Schwela, D. H., 1999, "Guidelines for Community Noise," World Health Organization.
[6] "Noise Mapping England: The London Road Traffic Noise Map," Department for Environment, Food and Rural Affairs (Defra), London 2004.
[7] Hall, C. A., and Crichton, D., 2005, "Engine and Installation Configurations for a Silent Aircraft," ISABE-2005-1164.
[8] Agarwal, A., and Dowling, A. P., 2005, "Low Frequency Acoustic Shielding of Engine Noise by the Silent Aircraft Airframe," Paper No. AIAA 2005-2996.
[9] Berrier, B. L., and Allan, A. G., 2004, "Experimental and Computational Evaluation of Flush-Mounted, S-Duct Inlets," Paper No. AIAA 2004-0764.
[10] Gliebe, P. R., and Janardan, B. A., 2003, "Ultra-High Bypass Engine Aeroacoustic Study," Paper No. NASA-2003-212525.
[11] Daggett, D. L., Brown, S. T., and Kawai, R. T., 2003, "Ultra-Efficient Engine Diameter Study," NASA CR-2003-212309.
[12] Dittmar, J. H., 1998, "A Fan Concept to Meet the 2017 Noise Goals," NASA-TM-1998-208663.
[13] Dittmar, J. H., Tweedt, D., Jeracki, R., Envia, E., Bartos, K., and Slater, J., 2003, "A Fan Design That Meets the NASA Aeronautics Noise Goals," NASA TM-2003-212322.
[14] Crichton, D., Tan, D., and Hall, C. A., 2004, "Required Jet Area For a Silent Aircraft at Take-off," presented at the 8th ASC-CEAS Workshop, Budapest University of Technology and Economics, Hungary.
[15] Stone, J. R., and Montegani, F. J., 1980, "An Improved Prediction Method for the Noise Generated in Flight by Circular Jets," NASA TM-81470.
[16] ESDU, 1977, "Evaluation of the Attenuation of Sound by a Uniform Atmosphere," item 78002 available from www.esdu.com.
[17] ESDU, 1982, "Estimation of Lateral Attenuation of Air-to-Ground Jet or Turbofan Aircraft Noise in One-Third Octave Bands," item 82027 available from www.esdu.com.
[18] ICAO, 1993, "Convention on International Civil Aviation—Annexe 16," Vol. 1, 3rd ed.
[19] ICAO, "PANS-OPS Volume 1 Part V: Noise Abatement Procedures."
[20] FAA, 1993, "AC 91-53A: Noise Abatement Departure Profiles."
[21] Hall, C. A., and Crichton, D., 2006, "Engine Design Studies for a Silent Aircraft," ASME Paper No. GT2006-90559.
[22] Woodward, R. P., and Lucas, J. G., 1976, "Acoustic and Aerodynamic Performance of a 1.83 Meter Diameter 1.25 Pressure Ratio Fan (QF-8)," NASA TN D-8130 TN D-8130.
[23] Ginder, R. B., and Newby, D. R., 1977, "An Improved Correlation for the Broadband Noise of High Speed Fans," J. Aircr., **14**, pp. 844–849.
[24] Hughes, C. E., Woodward, R. P., Podboy, G. G., and Jeracki, R. J., 2005, "The Effect of Bypass Nozzle Exit Area on Fan Aerodynamic Performance and Noise in a Model Turbofan Simulator," ASME Paper No. GT2005-68573.
[25] Woodward, R. P., Hughes, C. E., Jeracki, R., and Miller, C. J., 2002, "Fan Noise Source Diagnostic Test—Far Field Acoustic Results," presented at the 8th AIAA/CEAS Aeroacoustics Conference & Exhibit, Breckenridge, CO.
[26] Heidmann, M. F., 1979, "Interim Prediction Method for Fan and Compressor Source Noises," NASA TM X-71763.
[27] ESDU, 1998, "Prediction of Noise Generated by Fans and Compressors in Turbojet and Turbofan Engines," item 98008 available from www.esdu.com.
[28] Topol, D. A., Ingram, C. L., Larkin, M. J., Roche, C. H., and Thulin, R. D., 2004, "Advanced Subsonic Technology (AST) 22-Inch Low Noise Research Fan Rig Preliminary Design of ADP-Type Fan 3," NASA CR-2004-212718.
[29] Xu, L., 2004, "Shockwave and Noise Abatement of Transonic Fans," presented at the ASME Turbo Expo: Power for Land, Sea and Air, Vienna, Austria.
[30] Prasad, A., and Prasad, D., 2005, "Unsteady Aerodynamics and Aeroacoustics of a High-Bypass Ratio Fan Stage," ASME J. Turbomach., **127**, pp. 64–75.
[31] Morfey, C. L., and Fisher, M. J., 1970, "Shock-Wave Radiation from a Supersonic Ducted Rotor," Aeronaut. J., **74**, pp. 579–585.
[32] Wennerstrom, A. J., 2000, "Design of Highly Loaded Axial-Flow Fans and Compressors," ISBN 0-933283-11-3.
[33] Denton, J. D., and Xu, L., 2002, "The Effects of Lean and Sweep on Transonic Fan Performance," ASME Paper No. GT-2002-30327.
[34] Hobbs, D. E., and Weingold, H. D., 1984, "Development of Controlled Diffusion Airfoils for Multistage Compressor Application," ASME J. Eng. Gas Turbines Power, **106**, pp. 271–278.